

**CAVITY RINGDOWN SPECTROSCOPY, KINETICS, AND QUANTUM
CHEMISTRY OF ATMOSPHERICALLY RELEVANT REACTIONS**

Thesis by

Matthew Kiran Sprague

In Partial Fulfillment of the Requirements

for the Degree of

Doctor of Philosophy



California Institute of Technology

Pasadena, California

2012

(Defended May 18, 2012)

© 2012

Matthew Kiran Sprague

All Rights Reserved

Acknowledgements

In front of you is a huge book, a thesis full of research results. (Well, if you are anything like me, it's an electronic file instead of a book...) This book is a culmination of my graduate research: seven years of work packed into one tome. But really, there is far more than seven years of work that has gone into this thesis. And most of it has not come at my hands: the wonderful people in my life for the last 28 years have shaped everything that you will read about here. If you are reading this, you know my style: very precise, detailed, and perhaps long-winded. So bear with me as I spend a few pages thanking everyone that has helped make this thesis possible.

The first two people that I would like to thank are my advisors: Professor Mitchio Okumura and Dr. Stanley Sander. Mitchio and Stan have been incredible advisors: they have taught me how to do precise, high-impact science. They have taught me how to continually question my own work, always striving for the best possible results. They have kept me guided toward our research goals, yet at the same time let me wander in interesting research directions (most shown by their “tolerance” of all of my theoretical and computational interests!). But perhaps most importantly, both Mitchio and Stan are wonderful people, and have made sure that I remained a “happy graduate student” during my career here. This thesis would not have been possible without Mitchio's and Stan's expert guidance, and I thank them for shaping my future as a scientist.

One of Mitchio's skills has been to maintain a research group full of people that are hard working, intelligent, and fun to be around. It has been a joy to come into work each day and see the members of the Okumura group. Thank you to the graduate students, postdocs, and staff scientists that I have had the good fortune to work with: Andrew

Mollner, David Robichaud, Aaron Noell, Laurence Yeung, Kana Takematsu, Kathleen Spencer, David Long, Nathan Eddingsaas, Aileen Hui, Sigrid Barklund, Thinh Bui, Nathan Honsowetz, Heather Widgren, Kathryn Pérez, Leah Dodson, Milinda Rupasinghe, Ralph Page, Marissa Weichman, Laura Mertens, and Linhan Shen.

I would like to single out a few of my co-workers. Andrew Mollner was my mentor for the first two years at Caltech and taught me everything that I needed to know to run a cavity ringdown lab. Andrew is one of the most patient, nicest, and skilled teachers that I have met, and I know that his future students will be in good hands. Laurence Yeung was my officemate in 101D Noyes for over 4 years. He kept me honest on the love of experiments, food, and life, and a large portion of what I have learned in graduate school came from our office chats. Heather Widgren and Marissa Weichman were my two awesome undergraduate students, and I hope that they enjoyed working in the lab as much as I enjoyed hosting them. Ralph Page was a staff scientist in our lab who helped improve my experiments. That is a short sentence, but about 1/3 of this thesis would not exist without Ralph's help. Ralph's strength was helping me cut through all of the "noise" to solve problems quickly, and I can't thank him enough for that. Finally, Laura Mertens is taking over for me as the graduate student in the IR-CRDS / quantum chemistry lab. She has been an enthusiastic learner and hard worker, and I know she will keep the lab in great care. Thanks for putting up with me!

In science, nothing gets done unless you have people to work with, talk to, and bounce ideas off of. Another of Mitchio's and Stan's strengths is how many great collaborators they attract. I was lucky enough to work with Professor Anne McCoy (Ohio State) on a quantum chemistry project. Thanks, Anne, for lending me your resources,

discussing science with me, helping me improve my writing skills, letting me learn from you, and most importantly, being a great person to work with. I would also like to thank the members of my candidacy and thesis committees for all of their advice and support: Professors Geoffrey Blake, Paul Wennberg, Vincent McKoy, and Jacqueline Barton.

It takes a lot to keep a laboratory running, especially when a certain somebody (me) keeps breaking things. Rick Gerhart has bailed me out of a lot of trouble with glassware, Tom Dunn has helped me fix burnt-out electronics, and both Mike Roy and Dave Natzic have bailed me out of trouble with machined parts. (Yes, I'm good at breaking things!) Thanks for all of your help and your talks about football, Hawaii, and classic cars. Similarly, it takes a lot to keep a graduate student running: lots of support staff to keep paperwork in line, packages and mail flowing, and smiles to go around. Thank you to Joe Drew, Anne Penney, Dian Buchness, Laura Howe, and Agnes Tong for all of your help along the way. It has been great to work with such friendly people. And Joe, as long as they're not playing my Bills, go Cleveland Browns!

My good fortune extends past Caltech: I have had many great research mentors, professors, and teachers that have helped shape me into a chemist. My undergraduate education at Ithaca College was top-notch, and I thank Professors Vincent DeTuri and Anna Larsen for the research opportunities that they extended to me. My time at Ithaca also helped develop my passion for teaching, and this is thanks to Vince, Anna, and Professor Michael "Bodhi" Rogers, who all gave me an opportunity to teach as many students as I could handle. I also was lucky enough to work at Sandia National Laboratories for three summers, and I would like to thank LeRoy Whinnery and Blake

Simmons for making my time at Sandia memorable. It is really amazing how the two of you could teach me so much about independent research in three summers.

I'm pretty sure that you can't finish a thesis unless you are healthy and happy. And I have a lot of people to thank for this. First, a big thank you to Bill Bing, director of the Caltech Bands. Bill is the perfect person to work at Caltech: he pushes students to a high performance level, he is a skilled trumpet player and teacher, and he knows how to keep everything fun. Bill, never retire! I have also been able to play in a couple of outside jazz bands thanks to meeting people through the Caltech music program, and I would like to thank Pat Olguin, Brenda Goforth Adelante, and Eric Kulczycki for giving me the opportunity to play in their bands. I am also an avid football fan – go Buffalo Bills! I thank the Los Angeles Bills Backers, and club president Joy Ammann, for giving me the opportunity to spend my Sundays enjoying football with you. By the way, how do I stay healthy? Great medical care from doctors and nurses. Thank you to Alice Sogomonian, Divina Bautista, Linda Schutz, Dr. Helena Kopecky, Dr. Susanna Friedlander, Dr. Maria Oh, and Dr. Mariel Tourani for all of your help. This thesis would not be possible without all of you.

I have made some great friends at Caltech and Ithaca, and there aren't enough words for me to express how much I value their support and friendship. Thank you Dan Prugel, the one crossover that I have between Rochester and Caltech, and who shares more of my values than either one of us would care to admit. Thank you to my Ithaca College friends, Eric Leibensperger, Beth Gardiner, Eric Callahan, Tasha Kates, and Matt Libera (and many others that won't fit in the allotted space), for 4 years of fun at Ithaca, 7 years of visits and online chats, and many more years of fun to come. Thank you to

Kathryn Pérez and Kathleen Spencer, two of my Caltech friends to whom I will be eternally indebted for helping me through my most difficult graduate school trials. To all of my friends: thank you, I am happy every day because of you.

They say that you save the best for last. In this case, I saved my largest thanks for my parents, Nancy Sprague and Jeffery Sprague, and my stepparents, Greg Lewis and Esta Sullivan. 28 years ago, you decided to spend a lot of money to adopt a small child from India. In the years since then, you have taught him everything that he knows: how to learn, how to work hard, how to enjoy life, how to succeed in endeavors, how to endure the trials in life, how to appreciate friends, and how to love family. Most of all, the four of you have given him your love unconditionally. I cannot thank you enough for always pushing me to follow my dreams wherever they may take me, but always keeping a place for me to call home, where I will always know that I am loved. This thesis may satisfy the requirements for a Ph.D. at Caltech, but it was written for the four of you.

Abstract

This thesis describes laboratory experiments and electronic structure calculations on three chemical systems relevant to tropospheric ozone chemistry: peroxyxynitrous acid (HOONO), hydroxymethylperoxy radical formed from $\text{HO}_2 + \text{HCHO}$ (R1), and products of alkoxy isomerization (R2). R1 and R2 were studied experimentally using a gas flow cell that combined UV photolysis with cavity ringdown spectroscopy (CRDS). All chemical systems were studied using electronic structure calculations and kinetics modeling.

HOONO is one of the products of the reaction $\text{OH} + \text{NO}_2$, and acts as a temporary reservoir for HO_x and NO_x in the atmosphere. Torsional excitation of HOONO will break its internal hydrogen bond, leading to sequence band formation in the OH stretch spectrum. Chapter 3 describes a calculated 3-dimensional potential energy surface to examine torsional mode coupling and sequence band formation. We apply these results to previous CRDS kinetics studies of HOONO.

The reaction of HO_2 with carbonyls is believed to be a major sink of HO_x and carbonyl compounds at reduced temperatures. R1 is the simplest of these reactions. Despite numerous previous studies, considerable uncertainty exists on the activation energy and rate constant of R1. Chapters 4–6 describe CRDS and electronic structure studies on the isomerization product, hydroxymethylperoxy. CRDS was used to make the first measurements of the OH stretch and A-X electronic spectra, and the kinetics of hydroxymethylperoxy chemistry. Electronic structure calculations were used to simulate the spectroscopic bands and examine the conformers of hydroxymethylperoxy and 2-hydroxyisopropylperoxy.

Atmospheric alkoxy radicals can isomerize or react with O₂, and each pathway has a different impact on ozone chemistry. Chapters 7–10 describe cavity ringdown spectroscopy, kinetics, and electronic structure calculations on the *n*-butoxy and 2-pentoxy isomerization products, specifically $\delta\text{-HOC}_4\text{H}_8\bullet$, $\delta\text{-HOC}_4\text{H}_8\text{OO}\bullet$, $\delta\text{-HO-1-C}_5\text{H}_{10}\bullet$, and $\delta\text{-HO-1-C}_5\text{H}_{10}\text{OO}\bullet$. CRDS was used to make the first measurements of the A-X electronic spectrum of $\delta\text{-HOC}_4\text{H}_8\text{OO}\bullet$ and clean OH stretch spectra of all four radicals. Relative kinetics data previously obtained using CRDS were reanalyzed to include the effects of additional alkoxy reactions. Electronic structure calculations were performed to explain the observations that the OH stretch absorption cross section differs between HOR \bullet and HOROO \bullet .

Table of Contents

Acknowledgements	iii
Abstract	viii
Table of Contents	x
List of Figures	xvii
List of Tables	xxi
<u>Part 1—Introduction and Description of Cavity Ringdown Spectrometer...</u>	<u>1</u>
Chapter 1—Introduction	2
Atmospheric Chemistry.....	2
Specific Chemical Systems of Interest.....	6
Torsion-Torsion Coupling in Peroxynitrous Acid (HOONO).....	7
HO ₂ +HCHO: Spectroscopy, Kinetics, and Electronic Structure of HOCH ₂ OO•.....	9
Alkoxy (RO•) Isomerization: Spectroscopy, Kinetics, and Electronic Structure of Primary Products.....	11
Chapter 2—Description of Cavity Ringdown Spectrometer	13
Abstract.....	13
Introduction.....	13
Cavity Ringdown Spectroscopy.....	13
Considerations of Tunable Light Ranges.....	19
Optical Parametric Amplifier: Mid-IR Light (2.7–3.7 μm).....	21
Hydrogen Gas Raman Shifter: Near-IR Light (1.2–1.4 μm).....	22
Experimental Details.....	23
Pulsed Laser Photolysis-Cavity Ringdown Spectroscopy (PLP-CRDS) Apparatus.....	23
Gas Kinetics Cell.....	27
Optical Cavity.....	28
Optical Parametric Amplifier Setup.....	28
Raman Shifter Setup.....	30
Excimer Laser and Timing Control.....	31
Data Acquisition and Processing.....	31
Performance of CRDS Apparatus.....	32
Laser Performance.....	32
Detector Performance.....	34
Mirror Reflectivity vs Wavelength.....	36
Sensitivity of the CRDS Apparatus.....	39
Calibration of Spectrometer Frequency.....	41
Conclusions.....	42
Acknowledgements.....	43

Part 2—Quantum Chemistry Studies of Peroxynitrous Acid (HOONO)..... 44

Chapter 3—A 3-Dimensional Potential Energy Surface and Dipole Moment Surface for Modeling the Torsion-Torsion Coupling in cis-cis HOONO..... 45

Abstract.....	45
Introduction.....	46
Methods.....	52
Generation of Potential Energy Surface and Dipole Moment Surface... 52	
Simulation of Spectra.....	54
Results.....	55
Torsional Potential Energy Surface.....	56
Comparison of CCSD(T) and B3LYP Potential Energy Surface.....	60
OH Stretch Potential Energy Surface.....	62
Calculation of the Dipole Moment Surface.....	64
Wavefunctions.....	72
Discussion.....	73
Simulated OH Stretch Spectra (Fundamental, Overtone).....	73
Torsional Spectrum.....	75
Correction factor to $\alpha(p,298K)$	77
Conclusions.....	78
Acknowledgements.....	78

Part 3—Spectroscopy, Kinetics, and Quantum Chemistry of the Hydroxymethylperoxy Radical (HOCH₂OO•, HMP)..... 80

Chapter 4—The OH Stretch and A-X Electronic Cavity Ringdown Spectra of the Hydroxymethylperoxy Radical (HOCH₂OO•)..... 81

Abstract.....	81
Introduction.....	82
Methods.....	90
Apparatus and Chemicals.....	90
Experimental and Flow Conditions.....	92
Results.....	95
Chemistry.....	95
HMP ν_1 Spectrum.....	100
HMP A-X Spectrum.....	107
Discussion.....	114
Comparison of HMP ν_1 Spectrum to Methanol and Ethanol.....	114
Comparison of HMP A-X Spectrum to Methylperoxy.....	115
Conclusions.....	117
Acknowledgements.....	118

Chapter 5—Predicted A-X Transition Frequencies and 2-Dimensional Torsion-Torsion Potential Energy Surfaces of HOCH₂OO• and HOC(CH₃)₂OO•	119
Abstract.....	119
Introduction.....	120
Methods.....	122
Results.....	124
Torsion-Torsion Potential Energy Surfaces of HMP.....	125
Calculated A-X Transition Frequencies.....	132
Electronic, Torsional, and OH Str. Frequencies for HMP Conformer B	143
Calculated Potential Energy Surfaces and Spectroscopic Frequencies of 2-HIPP.....	144
Discussion.....	147
Preliminary Thoughts on the Appropriate Level of Theory for Substituted Alkyl Peroxies.....	147
Normal Mode Coupling and its Effect on Vibrational Frequencies, Sequence Bands.....	149
Conclusions.....	150
Acknowledgements.....	151
Chapter 6—Kinetics of HO₂ + HCHO and Further Reaction of the Hydroxymethylperoxy Radical (HOCH₂OO•)	152
Abstract.....	152
Introduction.....	153
Methods.....	155
Apparatus and Chemicals.....	155
Experimental and Flow Conditions.....	157
Results.....	160
Predicted HO ₂ + HCHO Kinetics.....	161
Kinetics of HMP by ν_1 Absorption.....	165
Kinetics of HMP by A-X Absorption.....	169
Discussion.....	171
Comparison of HO ₂ + HCHO Kinetics Results (ν_1) to Literature.....	171
Comparison of HMP Destruction Kinetics (A-X) to Existing Model...	172
Application of Our Kinetics Methods to HO ₂ +acetone.....	174
Conclusions.....	177
Acknowledgements.....	178

Part 4—Spectroscopy, Kinetics, and Quantum Chemistry of Alkoxy**Isomerization..... 179****Chapter 7—Direct Detection of the Primary Products of Alkoxy**

Isomerization: The OH Stretch Spectra of δ-HOC₄H₈•, δ-HOC₄H₈OO•, δ-HO-1-C₅H₁₀•, and δ-HO-1-C₅H₁₀OO•.....	180
Abstract.....	180
Introduction.....	181
Methods.....	188
Apparatus and Chemicals.....	188
Experimental and Flow Conditions.....	190
Results.....	195
Chemistry.....	196
Kinetics Modeling.....	201
OH Stretch Spectra of δ -HOC ₄ H ₈ •, δ -HOC ₄ H ₈ OO•, δ -HO-1-C ₅ H ₁₀ •, and δ -HO-1-C ₅ H ₁₀ OO•.....	202
Change in OH Stretch Spectrum with [RO•] and Timing.....	209
Determination of the Relative Kinetic Rate $k_{\text{isom}}/k_{\text{O}_2}$	214
Analysis of Our 2-pentyl nitrite Sample.....	218
Conclusions.....	225
Acknowledgements.....	225

Chapter 8—Reanalysis of the Alkoxy $k_{\text{isom}}/k_{\text{O}_2}$ OH Stretch Experiment and a New Interpretation of Alkoxy Relative Kinetics Experiments.....

227	227
Abstract.....	227
Introduction.....	228
Methods.....	236
Recalculation of Gas Concentrations.....	237
Recalculation of [RONO] and [RO•].....	238
Rescaling of Alkoxy Concentrations and Calculation of Relative Absorbance A_0/A	241
Choosing the Best Fits to Obtain the Overall Data Set for $k_{\text{isom}}/k_{\text{O}_2}$	243
Derivation of Dependence of A_0/A on [O ₂].....	244
Neglect of Prompt Decomposition.....	244
Treatment of the Remaining Pathways.....	246
Determination of $k_{\text{isom}}/k_{\text{O}_2}$	248
Results.....	249
Selected Gas Flow Data.....	250
How Scaling Method Affects A_0/A vs [O ₂].....	252
Overall Data Set of A_0/A vs [O ₂] and Calculated <i>int/slope</i>	254
Required Parameters and Rate Constants.....	260
Prompt Isomerization: Determination of ϕ_{pi}	262
Calculation of $k_{\text{isom}}/k_{\text{O}_2}$, Comparison of Data Fits.....	264
Discussion.....	267
Comparison of $k_{\text{isom}}/k_{\text{O}_2}$ Values to the Literature.....	267
Sensitivity of Correction Factors to Parameters.....	271

Products Being Detected at 110 μ s.....	275
Conclusions.....	280
Acknowledgements.....	281
Chapter 9—A Quantum Chemistry Explanation of the Alkoxy Relative Kinetics “Low [O₂] Anomaly”.....	282
Abstract.....	282
Introduction.....	283
Methods.....	288
Kinetics Model.....	288
Quantum Chemistry Calculations.....	292
Results.....	295
Kinetics Model for <i>n</i> -butoxy.....	296
Quantum Chemical Calculations.....	301
Spectroscopic Properties as a Function of Level of Theory and Basis... 303	
Comparison of <i>n</i> -butoxy Conformer OH Stretch Properties.....	306
Effect of Functional Group Positions on the OH Stretch Properties....	307
Calculation of OH Stretch Properties for the Kinetics Model.....	313
Simulation of A_0/A vs [O ₂].....	315
Discussion.....	318
OH Groups Formed Through Nonisomerization Pathways.....	319
Reduced Kinetics Model Simulations of A_0/A vs [O ₂].....	321
Persistence of Low [O ₂] Anomaly for Other Values of $k_{\text{isom}}/k_{\text{O}_2}$	324
Conclusions.....	326
Acknowledgements.....	327
Chapter 10—Cavity Ringdown Spectroscopy and Kinetics of <i>n</i>-butoxy Isomerization: The A-X Electronic Spectrum of HOC₄H₈OO•.....	328
Abstract.....	328
Introduction.....	329
Methods.....	333
Apparatus and Chemicals.....	333
Experimental and Flow Conditions.....	334
FTIR—Apparatus, Chemicals, Methods.....	337
Results.....	338
A-X Spectrum of HOC ₄ H ₈ OO•.....	339
Kinetics.....	342
Determination of the Relative Rate Constant $k_{\text{isom}}/k_{\text{O}_2}$	346
FTIR Analysis of <i>n</i> -butyl nitrite.....	349
Discussion.....	358
Measuring the A-X Spectrum of δ -HO-1-C ₅ H ₁₀ OO•.....	358
Conclusions.....	360
Acknowledgements.....	361

Part 5—Appendices..... 362

Appendix A—Classification of Laser System Performance.....	363
Introduction.....	363
Average Energy Measurement Methods.....	364
Pulse-to-Pulse Energy Fluctuation Measurement Methods.....	368
Issue with Saving “MultiRec” ASCII Waveforms.....	371
Appendix B—Nd:YAG Laser Stability Issues and Repairs.....	376
Introduction.....	376
Initial Measurements and Classification of the Unrepaired Laser System...	379
Energy Distribution Results and Analysis.....	379
Temporal Distribution Results and Analysis.....	383
Laser Repair Information.....	387
Jitter Between the Marx Bank Signal and the DDG.....	388
Amplification Circuit for the Marx Bank.....	389
Modifications to Charge and Fire Signal Lines.....	391
The 60 V Spike and Replacement of the CB631 Capacitor Bank.....	392
Replacing the Power Pill Thermostat.....	393
Laser Head Cleaning and Replacement of O-rings.....	396
Result of Repairs.....	397
Conclusions.....	401
Appendix C—Calculating Excited States Using Gaussian.....	403
(1) Configuration Interaction Singles (CIS).....	403
(2) Time Dependent HF and DFT (TD-HF and TD-DFT).....	406
(3) Exploiting Orbital Symmetry.....	410
(4) Freezing the Initial Orbital Guess Using Guess=(Alter,Always).....	413
(5) Scaling of Transition Frequencies.....	415
(6) Composite Quantum Chemistry Methods: G2, CBS-QB3, and W1...	416
(7) Generating Potential Energy Surfaces.....	423
(8) A Caution on Using Equation of Motion (EOM) Methods.....	428
Acknowledgements.....	428
Appendix D—Simulating Spectroscopic Bands using Gaussian and	
PGopher.....	429
(1) Calculation of Vibrational Dipole Derivatives.....	429
(2) Estimation of the A-X Dipole Derivative.....	431
(3) Calculation of Anharmonic Rotational Constants.....	432
(4) Simulation of the Spectroscopic Band.....	434

Appendix E—The “Global Kinetics Model”: OH + (NO₂,CO,O₂) and HO₂ + (HCHO,NO).....	441
(1) Setting Up Kintecus 3.95.....	441
(2) Calculation of Termolecular Rate Constants.....	444
(3) Calculation of Other Reaction Rate Constants.....	445
(4) Reactions Included in the “Global Kinetics Model”.....	448
<u>Part 6—References.....</u>	<u>452</u>

List of Figures

Chapter 1

Figure 1.1. Days per year that ozone concentrations exceeded 75 ppb.....	3
Figure 1.2. Potential energy surface for OH + NO ₂	7
Figure 1.3. Potential energy surface for HO ₂ + HCHO.....	10

Chapter 2

Figure 2.1. Sample ringdown traces at 3525.2 cm ⁻¹	18
Figure 2.2. Schematic of an optical parametric amplifier (OPA).....	21
Figure 2.3. Energy diagram illustrating the Raman effect.....	22
Figure 2.4. Diagram of the first kinetics cell.....	25
Figure 2.5. Diagram of the second kinetics cell.....	25
Figure 2.6. Optical setup for mid-infrared light (2.7–3.7 μm).....	26
Figure 2.7. Optical setup for near-infrared light (1.2–1.4 μm).....	26
Figure 2.8. Reflectivity curves for the cavity ringdown mirrors.....	38

Chapter 3

Figure 3.1. Potential energy surface for OH + NO ₂	47
Figure 3.2. The three conformers of HOONO.....	47
Figure 3.3. Potential energy surface of HOONO as a function of τ _{HOON} , τ _{OONO}	57
Figure 3.4. Potential energy surfaces: B3LYP and CCSD(T).....	61
Figure 3.5. Potential energy surface vs OH bond length change.....	63
Figure 3.6. μ _a for cis-cis HOONO vs r _{OH} -r _e	68
Figure 3.7. μ _b for cis-cis HOONO vs r _{OH} -r _e	70
Figure 3.8. Wavefunctions for the 8 lowest energy torsional states of HOONO....	73
Figure 3.9. Calculated OH stretch spectra for HOONO.....	74
Figure 3.10. Simulated torsional spectrum of HOONO.....	76

Chapter 4

Figure 4.1. B-X spectra of HMP, HO ₂ , CH ₃ OO•.....	86
Figure 4.2. Kinetics simulations for HO ₂ + HCHO experiments.....	100
Figure 4.3. Unsubtracted mid-infrared cavity ringdown spectra.....	101
Figure 4.4. ν ₁ (OH stretch) spectrum of HOCH ₂ OO• (HMP).....	101
Figure 4.5. ν ₁ /ν ₅ (OH stretch) spectrum of H ₂ O ₂	102
Figure 4.6. Subtraction of H ₂ O ₂ and HCOOH to obtain a pure HMP ν ₁ spectrum	103
Figure 4.7. Absorption cross sections of the ν ₁ band of HMP.....	106
Figure 4.8. ν ₁ spectra of HMP taken under poor conditions.....	107
Figure 4.9. A-X spectrum of HMP.....	108
Figure 4.10. Spectra of individual HMP A-X bands.....	109
Figure 4.11. Comparison of HMP experimental kinetics to simulation.....	110
Figure 4.12. Comparison of observed A-X bands to simulation.....	112
Figure 4.13. Absorption cross sections for the A-X region of HMP.....	113
Figure 4.14. Absorption cross sections for the four A-X bands of HMP.....	114
Figure 4.15. ν ₁ spectra of HMP, CH ₃ OH, and C ₂ H ₅ OH.....	115

Figure 4.16. A-X spectra of HMP and CH ₃ OO•.....	116
--	-----

Chapter 5

Figure 5.1. B3LYP potential energy surfaces and conformers of HMP.....	126
Figure 5.2. CCSD and B3LYP potential energy surfaces of HMP.....	127
Figure 5.3. MP2 and MP4 potential energy surfaces of HMP.....	129
Figure 5.4. Deviation of calculated A-X frequency of HMP from experiment.....	134
Figure 5.5. Deviation of calculated OOCO torsion frequency from experiment....	136
Figure 5.6. Deviation of calculated OOCO torsion frequency from experiment....	138
Figure 5.7. Deviation of calculated OH stretch frequency from experiment.....	140
Figure 5.8. 2-HIPP X state potential energy surfaces.....	145
Figure 5.9. 2-HIPP A state potential energy surfaces.....	146

Chapter 6

Figure 6.1. Kinetics traces of HMP using two frequencies within the ν_1 band.....	165
Figure 6.2. Kinetics traces of HMP over the first 75 μ s of reaction.....	166
Figure 6.3. [HMP](t) measured by the ν_1 band.....	167
Figure 6.4. [HMP](t) at short times (75 μ s) measured by the ν_1 band.....	168
Figure 6.5. Kinetics traces of HMP using three frequencies within the A-X bands..	170
Figure 6.6. [HMP] and [HMP]/[HMP] _{max} as measured (A-X) and modeled.....	173

Chapter 7

Figure 7.1. Reaction map and energy diagram for the reactions of alkoxy radicals..	183
Figure 7.2. Modeled concentrations (100 μ s) for -OH species, <i>n</i> -butoxy.....	202
Figure 7.3. Cavity loss for precursor chemicals and products of alkoxy.....	203
Figure 7.4. ν_1 spectra of <i>n</i> -butoxy chem.: δ -HOC ₄ H ₈ • and δ -HOC ₄ H ₈ OO•.....	204
Figure 7.5. ν_1 spectra of 2-pentoxy chem.: δ -HO-1-C ₅ H ₁₀ • and δ -HO-1-C ₅ H ₁₀ OO•	205
Figure 7.6. Overlaid spectra of HOR• and HOROO•.....	206
Figure 7.7. Infrared spectra of photolysis products of isobutyl and <i>t</i> -butyl nitrite...	208
Figure 7.8. Absorbance (3662 cm ⁻¹) for <i>n</i> -butoxy as a function of time.....	210
Figure 7.9. Modeled concentrations (1000 μ s) for -OH species, <i>n</i> -butoxy.....	211
Figure 7.10. ν_1 spectra of <i>n</i> -butoxy isomerization, varied conditions.....	212
Figure 7.11. A_0/A vs [O ₂] for <i>n</i> -butoxy and 2-pentoxy from ν_1 band.....	216
Figure 7.12. FTIR spectrum of our 2-pentyl nitrite after distillation.....	218
Figure 7.13. Individual FTIR bands for major and minor species in pentyl nitrite..	220
Figure 7.14. Apparatus used to measure the vapor pressure of 2-pentyl nitrite.....	223
Figure 7.15. Clausius-Clapeyron plot for 2-pentyl nitrite.....	224

Chapter 8

Figure 8.1. A_0/A vs [O ₂] from Mollner thesis.....	229
Figure 8.2. Plots of A_0/A vs [O ₂] for <i>n</i> -butoxy data set, different scaling.....	253
Figure 8.3. Plots of A_0/A vs [O ₂] for the overall <i>n</i> -butoxy data set.....	257
Figure 8.4. Plots of A_0/A vs [O ₂] for the overall 2-pentoxy data set.....	259
Figure 8.5. Fits of A_0/A vs [O ₂] to CRDS data.....	266
Figure 8.6. Variation of correction factors with respect to parameters.....	274
Figure 8.7. Kinetics model of -OH stretch contributors in <i>n</i> -butoxy.....	278

Chapter 9

Figure 9.1. A_0/A vs $[O_2]$ for <i>n</i> -butoxy.....	285
Figure 9.2. Concentration vs time for –OH containing species.....	296
Figure 9.3. Description of -OH containing products of <i>n</i> -butoxy.....	299
Figure 9.4. A_0/A vs $[O_2]$ simulation vs experiment.....	317
Figure 9.5. Fraction of OH stretch intensity from nonisomerization.....	321
Figure 9.6. Comparison of reduced kinetics model simulations to experiment.....	324
Figure 9.7. A_0/A vs $[O_2]$ simulation for different k_{isom}/k_{O_2}	325

Chapter 10

Figure 10.1. Cavity ringdown spectrum of the A-X transition of $\delta\text{-HOC}_4\text{H}_8\text{OO}\cdot$...	340
Figure 10.2. Direct kinetics measurements of $\text{HOC}_4\text{H}_8\text{OO}\cdot$ via the A-X band.....	343
Figure 10.3. Kinetics simulations of $\text{HOC}_4\text{H}_8\text{OO}\cdot$ and other peroxy species.....	345
Figure 10.4. A_0/A vs $[O_2]$ for <i>n</i> -butoxy, A-X peak.....	347
Figure 10.5. FTIR spectra of <i>n</i> -butyl nitrite, fresh, freeze pumped.....	350
Figure 10.6. FTIR spectra of NO band region of <i>n</i> -butyl nitrite samples.....	352
Figure 10.7. FTIR spectra of <i>n</i> -butyl nitrite, fresh, not freeze pumped.....	353
Figure 10.8. FTIR spectra of <i>n</i> -butyl nitrite, not fresh.....	354
Figure 10.9. Reference spectra fits to FTIR <i>n</i> -butyl nitrite spectra.....	355
Figure 10.10. Sample ON-O stretch FTIR spectrum of <i>n</i> -butyl nitrite.....	357
Figure 10.11. Kinetics simulations for 2-pentoxy system.....	359

Appendix A

Figure A.1. Waveforms collected for a sine wave input.....	369
Figure A.2. 532 nm light scattered to a Si photodiode, 50 Ω vs 1 M Ω	371
Figure A.3. “Split MulRec” box.....	372
Figure A.4. 4 pulse records of 255 consecutive NIR pulses in GageScope 3.0.....	373
Figure A.5. 4 pulse records of 255 consecutive NIR pulses, ASC, Split MulRec.....	374
Figure A.6. 4 pulse records of 255 consecutive NIR pulses, ASC, single file.....	375

Appendix B

Figure B.1. NIR spectrum of $\text{HO}_2 + \text{HCHO}$, considerable noise.....	377
Figure B.2. Sample ringdown data when peak voltage exceeds scale of scope....	378
Figure B.3. Energy distribution for 255 laser pulses, 1.28 kV.....	380
Figure B.4. Energy distribution for 255 laser pulses, 1.34 kV.....	382
Figure B.5. Time distribution for 255 laser pulses, 1.28 kV.....	384
Figure B.6. Time distribution for 255 laser pulses, 1.34 kV.....	385
Figure B.7. Pulse Time vs Energy for Nd:YAG.....	386
Figure B.8. Q-switch amplification circuit for YG-661 laser.....	390
Figure B.9. Circuit diagram for the optoisolator box.....	392
Figure B.10. Nd:YAG pulse energy vs flashlamp fire time.....	394
Figure B.11. Cooling water temperature vs time since flashlamps were started....	395
Figure B.12. Energy histograms after repair.....	399
Figure B.13. Peak timing histograms after repair.....	400

Appendix C

Figure C.1. Screenshot of the G2 energy calculator spreadsheet.....	420
Figure C.2. Visualization of energies, 2-dimensional potential energy scan.....	427

Appendix D

Figure D.1. Molecular orbitals involved in the A-X transition of HMP.....	431
Figure D.2. Simulated ν_1 band of CH ₃ OH, B3LYP/6-31+G(d,p).....	439
Figure D.3. Comparison of experimental and simulated ν_1 bands of CH ₃ OH.....	440

Appendix E

Figure E.1. Portion of a kinetics model entered into a Kintecus Excel spreadsheet	442
Figure E.2. Portion of concentrations entered into a Kintecus Excel spreadsheet	442
Figure E.3. Simulation parameters entered into a Kintecus Excel spreadsheet.....	442
Figure E.4. Termolecular falloff kinetics calculator worksheet.....	445
Figure E.5. Equilibrium reaction rate kinetics calculator worksheet.....	447

List of Tables

Chapter 1

Chapter 2

Table 2.1. Typical laser performance.....	33
Table 2.2. Expected ringdown peak voltages for MIR and NIR experiments.....	36
Table 2.3. Summary of cavity ringdown mirror specifications.....	37

Chapter 3

Table 3.1. Dipole moments for HOONO, no Density=Current command.....	65
Table 3.2. Calculated values of μ_a for cis-cis HOONO.....	68
Table 3.3. Calculated values of μ_b for cis-cis HOONO.....	69

Chapter 4

Table 4.1. Experimental conditions for HMP spectroscopy experiments.....	93
Table 4.2. Summary of lifetimes and estimated [HMP] from chemistry analysis....	98
Table 4.3. Summary of lifetimes and estimated [HMP] from kinetics model.....	99
Table 4.4. Comparison of observed band positions to quantum chemistry.....	111

Chapter 5

Table 5.1. Summary of levels of theory and bases used for HMP calculations.....	124
Table 5.2. Calculated A-X transition frequencies of HMP conformers A and B.....	133
Table 5.3. Calculated OOCO torsion (A state) of HMP conformer A.....	135
Table 5.4. Calculated OOCO torsion (X state) of HMP conformer A.....	137
Table 5.5. Calculated OH stretch frequency of HMP conformer A.....	139
Table 5.6. Summary of acceptable and unacceptable levels of theory.....	142
Table 5.7. Calculated A-X, OOCO torsion, and OH stretch of HMP conformer B..	143
Table 5.8. Calculated A-X, OOCO torsion, and OH stretch of 2-HIPP.....	147

Chapter 6

Table 6.1. Experimental conditions for HMP kinetics experiments.....	159
Table 6.2. Orders of magnitude for kinetics terms.....	162
Table 6.3. Determination of k_1 from CRDS ν_1 absorption data.....	168
Table 6.4. Comparison of rate constant $k_{\text{HO}_2+\text{HCHO}}$ to literature values.....	171
Table 6.5. Equilibrium constants for $\text{HO}_2 + \text{acetone}$ from theory and experiment	176
Table 6.6. Rate constants for $\text{HO}_2 + \text{acetone}$ from theory and experiment.....	176

Chapter 7

Table 7.1. Comparison of previous $k_{\text{isom}}/k_{\text{O}_2}$ for <i>n</i> -butoxy and 2-pentoxy.....	186
Table 7.2. Experimental conditions for <i>n</i> -butoxy experiments.....	192
Table 7.3. Experimental conditions for 2-pentoxy experiments.....	193
Table 7.4. Compare our results to previous $k_{\text{isom}}/k_{\text{O}_2}$ for <i>n</i> -butoxy and 2-pentoxy	217
Table 7.5. Calculated integrated intensities for alkyl nitrites.....	221

Chapter 8

Table 8.1. Compare Mollner's results to previous $k_{\text{isom}}/k_{\text{O}_2}$	230
Table 8.2. One set of gas flow conditions.....	250
Table 8.3. Comparison of initial analysis of gas concentrations to reanalysis.....	251
Table 8.4. Slopes, intercepts, $k_{\text{isom}}/k_{\text{O}_2}$, and standard error for <i>n</i> -butoxy.....	260
Table 8.5. Slopes, intercepts, $k_{\text{isom}}/k_{\text{O}_2}$, and standard error for 2-pentoxy.....	260
Table 8.6. Rate constants and uncertainties for <i>n</i> -butoxy and 2-pentoxy.....	261
Table 8.7. Parameters, correction factors, and $k_{\text{isom}}/k_{\text{O}_2}$	265
Table 8.8. Comparison of our reanalyzed $k_{\text{isom}}/k_{\text{O}_2}$ to Mollner and literature....	270
Table 8.9. Sensitivity of correction factors to parameters.....	273

Chapter 9

Table 9.1. Kinetics model for <i>n</i> -butoxy.....	288
Table 9.2. Kinetics model parameters.....	292
Table 9.3. Chemical species calculated for this study.....	294
Table 9.4. Harmonic frequencies and intensities, straight chain, B3LYP.....	302
Table 9.5. Harmonic frequencies and intensities, straight chain, B3LYP vs CCSD	305
Table 9.6. Harmonic frequencies and intensities, 6-31+G(d,p) vs aug-cc-pVTZ....	305
Table 9.7. Energies and frequencies of HOC ₄ H ₈ • and HOC ₄ H ₈ OO• conformers...	307
Table 9.8. Harmonic frequencies and intensities, functional group positions.....	309
Table 9.9. Harmonic frequencies and intensities for <i>n</i> -butoxy model species.....	314
Table 9.10. First reduced kinetics model for <i>n</i> -butoxy.....	322
Table 9.11. Second reduced kinetics model for <i>n</i> -butoxy.....	322

Chapter 10

Table 10.1. Experimental conditions for alkoxy experiments.....	335
Table 10.2. Experimental conditions for FTIR spectra of butyl nitrite samples....	338
Table 10.3. Absolute and relative absorbances for A-X peaks.....	342
Table 10.4. Observed and modeled HOC ₄ H ₈ OO• lifetime.....	344
Table 10.5. Parameters used for calculation of correction factors, $k_{\text{isom}}/k_{\text{O}_2}$	348
Table 10.6. Comparison of $k_{\text{isom}}/k_{\text{O}_2}$ to literature.....	349
Table 10.7. Scale factors and [NO] in <i>n</i> -butyl nitrite samples.....	358

Appendix A

Table A.1. Laser performance with Quantel YG-661 Nd:YAG laser.....	366
Table A.2. Laser performance with Continuum Surelite III Nd:YAG laser.....	367

Appendix B

Table B.1. Comparison of energy and fluctuations before and after repairs.....	398
--	-----

Appendix C

Table C.1. Comparison of CIS/6-31+G(d,p) to experiment, A-X of peroxy.....	406
Table C.2. Comparison of TD-HF, TD-DFT to experiment, A-X of peroxy.....	409
Table C.3. Comparison of Guess=(Alter,Always) to experiment, A-X of peroxy...	415
Table C.4. Comparison of scaled frequencies to experiment, A-X of peroxy.....	416

Table C.5. Comparison of G2 frequencies to experiment, A-X of peroxy.....	421
Table C.6. Comparison of CBS-QB3 frequencies to experiment, A-X of peroxy...	422

Appendix D

Appendix E

Table E.1. Reactions included in the “Global Kinetics Model”.....	448
---	-----

This page intentionally left blank

**Part 1—Introduction and Description of Cavity Ringdown
Spectrometer**

Chapter 1—Introduction

Atmospheric Chemistry

The earth's atmosphere has been described as a complex photochemical reactor, yet the vast majority of the earth's atmosphere consists of closed shell species (all electrons paired). Over 99% of the atmosphere consists of N_2 , O_2 , and Ar. Other major closed shell species include CO_2 , Ne, He, Kr, H_2 , and N_2O .¹⁻³ In the troposphere, these species are chemically inert, and will not undergo any chemical reactions.

The complexity of earth's chemistry comes from the presence of trace species. These chemical species have abundances on the order of parts per million (ppm), parts per billion (ppb), or parts per trillion (ppt). The most reactive of these species are open shell radicals (at least one unpaired electron). These species include ozone (O_3), reactive hydrogen (HO_x , defined as OH and HO_2), reactive nitrogen (NO_x , defined as NO, NO_2 , and NO_3), and various organic species (alkanes, alkenes, carbonyls, radicals).¹⁻³ The chemical reactions amongst all of these species directly determine local air quality and global climate change.

Of particular interest to the Los Angeles community is the chemistry governing smog formation. Smog consists of anthropogenic aerosols combined with elevated levels of toxic gases, such as O_3 . Although stratospheric ozone is considered "good ozone" due to its ability to block ultraviolet radiation from penetrating through the atmosphere, tropospheric ozone is considered "bad ozone" due to its adverse health effects on humans. Exposure to elevated concentrations of ozone can lead to a decrease in lung function, aggravation of asthma, throat irritation and cough, chest pain and shortness of breath, inflammation of lung tissue, and higher susceptibility to respiratory infection.⁴ Recent

studies have also shown that long-term exposure to ozone can lead to fatal cardiovascular or pulmonary conditions.⁴ The EPA recommends that to maintain good air quality, O₃ levels stay below 75 ppb, and should not exceed this limit for more than three days per year.^{2, 5} Although the air quality in Los Angeles has drastically improved in the last 30 years, the ozone levels still regularly exceed this limit. Figure 1.1 shows ozone levels in the Los Angeles basin from the last 30 years.⁵ In 2008, the ozone level in the Los Angeles basin exceeded the federal standard (75 ppb) for 120 days, posing a very serious health risk.

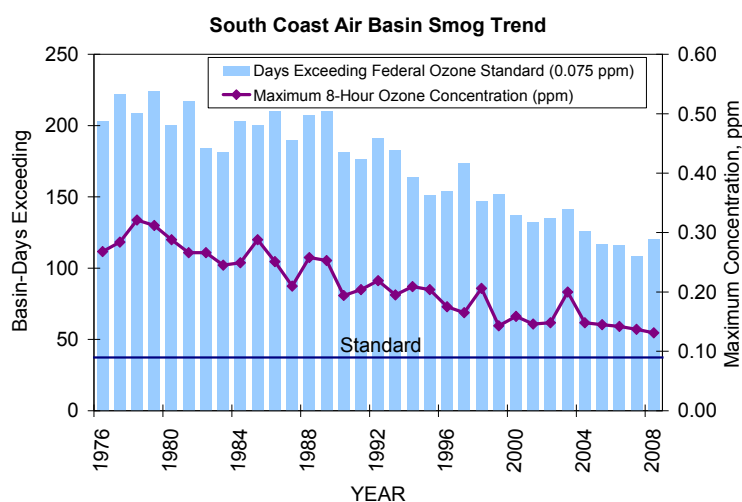


Figure 1.1. Days per year that ozone concentrations in the Los Angeles basin have exceeded the federal standard of 75 ppb, from 1976 to 2008. The number of days with excessive ozone has decreased over the last 30 years. However, even as recently as 2008, ozone levels exceeded the federal standard for 1/3 of the year. Reprinted with permission from South Coast Air Quality Management District, Copyright 2012.⁵

A better understanding of the complex chemistry behind ozone formation will allow us to refine our air quality regulations to reduce smog. The main source of ozone in the troposphere is from a series of reactions beginning with either CO or CH₄.² The net reactions are:



CO, O₂, and CH₄ are all unreactive closed shell species. Without a catalyst, Reactions 1.1 and 1.2 will never occur. The mechanism for Reaction 1.1 (shown in Reactions 1.3–1.6) reveals that HO_x and NO_x are the catalysts to ozone formation.² **We therefore expect any other atmospheric reaction involving HO_x and NO_x to affect ozone and smog formation.** HO_x and NO_x concentrations can be significantly increased due to industrial and automotive emissions. Studying chemical reactions involving HO_x and NO_x will allow us to determine the best approaches to reducing tropospheric ozone concentrations.



There are three main approaches to studying atmospheric chemistry. Laboratory studies focus on the basic physical chemistry of atmospheric molecules. These studies measure spectroscopy, kinetics, and dynamics of the individual reactions that take place in the atmosphere. Field studies focus on applying the results of laboratory studies to detection of chemicals in the atmosphere. These studies show us how reactions proceed under actual atmospheric conditions. Modeling studies use the results of the laboratory and field studies to simulate the earth's atmosphere. The atmospheric models allow us to predict the future of the atmosphere for different anthropogenic emissions, allowing us to develop appropriate climate policies. Results from the field and modeling studies can

often indicate basic reactions that are either missing or have clearly incorrect rate constants, suggesting new laboratory studies to be undertaken. All three types of studies are important, and each method relies on the other two to generate meaningful results.

The experiments described in this thesis consist of basic physical chemistry experiments and electronic structure calculations on radical reactions of atmospheric interest. **We focus on direct spectroscopic detection of each chemical reaction's primary products.** In contrast to our methods, many laboratory studies use end-product analysis and kinetics modeling to back out the rate constants of interest. By utilizing a direct detection method, our kinetics results have minimal reliance on other reactions' rate constants, and are thus subject to lower uncertainties than end-product studies. The experimental technique that we employ is infrared cavity ringdown spectroscopy (IR-CRDS), a sensitive method that utilizes an optical cavity to obtain infrared spectra for absorptions on the order of ppm.⁶⁻¹¹ A major advantage to using IR-CRDS is that radical concentrations can be kept low, preventing appreciable amounts of secondary chemistry from occurring. The principles of IR-CRDS and details of our experimental apparatus are described in the remainder of Part 1 of this thesis (Chapter 2).

The interpretation of CRD spectra can be difficult. Our goal is to make accurate kinetics measurements for use in atmospheric models. However, individual peaks must be assigned to chemical species with confidence before it is possible to make kinetics measurements. Some spectroscopic peaks lack structure, making it difficult to *a priori* unambiguously assign the peak to a molecule. Additionally, many peaks will appear in similar spectral regions, further complicating assignment of the spectrum. **To aid in interpreting the spectra, we perform electronic structure calculations to simulate**

spectroscopy and kinetics results. These calculations give us further insight into the chemical physics that governs our experiments. By combining the electronic structure calculations with a kinetics study, we can compare our experimental measurements to simulation, and further refine our understanding of the chemical system being studied.

Specific Chemical Systems of Interest

The work described in this thesis examines three chemical systems of atmospheric interest using a combination of experimental and theoretical techniques. The chemical systems and techniques used are

- Peroxynitrous acid (HOONO)—electronic structure calculations to interpret previous spectroscopic experiments on the branching ratio of OH + NO₂
- HO₂ + HCHO—CRDS detection of the OH stretch and $\tilde{A} - \tilde{X}$ transitions of the primary product, hydroxymethylperoxy (HMP, HOCH₂OO•); electronic structure calculations to model the spectroscopic bands and evaluate appropriate computational methods for hydroxyalkylperoxy systems; kinetics experiments and modeling to show that the existing chemical mechanism is incomplete
- Alkoxy radicals (RO•)—electronic structure calculations to determine how the chemical structure of alkoxy radicals affects the OH stretch spectrum; electronic structure calculations and kinetics modeling to interpret the “*n*-butoxy low [O₂] isomerization anomaly” observed in previous experiments; reanalysis of previously obtained relative kinetics data, CRDS detection of the OH stretch and $\tilde{A} - \tilde{X}$ transitions of the alkoxy isomerization products HOR• and HOROO•

A brief description of each chemical system is given below. More detailed descriptions of the chemical systems and experiments can be found in the individual chapters of this thesis.

Torsion-Torsion Coupling in Peroxynitrous Acid (HOONO)

The reaction of OH with NO_2 can go through one of two pathways: formation of HOONO (Reaction 1.7), or formation of nitric acid (HONO_2 , Reaction 1.8).¹²



The energy diagram for this chemical system is shown in Figure 1.2. HOONO is a weakly bound molecule ($D_0 = 19.6 \text{ kcal mol}^{-1}$) and will rapidly dissociate back to OH and NO_2 , therefore acting as a temporary reservoir for HO_x and NO_x .¹² In contrast, nitric acid is strongly bound ($D_0 = 47.2 \text{ kcal mol}^{-1}$) and acts as a permanent reservoir for HO_x and NO_x . It is therefore important to determine the branching ratio $k_{\text{HOONO}}/k_{\text{HONO}_2}$, in order to accurately ascertain how these reactions will affect the ozone budget.

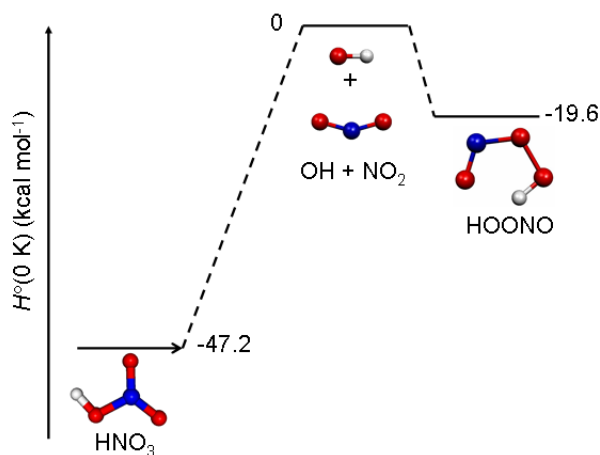


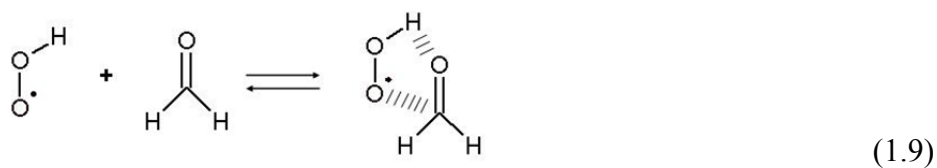
Figure 1.2. Potential energy surface for $\text{OH} + \text{NO}_2$. From Mollner et al.¹² Reprinted with permission from AAAS

The existence of a HOONO pathway has been postulated for 30 years.¹³ However, direct detection of HOONO in the gas phase^{14, 15} and kinetics measurements¹² have only been performed recently. Both experiments have measured the OH stretch spectra for HOONO and HONO₂, making use of the ratio of the integrated absorbances of each band and theoretical absorption cross sections¹⁶ to determine the branching ratio $k_{\text{HOONO}}/k_{\text{HONO}_2}$. However, this simple procedure ignores the possibility of sequence band formation within the OH stretch spectrum. Torsionally excited HOONO has a higher OH stretch frequency than ground state HOONO. We expect that the thermal population of torsional modes will create a set of OH stretch “sequence bands.” Some of these bands will fall under other peaks, and will therefore be missing from a simple integration of the observed HOONO band. In order to obtain an accurate branching ratio, a correction factor must be applied to the CRDS results to account for the unobserved intensity in the sequence bands.

Part 2 of this thesis (Chapter 3) describes a 3-dimensional potential energy surface used to model the sequence band formation in HOONO. Analysis of the potential energy surface shows us that the two torsional motions of HOONO are coupled by the internal hydrogen bond. Both torsions contribute to the formation of sequence bands. The energy levels generated from the potential energy surface show us how much OH stretch intensity is shifted out of the main HOONO peak, and give us a correction factor to apply to the experimentally determined $k_{\text{HOONO}}/k_{\text{HONO}_2}$.

HO₂ + HCHO: Spectroscopy, Kinetics, and Electronic Structure of HOCH₂OO•

The reaction of hydroperoxy radical (HO₂) with carbonyl compounds has been proposed as a major sink for carbonyl compounds in the upper troposphere/lower stratosphere (UTLS).¹⁷ The reaction of HO₂ with formaldehyde (HCHO) is the simplest of these reactions. The reaction proceeds through a hydrogen bound intermediate (Reaction 1.9) before isomerizing into a hydroxyalkylperoxy product (Reaction 1.10).



Ab initio calculations have shown that reaction of HO₂ + HCHO will proceed at room temperature.¹⁸⁻²⁰ A potential energy diagram for HO₂ + HCHO is shown in Figure 1.3.¹⁸ There is no activation barrier to Reaction 1.9. The activation barrier to Reaction 1.10 is lower than dissociation back to HO₂ + HCHO.^{18, 19, 21} The combination of these two factors indicates that the isomerization reaction will occur in the atmosphere, and that Reaction 1.9 should have an increased rate at reduced temperatures. In contrast, it is currently unknown whether the reaction of HO₂ with larger carbonyls (acetaldehyde, acetone) will form isomerization product, because the barrier to isomerization may or may not be higher than dissociation back to products.^{19, 22, 23}

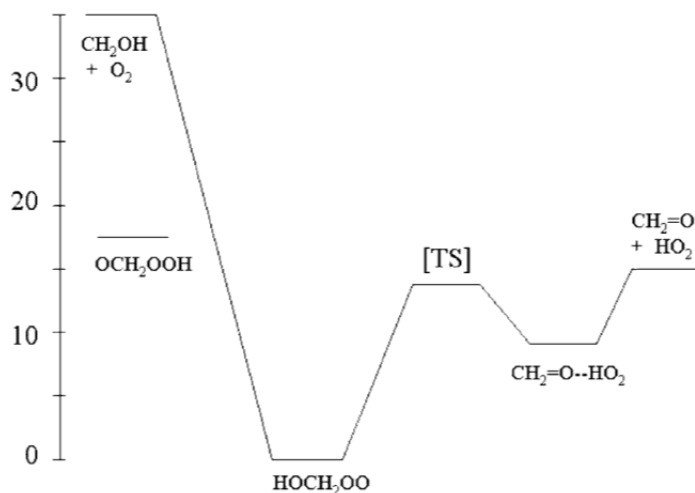


Figure 1.3. Potential energy surface for $\text{HO}_2 + \text{HCHO}$. Reprinted from Dibble (2002) with permission from Elsevier.¹⁸

Previous experiments have measured the kinetics of $\text{HO}_2 + \text{HCHO}$ by FTIR spectra of the end-products,²⁴ or via the $\tilde{B}-\tilde{X}$ band of the direct reaction product, hydroxymethylperoxy ($\text{HOCH}_2\text{OO}\cdot$, or HMP).^{25, 26} Despite these measurements, considerable uncertainty still exists in the activation energy ($\pm 80\%$, 2σ).²⁷ One source of this uncertainty is interference from other species (HO_2 , CH_3O_2) within the structureless $\tilde{B}-\tilde{X}$ spectrum of HMP. Detection of this intermediate by other spectroscopic transitions (free from interferences from other chemical species and structured to provide validation of the spectral assignment) could lead to improved kinetic rate constants and give rise to the possibility of studying reactions of HO_2 with larger carbonyls.

Part 3 of this thesis (Chapters 4–6) describes experimental and theoretical work on the spectroscopy and kinetics of HMP. We used CRDS to make the first detection of the OH stretch vibrational spectrum and the $\tilde{A}-\tilde{X}$ electronic spectrum. We performed quantum chemical calculations to verify the assignment of the spectroscopic bands to HMP, assess coupling between the HOCO and OOCO torsional motions, and to show

which levels of theory are appropriate for use in further studies of hydroxyalkylperoxy radicals. The kinetics data that we obtain from these spectroscopic bands are in excellent agreement with the existing kinetics model. This indicates that the rate constants and secondary chemistry from previous studies are well modeled.

Alkoxy (RO•) Isomerization: Spectroscopy, Kinetics, and Electronic Structure of Primary Products

Alkoxy radicals (RO•) are an important intermediate in the reactions of volatile organic compounds. The oxidation of alkanes (RH) in the presence of NO_x, leads to atmospheric alkoxy formation (Reactions 1.11–1.13). Once formed, these radicals can undergo decomposition (Reaction 1.14), isomerization and subsequent reaction with O₂ (Reactions 1.15 and 1.16), or direct reaction with O₂ (Reaction 1.17). Because HO_x and NO_x are produced and consumed, these reactions directly impact ozone chemistry.



Previous experiments have determined the relative rate $k_{\text{isom}}/k_{\text{O}_2}$, typically by end-product analysis.²⁸ In contrast, previous work in the Okumura group has used CRDS

to measure the OH stretch of the primary isomerization products, HOR• or HOROO•.^{29, 30} CRDS of the primary products should yield a value of $k_{\text{isom}}/k_{\text{O}_2}$ with lower uncertainty than an end-product study because secondary chemistry does not affect the CRDS experiment. However, numerous issues plagued the previous CRDS experiment. First, gas concentrations and scaling of absorbances to [RO•] were not done properly. Second, the spectra previously reported also were taken at times where secondary chemistry affected the experiment, and are therefore not “clean” spectra of HOR• or HOROO•. Third, anomalous behavior in the relative kinetics data is observed at low [O₂] (less than 1 torr); the yield of isomerization product increases as [O₂] is increased. Finally, the effects of alkoxy decomposition, recombination with NO, and prompt processes were not considered in deriving $k_{\text{isom}}/k_{\text{O}_2}$, a problem common to all alkoxy studies in the past 30 years.²⁸

Part 4 of this thesis (Chapters 7–10) describe experimental and theoretical work on the spectroscopy and relative kinetics of alkoxy isomerization. We used CRDS to make the first detection of the $\tilde{A}-\tilde{X}$ band of $\delta\text{-HOC}_4\text{H}_8\text{OO}\bullet$, the isomerization product of *n*-butoxy. We also report the first clean OH stretch spectra of $\delta\text{-HOC}_4\text{H}_8\bullet$, $\delta\text{-HOC}_4\text{H}_8\text{OO}\bullet$, $\delta\text{-HOC}_5\text{H}_{10}\bullet$, and $\delta\text{-HOC}_5\text{H}_{10}\text{OO}\bullet$, the isomerization products of *n*-butoxy and 2-pentoxy. The results of our electronic structure calculations show clear differences in the OH stretch absorption cross sections of HOR• and HOROO•, and clear patterns for how the relative locations of the hydroxyl and peroxy groups affect the OH stretch intensity. We also reanalyzed the previously acquired relative kinetics data to correct for calculation errors and to show that decomposition, recombination with NO, and prompt processes clearly affect the derived value of $k_{\text{isom}}/k_{\text{O}_2}$.

Chapter 2—Description of Cavity Ringdown Spectrometer

Experimental apparatus section: Reproduced in part with permission from Sprague et al.,³¹ Copyright 2012 American Chemical Society.

Abstract

Cavity ringdown spectroscopy (CRDS) is a sensitive technique that makes use of an optical cavity to measure absorptions on the order of parts per million. By choosing appropriate tunable light sources, we can measure the spectroscopy and kinetics of the chemical systems described in Chapter 1. This chapter summarizes the operating principles and specifications of our cavity ringdown spectrometer. Tunable infrared light is generated by sending the output of a Nd:YAG pumped dye laser into either an optical parametric amplifier or a hydrogen-filled Raman shifter. The infrared light is sent into the gas kinetics and ringdown cell. Radical chemistry is initiated by pulsed laser photolysis of precursor chemicals using an excimer laser. To assess the performance of the spectrometer, laser power, pulse energy fluctuations, timing jitter, mirror reflectivity, and minimum detectable absorbance were all measured. The spectrometer was calibrated using known spectroscopic lines and a readout on the dye laser indicating its position.

Introduction

Cavity Ringdown Spectroscopy

Absorption spectroscopy is governed by the Beer-Lambert Law:

$$A = \ln\left(\frac{I_0}{I}\right) = \sigma L_{abs} N, \quad (2.1)$$

where A is the absorbance, I_0 is the initial light intensity, I is the transmitted light intensity, σ is the absorption cross section, L_{abs} is the path length of light through the absorber, and N is the number density of absorber molecules (per unit volume). For molecules with small cross sections, a detectable absorbance can be attained by two methods: increasing the concentration of absorber molecules, or by increasing the physical absorption path length using long pass absorption spectroscopy.

In many cases, neither of these options is viable. Increasing the concentration of chemical absorbers in radical chemistry studies can lead to unwanted secondary chemistry effects. For example, consider a kinetics experiment on the reaction of the hydroperoxy radical (HO_2) with an excess amount of formaldehyde (HCHO), the chemical system described in Part 2 of this thesis. The goal of the study is to determine the rate constant of the reaction between HO_2 and HCHO . If these two chemicals are the only reactive species present, then two possible reactions can occur:



Since HO_2 is consumed in both reactions, and HCHO is in excess, we must measure the formation of $\text{HOCH}_2\text{OO}\cdot$ in order to determine the rate constant for Reaction 2.2. One way to do this is to measure the OH stretch spectrum of $\text{HOCH}_2\text{OO}\cdot$. In order to obtain a detectable concentration of $\text{HOCH}_2\text{OO}\cdot$, we could increase $[\text{HO}_2]$. This will, however, also increase the rate of Reaction 2.3, producing H_2O_2 , a chemical that will interfere with the spectroscopic detection of $\text{HOCH}_2\text{OO}\cdot$. A doubling of $[\text{HO}_2]$ will double the rate of Reaction 2.2, but quadruple the rate of Reaction 2.3. At high concentrations, the only product that will be detected is H_2O_2 , making the kinetics experiment impossible.

Additionally, increasing the physical sample path length is often cumbersome or impossible. For the chemical systems studied in our laboratory, photolysis of precursor chemicals is necessary to generate the reactants necessary to initiate chemistry. Using a long pass cell would prove unwieldy, as the photolysis beam would need a very large flux in order to photolyze precursors in the entire cell. For example, consider a 10 m long White cell with a minimum detectable absorbance of 10^{-5} used for detecting the OH stretch of the $\delta\text{-HOC}_4\text{H}_8\bullet$ radical ($\sigma_{\text{peak}} = 7.5 \times 10^{-20} \text{ cm}^2$), one of the alkoxy isomerization products discussed in Part 4 of this thesis. The minimum concentration of reactant radicals necessary for detection is $1.3 \times 10^{11} \text{ molecules cm}^{-3}$, which is low enough to prevent secondary chemistry effects. However, these reactant radicals are generated from photolysis of precursor alkyl nitrites, with a UV cross section of $8 \times 10^{-20} \text{ cm}^2$ at 351 nm.³² In order to prevent secondary chemistry due to the presence of excess alkyl nitrites, a typical experiment aims for 1% photolysis. This requires a photon flux of $1.0 \times 10^{17} \text{ cm}^{-2}$. For a 10 m long cell and a 0.5 cm high photolysis beam, a laser with an energy output of 32 J/pulse is required. Even if such a high powered laser was commercially available, it would be dangerous to operate and uneconomical to purchase.

Since neither long-pass absorption spectroscopy nor increasing the radical concentrations are acceptable ways to improve sensitivity, we must take a different approach. One way to do this is by increasing the effective path length via an optical cavity. Cavity ringdown spectroscopy (CRDS)^{6-11, 33} is a suitable experimental technique for detection of small absorbances. The technique requires two highly reflective mirrors ($R > 99.9\%$) to create an optical cavity. Laser light is injected into the cavity, and the small amount of light that is transmitted through the mirrors is detected. The intensity of

the transmitted light is proportional to the intensity of light in the cavity. Over time, the amount of light reaching the detector decays exponentially. This decay is called “ringdown,” named such because of the similarity to the sound decay of a ringing bell.

If the only loss process for light is leakage through the mirrors, the ringdown is characterized by

$$I = I_0 \exp\left(\frac{-t}{\tau_0}\right), \text{ with } \tau_0 = \frac{t_r}{2(1-R)} = \frac{L_{opt}}{c(1-R)}, \quad (2.4)$$

where t_r is the roundtrip time for light in the cavity, R is the mirror reflectivity, L_{opt} is the distance between the two mirrors, c is the speed of light, and τ_0 is the 1/e decay time of the light (called the ringdown lifetime).

When an absorber is present in the cavity, Equation 2.4 must be modified to

$$I = I_0 \exp\left(-\frac{t}{\tau}\right), \text{ with } \frac{1}{\tau} = \frac{1}{\tau_0} + (\sigma L_{abs} N) \left(\frac{c}{L_{opt}}\right), \quad (2.5)$$

where L_{abs} is the path length of the absorber and τ is the 1/e decay time for light in the presence of the absorber. The absorbance can be calculated from equations 2.4 and 2.5:

$$A = \frac{L_{opt}}{c} \left(\frac{1}{\tau} - \frac{1}{\tau_0} \right). \quad (2.6)$$

Equation 2.6 is valid for comparison of a cavity in the presence of chemical absorbers (with ringdown time τ) to a cavity in a reference state without the chemical absorbers (with ringdown time τ_0). The reference state does not necessarily have to be an empty cavity. For an experiment in which photolysis initiates chemistry, the reference state is chosen to be the cavity filled with reactant gases, prior to photolysis. By choosing this reference state, we effectively subtract out any background absorption from the

precursor chemicals. Ringdown decays are measured before and after photolysis. These decays are fit to a single exponential to calculate the characteristic lifetimes τ_0 and τ . By carefully controlling the time between photolysis and measuring the ringdowns, formation of photolysis products can be monitored.

To illustrate a typical ringdown measurement, we can examine the R(3) line of the ν_1 absorption of HO₂.³⁴⁻³⁶ Figure 2.1 shows two ringdown traces obtained at 3525.2 cm⁻¹, in the absence (blue curve) and presence (pink curve) of HO₂. The traces have been normalized to the same peak voltage. Note that when HO₂ is present, the intensity of light reaching the detector decays faster, indicating absorption. The ringdown lifetimes are $\tau_0 = 3.95 \mu\text{s}$ (without HO₂), and $\tau = 3.75 \mu\text{s}$ with HO₂. Using Equation 2.6 ($L_{\text{opt}} = 55 \text{ cm}$), we obtain an absorbance of 25 ppm for this HO₂ line. This is a relatively large absorption to measure with CRDS. For very large absorptions ($A > 0.1 \times (1-R)$) and very sharp spectral peaks (less than 1/400 of the light's linewidth), equations 4–6 are not quantitatively correct. To obtain accurate absorbances, correction factors must be applied to the CRDS data.^{11, 30}

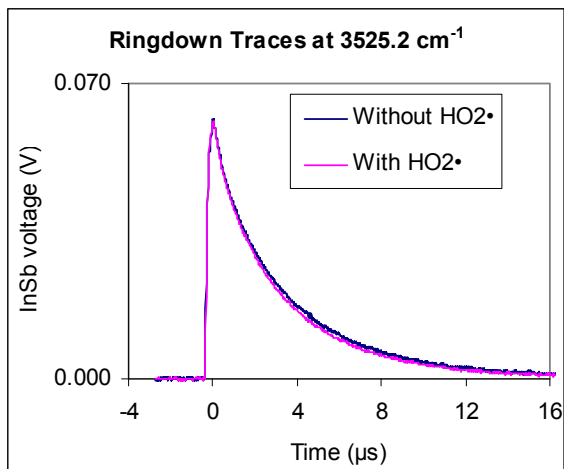


Figure 2.1. Sample ringdown traces at 3525.2 cm^{-1} in the absence of HO_2 (blue line, top) and in the presence of HO_2 (pink line, bottom). This frequency corresponds to the R(3) line of the ν_1 absorption of HO_2 .³⁴⁻³⁶ The two traces have been normalized to the same peak voltage. The ringdown lifetimes are $\tau_0 = 3.95\ \mu\text{s}$ (without HO_2) and $\tau = 3.75\ \mu\text{s}$, giving an absorbance by HO_2 of 25 ppm ($L_{\text{opt}} = 55\text{ cm}$).

Pulsed ringdown systems (such as the one used for the work in this thesis) typically can obtain sensitivities of $0.1\text{--}1\text{ ppm Hz}^{-1/2}$, depending on mirror reflectivity, optical cavity length, and absorption by background gases.³⁷ This is approximately three orders of magnitude more sensitive than a single-pass direct absorption method. It is possible for multipass absorption methods such as cavity enhanced absorption spectroscopy (CEAS) to approach the sensitivity of pulsed ringdown.³⁸ However, CRDS has a distinct advantage over CEAS and traditional absorption techniques. CRDS measurements are insensitive to laser power fluctuations because only the rate of signal decay is the quantity of interest. In contrast, CEAS and traditional absorption methods rely on the absolute signal intensity, making these methods susceptible to laser power fluctuations.

It is possible to obtain greater sensitivity using continuous wave light sources (cw-CRDS, sensitivity 1 ppb), or by combining an optical cavity with frequency

modulation detection (NICE-OHMS, sensitivity 1 ppt).³⁹ However, these methods come with their own drawbacks. Both methods require a continuous wave light source, such as a diode laser. Diode lasers generally have a smaller range of tunability than can be achieved in a pulsed light source system, making diode lasers inappropriate for use in preliminary spectroscopic studies. Additionally, NICE-OHMS is only an appropriate technique for very weak absorptions. If an absorption line is too strong, too much power will build up in the cavity, causing the detector signal to saturate.

Considerations of Tunable Light Ranges

The ranges of tunable light required for our experiments are determined by the properties of the atmospheric species being studied. Two functional groups are prevalent in the chemical systems described in Chapter 1: hydroxy groups (-OH) and peroxy groups (-OO•). Hydroxy groups are formed through reaction of organic species with HO_x. Peroxy groups are present in the atmosphere due to association reactions of oxygen with radical species.¹⁻³ A spectrometer with the ability to detect molecules containing these two functional groups can be used to study a wide variety of atmospherically relevant reactions.

Molecules with either of these two functional groups have distinct features in their spectra. Species containing a hydroxy group will have spectra with a broad, generally structureless peak around 2.7 μm (3680 cm⁻¹), resulting from the molecule's OH stretch normal mode. The position of this peak is sensitive to hydrogen bonding. A free OH group (i.e., not hydrogen bound) will have an OH stretch frequency near 3680 cm⁻¹, as observed in gas phase methanol.⁴⁰ However, a hydrogen bound OH group will have a

red-shifted OH stretch frequency, by as much as 400 cm^{-1} . This effect is most pronounced in condensed phase spectra; for example, liquid phase methanol has an OH stretch frequency of 3328 cm^{-1} .⁴¹ However, the effect is also important in gas phase molecules with internal hydrogen bonding, such as peroxyacid (HOONO). The magnitude of these frequency shifts can be highly dependent on molecular geometry and the excitation of other modes, possibly leading to sequence band formation over a range of hundreds of wavenumbers.^{42, 43} Measurement of OH stretch groups therefore requires a large range of light tunability.

Species containing a peroxy group will have spectra with a weak, highly structured peak around $1.3\text{ }\mu\text{m}$ (7400 cm^{-1}). This peak arises from the first electronic ($\tilde{A}-\tilde{X}$) transition. The position of this peak is sensitive to the local chemical environment of the peroxy group. Alkane chain length and proximity to different functional groups can change the electronic transition frequency by $\pm 500\text{ cm}^{-1}$.^{44, 45} Furthermore, different conformers of the same molecule can have vastly different transition frequencies, by as much as 1000 cm^{-1} , as observed in the hydroxymethylperoxy radical (Part 3 of this thesis). The large shifts in $\tilde{A}-\tilde{X}$ transition frequency also highlight the need for a wide range of tunability.

Taking the above factors into account, we choose two techniques to generate light in two frequency ranges. To measure OH stretch spectra, we use optical parametric amplification to obtain tunable light over the range $2.7\text{--}3.7\text{ }\mu\text{m}$. To measure the peroxy $\tilde{A}-\tilde{X}$ spectra, we use a hydrogen gas Raman shifter to obtain tunable light over the range $1.2\text{--}1.4\text{ }\mu\text{m}$.

Optical Parametric Amplification: Mid-IR light (2.7-3.7 μm)

An optical parametric amplifier (OPA) system is used to obtain 2.7-3.7 μm light.^{46, 47} A basic schematic of an OPA system is shown in Figure 2.2.

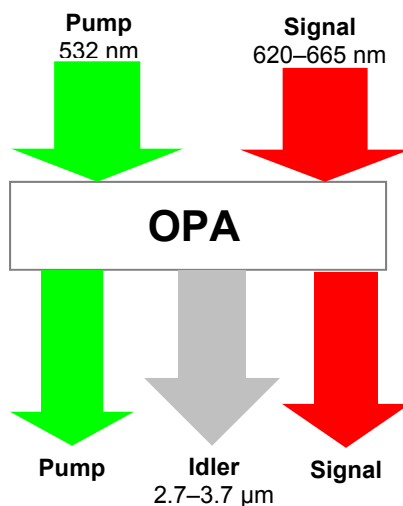


Figure 2.2. Schematic of an optical parametric amplifier (OPA). The wavelengths listed for the pump, signal, and idler beams are the wavelengths used in our apparatus. Note that in actual operation, the pump and signal beams are spatially and temporally matched.

A signal beam and a pump beam (of shorter wavelength than the signal beam) are sent through a nonlinear medium. Both beams must be matched spatially and temporally. Inside of the nonlinear medium, some of the pump beam photons are converted into two photons: one photon of the signal beam wavelength, and a second photon (idler) with a wavelength corresponding to the difference in pump and signal photon energies. In our setup, the pump photons are a fixed wavelength (532 nm), and the signal photons have a tunable wavelength (620-665 nm). Because the signal photons are tunable, the resulting idler photons are also tunable (2.7–3.7 μm). Our OPA typically produces 1 mJ of idler light, for 160 mJ of pump energy and 9 mJ of signal energy. The idler linewidth is 1 cm^{-1} ,

limited by the linewidth of the pump (1 cm^{-1}). Further details about the OPA system can be found in the *Experimental Details* section.

Hydrogen Gas Raman Shifter: Near-IR light (1.2–1.4 μm)

Our second method for generating tunable infrared light is to use a hydrogen gas Raman shifter. This setup gives us tunable light in the range 1.2–1.4 μm . A Raman shifter converts light from one wavelength to another by making use of the Raman effect. Figure 2.3 contains an energy diagram illustrating the Raman effect.

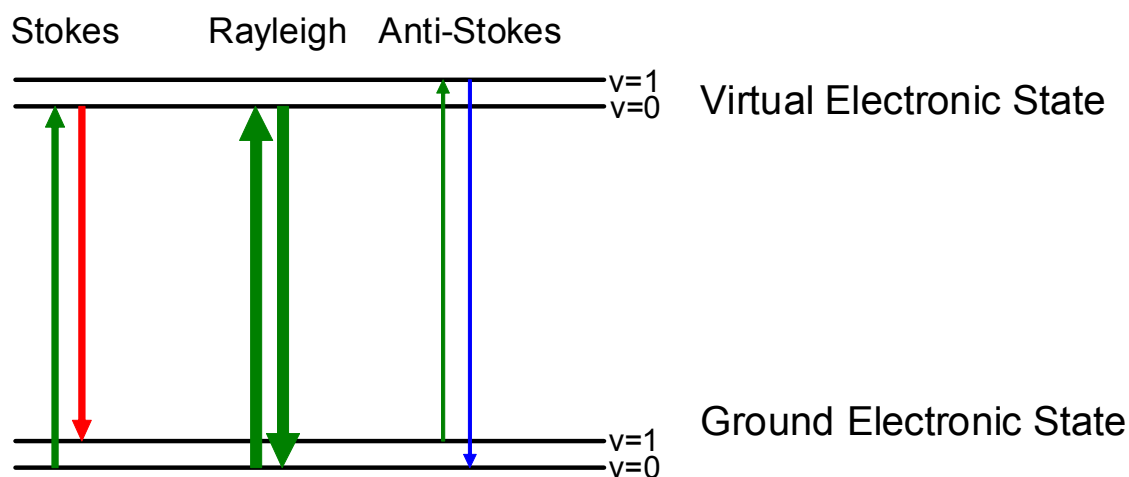


Figure 2.3. Energy diagram illustrating the Raman effect. Light of a given frequency excites polarizable molecules to a virtual state. The light produced when the molecule relaxes back to the ground state can be of lower frequency than the input (Stokes shifted), the same frequency as the input (Rayleigh scattered), or of higher frequency than the input (anti-Stokes shifted). The figure shows first Stokes and first anti-Stokes shifts. In our apparatus, we make use of the second Stokes shift in hydrogen gas (total shift 8310.4 cm^{-1}) to convert 620–665 nm light into 1.2–1.4 μm light.

When light enters a medium comprised of polarizable molecules, the molecules can be excited to virtual states. When the excited molecules relax back to their ground state, they can emit light of higher frequency (anti-Stokes shifted light), the same frequency (Rayleigh scattering), or lower frequency (Stokes shifted light). The frequency

shift between the incident and shifted photons is dependent on the medium used. We utilize hydrogen gas, which has a frequency shift is 4155.2 cm^{-1} . In our setup, the incident light is tunable over the range 620-665 nm. The second Stokes shifted light (total shift of 8310.4 cm^{-1}) gives us photons in the range 1.2-1.4 μm . The total energy of the Raman shifted light varies exponentially with the path length through the Raman shifter and incident power,⁴⁸ thus making multipass Raman shifter cells desirable. Additionally, focusing the beam within the Raman cell will also increase the energy of Raman shifted light. Our Raman shifter typically produces 90 μJ of infrared light for 30 mJ of incident red light. The linewidth of the Raman shifted light is 0.1 cm^{-1} , the same as the incident light. Further details of our Raman apparatus can be found in the *Experimental Details* section.

Experimental Details

Pulsed Laser Photolysis-Cavity Ringdown Spectroscopy (PLP-CRDS) Apparatus

The PLP-CRDS apparatus that was used in this thesis is the end result of 15 years of construction and repairs. Todd Fuelberth⁴⁹ and Eva Garland²⁹ constructed the optical parametric amplifier system currently in use. Andrew Mollner³⁰ installed the current excimer laser and gas flow system. My work has focused on laser installations and repair (see Part 5 of this thesis), replacement of the vacuum pump, and installation of the Raman shifter.

Figures 2.4 and 2.5 contain diagrams of the optical cavity and the two gas kinetics cells used. Figures 2.6 and 2.7 contain diagrams of the laser system. A full discussion of each component of the spectrometer can be found below; however, a brief overview is

warranted to orient the reader to each part of the spectrometer. The gas kinetics cells were constructed of stainless steel or quartz, with flat quartz windows to allow for the photolysis of chemicals within the cell. The cell was coupled to an optical cavity via mirror mounts. Light for the spectrometer was generated from Nd:YAG and dye lasers. To generate mid-infrared light, the Nd:YAG and dye laser outputs were mixed within an optical parametric amplifier. To generate near-infrared light, the dye laser output was sent through a hydrogen gas Raman shifter. An excimer laser was used to photolyze the chemicals within the kinetics cell. Digital delay generators controlled the timing between the excimer and Nd:YAG pulses. Ringdown data were collected using a photodiode connected to a PC oscilloscope.

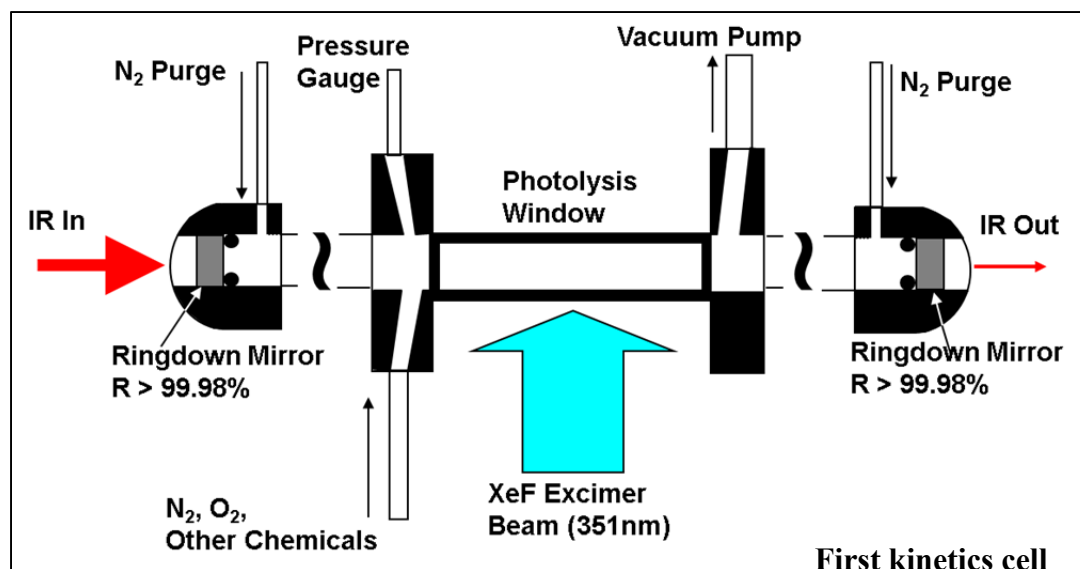


Figure 2.4. Diagram of the first kinetics cell (room temperature only).

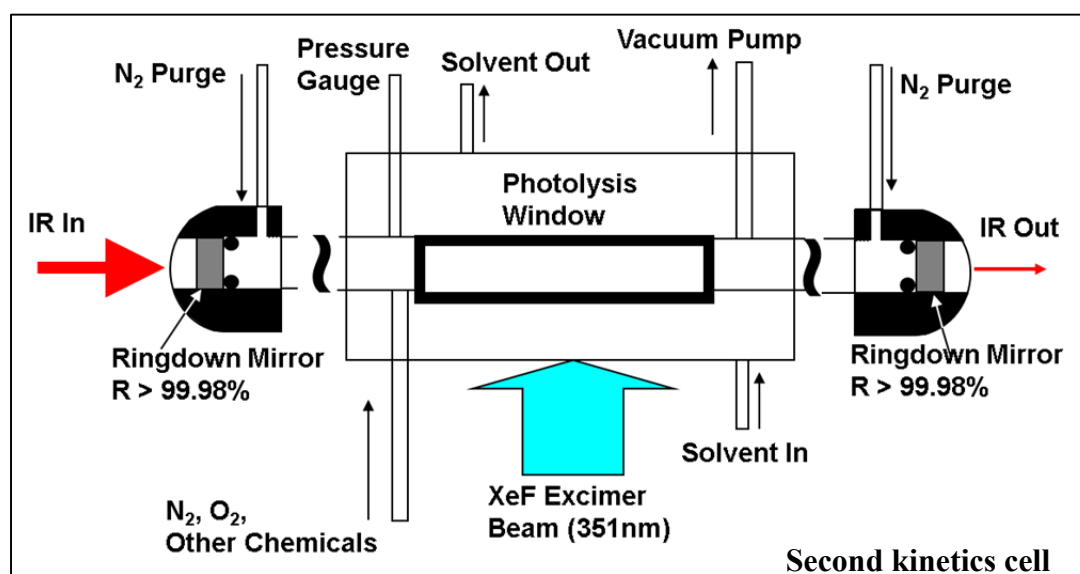


Figure 2.5. Diagram of the second kinetics cell (capable of temperature control).

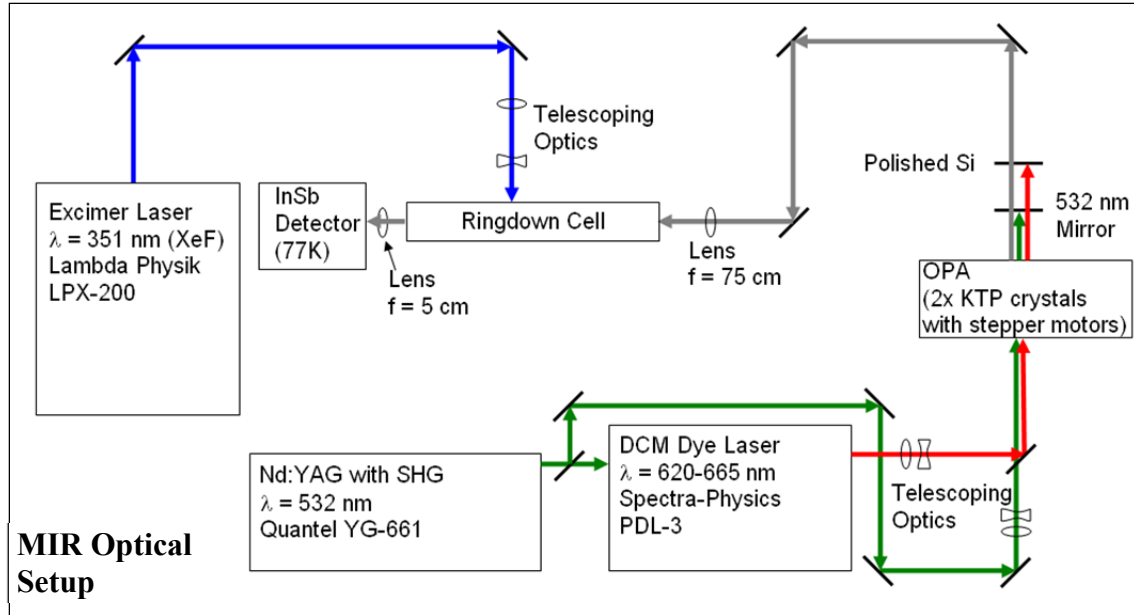


Figure 2.6. Optical setup for mid-infrared light ($2.7\text{--}3.7 \mu\text{m}$, using the OPA).

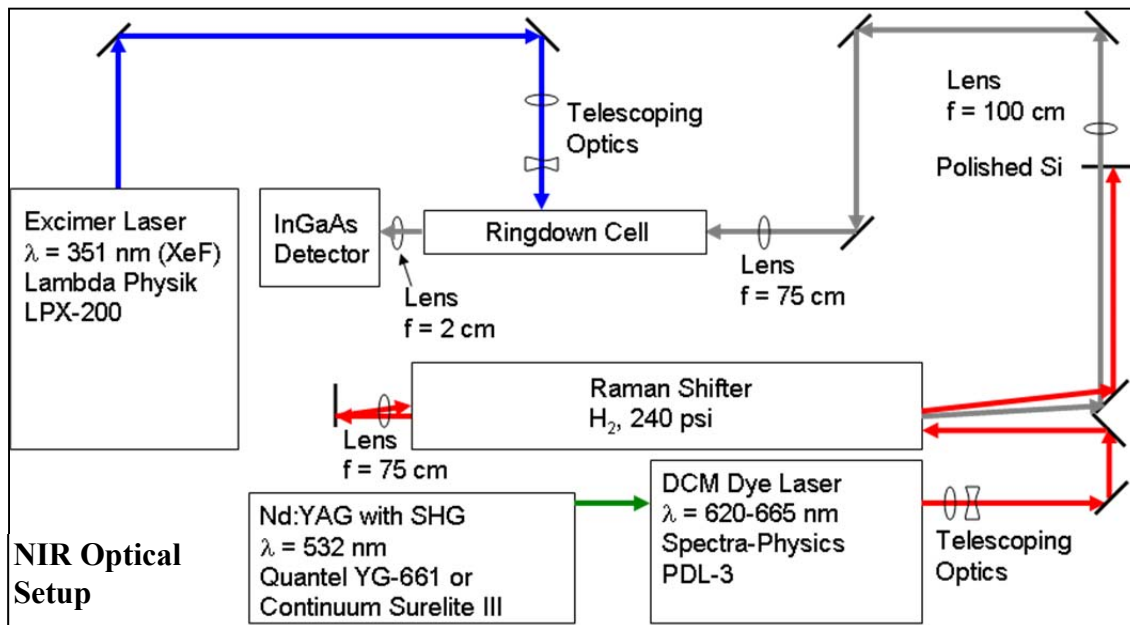


Figure 2.7. Optical setup for near-infrared light ($1.2\text{--}1.4 \mu\text{m}$, using the Raman shifter).

Gas kinetics cell

The first gas kinetics cell (used for the OH stretch measurements of HOCH₂OO• described in Part 3) is illustrated in Figure 2.4. The gas kinetics cell was a 7 cm long stainless steel tube with a square cross section of 1 cm². The cell was coated with a fluoropolymer (FluoroPel PFC 801A/coFS) in order to prevent chemicals from sticking to or reacting with the cell walls. The sides of the cell had 6 cm long quartz windows to allow light to pass through for photolysis. The cell was coupled to the ringdown mirrors through Teflon blocks. The Teflon blocks also had gas ports to allow for introduction of gases to the cell. A pressure gauge (MKS Baratron) was attached to one of the Teflon blocks in order to monitor the pressure inside the cell.

The second gas kinetics cell (used for all other experiments described in this thesis) is illustrated in Figure 2.5. The gas kinetics cell was a 37 cm long quartz tube with a circular cross section of 1 cm². The cell contained three ¼" ports. Two of the ports were used for introduction of the sample gases and the vacuum system, creating a 5 cm sample length within the cell. A pressure gauge (MKS Baratron) was attached to the third port in order to monitor the pressure inside the cell. A quartz jacket around the central tube allows for heated or chilled solvent to flow around the sample. A flat quartz window on the front side of the solvent jacket allows light to pass through for photolysis, while ensuring a minimum of light is reflected off of the cell.

For all experiments, gas flows were measured by a set of mass flow transducers. Inert gases were sent through an Omega flowmeter, model number FMA1720 (brass, 0 to 10000 sccm), FMA1716 (brass, 0 to 2000 sccm), or FMA1712 (brass, 0 to 500 sccm). Corrosive gases were sent through an Edwards flowmeter, model number 831MF

(stainless steel, 0 to 1000 sccm) or model number 831MFT (stainless steel, 0 to 100 sccm). The voltage from each flowmeter was sent to both a digital display box and an SCSI card in the PC.

Optical Cavity

Ringdown mirrors (Los Gatos Research, Newport, ATFilms, Layertec) were placed in commercially available mounts (Los Gatos Research) and connected to the ends of the kinetics cell. The mirrors were placed 55 cm apart in the initial stainless steel cell (Figure 2.4), and 52 cm apart in the final quartz cell (Figure 2.5). Inert gas was flowed over the mirrors and through 24 cm long glass tubes to protect the mirrors from chemical damage. These tubes were coupled to the mirror mounts by UltraTorr adaptors.

Different mirrors were used in each spectral region. The mid-infrared mirrors (used for the OH stretch spectra described in Chapter 4) had a peak reflectivity of 99.975% at 2.8 μm . The near-infrared mirrors (used for the electronic spectra described in Chapter 3) had a peak reflectivity of 99.985% at 1.32 μm . Further details on mirror performance can be found in the "*Performance of Apparatus*" section.

Optical Parametric Amplifier Setup

Tunable mid-infrared (MIR) light over the range 2.7–3.7 μm was generated using an optical parametric amplifier (OPA) system similar to the one described by Reid and Tang.⁴⁷ The laser system is illustrated in Figure 2.6. The pump beam was 532 nm light obtained from second harmonic generation of a Nd:YAG (Quantel YG-661 or Continuum Surelite III) beam. While the YG-661 had a built in second harmonic generator, the

Surelite III did not. An external harmonic generator and crystal oven (Inrad 5-301) was installed to obtain 532 nm light. The lasers were run at a repetition rate of 10 Hz with a typical energy output of 160 mJ/pulse. 30%–50% of the 532 nm light was sent into a dye laser (Spectra Physics PDL3). DCM dye (4-dicyanomethylene-2-methyl-6-p-dimethylaminostyryl-4H-pyran) was used to generate tunable red light in the range 620–665 nm. The green and red laser beams were overlapped spatially and temporally, and sent through two potassium titanyl phosphate (KTP) crystals to generate infrared light in the range 2700–3700 cm^{-1} . The infrared light was tunable by adjusting the dye laser light frequency. The KTP crystals were connected to a stepper motor to allow for adjustment of the crystal orientation in order to maximize the infrared power at each frequency. The dye laser output and KTP crystal stepper motors were controlled using a LabView program. For typical energies of 160 mJ/pulse of 532 nm light, 9 mJ/pulse of red light was produced. Optical parametric amplification of these beams gave a typical infrared energy of 1 mJ/pulse. The linewidth of the light exiting the OPA was 1 cm^{-1} , limited by the linewidth of the 532 nm light (also 1 cm^{-1}).

Red and green light were separated from the infrared beam using sapphire optics with an antireflective coating. Remaining red light was removed by a polished silicon optic placed at Brewster's angle. The infrared beam was found to be slightly diverging. To correct for this, the beam was sent through a long focal length (75 cm) lens immediately prior to entering the optical cavity.

Raman Shifter Setup

Tunable near-infrared (NIR) light over the range 1.2–1.4 μm was generated using a hydrogen gas Raman shifter. The laser system is illustrated in Figure 2.7. The dye laser pump beam was 532 nm light obtained from second harmonic generation of a Nd:YAG (Quantel YG-661 or Continuum Surelite III) beam. While the YG-661 had a built in second harmonic generator, the Surelite III did not. An external harmonic generator and crystal oven (Inrad 5-301) was installed to obtain 532 nm light. The lasers were run at a repetition rate of 10 Hz. Typical 532 nm energy output of the Nd:YAG laser was 285 mJ/pulse for the YG-661, and 370 mJ/pulse for the Surelite III. All of the 532 nm light was sent into a dye laser (Spectra Physics PDL3). DCM dye was used to generate tunable red light in the range 620–665 nm. The red light was then telescoped to 0.5 mm beam diameter and sent through a two-pass Raman shifter (1.25 m per pass, 240 psi of H_2 gas). Lenses were placed in the optical path to ensure that the beam focused in the middle of the Raman shifter during both passes. The light was then passed through a polished silicon optic at Brewster's angle to isolate the near infrared (NIR) light produced from the 2nd Stokes shift (1.2–1.4 μm). For typical energies of 285 mJ/pulse of 532 nm light (YG-661), 20 mJ/pulse of red light was produced, leading to typical NIR light energies of 50 μJ /pulse. For typical energies of 370 mJ/pulse of 532 nm light (Surelite III), 30 mJ/pulse of red light was produced, leading to typical NIR light energies of 90 μJ /pulse. The linewidth of the NIR light was 0.1 cm^{-1} , limited by the linewidth of the dye laser (also 0.1 cm^{-1}).

Excimer Laser and Timing Control

Photolysis inside the gas cell was initiated by an excimer laser (Lambda-Physik LPX210i). For the experiments in this thesis, the gas mixture used was XeF, producing 351 nm light. The laser repetition rate was 10 Hz, with typical energies of 150–200 mJ/pulse. The laser beam size was 3 cm × 1 cm directly out of the excimer. The beam was focused vertically and expanded horizontally to a size of 5 cm × 0.3 cm before it entered the kinetics cell. Typical photon flux was 1.0×10^{17} photons cm⁻².

In order to determine the growth of spectral features with time, precise control over the relative fire times between the excimer and Nd:YAG lasers fire was required. To achieve this, the relative timing of the two lasers was controlled by two digital delay generators (Stanford Research Systems DG535). While the timing resolution of the delay generators is on the order of picoseconds, the overall timing precision of the experiment is determined by either the ringdown lifetime or relative timing jitter between the excimer and YAG laser pulses (whichever is larger). In the absence of jitter between the excimer and YAG pulses, the overall time resolution is 5 μs, equal to the ringdown lifetime. The resolution is worse (>10 μs) if significant timing jitter is present, as was the case when the YG-661 was installed incorrectly. See Appendix B for a detailed description of how the jitter between the excimer and YAG was eliminated.

Data Acquisition and Processing

Ringdown signals were detected by focusing the light exiting the optical cavity onto a photodiode detector with a short focal length lens. For the mid-IR experiments, an indium-antimony photodiode cooled to 77 K (InSb, Judson J10D-M204-R01M-60) was

used in conjunction with a 5 cm focal length CaF_2 lens. The signal coming out of the detector was sent through a voltage amplifier (Analog Modules 351A-3). For the near-IR experiments, a room temperature indium-gallium-arsenide detector (InGaAs, ThorLabs PDA-400) was used in conjunction with a 2 cm focal length CaF_2 lens. The PDA-400 has a built-in transimpedance amplifier, and no further amplification of the ringdown signal was necessary. For both sets of experiments, the amplified signal was sent through a ferrite choke and high pass filter before being sent to a PC oscilloscope board (GageScope CS1450). The sample rate of the card and data collection time were both dependent on the reflectivity of the cavity ringdown mirrors. Ringdown data were collected for 80 μs after the Nd:YAG laser fired at a sampling rate of 25 MS/s. Ringdowns from 16 or 64 shots (actual number dependent on the experiment) were averaged to obtain a ringdown trace. These traces were log-linear fit to obtain a preliminary ringdown lifetime. In order to reduce the effects of noise near the peak of the signal, data from the first 12.5% of the preliminary lifetime were cut. The remaining part of the trace was then refit using a Levenberg-Marquardt algorithm. All fitting was done in a LabVIEW program.³⁰

Performance of CRDS Apparatus

Laser Performance

The tunable infrared light used to obtain cavity ringdown spectra is generated through multiple nonlinear processes. Therefore, it is critical that the lasers used to generate this infrared light are performing optimally. Three properties of the laser light must be classified: average pulse energy, pulse-to-pulse energy fluctuations, and timing

jitter (i.e., how much does the opening of the q-switch move in time, relative to the firing of the flashlamps). A low average pulse energy will reduce the signal-to-noise ratio for the ringdowns, while very large energy fluctuations or timing jitter will make it impossible to collect high-quality ringdown traces due to individual ringdowns exceeding the scale of the oscilloscope board.

Table 2.1 contains typical laser pulse energies and pulse-to-pulse energy fluctuations for each wavelength of light under operating conditions (1064 and 532 nm light from the Nd:YAG laser, 640 nm light from the dye laser, and the infrared light generated from the OPA and Raman shifter). A full report of performance at reduced energies (by reducing flashlamp voltage or by changing the q-switch delay time) as well as details on the methods used to classify laser performance can be found in Appendix A.

Table 2.1. Typical laser performance (energy per pulse, pulse to pulse 1σ energy fluctuation, and YAG timing jitter)

Pump Laser and Setup	1064 nm, YAG oscillator	1064 nm, YAG amplifier	532 nm, YAG SHG	640 nm, Dye	1.37 μm , Raman	2.8 μm , OPA	YAG Timing Jitter
Quantel YG-661*, OPA Setup	75 mJ	350 mJ	120 mJ	1 mJ	N/A	1 mJ	± 5000 ns
Continuum Surelite III, OPA Setup	394 mJ ($\pm 0.7\%$)	N/A	160 mJ ($\pm 2.2\%$)	9 mJ	N/A	1 mJ	± 8 ns
Quantel YG-661, Raman Setup	169 mJ ($\pm 0.5\%$)	625 mJ	285 mJ ($\pm 1.1\%$)	20 mJ ($\pm 5.0\%$)	51 μJ ($\pm 16\%$)	N/A	± 8 ns
Continuum Surelite III, Raman Setup	757 mJ ($\pm 0.25\%$)	N/A	376 mJ ($\pm 1.5\%$)	30 mJ	92 μJ ($\pm 20\%$)	N/A	± 8 ns

* YG-661 installed incorrectly while used with the OPA

It should be noted that the YG-661 was not functioning properly when experiments using the OPA setup were being performed. Energy fluctuations were quite large, due to fluctuations in the timing of the laser's q-switch and damage to the capacitor

bank. Repairs were made to the laser prior to using the YG-661 with the Raman shifter. Information about these repairs can be found in Appendix B of this thesis.

Detector Performance

It is important that the signal-to-noise ratio of the recorded ringdowns be as large as possible. The sensitivity of the instrument can be greatly improved simply by collecting and fitting the data over a large number of ringdown lifetimes. By choosing a detector appropriate for our laser power and ringdown mirrors, we can maximize our signal-to-noise ratio.

We can estimate the expected peak ringdown voltage as a function of mirror reflectivity. Comparing this value to the noise specification of the detector gives us a reasonable estimate of the signal-to-noise ratio. We first approximate the power reaching the detector as

$$P = \frac{E_{cavity}}{\tau_0} = \frac{(1-R)E_{IR}}{\left(\frac{L_{opt}}{c(1-R)}\right)}(X) = \frac{(1-R)^2 cE_{IR}}{L_{opt}}(X), \quad (2.8)$$

where P is the power reaching the detector, E_{cavity} is the IR energy stored in the ringdown cavity, τ_0 is the vacuum ringdown time, L_{opt} is the cavity length, c is the speed of light, R is the cavity ringdown mirror reflectivity, E_{IR} is the energy per pulse of the incident infrared light, and X is the fraction of light entering the cavity that actually couples to cavity modes. Given this approximation, the detector responsivity, and the detector amplification, the expected ringdown amplitude is

$$V_0 = \mathfrak{R} \times A \times P = \mathfrak{R} \times A \times \frac{(1-R)^2 cE_{IR}}{L}(X), \quad (2.9)$$

where V_0 is the ringdown amplitude, \mathfrak{R} is the photovoltaic responsivity (in A/W), and A is the transimpedance amplification (in V/A).

The noise level for a detector can be calculated by Equation 2.10:

$$V_{noise} = \mathfrak{R} \times A \times NEP \times \sqrt{BW}, \quad (2.10)$$

where V_{noise} is the noise level in volts, NEP is the Noise Equivalent Power (watts $\text{Hz}^{-1/2}$), and BW is the detector bandwidth (Hz). NEP is proportional to the square root of the detector area, so smaller detectors will have less noise. For some detector/amplifier combinations (such as the PDA400), V_{noise} is directly reported in the spec sheet.

The detector properties and signal-to-noise ratio for the MIR and NIR setups are summarized in Table 2.2. Additionally, the number of ringdown lifetimes that can be measured before the ringdown signal falls below the noise is calculated via Equation 2.11:

$$\# \text{ of lifetimes} = \ln(SNR) \quad (2.11)$$

where SNR is the signal-to-noise ratio. Each of the experimental setups (MIR, NIR) is expected to be capable of measuring at least 3.5 ringdown lifetimes before the signal falls below the detector's noise level.

Table 2.2. Expected ringdown peak voltages for MIR and NIR experiments

	Mid-IR (YG-661)	Mid-IR (Surelite III)	Near-IR (YG-661)	Near-IR (Surelite III)
Detector	Judson J10D-M204 (InSb, 77 K)	Judson J10D-M204 (InSb, 77 K)	ThorLabs PDA400 (InGaAs)	ThorLabs PDA400 (InGaAs)
Mirrors	Los Gatos, 2.8 μ	Los Gatos, 2.8 μ	Los Gatos, 1.35 μ	Los Gatos, 1.35 μ
Freq. (cm⁻¹)	3620 cm ⁻¹	3620 cm ⁻¹	7540 cm ⁻¹	7540 cm ⁻¹
E_{IR} (μJ/pulse)	500	1000	15	90
L (cm)	55	55	60	60
R	0.9997	0.9998	0.9998	0.9998
\Re (A/W)	3.0	3.0	7.5×10^3	7.5×10^3
A (V/A)	50	50	0.95	0.95
V₀/X (calc) (V)	3.68	3.27	4.80	28.8
V₀ (actual) (V)	0.145	0.075	0.277	1.2
X	0.04	0.02	0.06	0.04
NEP (W Hz^{-1/2})	8×10^{-13}	8×10^{-13}		
BW (Hz)	3.5×10^6	3.5×10^6		
V_{noise} (V)	2.2×10^{-3}	2.2×10^{-3}	3.3×10^{-4} ^a	3.3×10^{-4} ^a
SNR	66	34	839	3636
# of lifetimes	4.2	3.5	6.7	8.2

a) Noise level reported directly on detector specification sheet

Mirror Reflectivity vs Wavelength

The cavity ringdown spectrometer's performance is intimately related to the reflectivity of the mirrors used. As seen in the previous section, a long ringdown lifetime allows for more data to be collected before the ringdown falls below the detector's signal-to-noise. In the center of the mirror's range, the reflectivity is the largest, and the ringdown lifetime will be longest. Further away from the central wavelength, the mirror reflectivity decreases, causing the ringdown lifetime to decrease. To properly classify the spectrometer performance, it is important to know the mirror reflectivity as a function of wavelength.

Equation 2.4 can be rearranged to solve for the mirror reflectivity:

$$R = 1 - \frac{L_{opt}}{c\tau_0}. \quad (2.12)$$

In order to determine the mirror reflectivity, vacuum ringdown data are recorded across the range of the mirrors. The ringdown lifetimes are then converted to mirror reflectivities via Equation 2.12.

The experiments described in this thesis used three sets of mirrors. The specifications for each set of mirrors are summarized in Table 2.3. The reflectivity curves for each set of mirrors can be found in Figure 2.8. The apparent dips in reflectivity observed in all of the reflectivity curves are due to water absorptions. Note that over time, mirror surfaces and coatings can become damaged, leading to a decrease in reflectivity. In particular, the Newport 1.35 μm mirrors suffered a large decrease in reflectivity over time, from 99.975% to 99.945%, as illustrated in Figures 2.8c and 2.8d. To avoid this phenomenon in the future, care must be taken to keep the mirrors as clean as possible to avoid the need for repeated washings.

Conversely, the Los Gatos 2.8 μm mirrors' reflectivity increased with repeated washings, from 99.97% in 2006 to 99.98% in 2011. This is a direct result of cleaning the mirrors carefully and purging the mirrors properly to avoid any contamination during experiments. Thus, one should not be afraid to clean the mirrors when necessary.

Table 2.3. Summary of cavity ringdown mirror specifications

Manufacturer	Los Gatos 2.8 μm	Los Gatos 1.32 μm	Newport 1.35 μm
Peak Reflectivity	99.975%	99.985%	99.975%
Mirror Center	3300 cm^{-1}	7590 cm^{-1}	7280 cm^{-1}
Mirror Range	2900–3800 cm^{-1}	7100–8000 cm^{-1}	6900–7800 cm^{-1}

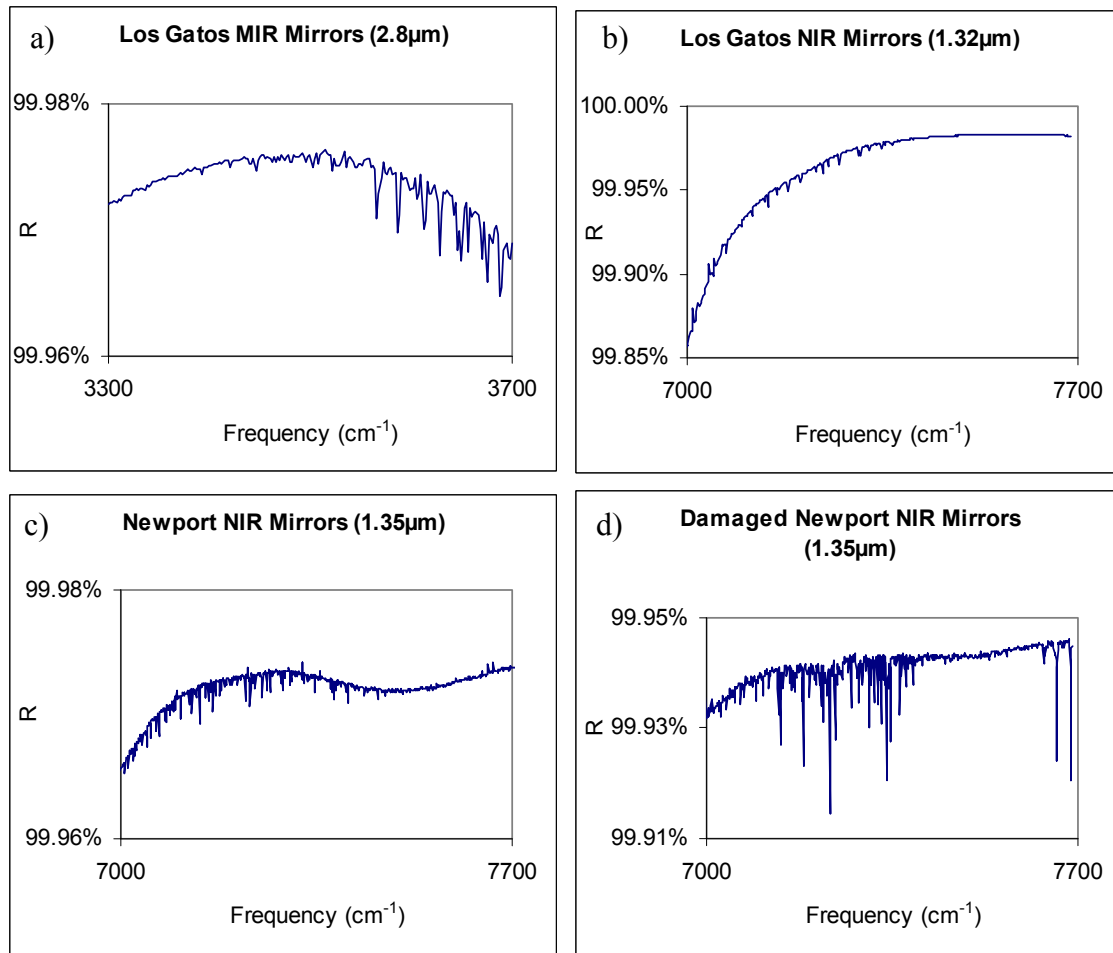


Figure 2.8. Reflectivity curves for the cavity ringdown mirrors used in this thesis: Los Gatos mirrors centered at 2.8 μm (a), Los Gatos mirrors centered at 1.32 μm (b), Newport mirrors centered at 1.35 μm (c), and damaged Newport mirrors centered at 1.35 μm (d). The apparent dips in reflectivity are due to absorptions by water.

It is not practical to simply use the most reflective mirrors available in the apparatus. As the mirror reflectivity increases, the ringdown lifetime also increases, which should result in the ability to fit larger amounts of data, increasing the effectiveness of the spectrometer. However, the relationship between mirror reflectivity and ringdown amplitude in Equation 2.9 also needs to be considered:

$$V_0 = \mathfrak{R} \times A \times \frac{(1-R)^2 c E_{IR}}{L} (X). \quad (2.9)$$

If the mirror reflectivity (R) is too high, then not enough light will be able to enter the cavity, and the peak ringdown voltage (V_0) will become too small to detect. It is therefore important to choose mirrors with a high enough reflectivity to create large ringdown times, while simultaneously transmitting enough light to be detected.

It is also important to consider the detector's responsivity (\mathfrak{R}) and amplification (A) when choosing mirrors. If \mathfrak{R} and A are large, then smaller signals can be detected, and more highly reflective mirrors can be used. However, one should not simply choose a detector with the highest \mathfrak{R} and A available. As the detector's amplification increases, the detector bandwidth will decrease. If the bandwidth is too small, then the recorded ringdowns will be distorted. Typically, the bandwidth of the detector must be greater than $5/\tau$ in order to avoid this effect. For our experiments, the minimum acceptable detector bandwidth is approximately 3 MHz.

Sensitivity of the CRDS Apparatus

In theory, the exact ringdown lifetime can be calculated given knowledge of the mirror reflectivity, absorber concentrations, and absorbance cross sections. In practice, small changes in cavity length, mirror alignment, sample composition, and imperfect ringdown fitting cause a statistical scatter in measured ringdown lifetimes. The size of this statistical scatter can be used to determine the minimum detectable absorbance, via Equation 2.6:

$$A = \frac{L_{opt}}{c} \left(\frac{1}{\tau} - \frac{1}{\tau_0} \right). \quad (2.6)$$

Suppose a large number of ringdowns are collected and fit at a particular wavelength.

The ringdown times have an average value $1/\tau_0$ and standard deviation σ_{1/τ_0} . The relative standard deviation (labeled as $\Delta\tau/\tau$) is given by Equation 2.13:

$$\frac{\sigma_{1/\tau_0}}{1/\tau_0} = \frac{\Delta\tau}{\tau}. \quad (2.13)$$

For the experiments in this thesis, the minimum detectable absorbance (A_{\min}) corresponds to 2 standard deviations in absorbance (σ_A), or

$$A_{\min} = 2\sigma_A = \frac{2L_{opt}}{c} \left(\frac{\Delta\tau}{\tau} \right) \left(\frac{1}{\tau_0} \right). \quad (2.14)$$

It can be observed that $\Delta\tau/\tau$ generally remains constant regardless of the ringdown lifetime τ_0 . Thus, $\Delta\tau/\tau$ can be considered a wavelength-independent measure of spectrometer performance. Additionally, $\Delta\tau/\tau$ should behave statistically with respect to the number of averaged ringdowns per trace (N):

$$\frac{\Delta\tau}{\tau} \propto \frac{1}{\sqrt{N}}. \quad (2.15)$$

Equation 2.14 also reveals one other key idea: A_{\min} is proportional to $1/\tau_0$. This means that the sensitivity of our apparatus will decrease if the reference ringdown time is too small. It is therefore important to keep the background $1/\tau_0$ small by choosing precursor chemicals with small absorbances in the spectral region being measured.

The MIR setup typically had a $\Delta\tau/\tau$ of 0.4% (16 shots averaged) with the Los Gatos 2.8 μm mirrors, leading to a minimum detectable absorbance of 2.6 ppm $\text{Hz}^{-1/2}$. The NIR setup typically had a $\Delta\tau/\tau$ of 0.2% (16 shots averaged) with the Los Gatos 1.32 μm mirrors, leading to a minimum detectable absorbance of 0.8 ppm $\text{Hz}^{-1/2}$. It was observed

that increasing the fitting window from 40 μs to 80 μs was the most important factor in reducing $\Delta\tau/\tau$, likely because the baseline for the ringdown is better defined. However, further increases to the fitting window will not improve $\Delta\tau/\tau$. At longer times than 80 μs , the ringdown trace will fall below the detector noise level.

Calibration of Spectrometer Frequency

Spectroscopic measurements are of limited value without precise knowledge of the frequency of light being used. In general, a spectrometer must provide some means of determining the wavelength of light being used. There are two approaches to this calibration: external equipment to verify the frequency of light being used, or measurement of internal standard compounds within the spectrometer. Many spectrometers make use of atomic lamp absorptions as a means of externally measuring the dye laser frequency.^{50, 51} This technique is sufficient for Raman shifter setups, since the dye laser light and the Raman shift of H_2 are the only factors determining the wavelength of the IR light. However, the atomic lamp technique is not acceptable when using an OPA, because the frequency of the light from the YAG also affects the final IR wavelength. If the YAG is not precisely at 532 nm, then the calculated and actual IR frequencies out of the OPA will be different.

Rather than attempt to simultaneously measure the frequencies YAG and dye laser light, we measure the spectra of known absorbers within our cavity ringdown spectrometer in order to determine the frequency of IR light. A numerical readout on the dye laser indicates the position of its diffraction grating. By measuring well-known spectroscopic bands, we observe that the relationship between the numerical readout and

the wavelength of light produced is constant (within 0.1 cm^{-1} , the linewidth of the dye laser). Two different, stable (i.e., nonradical) absorbers are required for each setup (OPA, Raman). By using two separate absorbers, we are able to calibrate the absolute position as well as the dye laser motor step size.

For the OPA setup (2.7–3.7 μm), we used the $2\nu_2$ band of formaldehyde (3471.7 cm^{-1})^{52, 53} and the ν_1 band of water (3657 cm^{-1})⁴⁰ to calibrate the spectrometer. The calibration was confirmed by measuring band positions of H_2O_2 ($\nu_1=3609 \text{ cm}^{-1}$, $\nu_5=3618 \text{ cm}^{-1}$) and *n*-butanol ($\nu_1=3675 \text{ cm}^{-1}$).⁴⁰ For the Raman shifter setup (1.2–1.4 μm), we used the $2\nu_1$ band of methanol (7199 cm^{-1})⁴⁰ and the $\nu_1+4\nu_4$ band of HCHO (7374 cm^{-1}).^{52, 53} The calibration was confirmed by the A-X electronic transition of HO_2 (7029.4 cm^{-1}).^{54, 55}

Conclusions

We have installed and characterized a pulsed laser photolysis-cavity ringdown spectrometer in order to study the spectroscopy and kinetics of atmospherically relevant chemical species. Tunable infrared light is generated using an optical parametric amplifier (2.7–3.7 μm) or a Raman shifter (1.2–1.4 μm), pumped by pulsed Nd:YAG and dye lasers. Photolysis of the chemical reactants is achieved by sending light from an excimer laser through the cavity ringdown cell. The instrument is capable of measuring absorptions as low as $2.6 \text{ ppm Hz}^{-1/2}$ (mid-IR) or $0.8 \text{ ppm Hz}^{-1/2}$ (near-IR), with a time resolution of 5 μs . The spectrometer has been calibrated along its frequency axis by measuring known spectroscopic bands. With the spectrometer verified to be in good

operating condition, we now turn our attention to the specific chemical systems discussed in Chapter 1.

Acknowledgements

We thank Eva R. Garland and Todd L. Fuelberth for construction of the OPA stage, Andrew K. Mollner for installation of the excimer laser and gas lines, David J. Robichaud for LabVIEW programming, Dave Natzic for machining the ends of the Raman shifter, Rick Gerhart and Mike Roy for construction of the gas kinetics cells, and Ralph H. Page for improvements to the optical setup. The apparatus described in this chapter were funded under NASA Upper Atmosphere Research Program Grants NAG5-11657, NNG06GD88G, and NNX09AE21G2, California Air Resources Board Contract 03-333 and 07-730, and a Department of Defense National Defense Science and Engineering Graduate Fellowship (NDSEG).

Part 2—Quantum Chemistry Studies of Peroxynitrous Acid
(HOONO)

The work presented in Part 2 of this thesis (Chapter 3) has been published as part of our theoretical paper on torsion-torsion coupling and vibrational spectroscopy of HOONO. Reproduced in part with permission from McCoy et al.⁴³ Copyright 2010 American Chemical Society.

Chapter 3—A 3-Dimensional Potential Energy Surface and Dipole Moment Surface for Modeling the Torsion-Torsion Coupling in cis-cis HOONO

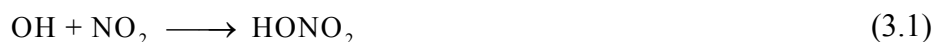
Abstract

The reaction of the hydroxyl radical (OH) with the nitrogen dioxide radical (NO_2) can form one of two products: peroxyxynitrous acid (HOONO), or nitric acid (HONO_2). Because HOONO is a temporary reservoir for OH and NO_2 , while HONO_2 is a permanent reservoir, the branching ratio of these two reaction channels is atmospherically significant. Previous experiments have measured the OH-stretch cavity ringdown spectra of HOONO and HONO_2 formed from $\text{OH} + \text{NO}_2$ to assess the branching ratio. However, the torsional modes of HOONO are coupled to the OH-stretch, leading to a series of sequence bands that complicate the OH-stretch spectrum. These sequence bands must be accounted for in order to obtain a quantitatively correct branching ratio. This chapter describes a 3-dimensional potential energy surface and dipole moment surface for HOONO to study the torsion/torsion coupling to the OH stretch. Geometries and energies were computed at the CCSD(T)/cc-pVTZ level of theory and basis, as a function of the HOON and OONO dihedral angles and the OH bond length. Dipole moments were then calculated at the CCSD/aug-cc-pVDZ level of theory and basis. The resulting surfaces were used to compute the wavefunctions, energies, and two simulated spectra of HOONO: the OH stretch spectrum, and the HOON and OONO torsional spectrum. These data were used in conjunction with the previous cavity ringdown spectra to obtain the true branching ratio for the two channels of $\text{OH} + \text{NO}_2$, and to make assignments in the matrix spectrum of HOONO.

Introduction

The reaction of the hydroxyl radical (OH) with nitrogen dioxide (NO₂) is a very important reaction in the troposphere. As stated in Chapter 1, HO_x and NO_x radicals catalyze tropospheric ozone formation, causing air pollution and health hazards. Both OH and NO₂ are formed from industrial and automotive emissions: OH from the oxidation of methane, and NO₂ directly from combustion engine and industrial plant emissions.¹⁻³ Because of the large impact on air quality, it is important to understand how OH and NO₂ will react with each other in the atmosphere.

Until thirty years ago, it was assumed that OH + NO₂ formed only nitric acid (HONO₂).^{56, 57} However, Robertshaw et al. noticed that their data did not fit to a single termolecular falloff curve. They suggested the possibility of two reaction pathways, one of which was a “weakly bound state.”¹³ Spectroscopic studies by Lee (matrix IR) identified this product as peroxyxynitrous acid (HOONO).⁵⁸⁻⁶¹ Thus, there are two reaction pathways for OH + NO₂:



The geometry and energetics of HOONO has been determined by many theoretical and experimental studies.^{12, 16, 42, 43, 62-72} The ground state of HOONO is bound by 19.6 kcal mol⁻¹ below the dissociation limit to OH + NO₂. In contrast, HONO₂ is 47.2 kcal mol⁻¹ below the dissociation limit (Figure 3.1).¹²

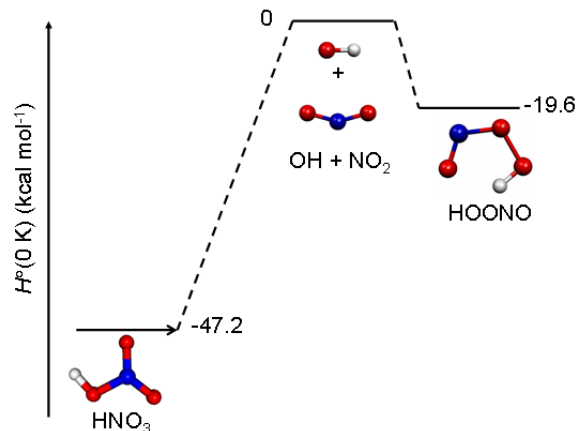


Figure 3.1. Potential energy surface for OH + NO₂. From Mollner et al.¹² Reprinted with permission from AAAS.

HOONO exists as three conformers: cis-cis, cis-perp, and trans-perp (Figure 3.2). The labels cis, perp, and trans refer to HOON and OONO dihedral angles of 0°, 90°, and 180° respectively. Of the three conformers, cis-cis HOONO is the most stable, 3 kcal mol⁻¹ lower than the trans-perp conformer.⁷⁰ The energy stabilization of the cis-cis conformer arises from the internal hydrogen bond formed between the terminal H and O atoms. While the cis-cis and trans-perp conformers have been located numerous times in theoretical studies, the existence of the cis-perp conformer is still debated. Depending on the level of theory, the cis-perp isomer is either a local minimum that supports at least one bound state,⁴² or is simply a shelf along the potential energy surface that does not support any bound states, but will have increased wavefunction amplitude.⁶⁸

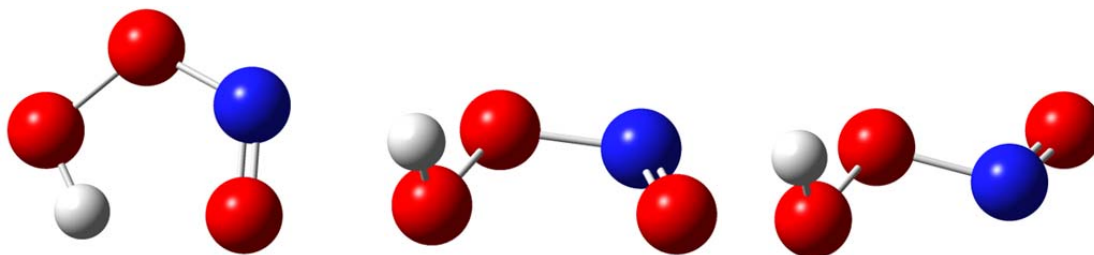


Figure 3.2. The three conformers of HOONO: cis-cis (left), cis-perp (center), and trans-perp (right).

Because HOONO is so weakly bound, the question arises as to whether HOONO formation is atmospherically relevant. Initial spectroscopic studies used Fourier transform infrared (FTIR) spectroscopy, and could not detect HOONO, leading to the conclusion that HOONO was not atmospherically important.⁷³ In the last decade, more sensitive gas phase experiments have been performed, utilizing cavity ringdown spectroscopy (CRDS) to directly detect the OH stretch fundamental^{12, 15} and overtone spectra,^{14, 42, 74} and action spectroscopy to detect the OH stretch overtone spectra.^{67, 68, 70, 75, 76} These experiments have detected gas phase HOONO in both the cis-cis and trans-perp conformers. Additionally, Li et al. were able to observe the cis-perp conformer using a pulsed supersonic expansion. The abundance of positive gas phase detections leads to the conclusion that HOONO is likely formed in the atmosphere.

The fate of HOONO in the atmosphere is very different than HONO₂. Because HOONO is weakly bound, it will rapidly dissociate back to OH + NO₂. This means that HOONO acts as a temporary sink for HO_x and NO_x. In contrast, HONO₂ is very strongly bound, and acts as a permanent sink for HO_x and NO_x. Knowing the amount of HOONO formed will give us a better understanding of the HO_x and NO_x budgets, and will allow us to refine our atmospheric models. We therefore are interested in determining the branching ratio (α) of the two channels of Reactions 3.1 and 3.2, defined as

$$\alpha(T, p) = \frac{k_{HOONO}(T, p)}{k_{HONO_2}(T, p)}. \quad (3.3)$$

The most recent experiment to evaluate Equation 3.3 was performed by Mollner et al.¹² This experiment used laser induced fluorescence (LIF) measurement of OH disappearance to obtain the overall rate constant for OH + NO₂, and CRDS measurements

of cis-cis HOONO and HONO₂ to obtain $\alpha(298K,p)$. The CRDS measurements made use of the OH stretch spectra of both species (cis-cis HOONO at 3306 cm⁻¹, and HONO₂ at 3551 cm⁻¹). It should be noted that typical OH stretch frequencies are found in the range 3500–3700 cm⁻¹. The large red shift in OH stretch frequency for cis-cis HOONO arises from the internal hydrogen bond.^{15, 42} The branching ratio was then calculated by using the integrated CRDS peak intensities:

$$\alpha(298K,p) = \frac{\int \text{Abs}_{\text{HOONO}}}{\int \text{Abs}_{\text{HONO}_2}} \times \frac{\sigma_{\text{HONO}_2}}{\sigma_{\text{HOONO}}}, \quad (3.4)$$

where $\frac{\sigma_{\text{HONO}_2}}{\sigma_{\text{HOONO}}}$ is taken from high level calculations (CCSD(T)/ANO).¹⁶

The one remaining problem with the kinetic analysis presented so far is that the OH stretch normal mode in cis-cis HOONO is coupled to the HOON and OONO torsional modes. This coupling arises from the internal hydrogen bond: the same hydrogen bond that is responsible for HOONO's large red shift in the OH stretch frequency. As the HOON or OONO dihedral angles increase (due to excitation of the two torsional normal modes), the internal hydrogen bond breaks, and the OH stretch frequency will increase. The end result is the formation of sequence bands in the spectrum. A sequence band of a transition is defined as the same change in energy quanta as the fundamental transition, but with the initial molecule not in the ground state. For example, the fundamental transition of the OH stretch is defined as

$$(n_{\text{OH}} = 0, n_{\text{HOON}} = 0, n_{\text{OONO}} = 0, \dots) \rightarrow (n_{\text{OH}} = 1, n_{\text{HOON}} = 0, n_{\text{OONO}} = 0, \dots). \quad (3.5)$$

In Equation 3.5, $\Delta n_{\text{OH}} = 1$, while all of the other normal modes remain in their ground state. One of the possible sequence bands involves a HOONO molecule that starts off

with one quantum of energy in the HOON torsion. The sequence band is therefore defined as

$$(n_{OH} = 0, n_{HOON} = 1, n_{OONO} = 0, \dots) \rightarrow (n_{OH} = 1, n_{HOON} = 1, n_{OONO} = 0, \dots). \quad (3.6)$$

In Equation 3.6, Δn_{OH} is still 1, but the HOON torsion has one quantum of energy in both the initial and final states. Similar sequence bands can be defined for any of the other normal modes, or combinations of the normal modes.

The torsional modes of HOONO have somewhat low frequencies, on the order of 300 cm^{-1} and 500 cm^{-1} for the HOON and OONO modes respectively. At room temperature, significant amounts of HOONO will be torsionally excited, and the OH stretch frequency of these excited molecules will increase. If the OH stretch frequency increases too much, OH stretch intensity will be shifted outside of the main HOONO spectroscopic band, and the simple integration in Equation 3.4 will not account for this intensity. **If the effects of sequence band formation are not explicitly accounted for, the branching ratio calculated from the CRDS experiment will be too low.**

Normal mode coupling also significantly affects the matrix spectrum of Zhang et al.¹⁶ Zhang's experiment measures the HOONO spectrum in the region $400\text{-}1000 \text{ cm}^{-1}$. This spectroscopic region contains the torsional fundamentals, overtones, and combination bands. Because the torsional modes are coupled, assignment of the peaks is not straightforward. Explicitly modeling the coupling between the two normal modes will allow for a more confident assignment of the matrix spectrum.

There have been two previous studies on normal mode coupling in cis-cis HOONO. McCoy et al. examined how the HOON torsional mode coupled to the OH stretch.⁴² Using a CCSD(T)/cc-pVTZ potential energy surface and a HF/aug-cc-pVTZ

dipole moment surface, McCoy determined that 15% of the OH stretch intensity is shifted into sequence bands. Matthews et al. examined how both the HOON torsional mode and HOO bend mode coupled to the OH stretch.⁶⁷ Matthews concluded that the HOO angle had minimal effect on top of the HOON torsional motion. Both studies examined the minimum energy path (MEP), allowing all other degrees of freedom to relax. Until our current work,⁴³ no studies have examined how the OONO torsional mode couples to the OH stretch. Since this mode will also break the internal hydrogen bond, we expect that it is necessary to explicitly account for this mode in order to accurately account for sequence band formation.

This thesis chapter presents a 3-dimensional potential energy surface and dipole moment surface for HOONO, as a function the OH bond length, the HOON dihedral angle, and the OONO dihedral angle. The shape of the potential energy surface and minimum energy path is analyzed to determine the extent of the coupling. Our potential energy surface will allow us to assess whether cis-perp conformer of HOONO exists as a shelf or as a local minimum. The energy levels and wavefunctions (calculated by Professor Anne McCoy) are then used to predict the sequence band positions and intensities in the OH stretch spectrum, and to predict the torsional fundamental and overtone spectrum.⁴³ The sequence bands are used to derive a correction factor for Mollner's calculated branching ratio.¹² The simulated torsional spectrum allows us to propose assignments for Zhang's matrix spectrum.¹⁶

Methods

Our main goals for this study are to obtain the OH stretch spectrum and the torsional spectrum for cis-cis HOONO. In order to obtain these, we need to map out approximately 6000 cm^{-1} of the potential energy surface. This will be enough to simulate the OH stretch spectrum as well as the torsional spectrum. Mapping the surface out this far will also allow us to assess whether the cis-perp conformer of HOONO exists as a local minimum or as a shelf.

All quantum chemistry computations (geometry optimizations, dipole moments) were carried out in Gaussian 98W,⁷⁷ Gaussian 03,⁷⁸ and Gaussian 03W.⁷⁹ We used four single processor, single core, Windows XP PCs (Caltech) and one multiprocessor Unix Beowulf cluster (Ohio State) to perform the calculations. Generation of wavefunctions, energy levels, and transition intensities was performed by Professor Anne McCoy (Ohio State), and will only be briefly discussed in this chapter to put the spectroscopy results into context.

Generation of Potential Energy Surface and Dipole Moment Surface

Our three dimensional potential energy surface was a function of the HOON dihedral angle (τ_{HOON}), the OONO dihedral angle (τ_{OONO}), and the OH bond length (r_{OH}). Our approach adiabatically separated the OH stretch motion from the torsional motion. We allowed τ_{HOON} to vary from 0° to 180° , and τ_{OONO} from 0° to 50° . We then optimized the geometries at each pair of dihedral angles, allowing the remaining degrees of freedom to relax. Geometries were optimized at the CCSD(T)/cc-pVTZ level of theory and basis.⁸⁰⁻⁸³ This level of theory has been used in previous studies of HOONO,⁴² and has

been shown to give results in good quantitative agreement with experiment. We did not directly optimize geometries at this level of theory. To use CPU time more efficiently, the optimizations were carried out in a series of steps. Optimizations were carried out in the order MP2/cc-pVDZ,^{84, 85} CCD/cc-pVDZ, CCSD(T)/cc-pVDZ, and finally CCSD(T)/cc-pVTZ. We then calculated the single point energies at values of r_{OH} of $r_e - 0.15 \text{ \AA}$ to $r_e + 0.25 \text{ \AA}$ in increments of 0.05 \AA , where r_e is the equilibrium OH bond length at each pair of τ_{HOON} and τ_{OONO} , keeping all other degrees of freedom fixed.

We did not optimize every combination of dihedral angles in the range ($0^\circ < \tau_{\text{HOON}} < 180^\circ$, $0^\circ < \tau_{\text{OONO}} < 50^\circ$). Instead, we used an irregular grid of points. More geometries were calculated near the cis-cis HOONO potential minimum, and fewer geometries were calculated at points further away. The rationale for this choice of grid and the convergence of our surface will be explained in the *Results* section.

It was initially unclear what level of theory and basis set were appropriate for calculating the dipole moment surface. Previous calculations were found to have used Hartree-Fock theory, which is woefully inadequate for describing the dipole moment of HOONO.⁴² We performed diagnostic tests on the dipole moment of cis-cis geometry of HOONO, varying r_{OH} from $r_e - 0.30 \text{ \AA}$ to $r_e + 0.30 \text{ \AA}$ in steps of 0.05 \AA , using six levels of theory and basis set combinations: QCISD/cc-pVDZ,⁸⁶ QCISD/aug-cc-pVDZ, QCISD/cc-pVTZ, CCSD/cc-pVDZ, CCSD/aug-cc-pVDZ, and CCSD/cc-pVTZ. As a result of these diagnostic tests (see the *Results* section for details), we calculated the entire dipole moment surface at the CCSD/aug-cc-pVDZ level of theory and basis. The dipole moments were converted into the principal axis coordinates to permit comparison to the previous dipole calculations of McCoy et al.⁴²

Simulation of Spectra

Fitting of the potential energy surfaces, generation of wavefunctions and energy levels, and simulation of the OH stretch and torsional spectra was the work of Professor Anne McCoy (Ohio State). The procedure and results are only briefly summarized here to put the branching ratio correction and torsional spectral assignments into context. A full description of the methods used can be found in the literature.⁴³

The energies obtained from the geometry optimizations were fit to the function

$$V(r_{OH}, \tau_{HOON}, \tau_{OONO}) = \sum_{n=0,2-4} \sum_{m=0}^{23} c_{n,m} y^n f_m(\tau_{HOON}, \tau_{OONO}), \quad (3.7)$$

where

$$y = 1 - \exp[-\alpha \Delta r_{OH}], \quad (3.8)$$

α is a constant, and the f_m are a series of trigonometric functions (sines and cosines) of τ_{HOON} and τ_{OONO} .

The dipoles were converted to an Eckart frame, then fit to the following two equations (for the a/b component and the c component respectively)

$$\mu_{a/b}(r_{OH}, \tau_{HOON}, \tau_{OONO}) = \sum_{n=0}^3 \sum_{m=0}^{23} d_{n,m}^{(a)/(b)} \Delta r_{OH}^n f_m(\tau_{HOON}, \tau_{OONO}), \quad (3.9)$$

$$\mu_c(r_{OH}, \tau_{HOON}, \tau_{OONO}) = \sum_{n=0}^3 \sum_{m=1}^{23} d_{n,m}^c \Delta r_{OH}^n g_m(\tau_{HOON}, \tau_{OONO}), \quad (3.10)$$

where the f_m are the same functions used in Equation 3.7, and the g_m are slightly different trigonometric functions based on the A'' symmetry of the c component of the dipole. These functional forms are then used to solve the Schrödinger equation in two steps: first the one-dimensional equation for the OH stretch, then the two-dimensional equation for the two dihedral angles.

The resulting wavefunctions can be combined with the dipole moment surface to generate the transition moments necessary for simulating the OH stretch spectrum:

$$\vec{\mu}_{\nu_{OH\leftarrow 0}}(\tau_{HOON}, \tau_{OONO}) = \langle \psi_0 | \vec{\mu} | \psi_{OH} \rangle \quad (3.11)$$

Similar equations are used to determine the transition moments for the torsional spectrum.

Results

Although the potential energy surface that we generated is in three dimensions, it is easiest to first consider two dimensions in order to observe the torsion-torsion coupling between the HOON and OONO torsional normal modes. The coupling of the torsional modes to the OH stretch is most easily shown by examination of the sequence bands present in the OH stretch spectrum. Therefore, we present the results in four parts. First, we present the potential energy surface as a function of the two dihedral angles, and comment on the coupling of the two torsional normal modes. Second, we show how the OH stretch potential energy surface varies as a function of τ_{HOON} and τ_{OONO} , indicating that the OH stretch is coupled to both torsional motions. Third, we show the logic behind the choice of the level of theory used for computing the dipole moment surface. Fourth, we present the wavefunctions, energy levels, and OH stretch and torsional spectra (all calculated by Professor McCoy), showing the effects of the coupling between the torsional modes and the OH stretch.

Torsional Potential Energy Surface

The plot of the potential energy surface of HOONO as a function of the HOON and OONO dihedral angles is illustrated in Figure 3.3. This surface makes use of the adiabatic approximation for r_{OH} , assuming that the OH bond length adjusts to its equilibrium value at each point along the surface. The cis-cis conformer of HOONO is located at the center of the plot. The black dots represent the points where geometries were optimized and energies were calculated. The points along the line $\tau_{\text{OONO}} = 0^\circ$ were taken from previously reported calculations.⁴² The grey stars represent the final points calculated, which will become important during the discussion about the choice of points along our irregular grid.

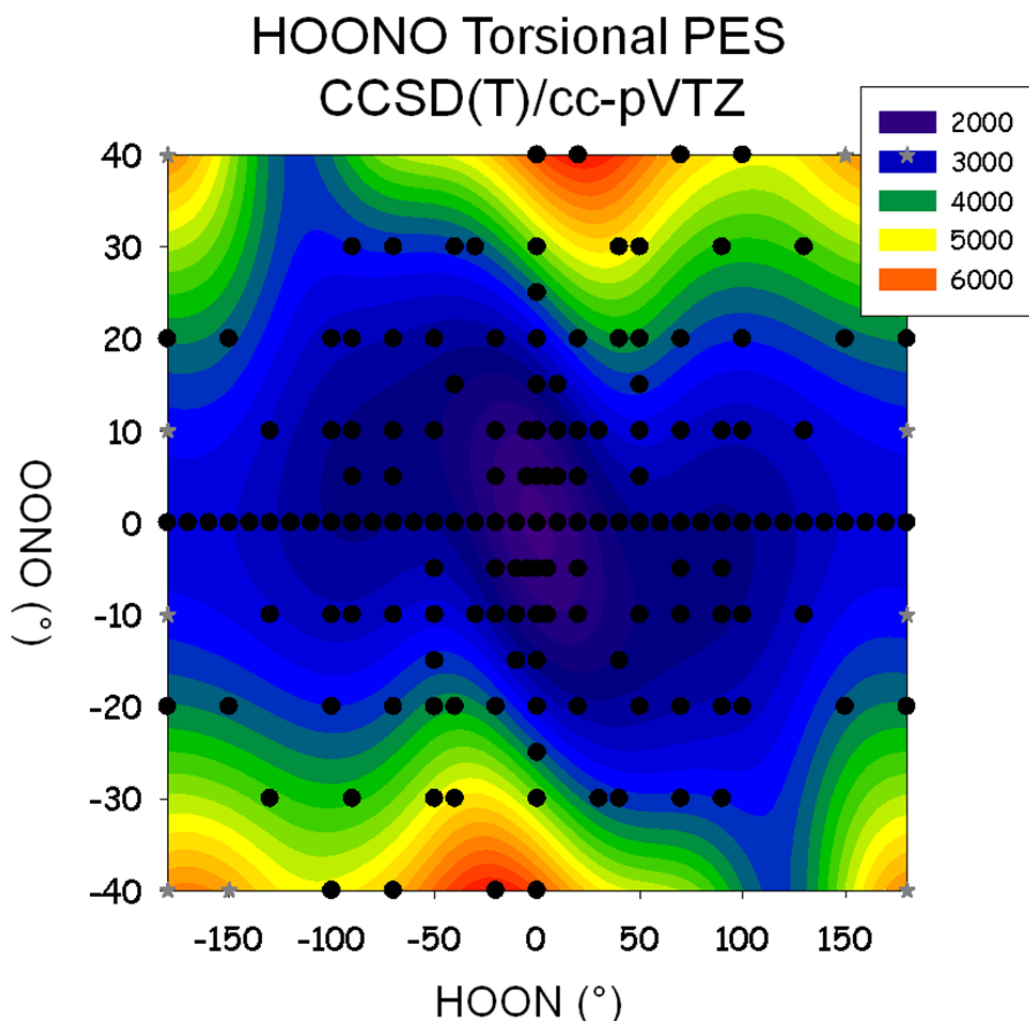


Figure 3.3. Potential energy surface of HOONO as a function of the two torsional angles τ_{HOON} and τ_{ONOO} . All other degrees of freedom were allowed to relax, including the OH bond length (r_{OH}). Energies were computed at selected points on the plot (black and silver dots) the CCSD(T)/cc-pVTZ level of theory and basis. Energies reported in cm^{-1} . Adapted with permission from McCoy et al.⁴³ Copyright 2010 American Chemical Society.

Before describing the shape and features of the potential energy surface, it is worthwhile to discuss the rationale behind the irregular grid of points used, and why this grid gives an accurate result for the PES. The goal of using the irregular grid was to save computational time. A single CCSD(T) geometry optimization took approximately one week of CPU time, whether on one node of Ohio State's Beowulf cluster or on one of our Windows XP computers. Thus, careful selection of points to optimize was critical for

completing this computational study in a reasonable amount of time. More geometries were chosen close to the bottom of the potential energy well (i.e., closer to cis-cis HOONO) to accurately map out the parts of the surface most likely to affect the torsional coupling and the sequence band formation in the OH stretch spectrum. We also chose more points near the cis-perp shelf/potential minimum, in order to accurately assess the contribution of cis-perp HOONO to the spectroscopy of HOONO. Fewer points were chosen outside of the cis-cis and cis-perp regions because the two torsional modes uncouple from each other, making the potential energy surface easier to fit. We did not optimize geometries where the energy would be above 6000 cm^{-1} relative to cis-cis HOONO, as these points would have minimal effect on the simulated spectra.

To evaluate whether the potential energy surface was converging, we performed fits to incomplete surfaces, with each surface containing two to six new points. We then computed the RMS error for the fit, and were satisfied with the number of points on the surface when the RMS error stopped changing. This criterion was satisfied when the final points of the potential energy surface were computed (grey stars on Figure 3.3). Considering all three dimensions (r_{OH} , τ_{HOON} , τ_{OONO}), the RMS error for the potential was 28 cm^{-1} . Along the torsional PES shown in Figure 3.3, the RMS error is an order of magnitude lower, 2.6 cm^{-1} .⁴³ The accurate mapping of the potential well combined with the convergence of the fit to the surface allows us to proceed with our analysis.

There are several features of the torsional potential energy surface that should be noted. The first feature is the shape of the potential energy well near the cis-cis HOONO minimum. The well is off-axis from the HOON and OONO dihedral angles, indicating that the two torsional normal modes involve motions that simultaneously affect both

angles. As the HOONO molecule moves out of the cis-cis well, the two torsions uncouple from each other, and motions along the HOON and OONO dihedral angles are independent from each other. This is most easily seen for $\tau_{\text{HOON}} > 100^\circ$.

Second, we note the large barrier to torsional motion along the OONO axis compared to the HOON axis. The energy difference between cis-cis HOONO and the trans-cis transition state ($\tau_{\text{HOON}} = 180^\circ$, $\tau_{\text{OONO}} = 0^\circ$) is only 1212 cm^{-1} . In contrast, consider a much smaller change in the OONO dihedral angle. The energy difference between cis-cis HOONO and ($\tau_{\text{HOON}} = 0^\circ$, $\tau_{\text{OONO}} = 40^\circ$) is 4202 cm^{-1} . Our potential energy surface indicates that the barrier to the trans-perp region of HOONO is greater than 6000 cm^{-1} , in agreement with previous theoretical and experimental studies.^{42, 67, 68, 70, 75, 76, 87, 88}

Third, our potential energy surface sheds light on the nature of the cis-perp conformer of HOONO. Previous theoretical attempts at locating a stable cis-perp minimum have been unsuccessful.^{16, 65, 67, 68, 74} McCoy et al. are able to find a local minimum for cis-perp HOONO when τ_{OONO} is restricted to 0° .⁴² However, because of this restriction, they note that they “do not ascribe too much significance to the predicted depth (or lack) of the well”. Our potential energy surface is a superset of McCoy’s surface, allowing us to determine the nature of the cis-perp minimum that they calculated. The cis-perp minimum observed in McCoy’s study does not lie along the minimum energy path (MEP) out of the cis-cis HOONO potential energy well. Rather, for a dihedral angle of $\tau_{\text{HOON}} = 90^\circ$, the minimum energy occurs near $\tau_{\text{OONO}} = -5^\circ$ (not 0°). Furthermore, our surface indicates that along our MEP, there is no local minimum at

$\tau_{\text{HOON}} = 90^\circ$; rather, the potential energy surface forms a shelf. Based on our potential energy surface, the cis-perp conformer of HOONO cannot be isolated.

Despite the lack of a local minimum at $\tau_{\text{HOON}} = 90^\circ$, we do not conclude that cis-perp HOONO is spectroscopically unimportant. Our surface is in agreement with previous theoretical studies: the potential energy surface has a shelf near $\tau_{\text{HOON}} = 90^\circ$. As will be shown in the *Wavefunctions* section, the potential energy shelf will give rise to a buildup of wavefunction intensity in the torsionally excited states of HOONO. We would therefore expect cis-perp character to be present in the experimental spectra, in agreement with the action spectroscopy experiments.⁷⁶

Comparison of CCSD(T) and B3LYP Torsional Potential Energy Surface

Figure 3.4 shows the 2D torsional potential energy surface of HOONO calculated at B3LYP/6-31+G(d,p) (left) and CCSD(T)/cc-pVTZ (right). B3LYP energies were calculated with regular spacing, $\Delta\tau_{\text{HOON}} = 10^\circ$, $\Delta\tau_{\text{OONO}} = 10^\circ$. The contour scales for both plots are equal (4000 cm^{-1} range), so the colors correspond to the same energies relative to cis-cis HOONO.

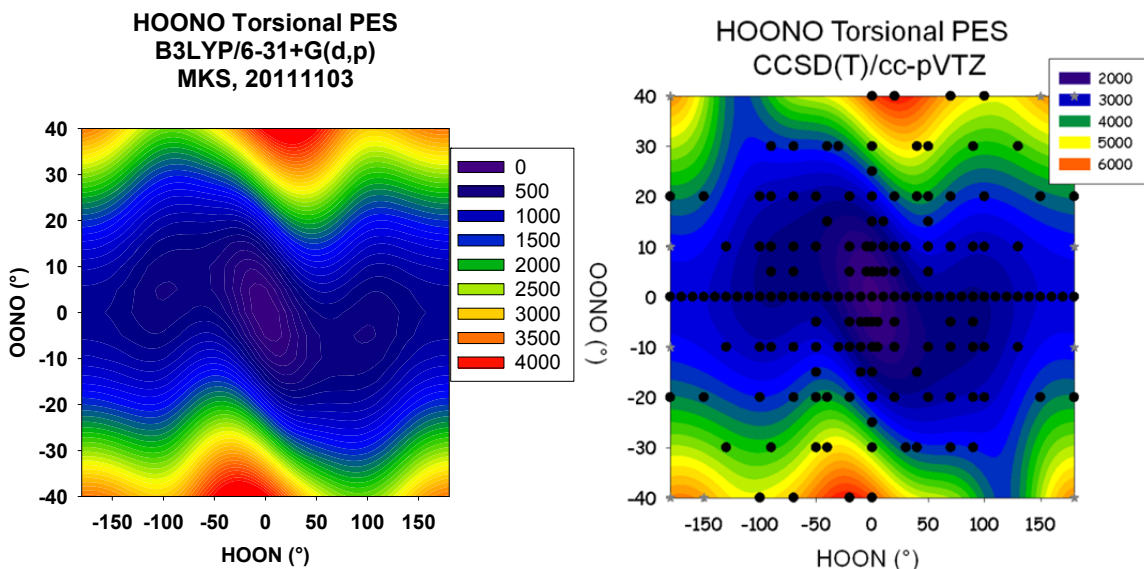


Figure 3.4. Potential energy surface of HOONO as a function of the two torsional angles τ_{HOON} and τ_{OONO} . Left: B3LYP/6-31+G(d,p). Right: CCSD(T)/cc-pVTZ.⁴² All other degrees of freedom were allowed to relax, including the OH bond length (r_{OH}). Energies on the B3LYP surface were calculated at regular intervals ($\Delta\tau_{\text{HOON}} = 10^\circ$, $\Delta\tau_{\text{OONO}} = 10^\circ$). Energies on the CCSD(T) surface were computed at selected points on the plot (black and silver dots). All energies reported in cm^{-1} . Right panel adapted with permission from McCoy et al.⁴³ Copyright 2010 American Chemical Society.

We note two features of interest when comparing the two potential energy surfaces. First, the potential energy well is more off-axis in the lower level B3LYP calculation than in the higher level CCSD(T) calculation, indicating that the two methods disagree with respect to the strength of mode coupling. Second, the barriers to the trans-perp region at $(100^\circ, -40^\circ)$ and $(-100^\circ, 40^\circ)$ are higher in the B3LYP calculation (2000 cm^{-1}) than in the CCSD(T) calculation (1000 cm^{-1}). This is likely an artifact in the CCSD(T) calculation due to the choice of points in the irregular grid.

It is useful to compare the qualitative features of our CCSD(T) potential energy surface to lower levels of theory, as done in Figure 3.4. There has been recent interest in the energetics and spectroscopy of ROONO molecules,⁸⁹⁻⁹⁴ and potential future studies may include hydroxylated ROONO (HOROONO). Similar to HOONO, torsional

coupling may play a significant role in the energetics and spectroscopy of HOROONO, and explicit modeling of the torsional potential energy surfaces will be necessary to obtain accurate energy levels and simulated spectra. Depending on the size of the R group, it may become too computationally expensive to perform CCSD studies, and quantum chemists will be limited to lower levels of theory. The surfaces in Figure 3.4 show that the qualitative features of torsional mode coupling can be reproduced at lower levels of theory. However, the differences in the extent of coupling will produce quantitatively different energy levels and infrared spectra. It may be worthwhile to perform a systematic study to determine the minimum level of theory and basis required to obtain an accurate description of HOONO and HOROONO energetics.

OH Stretch Potential Energy Surface

As stated earlier, we calculated an OH stretch potential for each geometry on the torsional potential energy surface. Rather than present all of the OH stretch potentials in this section, we choose a few potential energy slices that illustrate how the OH stretch motion is coupled to the two torsional motions. The easiest way to do this is to compare the OH stretch potential at the cis-cis minimum to two other points: one with $\tau_{\text{HOON}} > 0^\circ$, and one with $\tau_{\text{OONO}} > 0^\circ$.

Figure 3.5 shows plots of $V(r_{\text{OH}}) - V(r_e)$ vs $r_{\text{OH}} - r_e$ for three pairs of dihedral angles: ($\tau_{\text{HOON}} = 0^\circ$, $\tau_{\text{OONO}} = 0^\circ$) (a), ($\tau_{\text{HOON}} = 90^\circ$, $\tau_{\text{OONO}} = 0^\circ$) (b), and ($\tau_{\text{HOON}} = 0^\circ$, $\tau_{\text{OONO}} = 40^\circ$) (c). Each plot shows the potential over the range $-0.15 \text{ \AA} < r_{\text{OH}} - r_e < 0.25 \text{ \AA}$. Additionally, all three potential energy slices are shown overlaid on each other, with the minimum of each potential energy slice set to 0 cm^{-1} (d).

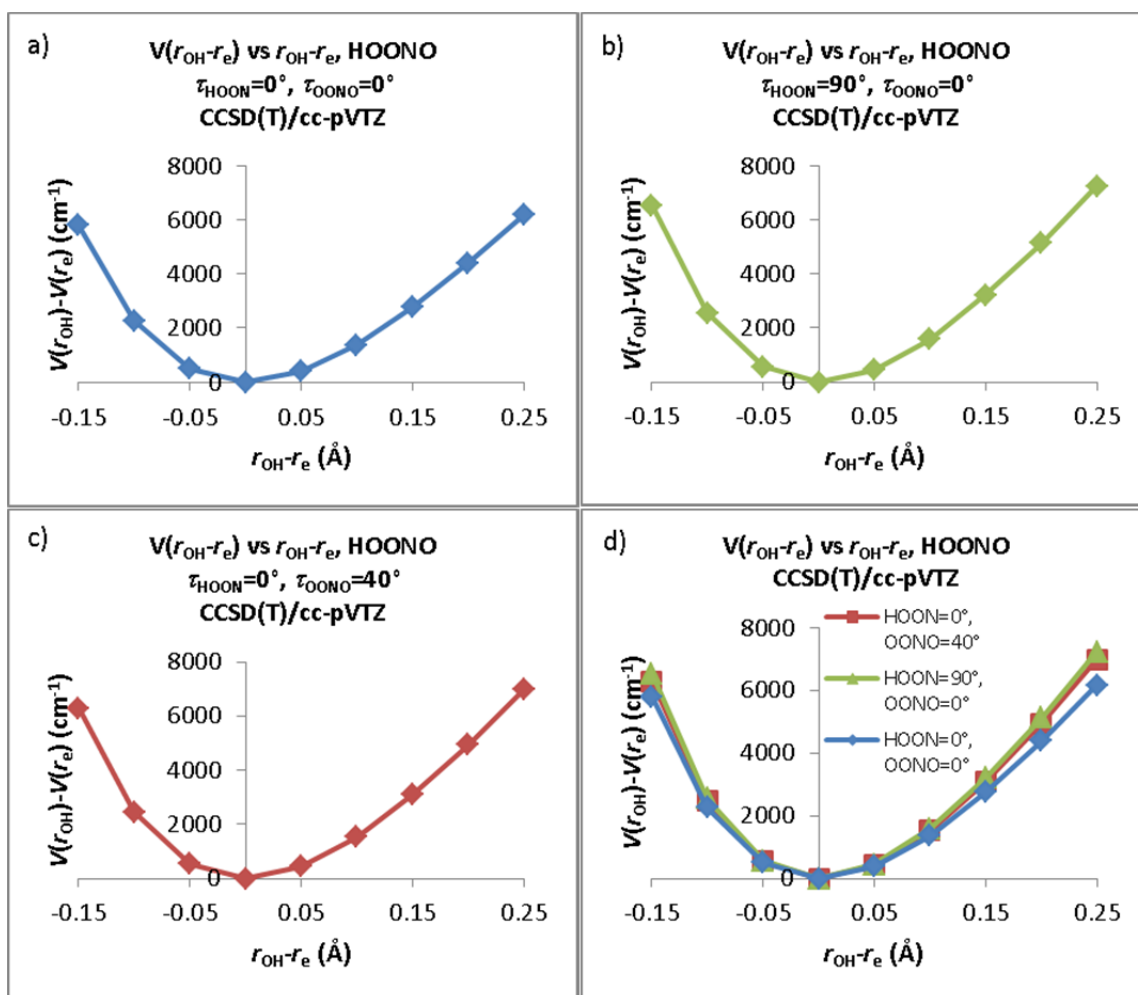


Figure 3.5. Potential energy of HOONO (in cm^{-1}) vs OH bond length change ($r_{\text{OH}} - r_e$) for three sets of dihedral angles: ($\tau_{\text{HOON}} = 0^\circ$, $\tau_{\text{OONO}} = 0^\circ$) (a), ($\tau_{\text{HOON}} = 90^\circ$, $\tau_{\text{OONO}} = 0^\circ$) (b), and ($\tau_{\text{HOON}} = 0^\circ$, $\tau_{\text{OONO}} = 40^\circ$) (c). In part d, all three plots are overlaid, with the minima of each plot set to 0 cm^{-1} . Energies were calculated at the CCSD/cc-pVTZ level of theory and basis.

Figure 3.5d allows us to analyze the curvature of each potential energy surface, and determine how increasing the two dihedral angles will affect the OH stretch. We notice that an increase in either of the dihedral angles causes the potential energy well to become narrower. This is due to the internal hydrogen bond in cis-cis HOONO breaking. The end result would be an increase in OH stretch frequency, in agreement with the

physical picture of HOONO built up over the last decade. While previous work showed that the HOON torsion was coupled to the OH stretch, we show that the OONO torsion also couples to the OH stretch (Figures 3.5c and 3.5d), and should be explicitly accounted for when modeling torsional coupling.

Calculation of the Dipole Moment Surface

In contrast to the potential energy surface described above, the 3-dimensional dipole moment surface reported in this thesis is not a superset of the 2-dimensional surface in McCoy's 2005 paper. The reason for this was that McCoy's dipole moments were actually calculated at a lower level of theory (HF/aug-cc-pVTZ) than reported in their paper (QCISD/aug-cc-pVTZ).⁴² We eventually decided to recalculate the entire dipole moment surface at CCSD/aug-cc-pVDZ.

Before discussing the logic that went into choosing the level of theory for our surface, it is instructive to go through how we determined that the dipoles were being calculated incorrectly. There were two pieces of evidence that showed how the original dipole surface was incorrectly calculated. First, we took two of the original Gaussian 03 input files used for McCoy's 2005 paper and changed only the level of theory for the dipole calculation: HF, QCISD, QCISD(T), CCSD, and CCSD(T). The two files only differed by basis set (cc-pVTZ and aug-cc-pVTZ). Table 3.1 shows the resulting dipole moments from these calculations. **Each calculation for a given basis set yields the same dipole moment, independent of the level of theory.** This result is clearly absurd: the electronic properties of the molecule change as a function of the level of theory, and therefore the electric dipole should also change. The problem is that the previous input

files did not include the `Density=Current` keyword, which indicates that the QCISD or CCSD wavefunctions should be used in calculation of molecular properties.⁷⁷ Without this keyword, the HF wavefunction is instead used. Therefore, the previously reported dipole surface used the Hartree-Fock dipoles. As will be shown later in this section, this level of theory is inadequate for describing the dipole surface.

Table 3.1. Dipole moments for HOONO with $\tau_{\text{HOON}} = 70^\circ$, $\tau_{\text{OONO}} = 20^\circ$, $r_{\text{OH}} = r_e - 0.15 \text{ \AA}$, calculated without the `Density=Current` keyword

Level of Theory	Basis	μ_x (Debye)	μ_y (Debye)	μ_z (Debye)	$ \mu $ (Debye)
HF	cc-pVTZ	0.2609	-0.4355	1.6088	1.6870
QCISD	cc-pVTZ	0.2609	-0.4355	1.6088	1.6870
QCISD(T)	cc-pVTZ	0.2609	-0.4355	1.6088	1.6870
CCSD	cc-pVTZ	0.2609	-0.4355	1.6088	1.6870
CCSD(T)	cc-pVTZ	0.2609	-0.4355	1.6088	1.6870
HF	aug-cc-pVTZ	0.2538	-0.4540	1.5570	1.6416
QCISD	aug-cc-pVTZ	0.2538	-0.4540	1.5570	1.6416
QCISD(T)	aug-cc-pVTZ	0.2538	-0.4540	1.5570	1.6416
CCSD	aug-cc-pVTZ	0.2538	-0.4540	1.5570	1.6416
CCSD(T)	aug-cc-pVTZ	0.2538	-0.4540	1.5570	1.6416

The second piece of evidence that the previous calculations were not run at the reported level of theory comes from unsuccessful attempts to correct the previous calculations. Since the original goal was to run the dipole moment surface at QCISD/aug-cc-pVTZ, we attempted to re-run some of the original dipole files using the `Density=Current` keyword. Each calculation crashed while using this keyword. The reason for this crash was that the QCISD/aug-cc-pVTZ and CCSD/aug-cc-pVTZ calculations require more memory than the 16 GB scratch space limit inherent to the 32-bit version of Gaussian. In contrast, HF/aug-cc-pVTZ does stay within the 16 GB limit, explaining why McCoy's previous calculations did not crash. There are two

solutions to this problem. One would be to run the calculations on a 64-bit version of Gaussian (or another 64-bit computational chemistry package). However, even with access to these programs, QCISD/aug-cc-pVTZ and CCSD/aug-cc-pVTZ are simply too expensive to feasibly use for calculation of our dipole moment surface, given the computing resources available at the time of this study (2006-2008). **This is why we devoted time to the second solution: finding another level of theory and basis at which to compute the dipole moment surface.**

The levels of theory that are within reason for our computing resources are QCISD and CCSD. We do not include perturbative triples (T) for either method because the inclusion of triples makes all of the dipole derivative computations numerical instead of analytic, and therefore too expensive. We have three basis sets that we can examine: cc-pVDZ, aug-cc-pVDZ, and cc-pVTZ. This allows us to determine the effect of adding diffuse and polarization functions, and the effect of triple zeta vs double zeta. We therefore calculate the dipoles using the following six methods (abbreviations listed in parentheses):

- QCISD/cc-pVDZ (Q/D)
- QCISD/aug-cc-pVDZ (Q/aD)
- QCISD/cc-pVTZ (Q/T)
- CCSD/cc-pVDZ (C/D)
- CCSD/aug-cc-pVDZ (C/aD)
- CCSD/cc-pVTZ (C/T)

To ensure that the electronic populations and dipole moments were computed from the correlated wavefunction rather than the SCF wavefunction, the keyword `Density=Current` was used in the route line of the input file. The Cartesian dipoles reported by Gaussian were then transformed into the normal mode coordinates. Dipoles were calculated varying the OH bond length from $r_{\text{OH}} = r_e - 0.3\text{\AA}$ to $r_{\text{OH}} = r_e + 0.3\text{\AA}$, in

steps of 0.05\AA , essentially repeating McCoy's HF/aug-cc-pVTZ (H/aT) calculations.⁴²

By transforming the dipoles into the normal mode coordinates and using these r_{OH} values, we can directly assess whether the dipole moment surface is improved by a higher level of theory. Dipole derivatives at $r_{\text{OH}} = r_e$ were approximated by Equation 3.12:

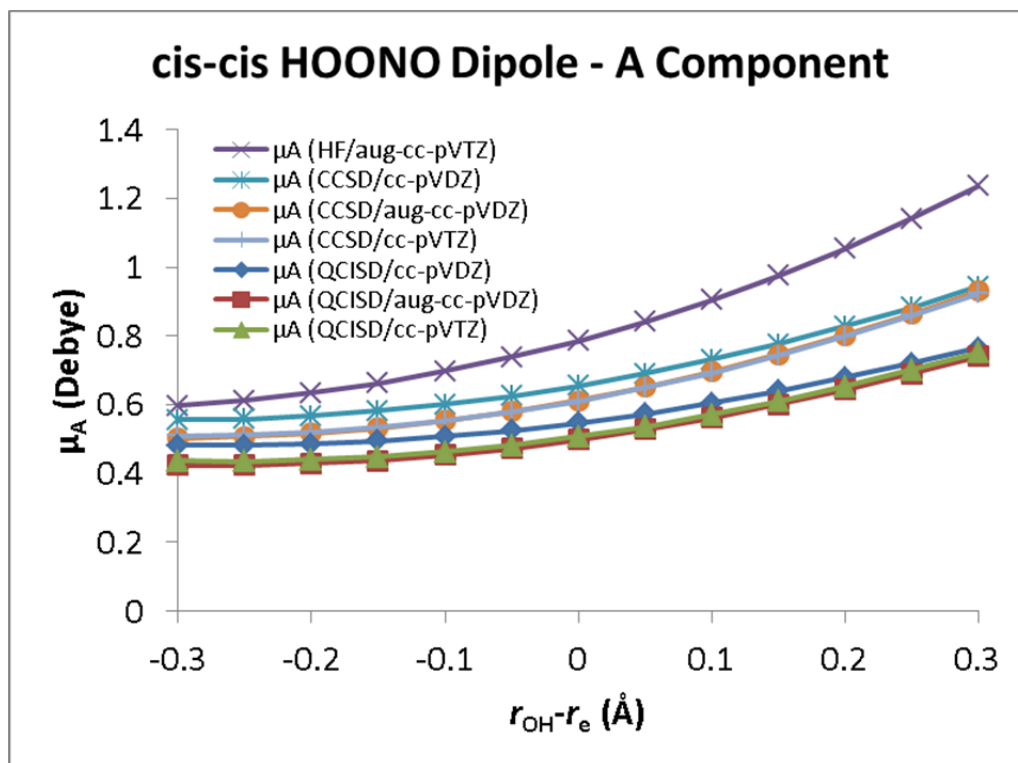
$$\frac{d\mu_i}{dr_{\text{OH}}} \approx \frac{[\mu_{i,r_e+0.05\text{\AA}} - \mu_{i,r_e-0.05\text{\AA}}]}{0.1\text{\AA}}, \quad (3.12)$$

where $\mu_{i,r}$ is the value of the i component of the dipole at $r_{\text{OH}} = r$.

The values of μ_a are tabulated in Table 3.2, and plotted in Figure 3.6. At $r_{\text{OH}} = r_e$, the HF/aug-cc-pVTZ dipole is 58% larger than the QCISD/aug-cc-pVDZ dipole, and 28% larger than the CCSD/aug-cc-pVTZ dipole. Similarly, the HF/aug-cc-pVTZ dipole derivative is twice as large as the QCISD/aug-cc-pVDZ dipole derivative, and 45% larger than the CCSD/aug-cc-pVDZ dipole derivative. Simultaneously, we notice that within the QCISD and CCSD methods, changing the basis set has a much smaller impact on the calculated dipole moments or the dipole derivative. The level of theory is the largest factor in determining the electric dipole properties. Based on the tabulated dipole values, the aug-cc-pVDZ and cc-pVTZ calculations give similar dipole and dipole derivative data at both levels of theory.

Table 3.2. Calculated values of μ_a (debye) for cis-cis HOONO, $r_{\text{OH}} = r_e - 0.3 \text{ \AA}$ to $r_e + 0.3 \text{ \AA}$

$r_{\text{OH}}-r_e$	$\mu_a(\text{Q/D})$	$\mu_a(\text{Q/aD})$	$\mu_a(\text{Q/T})$	$\mu_a(\text{HF/aT})$	$\mu_a(\text{C/D})$	$\mu_a(\text{C/aD})$	$\mu_a(\text{C/T})$
-0.30	0.482	0.424	0.437	0.598	0.556	0.503	0.509
-0.25	0.481	0.424	0.436	0.613	0.559	0.508	0.512
-0.20	0.485	0.429	0.440	0.635	0.568	0.517	0.520
-0.15	0.494	0.438	0.448	0.663	0.582	0.533	0.534
-0.10	0.507	0.453	0.463	0.697	0.601	0.554	0.553
-0.05	0.525	0.473	0.482	0.738	0.625	0.580	0.579
0.00	0.547	0.498	0.507	0.786	0.655	0.613	0.611
0.05	0.574	0.528	0.536	0.841	0.690	0.651	0.649
0.10	0.605	0.562	0.571	0.904	0.731	0.696	0.693
0.15	0.640	0.601	0.611	0.975	0.777	0.746	0.742
0.20	0.679	0.644	0.654	1.054	0.828	0.802	0.798
0.25	0.720	0.691	0.702	1.141	0.883	0.864	0.859
0.30	0.764	0.741	0.752	1.236	0.943	0.931	0.924
$d\mu_a/dr_{\text{OH}}$ (at $r_{\text{OH}}=r_e$)	0.491	0.545	0.545	1.031	0.648	0.711	0.696

**Figure 3.6.** μ_a (Debye) for cis-cis HOONO, for $r_{\text{OH}} = r_e - 0.3 \text{ \AA}$ to $r_e + 0.3 \text{ \AA}$, at seven combinations of level of theory and basis. The HF/aug-cc-pVTZ data are taken from McCoy et al.⁴² The dipole value and dipole derivative are most sensitive to the level of theory, with a slight contribution from changing the basis set. In both the CCSD and QCISD cases, the aug-cc-pVDZ and cc-pVTZ bases give similar results.

Having considered the A component of the dipole, we now turn our attention to the B component. The values of μ_a are tabulated in Table 3.3, and plotted in Figure 3.7. We notice that near $r_{\text{OH}} = r_e$, μ_b is relatively constant across methods compared to the A component (10% difference between the largest and smallest values of μ_b). However, we also notice that the HF/aug-cc-pVTZ dipole derivative is roughly 50% larger than the derivative calculated by other methods. The QCISD and CCSD methods give somewhat similar results. In both cases, the aug-cc-pVDZ dipoles are closer to the cc-pVDZ dipoles at small r_{OH} , and closer to the cc-pVTZ dipoles at large r_{OH} . Additionally, the cc-pVDZ and cc-pVTZ dipole derivatives at $r_{\text{OH}} = r_e$ agree with each other, while the aug-cc-pVDZ derivative is 10% smaller.

Table 3.3. Calculated values of μ_b (Debye) for cis-cis HOONO, $r_{\text{OH}} = r_e - 0.3 \text{ \AA}$ to $r_e + 0.3 \text{ \AA}$

$r_{\text{OH}} - r_e$	$\mu_b(\text{Q/D})$	$\mu_b(\text{Q/aD})$	$\mu_b(\text{Q/T})$	$\mu_b(\text{HF/aT})$	$\mu_b(\text{C/D})$	$\mu_b(\text{C/aD})$	$\mu_b(\text{C/T})$
-0.30	-0.604	-0.596	-0.576	-0.508	-0.626	-0.619	-0.596
-0.25	-0.649	-0.634	-0.617	-0.555	-0.671	-0.658	-0.637
-0.20	-0.692	-0.670	-0.656	-0.602	-0.715	-0.694	-0.677
-0.15	-0.733	-0.704	-0.694	-0.649	-0.756	-0.729	-0.714
-0.10	-0.771	-0.736	-0.730	-0.695	-0.794	-0.762	-0.751
-0.05	-0.806	-0.767	-0.764	-0.741	-0.829	-0.792	-0.785
0.00	-0.837	-0.795	-0.796	-0.787	-0.861	-0.821	-0.817
0.05	-0.866	-0.821	-0.826	-0.833	-0.890	-0.848	-0.848
0.10	-0.892	-0.845	-0.855	-0.880	-0.916	-0.872	-0.876
0.15	-0.915	-0.867	-0.881	-0.929	-0.939	-0.895	-0.902
0.20	-0.935	-0.888	-0.905	-0.979	-0.959	-0.916	-0.927
0.25	-0.953	-0.908	-0.929	-1.031	-0.976	-0.936	-0.950
0.30	-0.969	-0.928	-0.951	-1.086	-0.992	-0.956	-0.972
$d\mu_b/dr_{\text{OH}}$ (at $r_{\text{OH}} = r_e$)	-0.606	-0.541	-0.625	-0.924	-0.611	-0.552	-0.630

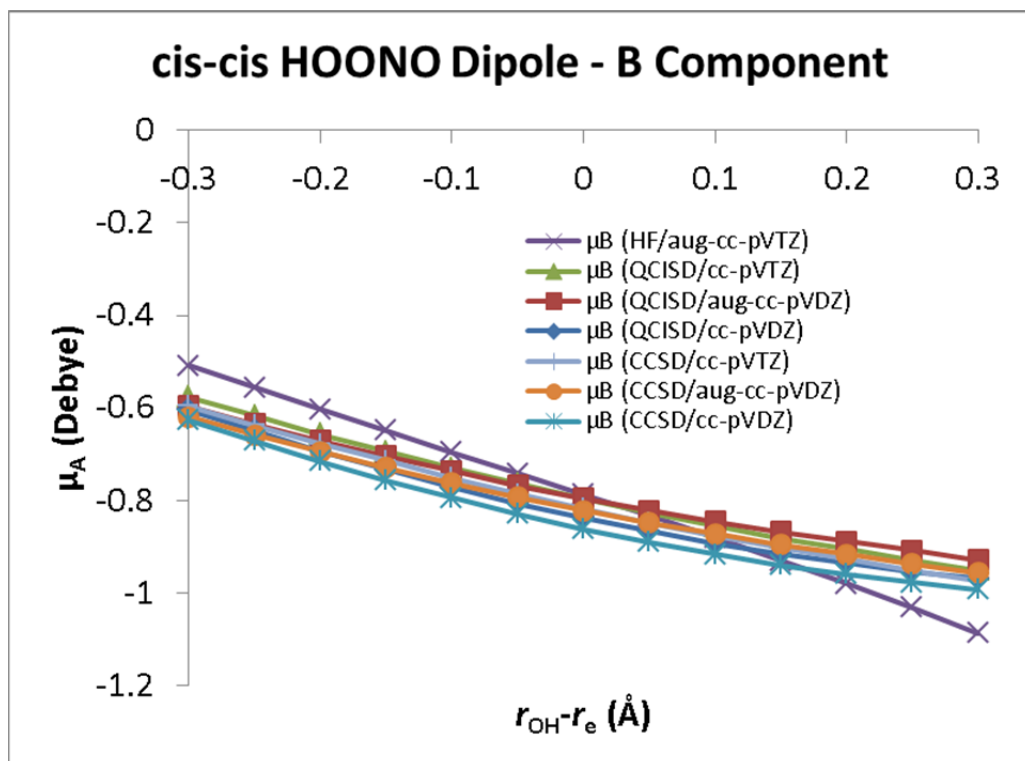


Figure 3.7. μ_b (Debye) for cis-cis HOONO, for $r_{\text{OH}} = r_e - 0.3 \text{ \AA}$ to $r_e + 0.3 \text{ \AA}$, at seven combinations of level of theory and basis. The HF/aug-cc-pVTZ data are taken from McCoy et al.⁴² The dipole value and dipole derivative are sensitive to both the level of theory and basis set. The HF-aug-cc-pVTZ dipole derivative is larger than any of the other methods. The QCISD and CCSD methods produced dipole components in relatively good agreement with each other, although the dipole derivatives for the aug-cc-pVDZ calculations were 10% lower than the cc-pVDZ and cc-pVTZ calculations.

We are able to select an appropriate method for calculating the dipole moment surface by considering the dipole moment data in Tables 3.2 and 3.3, and Figures 3.6 and 3.7. We first note that the HF/aug-cc-pVTZ dipole components do not qualitatively or quantitatively agree with the higher levels of theory (CCSD, QCISD). While the QCISD and CCSD plots of μ_A and μ_B vs r_{OH} are roughly the same shape across all basis sets, the HF plots show a much steeper slope, and therefore a larger dipole derivative. Additionally, the absolute magnitudes of the HF dipoles differ from the QCISD and CCSD dipoles: across the entire plot for the A component, and for small and large r_{OH} for the B component. **For these reasons, we therefore conclude that the HF/aug-cc-pVTZ**

dipole surface used by McCoy et al. is inadequate for modeling the spectroscopy of HOONO.

Next, consider the effect of changing the basis set. For both the A and B dipole components, increasing the basis beyond cc-pVDZ changes the dipole moment values and dipole derivative. This indicates that we have to use a larger basis set than cc-pVDZ. The dipole magnitude and dipole derivative for the A component is basically unaffected by choosing aug-cc-pVDZ or cc-pVTZ. The same does not hold true for the B component. Near $r_{\text{OH}} = r_e$, the dipole magnitudes are roughly equal. However, the dipole derivatives are different: cc-pVTZ gives a dipole derivative equal to cc-pVDZ, while aug-cc-pVDZ is lower by 10%. It is likely that the extra flexibility of the augmented basis set (polarization and diffuse functions) is necessary to model HOONO, especially given the change in the B component of the dipole as these functions are added. **We therefore choose to use the aug-cc-pVDZ basis set to model our dipole moment surface.**

The final consideration is whether to use QCISD or CCSD. CCSD is generally considered to be a more accurate level of theory than QCISD;⁹⁵ however, CCSD is also more computationally expensive. Given our computational resources, if the CCSD surface would take too long to calculate, we would be left with no choice but to use QCISD. Gaussian Inc. does not allow us to make any timing data public as part of our license agreement. What we can state is that the CCSD calculations were more expensive than the QCISD calculations by about a factor of 2, and that this factor did not put the CCSD calculations out of our reach. **Therefore, we chose to run the dipole moment surface at CCSD/aug-cc-pVDZ.**

Wavefunctions

Figure 3.8 shows the first 8 wavefunctions obtained from the torsional potential energy surface. The states are denoted as $(n_{\text{HOON}}, n_{\text{OONO}})$, representing the number of quanta of energy in each torsional mode. Each plot shows the potential energy surface contours from Figure 3.3 underneath the wavefunctions. There are two key features of these wavefunctions to note. First, the wavefunctions confirm the observations we made from the potential energy surface regarding the torsional mode coupling. The wavefunctions are off-axis near the bottom of the potential well, giving us another indication of the coupling between the two torsional modes. This is illustrated best in the ground state, $(1, 0)$, and $(0, 1)$ wavefunctions. As we move away from the potential minimum, the wavefunctions move back to being on-axis, representing the uncoupling of the normal modes due to breaking of the internal hydrogen bond. This is best illustrated in the $(4, 0)$ and $(5, 0)$ wavefunctions. Second, we notice a buildup of wavefunction intensity in the cis-perp region for many of the excited states: $(2, 0)$, $(3, 0)$, $(4, 0)$, $(5, 0)$, and $(1, 1)$. The large amount of intensity indicates that these states will have cis-perp character, despite the fact that there is no cis-perp minimum on our surface, supporting the experimental studies that indicate the spectroscopic importance of the cis-perp conformer.

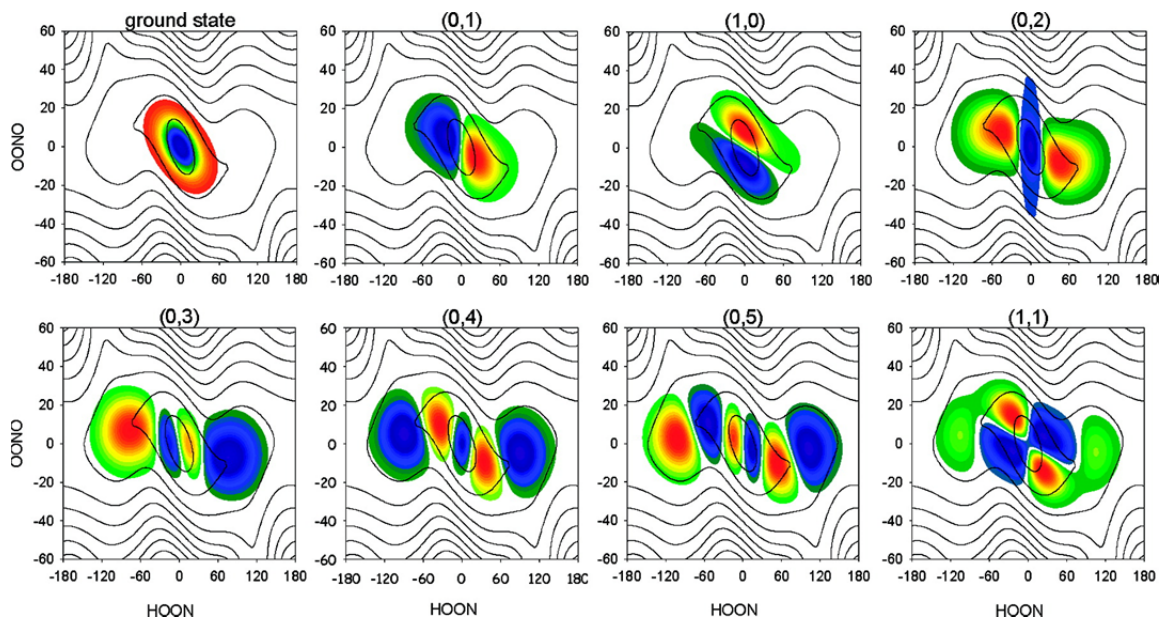


Figure 3.8. Wavefunctions for the 8 lowest energy torsional states of HOONO overlaid on the potential energy surface from Figure 3.3. The labels for each wavefunction are of the form $(n_{\text{HOON}}, n_{\text{OONO}})$, representing the quanta of energy in each torsional mode. Near the potential energy minimum, the wavefunctions are off-axis, indicating coupling between the two torsional modes. Further from the potential energy minimum, the wavefunctions return to being on-axis, indicating decoupling of the two torsional modes. The (2, 0), (3, 0), (4, 0), (5, 0), and (1, 1) states show a buildup of wavefunction intensity in the cis-perp region ($\tau_{\text{HOON}} = 90^\circ$, $\tau_{\text{OONO}} = 0^\circ$). Reprinted with permission from McCoy et al.⁴³ Copyright 2010 American Chemical Society.

Discussion

Simulated OH Stretch Spectra (Fundamental, Overtone)

Simulations of the OH stretch spectra of HOONO based on our 3-dimensional potential energy surface were carried out by Professor Anne McCoy.⁴³ The results are shown here to illustrate the effects of using our new potential energy surface and dipole moment surface. Figure 3.9 shows two simulations for the fundamental spectrum (left) and first overtone spectrum (right). The black lines are the spectra obtained using the 3-dimensional PES and dipole moment surface presented in this chapter. The blue lines are

the spectra obtained from a reduced (2-dimensional) potential energy surface, varying τ_{HOON} , and letting τ_{OONO} relax along the minimum energy path.

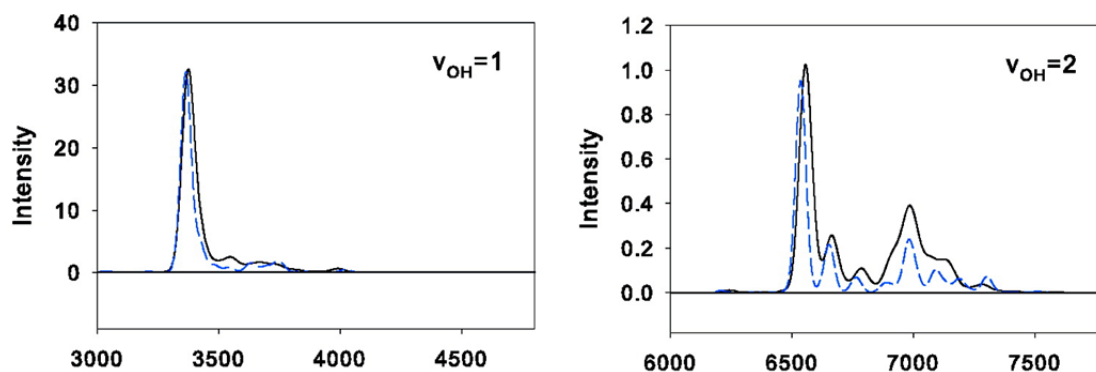


Figure 3.9. Calculated OH stretch spectra for HOONO based on our CCSD(T)/cc-pVTZ potential energy surface (Figure 3.3) and our CCSD/aug-cc-pVDZ dipole moment surface. The fundamental is shown in the left panel, while the first overtone is shown in the right panel. Spectra are convoluted with a 60 cm^{-1} Gaussian. Black line: fit to full 3-dimensional surfaces. Blue line: reduced dimensionality (2-dimensional, minimum energy path as a function of τ_{HOON}). Sequence band intensity is observed in all spectra, with significant intensity observed in the overtone spectrum. Reprinted with permission from McCoy et al.⁴³ Copyright 2010 American Chemical Society.

We note the following key features of the spectra in Figure 3.9. First, significant OH stretch intensity is found in sequence bands, roughly the same fraction whether the 2-dimensional or 3-dimensional PES is used. However, the shape of the sequence band spectrum is different between the two surfaces. This is most apparent in the overtone spectrum (right panel of Figure 3.9). Second, a greater fraction of intensity is found in the sequence bands for the overtone spectrum compared to the fundamental spectrum. This is a direct result of accessing the cis-perp shelf in the overtone spectrum. Third, the reduced dimensionality treatment (blue line) underestimates the fraction of intensity in the sequence bands. This illustrates the point that explicitly accounting for τ_{OONO} is necessary to develop an accurate picture of HOONO spectroscopy.

Torsional Spectrum

On the basis of our 2-dimensional potential energy surface (τ_{HOON} , τ_{OONO}) shown in Figure 3.3, we can simulate the pure torsional spectrum of HOONO and DOONO. In Figure 3.10, we compare our simulated torsional stick spectra (bottom) to the matrix IR spectra of HOONO (left) and DOONO (right) of Zhang et al.¹⁶ Zhang's band assignments are marked on their matrix spectra. Since our potential energy surface only is a function of τ_{HOON} and τ_{OONO} , we only obtain ν_9 (ν_{HOON}) and ν_8 (ν_{OONO}) transitions; the simulated spectra do not contain any ν_4 , ν_5 , ν_6 , or ν_7 lines. Previous work has shown that the $\nu_8 + \nu_9$ intensity is equal to the ν_4 intensity.¹⁶ We have scaled the matrix and calculated spectra to reflect this.

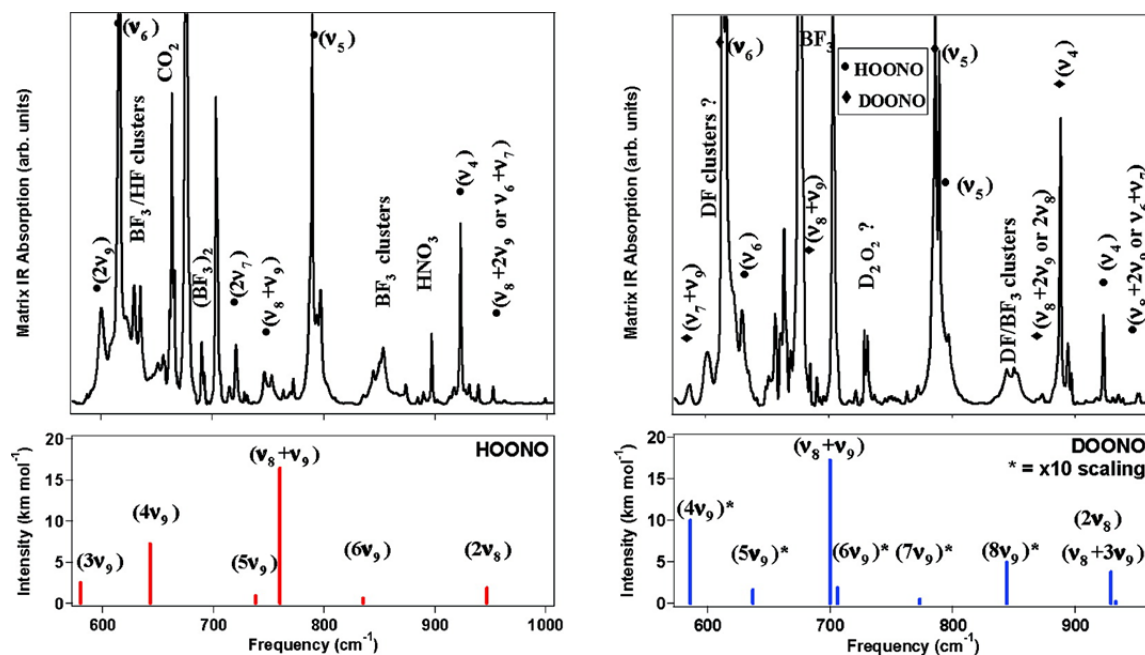


Figure 3.10. Simulated torsional spectrum (bottom) and experimental matrix spectra (top)¹⁶ for HOONO (left) and DOONO (right). The simulated spectra are based off of our CCSD(T)/cc-pVTZ potential energy surface (Figure 3.3), and only contain transitions involving ν_9 (ν_{HOONO}) and ν_8 (ν_{DOONO}). Zhang's assignments are marked on the matrix spectra. The matrix spectra have been scaled so that the calculated $\nu_8+\nu_9$ frequency is equal to the observed ν_4 frequency.¹⁶ Transitions marked with an asterisk have been scaled up by a factor of 10 to improve visibility. Reprinted with permission from McCoy et al.⁴³ Copyright 2010 American Chemical Society.

While many of the simulated bands fall within dense clusters of other peaks, we can suggest two reassignments based on our simulated spectra. First, Zhang et al. assign their HOONO band at 601 cm^{-1} to $2\nu_9$ on the basis of VPT2 calculations.¹⁶ Our simulated spectra suggest that this band should be assigned to $3\nu_9$ (calculated from our PES at 580 cm^{-1}). Second, we suggest that the observed DOONO band at 950 cm^{-1} arises from a combination of $2\nu_8$ and $\nu_8+3\nu_9$, two states that heavily mix.⁴³ It is unlikely that these bands arise from $\nu_8+2\nu_9$ as assigned by Zhang *et al.* because of the large difference between the calculated frequency (863 cm^{-1}) and observed band (950 cm^{-1}). It is more likely that Zhang's assignment of their peak at 870 cm^{-1} to $\nu_8+2\nu_9$ is correct.

Correction factor to $\alpha(p,298K)$

One of the goals of our study was to determine the extent to which sequence band formation would affect spectroscopic measurements of the OH + NO₂ branching ratio (Reactions 3.1 and 3.2). As stated in the Introduction, any HOONO intensity that is in its sequence bands will not be accounted for, and [HOONO] will be underestimated. To correct for this, we modify Equation 3.4 to reflect our interpretation of the CRDS experiment:

$$\alpha(298K,p) = \frac{\int_{3250 \text{ cm}^{-1}}^{3400 \text{ cm}^{-1}} A_{HOONO} d\bar{\nu}}{\int_{3480 \text{ cm}^{-1}}^{3620 \text{ cm}^{-1}} A_{HONO_2} d\bar{\nu}} \times \frac{\sigma_{HONO_2}}{\sigma_{HOONO}} \times K_{CRDS} \times K_{seq,3400,298K}, \quad (3.13)$$

where K_{CRDS} corrects for nonlinearities in the measured absorbances,³⁰ and $K_{seq,3400,298K}$ is the correction factor for HOONO sequence band intensity at frequencies above 3400 cm⁻¹ at 298 K. The integral limits are the same limits used by Mollner et al. in their experiment.³⁰

On the basis of the OH stretch fundamental spectrum in Figure 3.9, we determine 17% of the HOONO intensity to be in sequence bands at frequencies greater than 3400 cm⁻¹. This value is slightly greater than McCoy's value of 15% based on their 2-dimensional potential energy surface:⁴² another indication that inclusion of the OONO torsional mode in our theoretical treatment of HOONO impacts the derived energy levels, spectroscopy, and interpretations of experiments. We therefore set $K_{seq,3400,298K} = 1.17$, and use this value for Mollner's calculation of $\alpha(298 \text{ K}, p)$.³⁰

Conclusions

In this chapter, we have reported a 3-dimensional potential energy surface at the CCSD(T)/cc-pVTZ level of theory and basis and a 3-dimensional dipole moment surface at the CCSD/aug-cc-pVDZ level of theory and basis for peroxyxynitrous acid (HOONO). These surfaces are functions of the two torsional modes (ν_{HOON} , ν_{OONO}) and the OH stretch mode (ν_{OH}). Significant coupling between the HOON and OONO torsions is observed on the torsional potential energy surface near the cis-cis minimum. The derived wavefunctions also show coupling near the cis-cis minimum, and considerable intensity buildup near the cis-perp shelf for when energy is placed into the HOON torsion. The simulated vibrational and torsional spectra obtained from our surfaces were used to assess sequence band formation, revise assignments to previous matrix spectra of HOONO, and interpret cavity ringdown spectroscopy measurements of the branching ratio of OH + NO₂.

Acknowledgements

We thank Professor Anne McCoy for fitting of the potential energy surface, calculation of wavefunctions, simulated spectra, and provision of computer time for this project, Sara Ray for patience and assistance with running calculations on the Ohio State server, Andrew Mollner and Markus Keller for initial geometry and energy calculations, Jonathan Chen for installation of Q-Chem on the Okumura group server, and NASA/JPL for provision of computer time for this project. The experiments performed in this chapter were funded under NASA Upper Atmosphere Research Program Grants NAG5-11657, NNG06GD88G, and NNX09AE21G2, California Air Resources Board Contract 03-333

and 07-730, National Science Foundation CHE-0515627, and a Department of Defense National Defense Science and Engineering Graduate Fellowship (NDSEG).

**Part 3—Spectroscopy, Kinetics, and Quantum Chemistry of
the Hydroxymethylperoxy Radical (HOCH₂OO•, HMP)**

Chapter 4—The OH Stretch and A-X Electronic Cavity Ringdown Spectra of the Hydroxymethylperoxy Radical (HOCH₂OO•)

Abstract

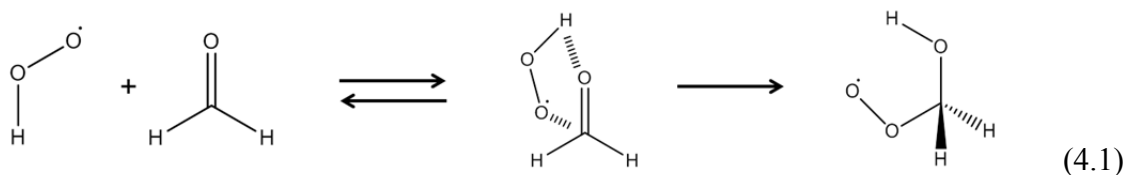
The reactions of HO₂ with carbonyl compounds have been proposed to be a sink for carbonyl compounds in the upper troposphere/lower stratosphere. The reaction of HO₂ with the simplest carbonyl, formaldehyde (HCHO), proceeds at room temperature, and thus serves as a prototype for this class of reactions. HO₂ and HCHO first form a hydrogen bound complex before isomerizing into the hydroxymethylperoxy radical (HOCH₂OO•, or HMP). Considerable uncertainty exists on the reaction rate of HO₂ + HCHO, underscoring the need to find clean spectroscopic bands of HMP. **In this chapter, we report the ν_1 (OH stretch) and A-X electronic cavity ringdown spectra of the HMP radical.** HMP was formed from the reaction of HCHO with HO₂, using Cl₂ photolysis in the presence of HCHO as the HO₂ source. HMP was detected 100 μ s after photolysis. The ν_1 band of HMP is centered at 3622 cm⁻¹ with strong and broad P and R branches. Careful selection of experimental conditions minimizes interference from H₂O₂, HCOOH, and HOCH₂OOH. Rotationally resolved electronic transitions of HMP were detected at 7391 cm⁻¹ (A-X origin), 7561 cm⁻¹ (combination band with the OOCO torsion), 7719 cm⁻¹ (combination band with OOCO torsion overtone), and 7275 cm⁻¹ (hot band of the OOCO torsion). The band assignments are made on the basis of the quantum chemistry calculations presented in Chapter 5, and the observed positions are in excellent agreement with the predicted values.

Introduction

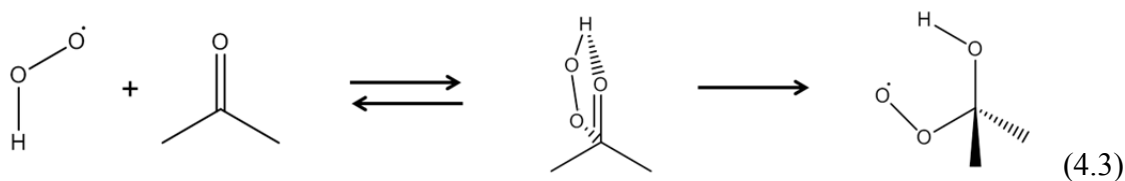
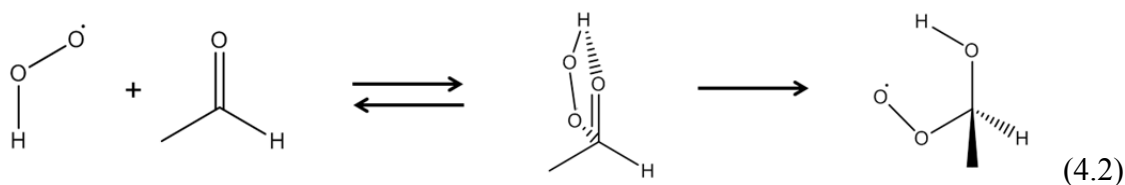
The reactions of the hydroperoxy radical (HO_2) with carbonyl compounds ($\text{RC(=O)R}'$) are interesting and important from both an atmospheric chemistry perspective as well as a chemical physics perspective. More than 30 years of experimental^{17, 23-26, 96-103, 18, 104-107} and theoretical studies^{19-22, 107-112} on this class of reactions have been performed. The basic picture that has evolved is that these reactions become more important at reduced temperatures; in other words, the rate of these reactions increases as temperature decreases. In the Upper Troposphere/Lower Stratosphere (UTLS), a boundary between atmospheric layers with temperature of 200–220 K, the reactions of HO_2 with carbonyl compounds are believed to be a major sink for both HO_2 and carbonyl compounds.^{17, 19, 20} Most of the previous studies have focused on the formaldehyde (HCHO), the smallest carbonyl compound.^{17, 21, 24-26, 96, 98-100, 102, 103, 109, 110} More recent studies have examined both acetaldehyde (CH_3CHO) and acetone (CH_3COCH_3).^{19, 20, 22, 23, 97, 108}

The experimental and theoretical studies on $\text{HO}_2 + \text{HCHO}$ paint a consistent picture of the reaction mechanism (Reaction 4.1). All of the experimental studies observe an increase in rate with decreasing temperature. This observation implies that the reaction has a negative activation energy: in other words, an intermediate chemical complex $[\text{HO}_2\cdots\text{HCHO}]$ is formed that is of lower energy than the reactants. Theoretical studies show that the most stable intermediate is formed by two hydrogen bonds, with the hydrogen of HO_2 bound to the carbon of HCHO , and the terminal oxygen of HO_2 bound to a hydrogen on HCHO . For this complex, HO_2 and HCHO lie in the same plane. The best available calculations place this complex $5\text{--}7 \text{ kcal mol}^{-1}$ below the reactants.²¹ The

hydrogen bound complex then isomerizes, with an activation energy that is lower than the dissociation energy of the complex (3–4 kcal mol⁻¹).²¹ The final isomerization product is the hydroxymethylperoxy radical, HOCH₂OO•, or HMP, and is more stable than the complex (-17 kcal mol⁻¹ compared to the reactants).²¹



In contrast to reaction with HCHO, the studies on the reactions of HO₂ with CH₃CHO (Reaction 4.2) and CH₃COCH₃ (Reaction 4.3) do not yet paint a consistent picture. Theoretical studies have identified the most likely candidates for the intermediate complexes and the products. Unlike the HCHO case, both the [HO₂---CH₃CHO] and [HO₂---CH₃COCH₃] complexes are not planar: the HO₂ radical is out of plane from the carbonyl molecule.²²



A far more disturbing departure from the HCHO case is that the theoretical studies have not yet come to a consensus as to whether the isomerization reaction's activation energy is higher or lower than the complex's dissociation energy. This has far reaching consequences: kinetic rate constants cannot be predicted accurately. In fact, the two theoretical studies on HO₂ + CH₃COCH₃ predict rate constants that differ by four

orders of magnitude.^{19, 22} It is therefore unsurprising that to date, nobody has been able to detect the products of either reaction. With such large uncertainties on the reaction's rate constants, it is impossible to predict whether either reaction will be atmospherically relevant. Gierczak et al. examined the reactions of HO₂ with various ketones, and observed rates of reaction at 298 K that are atmospherically insignificant (less than 10⁻¹⁵ cm³ molec⁻¹ s⁻¹).⁹⁷ Recent experimental studies by Grieman et al. suggest that at reduced temperature, reactions of HO₂ with ketones are important; their kinetics data show that the rate of HO₂ disappearance significantly increases in the presence of acetone.²³ Grieman's study cannot yet determine whether this effect can be attributed to a reaction of HO₂ with acetone similar to the reaction of HO₂ with HCHO.

Ideally, we would like to design a highly sensitive experiment that could determine whether or not HO₂ will react with acetaldehyde or acetone, and what the kinetic rate constants will be. In order to choose an appropriate method, it is best to first examine HO₂ + HCHO, a reaction that is known to proceed to completion even at room temperature. The first studies on HO₂ + HCHO by Su et al. in 1979⁹⁹ made use of end-product analysis by FTIR detection of the stable end-products hydrogen peroxide (Reaction 4.4), hydroxymethylhydroperoxide (HOCH₂OOH, or HMHP, Reaction 4.5), formic acid (HCOOH), and methanediol (HOCH₂OH, pathways described by Reactions 4.6–4.9).





By combining end-product measurements with a kinetics model, Su et al. were able to back out a kinetic rate constant for $\text{HO}_2 + \text{HCHO}$ on the order of $10^{-14} \text{ cm}^3 \text{ molec}^{-1} \text{ s}^{-1}$. Their detection of HMHP and HCOOH was a good indication that HMP was being formed. However, the rate constant for formation of HMP was subject to large uncertainties because their rate constant for HMP formation was dependent on every other rate constant in the kinetics model.

Any end-product study of HMP kinetics will suffer from two problems. The first problem is that assumptions must be made regarding individual rate constants entered into the kinetics model. Additionally, important reactions may be missing from the model, or assumed to be negligible. Any errors or uncertainties on the kinetics model being used will lead to a derived rate constant that is incorrect or subject to large errors. The second problem is that no verification of a proposed mechanism can be made. If end-product studies are the only experiments performed, then there is no way to confirm that Reactions 4.1–4.9 actually proceed as proposed.

One way to avoid the additional uncertainties inherent in any end-product analysis is to directly detect the HMP radical. Veyret et al. and Burrows et al. performed two such studies in 1989.^{25, 26} These studies measure the B-X electronic transition of the HMP radical, centered around 230 nm. The observed transition is very broad, structureless, and has a very large width (full width half maximum of approximately 80 nm). All peroxy radicals exhibit this characteristic B-X electronic transition: a very broad peak centered at 220-240 nm. An example of this is shown in Figure 4.1, which contains the B-X spectra

of HO₂ and methyl peroxy. These spectra look qualitatively similar to the B-X spectrum of HMP. Because all peroxy radicals absorb in the same region, it is very difficult to decouple individual spectra from each other. Additionally, many other molecules, such as the end-product HOCH₂OOH, will also absorb in the UV.¹¹³ This may cause further spectral interference.

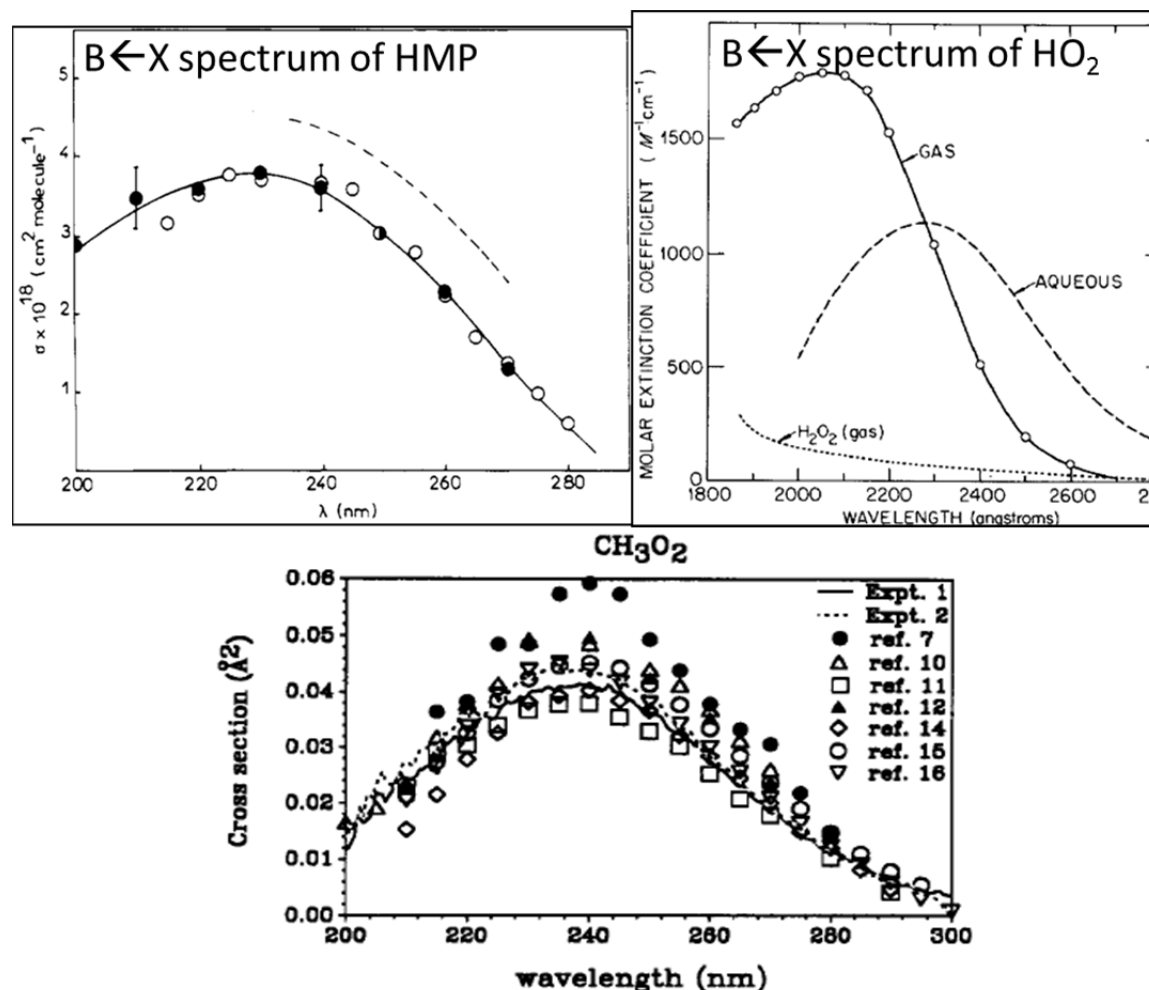


Figure 4.1. B-X spectra of HMP,²⁶ HO₂,³⁵ and CH₃OO.¹¹⁴ All of the spectra exhibit broad absorptions in the region 200-280 nm. HMP B-X spectrum and CH₃OO B-X spectrum are reprinted with permission from Veyret *et al.*²⁶ and Maricq *et al.*¹¹⁴ respectively. Copyright 1989 and 1992 American Chemical Society. HO₂ B-X spectrum reprinted with permission from Hochenad *et al.*³⁵ Copyright 1972, American Institute of Physics.

It is unsurprising that the rate constant of $\text{HO}_2 + \text{HCHO}$ suffers from a somewhat large uncertainty, although far less than for HO_2 and larger carbonyls. Veyret and Burrows report a rate constant for $\text{HO}_2 + \text{HCHO}$ of $k_1 = 7.7 \times 10^{-15} \times \exp[(625 \pm 550) / T]$ $\text{cm}^3 \text{ molec}^{-1} \text{ s}^{-1}$, or $k_1(298 \text{ K}) = (6.3[+33.4, -5.3]) \times 10^{-14} \text{ molec cm}^{-3}$.^{25, 26} The current recommendation by the NASA/JPL kinetics panel recommends a rate constant of $k_1 = 6.7 \times 10^{-15} \times \exp[600 / T]$ $\text{cm}^3 \text{ molec}^{-1} \text{ s}^{-1}$, or $k_1(298 \text{ K}) = 5.0 \times 10^{-14} \text{ molec cm}^{-3}$, with a factor of 5 uncertainty.²⁷ In order to gain a better understanding of important $\text{HO}_2 + \text{carbonyl}$ is in the atmosphere, we must first start by reducing the uncertainty in the rate constant of $\text{HO}_2 + \text{HCHO}$.

Direct spectroscopic detection through bands unique to $\text{HOCH}_2\text{OO}\cdot$ would pave the way to making a more precise measurement of the rate constant of $\text{HO}_2 + \text{HCHO}$ than currently available. Until this point, only the B-X spectrum of $\text{HOCH}_2\text{OO}\cdot$ has been within reach because of its large absorption cross section ($\sigma_{\text{peak}} = 3.5 \times 10^{-18} \text{ cm}^2 \text{ molec}^{-1}$), allowing for ease of detection despite the relatively few $\text{HOCH}_2\text{OO}\cdot$ radicals formed (on the order 10^{13} – $10^{15} \text{ molec cm}^{-3}$).

As described in Chapter 2, our pulsed cavity ringdown spectroscopy (CRDS) can detect absorbances as low as 0.1 ppm, allowing for detection of much weaker bands of these radical species ($\sigma_{\text{peak}} = 10^{-21}$ – $10^{-20} \text{ cm}^2 \text{ molec}^{-1}$). Thus, we are not limited to the UV transitions of HMP, we can search for other spectroscopic bands.

The structure of $\text{HOCH}_2\text{OO}\cdot$ suggests two possible bands to measure: the ν_1 (OH stretch) band located in the mid-IR (3600 – 3700 cm^{-1}), or the A-X electronic band (7000 – 8000 cm^{-1}). Each of these spectroscopic bands carries with it an advantage and a disadvantage. The ν_1 band is typically a broad and relatively strong band, and has been

used in our group for studies of HOONO (Chapter 3) and alkoxy isomerization (Chapters 7–10).^{12, 29-31} For example, the peak cross section of the ν_1 band (P/R branch) of methanol is $6 \times 10^{-20} \text{ cm}^2 \text{ molec cm}^{-1}$.⁴⁰ Although this is a factor of 50 weaker than the B-X transition of HOCH₂OO•, the detection limit of methanol (a similar molecule) using CRDS is only $1.6 \times 10^{12} \text{ molecules cm}^{-3} \text{ Hz}^{-1/2}$. It is relatively easy to generate an equivalent amount of HOCH₂OO• during an experiment. However, the disadvantage to using the ν_1 band is that any molecule containing an OH stretch mode will absorb in the same region as HOCH₂OO•, notably H₂O₂ formed from Reaction 4.4 and HMHP formed from Reaction 4.5. If the initial experimental conditions are chosen improperly or if products are measured at long times after HOCH₂OO• formation, the ν_1 spectrum will become contaminated.

All peroxy radicals have a characteristic A-X electronic transition in the near-IR (7000–8000 cm^{-1}), with the exact position dependent on the structure and functional groups of the peroxy radical.⁴⁴ Smaller peroxy radicals, such as methyl and ethyl peroxy, have a series of sharp band heads representing the electronic origin and combination bands of each conformer of the radical. The bandheads are clearly distinct from each other (i.e., different positions and shapes for HO₂, CH₃OO•, C₂H₅O₂•, etc.), and thus should provide a unique measure of [HOCH₂OO•] over a large range of experimental conditions and times. The main disadvantage is that the A-X bandhead is very weak (for example, $\sigma_{\text{peak}}(\text{C}_2\text{H}_5\text{OO}\bullet, \text{A-X}) = 5.29 \times 10^{-21} \text{ cm}^2 \text{ molec}^{-1}$, giving a detection limit on our CRDS apparatus of $2 \times 10^{13} \text{ molec cm}^{-3} \text{ Hz}^{-1/2}$).¹¹⁵ Thus, a larger [HOCH₂OO•] is required for detection and subsequent kinetics measurements using the A-X band compared to using the ν_1 band.

A final consideration that must be taken into account is the effect of internal hydrogen bonding on the spectra of HOCH₂OO•. Anglada et al. carried out electronic structure calculations on the HO₂ + HCHO potential energy surface, including one conformer of HOCH₂OO•.²¹ Though not explored in the text, the calculated geometry of HOCH₂OO• suggests a weak intramolecular hydrogen bond, with the distance between the OH and OO• groups about 2.5 Å. If there is a hydrogen bond, the effects on HMP spectroscopy must be considered. Our spectroscopic and computational studies on HOONO (Chapter 3) clearly show that internal hydrogen bonding will shift the ν_1 frequency and possibly lead to sequence band formation (defined as ν_1 intensity outside of the main absorption band due to torsional excitation breaking or strengthening the hydrogen bond).⁴³ Furthermore, the hydrogen bond lowers some of the electronic energy levels of HMP, and may therefore have an effect on the A-X transition frequency. Finally, it is possible that not all of the HMP in our experiment will be hydrogen bound; the hydroxyl and peroxy groups can be rotated away from each other to yield conformers without hydrogen bonding. All of the above possibilities may affect the position, width, and intensity of the ν_1 and A-X bands that we seek to measure.

Part 3 of this thesis (Chapters 4–6) describes the cavity ringdown spectroscopy, quantum chemistry, and kinetics of the hydroxymethylperoxy radical (HOCH₂OO•, HMP), the primary isomerization product of the HO₂ + HCHO reaction. This chapter (Chapter 4) describes the first detection of the ν_1 and A-X bands of HMP via cavity ringdown spectroscopy. Similar to previous experiments,^{25, 26} we generate HMP by reaction of HCHO with HO₂, formed through photolysis of Cl₂ in the presence of HCHO and O₂. Cavity ringdown spectroscopy was used to measure the resulting mid-IR and

near-IR spectra over the ranges $3500\text{--}3700\text{ cm}^{-1}$ (ν_1) and $7100\text{--}8000\text{ cm}^{-1}$ (A-X), $100\text{ }\mu\text{s}$ after photolysis. We show in this chapter that under our experimental conditions these bands provide a clean, unique measurement of HMP. The bands are compared to simulated spectra, and the agreement between experiment and simulation helps verify our assignment of the spectra.

The remaining chapters in Part 3 describe electronic structure calculations and kinetics measurements of HMP. 2-dimensional potential energy surfaces, calculated transition frequencies, and an assessment of appropriate levels of theory for calculations of hydroxylated peroxy radicals are presented in Chapter 5. The kinetics of HMP formation and destruction, measured by the ν_1 and A-X bands, are presented in Chapter 6.

Methods

Apparatus and Chemicals

The cavity ringdown spectrometer, laser system, and gas kinetics flow cell have been described in detail in Chapter 2 (Figures 2.5, 2.7, 2.8), and only a brief summary of the mid-IR (MIR) and near-IR (NIR) configurations is presented here.

Tunable MIR light used to measure the ν_1 spectrum was generated using an optical parametric amplifier. For 65 mJ of 532 nm light and $4\text{--}12\text{ mJ}$ of tunable red light ($620\text{--}665\text{ nm}$), $0.6\text{--}0.8\text{ mJ}$ of tunable infrared light was generated ($2900\text{--}3800\text{ cm}^{-1}$). The infrared light was sent into an optical cavity consisting of two highly reflective mirrors (Los Gatos Research, $2.8\text{ }\mu\text{m}$ peak, $R = 99.98\%$). Ringdown traces were collected with a liquid nitrogen cooled InSb detector (Judson J10D-M204-R01M-60) connected to a voltage amplifier (Analog Modules 351A-3) and PC oscilloscope card (GageScope

CS1450). 80 μs of ringdown data were collected per shot, and 16 ringdowns were collected and averaged before being fit. The first eighth of the ringdown lifetime was removed before the data were refit in order to eliminate errors caused from noise near the peak of the ringdown.

Tunable NIR light used to measure the spectrum ($6900\text{--}8500\text{ cm}^{-1}$, $100\text{ }\mu\text{J/pulse}$) was generated by sending the output from a Nd:YAG (532 nm, 370 mJ/pulse) pumped dye laser (DCM, Rh 640, or Rh 610 dye, 590–660 nm, 40 mJ/pulse peak) into a H_2 filled Raman shifter. The infrared light was sent into an optical cavity consisting of two highly reflective mirrors (Los Gatos Research, 1.35 or 1.20 μm peak, $R = 99.98\%$ or 99.99%). Ringdown traces were collected with an amplified InGaAs detector (ThorLabs PDA400) connected to a PC oscilloscope card (GageScope CS1450). 80 μs of ringdown data were collected per shot, and 16 ringdowns were collected and averaged before being fit. The first 1/20 of the ringdown lifetime was removed before the data were refit in order to eliminate errors caused from noise near the peak of the ringdown.

The hydroxymethylperoxy radicals ($\text{HOCH}_2\text{OO}\cdot$, HMP) measured in this experiment were generated by photolysis of Cl_2 in the presence of HCHO and O_2 (Reactions 4.10–4.12 and 4.1). Photolysis was initiated by 351 nm light from the excimer laser described in Chapter 2. The absorption cross section of Cl_2 at 351 nm is $\sigma_{351\text{nm}} = 1.9 \times 10^{-19}\text{ cm}^2\text{ molec}^{-1}$.²⁷ For the MIR experiments, the UV flux was kept at $1.8 \times 10^{17}\text{ molec cm}^{-3}$, resulting in 3.2% of the Cl_2 being photolyzed. For the NIR experiments, the UV flux was kept at $4.4 \times 10^{17}\text{ photons cm}^{-2}$, resulting in 8.0% of the Cl_2 being photolyzed.





Cl_2 was introduced to the cell from a gas cylinder consisting of 3.5% Cl_2 in He (Air Liquide or Matheson Tri-Gas). HCHO was introduced to the cell by flowing N_2 gas through a vessel of paraformaldehyde (Sigma-Aldrich, 95%) heated to 110 °C. Heating paraformaldehyde leads to the formation of HCHO monomers and oligomers. To trap the oligomers, the N_2/HCHO gas was sent to a dry ice/acetone trap before being sent to the CRDS cell. This method was verified to produce a consistent [HCHO] ($\pm 10\%$ between experiments) as measured by the $2\nu_2$ R branch ($3510\text{--}3520\text{ cm}^{-1}$)⁴⁰ and A-X bands (300–310 nm).¹¹⁶

Experimental and Flow Conditions

The majority of ν_1 and A-X spectra were taken at a single set of conditions appropriate for each region. In both regions, [HCHO] was factor of 30–1000 higher than [HO_2], with [HCHO] = 1×10^{17} molec cm^{-3} and [HO_2] = 1×10^{14} molec cm^{-3} (MIR) or 3×10^{15} molec cm^{-3} (NIR). By keeping [HCHO] high, HO_2 is more likely to react with HCHO to form HMP (Reaction 4.1), rather than self-react to form H_2O_2 (Reaction 4.4). Higher [HO_2] was required in the NIR in order to generate the higher [HMP] necessary to detect the weak A-X bands.

The HMP spectra were measured by scanning across a range of frequencies in the MIR ($3520\text{--}3700\text{ cm}^{-1}$, step size 0.2 cm^{-1}) and NIR ($7100\text{--}8000\text{ cm}^{-1}$, step size 0.1 cm^{-1}) while at a constant time after photolysis of Cl_2 (100 μs). Spectra were also recorded at

longer times after photolysis (1000 μ s) under alternate conditions in order to show the formation of end-products.

The experimental conditions for the HMP spectroscopy experiments are summarized in Table 4.1. Gas flows were measured using the flowmeters discussed in Chapter 2. The temperature of the gas kinetics cell was taken to be room temperature: no temperature control of any kind was attempted.

Table 4.1. Experimental conditions (gas flows, photolysis parameters, chemical concentrations, and spectrometer performance) for HMP spectroscopy experiments

	HMP, ν_1 (MIR)	HMP, A-X (NIR)
N ₂ Purge Flow – Left Mirror	450 sccm	450 sccm
N ₂ Purge Flow – Right Mirror	450 sccm	450 sccm
N ₂ /HCHO Flow	250 sccm	250 sccm
3.5% Cl ₂ / He Flow	14 sccm	170 sccm
N ₂ Dilution Flow	1250 sccm	1250 sccm
O ₂ Flow	650 sccm	650 sccm
Cell Pressure	300 torr	330 torr
Temperature (room)	293 \pm 2 K	293 \pm 2 K
Flush Time	30 ms	25 ms
Photolysis Window Length	5 cm	5 cm
Excimer Energy at 351 nm	160 \pm 10 mJ/pulse	160 \pm 10 mJ/pulse
% Cl ₂ Photolyzed	3.2%	8.0%
[Cl•] ₀ ~ [HO ₂] ₀	1 \times 10 ¹⁴ cm ⁻³	3 \times 10 ¹⁵ cm ⁻³
[HCHO]	1 \times 10 ¹⁷ cm ⁻³	1.1 \times 10 ¹⁷ cm ⁻³
[O ₂]	2.0 \times 10 ¹⁸ cm ⁻³	2.2 \times 10 ¹⁸ cm ⁻³
Optical Cell Length	52 cm	52 cm
1/ τ_0 (purge only)	1.3 \times 10 ⁵ Hz, 3638 cm ⁻¹	1.2 \times 10 ⁵ Hz, 7550 cm ⁻¹
1/ τ (background gases)	1.4 \times 10 ⁵ Hz, 3638 cm ⁻¹	1.3 \times 10 ⁵ Hz, 7550 cm ⁻¹
$\Delta\tau/\tau^a$	0.34%	0.28%
Sensitivity (2 σ)	2.1 ppm Hz ^{-1/2}	1.6 ppm Hz ^{-1/2}

a) $\Delta\tau/\tau$ reported for averaging 16 ringdown traces per point

The cell flush time, [Cl₂], and [Cl•] are calculated from the experimental parameters Table 4.1. Derivations of these equations are presented in Chapter 8; therefore,

only the final results are presented here. The flush time is defined as the amount of time to remove the chemicals within the photolysis length from the ringdown cavity, and is calculated from Equation 4.13:

$$t_{flush} = \left(\frac{V_{in-out}}{\sum_{flush} f_i} \right) \times \left(\frac{P_{cell}}{P_{st}} \right), \quad (4.13)$$

where t_{flush} is the flush time for the chemical sample, V_{in-out} is the volume between the inlet for butyl nitrite and vacuum outlet ($V_{in-out} = 3.93 \text{ cm}^3$ for the cell used in these experiments), $\sum_{flush} f_i$ is the total flow rate of gases in the direction of flushing (in sccm), p_{cell} is the pressure in the CRDS cell, and p_{st} is the standard pressure (760 torr).

The fraction of Cl_2 that is photolyzed can be calculated from Equation 4.14:

$$\%_{photolysis} = \frac{\left(\frac{P_{excimer}}{A_{meter}} \right)}{F_{excimer}} \left(\frac{\lambda}{hc} \right) (\sigma_{\text{Cl}_2, \lambda}) (X) \left(\frac{A_{UV, laser}}{A_{UV, CRDS}} \right), \quad (4.14)$$

where $\%_{photolysis}$ is the fraction of RONO that is photolyzed, $(P_{excimer}/A_{meter})$ is the power per unit area of the UV light (read directly from the power meter), $F_{excimer}$ is the rep rate of the excimer laser (10 Hz), h is Planck's constant, c is the speed of light, λ is the wavelength of the excimer light (351 nm), $\sigma_{\text{Cl}_2, \lambda}$ is the absorption cross section of Cl_2 at the excimer wavelength ($1.9 \times 10^{-19} \text{ cm}^2 \text{ molec}^{-1}$ at 351 nm), X is the quantum yield for photolysis (taken to be 1), $A_{UV, laser}$ is the area of excimer beam measured at the excimer laser output, and $A_{UV, CRDS}$ is the area of excimer beam measured at the CRDS cell. For

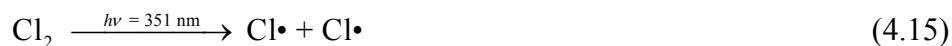
the v_1 experiment, $\frac{A_{UV, laser}}{A_{UV, CRDS}} = 2$. For the A-X experiment, $\frac{A_{UV, laser}}{A_{UV, CRDS}} = 5$.

Results

We present the results of our spectroscopy study in three parts. First, we discuss the chemistry relevant to our experiment following photolysis of the chlorine. Under each set of experimental conditions, we show that after 100 μ s, the majority of products being detected are HMP. Second, we present the ν_1 spectrum at various times after photolysis and $[\text{HO}_2]:[\text{HCHO}]$ ratios. Under our best conditions, we observe a clean HMP ν_1 band centered at 3622 cm^{-1} , with broad P and R branches. Under all conditions, we observe interference from secondary products (HCOOH , H_2O_2 , HOCH_2OOH), though these can be greatly minimized through a judicious choice of starting conditions and measurement time. Third, we present the A-X spectrum of HMP over the range $7100\text{-}8000 \text{ cm}^{-1}$. We observe the origin and many combination/hot bands, assigned on the basis of our quantum chemistry calculations (discussed in detail in Chapter 5). The qualitative shape of the spectrum is similar to methyl peroxy, though relative intensities and band positions are different. In both spectra sections, we compare our experimental spectra to simulated spectra (based on the parameters calculated in Chapter 5). We observe excellent agreement between the experiment and simulation, giving us confidence that we have detected HMP.

Chemistry

Our radical chemistry is initiated by photolysis of Cl_2 with UV light (351 nm, $\sigma_{351} = 1.8 \times 10^{-19} \text{ cm}^2 \text{ molec}^{-1}$).²⁷



Simultaneously, HCHO can also photolyze (Reaction 4.16), although this pathway is minor ($\sigma_{351} = 8.9 \times 10^{-22} \text{ cm}^2 \text{ molec}^{-1}$, $\phi_{16} = 0.35$).²⁷



For our photon fluxes, $(1.8\text{--}4.4) \times 10^{17} \text{ photons cm}^{-2}$, only 0.006%–0.014% of the HCHO will photolyze. For $[\text{HCHO}] = 1 \times 10^{17} \text{ molec cm}^{-3}$, this translates to $(5.6 \times 10^{12}\text{--}1.4 \times 10^{13}) \text{ molec cm}^{-3}$ of HCHO that is photolyzed.

Following photolysis, $\text{Cl}\cdot$ reacts rapidly with HCHO to form HCl and $\text{HCO}\cdot$ (Reaction 4.17, $k_{298\text{K}} = 7.3 \times 10^{-11} \text{ cm}^3 \text{ molec}^{-1} \text{ s}^{-1}$).²⁷ $\text{HCO}\cdot$ then reacts with O_2 to form CO and HO_2 (Reaction 4.18, $k_{298\text{K}} = 5.2 \times 10^{-11} \text{ cm}^3 \text{ molec}^{-1} \text{ s}^{-1}$).²⁷



For $[\text{HCHO}] = 10^{17} \text{ molec cm}^{-3}$, the lifetime of Reaction 4.17 is 0.14 μs . For $[\text{O}_2] = 2 \times 10^{18} \text{ molec cm}^{-3}$, the lifetime of Reaction 4.18 is 10 ns. Therefore, conversion of $\text{Cl}\cdot$ to HO_2 can be considered instantaneous compared to the time resolution of our experiment (empty cavity ringdown lifetime of 8 μs).

The vast majority of $\text{Cl}\cdot$ is converted to HO_2 , the two major side reactions are very slow compared. First, $\text{Cl}\cdot$ can react with O_2 to form $\text{ClOO}\cdot$ (Reaction 4.19, $k_{298\text{K},300\text{torr}} = 2.0 \times 10^{-14} \text{ cm}^3 \text{ molec}^{-1} \text{ s}^{-1}$, lifetime 25 μs).²⁷ Second, $\text{HCO}\cdot$ radicals can react with Cl_2 (Reaction 4.20, $k_{298\text{K}} = 7 \times 10^{-12} \text{ cm}^3 \text{ molec}^{-1} \text{ s}^{-1}$, lifetime 7 μs).¹¹⁷

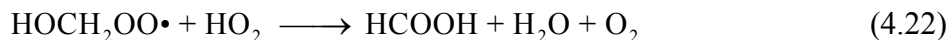


At this point, the HO_2 can undergo one of two reactions: reaction with HCHO to form HMP (Reaction 4.1, $k_{298\text{K}} = 5.7 \times 10^{-14} \text{ cm}^3 \text{ molec}^{-1} \text{ s}^{-1}$, lifetime 175 μs),^{25, 26} or

self-reaction to form H_2O_2 and O_2 (Reaction 4.4, $k_{298\text{K},300\text{torr}} = 2.0 \times 10^{-12} \text{ cm}^3 \text{ molec}^{-1} \text{ s}^{-1}$, initial lifetime 2.5 ms in the ν_1 experiment, 80 μs in the A-X experiment).²⁷ Note that lowering $[\text{HCHO}]:[\text{HO}_2]$ will cause HO_2 self-reaction to be favored. Since H_2O_2 causes spectral interference in the ν_1 experiment, it is crucial to keep $[\text{HCHO}]$ much higher than $[\text{HO}_2]$. Conversely, H_2O_2 does not absorb in the A-X region of HMP, and therefore we do not need to worry about $[\text{HCHO}]:[\text{HO}_2]$.



We now turn our attention to the pathways for HMP destruction. The major pathways for HMP destruction are reaction with HO_2 to form HOCH_2OOH (Reaction 4.21, $k_{298\text{K}} = 7.2 \times 10^{-12} \text{ cm}^3 \text{ molec}^{-1} \text{ s}^{-1}$) or formic acid (Reaction 4.22, $k_{298\text{K}} = 4.8 \times 10^{-12} \text{ cm}^3 \text{ molec}^{-1} \text{ s}^{-1}$), or self-reaction to form either hydroxymethoxy (Reaction 4.23, $k_{298\text{K}} = 5.2 \times 10^{-12} \text{ cm}^3 \text{ molec}^{-1} \text{ s}^{-1}$) or formic acid (Reaction 4.24, $k_{298\text{K}} = 7.0 \times 10^{-13} \text{ cm}^3 \text{ molec}^{-1} \text{ s}^{-1}$). The hydroxymethoxy can react with O_2 to form formic acid (Reaction 4.25, $k_{298\text{K}} = 3.5 \times 10^{-14} \text{ cm}^3 \text{ molec}^{-1} \text{ s}^{-1}$).^{25, 26}



Unimolecular reaction of HMP back to $\text{HO}_2 + \text{HCHO}$ is too slow to act as a loss mechanism (Reaction 26, lifetime 126 s^{-1}).^{25, 26}



We can calculate branching ratios of Reactions 4.1 and 4.4 based on their relative lifetimes, and therefore estimate $[\text{HMP}]$ and $[\text{H}_2\text{O}_2]$ in both the ν_1 and A-X experiments. These values are summarized in Table 4.2, along with conditions for other spectra reported in this chapter. For this calculation, we assume that Reactions 4.1 and 4.4 are the only relevant reactions of HO_2 within the timescale of HMP formation. We expect 94% of HO_2 to be converted to HMP in the ν_1 experiment and 31% in the A-X experiment.

Given the estimated $[\text{HMP}]$, we can also estimate the lifetime of HMP in our experiment. These lifetimes are also summarized in Table 4.2, and combine the lifetimes of Reactions 4.21–4.24. For this lifetime calculation, we use the $[\text{HO}_2]$ present after the listed lifetime of $\text{HO}_2 + \text{HCHO}$ for each condition. Because HO_2 is rapidly decreasing over the course of the experiment, we expect that all of the predicted HMP lifetimes are too low.

Table 4.2. Summary of lifetimes (μs), branching ratios, estimated $[\text{H}_2\text{O}_2]$ (molec cm^{-3}), and estimated $[\text{HMP}]$ (molec cm^{-3}) for $\text{HO}_2 + \text{HO}_2$ and $\text{HO}_2 + \text{HCHO}$ reactions under experimental conditions, as predicted by our analysis of chemistry.

Expt	$[\text{HO}_2]$	$[\text{HCHO}]$	$(\tau_{\text{HO}_2+\text{HO}_2})_0$	$\tau_{\text{HO}_2+\text{HCHO}}$	BR(HMP)	$[\text{H}_2\text{O}_2]$	$[\text{HMP}]$	τ_{HMP}
ν_1^a	1.0e14	1.0e17	2530	175	93.5%	6.5e12	9.4e13	660
A-X ^a	3.2e15	1.0e17	79	175	31.1%	2.2e15	1.0e15	75
$\nu_1 \#2^b$	1.2e15	5.0e15	211	3509	5.7%	1.1e15	6.8e13	1250
$\nu_1 \#3^b$	2.4e14	9.0e15	1054	1949	35.1%	1.6e14	8.4e13	860
A-X #2 ^b	1.5e15	1.0e17	169	175	49.0%	7.6e14	7.4e14	91

a) Conditions for reported spectra

b) Non-optimal conditions leading to unclear spectra or low $[\text{HMP}]$

Based on Table 4.2, we expect to form a detectable $[\text{HMP}]$ with minimal interference from $[\text{H}_2\text{O}_2]$ in the ν_1 region. To confirm this, we constructed a kinetics model using rate constants available in the literature.^{27, 117, 118} This kinetics model is summarized in Appendix E, as it is capable of modeling a number of reactions:

HO₂ + (HCHO,NO) and OH + (CO, NO₂, O₂). Table 4.3 summarizes [HO₂], [HCHO], lifetimes, [HMP], and HMP lifetime obtained from the model. We note $\tau_{\text{HO}_2+\text{HO}_2}$, $\tau_{\text{HO}_2+\text{HCHO}}$, the branching ratio, [H₂O₂], and [HMP] are in excellent agreement with our chemistry analysis (factor of 3). The lifetime of HMP from the kinetics model is longer than from our chemistry analysis because [HO₂] and [HMP] decrease over time, a factor not included in our simple chemistry analysis.

Table 4.3. Summary of lifetimes (μs), branching ratios, estimated [H₂O₂] (molec cm⁻³), and estimated [HMP] (molec cm⁻³) for HO₂ + HO₂ and HO₂ + HCHO reactions under experimental conditions, as predicted by our kinetics model.

Expt	[HO ₂]	[HCHO]	($\tau_{\text{HO}_2+\text{HO}_2}$) ^a	$\tau_{\text{HO}_2+\text{HCHO}}$	BR(HMP) ^b	[H ₂ O ₂]	[HMP]	τ_{HMP}
ν_1 ^c	1.0e14	1.0e17	1480 ^a	105	81%	1.6e12	6.8e13	>1000
A-X ^c	3.2e15	1.0e17	59 ^a	190	36%	6.2e14	3.5e14	450
ν_1 #2 ^d	1.2e15	5.0e15	198 ^a	6000 ^a	4%	3.9e14	1.8e13	>1000
ν_1 #3 ^d	2.4e14	9.0e15	646 ^a	2078 ^a	40%	4.3e13	2.9e13	>1000
A-X #2 ^d	1.5e15	1.0e17	110 ^a	220	59%	2.0e14	2.9e14	555

a) Initial lifetime

b) Branching ratio calculated as [HMP] / ([HMP]+[HO₂])

c) Conditions for reported spectra

d) Non-optimal conditions leading to unclean spectra or low [HMP]

Finally, on the basis of our kinetics model, we can find acceptable conditions for our experiments. For the ν_1 experiment, we must generate a large amount of HMP while keeping other species with OH stretches in low concentrations (notably H₂O₂, HOCH₂OOH, HCOOH). For the A-X experiment, we simply wish to generate as much HMP as possible. However, large quantities of HO₂ will increase the destruction rate of HMP (Reactions 4.21 and 4.22), and cause the concentration of HMP to vary over our data collection window (80 μs).

Figure 4.2 shows modeled kinetics of HMP and other species with OH groups for the ν_1 and A-X experimental conditions. We observe that the ideal detection time for both systems is 100 μs . This timing satisfies the requirements listed in the previous paragraph.

The rapid growth of HCOOH means that we cannot measure the maximum concentration of HMP in the ν_1 experiment (at 400 μs) without spectral interference.

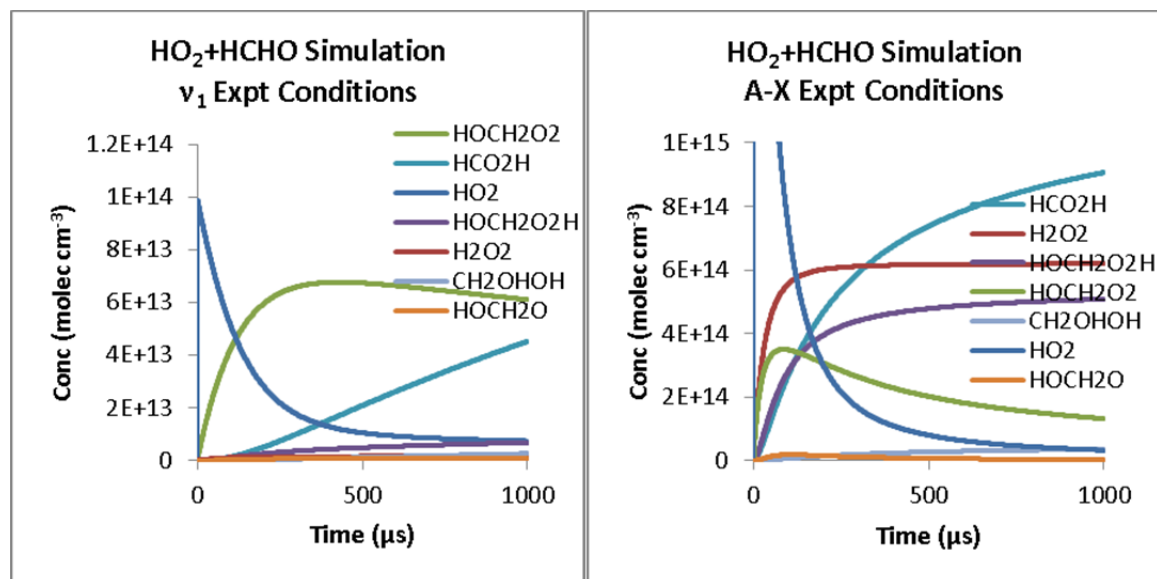


Figure 4.2. Kinetics simulations for our $\text{HO}_2 + \text{HCHO}$ experiments: ν_1 (left) and A-X (right). Conditions are listed in Table 4.1. In both systems, we make our measurements of HMP at 100 μs .

HMP ν_1 Spectrum

Figures 4.3–4.6 show a series of mid-infrared spectra obtained following the photolysis of Cl_2 in the presence of HCHO and O_2 . All spectra were taken with a 0.2 cm^{-1} step size, with different photolysis-probe delay times dependent on experimental conditions (noted with each figure). The spectra presented in Figure 4.3 are unsubtracted (i.e., the mirror reflectivity and absorption by the background gases have not been subtracted out). Figures 4.4–4.6 have had the background spectra in the absence of photolysis (excimer off) subtracted.

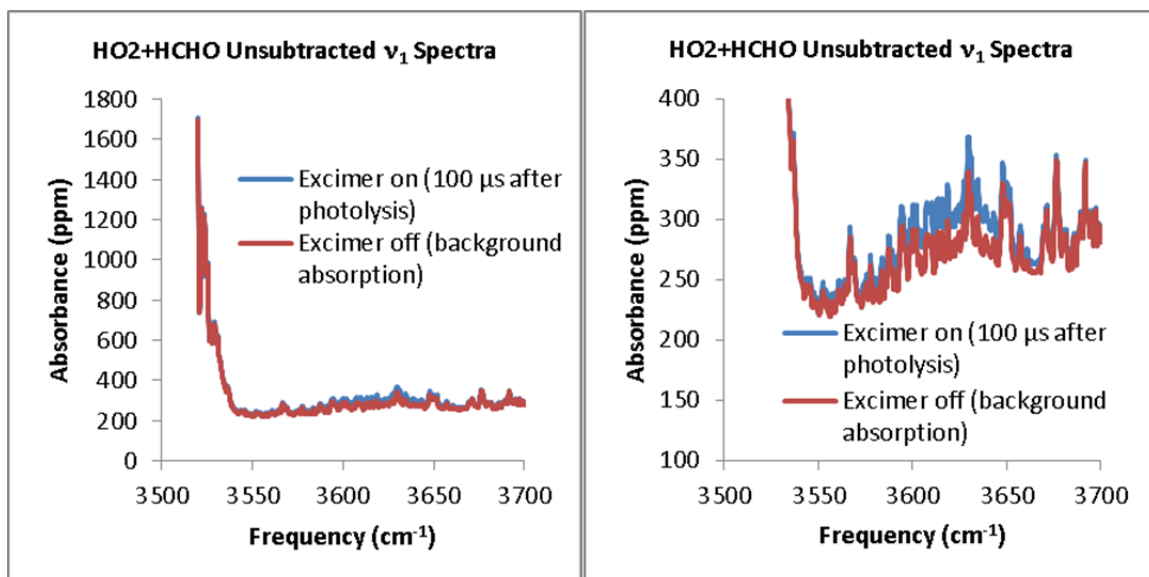


Figure 4.3. Cavity loss (mirror reflectivity plus absorption) of the precursor chemicals (excimer off) and the photolysis products (excimer on) in the mid-IR for Cl_2 in the presence of HCHO and O_2 . The right panel zooms in on the region 100–400 ppm to better illustrate those absorption features. The spectrum was taken at room temperature (295 ± 2 K) and $[\text{O}_2] = 2 \times 10^{18}$ molec cm^{-3} , 0.2 cm^{-1} between data points. The large absorption at $3500\text{--}3540 \text{ cm}^{-1}$ is from the $2\nu_2$ band of HCHO. Structured absorption across the entire spectrum is due to background H_2O . Additional absorption features are observed following photolysis of Cl_2 .

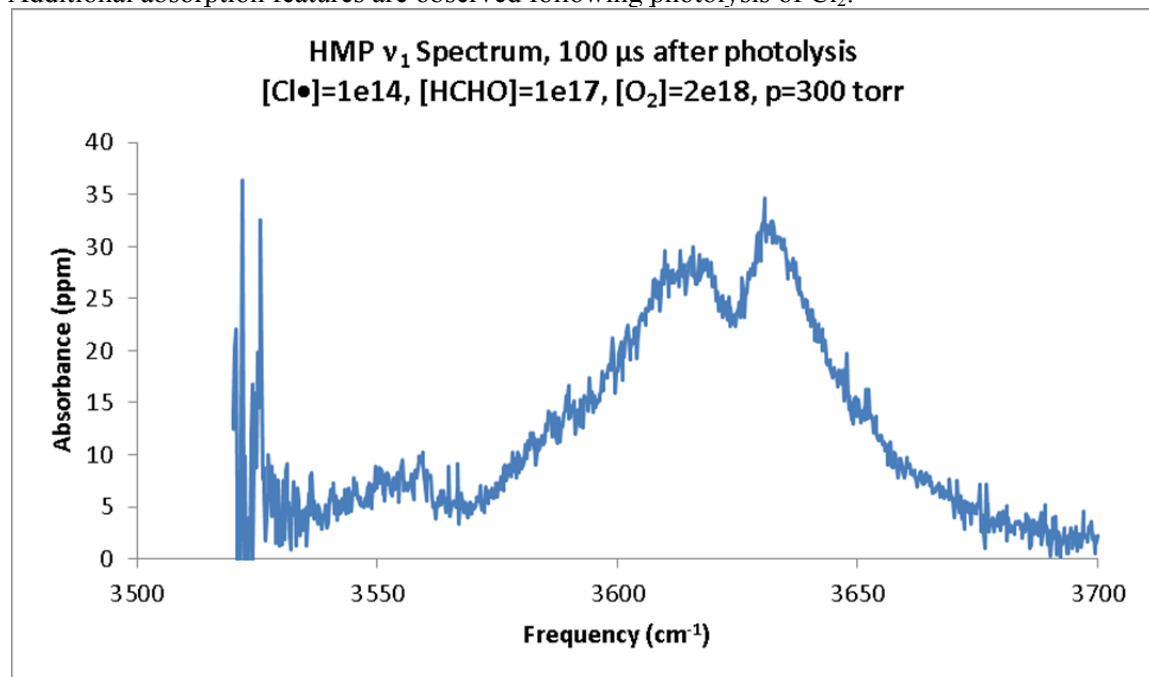


Figure 4.4. ν_1 (OH stretch) spectrum of $\text{HOCH}_2\text{OO}\cdot$ (HMP), the product of $\text{HO}_2 + \text{HCHO}$, taken under our most ideal conditions. The spectrum was recorded at 295 K, 300 torr, 0.2 cm^{-1} between data points, 100 μs after generation of HO_2 , $[\text{HO}_2] = 1 \times 10^{14}$ molec cm^{-3} , $[\text{HCHO}] = 1 \times 10^{17}$ molec cm^{-3} . The spectrum was signal averaged for 6.4 s per point. Based on our kinetics model, we predict $[\text{HMP}]:[\text{H}_2\text{O}_2] = 39$ and $[\text{HMP}]:[\text{HCOOH}] = 30$

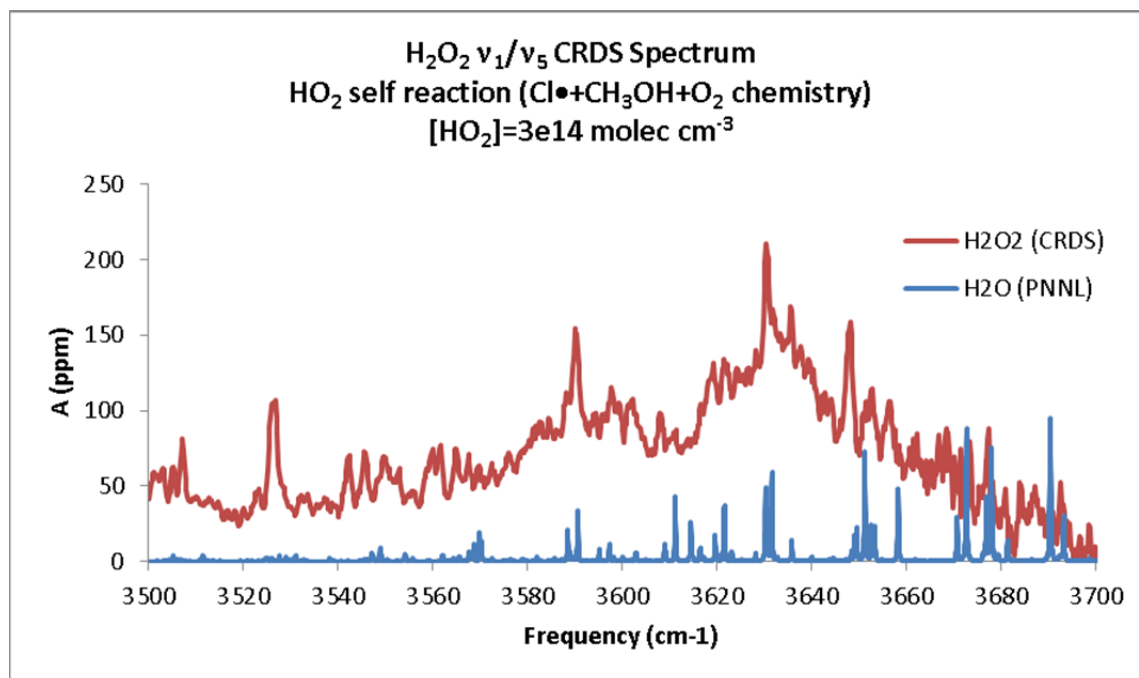


Figure 4.5. ν_1/ν_5 (OH stretch) spectrum of H₂O₂, formed from HO₂ self-reaction. HO₂ was generated by Cl• + CH₃OH + O₂ chemistry. [Cl•]= 3×10^{14} molec cm⁻³, [CH₃OH] = 1×10^{15} molec cm⁻³, [O₂] = 2×10^{18} molec cm⁻³, p = 300 torr, 0.2 cm⁻¹ step size. The spectrum is a composite of five scans (8.0 s average per point), ranging from 100–1000 μ s after Cl₂ photolysis. Spectral interference from CH₃OH loss has been subtracted out of the CRDS spectrum. A reference spectrum of H₂O⁴⁰ has been overlaid to indicate which peaks belong to water rather than H₂O₂. We note that the spectrum of H₂O₂ is qualitatively different than the HMP spectrum in Figure 4.4.

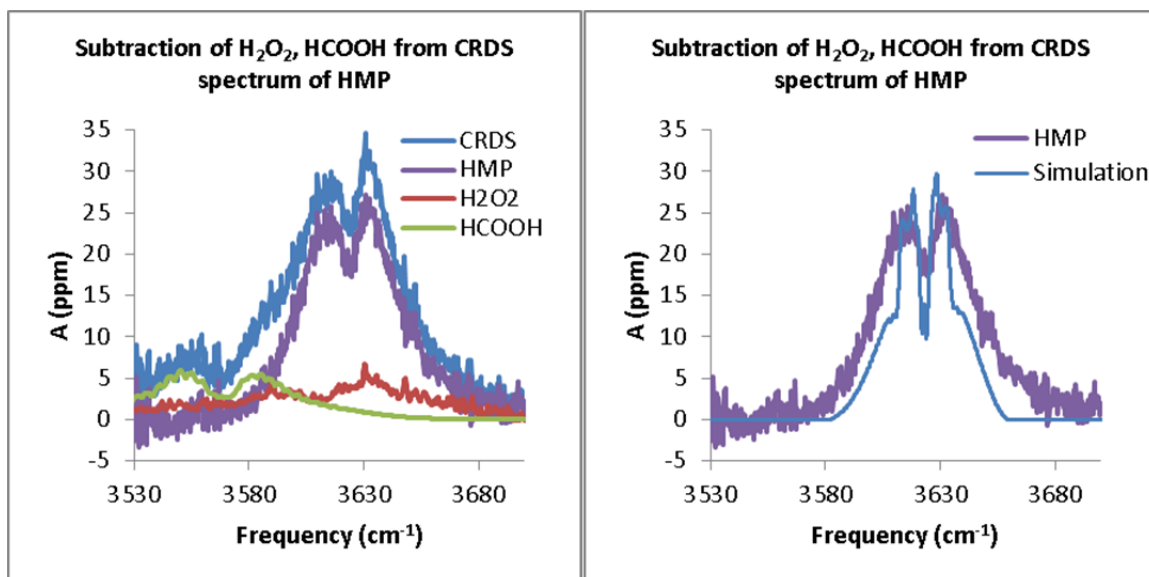


Figure 4.6. Left: Subtraction of H_2O_2 and HCOOH from the cavity ringdown spectrum to obtain the pure ν_1 spectrum of HMP. The integrated absorbance of the subtracted HMP ν_1 band is $1.3 \times 10^{-3} \text{ cm}^{-1}$. Assuming the B3LYP integrated cross section $8.8 \times 10^{-18} \text{ cm molec}^{-1}$, we estimate $[\text{HMP}] = 3.1 \times 10^{13} \text{ molec cm}^{-3}$, in excellent agreement with our kinetics model ($4.2 \times 10^{13} \text{ molec cm}^{-3}$). Right: Comparison of the ν_1 spectrum of HMP to simulation, B3LYP/6-31+G(d,p), anharmonic rotational constants. We observe good agreement between the CRDS and simulated ν_1 bands.

Figure 4.3 shows the background IR spectra of the reactants (excimer off) and the IR spectra of the background plus signal (excimer on). At frequencies less than 3540 cm^{-1} , the spectrum is dominated by the $2\nu_2$ band of HCHO. To better show the rest of the absorptions in this region, the right panel zooms in to absorptions of less than 400 ppm. We notice sharp peaks across the entire region, attributed mainly to residual water from the paraformaldehyde sample. Some of the peaks are likely also from HCHO.⁴⁰

Following photolysis of Cl_2 at 351 nm, an additional absorption is observed over the range $3550\text{--}3700 \text{ cm}^{-1}$. Figure 4.4 shows the IR spectrum of the products formed under the experimental conditions in Table 4.1, 100 μs after photolysis of Cl_2 in the presence of HCHO and O_2 . We observe a clear peak centered at 3622 cm^{-1} , with broad P and R branches ($\text{FWHM} = 60 \text{ cm}^{-1}$). The shape and position of this band are not

consistent with any of the other molecules discussed in the *Chemistry* section (HCOOH, H₂O₂, HOCH₂OOH).^{40, 119}

We do observe traces of spectral interference in Figure 4.4. The ν_1 band of HCOOH is clearly visible at 3570 cm⁻¹, although its peak absorbance is a factor of 6 weaker than the main band at 3622 cm⁻¹. There are also small peaks in the region 3645–3655 cm⁻¹. As discussed in the *Chemistry* section, one of the side products in our experiment is H₂O₂, and these peaks belong to the ν_1/ν_5 bands (OH symmetric and antisymmetric stretches) of H₂O₂. To confirm this, we measured the spectrum of H₂O₂ in our CRDS apparatus by generating HO₂ from Cl• / CH₃OH / O₂ chemistry, a “pure” source of HO₂ that will not form appreciable amounts of organic hydroxide species. This spectrum is shown in Figure 4.5. The H₂O₂ peaks match up with the weak peaks in Figure 4.4, indicating a very small amount of spectral interference from H₂O₂.

We can subtract out the contributions from HCOOH and H₂O₂, allowing us to compare the observed band to a simulation of HMP. Combined with our analysis in the *Chemistry* section, this would allow us to assign the observed absorption to the ν_1 band of HMP. Figure 4.6 shows this subtraction and simulation. The subtraction (left panel) was performed in two steps: first scaling the H₂O₂ spectrum to eliminate the peaks in the 3645–3655 cm⁻¹ region, then scaling the HCOOH spectrum to eliminate the observed ν_1 band at 3555–3570 cm⁻¹.

The ν_1 band of HMP was simulated using the PGopher program.¹²⁰ The geometry, dipole derivatives, and anharmonic rotational constants were calculated at the B3LYP/6-31+G(d,p) level of theory and basis using Gaussian 09W.¹²¹ We observe very good agreement between our simulation and the subtracted CRDS band (Figure 4.6, right

panel) with the main difference being that the FWHM of the simulated band (40 cm^{-1}) is narrower than the CRDS band (60 cm^{-1}). This may be due to the internal hydrogen bond formation (discussed in Chapter 5).

We assign the absorption band at 3622 cm^{-1} (Figure 4.4) to the ν_1 mode of HMP for the following two reasons. First, our two analyses in the *Chemistry* section (both from rate constants and from the kinetics model) show that under our experimental conditions, the species in our spectrometer should be mostly HMP. Second, the subtracted CRDS spectrum is in excellent agreement with our simulated ν_1 band (Figure 4.6).

We can use the integrated absorbance of the subtracted spectrum (Figure 4.6) and the theoretical integrated intensity (calculated during our simulation) to estimate [HMP]:

$$[\text{HMP}] = \frac{\int_{3530 \text{ cm}^{-1}}^{3700 \text{ cm}^{-1}} A d\bar{\nu}}{L_{\text{phot}} \int \sigma d\bar{\nu}}, \quad (4.27)$$

where $\int_{3530 \text{ cm}^{-1}}^{3700 \text{ cm}^{-1}} A d\bar{\nu}$ is the integrated absorbance of the subtracted band in Figure 4.6 ($1.3 \times 10^{-3} \text{ cm}^{-1}$), L_{phot} is the photolysis length (5 cm), and $\int \sigma d\bar{\nu}$ is the integrated cross section from our quantum chemistry calculations ($8.8 \times 10^{-18} \text{ cm molec}^{-1}$ at B3LYP/6-31+G(d,p)). Using Equation 4.27, we estimate $[\text{HMP}] = 3.1 \times 10^{13} \text{ molec cm}^{-3}$. This is in excellent agreement with the prediction from our kinetics model, $[\text{HMP}] = 4.2 \times 10^{13} \text{ molec cm}^{-3}$.

Using these either of concentrations (B3LYP or kinetics model), we can estimate the peak cross section of HMP. This plot is shown in Figure 4.7. It should be noted that these values are very crude estimates due to possible variations in [HCHO], [HO₂], and uncertainty on the absolute [HMP]. Nonetheless, we can estimate the peak cross section

to be on the order of $10^{-19} \text{ cm}^2 \text{ molec}^{-1}$. This is consistent with other small alcohols such as methanol ($8 \times 10^{-20} \text{ cm}^2 \text{ molec}^{-1}$), ethanol ($8 \times 10^{-20} \text{ cm}^2 \text{ molec}^{-1}$), or 1-propanol ($7 \times 10^{-20} \text{ cm}^2 \text{ molec}^{-1}$).

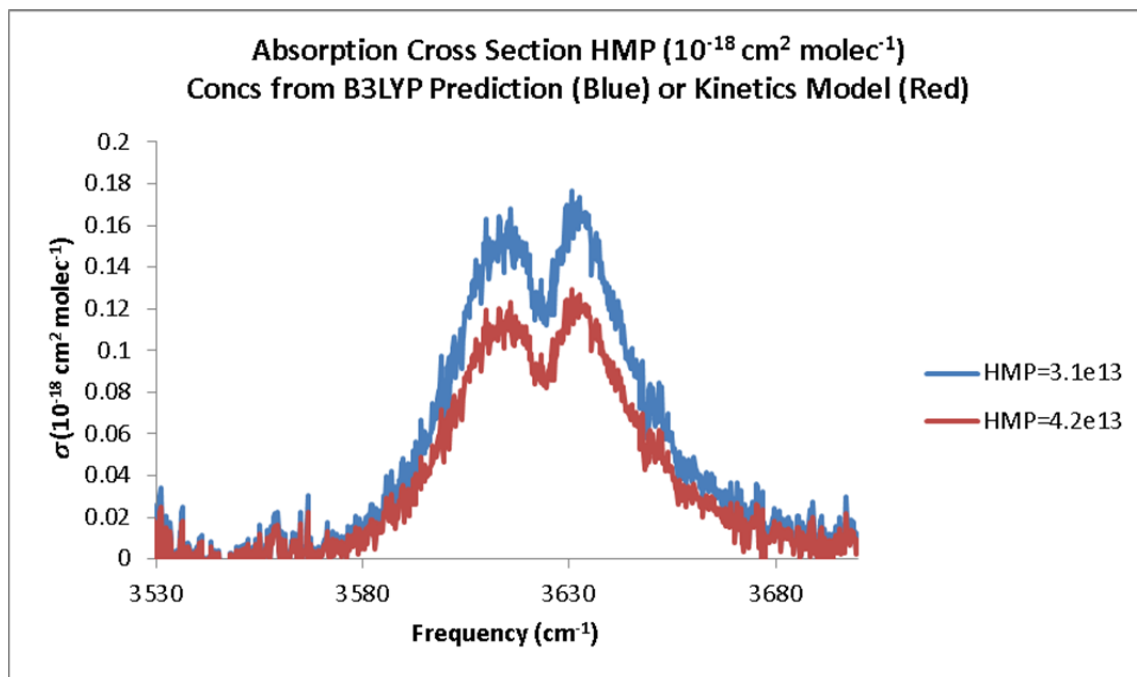


Figure 4.7. Absorption cross sections of the ν_1 band of HMP. The [HMP] used were taken from the B3LYP/6-31+G(d,p) intensity and CRDS integration (blue) and the kinetics model (red).

As mentioned in the *Chemistry* section, incorrect selection of initial conditions, notably the ratio [HCHO]:[HO₂] and the absolute reactant concentrations, will lead to severe spectral interference or large levels of noise. Figure 4.8 shows spectra for poor initial conditions. The left panel uses a very low [HCHO]:[HO₂] ratio compared to Figure 4.4 (4 vs 1000). The right panel uses a somewhat low [HCHO]:[HO₂] ratio (38), but with [HCHO] = $9 \times 10^{15} \text{ molec cm}^{-3}$, a factor of 11 lower than the spectrum in Figure 4.4. At very low [HCHO]:[HO₂] ratios, we observe a broad absorption across the entire region (3500–3700 cm^{-1}), indicative of H₂O₂ formation. In the right panel, we observe essentially the same spectrum as in Figure 4.4, but with much lower peak absorption (and

consequently a lower signal-to-noise ratio). The conclusion that we draw from Figure 4.8 is that we must be careful selecting initial conditions in our experiments, especially OH stretch experiments where secondary/side products will cause significant interference.

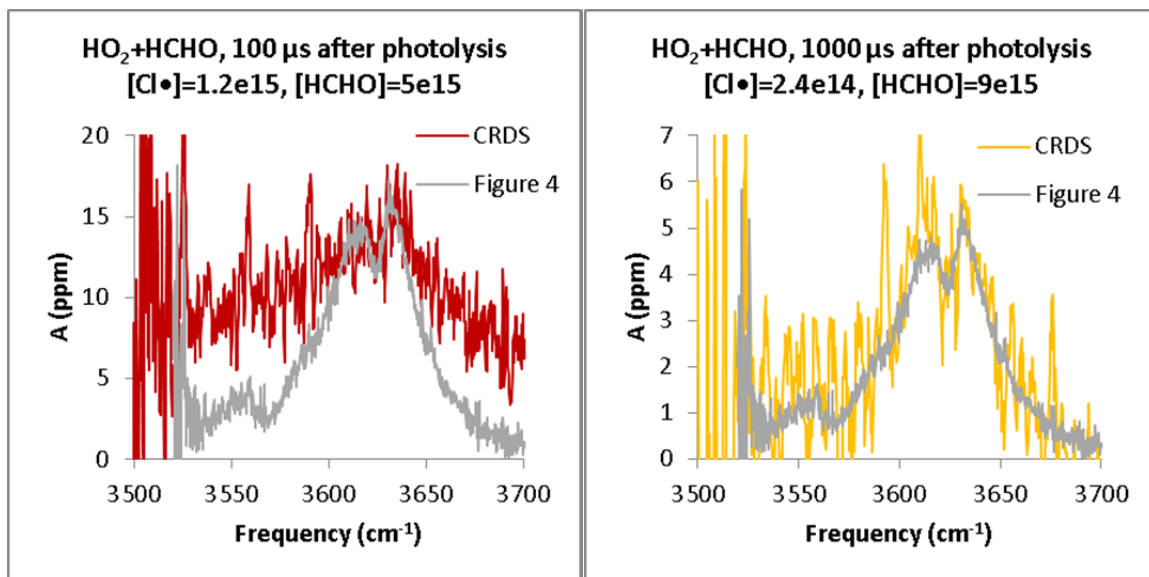


Figure 4.8. ν_1 (OH stretch) spectra of $\text{HOCH}_2\text{OO}\cdot$ (HMP), the product of $\text{HO}_2 + \text{HCHO}$, taken under poor conditions. Left: very low $[\text{HCHO}]:[\text{HO}_2]$ ratio. Right: Low absolute concentrations. The spectra were recorded at 295 K, 300 torr, 0.2 cm^{-1} between data points. Left: $[\text{HO}_2] = 1.2 \times 10^{15} \text{ molec cm}^{-3}$, $[\text{HCHO}] = 5 \times 10^{15} \text{ molec cm}^{-3}$, 100 μs after HO_2 formation. We observe significant interference from other species (HCOOH , H_2O_2), causing the spectrum to disagree with the spectrum presented in Figure 4.4 (shown in gray). Right: $[\text{HO}_2] = 2.4 \times 10^{14} \text{ molec cm}^{-3}$, $[\text{HCHO}] = 9 \times 10^{16} \text{ molec cm}^{-3}$, 1000 μs after HO_2 formation. The spectrum shape agrees with Figure 4.4, but the absolute absorbance is very low, resulting in a noisy spectrum.

HMP A-X spectrum

Figure 4.9 shows the A-X spectrum of HMP over the range $7100\text{--}8000 \text{ cm}^{-1}$. The reported spectrum is a composite of spectra taken over a period of 3 years (2009–2012) under similar experimental conditions (Table 4.1). Certain regions have been scanned in detail, these will be shown later in this section. In general, each point in the spectrum (0.1 cm^{-1} step size) has 3.2 s of averaging.

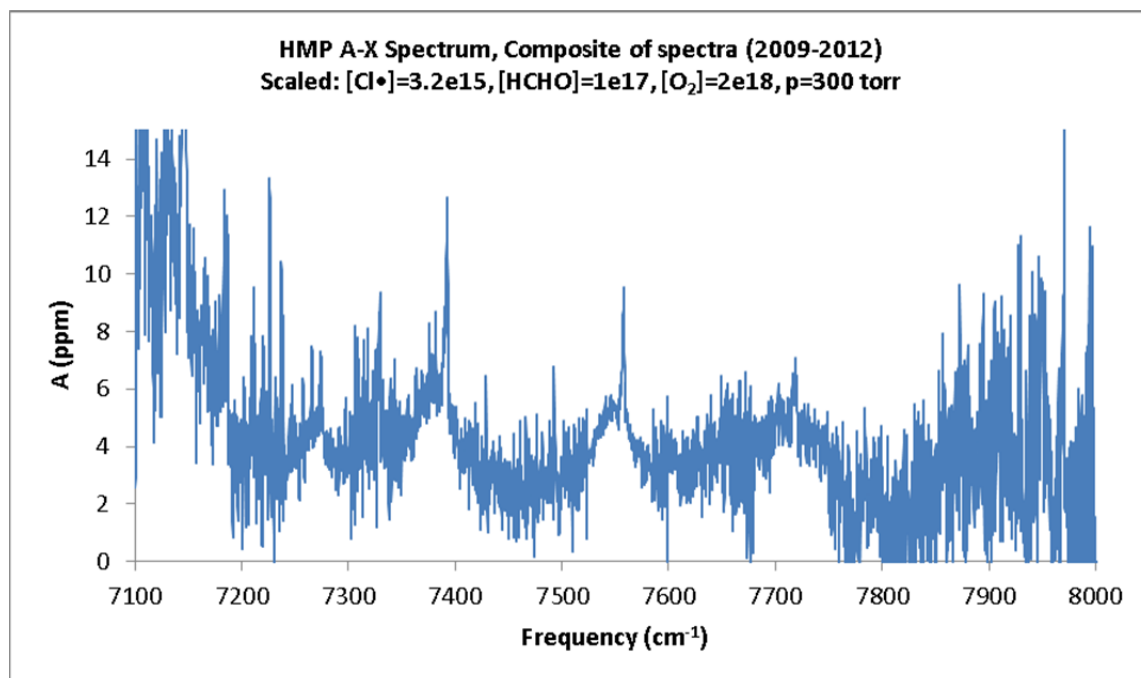


Figure 4.9. Cavity ringdown spectrum of the A-X electronic transition for the hydroxymethylperoxy radical ($\text{HOCH}_2\text{OO}\cdot$, HMP). We observe clear bandheads of HMP at 7275 cm^{-1} (15_1^0), 7391 cm^{-1} (0_0^0), 7561 cm^{-1} (15_0^1), and 7719 cm^{-1} (15_0^2) that are assigned to HMP. Peaks at 7146 , 7185 , 7930 , and 7975 cm^{-1} are assigned to HO_2 .

We immediately note seven peaks that belong to HO_2 :⁵⁴ 7146 , 7185 , 7230 , 7266 , 7330 , 7930 , and 7975 cm^{-1} . The first two peaks are part of the A-X origin, while the third and fourth peaks are part of the combination band with the OO stretch. The large intensities of the peaks close to the HO_2 transitions (7029 , 8050 cm^{-1})⁵⁴ prevents us from making meaningful observations in our spectrum at frequencies less than 7200 cm^{-1} or greater than 7900 cm^{-1} .

Despite interference from HO_2 , we observe four clean absorption bands in the rest of the spectrum. These bands are located at 7275 , 7391 , 7561 , and 7719 cm^{-1} . Figure 4.10 shows these bands in detail.

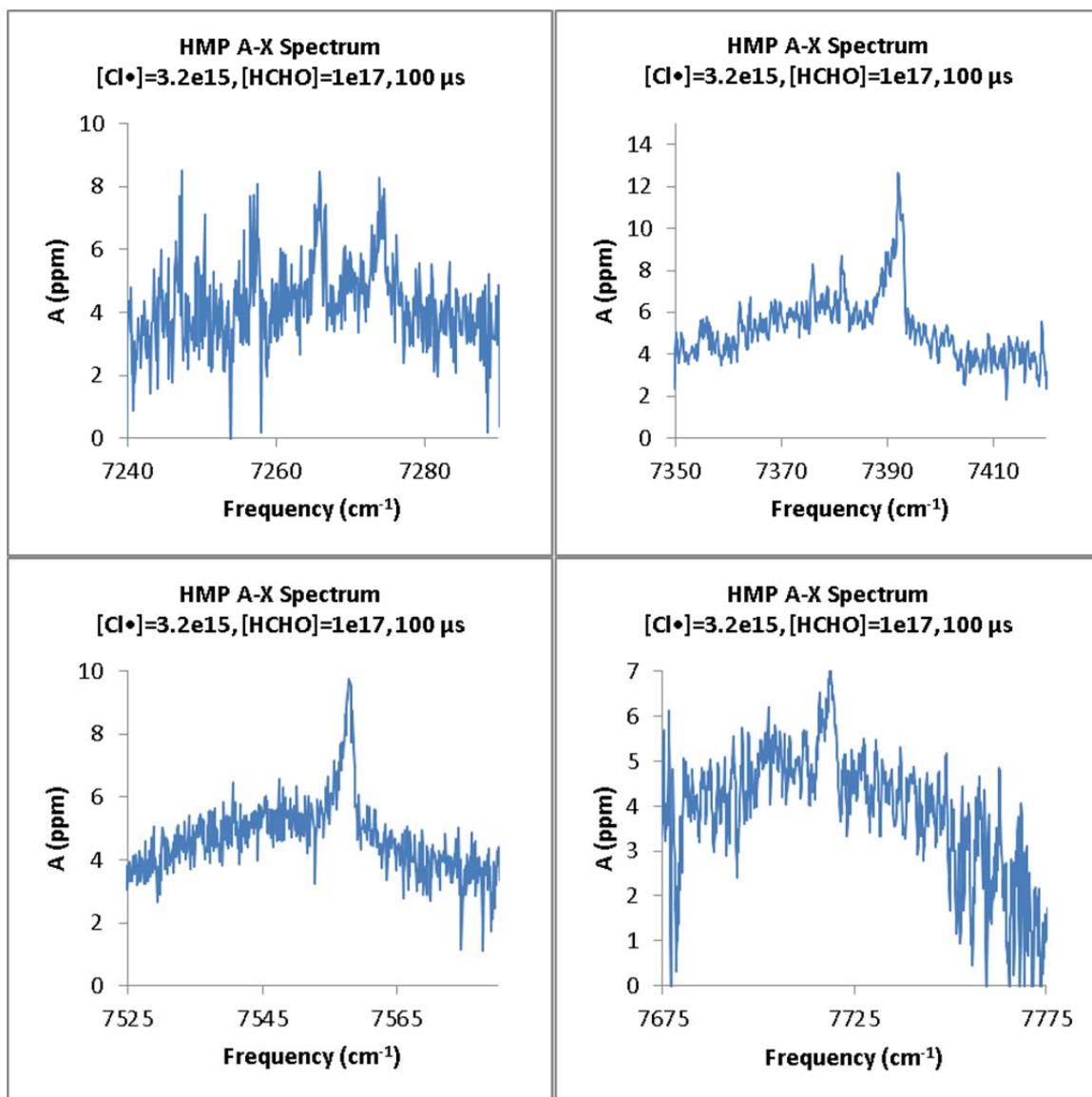


Figure 4.10. Cavity ringdown spectra of individual HMP A-X bands (from Figure 4.8). We assign these bands to HMP on the basis of simulated spectra, our quantum chemistry calculations (Chapter 5) and our kinetics studies (Chapter 6). We assign the bands as: 7275 cm^{-1} (15_1^0), 7391 cm^{-1} (0_0^0), 7561 cm^{-1} (15_0^1), and 7719 cm^{-1} (15_0^2).

We have many pieces of evidence that support assignment of these bands to HMP. First, the kinetics of these bands (discussed in detail in Chapter 6) are consistent with each other, and do not match the kinetics of the HO_2 peaks. Figure 4.11 compares the kinetics of the 7561 cm^{-1} peak to the simulation presented in Figure 4.2. The left panel is measured to the red of the bandhead, and is subject to more noise near the peak

absorption. The right panel is measured at the peak absorption, and is the best measure of the kinetics of the peak. The simulation and observed absorbances are in excellent agreement with each other.

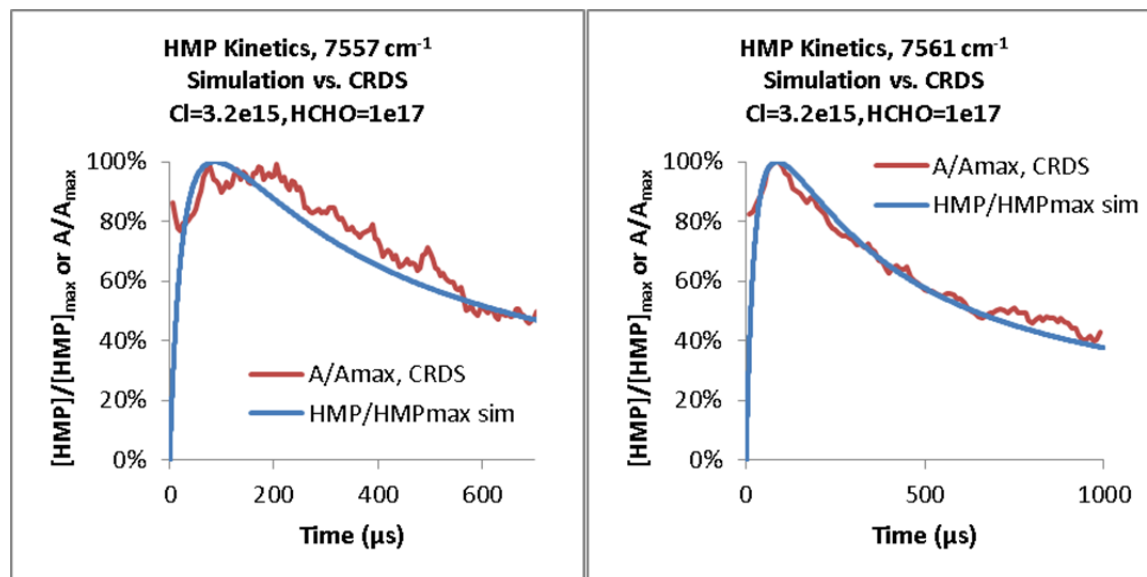


Figure 4.11. Comparison of experimentally measured HMP kinetics (CRDS, 15_0 band at 7561 cm^{-1}) to the kinetics simulation presented in Figure 4.2. The left panel was measured to the red of the peak absorbance (7557 cm^{-1}), while the right panel was measured at the bandhead peak. We observe excellent agreement between the experiment and simulation, supporting our assignment of the band to HMP. The other bands (7275 , 7391 , 7719 cm^{-1}) show similar kinetics (shown in Chapter 6).

The second piece of information supporting assignment of these bands to HMP is the calculated band positions according to quantum chemistry calculations (presented in detail in Chapter 5). Table 4.4 summarizes the A-X transition frequency and anharmonic vibrational modes of HMP in the X and A states. The transition frequency was calculated at CCSD/6-31+G(d,p), and the anharmonic frequencies were calculated at B3LYP/6-31+G(d,p). (Justification of these choices are given in Chapter 5.) These calculations were carried out in Gaussian 09W¹²¹ using the procedures described in Appendix C. Note that mode 15 is the OOCO torsion of HMP, and is the lowest

frequency vibrational mode. We observe excellent agreement between the calculated band positions and observed band positions.

Table 4.4 Comparison of observed transition and torsional frequencies to quantum chemistry predictions for HMP.

	Quantum Chemistry	CRDS	Difference
A-X Transition CCSD/6-31+G(d,p)	7424 cm ⁻¹	7391 cm ⁻¹	33 cm ⁻¹
ν_{15} (X) B3LYP/6-31+G(d,p)	110 cm ⁻¹	116 cm ⁻¹	6 cm ⁻¹
ν_{15} (A) B3LYP/6-31+G(d,p)	168 cm ⁻¹	170 cm ⁻¹	2 cm ⁻¹
$2\nu_{15}$ (A) B3LYP/6-31+G(d,p)	334 cm ⁻¹	328 cm ⁻¹	6 cm ⁻¹

Finally, we can simulate the A-X bands using PGopher¹²⁰ and compare to our experiment. We use the geometries and anharmonic rotational constants from our B3LYP/6-31+G(d,p) quantum chemistry calculations. The dipole derivative was estimated as the change in electron density of the OO• π^* orbital (most relevant to characteristic peroxy radicals). Figure 4.12 compares the four observed bands (7275, 7391, 7561, 7719 cm⁻¹) to simulations of 15_1^0 , 0_0^0 , 15_0^1 , and 15_0^2 respectively. Despite the high noise level in the 7275 cm⁻¹ and 7719 cm⁻¹ bands, we observe excellent agreement between the simulations and observed bands.

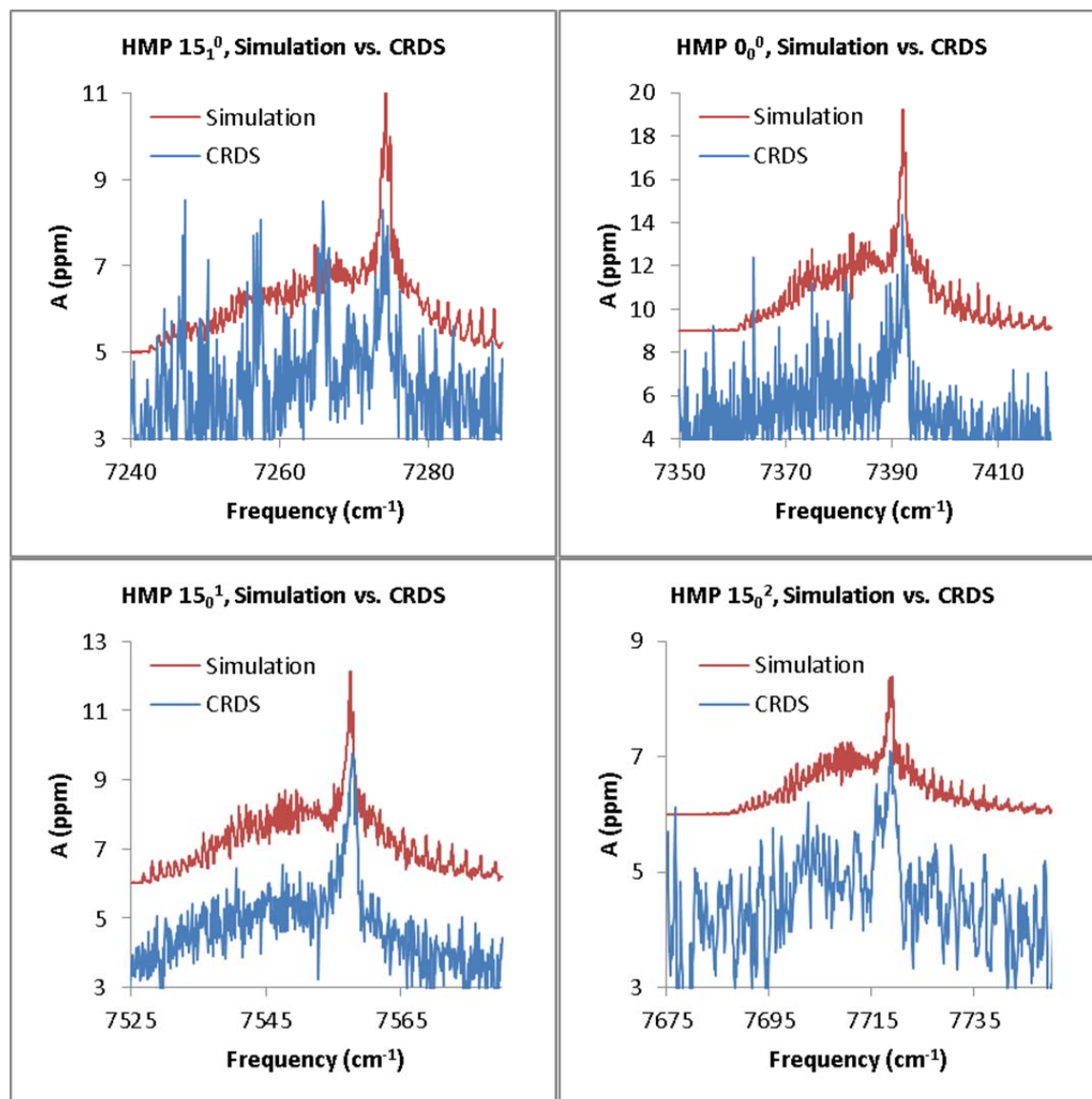


Figure 4.12. Comparison of observed A-X bands of HMP to simulation at B3LYP/6-31+G(d,p), anharmonic rotational constants. Shown above are the bands at 7275 cm^{-1} (15_1^0), 7391 cm^{-1} (0_0^0), 7561 cm^{-1} (15_0^1), and 7719 cm^{-1} (15_0^2).

Given the agreement between our CRDS experiment and theory for the kinetics, position, and shape of each spectroscopic band, we assign the observed bands at 7275 , 7391 , 7561 , and 7719 cm^{-1} to electronic transitions of HMP. The band at 7391 cm^{-1} is assigned as the electronic origin 0_0^0 , 7275 cm^{-1} as the OOCO torsion hot band 15_1^0 ,

7561 cm^{-1} as the OOCO torsion combination band 15_0^1 , and 7719 cm^{-1} as the OOCO torsion overtone combination band 15_0^2 .

Similar to the ν_1 band, we can estimate the absorption cross sections of the A-X bands in Figure 4.9. Since we do not have a theoretical prediction of the integrated absorbance, we must rely on the kinetics modeling to provide an estimate of [HMP] (3.5×10^{14} molec cm^{-3}). Figures 4.13 and 4.14 show the estimated cross sections for the A-X bands of HMP. We observe peak cross sections on the order 10^{-21} – 10^{-20} $\text{cm}^2 \text{ molec}^{-1}$ for the four A-X bands, in reasonable agreement with Melnik's experimentally determined cross section for ethylperoxy (5.29×10^{-21} $\text{cm}^2 \text{ molec}^{-1}$).¹¹⁵

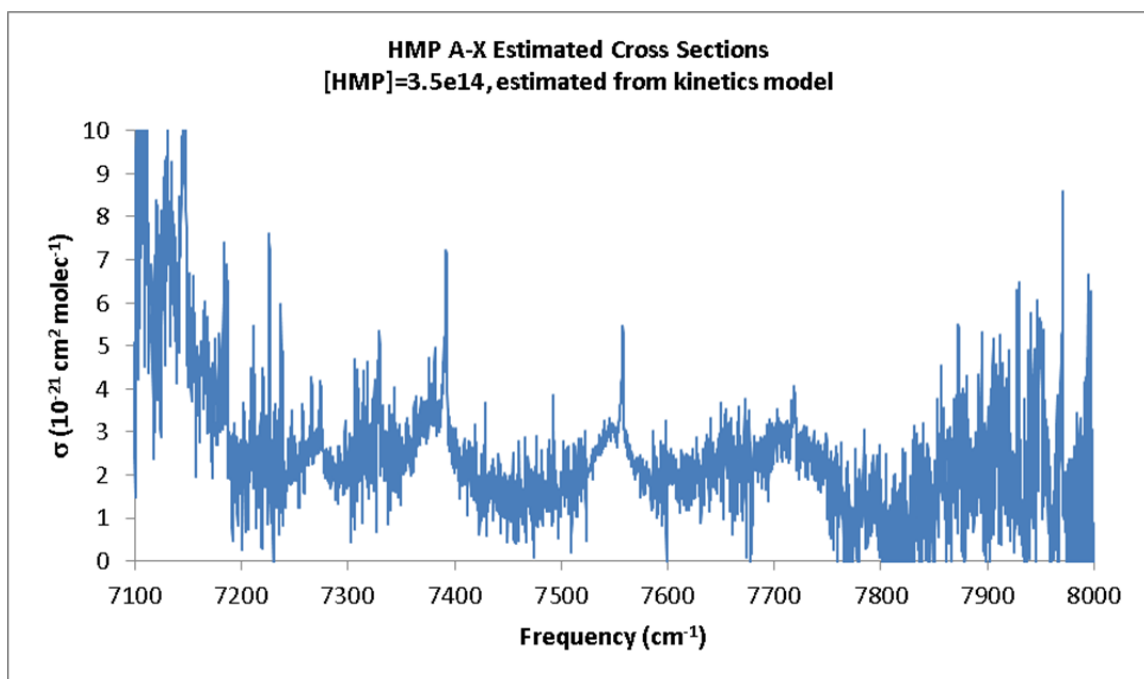


Figure 4.13. Absorption cross sections for the A-X region of HMP. The concentration of absorber used (3.5×10^{14} molec cm^{-3}) was taken to be [HMP] from the kinetics model (Figure 4.2).

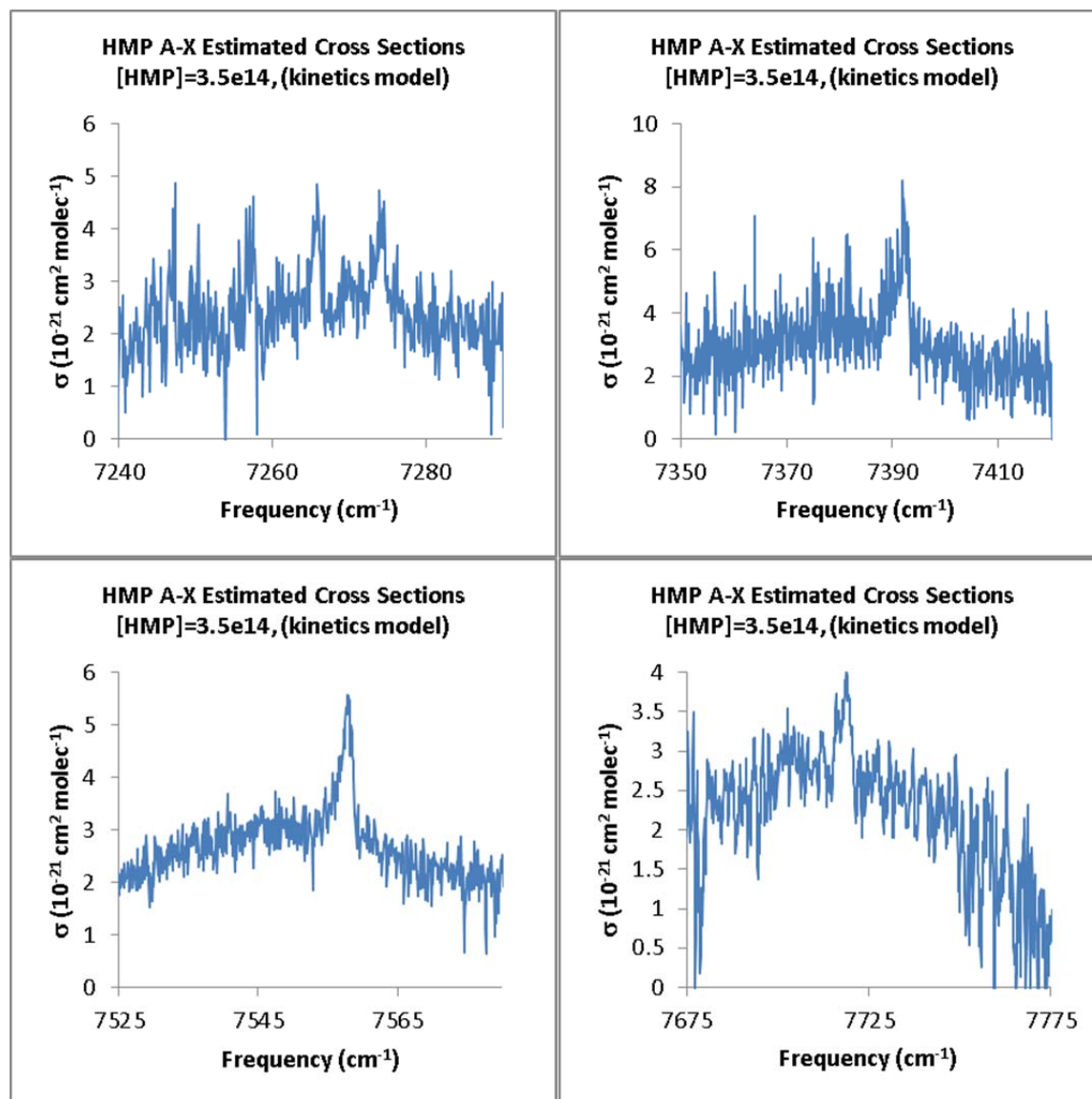


Figure 4.14. Absorption cross sections of the four A-X bands of HMP: 7275 cm^{-1} (15_1^0), 7391 cm^{-1} (0_0^0), 7561 cm^{-1} (15_0^1), and 7719 cm^{-1} (15_0^2). The $[\text{HMP}]$ used ($3.5 \times 10^{14}\text{ molec cm}^{-3}$) was taken from the kinetics model (Figure 4.2).

Discussion

Comparison of HMP ν_1 Spectrum to Methanol and Ethanol

Figure 4.15 compares the subtracted ν_1 band of HMP (Figure 4.6) to reference spectra of methanol and ethanol.¹²⁰ The reference spectra have been smoothed to 1 cm^{-1} , the linewidth of our mid-IR light (Chapter 2).

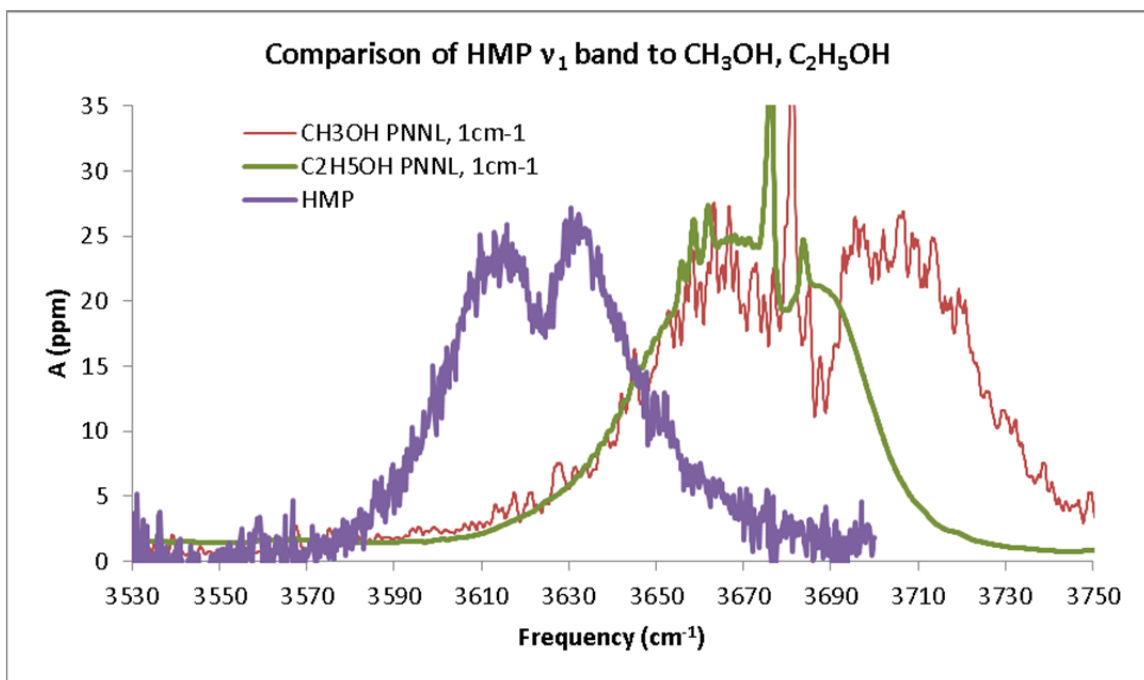


Figure 4.15. ν_1 (OH stretch) spectra of HMP (Figure 4.6), CH_3OH ,⁴⁰ and $\text{C}_2\text{H}_5\text{OH}$.⁴⁰ The reference spectra for CH_3OH and $\text{C}_2\text{H}_5\text{OH}$ have been smoothed to 1 cm^{-1} in order to match the linewidth of the HMP spectrum.

The shape of the HMP ν_1 band is similar to both methanol and ethanol. The FWHM of HMP (60 cm^{-1}) is equal to ethanol, but narrower than methanol (90 cm^{-1}), consistent with the difference in rotational constants between the three molecules. Second, the peak of HMP is red shifted from the alcohols by $55\text{--}60\text{ cm}^{-1}$. This is consistent with formation of a weak intramolecular hydrogen bond in HMP (discussed in detail in Chapter 5).

Despite the difference in band positions, the similarities in band shapes give us more confidence in our assignment of the observed absorption to the ν_1 band of HMP.

Comparison of HMP A-X Spectrum to Methylperoxy

We can also compare the A-X spectrum of HMP to the A-X spectrum of methylperoxy obtained by Chung et al.¹²² Figure 4.16 shows these two spectra. Chung

generates methylperoxy radicals by photolysis of acetone at 193 nm. Based on their reported experimental conditions, $[\text{CH}_3\text{OO}\cdot] = 7 \times 10^{15} \text{ molec cm}^{-3}$, with a photolysis length of 13 cm.

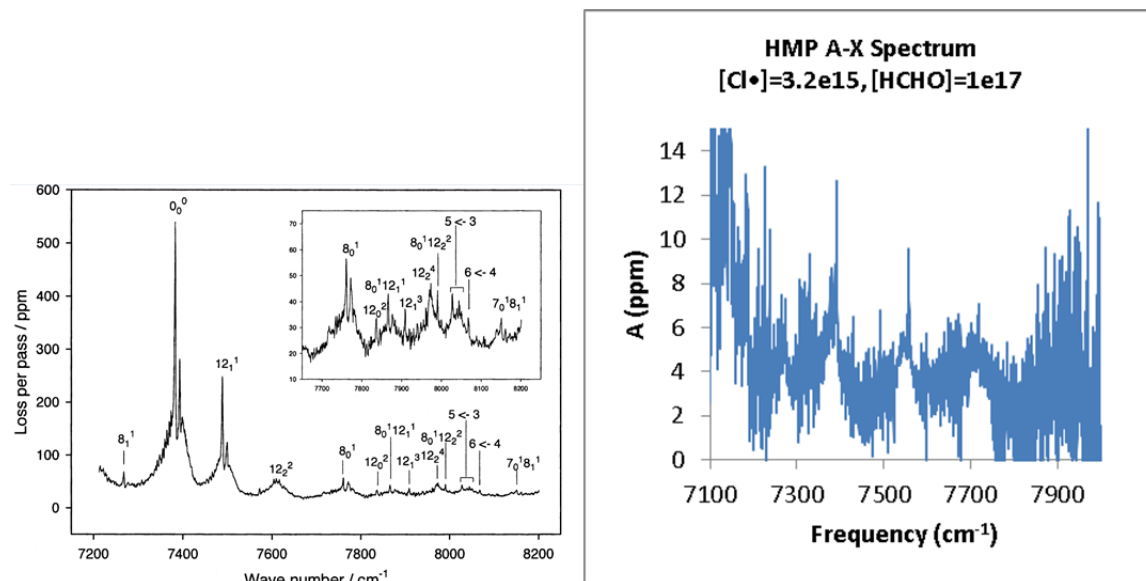


Figure 4.16. A-X electronic spectrum of methylperoxy (left) reported by Chung *et al.*,¹²² and our A-X spectrum of HMP (right). Left panel reprinted with permission from Chung *et al.*¹²² Copyright 2007, American Institute of Physics.

Chung's spectrum differs from our spectrum in two ways. First, Chung does not subtract out the mirror reflectivity (50 ppm). Second, Chung makes use of $[\text{CH}_3\text{OO}] \times L_{\text{phot}}$ a factor of 45 higher than our expected $[\text{HMP}] \times L_{\text{phot}}$, consequently making the absolute absorbances of each spectrum on different scales. Thus, the observed 0_0^0 peak absorbance of 550 ppm in Chung's spectrum would be equivalent to a peak absorbance of 11 ppm in our spectrum. We therefore observe good agreement in the linestrength of the pure A-X electronic transition between HMP and $\text{CH}_3\text{OO}\cdot$. Likewise, there is good agreement between the torsional overtone bands (12_0^2 in CH_3OO , 15_0^2 in HMP).

However, there are major differences between the two spectra over the range 7200–7600 cm^{-1} . In the CH_3OO spectrum, a sequence band involving the methyl torsion, 12_1^1 , is observed at 7480 cm^{-1} . The pure methyl torsion band, 12_0^1 , is not observed. In contrast, we do not observe the analogous sequence band 15_1^1 in the HMP spectrum, but we do see the “hydroxymethyl” torsion analog (OOCO torsion band) 15_0^1 at 7561 cm^{-1} . Similarly, Chung does not observe the torsional hot band 12_1^0 in the CH_3OO spectrum, although we see the analogous 15_1^0 band of HMP. These differences are likely due to the difference in molecular symmetry between HMP (C_1) and $\text{CH}_3\text{OO}\cdot$ (C_s), and differences in the dipole moment due to the hydroxyl group in HMP.

Conclusions

In this chapter, we have reported the first detection of the ν_1 (OH stretch) vibrational and A-X electronic spectra of the hydroxymethylperoxy radical ($\text{HOCH}_2\text{OO}\cdot$, HMP), the product of $\text{HO}_2 + \text{HCHO}$. The ν_1 spectrum is broad, with strong, structureless P and R branches. Under the experimental conditions used for the ν_1 spectrum, we observe relatively little interference from HCOOH and H_2O_2 , in good agreement with our predictions from kinetics modeling and chemistry analysis. We observe multiple electronic transitions corresponding to the pure A-X transition, and combination/hot bands with the OOCO torsion. Both the ν_1 and A-X bands agree well with simulation and spectra of similar molecules.

Assignment of the ν_1 and A-X bands were supported by quantum chemistry calculations and kinetics results. These topics are explored in detail in Chapters 5 and 6, respectively.

Acknowledgements

We thank Aileen O. Hui and Kathryn A. Pérez for assistance with calibration of the formaldehyde gas line, and Ralph H. Page for improvements to the optical setup. The experiments performed in this chapter were funded under NASA Upper Atmosphere Research Program Grants NAG5-11657, NNG06GD88G, and NNX09AE21G2, California Air Resources Board Contract 03-333 and 07-730, National Science Foundation CHE-0515627, and a Department of Defense National Defense Science and Engineering Graduate Fellowship (NDSEG).

Chapter 5—Predicted A-X Transition Frequencies and 2-Dimensional Torsion-Torsion Potential Energy Surfaces of HOCH₂OO• and HOC(CH₃)₂OO•

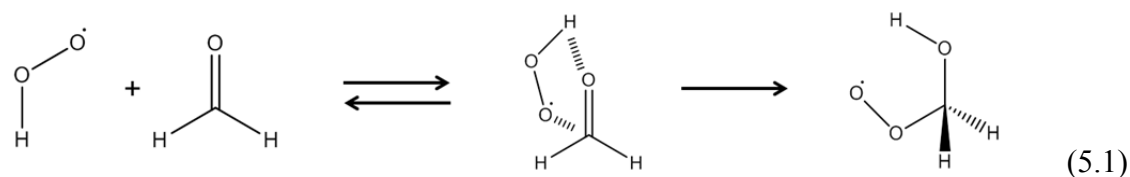
Abstract

In Chapter 4, we presented the ν_1 (OH stretch) vibrational and A-X electronic spectra of the hydroxymethylperoxy radical (HOCH₂OO•, or HMP). The slight red shift in the ν_1 absorption band suggests the formation of a weak intramolecular hydrogen bond, possibly leading to coupling of vibrational modes (similar to our observations of HOONO in Chapter 3). We observed four clear peaks in the A-X spectrum, consistent with assignment as the hot bands and combination bands with the OOCO torsional mode. We would like to make the most accurate assignment of the A-X spectrum and assessment of the torsional mode coupling. Although quantum chemistry methods for determining spectroscopic properties of alkyl peroxy radicals have been developed, these methods may or may not be applicable to substituted peroxy systems such as HMP.

In this thesis chapter, we predict the A-X electronic transition frequency and the extent of torsional mode coupling through quantum chemistry methods. We calculate potential energy surfaces as a function of the two torsional modes of HMP (OCOH, OOCO) for both the X and A states at a variety of levels of theory and bases. We also use composite methods to determine the A-X transition frequency. We also extend our methods to the product of HO₂ + acetone, HOC(CH₃)₂OO• (2-hydroxyisopropylperoxy, 2-HIPP) to provide predictions of spectroscopic bands for future studies. Our potential energy surfaces indicate that further studies must be carried out to determine the best overall method for calculation of the spectroscopic properties of substituted alkyl peroxies such as HMP.

Introduction

In Chapter 4, we presented the mid-IR and near-IR spectra of the products of the $\text{HO}_2 + \text{HCHO}$ reaction. Based on our chemistry analysis, kinetics modeling, band simulations, and preliminary quantum chemistry calculations, we assigned both spectra to the primary product $\text{HOCH}_2\text{OO}\cdot$ (HMP, Reaction 5.1): the mid-IR spectrum to the ν_1 (OH stretch) vibrational mode, and the near-IR spectrum to the A-X electronic transitions.



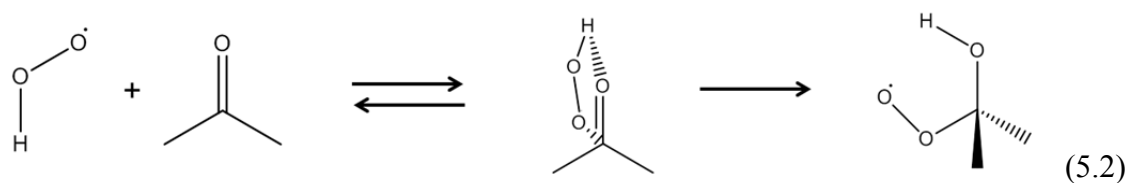
At the end of Chapter 4, we made two key observations about each spectrum when comparing to the spectra of similar molecules. First, the position of the ν_1 band of HMP (3622 cm^{-1}) is red shifted from the ν_1 bands of methanol (3681 cm^{-1}) and ethanol (3675 cm^{-1}).⁴⁰ We have already observed (HOONO, Chapter 3) that the formation of internal hydrogen bonds can cause red shifts in the OH stretch frequency. In HMP, interaction between the peroxy (OO) and hydroxy (OH) groups will cause this red shift. The bond is likely weaker than in HOONO due to the magnitude of the red shifts (60 cm^{-1} in HMP, 270 cm^{-1} in HOONO). Nonetheless, even a weak interaction may cause coupling between vibrational modes involving the peroxy and hydroxy groups, notably the two torsions OOCO (ν_{15}) and HOCO (ν_{13}), causing extra complexity in the vibrational spectrum.

Second, we observed some qualitative differences between the A-X spectrum of HMP and $\text{CH}_3\text{OO}\cdot$.¹²² In the HMP spectrum, we observe the OOCO torsional combination band 15_0^1 , but do not observe the sequence band 15_1^1 . The opposite holds true

in $\text{CH}_3\text{OO}\cdot$: Chung et al. observe the methyl torsion sequence band 12_1^1 , but not the combination band 12_0^1 . Given this discrepancy, it is important to confirm the assignment of our HMP spectrum. The possible torsional coupling suggested by the ν_1 spectrum makes this task harder, as all of the assigned bands could be affected by HMP's internal hydrogen bond.

Within the last 15 years, Terry Miller and co-workers have developed a general framework for modeling the electronic transitions of alkylperoxy radicals.⁴⁴ Miller uses G2,¹²³ a composite quantum chemistry method (explained in Appendix C) to obtain X and A state energies of alkylperoxies. The accuracy of these calculations is 10–200 cm^{-1} . Predictions are most accurate for small molecules (such as $\text{CH}_3\text{OO}\cdot$), and get worse with increasing size (such as 3-pentylperoxy)⁴⁴ or halogenation of the alkyl chain (such as $\text{CF}_3\text{OO}\cdot$).¹²⁴ Both molecules above can be thought of as substituted versions of methylperoxy (3-pentylperoxy replacing two of the H on $\text{CH}_3\text{OO}\cdot$ with C_2H_5 , $\text{CF}_3\text{OO}\cdot$ simply replacing all hydrogens with fluorines). Substitution may affect the electronic structure and interactions of the peroxy group with the rest of the radical. **Thus, there is no guarantee that the G2 method commonly employed for prediction of peroxy spectra will be adequate for HMP, a substituted alkylperoxy with internal hydrogen bonding involving the peroxy group.**

The “holy grail” of the spectroscopic studies presented in Chapter 4 is to detect the primary product of $\text{HO}_2 + \text{acetone}$ (Reaction 5.2): $\text{HOC}(\text{CH}_3)_2\text{OO}\cdot$ (2-hydroxyisopropylperoxy, or 2-HIPP).



Recent studies have shown that HO_2 disappears faster in the presence of acetone; however, by monitoring HO_2 alone, these studies cannot differentiate between Reaction 5.2 and an enhancement of HO_2 self-reaction. Direct spectroscopic detection of 2-HIPP would provide evidence that Reaction 5.2 does in fact take place. However, there are no predictions as to where the spectroscopic bands of 2-HIPP should be located. In order to make a meaningful prediction of the 2-HIPP spectrum, we must first determine an appropriate method for modeling 2-HIPP.

In this thesis chapter, we present two dimensional potential energy surfaces for the ground (X) and first excited (A) states of HMP, as a function of the OCOH and OOCO dihedral angles. These surfaces were analyzed to determine the extent of torsion-torsion coupling due to internal hydrogen bonding. We also determine the A-X transition frequency on the basis of these calculations. By carrying these calculations out at a wide variety of levels of theory and bases, we can determine appropriate methods for modeling substituted alkyl peroxies such as HMP. We then extend our results to predict the ν_1 and A-X spectra of 2-HIPP.

Methods

All quantum chemistry calculations in this chapter were performed in Gaussian 03W.⁷⁹ We used three single processor, single core, Windows XP PCs (Caltech). Potential energy surface data were compiled in GaussView 3.09,¹²⁵ and the resulting plots were generated in SigmaPlot 8.0.¹²⁶

We generated potential energy surfaces of HMP as a function of the two dihedral angles OCOH and OOCO by performing relaxed energy scans (i.e., for each set of dihedral angles (τ_{OCOH} , τ_{OOCO}), all other molecular coordinates were allowed to relax). A-X transition frequencies were obtained by performing a geometry optimization in both the A and X states, then subtracting the difference in energies. This transition frequency was scaled to HO₂ (Equation 5.3) to correct for systematic errors in the quantum chemistry method and zero point energy effects.

$$\left(E_{\text{A-X,HMP}}\right)_{\text{actual}} = \left(E_{\text{A-X,HMP}}\right)_{\text{calc}} \times \frac{\left(E_{\text{A-X,HO}_2}\right)_{\text{actual}}}{\left(E_{\text{A-X,HO}_2}\right)_{\text{calc}}} \quad (5.3),$$

where $\left(E_{\text{A-X,HO}_2}\right)_{\text{actual}} = 7029 \text{ cm}^{-1}$.⁵⁴

Based on the results of these potential energy surfaces, we examined the global minimum of the X state and the associated potential energy well of the A state in greater detail to obtain information about the A-X transition frequency. We calculated the geometries, energies, and vibrational frequencies of the wells in the X and A states, making use of anharmonic frequency calculations (VPT2) when available in Gaussian 03W. The resulting energy differences were scaled to HO₂ according to Equation 5.3 in order to make the best estimates of the A-X transition frequency.

Geometries and energies for the excited (A) state of HMP were obtained by “freezing” the electrons in the excited state configuration at each step of the self-consistent field calculation, similar to the method developed by Miller and co-workers (see Appendix C for details of this method).⁴⁴

The specific levels of theory and bases used for this study are summarized in Table 5.1. Note that in Gaussian 03W and 09W, anharmonic frequencies are only available at the HF, B3LYP, and MP2 levels of theory.

Table 5.1. Summary of levels of theory and bases used for HMP calculations

Level of Theory	Basis	A-X Transition	Anharmonic Frequencies ^a	Potential Energy Surface
B3LYP	6-31+G(d,p)	Yes	Yes	Yes
	6-311++G(2df,2p)	Yes	Yes	—
	cc-pVDZ	Yes	Yes	Yes
	aug-cc-pVDZ	Yes	Yes	—
CCSD	6-31+G(d,p)	Yes	—	Yes
	cc-pVDZ	Yes	—	—
	aug-cc-pVDZ	Yes	—	—
	cc-pVTZ	Yes	—	—
MP2(FC)	6-31+G(d,p)	Yes	Yes	Yes
MP2(Full)	6-31+G(d,p)	Yes	Yes	Yes
MP4(SDQ)	6-31+G(d,p)	Yes	—	Yes
MP4(SDTQ)	6-31+G(d,p)	Yes	—	—
QCISD	6-31+G(d,p)	Yes	—	—
CIS	6-31+G(d,p)	Yes	—	—
TD-HF	6-31+G(d,p)	Yes	—	—
TD-B3LYP	6-31+G(d,p)	Yes	—	—
	cc-pVDZ	Yes	—	—
EOM-CCSD	6-31+G(d,p)	Yes	—	—
	aug-cc-pVDZ	Yes	—	—
	cc-pVTZ	Yes	—	—
G1	—	Yes	—	—
G2	—	Yes	—	—
CBS-QB3	—	Yes	—	—
W1U	—	Yes	—	—

a) Anharmonic frequencies not available in Gaussian 03W for CCSD, MP4, QCISD, or composite methods

Results

We present the results of our study in three parts. First, we present the 2-dimensional torsional potential energy surfaces of HMP. We show the molecular geometries of the local minima in both the X and A states. The potential energy surfaces show evidence of torsional mode coupling in the X state, but not the A state. These surfaces show that density functional theory and coupled cluster methods are able to

locate all three conformers of HMP on the X state, but Möller-Plesset perturbation theory is not able to locate one of the conformers. Second, we present the vibrational and A-X transition frequencies calculated using density functional, coupled cluster, perturbation, equation of motion, and composite quantum chemistry methods. We observe generally good agreement between experiment and theory across most of these methods. We conclude that density functional, coupled cluster, and composite methods based on these levels of theory are appropriate for modeling HMP. Third, we extend our study to 2-HIPP, predicting the vibrational and A-X bands. We predict 2-HIPP to have an A-X frequency in the range 7900–8000 cm^{-1} , significantly to the blue of HMP.

Torsion-Torsion Potential Energy Surfaces of HMP

Figures 5.1–5.3 show a series of 2-dimensional potential energy surfaces of HMP as a function of the two dihedral angles τ_{COH} and τ_{OCO} . Figure 5.1 shows the B3LYP/6-31+G(d,p) calculated X and A surfaces with the three minima and $(\tau_{\text{COH}}, \tau_{\text{OCO}})=(0^\circ, 0^\circ)$ transition state (TS) labeled. Figure 5.2 shows the X and A state potential energy surfaces for the remaining DFT and coupled-cluster calculations: B3LYP/cc-pVDZ and CCSD/6-31+G(d,p). Figure 5.3 shows the surfaces from the three perturbation theory calculations: MP2(FC)/6-31+G(d,p), MP2(Full)/6-31+(d,p), and MP4(SDQ)/6-31+G(d,p).

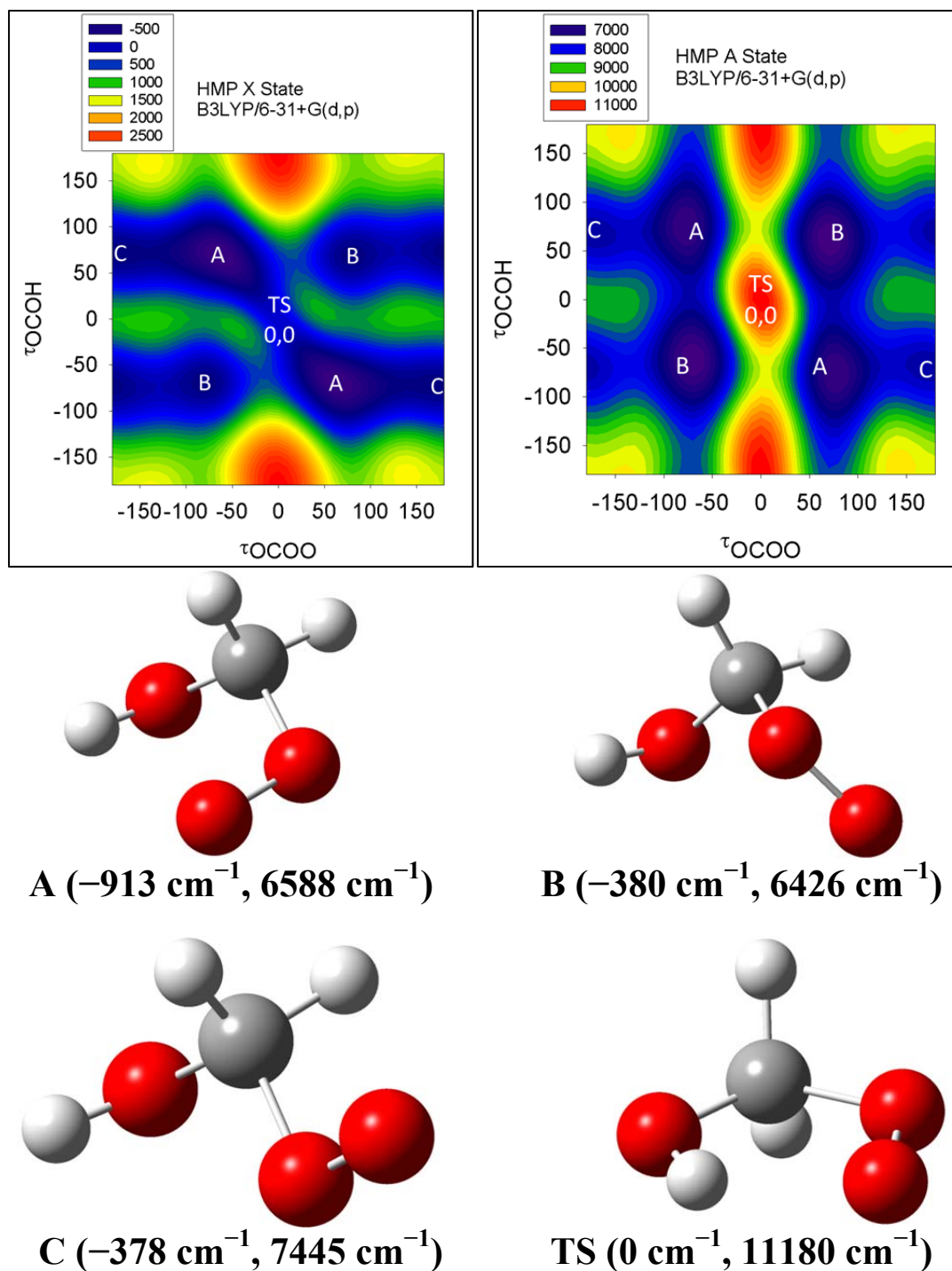


Figure 5.1. B3LYP/6-31+G(d,p) potential energy surfaces of HMP for the X state (left) and A state (right), as a function of the dihedral angles τ_{OCOH} and τ_{OOCO} . The local minima (A, B, C) at the X state geometries, and C_s transition state (TS), are labeled on each surface. The listed energies (X state, A state) are relative to the X state of TS, unscaled. The geometries of these conformers are shown below the surfaces. Energies on the potential energy surfaces are in cm^{-1} , relative to the X state C_s transition state energy.

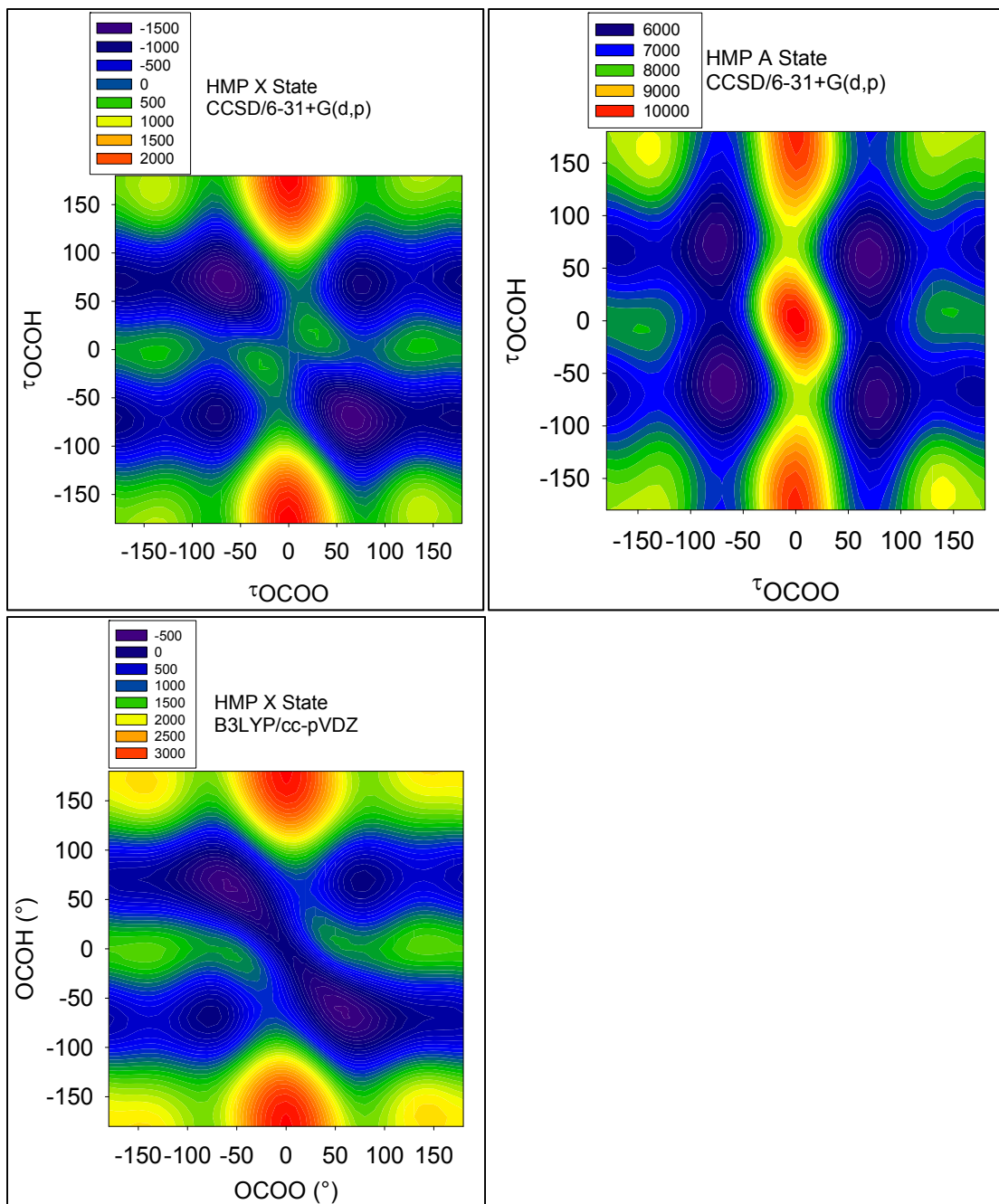
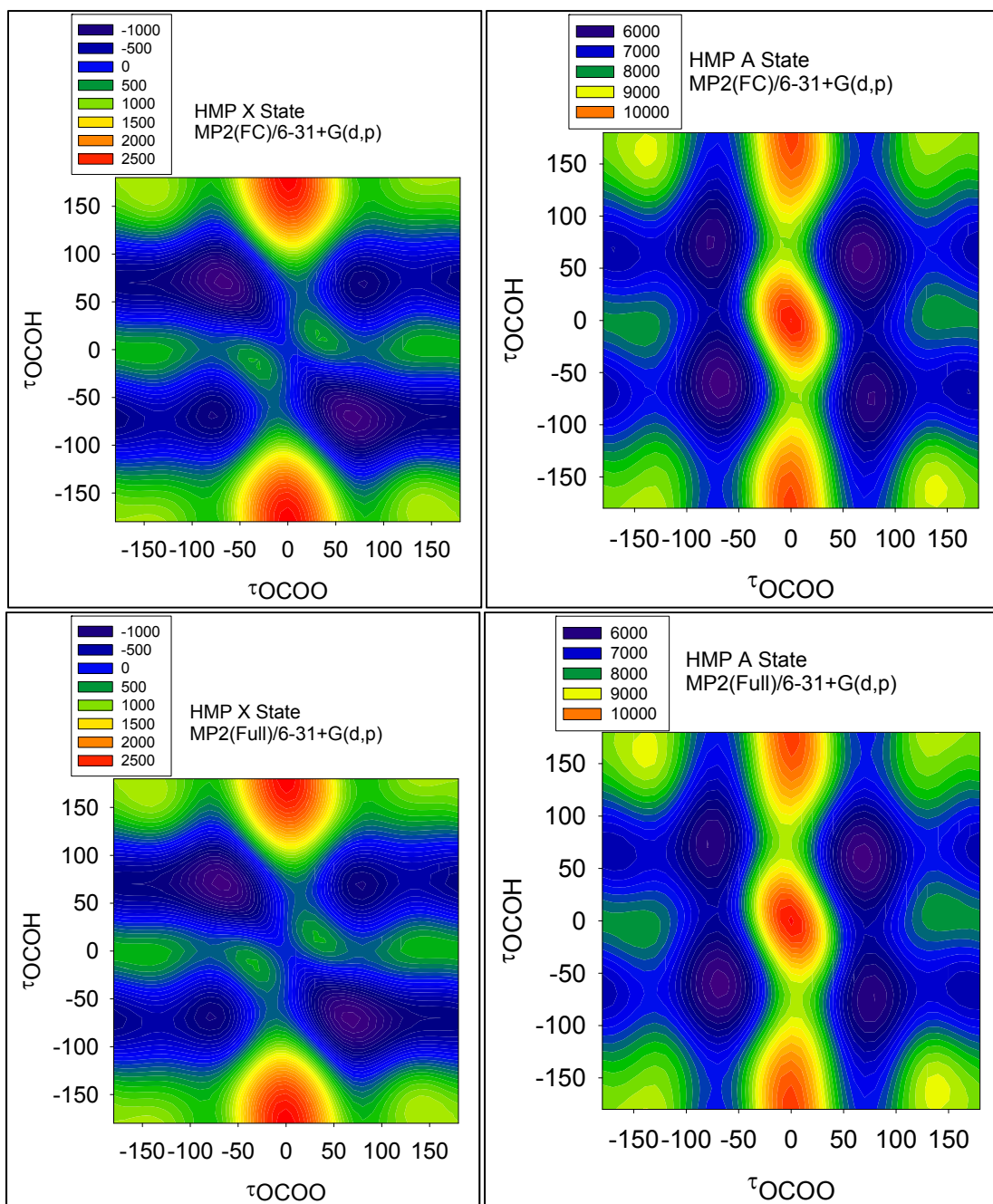


Figure 5.2. CCSD/6-31+G(d,p) (top) and B3LYP/cc-pVDZ (bottom) potential energy surfaces of HMP for the X state (left) and A state (right), as a function of the dihedral angles τ_{OCOH} and τ_{OOCO} . Energies on the potential energy surfaces are in cm^{-1} , relative to the X state C_s transition state energy.



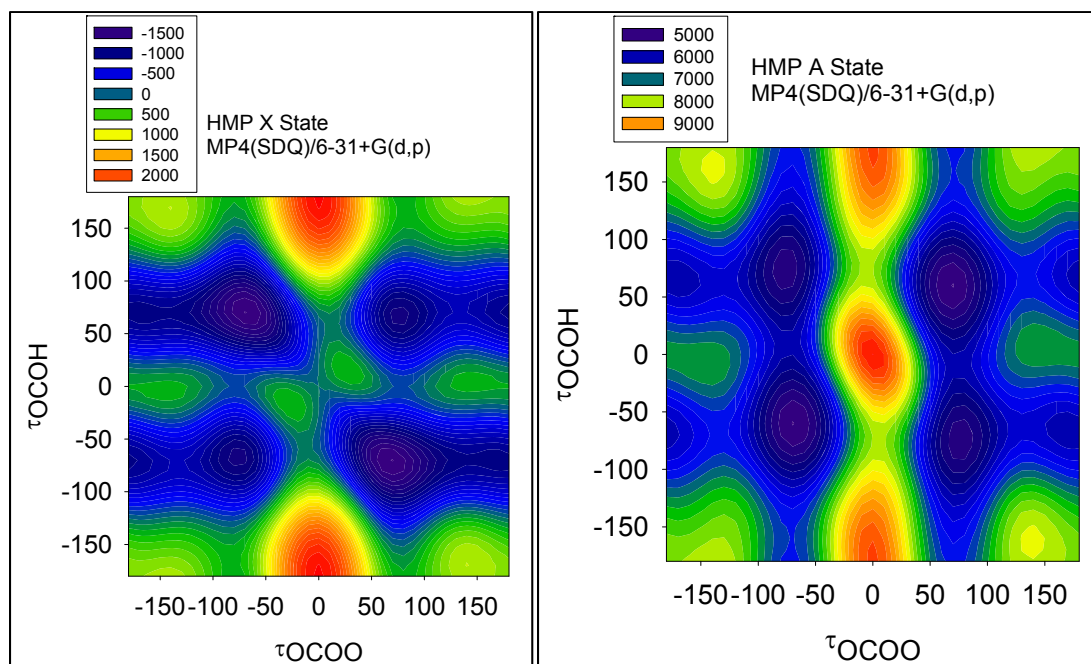


Figure 5.3. MP2(FC)/6-31+G(d,p) (top of previous page), MP2(Full)/6-31+(d,p) (bottom of previous page), and MP4(SDQ)/6-31+G(d,p) (this page) potential energy surfaces of HMP for the X state (left) and A state (right), as a function of the dihedral angles τ_{OCOH} and τ_{OCOO} . Energies on the potential energy surfaces are in cm^{-1} , relative to the X state C_s transition state energy.

First, consider the X state surface and energies presented in Figure 5.1 (B3LYP/6-31+G(d,p)). There are three nonequivalent minima on the potential energy surface representing rotation of the peroxy group, similar to the three equivalent minima observed for $\text{CH}_3\text{OO}\cdot$.¹²⁷ The global minimum conformer (Figure 5.1, labeled Conformer A) features an internal hydrogen bond. At B3LYP/6-31G(d,p), the energy stabilization provided by this hydrogen bond is 550 cm^{-1} , calculated by comparison to the two nonhydrogen bound conformers (B and C). The potential energy well is off axis (diagonal on the τ_{OCOH} , τ_{OCOO} plot), indicating that the two torsional modes are coupled to each other.

The TS is not a maximum on the surface; at least 1000 cm^{-1} is required to move from TS to B. Rather, it is a saddle point, and any HMP in the TS conformer will convert to conformer A without any energy barrier. Although the TS appears to have an internal hydrogen bond, it is actually higher in energy than the three minima, likely due to unfavorable orbital overlap from placing the OH and OO groups' relative orientation. Clearly there is interaction between these two groups in TS: the minimum energy path is also off axis.

Next consider the A state surface and energies in Figure 5.1. There are still three minima, but there are several qualitative differences compared to the X state surface. First, we observe that all three minima are on-axis, and the energy of Conformer A is approximately equal to Conformer B (in fact, Conformer B is now the global minimum by 150 cm^{-1}). These two facts imply that there is no hydrogen bonding in the A state of HMP. Second, TS is now a maximum on the surface rather than a saddle point. This affords the possibility of TS being converted into either Conformer A or B. Finally, we note that the positions of the minima on the X state (the positions of the letters) do not match exactly with the minima on the A state. In particular, the wells for conformer A are slightly shifted in τ_{OOCO} .

The potential energy surfaces in Figure 5.2, when compared to Figure 5.1, show the effects of increasing the level of theory (from B3LYP to CCSD) while keeping the basis set constant (6-31+G(d,p)), and changing the basis set (from 6-31+G(d,p) to cc-pVDZ) while keeping the level of theory constant (B3LYP). The CCSD/6-31+G(d,p) surfaces have the same qualitative features as the B3LYP/6-31+G(d,p) surfaces. On the X state surface, we still observe three local minima with one hydrogen bonded conformer

(normal modes coupled) stabilized by 550 cm^{-1} compared to the other two conformers. The A state still shows three minima, none with normal mode coupling, and Conformer B is slightly lower in energy than Conformer A (-200 cm^{-1}). The main difference between the CCSD/6-31+G(d,p) and B3LYP/6-31+G(d,p) surfaces is the relative energy of TS (900 cm^{-1} above conformer A at B3LYP, 1700 cm^{-1} at CCSD). Nonetheless, the qualitative agreement between the B3LYP and CCSD surfaces suggests that B3LYP may be a good method for modeling our $\text{HO}_2 + \text{carbonyl}$ systems.

Comparison of the B3LYP/cc-pVDZ surface to the B3LYP/6-31+G(d,p) surface reveals some similarities (three minima, one hydrogen bound) and some significant qualitative changes: widening of the TS saddle point and reduced barrier heights between conformers. This is likely due to the relative inflexibility of the cc-pVDZ basis set (no polarization or diffuse functions) compared to the 6-31+G(d,p) basis. Similar surfaces at aug-cc-pVDZ (not shown here) did agree qualitatively with the 6-31+G(d,p) surface, indicating that polarization and diffuse functions are required to model the HMP radical properly.

Finally, there is one disturbing difference between the perturbation method surfaces (Figure 5.3) and the B3LYP/CCSD surfaces (Figures 5.1 and 5.2). The barrier between Conformers C and A was 75 cm^{-1} (B3LYP/6-31+G(d,p)) or 100 cm^{-1} (CCSD/6-31+G(d,p)), and we can therefore calculate properties of conformer C at these two levels of theory. In contrast, at MP2(FC), MP2(Full), or MP4(SDQ), Conformer C is no longer a minimum; rather, it is a shelf (similar to the cis-perp region of HOONO from Chapter 3).

Calculated A-X Transition Frequencies

The most important conformers of HMP in our experiments will be conformers A and B. These potential energy wells are relatively deep (Figures 5.1–5.3); a radical in these conformations will be bound by $>900\text{ cm}^{-1}$ (conformer A) or 280 cm^{-1} (conformer B), as calculated at B3LYP/6-31+G(d,p). We therefore focus our attention on calculating the A-X transition frequencies out of these two conformations, with the global minimum (conformer A) being the most important due to its very deep well depth.

Tables 5.2–5.5 summarize the calculated A-X frequencies, OOCO torsion frequencies in the A and X states, and OH stretch frequencies. In Table 5.2, we scale all of the transition frequencies to HO_2 using Equation 5.3. In Tables 5.3–5.5, we calculate anharmonic frequencies using two methods: scaling the harmonic frequencies using known scaling factors,¹²⁸ or directly calculating anharmonic frequencies in Gaussian 09.¹²¹ In Figures 5.4–5.7, we show the deviations of each method's calculated frequencies to the experimentally determined values (Chapter 4). We discuss the data in these tables and figures after Figure 5.7.

Table 5.2. Calculated A-X transition frequencies (cm^{-1}) of HMP conformers A and B, scaled to HO_2 (7029 cm^{-1}).⁵⁴

Level of Theory	Basis	A-X, scaled, Conformer A ^a	A-X, scaled, Conformer B	$\frac{(\text{HO}_2)_{\text{actual}}}{(\text{HO}_2)_{\text{calc}}}$
B3LYP	6-31+G(d,p)	7272	6598	0.969
	6-311++G(2df,2p)	7182	6590	0.970
	cc-pVDZ	7326	6603	0.964
	aug-cc-pVDZ	7318	6697	0.962
CCSD	6-31+G(d,p)	7428	6634	1.040
	cc-pVDZ	7434	—	1.047
	aug-cc-pVDZ	7455	—	1.031
HF	6-31+G(d,p)	7061	6361	1.435
MP2(FC)	6-31+G(d,p)	7413	6574	1.028
MP2(Full)	6-31+G(d,p)	7409	6574	1.025
MP4(SDQ)	6-31+G(d,p)	7381	—	1.091
CIS	6-31+G(d,p)	6944	6446	1.110
TD-HF	6-31+G(d,p)	6941	6346	1.306
TD-B3LYP	6-31+G(d,p)	—	6548	0.879
	cc-pVDZ	7388	6607	0.885
EOM-CCSD	6-31+G(d,p)	—	—	1.073
	aug-cc-pVDZ	—	—	1.057
	cc-pVTZ	—	—	1.055
G1	—	7349 ^b	—	N/A ^b
G2	—	7424 ^b	—	N/A ^b
CBS-QB3	—	7479 ^b	—	N/A ^b
W1U	—	7443 ^b	—	N/A ^b

a) Observed A-X frequency of Conformer A is 7391 cm^{-1} (Chapter 4)

b) Composite methods are not scaled to HO_2

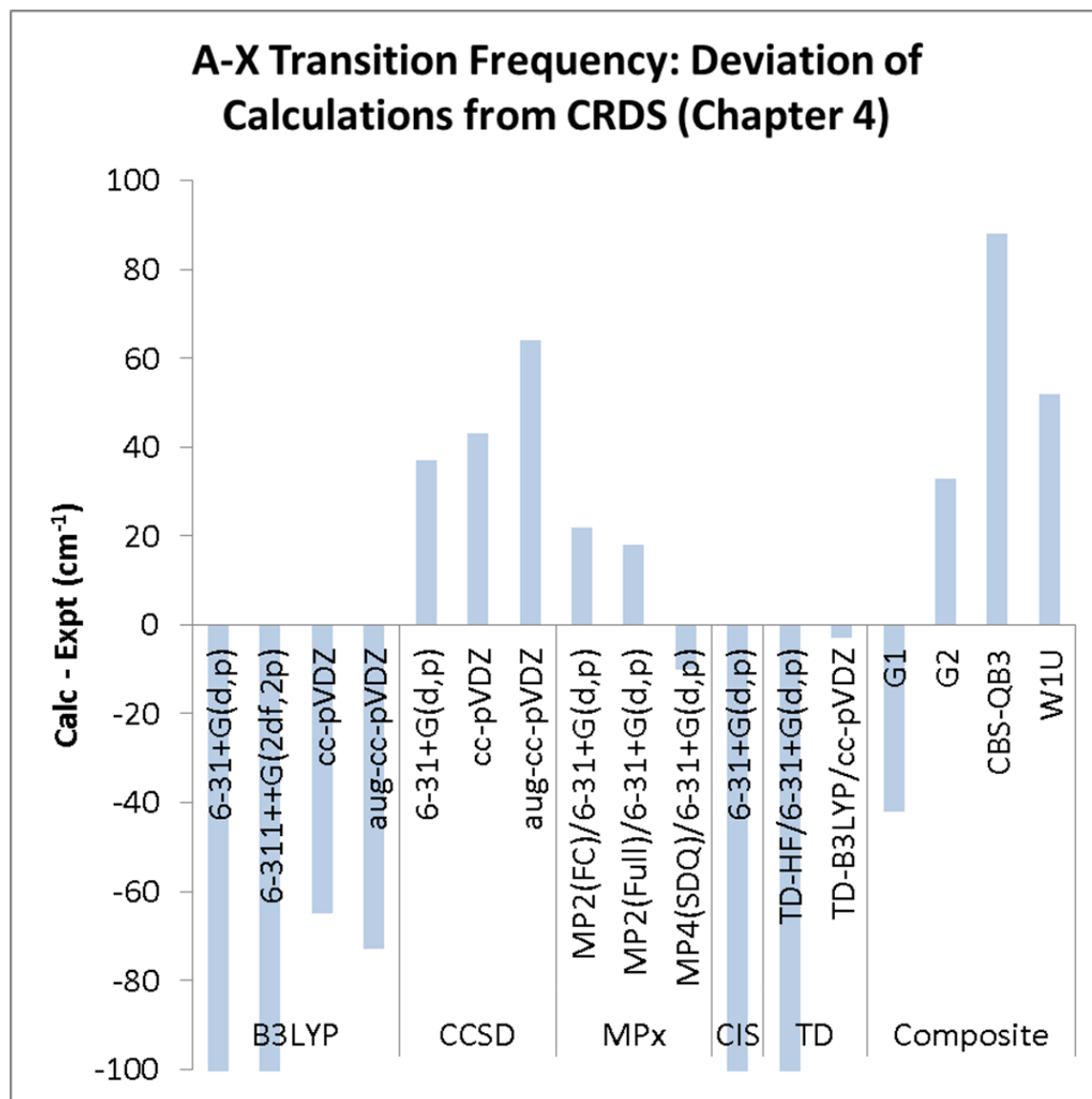


Figure 5.4. Deviation of calculated A-X frequency of HMP from experiment (CRDS, Chapter 4).

Table 5.3. Calculated ν_{15} (OOCO torsion) frequency for the A state of HMP conformer A, harmonic, harmonic scaled,¹²⁸ and anharmonic.

Level of Theory	Basis	ν_{15} A, harmonic ^a	ν_{15} A, harmonic, scaled ^a	ν_{15} A, anharmonic ^a
B3LYP	6-31+G(d,p)	175	168	168
	6-311++G(2df,2p)	176	170	168
	cc-pVDZ	176	170	169
	aug-cc-pVDZ	173	168	168
CCSD	6-31+G(d,p)	173	162	—
	cc-pVDZ	178	169	—
	aug-cc-pVDZ	175	167	—
HF	6-31+G(d,p)	176	159	—
MP2(FC)	6-31+G(d,p)	176	165	172
MP2(Full)	6-31+G(d,p)	177	165	173
MP4(SDQ)	6-31+G(d,p)	173	165	—
MP4(SDTQ)	6-31+G(d,p)	168	160	—
G2	—	175 ^b	165 ^b	—
CBS-QB3	—	177 ^b	171 ^b	—

a) Observed ν_{15} A state frequency is 170 cm^{-1} ($(15_0^1 - 0_0^0)$, Chapter 4)

b) Composite method frequencies taken from the zero-point energy calculation

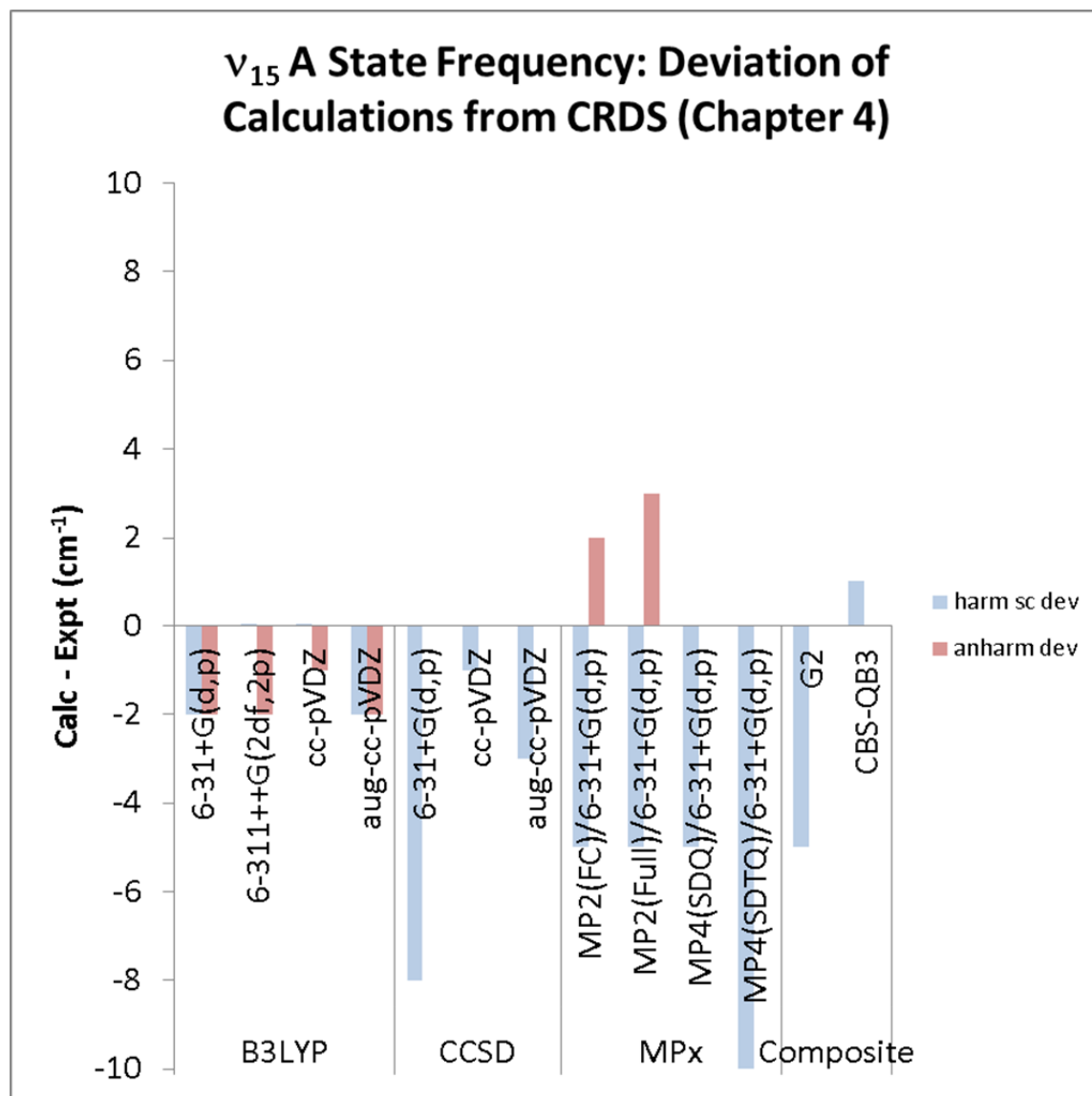


Figure 5.5. Deviation of calculated ν_{15} A state frequency of HMP from experiment (CRDS from $15_0^1 - 0_0^0$, Chapter 4).

Table 5.4. Calculated ν_{15} (OOCO torsion) frequencies (cm^{-1}) for the X state of HMP conformer A, harmonic, harmonic scaled,¹²⁸ and anharmonic.

Level of Theory	Basis	ν_{15} X, harmonic ^a	ν_{15} X, harmonic, scaled ^a	ν_{15} X, anharmonic ^a
B3LYP	6-31+G(d,p)	112	108	111
	6-311++G(2df,2p)	109	105	105
	cc-pVDZ	111	108	91
	aug-cc-pVDZ	109	106	108
CCSD	6-31+G(d,p)	140	131	—
	cc-pVDZ	143	136	—
	aug-cc-pVDZ	139	131	—
HF	6-31+G(d,p)	149	135	142
MP2(FC)	6-31+G(d,p)	124	116	116
MP2(Full)	6-31+G(d,p)	124	116	116
MP4(SDQ)	6-31+G(d,p)	132	126	—
G2	—	149 ^b	141 ^b	—
CBS-QB3	—	113 ^b	109 ^b	—

a) Observed ν_{15} X state frequency is 116 cm^{-1} ($(0_0^0 - 15_1^0)$), Chapter 4)

b) Composite method frequencies taken from the zero-point energy calculation

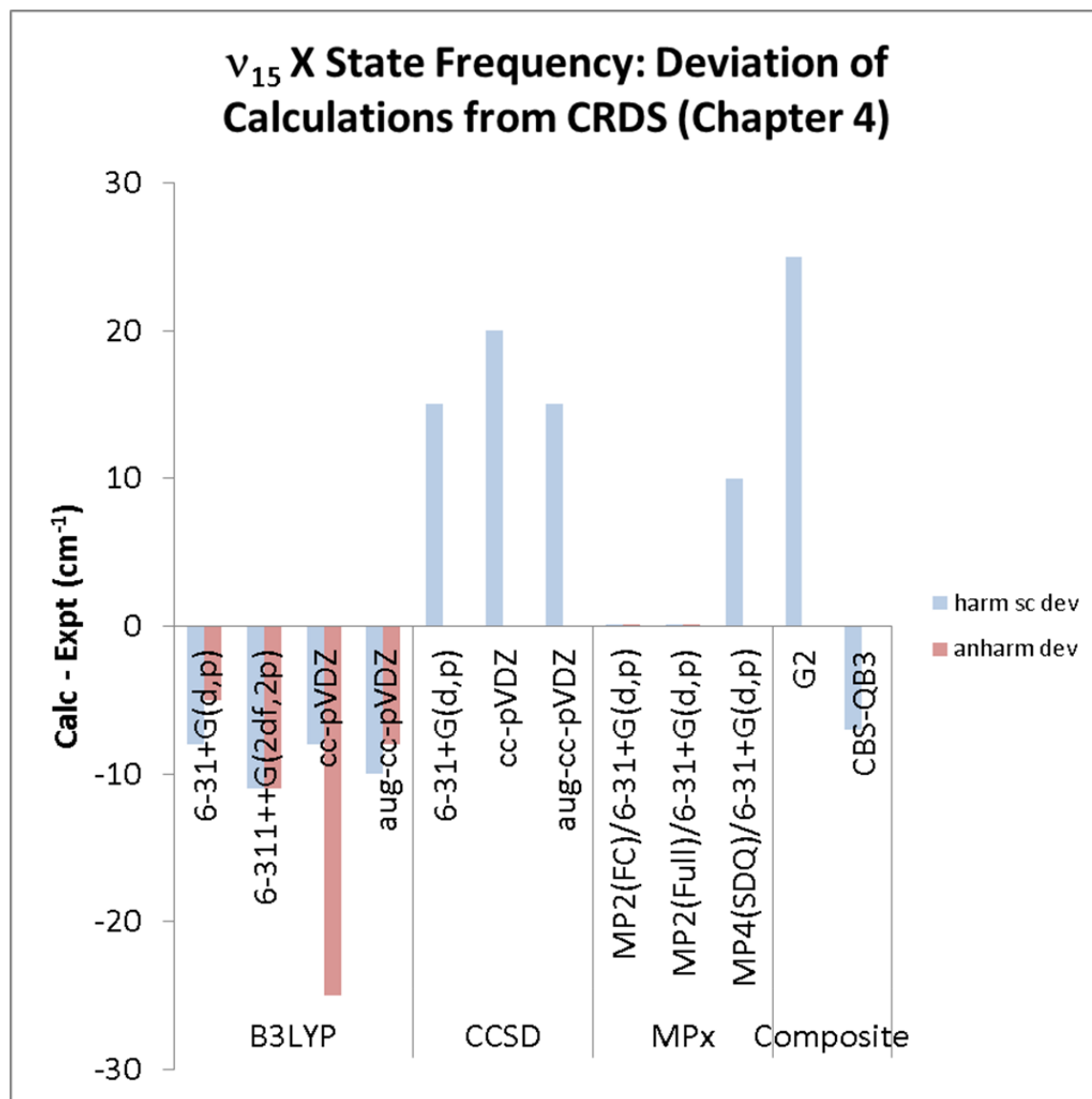


Figure 5.6. Deviation of calculated ν_{15} X state frequency of HMP from experiment (CRDS from $0_0^0 - 15_1^0$, Chapter 4).

Table 5.5. Calculated ν_1 (OH stretch) frequencies (cm^{-1}) for the X state of HMP conformer A, harmonic, harmonic scaled,¹²⁸ and anharmonic.

Level of Theory	Basis	ν_1 X, harmonic ^a	ν_1 X, harmonic, scaled ^a	ν_1 X, anharmonic ^a
B3LYP	6-31+G(d,p)	3800	3663	3602
	6-311++G(2df,2p)	3805	3676	3604
	cc-pVDZ	3730	3619	3519
	aug-cc-pVDZ	3783	3669	3580
CCSD	6-31+G(d,p)	3882	3626	—
	cc-pVDZ	3840	3637	—
	aug-cc-pVDZ	3825	3622	—
HF	6-31+G(d,p)	4175	3770	4001
MP2(FC)	6-31+G(d,p)	3859	3615	3667
MP2(Full)	6-31+G(d,p)	3861	3606	3669
MP4(SDQ)	6-31+G(d,p)	3886	3711	—
G2	—	4097 ^b	3864 ^b	—
CBS-QB3	—	3797 ^b	3672 ^b	—

a) Observed ν_1 frequency is 3622 cm^{-1} (Chapter 4)

b) Composite method frequencies taken from the zero-point energy calculation

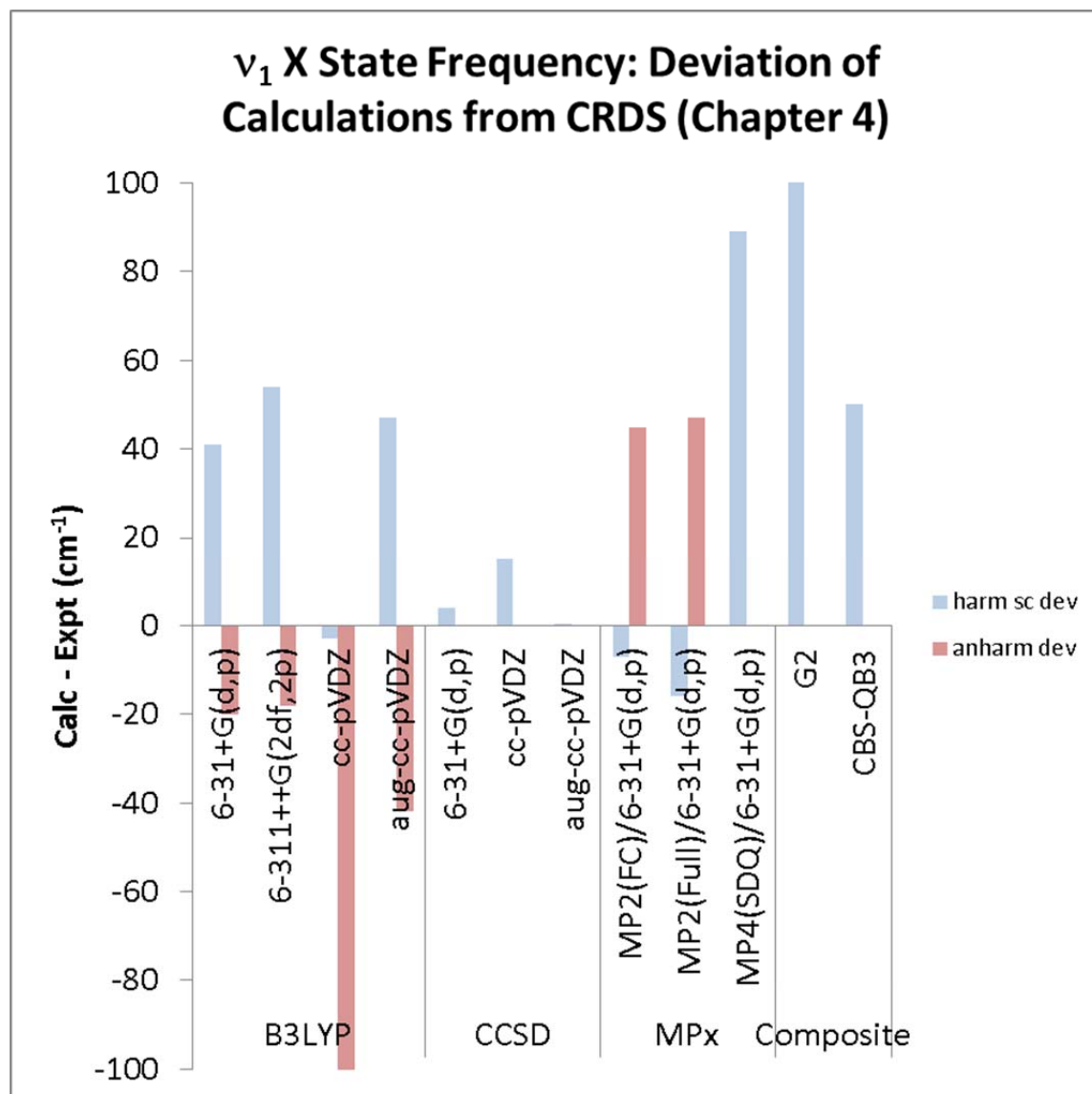


Figure 5.7. Deviation of calculated ν_1 frequency of HMP from experiment (CRDS, Chapter 4).

A-X transition frequency (Table 5.2, Figure 5.4) – Our desired accuracy for the calculated A-X bands is $\pm 50 \text{ cm}^{-1}$. Based on the existing studies of alkyl peroxy electronic transitions, we expect that this level of accuracy for HMP will allow us to make predictions of larger systems (2-HIPP) within 100 cm^{-1} . According to Figure 5.4, CCSD (across three basis sets), MP_x , and the composite chemistry methods all satisfy this requirement. B3LYP is only able to come within this accuracy using certain basis sets

(cc-pVDZ and aug-cc-pVDZ) or the time dependent formulation TD-B3LYP. We observe that CIS and TD-HF both predict the A-X frequency too low by 400 cm^{-1} , completely unacceptable.

$\nu_{15}(A)$ torsional frequency (Table 5.3, Figure 5.5) – We immediately note that nearly all of the methods tested can reproduce the ν_{15} A state frequency to within 10 cm^{-1} , with the exception of HF/6-31+G(d,p). The majority of the calculated torsional frequencies are lower than the observed frequency (170 cm^{-1}). Overall, the B3LYP calculations are the most consistent and accurate (-2 cm^{-1}).

$\nu_{15}(X)$ torsional frequency (Table 5.4, Figure 5.6) – In general, B3LYP (and even the associated composite method CBS-QB3) and MP2 can reproduce the ν_{15} X state frequency within 10 cm^{-1} . We see more signs of cc-pVDZ being too inflexible for modeling HMP: the B3LYP/cc-pVDZ anharmonic frequency is underpredicted by 25 cm^{-1} . Meanwhile, all of the CCSD calculations overpredict the torsional frequency by $15\text{--}20\text{ cm}^{-1}$.

$\nu_1(X)$ torsional frequency (Table 5.5, Figure 5.7) – CCSD does an excellent job of modeling the OH stretch, reproducing the ν_1 frequency within 15 cm^{-1} across all of the basis sets used. Scaled MP2 also is quite accurate. However, the anharmonic MP2 calculations, all B3LYP calculations, and the MP4 calculations perform poorly, with predictions off by at least 40 cm^{-1} .

Looking at all of the data in Tables 5.2–5.5 and Figures 5.4–5.7, we notice that each level of theory perform differently for each spectroscopic property. Table 5.6 summarizes which methods were considered acceptable for each spectroscopic band of HMP (A-X, ν_{15} A, ν_{15} X, and ν_1). Methods were considered acceptable if the results generally fit into the “acceptable range” (discussed above and listed in the table). There is no “perfect” method to model all four relevant bands. Nonetheless, with the exception of CIS and TD-HF calculations, reasonably accurate spectroscopic frequencies for HMP can be generated by using any of the quantum chemistry methods presented in this chapter.

Table 5.6. Summary of levels of theory that gave acceptable and unacceptable predictions of HMP spectroscopic bands

Band	Expt. (Chapter 4) (cm^{-1})	Acceptable range (cm^{-1})	Acceptable levels of theory	Unacceptable levels of theory
A-X	7391	± 100	B3LYP (Dunning) ^a CCSD MP _x TD-B3LYP G1/G2 CBS-QB3 W1	B3LYP (Pople) ^a CIS TD-HF
ν_{15} (A)	170	± 10	B3LYP CCSD MP _x	—
ν_{15} (X)	116	± 10	B3LYP MP _x	CCSD
ν_1	3622	± 20	CCSD	B3LYP MP _x

a) Dunning type basis sets yielded errors of -65 and -73 cm^{-1} . Pople type basis sets yielded errors of -119 and -209 cm^{-1} .

Calculated Potential Energy Surfaces and Spectroscopic Frequencies of 2-HIPP

Finally, we extend the methods presented in this chapter to generate potential energy surfaces and to predict of the spectroscopic properties of 2-HIPP. 2-HIPP has a greater number of atoms (13 vs 7) and electrons than HMP (49 vs 33). At a given level of theory and basis, calculations on 2-HIPP will be more expensive than HMP. Because of this, we report less data for 2-HIPP than for HMP.

Figure 5.8 shows the X state potential energy surface for 2-HIPP as a function of the two dihedral angles τ_{COH} and τ_{OCO} , at B3LYP/6-31+G(d,p), HF/6-31+G(d,p) MP2(FC)/6-31+G(d,p), and MP2(Full)/6-31+G(d,p). Figure 5.9 shows the A state surface of 2-HIPP at HF/6-31+G(d,p). Similar to Figures 5.1–5.3, all energies are in cm^{-1} , relative to the $(\tau_{\text{COH}}, \tau_{\text{OCO}}) = (0, 0)$ transition state.

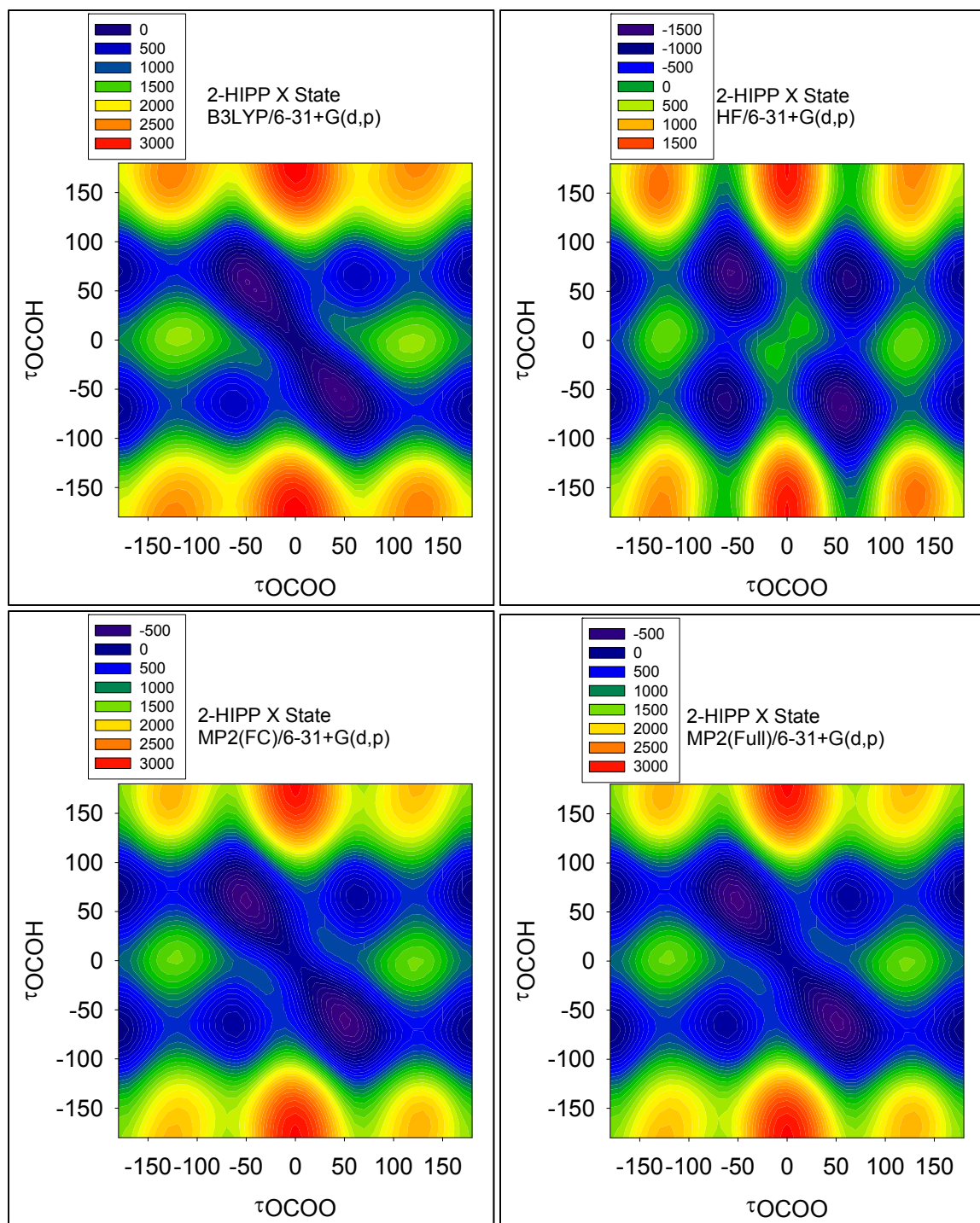


Figure 5.8. 2-HIPP X State potential energy surfaces as a function of the dihedral angles τ_{OCOH} and τ_{OOCO} . Surfaces calculated at B3LYP/6-31+G(d,p) (top left), HF/6-31+G(d,p) (top right), MP2(FC)/6-31+G(d,p) (bottom left), and MP2(Full)/6-31+G(d,p) (bottom right). Energies on the potential energy surfaces are in cm^{-1} , relative to the X state C_s transition state energy.

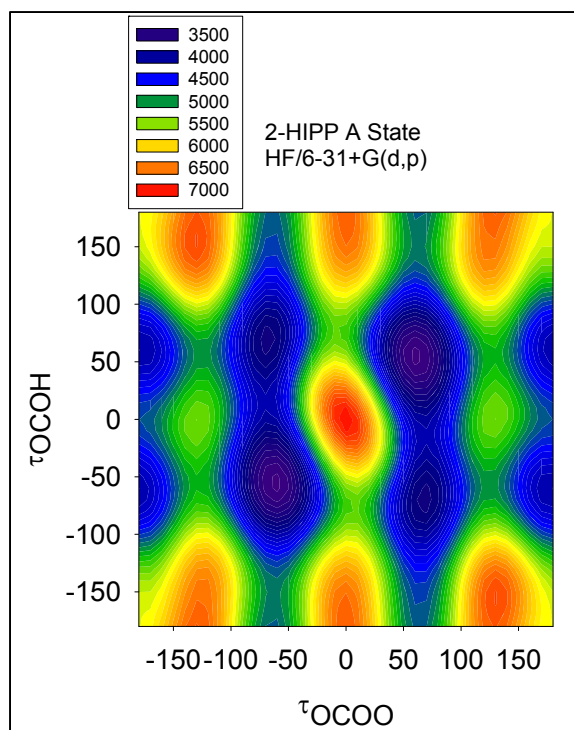


Figure 5.9. 2-HIPP A State potential energy surface as a function of the dihedral angles τ_{OCOH} and τ_{OOCO} . Surface calculated at HF/6-31+G(d,p). Energies in cm^{-1} , relative to the X state C_s transition state energy.

Comparing the 2-HIPP surfaces (Figures 5.8 and 5.9) to HMP (Figures 5.1–5.3), we note several similar features. On the X state, there are three energy minima. The global minimum, equivalent to Conformer A, is off-axis, indicating that hydrogen bonding is leading to coupling of normal modes (although this coupling is not evident on the low-quality HF surface). The A state of 2-HIPP also has three minima. Similar to HMP, the global minimum of the A state corresponds to the equivalent of Conformer B.

The main qualitative difference between HMP and 2-HIPP are the energetics of Conformers B and C. In 2-HIPP, Conformer C is more stable than Conformer B (-200 cm^{-1} for C vs 0 cm^{-1} for B), and has a higher barrier to conformational change via the OOCO torsion (600 cm^{-1} for C, 500 cm^{-1} for B). In HMP, the opposite held true: Conformer B was more stable energetically and had a higher barrier to conformational change.

Table 5.8 summarizes calculated spectroscopic parameters of Conformer A of 2-HIPP: the A-X transition frequency (scaled to HO₂), ν_{33} (OOCO torsion) frequency in the A and X states, and ν_1 (OH stretch) frequency. These parameters were only calculated at selected levels of theory and bases due to the increased computational expense of 2-HIPP calculations compared to HMP. We note that at the most reliable levels of theory (B3LYP, G1, G2), the A-X transition is predicted to be in the range 7900–8000 cm⁻¹, well to the blue of HMP (7391 cm⁻¹). The B3LYP vibrational calculation predicts that the ν_1 band should appear in a similar location as HMP (3620 cm⁻¹), red shifted from a typical alcohol due to the internal hydrogen bond.

Table 5.8. Calculated A-X, ν_{33} (OOCO torsion, A and X states), and ν_1 (OH stretch) frequencies (cm⁻¹) of 2-HIPP. A-X scaled to HO₂ (7029 cm⁻¹).⁵⁴

Level of Theory	Basis	A-X, scaled	ν_{33} A (harm / sc)	ν_{33} X (harm / sc)	ν_1 (harm / sc)
B3LYP	6-31+G(d,p)	7913	132 / 128	113 / 109	3756 / 3621
HF	6-31+G(d,p)	7572	137 / 124	151 / 136	4168 / 3764
CIS	6-31+G(d,p)	7195	—	—	—
TD-HF	6-31+G(d,p)	7204	—	—	—
TD-B3LYP	6-31+G(d,p)	7362	—	—	—
	cc-pVDZ	7440	—	—	—
G1	—	7877	—	—	—
G2	—	7988	—	—	—

Discussion

Preliminary Thoughts on the Appropriate Level of Theory for Substituted Alkyl Peroxies

The data presented in Figures 5.2–5.8 and Tables 5.1–5.9 show that no one single method can model all aspects of HMP accurately. Nonetheless, we can make preliminary

recommendations as to what methods should be used for modeling our HO₂+carbonyl products on the basis of our HMP data.

Regarding the A-X electronic transition frequencies of HMP (Table 5.2, Figure 5.4), we note that CCSD, MPx, G2, and W1 perform similarly (within 50 cm⁻¹ of the observed value). However, the MPx surfaces (Figure 5.3) do not predict X state Conformer C to be bound, in contrast to all of the other calculated surfaces. Consequently, G2 cannot predict a transition frequency for Conformer C, since it uses an MP2 geometry for all of its energy calculations.¹²³ **At this time, we recommend CCSD or W1 for calculation of the A-X transition frequencies and potential energy surface calculations.** Note that for larger systems such as 2-HIPP, these calculations will become very expensive, likely only accessible with a supercomputer. B3LYP can reproduce the qualitative features of the CCSD X and A surfaces and is much cheaper than CCSD. However, the absolute accuracy of the A-X transition suffers (± 150 cm⁻¹). B3LYP is likely an appropriate starting point for larger systems before embarking on the more expensive CCSD or W1 calculations.

Regarding the low lying OOCO torsional modes, we observe that B3LYP and MP2 are able to reproduce the frequency within 10% of the observed values. CCSD overestimates the ν_{15} X state significantly (15%) across all of the basis sets used. **Although limited data exist at this time, we recommend B3LYP or MPx for calculation of torsional mode frequencies.**

Regarding the OH stretch, only CCSD can consistently reproduce the observed frequency within 15 cm⁻¹. For B3LYP and MPx, the significant discrepancies between

the anharmonic and scaled harmonic frequencies raise questions about those methods' accuracy. **We recommend only CCSD for calculation of OH stretch frequencies.**

Normal Mode Coupling and its Effect on Vibrational Frequencies, Sequence Bands

The vibrational frequency analysis presented in Tables 5.2–5.5, 5.7, and 5.8 make use of the normal mode frequencies reported by Gaussian 09.¹²¹ The two torsional modes OOCO and OCOH are reported as pure torsions. However, the potential energy surfaces presented in Figures 5.1–5.3 show that the two modes should be coupled together due to the internal hydrogen bond. We therefore expect the actual vibrational modes to be mixed together, resulting in changes in the vibrational energy levels similar to HOONO (Chapter 3).

We also expect the internal hydrogen bond to affect the ν_1 spectrum. We may observe the formation of sequence bands due to torsionally excited HMP breaking the internal hydrogen bond, again similar to HOONO (Chapter 3). Unlike HOONO, this effect will likely not cause intensity to be shifted to the blue of the observed ν_1 band, because the frequency difference between HMP and similar alcohols is small (55 cm^{-1} , Chapter 4). Rather, we may observe significant sequence band formation to the red of the main band because the OH stretch frequency should decrease significantly as the geometry of HMP approaches the $(\tau_{\text{OCOH}}, \tau_{\text{OOCO}}) = (0, 0)$ TS state, where there is even greater interaction between the OH and OO groups.

In order to fully understand how hydrogen bonding and coupling between vibrational modes affects HMP, we would have to explicitly calculate the energy levels based on the potential energy surfaces presented in this chapter. This study would be

interesting and worthwhile; we have already observed slight discrepancies in the width of the simulated and observed ν_1 spectra (Chapter 4). Unfortunately, such a project is outside the scope of our research, and would have to be performed in collaboration with a theorist (such as we did for the HOONO project in Chapter 3).

Conclusions

In this chapter, we have modeled spectroscopic properties of hydroxymethylperoxy (HMP) by computing the ground (X) and excited (A) state 2-dimensional potential energy surfaces as a function of the two dihedral angles (τ_{OCOH} , τ_{OOCO}), A-X electronic transition frequency, OOCO torsional frequency, and OH stretch vibrational frequency. Our potential energy surfaces reveal coupling between the OCOH and OOCO torsions on the X state (an effect of internal hydrogen bonding in HMP), but not in the A state. We locate three conformers of HMP on each surface, although the third conformer on the X state is either a shallow well or a shelf depending on the level of theory used. Our calculated electronic and vibrational frequencies are in excellent agreement with the experimentally observed HMP vibrational and electronic spectra (Chapter 4). On the basis of our results, we make the following recommendations for modeling our HO₂ + carbonyl systems: CCSD for potential energy surfaces, CCSD or W1 for modeling electronic transitions, B3LYP or MPx for torsional frequencies, and CCSD for OH stretch frequencies. We applied these methods to 2-HIPP (HO₂ + acetone) and predicted the A-X, OOCO torsion, and OH stretch frequencies. The torsion-torsion coupling observed on our X state surfaces indicates that explicit calculation of torsional energy levels may be required to accurately simulate HMP spectra.

Acknowledgements

We thank Heather L. Widgren for computing some of the G2 energies. The computations performed in this chapter were funded under NASA Upper Atmosphere Research Program Grants NAG5-11657, NNG06GD88G, and NNX09AE21G2, California Air Resources Board Contract 03-333 and 07-730, National Science Foundation CHE-0515627, and a Department of Defense National Defense Science and Engineering Graduate Fellowship (NDSEG).

Chapter 6—Kinetics of HO₂ + HCHO and Further Reaction of the Hydroxymethylperoxy Radical (HOCH₂OO•)

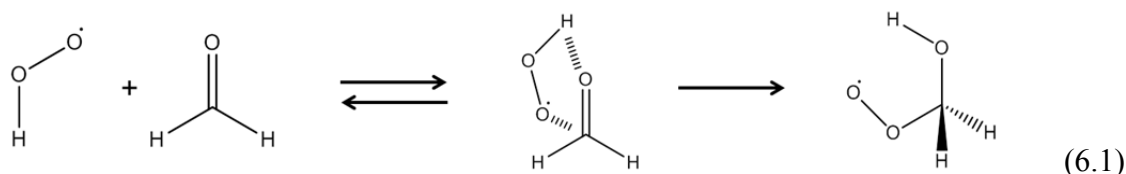
Abstract

In Chapters 4 and 5, we presented and assigned the ν_1 and A-X spectra of the isomerization product of HO₂ + HCHO: the hydroxymethylperoxy radical (HOCH₂OO•, HMP). Based on our chemistry analysis, the observed bands are unique to HMP (early times only for ν_1 , all times for A-X). In this thesis chapter, we use the ν_1 and A-X cavity ringdown spectra of HMP to measure its formation (HO₂ + HCHO) and destruction kinetics. We determine the rate constant $k_{\text{HO}_2+\text{HCHO}}$ by measuring the ν_1 absorption as a function of time under pseudo first order conditions ($[\text{HCHO}] \gg [\text{HO}_2]$). Destruction of HMP is monitored by measuring the A-X absorptions as a function of time and comparing to a kinetics model using existing rate constants. Using the ν_1 band, we report $k_{\text{HO}_2+\text{HCHO}} = (4.8 \pm 1.7) \times 10^{-14} \text{ cm}^3 \text{ molec}^{-1} \text{ s}^{-1}$ (2σ), in excellent agreement with previous studies. Our A-X study gives an HMP destruction rate in agreement with the existing kinetics model (for our conditions, lifetime 1 ms). These results indicate that the previous end-product and B-X (contaminated spectra) studies were able to model secondary chemistry and subtract out contaminations quite well.

The methods described in Chapters 4-6 can be readily extended to the HO₂ + acetone system: directly detecting 2-hydroxyisopropylperoxy (2-HIPP). We show in this chapter that in order to carry out CRDS measurements on 2-HIPP, we need to cool our kinetics cell to 190–250 K, depending on the exact equilibrium constant for the HO₂ + acetone reaction.

Introduction

Let us begin with a summary of what we have learned about $\text{HO}_2 + \text{HCHO}$ so far from our CRDS and quantum chemistry studies. Our spectroscopy studies in Chapter 4 support the current understanding of the $\text{HO}_2 + \text{HCHO}$ reaction (Reaction 6.1): formation of a complex followed by isomerization to form the hydroxymethylperoxy radical ($\text{HOCH}_2\text{OO}\cdot$, or HMP).



We have detected both the ν_1 (OH stretch) vibrational band of HMP, and the A-X electronic transition characteristic of all peroxy radicals. The intensities,¹²² positions, shapes of these spectroscopic bands are consistent with our quantum chemistry calculations (Chapter 5). Additionally, the chemistry analysis presented in Chapter 4 indicates that under our experimental conditions, our spectra are dominated by HMP. With all of these pieces of data, we are confident that our spectra can be assigned to HMP.

We now turn our attention to the kinetics of HMP: both formation (Reaction 6.1) and destruction (Reactions 6.2–6.6). The main destruction pathways of HMP are reaction with HO_2 (Reactions 6.2 and 6.3) or self-reaction (Reactions 6.4 and 6.5). Termination of Reaction 6.5 ($\text{HOCH}_2\text{O}\cdot$) occurs by reaction with O_2 .





Previous studies have measured the kinetics of HMP formation and destruction either by end-product analysis^{24, 99} or by direct measurement via the B-X band in the UV.^{25, 26} These two methods each come with their own set of problems. Any end-product study must make assumptions about the rest of the kinetics model in order to derive a rate constant for the reaction of interest ($\text{HO}_2 + \text{HCHO}$), subjecting $k_{\text{HO}_2+\text{HCHO}}$ (or other rate constants) to large uncertainties. The kinetics as measured by the B-X bands required corrections for other chemical species, notably HCOOH, which forms in large quantities over the timescales used for the previous experiments (1 s).^{25, 26}

We can use the spectroscopic bands of HMP from Chapter 4 to measure the kinetics of Reactions 6.1-6.6. Under the correct conditions, both of these bands (ν_1 , A-X) will provide direct detection and unique measures of HMP. Each spectroscopic band carries its own advantages and disadvantages. The ν_1 band is unique to HMP at early times (shown in Chapter 4, Figure 4.2) and is very strong ($\sigma = 10^{-19} \text{ cm}^2 \text{ molec}^{-1}$), making it ideal for measuring the formation rate of HMP ($k_{\text{HO}_2+\text{HCHO}}$, Reaction 6.1). However, as observed from Reactions 6.2–6.6, other ν_1 bands (HOCH_2OOH , $\text{HOCH}_2\text{O}\cdot$, HCOOH) will interfere with the spectrum at later times, making measurements of HMP destruction impossible. Conversely, the A-X bands are weak ($\sigma = 10^{-21} \text{ cm}^2 \text{ molec}^{-1}$), making measurements of $k_{\text{HO}_2+\text{HCHO}}$ difficult due to the fast rise time of the HMP absorption. Because the A-X bands are unique measures of HMP, these bands are well-suited for making measurements of the relatively slow HMP destruction (lifetime 1 ms under our conditions, as shown in Chapter 4).

In our spectroscopy study, we made use of a large excess of [HCHO] (a factor of 30–1000 greater than [HO₂]), in effect keeping [HCHO] constant during the experiment. By using similar conditions in our kinetics study, we can obtain pseudo-first-order kinetics when analyzing the HMP formation (Reaction 6.1).

This thesis chapter describes the first kinetics measurements on HMP formation and destruction as measured via the ν_1 vibrational and A-X electronic bands of HMP. Similar to the experiments in Chapter 4, HMP was generated by pulsed laser photolysis of Cl₂ in the presence of formaldehyde and O₂. Cavity ringdown spectroscopy was used to measure the formation and destruction of HMP by monitoring the ν_1 and A-X absorptions as a function of time (0–1000 μ s) after HO₂ formation. The formation kinetics were measured as a function of [HO₂] in order to determine the rate constant $k_{\text{HO}_2+\text{HCHO}}$. The destruction kinetics were compared to a kinetics model to assess the quality of existing rate constants.

Methods

Apparatus and Chemicals

The cavity ringdown spectrometer, laser system, and gas kinetics flow cell have been described in detail in Chapter 2 (Figures 2.5, 2.7, 2.8), and only a brief summary of the mid-IR (MIR) and near-IR (NIR) configurations is presented here.

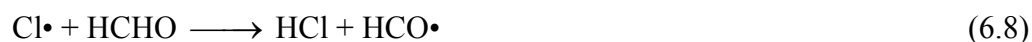
Tunable MIR light used to measure kinetics via the ν_1 absorption of HMP was generated using an optical parametric amplifier. For 65 mJ of 532 nm light and 4–12 mJ of tunable red light (620–665 nm), 0.6–0.8 mJ of tunable infrared light was generated (2900–3800 cm⁻¹). The infrared light was sent into an optical cavity consisting of two

highly reflective mirrors (Los Gatos Research, 2.8 μm peak, $R = 99.98\%$). Ringdown traces were collected with a liquid nitrogen cooled InSb detector (Judson J10D-M204-R01M-60) connected to a voltage amplifier (Analog Modules 351A-3) and PC oscilloscope card (GageScope CS1450). 80 μs of ringdown data were collected per shot, and 16 ringdowns were collected and averaged before being fit. The first eighth of the ringdown lifetime was removed before the data were refit in order to eliminate errors caused from noise near the peak of the ringdown.

Tunable NIR light used to measure kinetics via the A-X absorptions of HMP (6900–8500 cm^{-1} , 100 $\mu\text{J/pulse}$) was generated by sending the output from a Nd:YAG (532 nm, 370 mJ/pulse) pumped dye laser (DCM, Rh 640, or Rh 610 dye, 590–660 nm, 40 mJ/pulse peak) into a H_2 filled Raman shifter. The infrared light was sent into an optical cavity consisting of two highly reflective mirrors (Los Gatos Research, 1.35 or 1.20 μm peak, $R = 99.98\%$ or 99.99%). Ringdown traces were collected with an amplified InGaAs detector (ThorLabs PDA400) connected to a PC oscilloscope card (GageScope CS1450). 80 μs of ringdown data were collected per shot, and 16 ringdowns were collected and averaged before being fit. The first 1/20 of the ringdown lifetime was removed before the data were refit in order to eliminate errors caused from noise near the peak of the ringdown.

The hydroxymethylperoxy radicals ($\text{HOCH}_2\text{OO}\cdot$, HMP) measured in this experiment were generated by photolysis of Cl_2 in the presence of HCHO and O_2 (Reactions 6.7-6.9 and 6.1). Photolysis was initiated by 351 nm light from the excimer laser described in Chapter 2. The absorption cross section of Cl_2 at 351 nm is $\sigma_{351\text{nm}} = 1.9 \times 10^{-19} \text{ cm}^2 \text{ molec}^{-1}$.²⁷ For the MIR experiments, the UV flux was kept at 1.8×10^{17}

molec cm⁻³, resulting in 3.2% of the Cl₂ being photolyzed. For the NIR experiments, the UV flux was kept at 4.4×10^{17} photons cm⁻², resulting in 8.0% of the Cl₂ being photolyzed.



Cl₂ was introduced to the cell from a gas cylinder consisting of 3.5% Cl₂ in He (Air Liquide or Matheson Tri-Gas). HCHO was introduced to the cell by flowing N₂ gas through a vessel of paraformaldehyde (Sigma-Aldrich, 95%) heated to 110 °C. Heating paraformaldehyde leads to the formation of HCHO monomers and oligomers. To trap the oligomers, the N₂/HCHO gas was sent to a dry ice/acetone trap before being sent to the CRDS cell. This method was verified to produce a consistent [HCHO] ($\pm 10\%$ between experiments) as measured by the 2v₂ R branch (3510–3520 cm⁻¹)⁴⁰ and A-X bands (300–310 nm).¹¹⁶

Experimental and Flow Conditions

In our experiments, [HCHO] was factor of 30–1000 higher than [HO₂], with [HCHO] = 1×10^{17} molec cm⁻³ and [HO₂] = (1–30) $\times 10^{14}$ molec cm⁻³. We showed in Chapter 4 that by keeping [HCHO]:[HO₂] high, our v₁ spectrum is relatively free of interference from H₂O₂. Higher [HO₂] was required in the NIR in order to generate the higher [HMP] necessary to make measurements via the weak A-X bands (Chapter 4).

Kinetics measurements were made by keeping the spectrometer at a constant frequency and varying the photolysis-probe delay time over the range 0–1000 μs . As shown in the *Results* section, only the first 50 μs of data were used in the MIR (ν_1) experiment due to interference from other species at longer times (HMHP, HCOOH, H₂O₂). The entire range of photolysis-probe times was used for the NIR (A-X) experiment.

The experimental conditions for the HMP kinetics experiments are summarized in Table 6.1. Gas flows were measured using the flowmeters discussed in Chapter 2. The temperature of the gas kinetics cell was taken to be room temperature: no temperature control of any kind was attempted.

Table 6.1. Experimental conditions (gas flows, photolysis parameters, chemical concentrations, and spectrometer performance) for HMP kinetics experiments

	HMP, v_1 (MIR)	HMP, A-X (NIR)
N ₂ Purge Flow – Left Mirror	450 sccm	450 sccm
N ₂ Purge Flow – Right Mirror	450 sccm	450 sccm
N ₂ /HCHO Flow	250 sccm	250 sccm
3.5% Cl ₂ / He Flow	14–70 sccm	170 sccm
N ₂ Dilution Flow	1250 sccm	1250 sccm
O ₂ Flow	650 sccm	650 sccm
Cell Pressure	300 torr	330 torr
Temperature (room)	293 ± 2 K	293 ± 2 K
Flush Time	30 ms	25 ms
Photolysis Window Length	5 cm	5 cm
Excimer Energy at 351 nm	160 ± 10 mJ/pulse	160 ± 10 mJ/pulse
% Cl ₂ Photolyzed	3.2%	8.0%
[Cl•] ₀ ~ [HO ₂] ₀	(1–5) × 10 ¹⁴ cm ⁻³	3 × 10 ¹⁵ cm ⁻³
[HCHO]	1 × 10 ¹⁷ cm ⁻³	1 × 10 ¹⁷ cm ⁻³
[O ₂]	2.0 × 10 ¹⁸ cm ⁻³	2.2 × 10 ¹⁸ cm ⁻³
Optical Cell Length	52 cm	52 cm
1/τ ₀ (purge only)	1.3 × 10 ⁵ Hz, 3638 cm ⁻¹	1.2 × 10 ⁵ Hz, 7550 cm ⁻¹
1/τ (background gases)	1.4 × 10 ⁵ Hz, 3638 cm ⁻¹	1.3 × 10 ⁵ Hz, 7550 cm ⁻¹
Δτ/τ ^a	0.34%	0.28%
Sensitivity (2σ)	2.1 ppm Hz ^{-1/2}	1.6 ppm Hz ^{-1/2}

a) Δτ/τ reported for averaging 16 ringdown traces per point

The cell flush time, [Cl₂], and [Cl•] are calculated from the experimental parameters in Table 6.1. Derivations of these equations are presented in Chapter 8; therefore, only the final results are presented here. The flush time is defined as the amount of time to remove the chemicals within the photolysis length from the ringdown cavity, and is calculated from Equation 6.10:

$$t_{flush} = \left(\frac{V_{in-out}}{\sum_{flush} f_i} \right) \times \left(\frac{P_{cell}}{P_{st}} \right), \quad (6.10)$$

where t_{flush} is the flush time for the chemical sample, V_{in-out} is the volume between the inlet for butyl nitrite and vacuum outlet ($V_{in-out} = 3.93 \text{ cm}^3$ for the cell used in these

experiments), $\sum_{flush} f_i$ is the total flow rate of gases in the direction of flushing (in sccm),

p_{cell} is the pressure in the CRDS cell, and p_{st} is the standard pressure (760 torr).

The fraction of Cl_2 that is photolyzed can be calculated from Equation 6.11:

$$\%_{photolysis} = \frac{\left(\frac{P_{excimer}}{A_{meter}} \right)}{F_{excimer}} \left(\frac{\lambda}{hc} \right) (\sigma_{Cl_2, \lambda}) (X) \left(\frac{A_{UV, laser}}{A_{UV, CRDS}} \right), \quad (6.11)$$

where $\%_{photolysis}$ is the fraction of RONO that is photolyzed, $(P_{excimer}/A_{meter})$ is the power per unit area of the UV light (read directly from the power meter), $F_{excimer}$ is the repetition rate of the excimer laser (10 Hz), h is Planck's constant, c is the speed of light, λ is the wavelength of the excimer light (351 nm), $\sigma_{Cl_2, \lambda}$ is the absorption cross section of Cl_2 at the excimer wavelength ($1.9 \times 10^{-19} \text{ cm}^2 \text{ molec}^{-1}$ at 351 nm), X is the quantum yield for photolysis (taken to be 1), $A_{UV, laser}$ is the area of excimer beam measured at the excimer laser output, and $A_{UV, CRDS}$ is the area of excimer beam measured at the CRDS cell. For

the ν_1 experiment, $\frac{A_{UV, laser}}{A_{UV, CRDS}} = 2$. For the A-X experiment, $\frac{A_{UV, laser}}{A_{UV, CRDS}} = 5$.

Results

We present the results of our kinetics study in four parts. First, we analyze the kinetics of $HO_2 + HCHO$ to derive an equation for the rate constant k_{HO_2+HCHO} based on our CRDS measurements. Second, we show the kinetics of HMP formation using the ν_1 band. In this part, we derive k_{HO_2+HCHO} . We also show that at long times, absorbance in the ν_1 region remains constant despite formation of $HCOOH$, indicating that the ν_1 band of HMP cannot be used to measure its destruction rate. Third, we show the kinetics of

HMP as measured by the A-X band. These results clearly show the destruction of HMP, and we derive a lifetime of HMP under our experimental conditions. In the *Discussion* section, we compare our results to the existing kinetic rate constants and our kinetics model. Our results are in excellent agreement with the literature, indicating that secondary chemistry and spectral interferences were well modeled in the previous studies.

Predicted HO₂ + HCHO Kinetics

At the beginning of our experiment (<100 μs), we have very fast conversion of Cl• to HO₂ (see the analysis from Chapter 4). Thus, we only need to be concerned with two reactions: HO₂ + HCHO (Reaction 6.1) and HO₂ self-reaction (Reaction 6.12)



where (+M) indicates that there are bimolecular and termolecular pathways.

We would like to derive an expression for how [HMP] will vary in time as a function of known parameters ([HCHO]₀, [HO₂]₀). The differentiated rate law for [HMP] is

$$\frac{d[\text{HMP}]}{dt} = k_1 [\text{HO}_2][\text{HCHO}], \quad (6.13)$$

where k_1 represents the rate constant for Reaction 6.1 (HO₂ + HCHO). Since we have chosen to use a large excess of [HCHO], we can reduce Equation 6.13 to a pseudo-first-order kinetics equation:

$$\frac{d[\text{HMP}]}{dt} = k_{1,eff} [\text{HO}_2], \quad (6.14)$$

where $k_{1,eff} = k_1 \times [\text{HCHO}]$.

Although [HCHO] is constant, [HO₂] is not, and we must determine the time dependence of [HO₂]. HO₂ is consumed by Reactions 6.1 and 6.12. Define k_{12a} as the rate constant for HO₂ bimolecular self-reaction and k_{12b} as the rate constant for HO₂ termolecular self-reaction. Then the differentiated rate law for [HO₂] is

$$-\frac{d[\text{HO}_2]}{dt} = 2(k_{12a} + k_{12b}[\text{M}])[\text{HO}_2]^2 + k_{1,\text{eff}}[\text{HO}_2], \quad (6.15)$$

where the factor of 2 indicates that two HO₂ radicals are consumed during self-reaction.

Integrating Equation 6.15 and solving for [HO₂](t) gives us

$$[\text{HO}_2](t) = \frac{k_{1,\text{eff}}[\text{HO}_2]_0}{k_{1,\text{eff}}e^{k_{1,\text{eff}}t} + 2(e^{k_{1,\text{eff}}t} - 1)(k_{12a} + k_{12b}[\text{M}])[\text{HO}_2]_0}. \quad (6.16)$$

Substituting Equation 6.16 back into Equation 6.14 yields

$$\frac{d[\text{HMP}]}{dt} = \frac{k_{1,\text{eff}}^2[\text{HO}_2]_0}{k_{1,\text{eff}}e^{k_{1,\text{eff}}t} + 2(e^{k_{1,\text{eff}}t} - 1)(k_{12a} + k_{12b}[\text{M}])[\text{HO}_2]_0}. \quad (6.17)$$

Although Equation 6.17 looks complicated, we can make a few simplifications based on the order of magnitudes for each term. Table 6.2 summarizes the orders of magnitudes for each term in Equation 6.17 and the parameters used to obtain these estimates.

Table 6.2. Orders of magnitude for each term in Equation 6.17, assuming conditions for the v_1 experiment ($[\text{HO}_2]_0 = 10^{14}$ molec cm⁻³, [HCHO] = 10^{17} molec cm⁻³, [M] = 10^{19} molec cm⁻³).

Parameter / Term	Estimate
k_1 (298 K)	5.5×10^{-14} cm ³ s ⁻¹ molec ⁻¹ ^{25, 26}
$k_{1,\text{eff}} = k_1 \times [\text{HCHO}]$	5500 s ⁻¹
k_{12a} (298 K)	1.5×10^{-12} cm ³ molec ⁻¹ s ⁻¹
k_{12b} (298 K)	4.9×10^{-32} cm ⁶ molec ⁻² s ⁻¹
$k_{1,\text{eff}}^2[\text{HO}_2]_0$	3×10^{21} cm ³ molec ⁻¹ s ⁻²
$k_{1,\text{eff}}e^{k_{1,\text{eff}}t}$	7241 s ⁻¹ ($t = 50$ μs)
Series Approx. $k_{1,\text{eff}}e^{k_{1,\text{eff}}t} \approx k_{1,\text{eff}}(1 + k_{1,\text{eff}}t)$	7013 s ⁻¹ ($t = 50$ μs)
$2(e^{k_{1,\text{eff}}t} - 1)(k_{12a} + k_{12b}[\text{M}])[\text{HO}_2]_0$	126 s ⁻¹

To first order, the $2(e^{k_{1,eff}t} - 1)(k_{12a} + k_{12b}[M])[HO_2]_0$ term is negligible compared to the $k_{1,eff}e^{k_{1,eff}t}$ term (for the highest $[HO_2]_0 = 5 \times 10^{14}$ molec cm^{-3} , this term will still be less than 5% of $k_{1,eff}e^{k_{1,eff}t}$). We also note that replacing $k_{1,eff}e^{k_{1,eff}t}$ with its Taylor series $k_{1,eff}(1 + k_{1,eff}t)$ only gives a 3% error at 50 μs . Using this Taylor series, we simplify Equation 6.17 at small times to

$$\frac{d[HMP]}{dt} = k_{1,eff} \left(\frac{[HO_2]_0}{k_{1,eff}t + 1} \right), \quad (6.18)$$

with the caveat that Equation 6.18 only holds true for the v_1 experiment (small $[HO_2]_0$) at short times ($<100 \mu s$). Even with this caveat, Equation 6.18 predicts that the slope $\frac{d[HMP]}{dt}$ will have a small time dependence due to depletion of HO_2 .

We can solve Equation 6.18 for $k_{1,eff}$, and then obtain k_1 :

$$k_{1,eff} = \frac{d[HMP]/dt}{[HO_2]_0 - \left(\frac{d[HMP]}{dt} \right) t}, \quad (6.19)$$

$$k_1 = \frac{d[HMP]/dt}{[HCHO] \left([HO_2]_0 - \left(\frac{d[HMP]}{dt} \right) t \right)}. \quad (6.20)$$

We cannot eliminate the $\left(\frac{d[\text{HMP}]}{dt}\right)t$ term, as this term indicates how much $[\text{HO}_2]$ has been depleted. Instead, we make the approximation

$$[\text{HO}_2]_0 - \left(\frac{d[\text{HMP}]}{dt}\right)t \approx [\text{HO}_2]_0 - \left(\frac{d[\text{HMP}]}{dt}\right)t_{\text{avg}}, \quad (6.21)$$

where t_{avg} is taken to be half of the times being fit. For example, if 50 μs worth of data are used to obtain $\left(\frac{d[\text{HMP}]}{dt}\right)$, then $t_{\text{avg}} = 25 \mu\text{s}$. By making this substitution, we obtain the relation between k_1 and our kinetics data:

$$k_1 = \frac{\frac{d[\text{HMP}]}{dt}}{[\text{HCHO}] \left([\text{HO}_2]_0 - \left(\frac{d[\text{HMP}]}{dt}\right)t_{\text{avg}} \right)}. \quad (6.22)$$

Equation 6.22 would be the same equation obtained from a kinetics analysis assuming that HO_2 self-reaction (Reaction 6.12) is negligible. This is true for low $[\text{HO}_2]$, where Reaction 6.1 will dominate. At higher HO_2 , we cannot make these approximations, and the HO_2 dependence must be represented by Equation 6.17. This is yet another reason why k_1 cannot be well determined from the A-X experiment: $[\text{HO}_2]$ is much greater than in the v_1 experiment.

Our derivation of Equation 6.22 has at least 10% error on the calculation of k_1 , due to the approximations made going from Equations 6.17 to 6.18, and the approximation made in Equation 6.21. However, this is likely of little consequence. Equation 6.22 depends on the absolute $[\text{HMP}]$, which requires knowledge of the absorption cross section σ to convert between absorbance and $[\text{HMP}]$. We are using absorption cross sections generated from relatively low levels of theory

(B3LYP/6-31+G(d,p)), and we expect much larger errors on the cross section ($> 20\%$) than from Equation 6.22.

Kinetics of HMP by ν_1 Absorption

Figures 6.1–6.4 show a series of kinetics traces for HMP measured at the two peaks of the ν_1 absorption band: 3610 cm^{-1} and 3630 cm^{-1} . We have already observed (Chapter 4) that these two regions are affected differently by interfering species (3610 cm^{-1} weakly by HCOOH , 3630 cm^{-1} by HOCH_2OOH , both by H_2O_2). By measuring the kinetics at both points of the ν_1 band, we can check that our measurements are invariant to the exact frequency used.

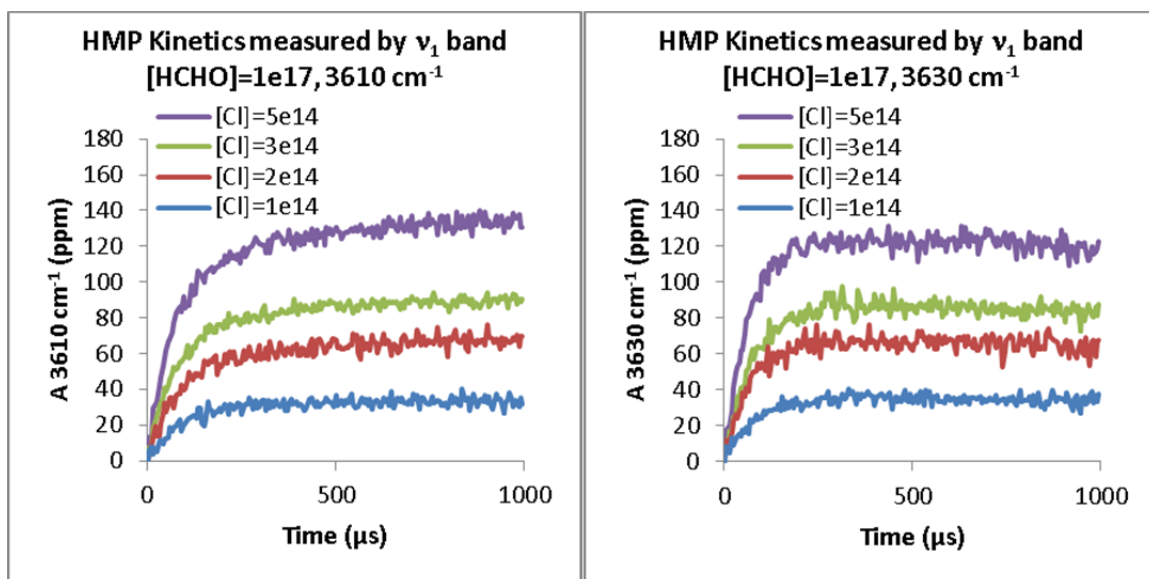


Figure 6.1. Kinetics traces of HMP using two frequencies within the ν_1 band: 3610 cm^{-1} (left) and 3630 cm^{-1} (right). Both plots were taken with $[\text{HCHO}] = 1 \times 10^{17}\text{ molec cm}^{-3}$, for $[\text{Cl}\cdot] = (1-5) \times 10^{14}\text{ molec cm}^{-3}$ (labeled on plots).

We note that the ν_1 absorbance scales with $[\text{Cl}\cdot]$ (and thus with $[\text{HO}_2]$), in accordance with Equation 6.13. We note that at long times (1 ms) where HMP is expected to be converted to other products, the ν_1 absorbance is remaining relatively

constant, despite an expected lifetime of HMP of at most 700 μs (Chapter 4, Table 4.2). This implies that side products or secondary products (H_2O_2 , HOCH_2OOH) are interfering with our HMP measurements at long times. Thus, we cannot use the ν_1 band to measure the kinetics of HMP destruction.

At short times, we have shown (Chapter 4) that the measured spectrum should be representative of HMP. Figure 6.2 shows the kinetics traces of HMP over the first 75 μs after HO_2 formation, as measured by the ν_1 band. Over this time range, we clearly observe pseudo-first-order kinetics effects within the first 50 μs : the growth of HMP is linear, with higher growth rates observed for higher $[\text{HO}_2]$. We also observe slight curvature beyond 50 μs , implying the loss of our pseudo-first-order kinetics conditions (likely due to $[\text{HO}_2]$ variance)

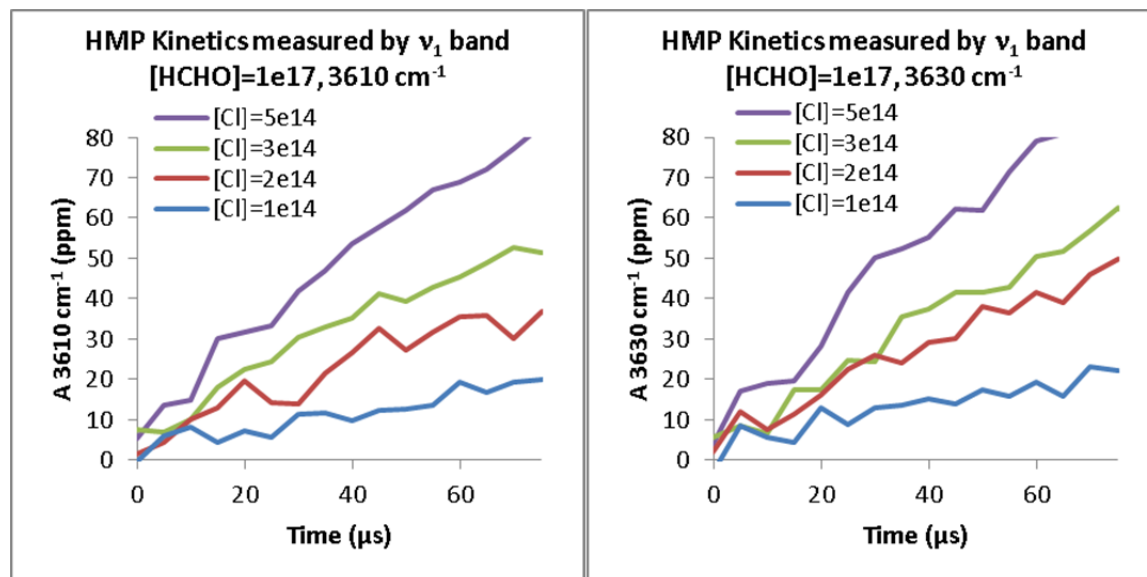


Figure 6.2. Kinetics traces of HMP over the first 75 μs of reaction, measured at 3610 cm^{-1} (left) and 3630 cm^{-1} (right). Both plots were taken with $[\text{HCHO}] = 1 \times 10^{17}$ molec cm^{-3} , for $[\text{Cl}\cdot] = (1-5) \times 10^{14}$ molec cm^{-3} (labeled on plots).

The kinetics data in Figures 6.1 and 6.2 are our raw spectroscopic data, and are presented in terms of absorbance. In order to calculate rate constants, we must convert

these data to absolute [HMP] using the absorption cross sections calculated in Chapter 4. For the two frequencies reported here, $\sigma_{\text{HMP},3610} = 1.3 \times 10^{-19} \text{ cm}^2 \text{ molec}^{-1}$ and $\sigma_{\text{HMP},3630} = 1.5 \times 10^{-19} \text{ cm}^2 \text{ molec}^{-1}$. These values are taken to be the average of the cross sections obtained by theoretical calculations (B3LYP/6-31+G(d,p)) and derived [HMP] from our kinetics model. These theoretical cross sections should be considered to have at least 20% uncertainty.

Using these cross sections, we can plot [HMP] vs time over 1 ms (Figure 6.3) and 75 μs , the range useful for calculating k_1 (Figure 6.4). At short times, we note that both bands are in excellent agreement with respect to [HMP] vs time, indicating very little interference from secondary products on short timescales. Over a 1 ms timescale, we note that the 3610 cm^{-1} measurements predict larger [HMP] than the 3630 cm^{-1} measurements for all $[\text{HO}_2]$, another indication that secondary species are causing spectral interference at longer times.

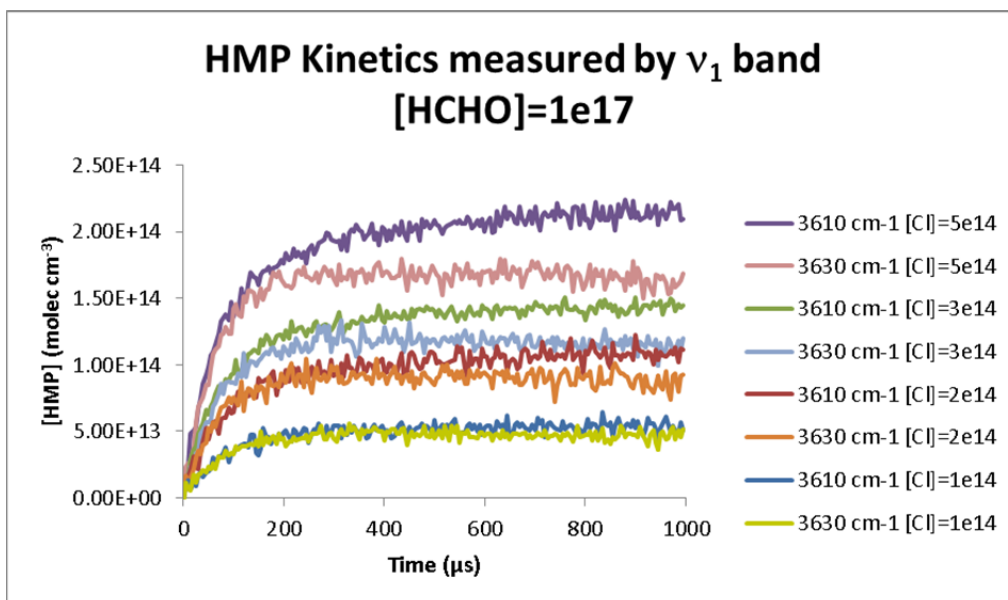


Figure 6.3. [HMP](t) measured by the ν_1 band (3610 cm^{-1} , 3630 cm^{-1}) for $[\text{Cl}\cdot] = (1-5) \times 10^{14} \text{ molec cm}^{-3}$. All data were taken with $[\text{HCHO}] = 1 \times 10^{17} \text{ molec cm}^{-3}$. Absolute [HMP] were calculated from absorbance data assuming $\sigma_{\text{HMP},3610} = 1.3 \times 10^{-19} \text{ cm}^2 \text{ molec}^{-1}$ and $\sigma_{\text{HMP},3630} = 1.5 \times 10^{-19} \text{ cm}^2 \text{ molec}^{-1}$.

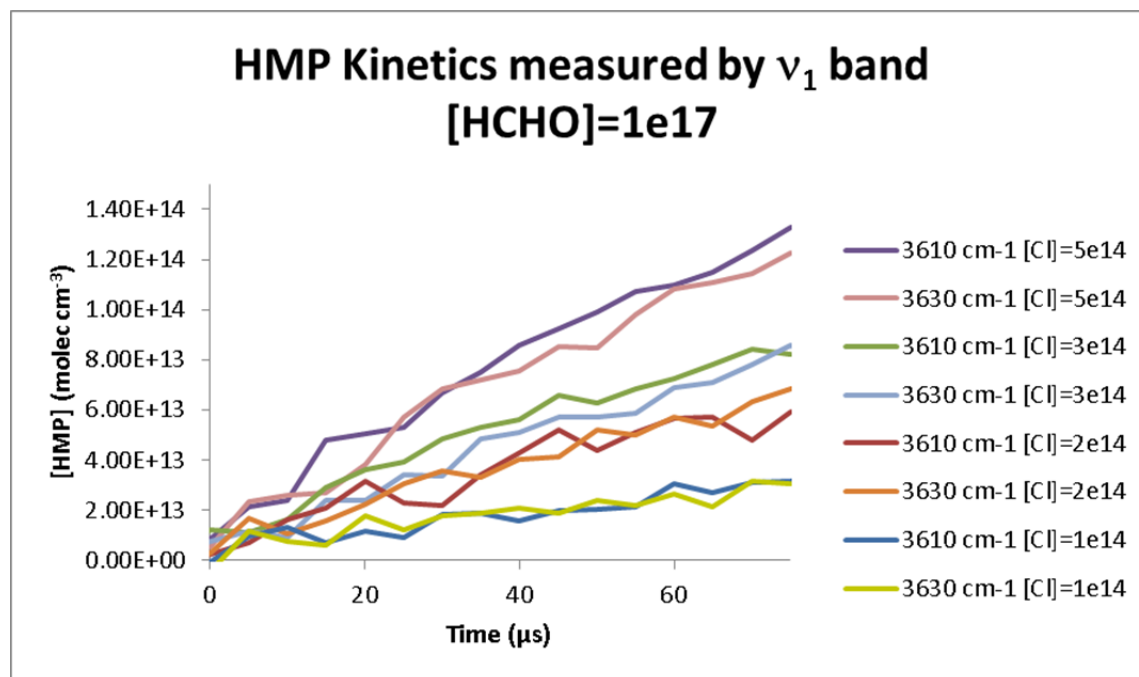


Figure 6.4. $[\text{HMP}](t)$ at short times ($75 \mu\text{s}$), measured by the ν_1 band (3610 cm^{-1} , 3630 cm^{-1}) for $[\text{Cl}\cdot] = (1-5) \times 10^{14} \text{ molec cm}^{-3}$. All data were taken with $[\text{HCHO}] = 1 \times 10^{17} \text{ molec cm}^{-3}$. Absolute $[\text{HMP}]$ were calculated from absorbance data assuming $\sigma_{\text{HMP},3610} = 1.3 \times 10^{-19} \text{ cm}^2 \text{ molec}^{-1}$ and $\sigma_{\text{HMP},3630} = 1.5 \times 10^{-19} \text{ cm}^2 \text{ molec}^{-1}$.

Given the data in Figure 6.4, we can calculate k_1 using Equation 6.22. These results are summarized in Table 6.3. We use only the absorption data within the first $50 \mu\text{s}$ of reaction to ensure that we still have pseudo first order conditions, and that the errors introduced from the approximations used to derive Equation 6.22 do not become too large.

Table 6.3. Determination of k_1 from CRDS ν_1 absorption data and Equation 6.22 (main text), $[\text{HCHO}] = 1 \times 10^{17} \text{ molec cm}^{-3}$, $t_{\text{avg}} = 25 \mu\text{s}$ ($50 \mu\text{s}$ of data used for determining $d[\text{HMP}]/dt$).

$\bar{\nu} (\text{cm}^{-1})$	3610	3610	3610	3610	3630	3630	3630	3630
$[\text{HO}_2]_0 (\text{cm}^{-3})$	1e14	2e14	3e14	5e14	1e14	2e14	3e14	5e14
$d[\text{HMP}]/dt (\text{cm}^{-3} \text{ s}^{-1})$	3.3e17	8.8e17	1.2e18	1.8e18	4.3e17	8.8e17	1.1e18	1.7e18
$k_1 (\text{cm}^3 \text{ s}^{-1})$	4.0e-14	5.7e-14	5.0e-14	4.4e-14	5.4e-14	5.6e-14	4.6e-14	4.0e-14

If we simply average the individual k_1 obtained from our data, we **obtain** $k_1 = (4.8 \pm 1.7) \times 10^{-14} \text{ cm}^3 \text{ molec}^{-1} \text{ s}^{-1}$ (**2 σ error**). The uncertainty on this rate constant includes the scatter of the k_1 data, 20% uncertainty on the IR absorption cross section of HMP and 10% uncertainty on k_1 due to the approximations made to obtain Equation 6.22.

Kinetics of HMP by A-X Absorption

As explained in the *Introduction*, our kinetics measurements using the A-X bands are well suited to measure HMP destruction, and therefore the lifetime of HMP in our experiment. While we were able to derive an accurate ($\pm 20\%$) expression for the rate constant of HMP formation, we cannot do the same for destruction of HMP for two reasons. First, destruction of HMP occurs by multiple pathways (Reactions 6.2–6.6). We cannot determine individual destruction rate constants; rather, we can only examine the overall destruction of HMP. Second, we observe that Reactions 6.3 and 6.6 regenerate HO_2 , restarting the $\text{HO}_2 + \text{HCHO}$ reaction. Therefore, the lifetime of HMP will be greater than a simple analysis of the rate constants of HMP destruction.

While we cannot extract exact rate constants, we are able to examine multiple A-X bands to determine whether or not the overall HMP decay kinetics are consistent between bands. These results can also be used in conjunction with a kinetics model to determine whether our data support or refute the existing HMP rate constants (*Discussion section*).

Figure 6.5 shows the kinetics of [HMP] as measured by the A-X bands at 7561 cm^{-1} and 7557 cm^{-1} (on and off peak of the 15_0^1 transition) and 7386 cm^{-1} (off peak of

the 0_0^0 transition). All absorbances have been converted to [HMP] via the absorption cross sections determined in Chapter 4.

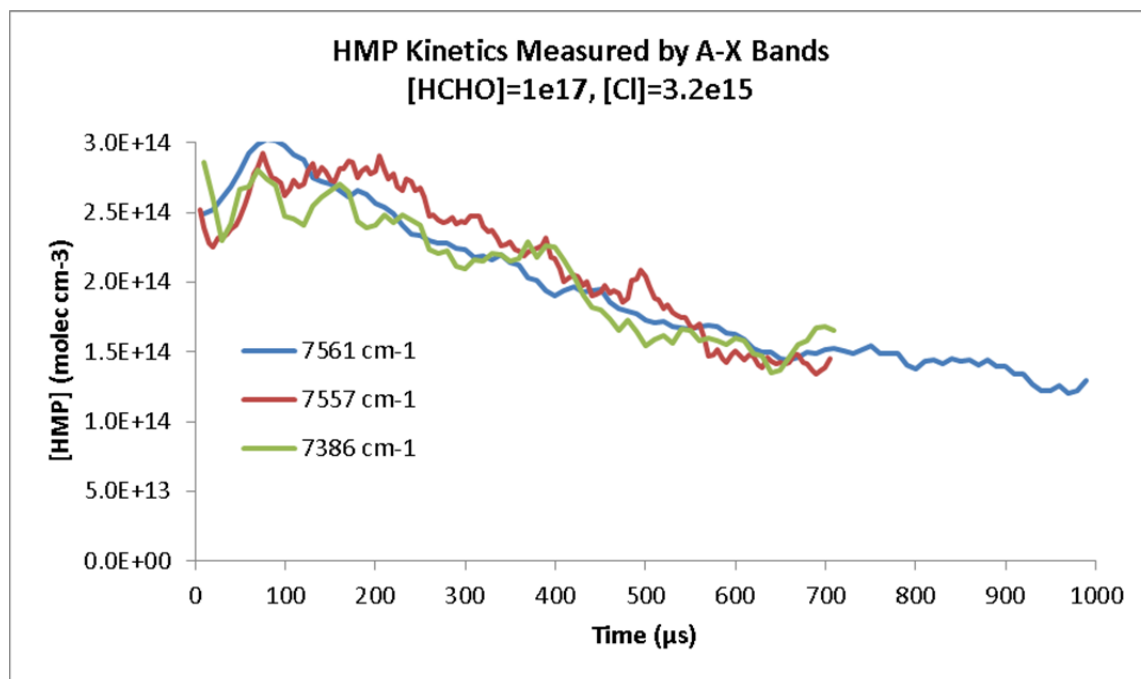


Figure 6.5. Kinetics traces of HMP using three frequencies within the A-X bands: 15_0^1 (peak 7561 cm^{-1} and off-peak 7557 cm^{-1}) and 0_0^0 (off-peak 7386 cm^{-1}). All data were taken with $[\text{HCHO}] = 1 \times 10^{17}\text{ molec cm}^{-3}$, $[\text{Cl}\cdot] = 3.2 \times 10^{15}\text{ molec cm}^{-3}$.

We observe excellent agreement in the calculation of [HMP] across the three measured frequencies. In all cases, we observe [HMP] reaching its maximum in the range 100–200 μs (error due to the noise in the kinetics traces). At 1 ms, we observe 41% of the maximum [HMP] in our system, implying a lifetime of HMP slightly longer than 1 ms for our experimental conditions.

The observed lifetime ($>1\text{ ms}$) is much larger than the “estimated” lifetimes from Chapter 4, Table 4.2 (75 μs). This is simply because the lifetimes in Chapter 4 were calculated by assuming $[\text{HO}_2]$ was at its maximum value throughout the experiment, an invalid assumption for the A-X conditions where $[\text{HO}_2]$ is high, but consumed by both

HO₂ + HCHO (Reaction 6.1) and self-reaction (Reaction 6.12). We should not be surprised that the actual lifetime of HMP is an order of magnitude greater than our relatively simple analysis.

Discussion

Comparison of HO₂ + HCHO Kinetics Results (ν₁) to Literature

Using the kinetics data obtained by measuring the ν₁ absorbance of HMP, we were able to calculate a 298 K rate constant for HO₂ + HCHO of $k_1 = (4.8 \pm 1.7) \times 10^{-14} \text{ cm}^3 \text{ molec}^{-1} \text{ s}^{-1}$. We compare this value to previous measurements in Table 6.4. Our value is in excellent agreement with the literature,^{96, 99} particularly the studies by Veyret and Burrows that directly detected HMP via its B-X absorption in the UV.^{25, 26} The current NASA/JPL Data Evaluation²⁷ recommends a rate of $5 \times 10^{-14} \text{ cm}^3 \text{ molec}^{-1} \text{ s}^{-1}$ with a factor of 5 uncertainty: we recommend the same rate constant with only 40% uncertainty.

Table 6.4. Comparison of rate constant $k_{\text{HO}_2+\text{HCHO}}$ to literature values.

Ref	$k_{\text{HO}_2+\text{HCHO}}$ (298 K) ($10^{-14} \text{ cm}^3 \text{ molec}^{-1} \text{ s}^{-1}$)	Molecule Detected	Method	Pressure (torr)
This work	4.8 ± 1.7	HOCH ₂ OO•, ν ₁	PLP-IR-CRDS, slow flow	300
Veyret, Burrows, 1989 ^{25, 26}	6.2 (factor of 5)	HOCH ₂ OO•, B-X	Flash Photolysis, slow flow, UV Absorption	85-170
Su, 1979 ⁹⁹	1.0 (order of magnitude)	HCOOH, H ₂ O ₂ , HOCH ₂ OOH	Photolysis, FTIR	700
Barnes, 1985 ⁹⁶	11 ± 4 (273 K) ^a	HOCH ₂ OONO ₂ , HNO ₄	Flash photolysis, FTIR	400
JPL/NASA ²⁷	5.0 (factor of 5)	N/A	Recommendation	N/A

a) Using Veyret's temperature dependence of $\exp[625/T]$, Barnes's rate constant is equivalent to $k_1(298\text{K}) = (9.1 \pm 3.3) \times 10^{-14} \text{ cm}^3 \text{ molec}^{-1} \text{ s}^{-1}$.

Comparison of HMP Destruction Kinetics (A-X) to Existing Model

The kinetics measurements made via the A-X predict an overall lifetime for HMP of slightly greater than 1 ms under our conditions ($[\text{HO}_2] = 3 \times 10^{15} \text{ molec cm}^{-3}$, $[\text{HCHO}] = 1 \times 10^{17} \text{ molec cm}^{-3}$). Because of the multiple destruction pathways of HMP and regeneration of HO_2 (Reactions 6.2-6.6), it is difficult to estimate whether or not this lifetime is reasonable. Instead, we compare our results to a kinetics model based on rate constants taken from the literature.^{27, 117, 118} Regarding HMP formation, we run our model using both Veyret's rate constant, $k_{1,298\text{K,Veyret}} = 6.3 \times 10^{-14} \text{ cm}^3 \text{ molec}^{-1} \text{ s}^{-1}$,²⁶ and the NASA/JPL recommendation, $k_{1,298\text{K,JPL}} = 5.0 \times 10^{-14} \text{ cm}^3 \text{ molec}^{-1} \text{ s}^{-1}$.²⁷ Our model is presented in Appendix E; here, we show only the results of the modeling.

We compare our A-X CRDS kinetics results to the model in Figure 6.6. Two plots are shown: absolute [HMP] (left), and the relative concentration $[\text{HMP}]/[\text{HMP}]_{\text{max}}$ (right). For clarity, we only show the kinetics as measured at 7561 cm^{-1} . This measurement carries two advantages: it is the strongest absolute absorbance measured, and there is no background H_2O that adds to the spectrometer noise in this region. We have already shown that the kinetics measurements at 7557 and 7386 cm^{-1} give similar results (Figure 6.5): therefore, the comparison in Figure 6.6 is generally valid across the A-X bands measured.

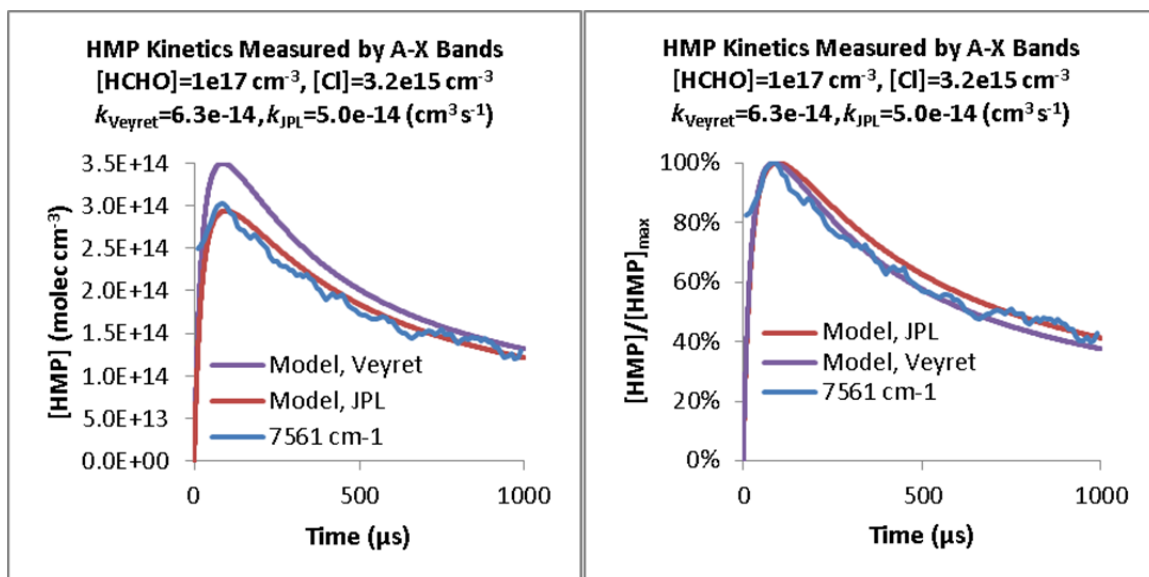
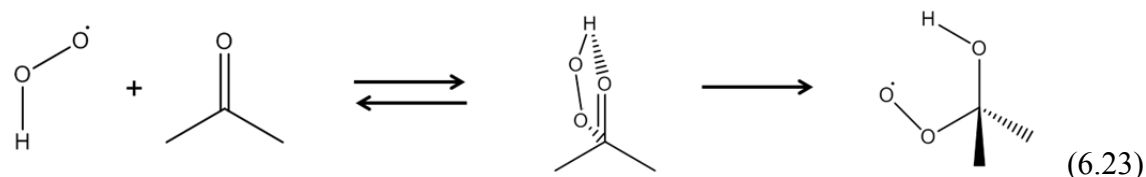


Figure 6.6. [HMP] (left) and the relative concentration $[\text{HMP}]/[\text{HMP}]_{\text{max}}$ (right), as experimentally measured (blue, CRDS A-X band) and modeled (purple and red). The purple curve uses Veyret's rate constant for $k_{\text{HO}_2+\text{HCHO}}$,²⁶ while the red curve uses the NASA/JPL data evaluation's recommendation.²⁷

The plots in Figure 6.6 show excellent agreement between our measured kinetics and the existing models. The absolute [HMP] predicted using either rate constant agrees within $\pm 25\%$. However, due to the large errors on the absorption cross section, this agreement may be accidental. The more significant data are the relative concentrations $[\text{HMP}]/[\text{HMP}]_{\text{max}}$. Regardless of the exact $k_{\text{HO}_2+\text{HCHO}}$ used, the models are in near perfect agreement with our data, predicting HMP lifetimes of 1 ms under our experimental conditions. Our data cannot differentiate between the individual destruction rate constants (Reactions 6.2–6.5); however, the agreement between model and experiment suggest that the sum of HMP destruction rates in the literature^{25, 26, 99} is quite accurate.

Application of Our Kinetics Methods to HO₂ + Acetone

As stated in Chapter 4, the “holy grail” of the HO₂ + carbonyl studies is direct detection of the isomerization product of HO₂ + acetone: 2-hydroxyisopropylperoxy (2-HIPP, Reaction 6.23).



Current experimental studies measuring show that HO₂ is consumed faster than expected (self-reaction) when acetone is present.²³ Because this study only detects [HO₂], it is not able to determine whether isomerization to 2-HIPP is taking place or if a Chaperone mechanism is causing a rate enhancement of the self-reaction.

The CRDS methods developed in Chapters 4-6 provide a method for direct detection and kinetics measurements of 2-HIPP. If we can obtain ν_1 and A-X spectra of 2-HIPP, then we will be able to measure its formation and destruction kinetics in a similar manner as we have done with HMP. Below, we provide an analysis of the experimental requirements for CRDS detection and kinetics measurements on 2-HIPP.

Since our detection method is spectroscopic in nature, we must first determine how the absorption cross sections of 2-HIPP compare to HMP. We can estimate the ν_1 cross section using quantum chemistry (B3LYP/6-31+G(d,p)) and compare to the cross section of HMP. At this level of theory, we obtain $\int \sigma_{\nu_1, 2\text{-HIPP}} d\bar{\nu} = 47 \text{ km mol}^{-1}$ and $\int \sigma_{\nu_1, \text{HMP}} d\bar{\nu} = 53 \text{ km mol}^{-1}$. To first order, we can assume that the absorption cross sections are equivalent. Regarding the A-X transition, the dipole moments of HMP and 2-HIPP are roughly equivalent, 2.1 debye for HMP, 2.2 debye for 2-HIPP at

B3LYP/6-31+G(d,p), with the magnitudes remaining constant between the A and X states. The dipole derivative is solely based on the change in direction of the π^* orbital on the O-O group, which is also the same between 2-HIPP and HMP. Finally, the potential energy surfaces in Chapter 5 show that both 2-HIPP and HMP have 3 deep torsional minima, and we should expect to see a series of bandheads much like HMP. A crude estimate of the strength of the 2-HIPP A-X bandheads is that they will be as strong as HMP. **Taken as a whole, this means that our goals are to generate nearly as much 2-HIPP as we did HMP.** Based on Figures 6.3 and 6.5, we should be able to make measurements of 2-HIPP kinetics for $[2\text{-HIPP}] = 10^{13}$ molec cm^{-3} (ν_1) experiment and 10^{14} molec cm^{-3} (A-X) experiment.

Next, consider the equilibrium (K_{eq}) and rate constants (k) for Reaction 6.23. There are currently three estimates of these constants: Hermans et al. (theory),¹⁹ Cours et al. (theory),²² and Grieman et al. (experiment).²³ The literature values are summarized in Tables 6.5 and 6.6. Hermans reports a temperature dependent equation for both K_{eq} and k : these equations are entered into the tables. Cours's and Grieman's studies do not report such equations, instead reporting K_{eq} and k for selected temperatures. Here, we fit these data over the range 200-300 K to aid in further analysis. These fits and 298 K rate constants are reported below.

Table 6.5. Equilibrium constants for HO₂ + acetone, from theory (Hermans, Cours) and experiment (Grieman), and for HO₂ + HCHO (Hermans). Temperature-dependent equations for Cours and Grieman were obtained by a fit to their data.

Ref	K_{eq} HO ₂ + Acetone (cm ³)	K_{eq} HO ₂ +HCHO (cm ³)	Ratio (Acetone/HCHO)
Hermans ¹⁹	$7.81 \times 10^{-28} \exp\left[\frac{7201}{T}\right]$ (2.44×10^{-17} at 298 K)	$4.44 \times 10^{-27} \exp\left[\frac{8007}{T}\right]$ (2.07×10^{-15} at 298 K)	$0.176 \times \exp\left[\frac{-806}{T}\right]$ (0.012 at 298 K)
Cours ²²	$1.14 \times 10^{-29} \exp\left[\frac{6085}{T}\right]$ (8.64×10^{-21} at 298 K)		
Grieman ²³	$2.88 \times 10^{-24} \exp\left[\frac{3961}{T}\right]$ (1.58×10^{-18} at 298 K)		

Table 6.6. Rate constants for HO₂ + acetone from theory (Hermans, Cours) and for HO₂ + HCHO (Hermans). Temperature-dependent equations for Cours were obtained by a fit to their data.

Ref	k HO ₂ + Acetone (cm ³ s ⁻¹)	k HO ₂ + HCHO (cm ³ s ⁻¹)	Ratio (Acetone/HCHO)
Hermans ¹⁹	$4.98 \times 10^{-15} \exp\left[\frac{1460}{T}\right]$ (6.68×10^{-13} at 298 K)	$5.68 \times 10^{-15} \exp\left[\frac{1209}{T}\right]$ (3.28×10^{-13} at 298 K)	$0.878 \times \exp\left[\frac{251}{T}\right]$ (2.04 at 298 K)
Cours ²²	$4.07 \times 10^{-16} \exp\left[\frac{-47}{T}\right]$ (3.49×10^{-16} at 298 K)		

We note that the equilibrium constants for HO₂ + acetone are much lower than for HO₂ + HCHO. At best (Hermans's calculation), K_{eq} for HO₂ + acetone is a factor of 100 less than HO₂ + HCHO. At worst (Cours), the difference is a factor of 10⁶. Grieman's experiment splits the middle of these studies. In order to observe 2-HIPP, we must reduce the temperature of our system such that K_{eq} of HO₂ + acetone is at least equal to our room temperature K_{eq} of HO₂ + HCHO.

Using the K_{eq} in Table 6.5, we must reduce the temperature of our system to 250 K (Hermans), 185 K (Cours), or 195 K (Grieman) in order to obtain $K_{\text{eq}} =$

$2.1 \times 10^{-15} \text{ cm}^3$, the same equilibrium constant that we attained for our $\text{HO}_2 + \text{HCHO}$ experiment. 250 K is accessible with the current CRDS apparatus (Chapter 2). However, modifications must be made to achieve temperatures below 200 K (in theory by improving the cell insulation and using liquid nitrogen as the coolant rather than dry ice/methanol).

Even once the $\text{HO}_2 + \text{acetone}$ complex is formed, we must now be concerned with how fast it will isomerize into 2-HIPP. Hermans's calculations (Table 6.6) imply that 2-HIPP formation has a rate constant equivalent to HMP formation. However, Cours's calculations disagree significantly, predicting 2-HIPP formation to be a factor of 1000 slower than HMP. If 2-HIPP formation is very slow, yet destruction of 2-HIPP is just as fast as HMP (analogous to Reactions 6.2–6.6), then we will observe very little 2-HIPP in our spectroscopy experiments, making kinetics measurements extremely difficult. However, if 2-HIPP formation is as fast HMP formation, then we should be able to make measurements on the kinetics of 2-HIPP, subject to the temperature control of our apparatus.

Conclusions

In this chapter, we have reported the kinetics of HMP formation (from $\text{HO}_2 + \text{HCHO}$) and destruction as measured by its ν_1 and A-X spectroscopic bands. The strong ν_1 band is a unique measure of HMP at short times, making it ideal for measurement of the $\text{HO}_2 + \text{HCHO}$ rate constant. The A-X bands are weaker, but are unique measures of HMP at long times, making them ideal for studying HMP destruction. We report a rate constant $k_{\text{HO}_2+\text{HCHO}} = (4.8 \pm 1.7) \times 10^{-14} \text{ cm}^3 \text{ molec}^{-1} \text{ s}^{-1}$ (2σ uncertainty)

on the basis of our ν_1 kinetics study. Our rate constant is in excellent agreement with previous reports and data evaluations, but with lower uncertainty.^{25-27, 96, 99} Under our experimental conditions for the A-X experiment ($[\text{HO}_2] = 3.2 \times 10^{15}$ molec cm^{-3} , $[\text{HCHO}] = 1 \times 10^{17}$ molec cm^{-3}), the lifetime of HMP was 1 ms, in excellent agreement with predictions made from our kinetics model consisting of rate constants from the literature.^{26, 27, 117, 118}

The spectroscopy, quantum chemistry, and kinetics results presented in Chapters 4–6 suggest that we can apply our methods to studying the $\text{HO}_2 + \text{acetone}$ reaction. We have made predictions regarding the ν_1 and A-X band positions for 2-HIPP (Chapter 5) and the experimental conditions (concentrations, temperatures) required to observe 2-HIPP in our apparatus (this chapter). Modification of our spectrometer to reach temperatures of 200 K or less should be sufficient to permit measurements of 2-HIPP.

Acknowledgements

We thank Andrew Mollner for assistance with obtaining the time dependent ν_1 spectra. The experiments performed in this chapter were funded under NASA Upper Atmosphere Research Program Grants NAG5-11657, NNG06GD88G, and NNX09AE21G2, California Air Resources Board Contract 03-333 and 07-730, National Science Foundation CHE-0515627, and a Department of Defense National Defense Science and Engineering Graduate Fellowship (NDSEG).

Part 4—Spectroscopy, Kinetics, and Quantum Chemistry of
Alkoxy Isomerization

Part of the work presented in Part 4 of this thesis (Chapters 7 and 8) has been published in our paper on the cavity ringdown spectroscopy and kinetics of alkoxy isomerization. Reproduced in part with permission from Sprague et al.³¹ Copyright 2012 American Chemical Society.

Chapter 7—Direct Detection of Primary Products of Alkoxy Isomerization: The OH Stretch Spectra of δ -HOC₄H₈•, δ -HOC₄H₈OO•, δ -HO-1-C₅H₁₀•, and δ -HO-1-C₅H₁₀OO•

Abstract

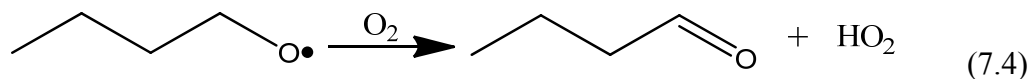
The primary products of *n*-butoxy and 2-pentoxy isomerization in the presence and absence of O₂ have been detected using Pulsed Laser Photolysis-Cavity Ringdown Spectroscopy (PLP-CRDS). Alkoxy radicals were generated by photolysis of alkyl nitrite precursors (*n*-butyl nitrite or 2-pentyl nitrite), and the isomerization products were detected by infrared cavity ringdown spectroscopy 20 μ s after the photolysis. We report the mid-IR OH stretch (ν_1) absorption spectra for δ -HOC₄H₈•, δ -HOC₄H₈OO•, δ -HO-1-C₅H₁₀•, and δ -HO-1-C₅H₁₀OO•. The observed ν_1 bands are similar in position and shape to their parent alcohols (*n*-butanol and 2-pentanol), although the HOROO• absorption is somewhat stronger than the HOR• absorption. We observe that these ν_1 spectra are constant over at least 800 μ s, indicating that secondary products have similar spectra to our primary products. We show here that the ν_1 spectra can be used to make relative rate measurements of alkoxy isomerization to reaction with O₂ (larger data sets in Chapter 8). We also report the thermodynamic properties of 2-pentyl nitrite ($p_{\text{vap}}(T)$, $\Delta_{\text{vap}}H$, and $T_{\text{boil,1atm}}$).

Introduction

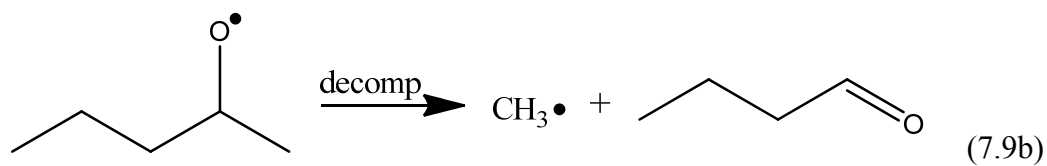
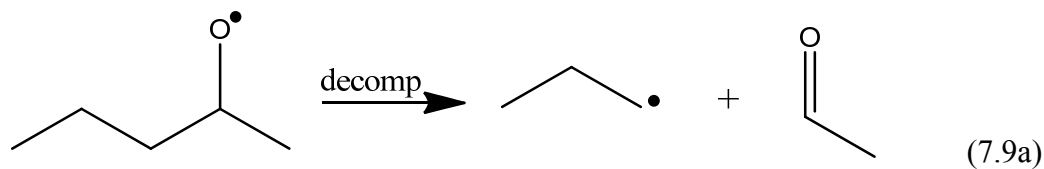
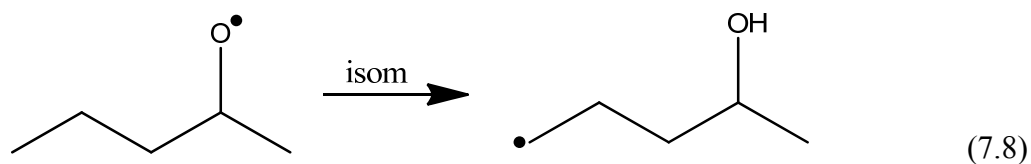
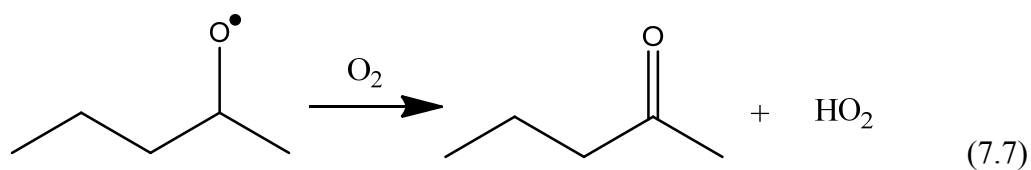
Alkoxy radicals (RO•) are an important intermediate species in the oxidation of volatile organic hydrocarbons through the HO_x and NO_x cycles in the atmosphere. Alkoxy radicals are formed predominantly by a chain of three reactions: first oxidation of a hydrocarbon with OH to form an alkyl radical (Reaction 7.1), immediate association with O₂ to form an alkyl peroxy radical (Reaction 7.2), then finally reaction of alkyl peroxy radicals with NO to form the alkoxy radical (Reaction 7.3).¹⁻³



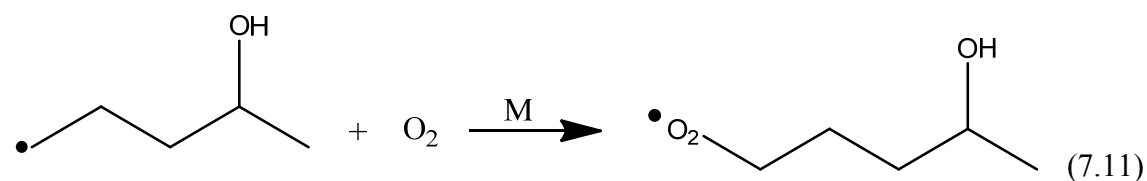
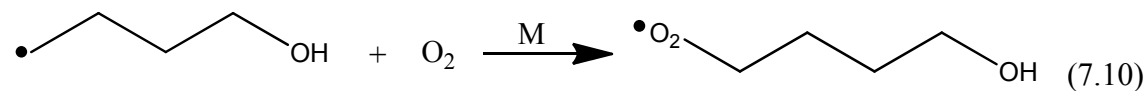
The alkoxy radicals react further via one of three mechanisms: α -hydrogen abstraction by O₂ to form a carbonyl and HO₂, unimolecular isomerization involving a 1,5-hydrogen shift via a cyclic transition state, or unimolecular dissociation via β -scission. These three reactions for the *n*-butoxy radical (a primary alkoxy radical) and the 2-pentoxy radical (a secondary alkoxy radical) are shown below.

n-butoxy:

2-pentoxy:



In the presence of O_2 , the δ -hydroxyalkyl radicals formed in Reactions 7.5 and 7.8 rapidly associate with O_2 to form δ -hydroxyalkylperoxy radicals, Reactions 7.10 and 7.11.



The computed energetics for the reactions of the *n*-butoxy radical are shown in Figure 7.1. The diagram is a composite of two different calculations; numerous *ab initio* calculations have been performed to calculate the energetics and RRKM reaction rates for decomposition and isomerization of alkoxy radicals,¹²⁹⁻¹⁴⁰ but very few calculations have been performed on the reaction with O₂.^{131, 133, 141} For the *n*-butoxy radical, Somnitz and Zellner^{136, 138} calculated barriers for decomposition and isomerization of 15.0 kcal mol⁻¹ and 10.2 kcal mol⁻¹, respectively, at the modified G2(MP2,SVP) level of theory. Jungkamp et al.¹³¹ calculate a barrier for reaction with O₂ of 8.2 kcal mol⁻¹, at the B3LYP/6-311+G(3df,2p)//B3LYP/6-31G(d,p) level of theory.

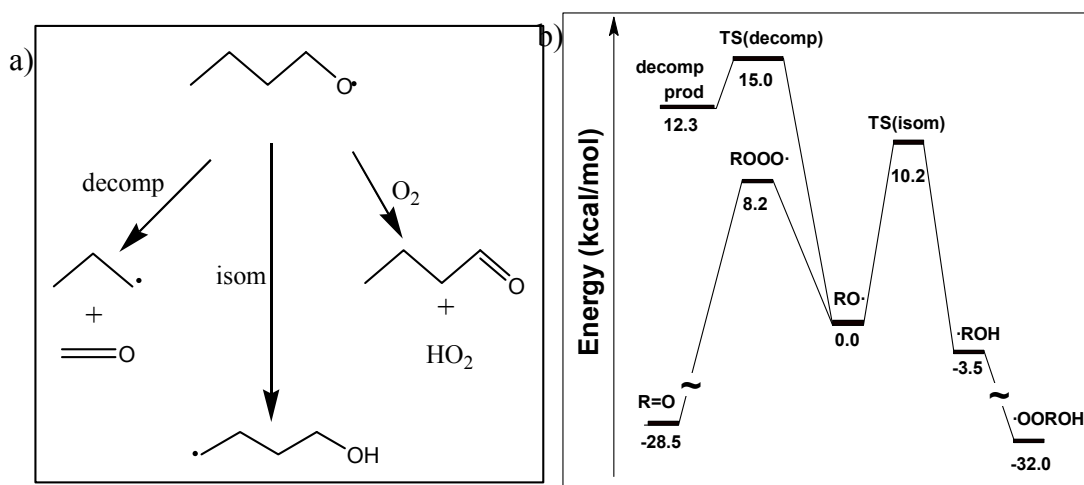


Figure 7.1. Reaction map (a) and energy diagram (b) for the decomposition, reaction with O₂, and isomerization reactions of alkoxy radicals. The energies listed are for *n*-butoxy. Energies for the isomerization and decomposition are taken from Somnitz and Zellner^{138, 139} at the modified G2(MP2,SVP) level of theory, while energies for the reaction with O₂ are taken from Jungkamp et al.¹³¹ at the B3LYP/6-311+G(3df,2p)//B3LYP/6-31G(d,p) level of theory. All energies listed are relative to the *n*-butoxy radical. Reprinted with permission from Sprague et al.³¹ Copyright 2012 American Chemical Society.

Many experimental and theoretical studies have shown that relative importance of the reaction pathways of alkoxy radicals depends critically upon the structure of the

alkoxy radical. Several reviews are available.^{118, 130, 142-144} For all alkoxy radicals, unimolecular decomposition is an available pathway, and the rate of decomposition is faster when the transition state is stabilized through substitution at the α - or β -carbon. Those alkoxy radicals containing an α -hydrogen can also undergo hydrogen abstraction reaction with O₂. Only radicals which can form a 6-membered ring transition state have a sufficiently low barrier for unimolecular isomerization to be atmospherically relevant,^{142, 145-148} and the isomerization rate is fastest when the product is a secondary or tertiary alkyl radical.¹⁴² For molecules in which all three pathways are possible, isomerization and reaction with O₂ dominate under atmospheric conditions. Measurements of k_{O_2} have generally yielded values within a factor of two of $1 \times 10^{-14} \text{ cm}^3 \text{ molec}^{-1} \text{ s}^{-1}$ at 298 K, with small dependencies on temperature and the structure of the alkoxy radical.^{143, 144} Variations in k_{isom} and k_{decomp} with pressure, temperature, and molecular structure are much larger, spanning many orders of magnitude because of the significant barriers involved and differences in the densities of states.^{129, 134, 135, 137, 139, 140, 149-152}

Isomerization has been a particularly difficult process to study experimentally due to the wide range of values of k_{isom} and fast secondary chemistry. In molecules which can form a 6-membered ring, isomerization generally occurs on the timescale of microseconds or less. In addition, the primary products of isomerization are hydroxyalkyl radicals with fast secondary reaction rates. As a result, the isomerization of alkoxy radicals has not yet been observed directly. Many previous studies of k_{isom} have focused on the simplest alkoxy radicals that can undergo isomerization: *n*-butoxy, 1-pentoxy, and 2-pentoxy. Under conditions relevant to the lower atmosphere (300 K, 1 bar, 21% O₂) the lifetime for reaction with O₂ is on the order 20 μs .²⁸ Previous relative rate

measurements have estimated the lifetimes for isomerization under these conditions to be on the order of 3 μs for Reaction 7.5 and shorter for Reaction 7.8.²⁸ The decomposition reactions have been estimated to occur on longer timescales: on the order 1 ms for Reaction 7.6 and 100 μs for Reaction 7.9. As a result, isomerization and reaction with O_2 are expected to be the dominant fates for these alkoxy radicals.

Most of the previous experimental work^{146, 148, 153-158} has measured the branching ratio of the isomerization and O_2 reaction channels, $k_{\text{isom}}/k_{\text{O}_2}$ by end-product analysis. Typically, butanal is detected, and a kinetics model is used to back out the relevant rate constants. Hein et al.¹⁵⁹ obtain an absolute value for k_{isom} by measuring the disappearance of OH and NO_2 . The resulting data are then fit to a kinetics model to back out k_{isom} . Although the majority of studies are in good agreement with each other (Table 7.1), it is possible for errors in the kinetics models to systematically affect all of the reported $k_{\text{isom}}/k_{\text{O}_2}$. Most of these prior experiments have included NO. In this case, the products of Reactions 7.10 and 7.11 react with NO via Reaction 7.3 to generate a secondary alkoxy radical. This secondary alkoxy radical can also undergo reaction via several pathways, leading to a large variety of possible end-products. Often, several reaction pathways can generate the same products, and so it can be difficult to deduce reaction mechanisms by relying on end-product data.¹³¹

Table 7.1. Comparison of previous relative rate constant determinations $k_{\text{isom}}/k_{\text{O}_2}$ and derived k_{isom} for *n*-butoxy and 2-pentoxy

	$k_{\text{isom}}/k_{\text{O}_2}$ (10^{19} cm^{-3}) ^a	k_{isom} (10^5 s^{-1}) ^b	Molecules detected	Method	<i>P</i> (<i>torr</i>)	Ref
<i>n</i>-butoxy	2.0 ± 0.4	2.7 ± 1.5	Butyl nitrite, Butanal,	Static, FTIR	700	Cassanelli ¹⁵⁵
	1.5 ± 0.4	2.1 ± 1.2	4-hydroxy butanal	Static, GC	760	Cox ¹⁵⁶
	1.9 ± 0.4	2.7 ± 1.4	Butane, Butanal	Static, FTIR	700	Niki ¹⁴⁸
	2.1 ± 0.5	2.9 ± 1.6	Butyl nitrite, Butanal	Slow flow, GC	760	Cassanelli ¹⁶⁰
	1.8 ± 1.1	2.5 ± 2.0	Butyl nitrite, Butanal	Slow flow, GC	760	Cassanelli ¹⁶⁰
	1.8 ± 0.6	2.5 ± 1.5	Butane, Butanal	Static, FTIR	760	Geiger ¹⁶¹
	0.25 ± 0.19 ^c	0.35 ± 0.20 ^c	Butanal, 4-hydroxy butanal	Fast flow, LIF	38	Hein ¹⁵⁹
	1.6	2.2	OH and NO ₂	Static, GC	740	Carter ¹⁵⁴
	2.1 ± 1.8 ^d	2.9 ± 1.4 ^d		Recommendation	760	IUPAC ¹¹⁸
2-pentoxy	3.1 ^e	2.5 ^e	2-pentanone	Static, GC	700	Atkinson ¹⁴⁵
	0.15	0.12 ^f	Acetone, Acetaldehyde, 2-hexanol	Static, GC	760	Dóbe ¹⁵⁷

a) All uncertainties are 2σ. All studies other than the current work treat all alkoxy reactions besides isomerization and reaction with O₂ as negligible.

b) Computed k_{isom} assuming literature value of $k_{\text{O}_2} = (1.4 \pm 0.7) \times 10^{-14} \text{ cm}^3 \text{ s}^{-1}$ for *n*-butoxy,²⁸ and $k_{\text{O}_2} = 8 \times 10^{-15} \text{ cm}^3 \text{ s}^{-1}$ for 2-pentoxy (no estimate available for the uncertainty).¹⁴²

c) Unlike the other studies, Hein directly measured k_{isom} . In this table, we calculate the ratio $k_{\text{isom}}/k_{\text{O}_2}$ from Hein's measurement using the literature value of k_{O_2} .

d) The IUPAC recommendation for $k_{\text{isom}}/k_{\text{O}_2}$ is computed from their individual recommendations of the isomerization and O₂ reactions

e) The uncertainty on $k_{\text{isom}}/k_{\text{O}_2}$ is reported by Atkinson as a factor of 2.

f) Dóbe's study calculates k_{isom} from the relative rate $k_{\text{isom}}/k_{\text{decomp}}$ and their measured rate $k_{\text{decomp}} = 1.2 \times 10^4 \text{ s}^{-1}$. The $k_{\text{isom}}/k_{\text{O}_2}$ reported in this table uses the literature value of $k_{\text{O}_2} = 8 \times 10^{-15} \text{ cm}^3 \text{ s}^{-1}$ for 2-pentoxy.¹⁴²

A better method for studying alkoxy chemistry is to directly detect the species involved in the primary reactions of alkoxy chemistry (Reactions 7.4–7.11). Such methods avoid the need for assumptions about secondary chemistry, and should lead to reduced uncertainty on the kinetic rate constants. Numerous spectroscopic studies on the alkoxy radicals themselves have been carried out, typically employing laser-induced fluorescence (LIF) to measure the A-X or B-X electronic transitions.¹⁶²⁻¹⁸² However, fluorescence is quenched for larger alkoxy radicals due to internal conversion, making LIF experiments inappropriate for studying the larger alkoxy radicals that can isomerize.

The approach previously taken in our laboratory has been direct detection of the primary isomerization products, HOR• (formed in Reactions 7.5 and 7.8), and HOROO• (Reactions 7.10 and 7.11), via the ν_1 (OH stretch) cavity ringdown spectra.^{29, 30} Measuring the ν_1 intensity as a function of $[O_2]$ will show how the isomerization reactions compete with the O_2 reactions. In principle, it should be possible to obtain clean ν_1 spectra of HOR• and HOROO• for appropriate experimental conditions (radical concentrations, timing of measurement). Careless choices of these conditions (very high radical concentrations, very long times after initial alkoxy radical generation) will lead to detection of a variety of secondary products with their own OH stretch spectra. Besides the fact that the reported spectra are not truly HOR• or HOROO•, the relative kinetics measurements may or may not be accurate if the ratios of secondary products change with $[O_2]$. By reducing radical concentrations and time after alkoxy generation, we can obtain cleaner spectra than previous experiments in our group were able to.

In this thesis chapter, we report the first clean OH stretch spectra of δ -HOC₄H₈•, δ -HOC₄H₈OO•, δ -HO-1-C₅H₁₀•, and δ -HO-1-C₅H₁₀OO•. Compared to the previous experiments performed by Garland and Mollner,^{29, 30} here we make use of shorter timescales, lower $[RO\bullet]$, and lower $[O_2]$ to obtain cleaner spectra. Similar to Garland and Mollner's previous experiments, HOR• and HOROO• (R = C₄H₈ or C₅H₁₀) were generated through pulsed laser photolysis of *n*-butyl nitrite or 2-pentyl nitrite in the absence or presence of O₂. Cavity ringdown spectroscopy was used to measure the resulting spectrum over the range 3610-3720 cm⁻¹, 20 μ s after photolysis. Additional spectra were recorded 800 μ s after photolysis in order to assess how the OH stretch peak changes as secondary chemistry proceeds, allowing us to determine the effects of

secondary chemistry on Garland and Mollner's experiments. The OH stretch peak heights were also measured as a function of $[O_2]$ to obtain k_{isom}/k_{O_2} , allowing us to determine if the previous measurements were affected by the mixture of products that were actually being detected.

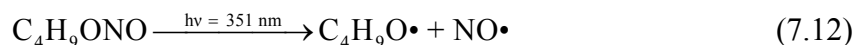
Methods

Apparatus and Chemicals

The cavity ringdown spectrometer, laser system, and gas kinetics flow cell have been described in detail in Chapter 2 (Figures 2.5, 2.7, 2.8). Briefly, the tunable near-infrared light used to measure the spectrum was generated using an optical parametric amplifier. For 65 mJ of 532 nm light and 4–12 mJ of tunable red light (620–665 nm), 0.6–0.8 mJ of tunable infrared light was generated ($2900\text{--}3800\text{ cm}^{-1}$). The infrared light was sent into an optical cavity consisting of two highly reflective mirrors (Los Gatos Research, 2.8 μm peak, $R = 99.98\%$). Ringdown traces were collected with a liquid nitrogen cooled InSb detector (Judson J10D-M204-R01M-60) connected to a voltage amplifier (Analog Modules 351A-3) and PC oscilloscope card (GageScope CS1450). 80 μs of ringdown data were collected per shot, and 16 ringdowns were collected and averaged before being fit. The first eighth of the ringdown lifetime was removed before the data were refit in order to eliminate errors caused from noise near the peak of the ringdown.

The δ -hydroxybutylperoxy radicals were formed by photolysis of *n*-butyl nitrite (95%, Sigma-Aldrich) in the presence of O_2 (Reactions 7.12, 7.5, and 7.10). Photolysis was initiated by 351 nm light from the excimer laser described in Chapter 2. Typical UV

flux was kept at 1.8×10^{17} photons cm^{-2} . The absorption cross section of *n*-butyl nitrite at 351 nm is $\sigma_{351\text{nm}} = 8.0 \times 10^{-20}$ $\text{cm}^2 \text{molec}^{-1}$,³² resulting in 1.5% of the alkyl nitrite being photolyzed.



n-butyl nitrite was introduced to the gas kinetics cell by flowing N_2 gas through a bubbler kept at 0 °C. Prior to usage, the *n*-butyl nitrite went through a minimum of three freeze-pump-thaw cycles in order to degas the sample of oxygen and to reduce the concentration of impurities (such as NO, nitrous oxides, aldehydes, and acids). Briefly, one cycle consists of freezing the nitrite in liquid nitrogen, vacuum pumping on the sample for 10–20 minutes, then isolating the sample and thawing. The gas bubbles that evolve represent impurities that have a higher vapor pressure than the nitrite. Cycles were repeated until minimal to no gas evolved during thawing.

The δ -hydroxy-1-pentylperoxy radicals were formed by photolysis of 2-pentyl nitrite in the presence of O_2 , similar to the chemistry for the *n*-butoxy system presented above. However, 2-pentyl nitrite is not commercially available, requiring us to synthesize the 2-pentyl nitrite according to standard protocol.¹⁸³ The synthesis was first performed on a small scale (listed chemical quantities) to verify the formation of 2-pentyl nitrite before scaling up. 22 g of NaNO_2 was dissolved in 88 mL of H_2O , and cooled to -5 °C. A mixture of 6 mL H_2O , 8.5 mL concentrated H_2SO_4 , and 33 mL of 2-pentanol was cooled to -5°C and added drop wise to the NaNO_2 solution over the course of 60 minutes. Solid Na_2SO_4 was filtered, and the upper layer containing 2-pentyl nitrite was separated. The

crude product was vacuum distilled at 30 torr to remove water and excess pentanol. Based on FTIR spectra of the 2-pentyl nitrite (shown in the *Results* section), $[\text{RONO}]:[\text{ROH}] = 24$, $[\text{RONO}]:[\text{NO}] = 240$, and $[\text{RONO}]:[\text{H}_2\text{O}] = 14$ (overall purity 90%). Approximately 15 mL of distilled 2-pentyl nitrite was yielded. After FTIR characterization, two batches of 2-pentyl nitrite (150 mL each) were synthesized: one for the CRDS experiment, and one to measure thermodynamic properties of 2-pentyl nitrite.

Quantum chemistry calculations suggest that $\sigma_{351\text{nm}}(\text{C}_5\text{H}_{11}\text{ONO}) = 0.75 \times \sigma_{351\text{nm}}(\text{C}_4\text{H}_9\text{ONO})$, or $6.0 \times 10^{-20} \text{ cm}^2 \text{ molec}^{-1}$. For a photolysis flux of 2.0×10^{17} photons cm^{-2} , 1.2% of the pentyl nitrite is photolyzed.

Experimental and Flow Conditions

The majority of the $\delta\text{-HOC}_4\text{H}_8\bullet$, $\delta\text{-HOC}_4\text{H}_8\text{OO}\bullet$, $\delta\text{-HO-1-C}_5\text{H}_{10}\bullet$, and $\delta\text{-HO-1-C}_5\text{H}_{10}\text{OO}\bullet$ spectra were acquired at a single set of conditions for each species in order to provide for signal averaging. The main difference between the conditions required for detection of the two species is that detections of $\delta\text{-HOC}_4\text{H}_8\bullet$ and $\delta\text{-HO-1-C}_5\text{H}_{10}\bullet$ were made at $[\text{O}_2] = 0$, while detections of $\delta\text{-HOC}_4\text{H}_8\text{OO}\bullet$ and $\delta\text{-HO-1-C}_5\text{H}_{10}\text{OO}\bullet$ were made at $[\text{O}_2] = 9 \times 10^{17} \text{ molec cm}^{-3}$. The spectra of both species were measured by scanning across a range of frequencies (3610-3720 cm^{-1} , step size 0.2 cm^{-1}) while at a constant time after photolysis of the alkyl nitrite (20 μs). As will be shown by the kinetics modeling in the *Results* section, the majority of the OH stretch absorption is due to $\text{HOR}\bullet$ or $\text{HOROO}\bullet$ at 20 μs (94% or 98% respectively). Spectra were also recorded at longer times after photolysis (800 μs) in order to determine how the OH stretch peak changed as secondary products formed.

Of particular note is the lower concentration of RONO used for the OH stretch measurements ($[\text{C}_4\text{H}_9\text{ONO}] = 7.1 \times 10^{15} \text{ molec cm}^{-3}$, $[\text{C}_5\text{H}_{11}\text{ONO}] = 8.1 \times 10^{15} \text{ molec cm}^{-3}$) compared to the A-X experiment ($[\text{C}_4\text{H}_9\text{ONO}] = 6.0 \times 10^{14} \text{ molec cm}^{-3}$, see Chapter 10). Alkyl nitrites have a structured absorption for frequencies $>3300 \text{ cm}^{-1}$ ⁴¹ (see the *Results* section for our measured spectrum). By keeping $[\text{RONO}]$ low, we minimize its background absorption, and therefore reduce the noise level of our spectrometer (Chapter 2). There are two key differences between this experiment and the A-X experiment that allow for this reduction in $[\text{RONO}]$. First, alkyl nitrites do not absorb in the near-IR region where the A-X transitions of HOROO• are located, thus allowing us to indiscriminately increase $[\text{RONO}]$. Second, the absorption cross sections of OH stretch peaks^{40, 41} are typically a factor of 10-100 larger than the cross section of the A-X peak for peroxy radicals.^{44, 115, 122, 124, 184, 185} While a decrease in $[\text{RONO}]$ would render the A-X band of HOROO• undetectable, the OH stretch band is strong enough to still allow for detection HOR• or HOROO•.

The relative kinetics experiments were conducted by varying $[\text{O}_2]$ ($0-8 \times 10^{18} \text{ molec cm}^{-3}$) at roughly constant pressure (300–330 torr) and measuring the resulting absorption at a constant frequency (HOC₄H₈OO• at 3662 cm^{-1} , HOC₅H₁₀OO• at 3660 cm^{-1}), over the range 20–60 μs after photolysis (0.5 μs step size). It can be observed that the intensity of the OH stretch peak does not change over the first 100 μs ,³⁰ and likely longer (see *Results* for more details). We can therefore average the absorptions across the entire timing range as a way to “signal average” our absorptions.

The conditions for the three experiments are summarized in Tables 7.2 (*n*-butoxy) and 7.3 (2-pentoxy). Gas flows were measured using the flowmeters discussed in

Chapter 2. The temperature of the gas kinetics cell was taken to be room temperature: no temperature control of any kind was attempted.

Table 7.2. Experimental conditions (gas flows, photolysis parameters, chemical concentrations, and spectrometer performance) for *n*-butoxy experiments

	HOC ₄ H ₈ OO• Spectrum, 300 torr	HOC ₄ H ₈ • Spectrum, 300 torr	Relative rate, 300-330 torr
N ₂ Purge Flow—Left Mirror	550 sccm	550 sccm	550 sccm
N ₂ Purge Flow—Right Mirror	500 sccm	500 sccm	500 sccm
N ₂ Bubbler Flow	48 sccm 171 sccm ^b	48 sccm	48 sccm
N ₂ Dilution Flow	2700 sccm	2700 sccm	0-2700 sccm ^a
O ₂ Flow	400 sccm	0 sccm	0-2700 sccm ^a
Cell Pressure	300 torr 310 torr ^b	270 torr	300 torr
Temperature (room)	293 ± 2 K	293 ± 2 K	293 ± 2 K
Flush Time	25 ms	25 ms	25 ms
Photolysis Window Length	5 cm	5 cm	5 cm
Excimer Energy at 351 nm	160 ± 10 mJ/pulse	160 ± 10 mJ/pulse	160 ± 10 mJ/pulse
% Alkoxy Photolyzed	1.47%	1.47%	1.47%
[C ₄ H ₉ ONO] _{cell}	7.1 × 10 ¹⁵ cm ⁻³ 2.4 × 10 ¹⁶ cm ⁻³ ^b	7.1 × 10 ¹⁵ cm ⁻³	7.1 × 10 ¹⁵ cm ⁻³
[C ₄ H ₉ O•]	1.1 × 10 ¹⁴ cm ⁻³ 3.6 × 10 ¹⁴ cm ⁻³ ^b	1.1 × 10 ¹⁴ cm ⁻³	1.1 × 10 ¹⁴ cm ⁻³
[O ₂]	9.0 × 10 ¹⁷ cm ⁻³ 8.0 × 10 ¹⁸ cm ⁻³ ^b	0 cm ⁻³	(1–8) × 10 ¹⁸ cm ⁻³
Optical Cell Length	52 cm	52 cm	52 cm
1/τ ₀ (3638 cm ⁻¹ , purge only)	1.2 × 10 ⁵ Hz	1.2 × 10 ⁵ Hz	1.2 × 10 ⁵ Hz
1/τ (3670 cm ⁻¹ , all background gases, no C ₄ H ₉ ONO)	1.6 × 10 ⁵ Hz	1.6 × 10 ⁵ Hz	1.6 × 10 ⁵ Hz
1/τ (3670 cm ⁻¹ , all background gases and C ₄ H ₉ ONO)	2.5 × 10 ⁵ Hz 4.9 × 10 ⁵ Hz ^b	2.5 × 10 ⁵ Hz	2.5 × 10 ⁵ Hz
Δτ/τ ^c	0.8%	0.8%	0.8%
Sensitivity (3670 cm ⁻¹ , with C ₄ H ₉ ONO background, 2σ)	6.9 ppm Hz ^{-1/2} 13.6 ppm Hz ^{-1/2} ^b	6.9 ppm Hz ^{-1/2}	6.9 ppm Hz ^{1/2}

a) The sum of O₂ and N₂ dilution flows was kept at 2700 sccm for the relative rate experiments to keep a constant pressure and flush time

b) Increased [RONO] and [O₂] only used for separate experiments. These scans were not averaged into the reported spectrum

c) Δτ/τ reported for averaging 16 ringdown traces per point

Table 7.3. Experimental conditions (gas flows, photolysis parameters, chemical concentrations, and spectrometer performance) for 2-pentoxy experiments

	HOC ₅ H ₁₀ OO• Spectrum, 320 torr	HOC ₅ H ₁₀ • Spectrum, 320 torr	Relative rate, 320 torr
N ₂ Purge Flow—Left Mirror	550 sccm	550 sccm	550 sccm
N ₂ Purge Flow—Right Mirror	500 sccm	500 sccm	500 sccm
N ₂ Bubbler Flow	83 sccm 265 sccm ^b	83 sccm	83 sccm
N ₂ Dilution Flow	2700 sccm	3300 sccm	0-2700 sccm ^a
O ₂ Flow	400 sccm	0 sccm	0-2700 sccm ^a
Cell Pressure	320 torr	320 torr	320 torr
Temperature (room)	293 ± 2 K	293 ± 2 K	293 ± 2 K
Flush Time	25 ms	25 ms	25 ms
Photolysis Window Length	5 cm	5 cm	5 cm
Excimer Energy at 351 nm	170 ± 10 mJ/pulse	170 ± 10 mJ/pulse	170 ± 10 mJ/pulse
% Alkoxy Photolyzed	1.19%	1.19%	1.19%
[C ₅ H ₁₁ ONO] _{cell}	8.1 × 10 ¹⁵ cm ⁻³ 2.5 × 10 ¹⁶ cm ⁻³ ^b	8.1 × 10 ¹⁵ cm ⁻³	8.1 × 10 ¹⁵ cm ⁻³
[C ₅ H ₁₁ O•]	9.6 × 10 ¹³ cm ⁻³ 3.0 × 10 ¹⁴ cm ⁻³ ^b	9.6 × 10 ¹³ cm ⁻³	9.6 × 10 ¹³ cm ⁻³
[O ₂]	9.5 × 10 ¹⁷ cm ⁻³	0 cm ⁻³	(1–8) × 10 ¹⁸ cm ⁻³
Optical Cell Length	52 cm	52 cm	52 cm
1/τ ₀ (3638 cm ⁻¹ , purge only)	1.2 × 10 ⁵ Hz	1.2 × 10 ⁵ Hz	1.2 × 10 ⁵ Hz
1/τ (3638 cm ⁻¹ , all background gases, no C ₅ H ₁₁ ONO)	1.4 × 10 ⁵ Hz	1.4 × 10 ⁵ Hz	1.4 × 10 ⁵ Hz
1/τ (3660 cm ⁻¹ , all background gases and C ₅ H ₁₁ ONO)	2.5 × 10 ⁵ Hz 5.5 × 10 ⁵ Hz ^b	2.5 × 10 ⁵ Hz	2.5 × 10 ⁵ Hz
Δτ/τ ^c	0.3%	0.3%	0.3%
Sensitivity (3660 cm ⁻¹ , with C ₅ H ₁₁ ONO background, 2σ)	3.3 ppm Hz ^{-1/2} 7.2 ppm Hz ^{-1/2} ^b	3.3 ppm Hz ^{-1/2}	3.3 ppm Hz ^{-1/2}

a) The sum of O₂ and N₂ dilution flows was kept at 2700 sccm for the relative rate experiments to keep a constant pressure and flush time

b) Increased [RONO] only used for a separate experiment. This scan was not averaged into the reported spectrum

c) Δτ/τ reported for averaging 16 ringdown traces per point

We can calculate the cell flush time, [RONO], and [RO•] based on the experimental parameters in Tables 7.2 and 7.3. Derivations of these equations are presented in Chapter 8 (reanalysis of previous experiments); therefore, only the final results are presented here. The flush time is defined as the amount of time to remove the chemicals within the photolysis length from the ringdown cavity, and is calculated from Equation 7.13:

$$t_{flush} = \left(\frac{V_{in-out}}{\sum_{flush} f_i} \right) \times \left(\frac{p_{cell}}{p_{st}} \right), \quad (7.13)$$

where t_{flush} is the flush time for the chemical sample, V_{in-out} is the volume between the inlet for butyl nitrite and vacuum outlet ($V_{in-out} = 3.93 \text{ cm}^3$ for the cell used in this experiment), $\sum_{flush} f_i$ is the total flow rate of gases in the direction of flushing (in sccm), p_{cell} is the pressure in the CRDS cell, and p_{st} is the standard pressure (760 torr).

[RONO] in the CRDS cell is determined by the vapor pressure of the alkyl nitrite and the dilution of the butyl nitrite carrier gas within the CRDS cell, and can be calculated from Equation 7.14:

$$\left(\frac{N}{V} \right)_{RONO,CRDS} = p_{vap} \left(\frac{N/V}{P} \right)_{conv} \left(\frac{T_{bubbler}}{T_{cell}} \right) \left(\frac{f_{bubbler}}{\sum f_i} \right), \quad (7.14)$$

where $\left(\frac{N}{V} \right)_{RONO,CRDS}$ is the concentration of butyl nitrite in the CRDS cell, p_{vap} is the vapor pressure of RONO in the bubbler, $T_{bubbler}$ is the temperature of the bubbler (273 K),

$\left(\frac{N/V}{P} \right)_{conv}$ is the conversion factor between pressure and number density of a gas

(3.24×10^{16} molec cm⁻³/torr), T_{cell} is the temperature of the gas kinetics cell (293 K), f_{bubbler} is the gas flow through the bubbler, and Σf_i is the sum of all gas flows through the gas kinetics cell. The vapor pressure of C₄H₉ONO (20.3 torr at 273 K) can be computed based on known thermodynamic properties ($\Delta_{\text{vap}}H$, $T_{\text{boil,1atm}}$). No thermodynamic data exist for 2-pentyl nitrite in the literature; thus, we relied on our measurements of $p_{\text{vap}}(T)$ (see the *Results* section) to obtain the vapor pressure of C₅H₁₁ONO (13.5 torr at 273 K).

The fraction of RONO that is photolyzed can be calculated from Equation 7.15:

$$\%_{\text{photolysis}} = \frac{\left(\frac{P_{\text{excimer}}}{A_{\text{meter}}} \right) \left(\frac{\lambda}{hc} \right) (\sigma_{\text{RONO},\lambda}) (X) \left(\frac{A_{\text{UV,laser}}}{A_{\text{UV,CRDS}}} \right)}{F_{\text{excimer}}}, \quad (7.15)$$

where $\%_{\text{photolysis}}$ is the fraction of RONO that is photolyzed, $(P_{\text{excimer}}/A_{\text{meter}})$ is the power per unit area of the UV light (read directly from the power meter), F_{excimer} is the rep rate of the excimer laser (10 Hz), h is Planck's constant, c is the speed of light, λ is the wavelength of the excimer light (351 nm), $\sigma_{\text{RONO},\lambda}$ is the absorption cross section of RONO at the excimer wavelength (8×10^{-20} cm² at 351 nm for *n*-butyl nitrite, 6×10^{-20} cm² for 2-pentyl nitrite), X is the quantum yield for photolysis (taken to be 1), $A_{\text{UV,laser}}$ is the area of excimer beam measured at the excimer laser output, and $A_{\text{UV,CRDS}}$ is the area of excimer beam measured at the CRDS cell. For these experiments, $\frac{A_{\text{UV,laser}}}{A_{\text{UV,CRDS}}} = 2$.

Results

We present the results of this study in four parts. First, we discuss the chemistry relevant to our experiment following photolysis of the alkyl nitrite. Within 20 μ s, we show that the majority of product being detected are the primary isomerization products,

HOR• ($[O_2] = 0$) or HOROO• (in the presence of O_2). Second, the OH stretch spectra of HOR• and HOROO• are shown at a constant time after photolysis (20 μ s) and a single starting alkoxy concentration ($[C_4H_9O\bullet] = 1.1 \times 10^{14}$ molec cm^{-3} , $[C_5H_{11}O\bullet] = 9.6 \times 10^{13}$ molec cm^{-3}). The OH stretches for δ -HOC₄H₈• and δ -HOC₄H₈OO• are located at 3675 cm^{-1} , while the OH stretches for δ -HO-1-C₅H₁₀• and δ -HO-1-C₅H₁₀OO• are located at 3660 cm^{-1} . We observe differences in peak intensity and shape between HOR• and HOROO• for both the butoxy and pentoxy systems. Third, we present the observed OH stretch spectra at longer times after alkoxy formation (800 μ s vs 20 μ s) and higher starting radical concentrations ($[RO\bullet] = 3 \times 10^{14}$ molec cm^{-3} vs 1×10^{14} molec cm^{-3}) to compare the band shapes of pure HOROO• and a mixture of HOROO• and secondary products. Fourth, we report the relative rate k_{isom}/k_{O_2} by using the newly measured OH stretch spectra of HOC₄H₈OO• and HOC₅H₁₀OO• to obtain A_0/A as a function of $[O_2]$. The relative rate obtained with our newly measured band is in agreement with all of the available data: previous literature,^{146, 148, 153-158} the reanalysis of the previous OH stretch experiment (Chapter 8), and the A-X experiment (Chapter 10). Finally, we present the analysis of our 2-pentyl nitrite sample: FTIR spectra, purity, vapor pressure measurements, and derived thermodynamic parameters.

Chemistry

Photolysis of the alkyl nitrites in the UV leads to prompt dissociation, with a typical reaction enthalpy of 40 kcal mol⁻¹.¹⁸⁶



For photolysis at 351 nm, the fragments contain 40 kcal mol^{-1} of available energy. The observations by Bruhlmann et al.¹⁸⁷ and Mestdagh et al.¹⁸⁸ of anisotropic product angular distributions in the photolysis of alkyl nitrites indicates that products are formed on timescales less than a rotational period ($<1 \text{ ps}$). $\text{RO}\cdot$ and NO are formed almost exclusively, most likely on the excited RONO electronic surface, with a minor channel leading to OH production.¹⁸⁹ If we assume that the quantum yield for dissociation is $\phi_{7.16} = 1$, then for our laser fluence ($2 \times 10^{17} \text{ photons cm}^{-2}$ at 351 nm), we expect $[\text{C}_4\text{H}_9\text{O}\cdot]_0 = 1 \times 10^{14} \text{ molec cm}^{-3}$. At 300 torr, vibrational relaxation will lead to thermal equilibrium on timescales $\ll 1 \text{ }\mu\text{s}$. Based on rate constants from the literature, isomerization for *n*-butoxy and 2-pentoxy radicals is expected to occur on time scales of $4 \text{ }\mu\text{s}$ ($k_{\text{isom}} = 2.5 \times 10^5 \text{ s}^{-1}$),²⁸



In the absence of O_2 , a small fraction of $\text{HOR}\cdot$ will undergo self-recombination, with lifetime $200 \text{ }\mu\text{s}$ ($k = 5 \times 10^{-11} \text{ cm}^3 \text{ molec}^{-1} \text{ s}^{-1}$).¹¹⁷



In the presence of O_2 , the hydroxy-alkyl radicals $\text{HOR}\cdot$ will associate to form peroxy radicals $\text{HORO}\cdot$ with a rate coefficient of roughly $7 \times 10^{-12} \text{ cm}^3 \text{ molec}^{-1} \text{ s}^{-1}$.²⁷



In most of our spectroscopy experiments, $[\text{O}_2] = 30 \text{ torr}$. Under these conditions, the pseudo-first order lifetime of $\text{HOR}\cdot$ is 150 ns . Thus, all of the $\text{HOR}\cdot$ will have been converted to $\text{HORO}\cdot$. (Note that for lower $[\text{O}_2]$, $0.1\text{--}1 \text{ torr}$, the lifetime of $\text{HOR}\cdot$ increases to $4\text{--}45 \text{ }\mu\text{s}$, and a mixture of $\text{HOR}\cdot$ and $\text{HORO}\cdot$ is detected. The consequences of this are explored in Chapter 9)

Decomposition of the alkoxy radicals occurs on timescales of 2 ms for *n*-butoxy ($k_{\text{decomp}} = 600 \text{ s}^{-1}$) and 50 μs for 2-pentoxy ($k_{\text{decomp}} = 2 \times 10^4 \text{ s}^{-1}$).¹¹⁷



The alkoxy radicals can also recombine with background and product NO to reform the alkyl nitrite. For our $[\text{NO}] = 10^{14} \text{ molec cm}^{-3}$, this reaction occurs on time scales of 300 μs ($k_{\text{NO}} \times [\text{NO}] = 3000 \text{ s}^{-1}$).³²



There are two concerns regarding secondary chemistry in our experiment. First, any side reactions of the alkoxy radical itself will have an impact on the initial $[\text{RO}\cdot]$ present, affecting both band strength and relative kinetics measurements. Second, hydrogen abstraction by $\text{RO}\cdot$, $\text{HOR}\cdot$, or $\text{HOROO}\cdot$ will lead to different species that contain hydroxyl groups. These species may have different ν_1 bands than $\text{HOR}\cdot$ or $\text{HOROO}\cdot$, and will cause interference in our reported spectra.

First, consider the reactions of the alkoxy radical itself. For our conditions, $[\text{RO}\cdot] = [\text{NO}] = 1 \times 10^{14} \text{ molec cm}^{-3}$. Recombination reactions of $\text{RO}\cdot$ with $\text{RO}\cdot$ or NO ,



are approximately two orders of magnitude slower than isomerization ($k_{\text{NO}} \times [\text{NO}] = 3000 \text{ s}^{-1}$).³² Thus, Reactions 7.5–7.11 will still be the dominant fate of the alkoxy radicals. The overall effect of Reactions 7.22 and 7.23 will be minor. Reaction 7.22 will be especially unimportant due to its quadratic dependence on $[\text{RO}\cdot]$.

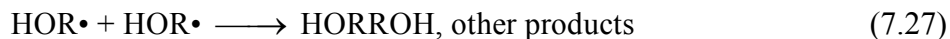
We next consider reactions of $\text{RO}\cdot$, $\text{HOR}\cdot$, and $\text{HOROO}\cdot$ that could lead to other products with hydroxyl groups. Continuing our analysis of $\text{RO}\cdot$, we note that alkoxy

radicals could abstract a hydrogen from RONO to form an alcohol (ROH, Reaction 7.24). Furthermore, HOR• could also abstract a hydrogen from RONO to form an alcohol (Reaction 7.25), or HOROO• could form a hydroxyalkylhydroperoxide (HOROOH, Reaction 7.26)



Analogous rate constants ($\text{R}\cdot + \text{R}$, $\text{R}\cdot + \text{ROH}$, $\text{RO}_2\cdot + \text{R}$, $\text{RO}_2\cdot + \text{ROH}$, $\text{RO}\cdot + \text{R}$) for $\text{R} = (\text{CH}_2, \text{C}_2\text{H}_4)$ are in the range 10^{-22} – $10^{-18} \text{ cm}^3 \text{ molec}^{-1} \text{ s}^{-1}$.¹¹⁷ For $[\text{RONO}] = 10^{16} \text{ molec cm}^{-3}$, the lifetime of these reactions would be 10^2 – 10^6 s . We conclude that hydrogen abstraction is unimportant over the timescale $20 \mu\text{s}$.

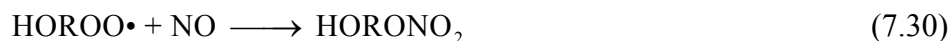
Next, we consider whether HOR• or HOROO• are removed through other (nonhydrogen abstraction) mechanisms. First, consider the fate of HOR• radicals in the absence of O₂: self-recombination or recombination with NO.



If we assume that the HOR• + HOR• recombination reactions are in the high pressure limit with rate constant $5 \times 10^{-11} \text{ cm}^3 \text{ molec}^{-1} \text{ s}^{-1}$, a rate constant similar to both HOCH₂• self-reaction and HOC₂H₄• self-reaction,¹¹⁷ then the initial lifetime for Reaction 7.27 is $200 \mu\text{s}$. The rate constant for Reaction 7.28 is unknown: analogous reactions have rate constants ranging from $6 \times 10^{-14} \text{ cm}^3 \text{ molec}^{-1} \text{ s}^{-1}$ ($\text{C}_3\text{H}_7\cdot + \text{NO}$) to $2 \times 10^{-11} \text{ cm}^3 \text{ molec}^{-1} \text{ s}^{-1}$ ($\text{HOCH}_2\cdot + \text{NO}$). For $[\text{NO}] = 1 \times 10^{14} \text{ molec cm}^{-3}$, we obtain $k_{28} \times [\text{NO}] = (6\text{--}2000) \text{ s}^{-1}$, or lifetimes of (0.5–170) ms. Regardless of the exact value of the rate

constant for $\text{HOR}\cdot + \text{NO}$, the reaction is at least two orders of magnitude less important than isomerization, and $[\text{HORNO}]$ can be considered negligible at 20 μs . Thus, at 20 μs , most (>90%) of the primary products will be $\text{HOR}\cdot$ monomers, with a small fraction recombining to form HORROH . The other products of Reaction 7.27 include hydrogen abstraction to form ROH and hydroxyl-butenes, but similar reaction channels in $\text{HOCH}_2\cdot$ or $\text{HOC}_2\text{H}_4\cdot$ self-reactions have a rate constant less than 10% of the overall rate for Reaction 7.27.¹¹⁷ Thus, ROH formation by $\text{HOR}\cdot$ hydrogen abstraction is negligible at 20 μs . The reaction rate for recombination with NO (Reaction 7.28) is too small to expect an appreciable contribution from HORNO . Similarly, a negligible amount of $\text{HOR}\cdot$ may have undergone hydrogen abstraction by NO to form butanol and a hydroxy-butene. The end result is that besides the small fraction of $\text{HOR}\cdot$ that recombines to form HORROH , no other reactions convert $\text{HOR}\cdot$ to other hydroxyl containing products over the timescale of our experiment (20 μs).

Finally, consider whether $\text{HORO}\cdot$ could be removed by other mechanisms. Further reaction of $\text{HORO}\cdot$ with NO will give a hydroxyalkoxy ($\text{HORO}\cdot$) and NO_2 (Reaction 7.29), with a rate coefficient of approximately $9 \times 10^{-12} \text{ cm}^3 \text{ molec}^{-1} \text{ s}^{-1}$. A minor association channel also exists, giving the hydroxyalkylnitrate HORONO_2 (Reaction 7.30), with a rate coefficient of approximately $4 \times 10^{-13} \text{ cm}^3 \text{ molec}^{-1} \text{ s}^{-1}$.¹¹⁸



At the low NO concentrations generated from the photolysis of precursor ($1 \times 10^{14} \text{ molec cm}^{-3}$), the pseudo-first-order lifetime of $\text{HORO}\cdot$ for reaction with NO is on the order of 1 ms: too long to be of importance. Assuming that the rate constant for the

HOROO• self-reaction is comparable to that for *n*-C₄H₉OO• self-reaction (4×10^{-13} cm³ molec⁻¹ s⁻¹),¹⁹⁰ no appreciable reaction of HOROO• will occur in less than 1 ms.

In theory, HOROO• could also abstract hydrogen through self-reaction:



The analogous rate constants (RO₂• + R, RO₂• + ROH) are on the order 10⁻²²–10⁻¹⁷ cm³ molec⁻¹ s⁻¹.¹¹⁷ For [HOROO•] = 10¹⁴ molec cm⁻³, the initial lifetime for Reaction 7.31 would be a minimum of 500 s. We reach a similar conclusion as the HOR• system: HOROO• does not react away to form other hydroxyl containing products over 20 μs. In the case of HOROO•, we do not have a contribution from recombination.

Based on all of the chemistry presented above, we expect that at 20 μs, only primary alkoxy chemistry (isomerization, reaction with O₂, decomposition, dimerization of HOR• in the absence of O₂, and formation of HOROO• in the presence of O₂) will contribute significantly to our experiment. Secondary reactions of RO•, HOR•, and HOROO• will not lead to spectral interference.

Kinetics Modeling

To further confirm that secondary chemistry effects are minimal, we constructed a kinetics model using rate constants available in the literature^{27, 117, 118} with the Kintecus kinetics modeling software.¹⁹¹ This kinetics model is one of the main tools used in Chapter 9, and is described in full detail there.

Figure 7.2 shows the simulated fractions of hydroxyl containing species present in our experiment over the range 0–100 μs after generating RO•. The modeled data are for *n*-butoxy, but similar results apply to 2-pentoxy. The conditions used for these

simulations are the same as in our CRDS experiment (Table 7.2). Our model shows that for $[O_2] = 0$, the cavity ringdown spectrum 20 μs after RONO photolysis will be predominantly $\text{HOR}\cdot$ (94%), with minor contributions from the recombination product HORROH (6%). For $[O_2] = 1 \times 10^{18} \text{ molec cm}^{-3}$, the measured spectrum should be $>98\%$ $\text{HOROO}\cdot$. At later times, a significant amount of the stable end-product $\text{HOR}'\text{CHO}$ is observed.

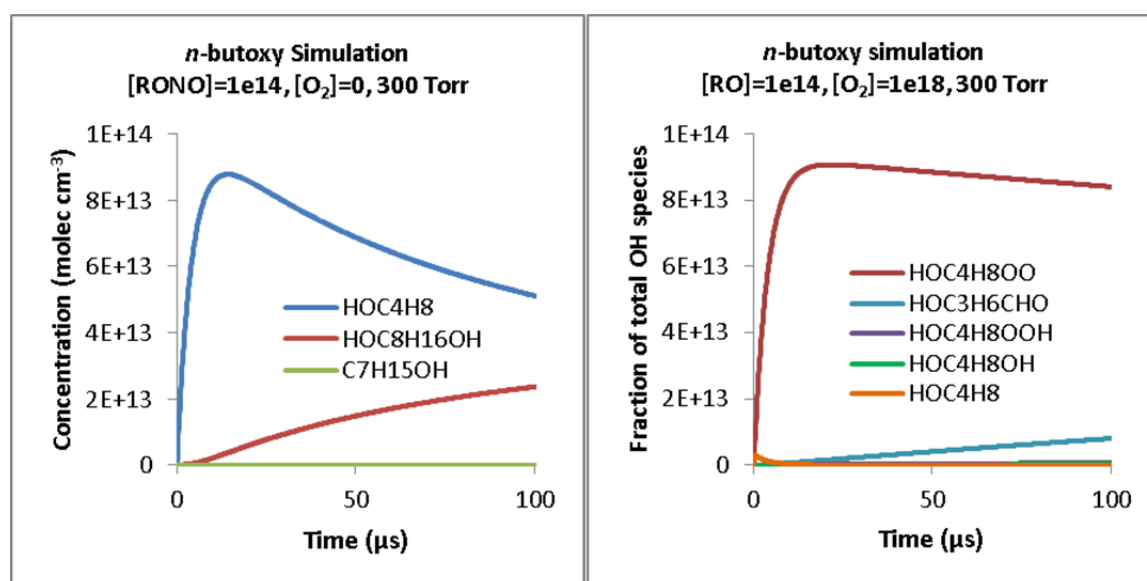


Figure 7.2. Modeled concentrations of $-\text{OH}$ containing species for n -butoxy chemistry, for $[O_2] = 0$ torr (left), and $[O_2] = 1 \times 10^{18} \text{ molec cm}^{-3}$ (right). Experimental conditions are the same as in Table 7.2. At 20 μs , we expect our spectra to be predominantly $\text{HOR}\cdot$ (94%, $[O_2] = 0$) or $\text{HOROO}\cdot$ (98%, $[O_2] = 1 \times 10^{18} \text{ molec cm}^{-3}$).

OH Stretch Spectra of $\delta\text{-HOC}_4\text{H}_8\cdot$, $\delta\text{-HOC}_4\text{H}_8\text{OO}\cdot$, $\delta\text{-HO-1-C}_5\text{H}_{10}\cdot$, and $\delta\text{-HO-1-C}_5\text{H}_{10}\text{OO}\cdot$

Figures 7.3–7.6 show a series of infrared spectra obtained following the photolysis of n -butyl nitrite or 2-pentyl nitrite precursors. All spectra shown were taken with a photolysis-probe delay of 20 μs , with a 0.2 cm^{-1} step size. The spectra presented in Figure 7.3 are unsubtracted (i.e., the mirror reflectivity and absorption by the background

gases have not been subtracted out). Figures 7.4–7.6 have had the background spectra in the absence of photolysis (excimer off) subtracted.

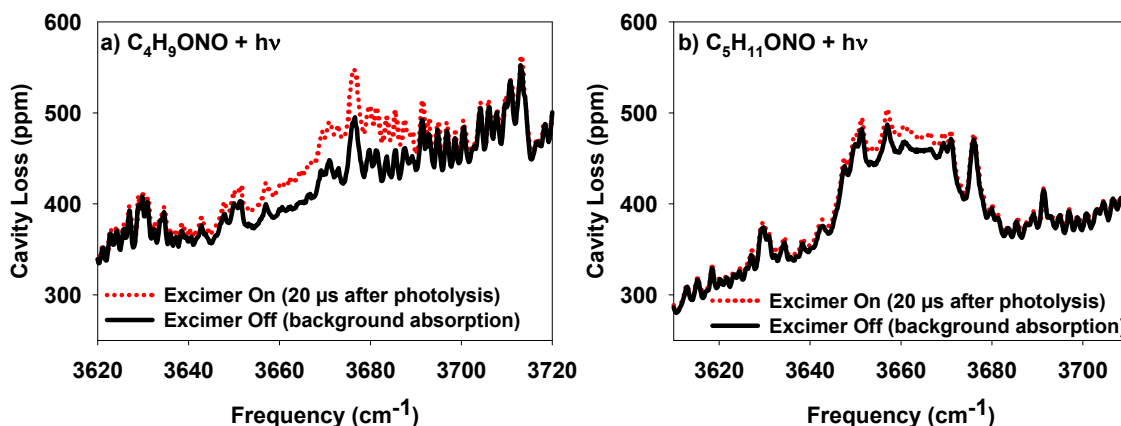


Figure 7.3. Cavity loss (mirror reflectivity plus absorption) of the precursor chemicals (excimer off) and the photolysis products (excimer on) in the mid-IR for *n*-butyl nitrite (a, 300 torr) and 2-pentyl nitrite (b, 315 torr). All spectra were taken at room temperature (295 ± 2 K) and $[O_2] = 1 \times 10^{18}$ molec cm⁻³, 0.2 cm⁻¹ between data points. The alkyl nitrite absorptions show considerable structure across the entire region. The large peak in the 2-pentyl nitrite spectrum centered at 3660 cm⁻¹ is due to residual 2-pentanol. Additional absorption features are observed following photolysis of the alkyl nitrite. Reprinted with permission from Sprague et al.³¹ Copyright 2012 American Chemical Society.

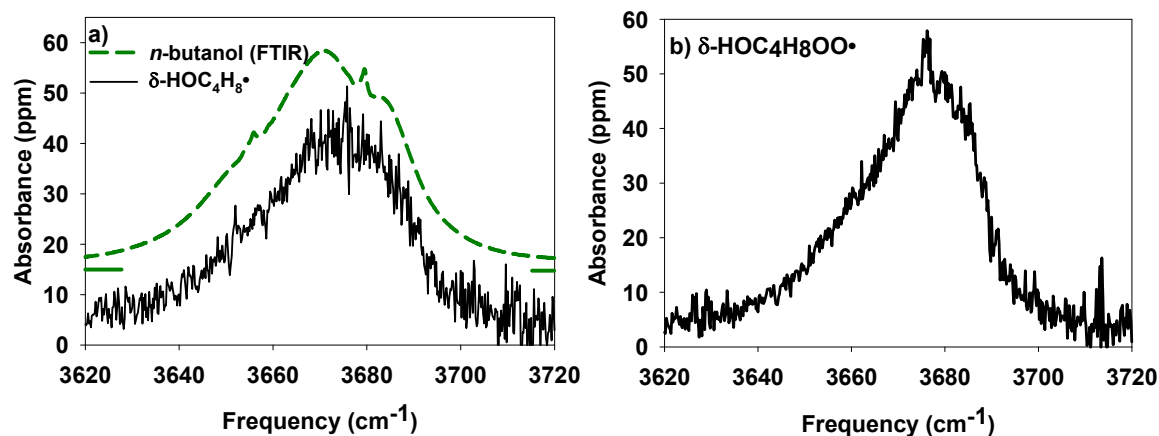


Figure 7.4. ν_1 (OH stretch) spectra of the isomerization of products of *n*-butoxy, in the absence ($\delta\text{-HOC}_4\text{H}_8\bullet$, a) and presence of O_2 ($\delta\text{-HOC}_4\text{H}_8\text{OO}\bullet$, b, $[\text{O}_2] = 9 \times 10^{17}$ molec cm^{-3}). Spectra were recorded at 295 K, 300 torr, 0.2 cm^{-1} between data points, 20 μs after photolysis of *n*-butyl nitrite, $[\text{RONO}] = 7 \times 10^{15}$ molec cm^{-3} , with a 1.5% photolysis ratio. The $\delta\text{-HOC}_4\text{H}_8\bullet$ spectrum was signal averaged for 4.8 s per point, while the $\delta\text{-HOC}_4\text{H}_8\text{OO}\bullet$ spectrum was signal averaged for 8.0 s per point. Both spectra are similar in position and shape to the FTIR spectrum of *n*-butanol (a, shown in green).⁴⁰ Assuming an isomerization rate constant $k_{\text{isom}} = 2.4 \times 10^5 \text{ s}^{-1}$, we predict that in the absence of O_2 , 94% of the product being measured is $\text{HOC}_4\text{H}_8\bullet$, and 6% is its dimer, $\text{HOC}_8\text{H}_{16}\text{OH}$. In the presence of O_2 , we predict that 98% of the product being measured is $\text{HOC}_4\text{H}_8\text{OO}\bullet$ and 2% are other secondary products. Reprinted with permission from Sprague et al.³¹ Copyright 2012 American Chemical Society.

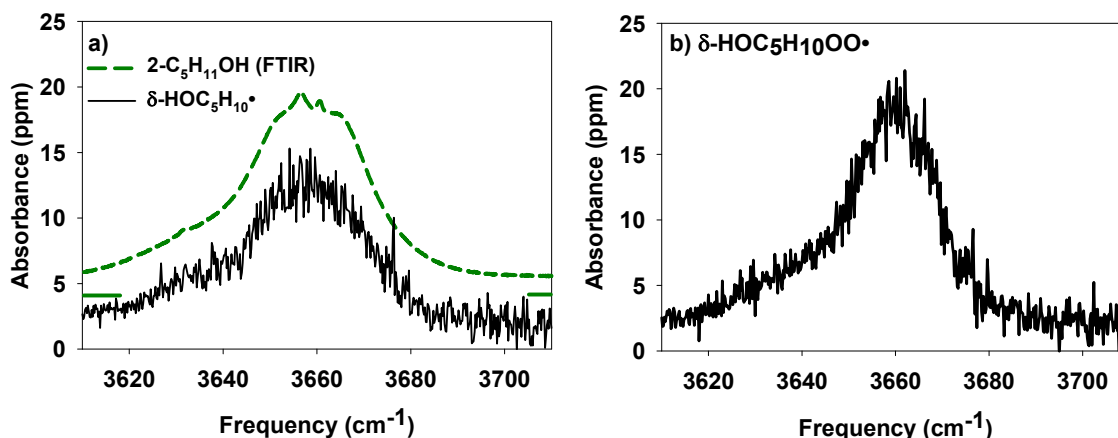


Figure 7.5. ν_1 (OH stretch) spectra of the isomerization of products of 2-pentoxyl, in the absence (δ -HO-1-C₅H₁₀•, a) and presence of O₂ (δ -HO-1-C₅H₁₀OO•, b, [O₂] = 1×10^{18} molec cm⁻³). Spectra were recorded at 295 K, 315 torr, 0.2 cm⁻¹ between data points, 20 μ s after photolysis of 2-pentyl nitrite, [RONO] = 8×10^{15} molec cm⁻³. The photolysis ratio is not well known: if the UV cross section of 2-pentyl nitrite is taken to be 0.75 times that of *n*-butyl nitrite, then [RO•]₀ = 1×10^{14} molec cm⁻³. The peak intensities suggest that [HOR•]₀ = 5×10^{13} molec cm⁻³. Both the δ -HO-1-C₅H₁₀• and δ -HO-1-C₅H₁₀OO• spectra were signal averaged for 11.2 s per point. Both spectra are similar in position and shape to the FTIR spectrum of 2-pentanol (a, shown in green).⁴⁰ Assuming an isomerization rate constant $k_{\text{isom}} = 2.4 \times 10^5$ s⁻¹, we predict that in the absence of O₂, 94% of the product being measured is δ -HO-1-C₅H₁₀•, and 6% is its dimer, HOC₁₀H₂₀OH. In the presence of O₂, we predict that 98% of the product being measured is δ -HO-1-C₅H₁₀OO• and 2% are other secondary products. Reprinted with permission from Sprague et al.³¹ Copyright 2012 American Chemical Society.

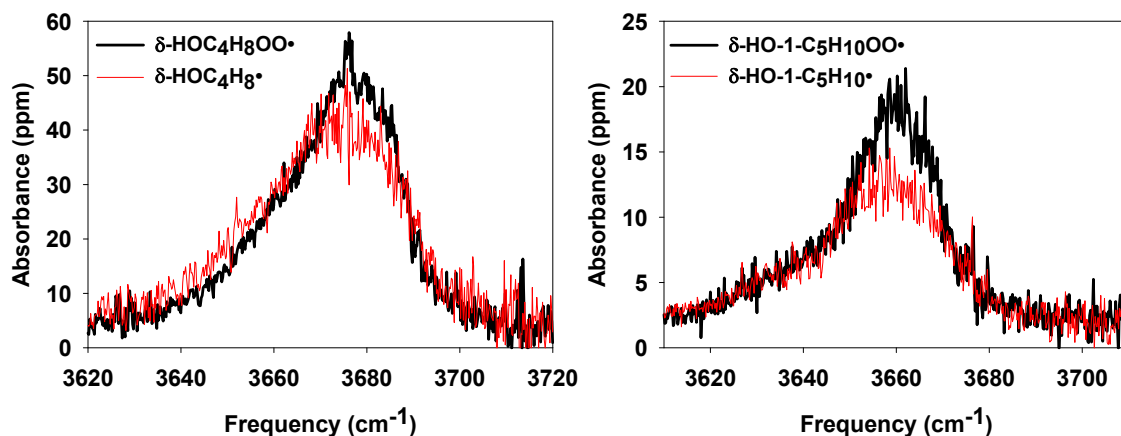


Figure 7.6. Overlaid spectra of δ -HOR• (red) and δ -HOROO• (black) for R = C₄H₈ (left, [HOROO•]/[HOR•] = 0.95) and R = 1-C₅H₁₀ (right, [HOROO•]/[HOR•] = 0.97). Relative concentrations were calculated assuming $k_{\text{isom}}/k_{\text{O}_2} = 1.7 \times 10^{19} \text{ cm}^{-3}$ (*n*-butoxy) or $3.4 \times 10^{19} \text{ cm}^{-3}$ (2-pentoxy), as determined in Chapter 8. We observe that the ν_1 band of HOROO• is narrower and stronger than HOR• for both systems. Reprinted with permission from Sprague et al.³¹ Copyright 2012 American Chemical Society.

Figure 7.3 shows the background IR spectra of the reactants (excimer off) and the IR spectra of the background plus signal (excimer on) for *n*-butyl nitrite (Figure 7.3a) and 2-pentyl nitrite photolysis (Figure 7.3b). Two species contribute to the background in both spectra: the parent alkyl nitrites (broad, structured absorption across the range 3610–3720 cm⁻¹) and water (sharp features at 3630, 3650, 3670, and 3690 cm⁻¹). In the 2-pentyl nitrite spectrum, an additional broad, structureless absorption from 2-pentanol is observed at 3660 cm⁻¹.

Following photolysis at 351 nm, absorption bands are observed, centered near 3675 cm⁻¹ in the *n*-butyl nitrite spectrum and 3660 cm⁻¹ for the 2-pentyl nitrite spectrum, on top of the background features. Figures 7.4 and 7.5 show the IR spectra of products formed following the generation of two different alkoxy radicals: *n*-butoxy (Figure 7.4), and 2-pentoxy (Figure 7.5), in the absence (Figures 7.4a and 7.5a) and presence (Figures

7.4b, 7.5b) of O₂. Following photolysis of *n*-butyl nitrite and 2-pentyl nitrite, clear peaks are observed in the OH-stretch region, located at 3675 cm⁻¹ for *n*-butyl nitrite, and 3660 cm⁻¹ for 2-pentyl nitrite. These absorption features are broad (FWHM > 30 cm⁻¹) and asymmetric, with more intensity observed to the red of the peak. The width and partial structure of these peaks suggest that multiple conformers contribute to each observed absorption band. Furthermore, the observed peaks are similar in shape and position to the parent alcohols of the alkoxy radicals being studied. In the *n*-butoxy system (Figure 7.4), the observed absorption band is similar to the ν_1 band of *n*-butanol (reference FTIR spectrum shown in green).⁴⁰ Similarly, for the 2-pentoxy system (Figure 7.5), the observed absorption band is similar to the ν_1 band of 2-pentanol.⁴⁰ It should be noted that the absorption bands are somewhat stronger and sharper in the presence of O₂ than in the absence of O₂. Figure 7.6 shows these bands overlaid to illustrate this point. Analogous peaks were not observed following the photolysis of isobutyl nitrite or *tert*-butyl nitrite, as shown in Figure 7.7.

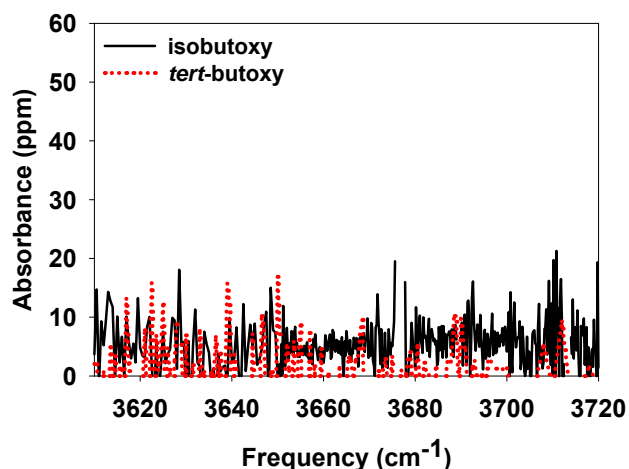


Figure 7.7. Infrared spectra of the products formed from photolysis of isobutyl nitrite and *tert*-butyl nitrite. Spectra were recorded at 295 K, 300 torr, 0.2 cm^{-1} between data points, 20 μs after photolysis of the alkyl nitrite, $[\text{RONO}] = 8.1 \times 10^{15} \text{ molec cm}^{-3}$, with a 1.2% photolysis ratio. No absorption features in the ν_1 region are observed, indicating that the products of isobutoxy and *tert*-butoxy chemistry do not contain hydroxyl groups. Reprinted with permission from Sprague et al.³¹ Copyright 2012 American Chemical Society.

We assign the absorption bands presented in Figures 7.4 and 7.5 to the primary alkoxy isomerization products for the following reasons. First, the absorption bands that we observe are similar to the ν_1 (OH stretch) bands of *n*-butanol and 2-pentanol. The primary isomerization products have structures similar to these alcohols (HOR• and HOROO• vs ROH), and we expect similar infrared spectra. Second, we only observe the absorption features for alkoxy radicals that are long enough to undergo a 1,5-hydrogen shift (*n*-butoxy and 2-pentoxy). Neither isobutoxy nor *tert*-butoxy are long enough to isomerize, and thus any absorptions in the *n*-butoxy and 2-pentoxy systems that belonged to isomerization products would be missing. Finally, the arguments presented in the *Chemistry* section indicate that the only significant products that we should be detecting under our experimental conditions are the primary isomerization products. The absence

of any OH stretch bands in the isobutoxy and *tert*-butoxy experiments provides reasonable confirmation that hydrogen abstraction is not leading to significant quantities of parent alcohol (ROH) being detected. We therefore assign the IR spectra in Figures 7.4 and 7.5 to δ -HOC₄H₈• (Figure 7.4a), δ -HOC₄H₈OO• (Figure 7.4b), δ -HO-1-C₅H₁₀• (Figure 7.5a), and δ -HO-1-C₅H₁₀OO• (Figure 7.5b).

The intensity of HOR• is predicted to be similar to the parent alcohol, ROH. We can therefore use the HOR• absorbance to estimate the initial concentration of alkoxy radicals, [RO•]₀. Our quantum chemistry calculations (Chapter 9) confirm that HOR• and the parent alcohol (ROH) have approximately the same absorption cross section. Taking the peak absorption cross section of the HOR• ν_1 peak to be equivalent to the parent alcohols (7.2×10^{-20} cm² molec⁻¹ for *n*-butanol, 6.0×10^{-20} cm² molec⁻¹ for 2-pentanol),⁴⁰ we obtain [HOC₄H₈•]₀ = 1×10^{14} molec cm⁻³ and [HOC₅H₁₀•]₀ = 5×10^{13} molec cm⁻³. These values are consistent with our estimate of the nascent alkoxy product yields (within a factor of 2).

Change in OH Stretch Spectrum with [RO•] and Timing

Spectra were also collected for photolysis-probe delays over the range 10–800 μ s. Figure 7.8 shows the time dependence of the absorbance observed in Figures 7.4 (at 3662 cm⁻¹). We observe that at this frequency, the OH stretch intensity rises with a lifetime of approximately 5 μ s, and reaches a maximum by 20 μ s. Mollner observed that the intensity remains constant for at least 200 μ s,³⁰ indicating that the ν_1 band is a reasonably good way to measure the overall concentration of species with hydroxyl groups. Note that

since the rise time (5 μs) is on the same timescale as our ringdown time (3–7 μs), we cannot use the rise time as a direct measure of the alkoxy isomerization rate constant.

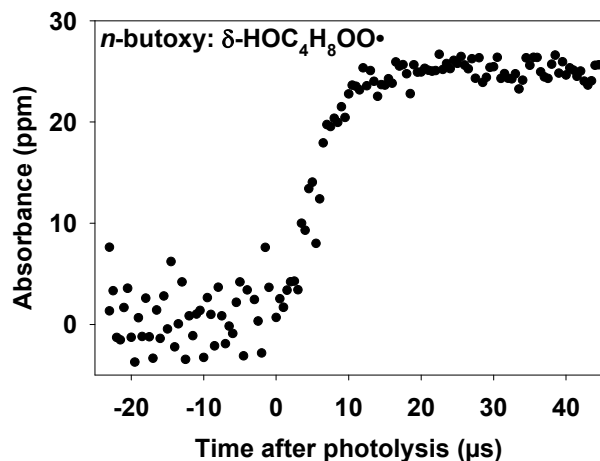


Figure 7.8. Absorbance at 3662 cm^{-1} for *n*-butoxy isomerization as a function of time after *n*-butyl nitrite photolysis. Data were recorded at 295 K, 300 torr, $[\text{O}_2] = 1 \times 10^{18}\text{ molec cm}^{-3}$, $[\text{RONO}] = 7 \times 10^{15}\text{ molec cm}^{-3}$, with a 1.6% photolysis ratio. The absorbance reaches its maximum within 20 μs of photolysis and remains constant thereafter. Reprinted with permission from Sprague et al.³¹ Copyright 2012 American Chemical Society.

Secondary chemistry changes the products being detected at 800 μs . Figure 7.9 shows the expected concentrations of OH containing species across 0–1000 μs based on our kinetics model, for $[\text{O}_2] = 10^{18}\text{ molec cm}^{-3}$, at two different alkoxy concentrations (left – $1 \times 10^{14}\text{ molec cm}^{-3}$, right – $3.7 \times 10^{14}\text{ molec cm}^{-3}$). At 800 μs , only 50% or 21% of the ν_1 band will be due to $\text{HOC}_4\text{H}_8\text{OO}\cdot$. The remaining contributions will be from the stable end-products $\text{HOC}_3\text{H}_6\text{CHO}$ (41% or 59%), $\text{HOC}_4\text{H}_8\text{OOH}$ (8% or 18%), and $\text{HOC}_4\text{H}_8\text{OH}$ (1% or 2%).

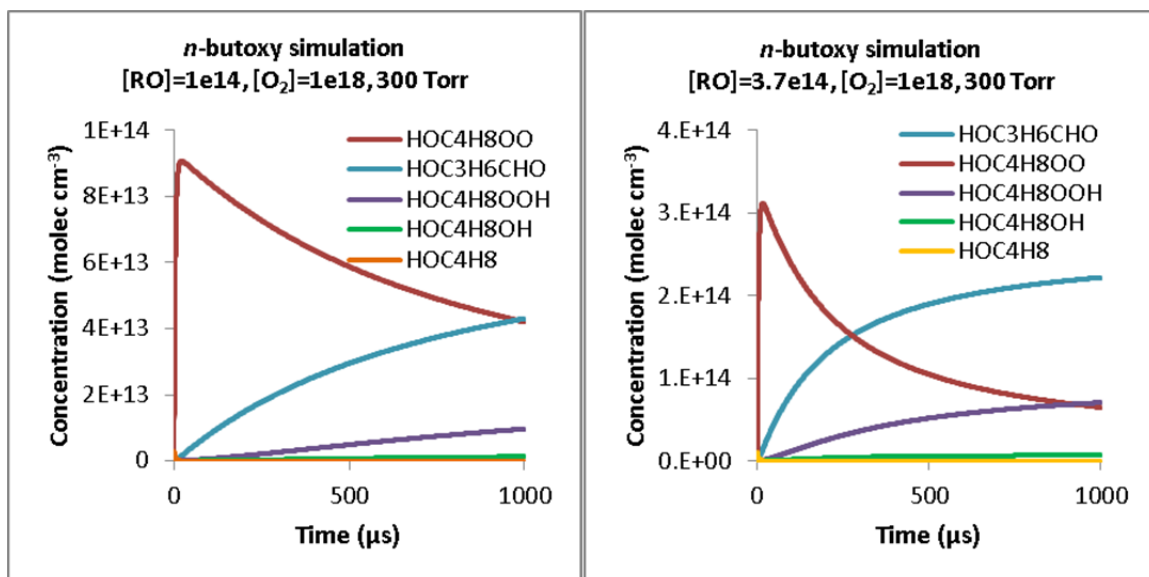


Figure 7.9. Modeled concentrations of $-OH$ containing species for n -butoxy chemistry, $[O_2] = 1 \times 10^{18}$ molec cm^{-3} . The initial alkoxy concentration was either 1×10^{14} molec cm^{-3} (left) or 3.7×10^{14} molec cm^{-3} (right). At 800 μs , we expect our spectra to be a mixture of $HOC_4H_8OO\cdot$ (50% or 21%), HOC_3H_6CHO (41% or 59%), HOC_4H_8OOH (8% or 18%), and HOC_4H_8OH (1% or 2%).

Figure 7.10 shows overlaid spectra comparing the products of alkoxy chemistry at 10 μs , 20 μs , and 800 μs . All spectra were taken at $[O_2] = 1 \times 10^{18}$ molec cm^{-3} . Figure 7.10a compares the 10 μs , 20 μs , and 800 μs spectra for $[RO\cdot] = 1 \times 10^{14}$ molec cm^{-3} . Figure 7.10b compares the 800 μs spectra for $[RO\cdot] = 1 \times 10^{14}$ molec cm^{-3} and 3.7×10^{14} molec cm^{-3} .

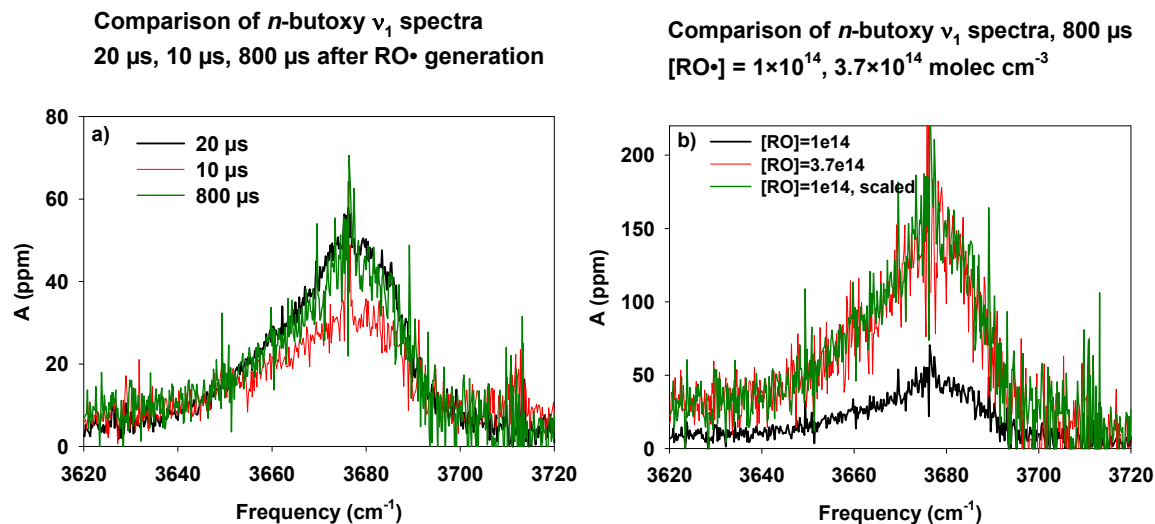


Figure 7.10. ν_1 spectra of *n*-butoxy isomerization products at various conditions. All spectra were taken with $[\text{O}_2] = 9 \times 10^{17} \text{ molec cm}^{-3}$. Figure 7.10a: $[\text{RO}\cdot] = 1 \times 10^{14} \text{ molec cm}^{-3}$, 20 μs (black), 10 μs (red), and 800 μs (green) after photolysis. Figure 7.10b: 800 μs after photolysis, $[\text{RO}\cdot] = 3.7 \times 10^{14} \text{ molec cm}^{-3}$ (red), $1.1 \times 10^{14} \text{ molec cm}^{-3}$ (black, scaled by a factor of 3.4 in green).

First, consider the 10 μs and 20 μs spectra in Figure 7.10a (red and black respectively). Ignoring the sharp spike at 3675 cm^{-1} , the peak absorbance at 10 μs is lower than at 20 μs a factor of 0.7 (33 ppm vs 48 ppm). The 10 μs spectrum (FWHM 35 cm^{-1}) is wider than the 20 μs spectrum (25 cm^{-1}). There are two possibilities to explain these differences, although only one of these is likely. First, isomerization may not be complete after only 10 μs . Given an isomerization lifetime of 5 μs ,^{146, 148, 153-158} we expect 86% of the alkoxy to have isomerized at 10 μs , and 98% at 20 μs , accounting for much of the intensity difference. Second, while it is possible that not all of the $\text{HOR}\cdot$ has been converted to $\text{HOROO}\cdot$ after only 10 μs , this is unlikely. The association of O_2 with $\text{HOR}\cdot$ is very fast ($k_{\text{HOR}+\text{O}_2} \times [\text{O}_2] = 7 \times 10^6 \text{ s}^{-1}$, or lifetime 0.14 μs).²⁷ After 10 μs , 100% of the $\text{HOR}\cdot$ should have been converted to $\text{HOROO}\cdot$.

Next, consider the 20 and 800 μs spectra in Figure 7.10a (black and green respectively). Both spectra have approximately the same shape and intensity, with slight discrepancies near the peak (48 ppm at 20 μs vs 47 ppm at 800 μs) and the baseline at 3620–3640 cm^{-1} (5 ppm at 20 μs vs 8 ppm at 800 μs). The spectra are equivalent in shape and absorbance at frequencies greater than 3680 cm^{-1} . The peak absorbance difference is within the noise of the 800 μs spectrum. The difference in baselines at 3620 cm^{-1} is likely due to absorbance by secondary products. Overall, the spectra are essentially equivalent over the range 3640–3720 cm^{-1} , indicating that the ν_1 band is a very robust measure of the overall number of OH groups in the system.

Third, consider the 800 μs spectra in Figure 7.10b, at low and high $[\text{RO}\cdot]$ (black/green and red respectively). By scaling the low $[\text{RO}\cdot]$ spectrum (black) up to high $[\text{RO}\cdot]$ concentration (green), we observe that the spectrum shape and relative absorbance is invariant to the initial radical concentration. We already have predicted that increasing $[\text{RO}\cdot]$ will change the products being detected at 800 μs (Figure 7.9). Thus, Figure 7.10b provides more evidence that secondary chemistry does not change the properties of the observed ν_1 band.

Finally, consider the sharp spikes in the 10, 20, and 800 μs spectra at 3630, 3650, 3675, and 3710 cm^{-1} . These spikes do not follow the same kinetics as our alkoxy peak; the spikes are largest in the 10 μs spectrum and much lower in the 20 and 800 μs spectra. The spikes likely belong to another chemical species, although we have not identified this species yet.

Determination of the Relative Kinetic Rate $k_{\text{isom}}/k_{\text{O}_2}$

The final goal of the study presented in this chapter was to remeasure $k_{\text{isom}}/k_{\text{O}_2}$ using our new OH stretch spectra of HOROO•, in order to determine whether the previous alkoxy kinetics results (reanalyzed in Chapter 8) obtained an accurate value using the mixed spectrum of HOROO• and HOR'CHO. The results of the previous section showed that the OH stretch spectra of pure HOC₄H₈OO• and a 1:1 mixture of HOC₄H₈OO• and HOC₃H₆CHO were exactly the same. Therefore, we expect our new measurements of $k_{\text{isom}}/k_{\text{O}_2}$ to be within the uncertainty of the previously reported measurements.

Details of how to derive $k_{\text{isom}}/k_{\text{O}_2}$ based on CRDS measurements will be presented with the kinetics analysis (Chapter 8), and only a brief overview is presented here. The relative rate constants of the isomerization channel (Reactions 7.5 and 7.8) and the O₂ channel (Reactions 7.4 and 7.7) can be determined by varying [O₂] and measuring [HOROO•]. By considering only the isomerization and O₂ reaction pathways, the resulting data should fit to Equation 7.32:

$$\frac{A_0}{A} = \frac{k_{\text{O}_2}}{k_{\text{isom}}}[\text{O}_2] + 1, \quad (7.32)$$

where A_0/A is defined as the ratio of absorbances at “[O₂] = 0” and the [O₂] of interest. Because of anomalous behavior in the relative kinetics measurements at low [O₂] (discussed in Chapter 9), “[O₂] = 0” is defined as the y-intercept of the fitted regression line to Equation 7.32, and not the literal absorbance at [O₂] = 0. We then apply a correction factor (Chapter 8) to account for additional reactions of the alkoxy radical. The true $k_{\text{isom}}/k_{\text{O}_2}$ is given by

$$\left(\frac{k_{\text{isom}}}{k_{\text{O}_2}}\right)_{\text{actual}} = \left(\frac{\partial\left(\frac{A_0}{A}\right)}{\partial[\text{O}_2]}\right)^{-1} \times X_{\text{tot}}, \quad (7.33)$$

where $(k_{\text{isom}}/k_{\text{O}_2})_{\text{actual}}$ is the true value of $k_{\text{isom}}/k_{\text{O}_2}$, $\frac{\partial\left(\frac{A_0}{A}\right)}{\partial[\text{O}_2]}$ is the value obtained by fitting to Equation 7.32 (only considering isomerization and reaction with O_2), and X_{tot} is the correction factor that accounts for all other reaction pathways (0.93 ± 0.02 for *n*-butoxy, 0.87 ± 0.04 for 2-pentoxy, 2σ).

Figure 7.11 shows the plots of A_0/A vs $[\text{O}_2]$ for *n*-butoxy (left) and 2-pentoxy (right), measured using the OH stretch spectrum peak. All measurements were made at 3662 cm^{-1} (butoxy) and 3660 cm^{-1} (pentoxy). These points were chosen to obtain a large absorbance while avoiding the sharp spike observed near the $\text{HOC}_4\text{H}_8\text{OO}\cdot$ OH stretch peak at 3675 cm^{-1} . The linear fit for *n*-butoxy is excellent given the low number of data points taken ($R^2 = 96.24\%$), while the fit for 2-pentoxy is somewhat worse ($R^2 = 84.66\%$).

For *n*-butoxy, with 2σ errors, the slope of the plot, $\frac{\partial\left(\frac{A_0}{A}\right)}{\partial[\text{O}_2]}$, is $(4.73 \pm 0.59) \times 10^{-20} \text{ cm}^3$, and the intercept, A_0/A at $[\text{O}_2] = 0$, is (1.00 ± 0.02) . Using $X_{\text{tot}} = 0.93 \pm 0.02$, **the resulting relative kinetic rate constants, $k_{\text{isom}}/k_{\text{O}_2}$, is reported as $(1.96 \pm 0.25) \times 10^{19} \text{ cm}^{-3}$ (2σ error).**

For 2-pentoxy, with 2σ errors, the slope of the plot, $\frac{\partial\left(\frac{A_0}{A}\right)}{\partial[\text{O}_2]}$, is $(2.30 \pm 0.98) \times 10^{-20} \text{ cm}^3$, and the intercept, A_0/A at $[\text{O}_2] = 0$, is (1.00 ± 0.04) . Using X_{tot}

$= 0.87 \pm 0.04$, the resulting relative kinetic rate constants, $k_{\text{isom}}/k_{\text{O}_2}$, is reported as $(3.78 \pm 1.62) \times 10^{19} \text{ cm}^{-3}$ (2σ error).

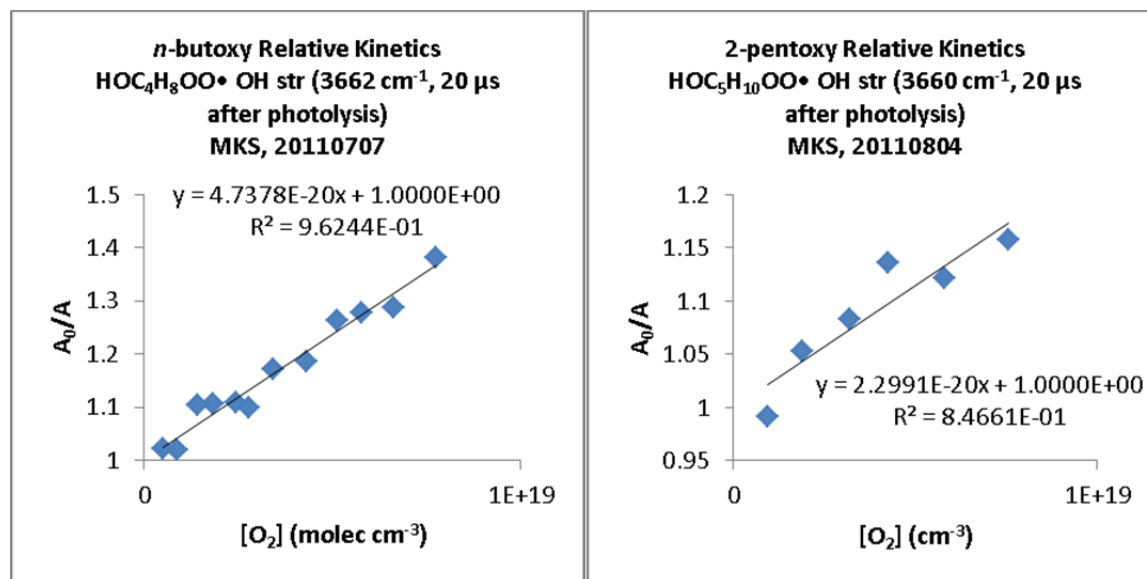


Figure 7.11. Plot of A_0/A vs $[\text{O}_2]$ for *n*-butoxy (left) and 2-pentoxy (right), as measured by the OH stretch peaks at 3662 cm^{-1} (shoulder of *n*-butoxy) or 3660 cm^{-1} (peak of 2-pentoxy). A_0/A is a measure of the percent yield of the isomerization channel as compared to the O_2 channel. For *n*-butoxy, the plot has a slope of $(4.73 \pm 0.59) \times 10^{-20} \text{ cm}^3$, and an intercept of (1.00 ± 0.02) . Applying the correction factor of 0.93 ± 0.02 to account for additional reaction pathways, the resulting $k_{\text{isom}}/k_{\text{O}_2}$ value for *n*-butoxy is determined to be $(1.96 \pm 0.25) \times 10^{19} \text{ cm}^{-3}$. For 2-pentoxy, the plot has a slope of $(2.30 \pm 0.98) \times 10^{-20} \text{ cm}^3$, and an intercept of (1.00 ± 0.04) . Applying the correction factor of 0.87 ± 0.04 to account for additional reaction pathways, the resulting $k_{\text{isom}}/k_{\text{O}_2}$ value for 2-pentoxy is determined to be $(3.78 \pm 1.63) \times 10^{19} \text{ cm}^{-3}$. All errors are reported to 2σ .

Table 7.4 contains a summary of the relative rate constants $k_{\text{isom}}/k_{\text{O}_2}$ for *n*-butoxy and 2-pentoxy from our CRDS experiments and the literature. We observe that the preliminary values of $k_{\text{isom}}/k_{\text{O}_2}$ obtained from the spectroscopic bands presented in this chapter are in very good agreement with all of the previous studies in the literature,^{146, 148, 153-158} including the previous CRDS experiments after reanalysis (Chapter 8) and the A-X electronic band (Chapter 10). The larger uncertainty reported for 2-pentoxy relative to *n*-

butoxy is due to two factors: background 2-pentanol absorption that increases our spectrometer noise, and considerably fewer data points used in the linear fit.

Table 7.4. Comparison of relative rate constant determinations $k_{\text{isom}}/k_{\text{O}_2}$ and derived k_{isom} for *n*-butoxy and 2-pentoxy

	$k_{\text{isom}}/k_{\text{O}_2}$ (10^{19} cm^{-3}) ^a	k_{isom} (10^5 s^{-1}) ^b	Molecules detected	Method	<i>P</i> (<i>torr</i>)	Ref
<i>n</i>-butoxy	1.96 ± 0.25	2.7 ± 1.4	δ-hydroxy- <i>n</i> -butyl peroxy	Slow flow, CRDS (OH Str)	330	This work
	1.39 ± 0.47	2.0 ± 1.2	δ-hydroxy- <i>n</i> -butyl peroxy	Slow flow, CRDS (A-X)	330	Chapter 10
	1.69 ± 0.15	2.4 ± 1.2	δ-hydroxy- <i>n</i> -butyl peroxy	Slow flow, CRDS (OH Str)	670	Chapter 8
	2.0 ± 0.4	2.7 ± 1.5	Butyl nitrite, Butanal,	Static, FTIR	700	Cassanelli ¹⁵⁵
	1.5 ± 0.4	2.1 ± 1.2	4-hydroxy butanal	Static, GC	760	Cox ¹⁵⁶
	1.9 ± 0.4	2.7 ± 1.4	Butane, Butanal	Static, FTIR	700	Niki ¹⁴⁸
	2.1 ± 0.5	2.9 ± 1.6	Butyl nitrite, Butanal	Slow flow, GC	760	Cassanelli ¹⁶⁰
	1.8 ± 1.1	2.5 ± 2.0	Butyl nitrite, Butanal	Slow flow, GC	760	Cassanelli ¹⁶⁰
	1.8 ± 0.6	2.5 ± 1.5	Butane, Butanal	Static, FTIR	760	Geiger ¹⁶¹
	0.25 ± 0.19 ^c	0.35 ± 0.20 ^c	Butanal, 4-hydroxy butanal	Fast flow, LIF	38	Hein ¹⁵⁹
	1.6	2.2	OH and NO ₂	Static, GC	740	Carter ¹⁵⁴
	2.1 ± 1.8 ^d	2.9 ± 1.4 ^d		Recommendation	760	IUPAC ¹¹⁸
2-pentoxy	3.78 ± 1.62	3.0	δ-hydroxy- <i>n</i> -pentyl peroxy	Slow flow, CRDS (OH Str)	330	This chapter
	3.37 ± 0.43 ^e	2.7	δ-hydroxy- <i>n</i> -pentyl peroxy	Slow flow, CRDS (OH Str)	670	Chapter 8
	3.1 ^e	2.5 ^e	2-pentanone	Static, GC	700	Atkinson ¹⁴⁵
	0.15	0.12 ^f	Acetone, Acetaldehyde, 2-hexanol	Static, GC	760	Dóbé ¹⁵⁷

a) All uncertainties are 2σ . All studies other than the current work treat all alkoxy reactions besides isomerization and reaction with O₂ as negligible.

b) Computed k_{isom} assuming literature value of $k_{\text{O}_2} = (1.4 \pm 0.7) \times 10^{-14} \text{ cm}^3 \text{ s}^{-1}$ for *n*-butoxy,²⁸ and $k_{\text{O}_2} = 8 \times 10^{-15} \text{ cm}^3 \text{ s}^{-1}$ for 2-pentoxy (no estimate available for the uncertainty).¹⁴²

c) Unlike the other studies, Hein directly measured k_{isom} . In this table, we calculate the ratio $k_{\text{isom}}/k_{\text{O}_2}$ from Hein's measurement using the literature value of k_{O_2} .

d) The IUPAC recommendation for $k_{\text{isom}}/k_{\text{O}_2}$ is computed from their individual recommendations of the isomerization and O₂ reactions

e) The uncertainty on $k_{\text{isom}}/k_{\text{O}_2}$ is reported by Atkinson as a factor of 2.

f) Dóbé's study calculates k_{isom} from the relative rate $k_{\text{isom}}/k_{\text{decomp}}$ and their measured rate $k_{\text{decomp}} = 1.2 \times 10^4 \text{ s}^{-1}$. The $k_{\text{isom}}/k_{\text{O}_2}$ reported in this table uses the literature value of $k_{\text{O}_2} = 8 \times 10^{-15} \text{ cm}^3 \text{ s}^{-1}$ for 2-pentoxy.¹⁴²

Analysis of Our 2-pentyl nitrite Sample

We now turn our attention to the properties of our 2-pentyl nitrite sample: purity, vapor pressure, and thermodynamic properties ($\Delta_{\text{vap}}H$, $T_{\text{boil,1atm}}$) of our sample. To the best of our knowledge, this is the first report of the thermodynamic properties of 2-pentyl nitrite.

The purity of our synthesized 2-pentyl nitrite (after distillation) can be determined through its FTIR spectrum ($1000\text{--}4000\text{ cm}^{-1}$), shown in Figure 7.12 (left: full spectrum, right: zoomed in to show smaller absorption features). The spectrum was recorded on a Nicolet FTIR spectrometer in Paul Wennberg's laboratory (Caltech), $L_{\text{FTIR}}=19\text{ cm}$. 2-pentyl nitrite was introduced to the spectrometer by evacuating the spectrometer cell, then allowing vapor from our sample into the spectrometer cell. Typical pressures in the spectrometer cell were 1-2 torr.

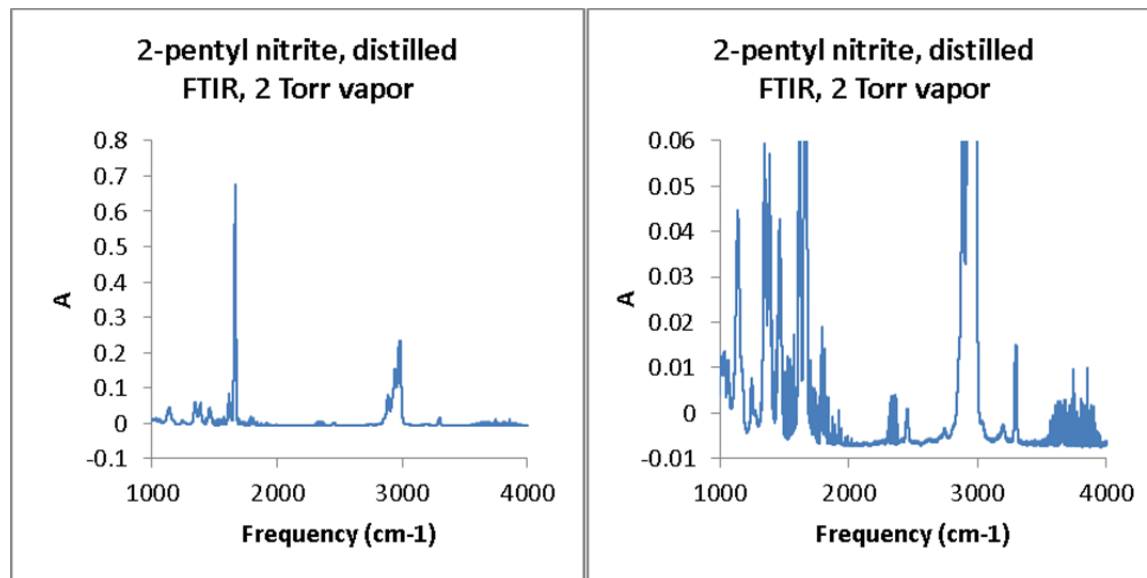


Figure 7.12. FTIR spectrum of our synthesized 2-pentyl nitrite after distillation. The left plot shows the entire spectrum. The right plot zooms in to better show the smaller absorption features. The spectrum was taken by introducing sample vapor to the FTIR. Cell length = 19 cm.

The main contaminants in our 2-pentyl nitrite sample are 2-pentanol (2-C₅H₁₁OH), NO, and H₂O. We use the IR bands of these species to determine their relative concentrations: ON-O stretch of 2-C₅H₁₁ONO (1550–1725 cm⁻¹), NO fundamental vibration (1840–1920 cm⁻¹), H₂O OH stretch modes (3600–3800 cm⁻¹), and the OH stretch of 2-C₅H₁₁OH (3600–3700 cm⁻¹). For H₂O, NO, and 2-C₅H₁₁OH, the individual bands are fit to reference spectra to determine their concentrations.⁴⁰ There is no reference spectrum for 2-C₅H₁₁ONO; thus, the concentration must be computed based on similar reference spectra and theoretical calculations, as described later in this section. Figure 7.13 shows the FTIR bands and fits used to determine the concentrations of each species. Fitting to the reference spectra reveals [H₂O] = 3.5 × 10¹⁵ molec cm⁻³, [NO] = 2 × 10¹⁵ molec cm⁻³, and [NO] = 1.8 × 10¹⁴ molec cm⁻³. A combination of quantum chemistry and reference spectra are required to obtain [2-C₅H₁₁ONO] = 4.8 × 10¹⁶ molec cm⁻³, as shown below.

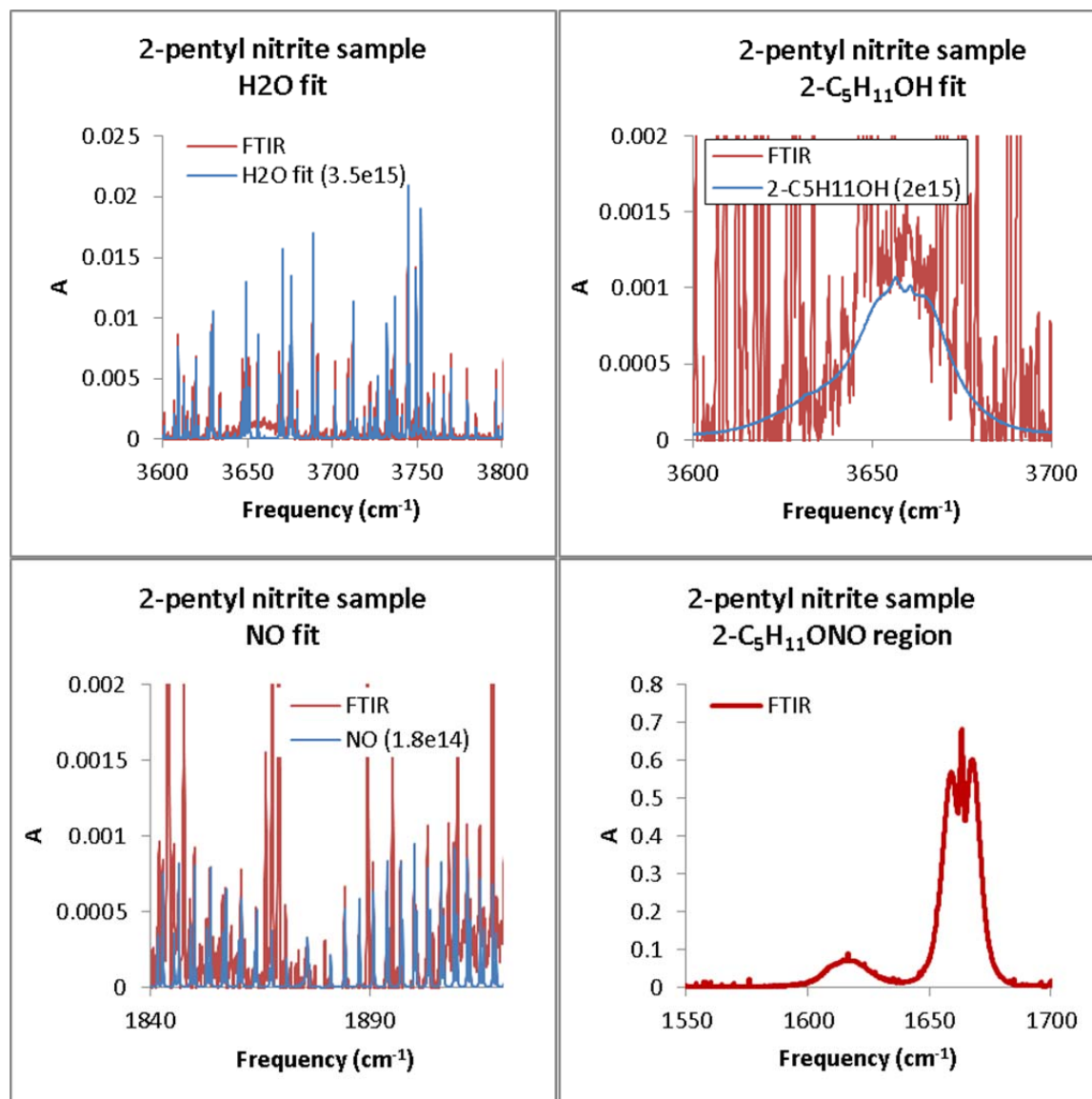


Figure 7.13. Individual FTIR bands for major and minor species in the 2-pentyl nitrite sample. Upper left: H₂O. Upper right: 2-pentanol. Lower left: NO. Lower right: 2-pentyl nitrite. Based on fits to reference spectra, we estimate $[\text{H}_2\text{O}] = 3.5 \times 10^{15} \text{ molec cm}^{-3}$, $[\text{NO}] = 2 \times 10^{15} \text{ molec cm}^{-3}$, and $[\text{NO}] = 1.8 \times 10^{14} \text{ molec cm}^{-3}$. Based on our quantum chemistry analysis, we conclude $[\text{2-C}_5\text{H}_{11}\text{ONO}] = 4.8 \times 10^{16} \text{ molec cm}^{-3}$.

We determine $[\text{2-C}_5\text{H}_{11}\text{ONO}]$ in three steps. First, we obtain the experimentally determined integrated intensities of the ON-O vibrational band from reference spectra of smaller nitrites (CH_3ONO and $\text{C}_2\text{H}_5\text{ONO}$).⁴⁰ Second, we compute relative intensities of relevant alkyl nitrites' ON-O vibrational modes to determine the trend in absorption cross

section. Third, we combine the results of the FTIR spectrum of 2-C₅H₁₁ONO, reference spectrum of smaller RONO, and relative cross sections between alkyl nitrites to obtain [2-C₅H₁₁ONO].

The relevant data needed to compute $\sigma_{2\text{-C}_5\text{H}_{11}\text{ONO}}$, and thus [2-C₅H₁₁ONO], are summarized in Table 7.5. Experimental integrated intensities for CH₃ONO and C₂H₅ONO were taken from reference spectra.⁴⁰ Integrated intensities for all alkyl nitrites were computed at the B3LYP/6-31+G(d,p) level of theory and basis using Gaussian 09W.¹²¹ Intensities were scaled to $I_{\text{calc}}/I_{\text{PNNL}}$ (CH₃ONO) or $I_{\text{calc}}/I_{\text{PNNL}}$ (C₂H₅ONO). The best value for the intensities were taken to be the average of the two scaled intensities.

Table 7.5. Calculated Integrated Intensities for alkyl nitrites, B3LYP/6-31+G(d,p). Intensities were scaled to reference spectra for CH₃ONO and C₂H₅ONO.⁴⁰

	I (PNNL) ^a (km mol ⁻¹)	ν calc (cm ⁻¹)	I calc ^a (km mol ⁻¹)	I , ^a scale to CH ₃ ONO	I , ^a scale to C ₂ H ₅ ONO	I_{best} ^a (km mol ⁻¹)
CH ₃ ONO	171	1686	193	171	175	171
C ₂ H ₅ ONO	182	1679	201	178	182	182
1-C ₃ H ₇ ONO		1678	207	184	188	186
1-C ₄ H ₉ ONO		1678	215	191	195	193
2-C ₅ H ₁₁ ONO		1676	211	187	191	189

a) All intensities converted to base e.

We calculate [2-C₅H₁₁ONO] from Beer's law (Equation 7.34):

$$[\text{C}_5\text{H}_{11}\text{ONO}] = \frac{\int_{1550\text{ cm}^{-1}}^{1700\text{ cm}^{-1}} A_{\text{ON-O}} d\bar{\nu}}{L_{\text{FTIR}} \times \left(\int \sigma_{\text{ON-O,avg}} d\bar{\nu} \right)}, \quad (7.34)$$

where $\int_{1550\text{ cm}^{-1}}^{1700\text{ cm}^{-1}} A_{\text{ON-O}} d\bar{\nu}$ is the observed (FTIR) integrated absorbance, L_{FTIR} is the cell

length (19 cm), and $\int \sigma_{\text{ON-O,avg}} d\bar{\nu}$ is the best value for the integrated intensity (I_{best}) from

Table 7.5. Based on the spectrum in Figure 7.13 and the quantum chemistry data in Table 7.5, we obtain $[2\text{-C}_5\text{H}_{11}\text{ONO}] = 4.8 \times 10^{16} \text{ molec cm}^{-3}$.

Given these calculated concentrations, we obtain the relative concentrations for our contaminants; $[2\text{-C}_5\text{H}_{11}\text{OH}]:[2\text{-C}_5\text{H}_{11}\text{ONO}] = 1:24$, $[\text{NO}]:[2\text{-C}_5\text{H}_{11}\text{ONO}] = 1:240$, and $[\text{H}_2\text{O}]:[2\text{-C}_5\text{H}_{11}\text{ONO}] = 1:14$. Thus, at least 90% of our sample consists of $[2\text{-C}_5\text{H}_{11}\text{ONO}]$.

We next turn our attention to the vapor pressure ($p_{\text{vap}}(T)$) and thermodynamic properties ($\Delta_{\text{vap}}H$, $T_{\text{boil,1atm}}$) of our 2-pentyl nitrite sample. We measured the temperature dependent vapor pressure using the experimental apparatus is shown in Figure 7.14. A 3-necked round-bottomed flask containing 50 mL of 2-pentyl nitrite was immersed in a water bath. The three necks of the flask were fit to a thermometer, two pressure gauges (MKS Baratron and Duniway thermocouple gauge), and an air/vacuum line to control pressure. Data were obtained by cooling the 2-pentyl nitrite sample, removing gas from the 2-pentyl nitrite flask to obtain the pressure of interest, and then slowly heating the water bath until boiling of the 2-pentyl nitrite sample was observed. Nitrogen gas was added to the flask in order to increase the pressure between measurements. Data points below room temperature were taken by using an ice water bath. Data points above room temperature were taken by heating the water bath. Vapor pressure data were taken over the temperature range 276–343 K.

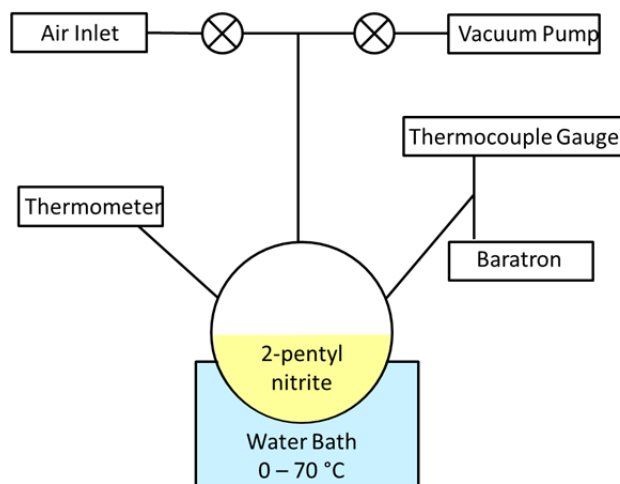


Figure 7.14. Apparatus used to measure the vapor pressure of 2-pentyl nitrite. Reprinted with permission from Sprague et al.³¹ Copyright 2012 American Chemical Society.

Figure 7.15 shows the natural logarithm of the vapor pressure of our sample plotted against the inverse boiling temperature. The plot is linear for temperatures up to 36 °C (309 K, $1000 / T > 3.23 \text{ K}^{-1}$). Above 36 °C, a brown gas evolved from the 2-pentyl nitrite sample, likely corresponding to decomposition of the sample. We observe a kink in the vapor pressure plot, indicating that we may no longer be measuring the properties of 2-pentyl nitrite above 36 °C.

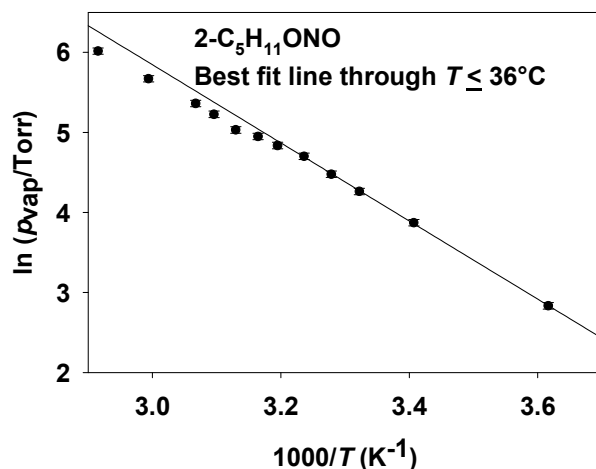


Figure 7.15. Clausius-Clapeyron plot for the 2-pentyl nitrite used for the spectra reported in this work. The data are nonlinear above 36 °C ($1000 / T < 3.23 \text{ K}^{-1}$) due to decomposition of the 2-pentyl nitrite. We report the 2σ uncertainty on each vapor pressure as $\pm 4\%$. The best-fit line to data points at or below 36 °C gives slope = $(-4900 \pm 150) \text{ K}$, intercept = 21 ± 1 . Using these values, $\Delta_{\text{vap}}H = 41 \pm 1 \text{ kJ mol}^{-1}$ and $T_{\text{boil}, 1 \text{ atm}} = (350 \pm 20) \text{ K}$. All uncertainties are reported to 2σ . Reprinted with permission from Sprague et al.³¹ Copyright 2012 American Chemical Society.

The data points prior to decomposition ($T < 36 \text{ °C}$) can be fit to the Clausius-Clapeyron equation:

$$\ln p_{\text{vap}} = \left(-\frac{\Delta_{\text{vap}}H}{R} \right) \left(\frac{1}{T_{\text{vap}}} \right) + \left(\frac{\Delta_{\text{vap}}H}{RT_{\text{boil}}} + \ln p_{\text{atm}} \right), \quad (7.35)$$

where p_{vap} is the vapor pressure at temperature T_{vap} , $\Delta_{\text{vap}}H$ is the enthalpy of vaporization, R is the universal gas constant, and T_{boil} is the boiling point at atmospheric pressure p_{atm} . We assume a 4% uncertainty (2σ) on the vapor pressure data. Including both the error on each vapor pressure data point and overall scatter in the data points, we obtain $\Delta_{\text{vap}}H = 41 \pm 1 \text{ kJ mol}^{-1}$ and $T_{\text{boil}, 1 \text{ atm}} = (350 \pm 20) \text{ K}$. All uncertainties are reported to 2σ .

Although our data fit very well to Equation 7.35, it is important to emphasize that our 2-pentyl nitrite sample was only 90% pure. The major contaminants were water

([H₂O]:[RONO] = 1:14), pentanol (1:24), and NO (1:240). If an azeotrope of 2-pentyl nitrite forms with water or 2-pentanol, then the vapor pressure data may have additional error.

Using our thermodynamic parameters, we determine $p_{\text{vap}}(273 \text{ K})=13.5 \text{ torr}$. We use this value in calculation of [2-C₅H₁₁ONO] for the experiment.

Conclusions

In this chapter, we have reported the first clean ν_1 (OH stretch) vibrational spectra of the primary products of *n*-butoxy and 2-pentoxy isomerization in the absence and presence of oxygen: $\delta\text{-HOC}_4\text{H}_8\bullet$, $\delta\text{-HOC}_4\text{H}_8\text{OO}\bullet$, $\delta\text{-HO-1-C}_5\text{H}_{10}\bullet$, and $\delta\text{-HO-1-C}_5\text{H}_{10}\text{OO}\bullet$. Under our experimental conditions, the recorded spectra are expected to be at least 94% (HOR \bullet) or 98% (HOROO \bullet) primary products. The ν_1 vibrational spectra are similar in shape and intensity to the parent alcohol ROH, with small differences in shape and intensity between HOR \bullet and HOROO \bullet . We observe that the spectra take 20 μs to reach their maximum absorption and remain constant in shape and intensity for at least 800 μs , indicating that secondary products have similar spectra to our HOROO \bullet radicals. We have shown that the ν_1 band can be used for measurement of alkoxy relative kinetics (explored further in Chapter 8). Finally, we make the first report of the vapor pressure and thermodynamic properties of 2-pentyl nitrite.

Acknowledgements

We thank Marissa L. Weichman and Laura A. Mertens for synthesis of the 2-pentyl nitrite used in these experiments and Nathan C. Eddingsaas for assistance with

acquiring the FTIR spectrum of 2-pentyl nitrite. The experiments performed in this chapter were funded under NASA Upper Atmosphere Research Program Grant NNX09AE21G2.

Chapter 8—Reanalysis of the Alkoxy $k_{\text{isom}}/k_{\text{O}_2}$ OH-stretch Experiment and a New Interpretation of Alkoxy Relative Kinetics Experiments

Abstract

In Chapter 7, we showed that the ν_1 band of the primary products of alkoxy isomerization could be used to measure the relative rate of isomerization to reaction with O_2 ($k_{\text{isom}}/k_{\text{O}_2}$). Previous studies within the Okumura group measured the relative kinetics of *n*-butoxy and 2-pentoxy via the ν_1 band, obtaining $k_{\text{isom}}/k_{\text{O}_2}$ values with low uncertainties, but generally higher than those reported in the literature. We find that the cause of this discrepancy is multiple errors in the analysis of the relative kinetics data.

Amongst these errors were the calculations of [RONO], [O_2], photolysis flux, and relative absorbance (A_0/A), due to errors in the CRDS program or errors in scaling data to [RONO]. Additionally, the effects of additional alkoxy reactions (decomposition, reaction with NO, prompt decomposition, and prompt isomerization) were not considered. A full reanalysis of all data (gas flows, [RONO] monitoring, CRDS absorption data, inclusion of all reaction pathways) gives new values of $k_{\text{isom}}/k_{\text{O}_2}$ of $(1.69 \pm 0.15) \times 10^{19} \text{ cm}^{-3}$ for *n*-butoxy, and $(3.37 \pm 0.43) \times 10^{19} \text{ cm}^{-3}$ for 2-pentoxy (2 σ error). The *n*-butoxy value of $k_{\text{isom}}/k_{\text{O}_2}$ is in much better agreement with the rest of the literature, but with a significantly smaller uncertainty than previous studies. The reanalyzed data give an estimate of ϕ_{pi} (the fraction of alkoxy radicals that undergo prompt isomerization following photolysis of alkyl nitrite at 351 nm) as 0.04 ± 0.02 for *n*-butoxy and 0.05 ± 0.02 for 2-pentoxy. We show that the previous experiments detected a mixture of primary and secondary products, although the results of Chapter 7 suggest that this does not affect the value of $k_{\text{isom}}/k_{\text{O}_2}$ obtained from our data.

Introduction

In Chapter 7, we showed that CRDS is capable of detecting the primary products of alkoxy isomerization, HOR• (in the absence of oxygen) and HOROO• (in the presence of oxygen), by measurement of the ν_1 (OH stretch) vibrational spectrum. We have also shown that this band can be used to measure the relative rate constant of alkoxy isomerization to reaction with O₂ ($k_{\text{isom}}/k_{\text{O}_2}$) for two reasons. First, the band intensity decreases with increasing [O₂], in agreement with our expectations for the alkoxy system. Second, the ν_1 band shape and intensity of HOROO• remain constant for at least 800 μs after reaching its maximum absorbance, making the ν_1 band a robust measure of [HOROO•].

In 2006, Mollner³⁰ (assisted by me in the laboratory) used the ν_1 bands of $\delta\text{-HOC}_4\text{H}_8\bullet$, $\delta\text{-HOC}_4\text{H}_8\text{OO}\bullet$, $\delta\text{-HO-1-C}_5\text{H}_{10}\bullet$, and $\delta\text{-HO-1-C}_5\text{H}_{10}\text{OO}\bullet$ to determine $k_{\text{isom}}/k_{\text{O}_2}$ for *n*-butoxy and 2-pentoxy. Mollner's relative kinetics data sets consisted of many more data points (177 for *n*-butoxy, 95 for 2-pentoxy) than the data presented in Chapter 7 (12 for *n*-butoxy, 7 for 2-pentoxy). Mollner's relative kinetics data are shown in Figure 8.1, and $k_{\text{isom}}/k_{\text{O}_2}$ values are compared to the chemical literature in Table 8.1. We immediately note that Mollner's *n*-butoxy value is larger than the rest of the measurements. Although Mollner's measurement is within the uncertainty of the end-product studies, it is in disagreement with the measurements reported from our alkoxy studies using the ν_1 (Chapter 7) and A-X bands (Chapter 10). Comparison of the 2-pentoxy values is a challenge because of the large errors associated with each $k_{\text{isom}}/k_{\text{O}_2}$.

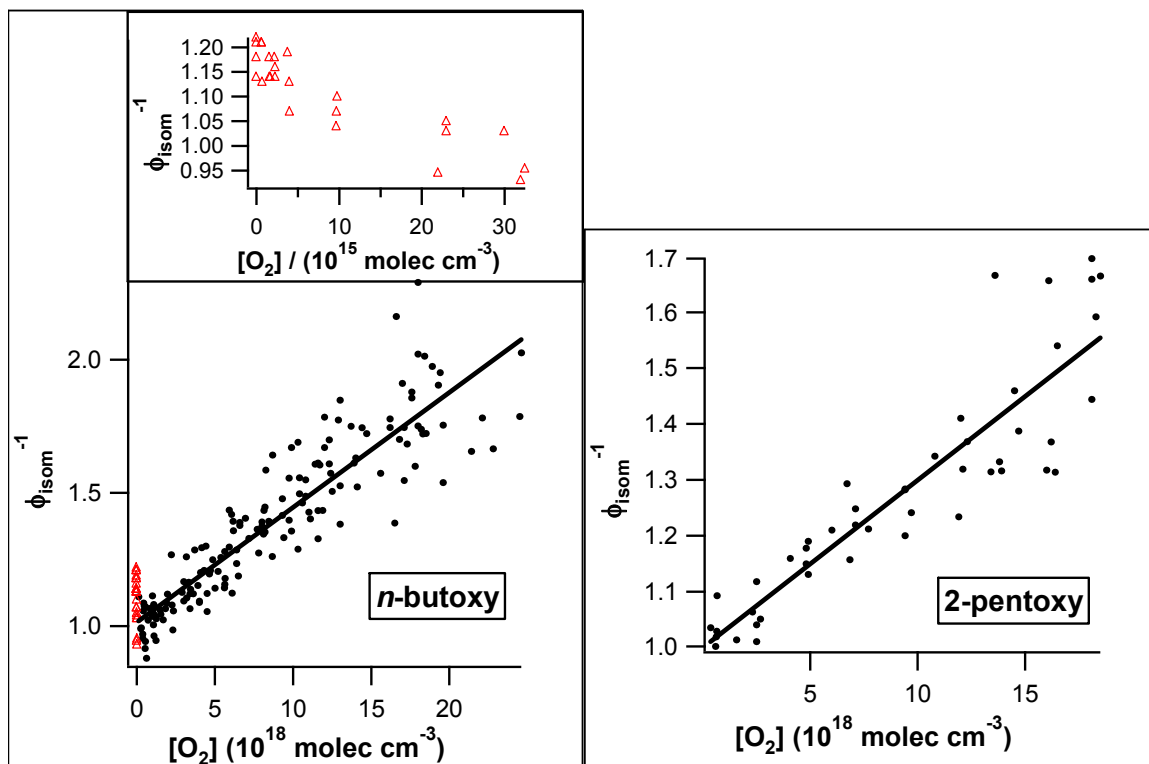


Figure 8.1. (caption and figure adapted from Mollner)³⁰ A_0/A (labeled as ϕ_{isom}^{-1}) plotted as a function of $[\text{O}_2]$ for n-butoxy (left) and 2-pentoxy (right). $[\text{HOR}\cdot]$, the concentration of all products formed through the isomerization channel, was calculated from the strength of the OH-stretch infrared peak. $[\text{RO}\cdot]$ was determined from the linear regression of individual data sets, assuming $\phi_{\text{isom}} = 1$ at $[\text{O}_2] = 0$. Both plots show the expected decrease in $[\text{HOR}\cdot]/[\text{RO}\cdot]$ with $[\text{O}_2]$. The inset to the n-butoxy plot shows an apparent increase in $[\text{HOC}_4\text{H}_8\cdot]$ with $[\text{O}_2]$ at very low $[\text{O}_2]$, as discussed in Chapter 9. Only the data with $[\text{O}_2] > 5 \times 10^{16}$ molecules cm^{-3} were used in the linear fits to determine $k_{\text{isom}}/k_{\text{O}_2}$. n-butoxy: slope = $(4.3 \pm 0.2) \times 10^{-20}$ cm^3 , intercept = 1.01 ± 0.02 , $k_{\text{isom}}/k_{\text{O}_2} = (2.3 [+0.2, -0.3]) \times 10^{19}$ cm^{-3} . 2-pentoxy: slope = $(3.0 \pm 0.3) \times 10^{-20}$ cm^3 , intercept = 1.00 ± 0.04 , $k_{\text{isom}}/k_{\text{O}_2} = (3.3 [+0.4, -0.6]) \times 10^{19}$ cm^{-3} . All errors are reported to 2σ , asymmetric error due to prompt isomerization.

Table 8.1. Comparison of relative rate constant determinations $k_{\text{isom}}/k_{\text{O}_2}$ and derived k_{isom} for *n*-butoxy using our initial analysis of CRDS data³⁰

	$k_{\text{isom}}/k_{\text{O}_2}$ (10^{19} cm^{-3}) ^a	k_{isom} (10^5 s^{-1}) ^b	Molecules detected	Method	<i>P</i> (<i>torr</i>)	Ref
<i>n</i>-butoxy	2.3 (+0.2, -0.3)	3.2 ± 1.6	δ-hydroxy-<i>n</i>-butyl peroxy	Slow flow, CRDS (OH Str)	670	Mollner³⁰
	1.96 ± 0.25	2.7 ± 1.4	δ-hydroxy- <i>n</i> -butyl peroxy	Slow flow, CRDS (OH Str)	330	Chapter 7
	1.39 ± 0.47	2.0 ± 1.2	δ-hydroxy- <i>n</i> -butyl peroxy	Slow flow, CRDS (A-X)	330	Chapter 10
	2.0 ± 0.4	2.7 ± 1.5	Butyl nitrite, Butanal,	Static, FTIR	700	Cassanelli ¹⁵⁵
	1.5 ± 0.4	2.1 ± 1.2	4-hydroxy butanal	Static, GC	760	Cox ¹⁵⁶
	1.9 ± 0.4	2.7 ± 1.4	Butane, Butanal	Static, FTIR	700	Niki ¹⁴⁸
	2.1 ± 0.5	2.9 ± 1.6	Butyl nitrite, Butanal	Slow flow, GC	760	Cassanelli ¹⁶⁰
	1.8 ± 1.1	2.5 ± 2.0	Butyl nitrite, Butanal	Slow flow, GC	760	Cassanelli ¹⁶⁰
	1.8 ± 0.6	2.5 ± 1.5	Butane, Butanal	Static, FTIR	760	Geiger ¹⁶¹
	0.25 ± 0.19 ^c	0.35 ± 0.20 ^c	Butanal, 4-hydroxy butanal	Fast flow, LIF	38	Hein ¹⁵⁹
	1.6	2.2	OH and NO ₂	Static, GC	740	Carter ¹⁵⁴
	2.1 ± 1.8 ^d	2.9 ± 1.4 ^d		Recommendation	760	IUPAC ¹¹⁸
2-pentoxy	3.3 (+0.4, -0.6)	2.7	δ-hydroxy-<i>n</i>-pentyl peroxy	Slow flow, CRDS (OH Str)	670	Mollner³⁰
	3.78 ± 1.62	3.0	δ-hydroxy- <i>n</i> -pentyl peroxy	Slow flow, CRDS (OH Str)	330	Chapter 7
	3.1 ^e	2.5 ^e	2-pentanone	Static, GC	700	Atkinson ¹⁴⁵
	0.15	0.12 ^f	Acetone, Acetaldehyde, 2-hexanol	Static, GC	760	Dóbe ¹⁵⁷

a) All uncertainties are 2σ. All studies other than the current work treat all alkoxy reactions besides isomerization and reaction with O₂ as negligible.

b) Computed k_{isom} assuming literature value of $k_{\text{O}_2} = (1.4 \pm 0.7) \times 10^{-14} \text{ cm}^3 \text{ s}^{-1}$ for *n*-butoxy,²⁸ and $k_{\text{O}_2} = 8 \times 10^{-15} \text{ cm}^3 \text{ s}^{-1}$ for 2-pentoxy (no estimate available for the uncertainty).¹⁴²

c) Unlike the other studies, Hein directly measured k_{isom} . In this table, we calculate the ratio $k_{\text{isom}}/k_{\text{O}_2}$ from Hein's measurement using the literature value of k_{O_2} .

d) The IUPAC recommendation for $k_{\text{isom}}/k_{\text{O}_2}$ is computed from their individual recommendations of the isomerization and O₂ reactions

e) The uncertainty on $k_{\text{isom}}/k_{\text{O}_2}$ is reported by Atkinson as a factor of 2.

f) Dóbe's study calculates k_{isom} from the relative rate $k_{\text{isom}}/k_{\text{decomp}}$ and their measured rate $k_{\text{decomp}} = 1.2 \times 10^4 \text{ s}^{-1}$. The $k_{\text{isom}}/k_{\text{O}_2}$ reported in this table uses the literature value of $k_{\text{O}_2} = 8 \times 10^{-15} \text{ cm}^3 \text{ s}^{-1}$ for 2-pentoxy.¹⁴²

Because Mollner's and my CRDS experiments for *n*-butoxy are in disagreement, I wanted to take another look at the OH-stretch data to make sure that nothing was wrong with the data. My expectation was that nothing would be wrong, and that the discrepancies could be explained by the lack of data points in my ν_1 (Chapter 7) and A-X (Chapter 10) relative kinetics data.

As I reviewed our lab notebook, I saw some disturbing notes. One entry noted that for a pressure of 700 torr, the concentration of O₂ in the cell was $2.46 \times 10^{19} \text{ cm}^{-3}$. In other words, the cell had a total pressure of 700 torr, with [O₂] = 760 torr, a physical impossibility. A manual calculation of [O₂] using the recorded flowmeter voltages and calibrations gave a value of [O₂] approximately 10% lower than the recorded value. A check of other entries in the lab notebook between March 2006 to October 2006 revealed the same problem throughout. The problem was an error in the LabVIEW program controlling the CRDS apparatus. A single flow was subtracted out of the total gas concentration, which happened to be the right purge flow (kept roughly at 10%). The protocol in the IR-CRDS lab since March 2006 (and likely far beyond then) was to blindly copy [O₂] reported by the program. **The result is that all [O₂] recorded for the alkoxy experiment are 7%–10% too high, directly affecting the reported $k_{\text{isom}}/k_{\text{O}_2}$ values that we report.** This issue prompted the full reanalysis of the alkoxy data.

As I performed the reanalysis of the alkoxy data, I noticed other errors in the analysis of the alkoxy data. First, **in some of the experiments, incorrect flowmeter calibrations were entered, causing additional errors in the derived gas concentrations.** At one point, zero-flow offsets for N₂ were entered into the computer, despite Ar being sent through the flowmeters. The result was major errors in the calculation of gas concentrations.

Second, [RONO] was not calculated correctly, a major problem because the measured absorptions must be scaled to the amount of alkyl nitrite before converting absorptions to A/A_0 . [RONO] in the CRDS cell is affected by the gas flow calculation problems mentioned above. Three methods can be used to obtain [RONO]:

1. Measurement of [RONO] in the RONO gas line using its UV absorption at 254 nm, then calculating its dilution in the CRDS cell based on the gas flows
2. Calculating [RONO] at the bubbler using thermodynamic properties (enthalpy of vaporization and boiling point), then calculating its dilution in the CRDS cell based on the gas flows
3. Measuring the background ringdown time in the CRDS experiment, since RONO has a broad absorption in the 3500-3700 cm^{-1} range where we are measuring the alkoxy isomerization product

We only scaled to [RONO] using method 3 during our previous experiments. Worse yet, we scaled our data to $1/\tau$, the absolute background ringdown time. This is an incorrect scaling method because the vacuum ringdown time, $1/\tau_0$, was not subtracted out. **Thus, we did not actually scale to the RONO absorption.** Furthermore, since any of the three methods are equally valid for scaling, we should have checked all three to see which one gives the best fit for each individual data set.

Third, the photolysis flux was likely calculated incorrectly for these experiments, resulting in the fraction of RONO that is photolyzed being incorrectly calculated. The amount of RONO that is photolyzed can be calculated from Equation 8.1:

$$\%_{\text{photolysis}} = \frac{\left(\frac{P_{\text{excimer}}}{A_{\text{meter}}} \right) \left(\frac{\lambda}{hc} \right) (\sigma_{\text{RONO},\lambda}) (X) \left(\frac{A_{\text{UV,laser}}}{A_{\text{UV,CRDS}}} \right)}{F_{\text{excimer}}}, \quad (8.1)$$

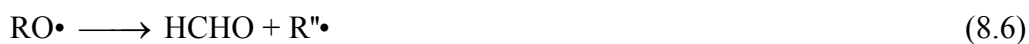
where $\%_{\text{photolysis}}$ is the fraction of RONO that is photolyzed, $(P_{\text{excimer}}/A_{\text{meter}})$ is the power meter reading directly out of the excimer laser (the power meter has a 1 cm^2 area), F_{excimer} is the repetition rate of excimer (10 Hz), h is Planck's constant, c is the speed of light, λ is the wavelength of the excimer light (351 nm), $\sigma_{\text{RONO},\lambda}$ is the absorption cross section of

RONO at the excimer wavelength ($8 \times 10^{-20} \text{ cm}^2 \text{ molec}^{-1}$), X is the quantum yield for photolysis (taken to be 1), $A_{\text{UV,laser}}$ is the area of excimer beam measured at the excimer laser output, and $A_{\text{UV,CRDS}}$ is the area of excimer beam measured at the CRDS cell.

At some point in the past, the excimer beam area at the CRDS cell was the same as the beam area directly out of the laser. Therefore, in the calculation of flux, the ratio of excimer beam areas will cancel out of the equation. However, this does not hold true when the beam areas are different, as has been true for all of the experiments in our laboratory since (and including) alkoxy. For the alkoxy experiments, $A_{\text{UV,laser}}/A_{\text{UV,CRDS}} = 2.5$, a factor that was accounted for in some of the early experiments, and not accounted for in other experiments. **The result is that [RO•] is inconsistently calculated. However, if the photolysis flux is kept constant for a set of relative kinetics data, then we will be insensitive to this mistake since $k_{\text{isom}}/k_{\text{O}_2}$ is derived from relative absorbance measurement: absolute [RO•] is largely irrelevant.**

Additionally, the relative absorbance A_{ν}/A was calculated in a very sloppy fashion. Rather than scale each regression line such that the y-intercepts were equal to 1, the previous analysis made use of the [RONO] measurements to scale all of the measured absorptions to [RO•] to $2 \times 10^{14} \text{ cm}^{-3}$. However, this is not a good way to calculate relative absorbances, because this method requires good knowledge of [RONO] and [RO•]. Given the variations in excimer flux and the incorrect scaling to [RONO], we cannot claim to know either concentration to very good precision. **The result is that our reported absorbance data are possibly incorrect, leading to even further scatter in our plot of relative absorbance vs [O₂], and added uncertainty in the derived $k_{\text{isom}}/k_{\text{O}_2}$.**

Finally, our previous interpretation of the alkoxy relative kinetics data ignored the effects of additional alkoxy reaction pathways. Alkoxy radicals in our experiments are generated from photolysis of an alkyl nitrite (RONO). The resulting alkoxy radicals that are formed are either in the vibrational ground state (denoted RO•, Reaction 8.2), or are vibrationally hot (denoted [RO•]*, Reaction 8.3). Once formed, the ground state alkoxy radicals can isomerize and associate with O₂ (Reaction 8.4), react with O₂ (Reaction 8.5), decompose (Reaction 8.6), or recombine with NO (Reaction 8.7). The hot alkoxy radicals can promptly isomerize (Reaction 8.8) or promptly decompose (Reaction 8.9), without regard for the thermal rate constants.



The typical analysis found in the literature considers only Reactions 8.4 and 8.5 relevant to alkoxy relative kinetics measurements; Reactions 8.6–8.9 are assumed to be negligible.^{146, 148, 153-158} However, there is evidence in the literature that this is an invalid assumption. First, the recombination of alkoxy radicals with NO is fast, with a rate constant $k_{\text{NO}} = 3.32 \times 10^{-11} \text{ cm}^3 \text{ s}^{-1}$.³² For $[\text{NO}] = (1-9) \times 10^{14} \text{ molec cm}^{-3}$ (typical values

of [NO] in alkoxy experiments),^{146, 148, 153-158} the relative rate of NO recombination to isomerization is $\frac{k_{NO} [\text{NO}]}{k_{isom}} = 0.01-0.12$. Second, while decomposition is slow for *n*-butoxy ($k_{decomp} = 600 \text{ s}^{-1}$, $k_{decomp}/k_{isom} = 2.4 \times 10^{-3}$), decomposition is non-negligible for 2-pentoxy, with theoretical estimates of $k_{decomp} = (0.5-3) \times 10^4 \text{ s}^{-1}$,¹¹⁷ and one experimental study obtaining $1.1 \times 10^4 \text{ s}^{-1}$.¹⁵⁷ For these decomposition rates, $k_{decomp}/k_{isom} = 0.02-0.12$.

Prompt processes may also be important (Reactions 8.8 and 8.9). The enthalpy of breaking the O-NO bond in *n*-butyl nitrite is 40 kcal mol^{-1} .¹⁸⁶ Photolysis using 351 nm light provides 80 kcal mol^{-1} of energy, resulting in 40 kcal mol^{-1} of excess energy distributed between the alkoxy radical and NO. Previous experiments have already estimated 10% prompt decomposition of *n*-butoxy following photolysis of *n*-butyl nitrite at $370 \pm 10 \text{ nm}$.¹⁵⁵ Furthermore, theoretical calculations have shown isomerization to have a barrier of only 10 kcal mol^{-1} .¹³⁶⁻¹³⁸ Therefore, some of the alkoxy radicals formed may isomerize immediately upon formation, without regard as to whether or not other reaction channels exist. These isomerization products are not indicative of the competition between isomerization and reaction with O_2 , and thus will affect spectroscopic measurements of k_{isom}/k_{O_2} .

Reactions 8.6–8.9 will consume alkoxy radicals, and therefore change the dependence of [HOROO•] on $[\text{O}_2]$. Since the magnitude of each reaction is on the same order of magnitude of our uncertainty for k_{isom}/k_{O_2} (10%), we cannot ignore these reactions in our analysis of our alkoxy relative kinetics data.

To summarize, the six errors in the previous alkoxy relative kinetics analysis were incorrect calculation of $[\text{O}_2]$, incorrect computation of gas flows, incorrect scaling of data

to [RONO], incorrect calculation of photolysis flux, incorrect calculation of A_0/A , and ignoring the additional reactions of $\text{RO}\cdot$. These six errors affect nearly all of the required analysis of the alkoxy data set. **Therefore, a full reanalysis of our CRDS alkoxy data must be performed.**

This thesis chapter describes the reanalysis and new interpretation of our previous alkoxy relative kinetics experiments. Gas flows and concentrations, alkoxy concentrations, scaling factors, and linear regressions were recalculated to correct the errors described above. We then derive the dependence of our CRDS absorbances on $[\text{O}_2]$, and how $k_{\text{isom}}/k_{\text{O}_2}$ can be extracted from our data.

Methods

A full description of the methods and equations used to reanalyze the alkoxy data can be found below. Briefly, reanalysis of the alkoxy data sets required five calculations:

1. Recalculation of all gas concentrations for each scan (and therefore $[\text{O}_2]$) based on the CRDS cell pressure, flowmeter voltages, zero flow offsets, and flowmeter calibrations recorded in the laboratory notebook
2. Recalculation of absolute [RONO] and $[\text{RO}\cdot]$ based on excimer flux, 254 nm absorption measurements, and the thermodynamic properties of the alkyl nitrites. Also, recalculation of relative [RONO] for each data set based on the background $1/\tau - 1/\tau_0$ at the peak OH stretch wavelength.
3. Rescaling of alkoxy absorptions to the three recalculated [RONO] in order to obtain correctly scaled A_0/A (absorbance at $[\text{O}_2] = 0$ relative to measured absorbance)

4. Choosing the best fits from each data set to obtain an overall data set of A_0/A
5. Derivation of the dependence of A_0/A on $[O_2]$ to determine how to extract k_{isom}/k_{O_2} from our data.

The resulting data sets were then used in our new analysis of the relative kinetics in order to extract k_{isom}/k_{O_2} . This analysis also allowed us to determine the fraction of prompt isomerization.

Recalculation of Gas Concentrations

The gas flow through a mass flowmeter can be calculated from Equation 8.10:

$$f = (V - V_0)(calib), \quad (8.10)$$

where f is the gas flow (in sccm), V is the voltage across the mass flowmeter for flow f (measured by a digital readout box), V_0 is the voltage across the mass flowmeter for zero gas flow (the zero flow offset), and $calib$ is the flowmeter's calibration factor (in sccm/volt). The calibration factor depends on the type of gas being used, and must be updated when gases are changed. The zero flow offset fluctuates from day to day and also depends on the type of gas being used.

Once all of the individual gas flows have been calculated, the concentrations of each gas can be computed from Equation 8.11:

$$[\text{gas}]_i = \frac{f_i}{\sum f_i} (p) \left(3.24 \times 10^{16} \frac{\text{molec}}{\text{cm}^3 \text{ Torr}} \right), \quad (8.11)$$

where $[\text{gas}]_i$ is the concentration of the gas from flow i in molec cm^{-3} , f_i is the flow of interest, $\sum f_i$ is the sum of all gas flows, and p is the pressure of the CRDS cell in torr. If

the gas of interest is on multiple gas lines, all of those lines must be added together to obtain the total concentration.

Recalculation of [RONO] and [RO•]

It is possible to obtain absolute [RONO] and [RO•] through two methods and relative [RONO] and [RO•] through a third method. The first method to obtain [RONO] makes use of the UV absorption of RONO at 254 nm. The absorption cross section for C₄H₉ONO is $\sigma_{\text{RONO},254\text{nm}} = 1.3 \times 10^{-18} \text{ cm}^{-2}$,^{32, 192} and our quantum chemistry calculations (CIS/6-31+G(d,p)) suggest that the cross section of 2-C₅H₁₁ONO is the same (linestrengths $f_{1\text{-C}_4\text{H}_9\text{ONO},376\text{nm}} = 0.0030$, $f_{2\text{-C}_5\text{H}_{11}\text{ONO}} = 0.0028$). A UV lamp and a Si photodiode were placed on opposite sides of a quartz cell (path length $L_{\text{UV}}=0.2125 \text{ cm}$). The voltage of the detector was recorded in the absence and presence of RONO. From these measurements, [RONO]_{gasline}, the concentration of alkyl nitrite in the bubbler gas line, can be calculated using Equation 8.12:

$$[\text{RONO}]_{\text{gasline}} = \frac{1}{\sigma_{\text{RONO},254\text{nm}} L_{\text{UV}}} \ln\left(\frac{I_0}{I}\right), \quad (8.12)$$

where I_0 is the detector voltage in the absence of RONO, and I is the detector voltage in the presence of RONO.

The second method to obtain [RONO] makes use of the thermodynamic properties of the alkyl nitrites. The first step is to calculate the vapor pressure of RONO in the bubbler. Assuming that the enthalpy of vaporization is independent of temperature, the vapor pressure can be calculated by Equation 8.13:

$$P_{\text{vap}} = P_{\text{ref}} \exp\left[\frac{-\Delta H_{\text{vap,ref}}}{R} \left(\frac{1}{T_{\text{bubbler}}} - \frac{1}{T_{\text{ref}}}\right)\right], \quad (8.13)$$

where p_{vap} is the vapor pressure of RONO in the bubbler, p_{ref} is the vapor pressure at a reference temperature, $\Delta H_{\text{vap,ref}}$ is the enthalpy of vaporization at a reference temperature, R is the universal gas constant, T_{bubbler} is the temperature of the bubbler, and T_{ref} is the reference temperature. For our experiments, *n*-butyl nitrite has a vapor pressure of 760 torr at 351 K, with $\Delta H_{\text{vap}} = 37 \text{ kJ mol}^{-1}$ (from the CRC handbook). Using these values with our bubbler temperature of 273 K gives us $p_{\text{vap}} = 20.3 \text{ torr}$. Based on our results from Chapter 7, 2-pentyl nitrite has a vapor pressure of 760 torr at 350 K, with $\Delta H_{\text{vap}} = 41 \text{ kJ mol}^{-1}$. Using these values with our bubbler temperature gives us $p_{\text{vap}} = 13.5 \text{ torr}$.

[RONO] can then be calculated by Equation 8.14:

$$[\text{RONO}]_{\text{gasline}} = p_{\text{vap}} \left(3.24 \times 10^{16} \frac{\text{molec}/\text{cm}^3}{\text{Torr}} \right). \quad (8.14)$$

With either method, [RONO] in the CRDS cell can be calculated by Equation 8.15:

$$[\text{RONO}]_{\text{CRDS}} = [\text{RONO}]_{\text{gasline}} \left(\frac{T_{\text{bubbler}}}{T_{\text{cell}}} \right) \left(\frac{f_{\text{bubbler}}}{\sum f_i} \right), \quad (8.15)$$

where $[\text{RONO}]_{\text{CRDS}}$ is the concentration of the alkyl nitrite in the gas kinetics cell, T_{bubbler} is the temperature of the bubbler (273 K), T_{cell} is the temperature of the gas kinetics cell (298 K), f_{bubbler} is the gas flow through the bubbler, and $\sum f_i$ is the sum of all gas flows through the gas kinetics cell. Although the absolute [RONO] from Equations 8.12 and 8.14 are not equal, it can be shown that they are nearly proportional, and thus both methods should give approximately the same quality fits (and the same $k_{\text{isom}}/k_{\text{O}_2}$).

Additionally, since we know the absolute [RONO], we can also calculate [RO•] using the results of Equations 8.1 and 8.15:

$$[\text{RO}\cdot] = [\text{RONO}] \left(\%_{\text{photolysis}} \right). \quad (8.16)$$

The third method to calculate [RONO] does not obtain an absolute value for [RONO], but rather a relative value for each data set, by measuring the background (excimer off) ringdown lifetime of a single frequency (3678 cm^{-1} for $\text{C}_4\text{H}_9\text{ONO}$, 3662 cm^{-1} for $\text{C}_5\text{H}_{11}\text{ONO}$). Assuming a pure sample of RONO (FTIR analysis of $\text{C}_4\text{H}_9\text{ONO}$ shows that after freeze pumping, very low concentrations of other organic contaminants are present in the sample), the background gases only consist of N_2 , O_2 , and RONO. Thus, the absorbance can be fully attributed to RONO, and should be proportional to [RONO]. We can therefore obtain a relative [RONO] by Equation 8.17:

$$[\text{RONO}]_{\text{CRDS}} \propto \left(\frac{1}{\tau} - \frac{1}{\tau_0} \right)_{\bar{\nu}}, \quad (8.17)$$

where $1/\tau$ is the inverse ringdown lifetime measured with RONO present in the cell, and $1/\tau_0$ is the inverse ringdown lifetime in the absence of RONO. Both measurements must be made at the same frequency, $\bar{\nu}$. There may be drifts in the proportionality of Equation 8.17 over the course of an experiment; therefore, an entire day's worth of data cannot be scaled to the first set of data taken. Rather, each set of seven or eight points can be scaled to each other. Such a method of scaling each set of data separately from each other is valid because at the end of our analysis, we only care about relative absorbances, not the absolute absorbances and concentrations.

Note that since we are only obtaining a relative [RONO] by scaling to the absorption background, we cannot obtain the absolute value of [RO•].

Rescaling of Alkoxy Concentrations and Calculation of Relative Absorbance A_0/A

We are interested in how the [HOROO•] changes with [O₂]. Rather than rely on an absolute measurement of [HOROO•], we can measure the fraction [HOROO•]₀/[HOROO•]; that is, the concentration of HOROO• at “[O₂] = 0” compared to [HOROO•] at the [O₂] of interest. This is equivalent to comparing the ν_1 absorbance for each condition, A_0/A .

A_0/A is determined by three steps: measurement of the peak absorbance of HOROO• (in actuality, any primary or secondary isomerization product with an OH group), scaling of the absorbance to [RONO], and conversion of the scaled absorbances to A_0/A .

Absorbances were determined by measuring $\left(\frac{1}{\tau_{exon}} - \frac{1}{\tau_{exoff}} \right)_{\bar{\nu}}$, the difference in inverse ringdown lifetimes between the CRDS cell contents after photolysis (excimer on, or “exon”) and before photolysis (excimer off, or “exoff”), at the peak absorption by HOROO•, $\bar{\nu}$. We use these values directly as a measure of the isomerization product formed.

It is theoretically possible to convert these values to [HOROO•] by Equation 8.18:

$$[\text{HOROO}\bullet] = \frac{1}{\sigma_{\bar{\nu}} c} \frac{L_{opt}}{L_{phot}} \left(\frac{1}{\tau_{exon}} - \frac{1}{\tau_{exoff}} \right)_{\bar{\nu}}, \quad (8.18)$$

where $\sigma_{\bar{\nu}}$ is the absorption cross section of HOROO• at frequency $\bar{\nu}$, L_{opt} is the optical path length of the CRDS cell (distance between the mirrors), and L_{phot} is the width of the photolysis beam (and therefore the path length of HOROO•). However, the quantum chemistry calculations presented in Chapter 9 show that the absorption cross sections of

HOROO• and the end-product HORCHO are quite different than •ROH (hydroxy alkyl radicals), ROH (alcohols), or other molecules with an –OH group. There is no guarantee that the OH stretch peak of HOROO• matches any other OH stretch peak in the literature. It is therefore inappropriate to assign a cross section to the peak of HOROO•, even with theoretical integrated absorption cross sections available.

In order to obtain quantitatively correct relative absorbances, we must account for the fact that each piece of data has a different [RONO] based on the gas flows, UV measurements, and background absorptions (Equations 8.12, 8.14, 8.17). We therefore scale each of the measured absorbances to a reference [RONO] using Equation 8.19:

$$\left(\frac{1}{\tau} - \frac{1}{\tau_0}\right)_{scaled} = \frac{[\text{RONO}]_{reference}}{[\text{RONO}]_{measured}} \left(\frac{1}{\tau} - \frac{1}{\tau_0}\right)_{measured}, \quad (8.19)$$

where $\left(\frac{1}{\tau} - \frac{1}{\tau_0}\right)_{scaled}$ is the scaled difference in ringdown times, $[\text{RONO}]_{reference}$ is the reference concentration of RONO (taken to be the first [RONO] in each data set) from Equations 8.12, 8.14, 8.17, and $[\text{RONO}]_{measured}$ is the concentration of RONO for the current piece of data, using the same equation for determining [RONO] as the reference equation.

Once the scaled absorbances have been calculated, A_0/A can be calculated. A plot of $\left[\left(\frac{1}{\tau} - \frac{1}{\tau_0}\right)_{scaled}\right]^{-1}$ vs $[\text{O}_2]$ was made for each data set of 7–10 data points, using each scaling method. The simplest analysis of alkoxy relative rate experiments predicts that A_0/A should depend linearly on $[\text{O}_2]$. (As will be shown later, nonlinearity is observed only in the case of significant prompt isomerization). Linear regression was performed

for each plot, and the y-intercept of each plot, $\left[\left(\frac{1}{\tau} - \frac{1}{\tau_0} \right)_{scaled} \right]^{-1}_{[O_2]=0}$, was taken to be

$A_0/A = 1$, the maximum [HORO•] absorbance possible for a given [RO•]. Thus, A_0/A can be calculated by Equation 8.20:

$$\frac{A_0}{A} = \frac{\left(\frac{1}{\tau_{exon}} - \frac{1}{\tau_{exoff}} \right)_{scaled}}{\left(\frac{1}{\tau_{exon}} - \frac{1}{\tau_{exoff}} \right)_{[O_2]=0}}. \quad (8.20)$$

We cannot use all of our A_0/A vs $[O_2]$ data in our linear regressions. Non-linearities are observed for $[O_2] < 10^{17}$ molec cm^{-3} due to the difference in absorption cross sections of HOR• and HOROO• (spectra shown in Chapter 7, explanation of nonlinearities in Chapter 9). As will be shown in the derivation of A_0/A vs $[O_2]$ section, prompt isomerization will cause non-linearity at high $[O_2]$. **Taking both factors into account, we only use data points in the range 1.0×10^{17} molec $cm^{-3} < [O_2] < 1.7 \times 10^{19}$ molec cm^{-3} in our linear regressions.**

Choosing the Best Fits to Obtain the Overall Data Set for k_{isom}/k_{O_2}

As stated in the previous section, it is important to scale the points within each experimental data set to [RONO] to ensure that the A_0/A values are quantitatively correct. Three equally valid scaling methods were presented, and in the absence of an overall “best” method, we must determine a way to determine which scaling method to use.

Performing linear regression on each data set of 7–10 points gives individual values and uncertainties of k_{isom}/k_{O_2} for each fit. One of the three scaling methods yields the lowest uncertainty; this scaling method was chosen as the “best” scaling method. The

data points A_0/A vs $[O_2]$ for each of the “best” points were then compiled into one large data set for both *n*-butoxy and 2-pentoxy. Five plots (and thus five k_{isom}/k_{O_2} values) were then computed using five overall data sets: unscaled data, scaling to UV measurements, scaling to thermodynamics, scaling to RONO background, and using the data from the best fits.

Derivation of Dependence of A_0/A on $[O_2]$

The absorbances that we are observing in the CRDS alkoxy experiments are measures of the ν_1 band (OH stretch) of the alkoxy isomerization product HOROO•, formed from “normal” isomerization (Reaction 8.4) and prompt isomerization (Reaction 8.8). Our goal in this section is to determine how the measured absorbance depends on $[O_2]$ given the six possible reactions of alkoxy (Reactions 8.4–8.9). We first show that prompt decomposition reduces the amount of starting alkoxy (and therefore the absolute absorbance measured), but does not affect A_0/A or any of the relative rate measurements. We then analyze the remaining five pathways.

Neglect of Prompt Decomposition

We begin our experiments by photolyzing an alkyl nitrite RONO into our alkoxy radical RO•. The alkoxy radicals that are initially formed $[RO\bullet]$ can be calculated from Equation 8.21:

$$[RO\bullet]_0 = [RONO] \times \%_{\text{photolysis}} \quad (8.21)$$

where $\%_{\text{photolysis}}$ can be calculated from Equation 8.1.

A fraction newly formed alkoxy radicals will promptly decompose (Reaction 8.9). Define this fraction as ϕ_{pd} . Then the amount of alkoxy radicals left for reaction, $[\text{RO}\cdot]_{\text{available}}$, is given by Equation 8.22:

$$[\text{RO}\cdot]_{\text{available}} = [\text{RO}\cdot]_0 \times (1 - \phi_{pd}) = [\text{RONO}] \times \left[\%_{\text{photolysis}} \times (1 - \phi_{pd}) \right]. \quad (8.22)$$

For a constant photolysis wavelength, $\%_{\text{photolysis}}$ and ϕ_{pd} are constant. We can therefore define an effective photolysis ratio, $\%_{\text{photolysis,eff}}$, calculated from Equation 8.23:

$$\%_{\text{photolysis,eff}} = \%_{\text{photolysis}} \times (1 - \phi_{pd}). \quad (8.23)$$

Substituting Equation 8.23 into Equation 8.22 gives us

$$[\text{RO}\cdot]_{\text{available}} = [\text{RONO}] \times \%_{\text{photolysis,eff}}. \quad (8.24)$$

The effects of prompt decomposition can be accounted for entirely in the photolysis ratio calculation. Therefore, prompt decomposition will have no effect on the relative kinetics analysis.

Prompt decomposition should not affect the OH stretch experiment at all, because the decomposition products cannot form secondary products with –OH groups on the timescales of Mollner’s experiments (20–110 μs).³⁰ However, it may affect the A-X spectroscopy and kinetics experiments. One of the products of decomposition is an alkyl radical. In the presence of O_2 , a rapid association reaction will occur, resulting in formation of an alkylperoxy radical (Reaction 8.25).



These peroxy radicals will have their own A-X spectroscopic bands, and may interfere with the HOROO• spectrum. It is therefore important to note that while prompt

decomposition will not fundamentally affect the relative kinetics experiments, spectroscopic interference still needs to be considered.

Treatment of the remaining pathways

Next consider the remaining 5 alkoxy reactions: isomerization, reaction with O₂, decomposition, recombination with NO, and prompt isomerization (Reactions 8.4–8.8). Here, we show that the relative rate constants $k_{\text{isom}}/k_{\text{O}_2}$ can be determined from the relative absorbances A_0/A .

We have defined A as the OH stretch absorbance for a given [O₂], and A_0 as the OH stretch absorbance for “[O₂] = 0” (actually an extrapolated value due to the low [O₂] anomaly described in Chapter 9). By Beer’s Law, the ratio A_0/A is

$$\frac{A_0}{A} = \frac{\sigma_{\text{HOROO}\cdot} L_{\text{phot}} ([\text{HOROO}\cdot])_{[\text{O}_2]=0}}{\sigma_{\text{HOROO}\cdot} L_{\text{phot}} [\text{HOROO}\cdot]} = \frac{([\text{HOROO}\cdot])_{[\text{O}_2]=0}}{[\text{HOROO}\cdot]}, \quad (8.26)$$

where $\sigma_{\text{HOROO}\cdot}$ is the ν_1 cross section of HOROO• and L_{phot} is the photolysis length (sample length of HOROO•). Furthermore, we can convert [HOROO•] to an isomerization yield ϕ_{isom} by Equation 8.27:

$$\frac{A_0}{A} = \frac{([\text{HOROO}\cdot])_{[\text{O}_2]=0} / [\text{RO}]_0}{[\text{HOROO}\cdot] / [\text{RO}]_0} = \frac{(\phi_{\text{isom}})_{[\text{O}_2]=0}}{\phi_{\text{isom}}}. \quad (8.27)$$

In Equation 8.27, ϕ_{isom} is defined as the isomerization yield of alkoxy radicals that did not undergo prompt decomposition. Using the five remaining alkoxy reactions

(Reactions 8.4–8.8), we obtain

$$\phi_{isom} = \phi_{pi} + (1 - \phi_{pi}) \frac{k_{isom}}{k_{isom} + k_{O_2} [O_2] + k_{decomp} + k_{NO} [NO]}, \quad (8.28)$$

where ϕ_{pi} is the fraction of alkoxy radicals that promptly isomerize (Reaction 8.8), and k_{isom} , k_{O_2} , k_{decomp} , and k_{NO} represent the rate constants for alkoxy isomerization, reaction with O_2 , decomposition, and reaction with NO respectively.

Substituting Equation 8.28 into Equation 8.27 gives us

$$\frac{A_0}{A} = \frac{\left(\frac{\frac{k_{O_2}}{k_{isom}}}{1 + \frac{k_{NO} [NO]}{k_{isom}} + \frac{k_{decomp}}{k_{isom}}} \right) [O_2] + 1}{\left(\frac{\phi_{pi} \frac{k_{O_2}}{k_{isom}}}{1 + \phi_{pi} \left(\frac{k_{NO} [NO]}{k_{isom}} + \frac{k_{decomp}}{k_{isom}} \right)} \right) [O_2] + 1}. \quad (8.29)$$

Although the relationship between A_0/A and $[O_2]$ is nonlinear, Equation 8.29 shows that we can extract k_{isom}/k_{O_2} from our CRDS absorbance data.

The typical analysis of alkoxy chemistry^{148, 154-156, 159, 160} assumes that decomposition, reaction with NO, and prompt isomerization are all negligible. In this limit, we recover the “classic” equation used in alkoxy relative kinetics analysis:

$$\lim_{k_{decomp}, k_{NO}, \phi_{pi} \rightarrow 0} \left(\frac{A_0}{A} \right) = \frac{k_{O_2}}{k_{isom}} [O_2] + 1. \quad (8.30)$$

Determination of k_{isom}/k_{O_2}

When only isomerization and reaction with O_2 are considered, a plot of A_0/A vs $[O_2]$ is linear with slope k_{O_2}/k_{isom} (Equation 8.30). We can therefore calculate k_{isom}/k_{O_2} by Equation 8.31:

$$\frac{k_{isom}}{k_{O_2}} = \left[\frac{\partial \left(\frac{A_0}{A} \right)}{\partial [O_2]} \right]^{-1} \quad (8.31)$$

The full dependence of A_0/A on $[O_2]$ (Equation 8.29) is approximately linear at low $[O_2]$, and the slope of the line should be related to k_{isom}/k_{O_2} . First start by calculating the derivative of Equation 8.29:

$$\left(\frac{\partial \left(\frac{A_0}{A} \right)}{\partial [O_2]} \right) = \frac{\frac{k_{O_2}}{k_{isom}}}{1 + \frac{k_{decomp}}{k_{isom}} + \frac{k_{NO} [NO]}{k_{isom}}} \times \frac{(1 - \phi_{pi}) \left[1 + \phi_{pi} \left(\frac{k_{decomp}}{k_{isom}} + \frac{k_{NO} [NO]}{k_{isom}} \right) \right]}{\left[1 + \phi_{pi} \left(\frac{k_{O_2} [O_2]}{k_{isom}} + \frac{k_{decomp}}{k_{isom}} + \frac{k_{NO} [NO]}{k_{isom}} \right) \right]^2} \quad (8.32)$$

At low $[O_2]$, Equation 8.32 reduces to

$$\left(\frac{\partial \left(\frac{A_0}{A} \right)}{\partial [O_2]} \right)_{[O_2]=0} = \frac{\frac{k_{O_2}}{k_{isom}}}{\left[1 + \frac{k_{decomp}}{k_{isom}} + \frac{k_{NO} [NO]}{k_{isom}} \right]} \times \left[\frac{(1 - \phi_{pi})}{1 + \phi_{pi} \left(\frac{k_{decomp}}{k_{isom}} + \frac{k_{NO} [NO]}{k_{isom}} \right)} \right] \quad (8.33)$$

Solving Equation 8.33 for k_{isom}/k_{O_2} gives

$$\frac{k_{isom}}{k_{O_2}} = \left[\left(\frac{\partial \left(\frac{A_0}{A} \right)}{\partial [O_2]} \right)_{[O_2]=0} \right]^{-1} \times \left[\frac{1}{1 + \frac{k_{decomp}}{k_{isom}} + \frac{k_{NO} [NO]}{k_{isom}}} \right] \times \left[\frac{(1 - \phi_{pi})}{1 + \phi_{pi} \left(\frac{k_{decomp}}{k_{isom}} + \frac{k_{NO} [NO]}{k_{isom}} \right)} \right] \quad (8.34)$$

According to Equation 8.34, the true k_{isom}/k_{O_2} is the product of three terms. The first term in Equation 8.34 is the k_{isom}/k_{O_2} that was calculated by assuming that the only

important alkoxy reactions are isomerization and reaction with O₂ (the typical analysis found in the literature). The second and third terms are “correction” factors for the other reaction pathways and prompt isomerization respectively. We can rewrite Equation 8.34:

$$\frac{k_{isom}}{k_{O_2}} = \left[\left(\frac{\partial \left(\frac{A_0}{A} \right)}{\partial [O_2]} \right)_{[O_2]=0} \right]^{-1} \times X_{kin} \times X_{prompt}, \quad (8.35)$$

where

$$X_{kin} = \frac{1}{1 + \frac{k_{decomp}}{k_{isom}} + \frac{k_{NO} [NO]}{k_{isom}}}, \quad (8.36)$$

$$X_{prompt} = \frac{(1 - \phi_{pi})}{1 + \phi_{pi} \left(\frac{k_{decomp}}{k_{isom}} + \frac{k_{NO} [NO]}{k_{isom}} \right)}, \quad (8.37)$$

X_{kin} is the correction factor for the missing kinetic reaction pathways (decomposition, reaction with NO), and X_{prompt} is the correction factor for prompt isomerization.

We can calculate the true k_{isom}/k_{O_2} by a relatively simple procedure. First, we perform linear regression to the relative kinetics data set to obtain the slope

$$\left(\frac{\partial \left(\frac{A_0}{A} \right)}{\partial [O_2]} \right)_{[O_2]=0}. \text{ Then, we apply the correction factors } X_{kin} \text{ and } X_{prompt} \text{ to obtain } k_{isom}/k_{O_2}.$$

Results

The results from this reanalysis are presented in four parts. First, a selected set of gas flow conditions is shown in order to illustrate how [O₂], [RONO], and [RO•] change

between the initial analysis and the reanalysis performed in this document. Second, a selected plot of A_0/A vs $[O_2]$ for an individual data set is shown to illustrate the changes in the plots between the initial analysis and the reanalysis, and to compare scaling methods. Third, the plots of A_0/A vs $[O_2]$ for the overall data sets of *n*-butoxy and 2-pentoxo are shown. Fourth, the best value of k_{isom}/k_{O_2} is derived by using our CRDS data and Equation 8.34, the full dependence of our relative kinetics data on $[O_2]$.

Selected Gas Flow Data

Combining the *n*-butoxy and 2-pentoxo experiments, 903 sets of gas flows and concentrations were recalculated; therefore, all of the recalculated data cannot be presented in this document. Instead, one set of experimental conditions will be reported in order to illustrate how $[O_2]$, $[RONO]$, and $[RO\bullet]$ change between the initial analysis and this reanalysis.

Table 8.2 contains the reanalyzed gas flows and concentrations from a single experimental scan, while Table 8.3 contains a comparison of $[O_2]$, $[RONO]$, and $[RO\bullet]$ between the initial analysis and the reanalysis.

Table 8.2. One set of gas flow conditions (from 9/28/06, Scan 1), $p = 670$ torr

Flow	Gas	Function	sccm/V	$V_{0,i}$	V_i	Flow (sccm)	[gas] (molec cm ⁻³)
1	N ₂	Dilution	2182.9	0.16	2.73	5610	1.56×10^{19}
2	N ₂	L-purge	184.2	0.023	4.01	734	2.04×10^{18}
3	O ₂	Dilution	-1940.6	-0.073	-0.36	557	1.55×10^{18}
4	N ₂	bubbler	101.5	0.42	1.92	152	4.23×10^{17}
5	N ₂	R-purge	415.8	0.165	1.99	759	2.11×10^{18}

Table 8.3. Comparison of the initial analysis of one set of gas concentrations to the reanalysis

	[O ₂] (molec cm ⁻³)	[RONO] (molec cm ⁻³)	[RO•] (molec cm ⁻³)
Initial Values	1.68×10^{18}	6.8×10^{15}	0.68×10^{14}
Reanalyzed Values	1.56×10^{18}	1.1×10^{16} (UV) 1.2×10^{16} (thermo)	1.9×10^{14} 2.0×10^{14}

Examination of Table 8.3 reveals striking differences between the initially calculated experimental conditions and the recalculated conditions. As explained in the introduction, the recalculated [O₂] is less than the initially calculated [O₂] (in this example, by 7%) because the right purge flow was not initially used in the calculation of total gas concentrations. The recalculations of [RONO] based on the UV measurements and thermodynamic parameters are greater than the values recorded in the lab notebook (in this example, by a factor of 1.5). It is likely that this discrepancy comes from two errors: the miscalculation of gas flows and concentrations that also affect the [O₂] calculation, and the use of incorrect flowmeter calibrations in the photolysis calculator and/or the gas flow calculator. This problem affects all of the N₂ bath gas data and much of the Ar bath gas data. Finally, the discrepancies in [RO•] are even greater than the previous two errors (in this case, a factor of 2.6), caused by the above two errors, and the miscalculation of photolysis flux described in the introduction.

Putting all of these errors together, we expect the derived value of $k_{\text{isom}}/k_{\text{O}_2}$ to change dramatically. The changes in [O₂] directly affect the plot of A_0/A vs [O₂], while the changes in [RONO] will affect how each individual data point is scaled. Because our data do not depend on the absolute value of [RO•] (we do not directly measure the kinetics of HOROO• formation and decay in the OH stretch experiment), the errors in [RO•] will not affect $k_{\text{isom}}/k_{\text{O}_2}$.

Recalculations on each data point of the entire alkoxy data set gives similar results to the example shown above. The actual $[O_2]$ values are lower than the previously recorded values by a factor of 7%–10%, $[RONO]$ is higher than the previously recorded values by a factor of 1.5–2, and $[RO\bullet]$ is higher than the previous values by a factor of 2–3.

How Scaling Method Affects A_0/A vs $[O_2]$

Since $[RONO]$ may vary during the course of an experiment, each data point in a single data set must be scaled to a reference $[RONO]$. As stated in the introduction, there are three methods that can be used: scaling to the UV absorption measurements (Equation 8.4), scaling by thermodynamic parameters (Equation 8.6), and scaling by background nitrite absorption (Equation 8.9). Since all three methods are equally valid ways to scale data points, the strategy is to use each individual method to scale the data points and determine which scaling method gives the best fit.

Figure 8.2 shows four plots of A_0/A vs $[O_2]$ for the same data set, without any scaling, and using each of the three described scaling methods. This data set was chosen to show that scaling method can often have a large effect on the quality of linear fit. However, for a typical data set, the UV and thermodynamic scaling methods usually gave

similar uncertainties and $\left[\frac{\partial \left(\frac{A_0}{A} \right)}{\partial [O_2]} \right]^{-1}$ (calculated as the ratio of the y-intercept to slope, or

int/slope) values. Scaling to the CRDS background usually gave *int/slope* values with the largest uncertainties, possibly due to interference by other molecules in the IR region.

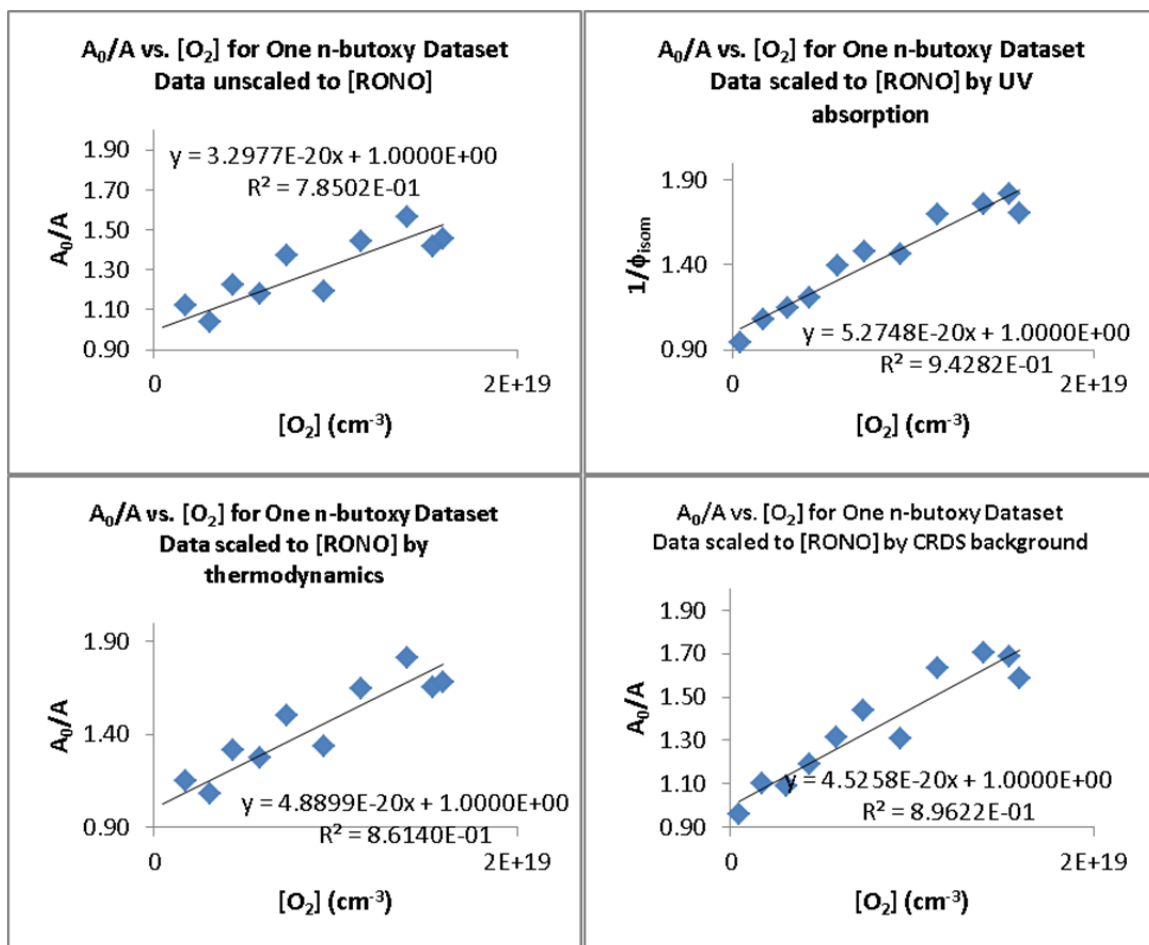


Figure 8.2. Plots of A_0/A vs $[O_2]$ for one n-butoxy data set (9/28/06, scans 73–105) using different scaling methods. Upper left: no scaling to [RONO], $int/slope = (3.0 \pm 0.6) \times 10^{19} \text{ cm}^{-3}$. Upper right: Scaling to [RONO] based on UV absorption measurements at 254 nm, $int/slope = (1.9 \pm 0.2) \times 10^{19} \text{ cm}^{-3}$. Lower left: Scaling to [RONO] based on thermodynamic parameters, $int/slope = (2.1 \pm 0.3) \times 10^{19} \text{ cm}^{-3}$. Lower right: Scaling to [RONO] based on CRDS background absorption at 3678 cm^{-1} , $int/slope = (2.2 \pm 0.3) \times 10^{19} \text{ cm}^{-3}$. All uncertainties are reported to 1σ . For this data set, scaling to UV absorption gives the smallest uncertainty on k_{isom}/k_{O_2} , although this is not true for all other data sets.

Visual inspection of the four plots in Figure 8.2 reveals that scaling to the UV absorption gives the best linear fit. Examination of the standard errors on the derived $int/slope$ values confirms this point. The $int/slope$ values, absolute 1σ uncertainties, and 1σ percent uncertainties for each fit are $(3.0 \pm 0.6) \times 10^{19} \text{ cm}^{-3}$ (18%) for the unscaled data, $(1.9 \pm 0.2) \times 10^{19} \text{ cm}^{-3}$ (9%) for the UV scaled data, $(2.1 \pm 0.3) \times 10^{19} \text{ cm}^{-3}$ (15%)

for the thermodynamics scaled data, and $(2.2 \pm 0.3) \times 10^{19} \text{ cm}^{-3}$ (12%) for the background scaled data. For this data set, scaling to the UV measurements yields the best linear fit. This is not the best method for every data set: some sets are best fit by scaling to the thermodynamic parameters, and a few sets are best fit to the background CRDS absorptions. None of the data sets are best fit by the unscaled data points.

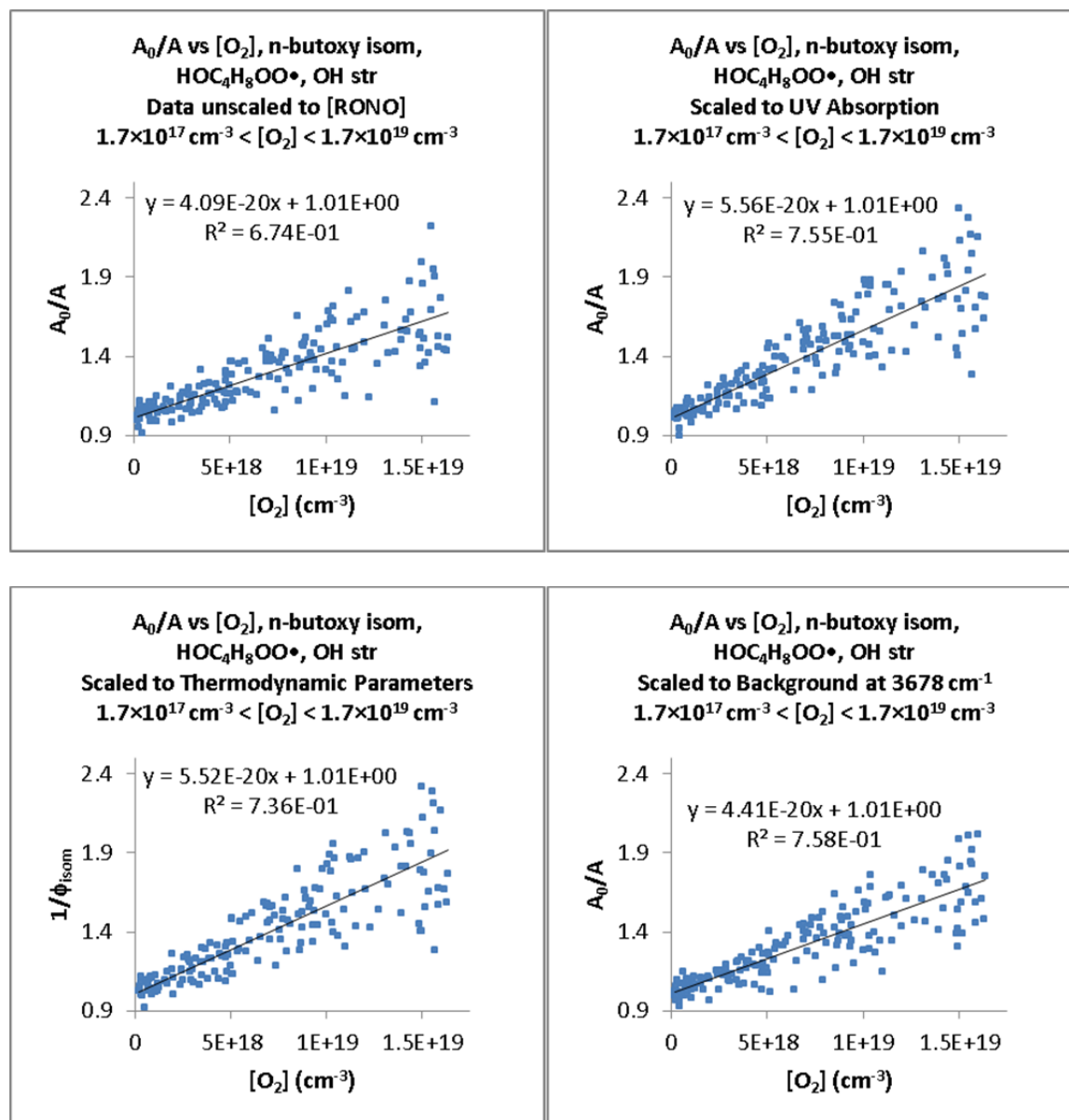
Overall Data Set of A_0/A vs $[O_2]$ and Calculated $int/slope$

The full data sets of A_0/A vs $[O_2]$ consist of 191 data points for *n*-butoxy and 76 data points for 2-pentoxy. Only 177 data points for *n*-butoxy were used for the linear fits to determine k_{isom}/k_{O_2} . Six points were measured at $[O_2] < 1.7 \times 10^{17} \text{ molec cm}^{-3}$, and are therefore subject to the low $[O_2]$ anomaly described in Chapter 9. Eight of the points were measured at $[O_2] > 1.7 \times 10^{19} \text{ molec cm}^{-3}$, and therefore may be subject to nonlinearities in A_0/A vs $[O_2]$ due to prompt isomerization. In contrast, all of the data points for 2-pentoxy were used because the $[O_2]$ used fell within the linear regime for A_0/A vs $[O_2]$.

There are five methods that can be used to generate full data sets of A_0/A vs $[O_2]$, and therefore to determine $int/slope$, based on the scaling procedures in the previous section. Four of the methods are to simply use the A_0/A values derived from the previous section (unscaled, scaled to UV absorption, scaled to thermodynamics, scaled to background CRDS absorption) to create four data sets of A_0/A vs $[O_2]$. The fifth method is to use the A_0/A values from each individual data set that gave the best linear fit, and combine each of these individual sets of A_0/A values into an overall data set. Each data set can then be fit to Equation 8.13 to obtain A_0/A . Presumably, the fifth data set should give a value of $int/slope$ with the lowest uncertainty.

The five plots of A_0/A vs $[O_2]$ for *n*-butoxy using each scaling method are shown in Figure 8.3, while the five plots for 2-pentoxy are shown in Figure 8.4. As expected, using the best fits from each individual data set give an overall data set with the lowest uncertainty on *int/slope*. Additionally, scaling to UV absorption measurements or thermodynamic parameters yields the same absolute value of *int/slope*, but with slightly higher uncertainties. The agreement between *int/slope* values strongly implies that using the best fits from each individual data set is a valid method for generating an overall data set.

Tables 8.4 and 8.5 summarize the derived *int/slope* parameters using each scaling method. By using the A_0/A generated from the best scaling method for each individual data set, we obtain *int/slope* = $(1.81 \pm 0.15) \times 10^{19} \text{ cm}^{-3}$ for *n*-butoxy, and $(3.86 \pm 0.45) \times 10^{19} \text{ cm}^{-3}$ for 2-pentoxy (reported to 2σ error).



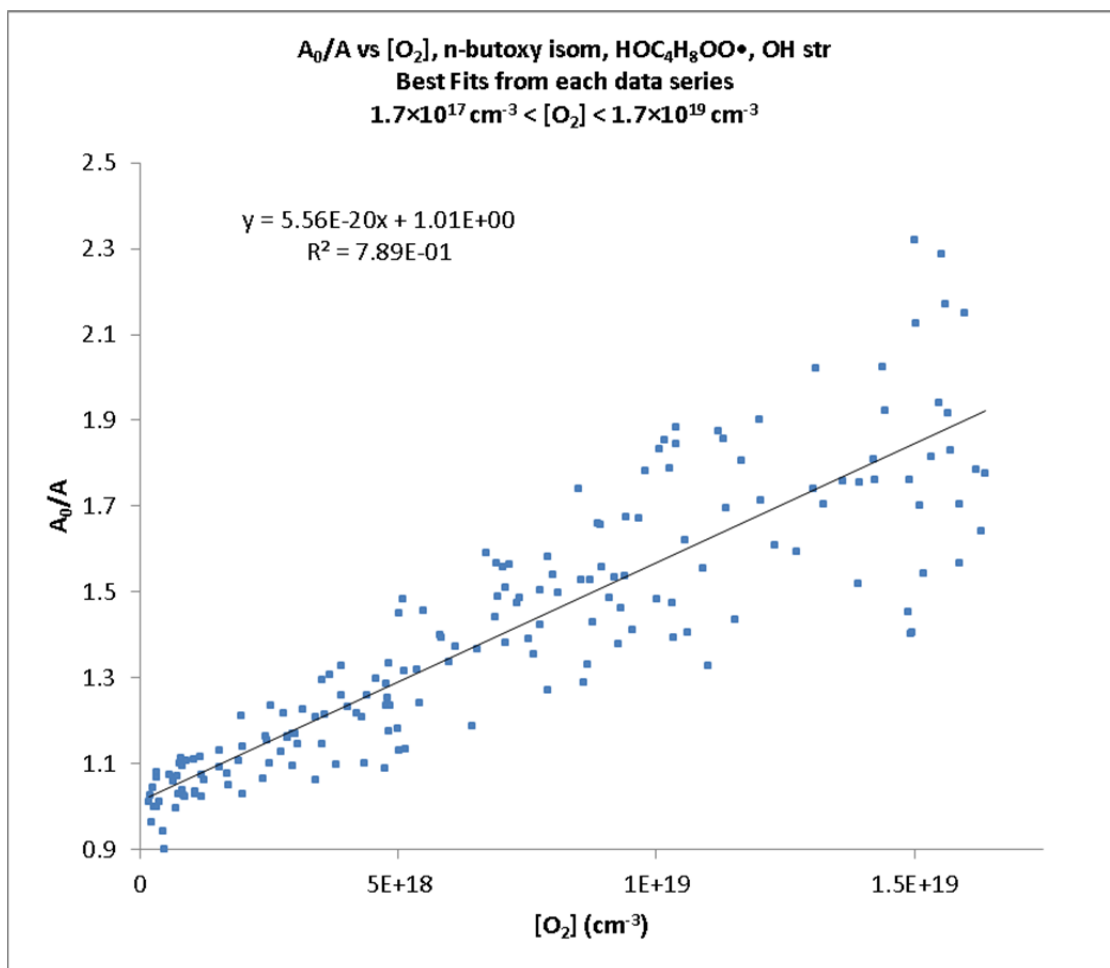
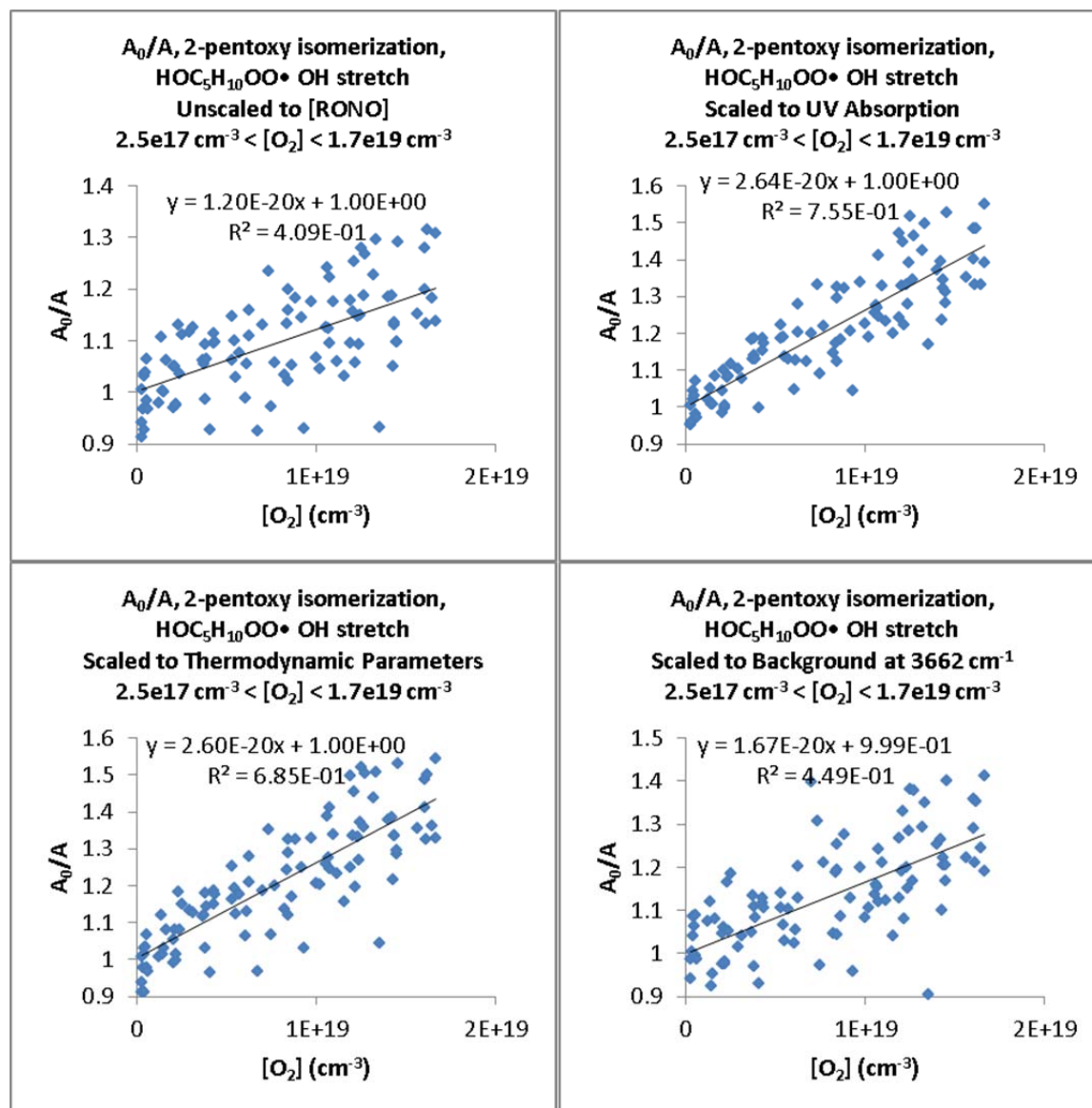


Figure 8.3. Plots of A_0/A vs $[O_2]$ for the overall *n*-butoxy data set, $1.7 \times 10^{17} \text{ molec cm}^{-3} < [O_2] < 1.7 \times 10^{19} \text{ molec cm}^{-3}$. On the previous page, Upper left: data unscaled to $[RONO]$, $int/slope = (2.47 \pm 0.27) \times 10^{19} \text{ cm}^{-3}$. Upper right: data scaled by UV absorption measurements, $int/slope = (1.82 \pm 0.17) \times 10^{19} \text{ cm}^{-3}$. Bottom left: data scaled by thermodynamic parameters, $int/slope = (1.83 \pm 0.18) \times 10^{19} \text{ cm}^{-3}$. Bottom right: data scaled by CRDS background at 3678 cm^{-1} , $int/slope = (2.29 \pm 0.21) \times 10^{19} \text{ cm}^{-3}$. This page: Combination of best fits to each individual data set, $int/slope = (1.81 \pm 0.15) \times 10^{19} \text{ cm}^{-3}$. All errors reported as 2σ . Standard errors on the slopes and intercepts can be found in Table 8.4. Final figure adapted with permission from Sprague et al.³¹ Copyright 2012 American Chemical Society.



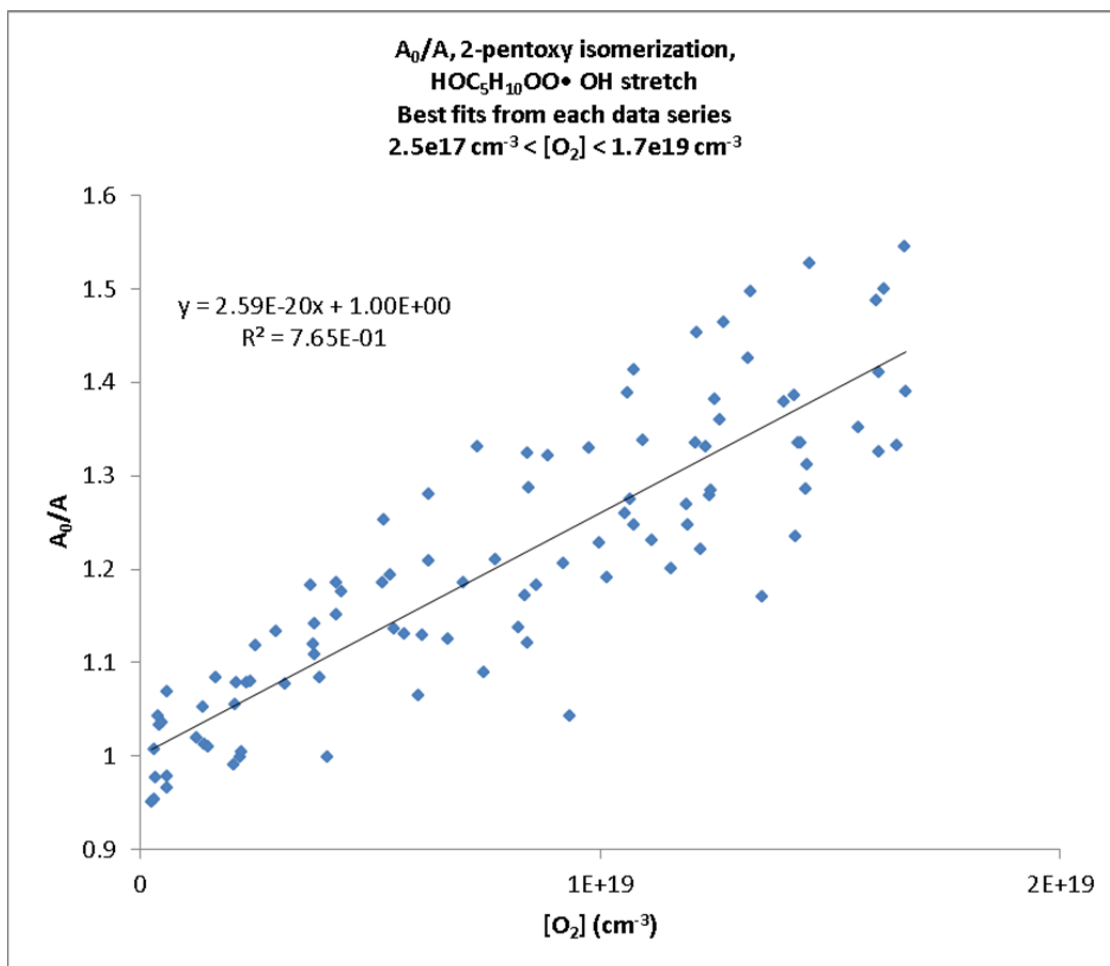


Figure 8.4. Plots of A_0/A vs $[\text{O}_2]$ for the overall 2-pentoxy data set, $1.7 \times 10^{17} \text{ molec cm}^{-3} < [\text{O}_2] < 1.7 \times 10^{19} \text{ molec cm}^{-3}$. On the previous page, Upper left: data unscaled to $[\text{RONO}]$, $\text{int/slope} = (8.35 \pm 2.05) \times 10^{19} \text{ cm}^{-3}$. Upper right: data scaled by UV absorption measurements, $\text{int/slope} = (3.79 \pm 0.45) \times 10^{19} \text{ cm}^{-3}$. Bottom left: data scaled by thermodynamic parameters, $\text{int/slope} = (3.86 \pm 0.55) \times 10^{19} \text{ cm}^{-3}$. Bottom right: data scaled by CRDS background at 3678 cm^{-1} , $\text{int/slope} = (5.99 \pm 1.37) \times 10^{19} \text{ cm}^{-3}$. This page: combination of best fits to each individual data set, $\text{int/slope} = (3.86 \pm 0.45) \times 10^{19} \text{ cm}^{-3}$. All errors reported as 2σ . Standard errors on the slopes and intercepts can be found in Table 8.5. Final figure adapted with permission from Sprague et al.³¹ Copyright 2012 American Chemical Society.

Table 8.4. Slopes, Intercepts, $k_{\text{isom}}/k_{\text{O}_2}$, and Standard Errors for *n*-butoxy Data Fits

Scaling Method	Slope (10^{-20} cm^3)	St. Error (2σ) (10^{-20} cm^3)	y-Intercept	St. Error (2σ)	<i>int/slope</i> (10^{19} cm^{-3})	St. Error (2σ) (10^{19} cm^{-3})
Unscaled	4.09	0.42	1.00	0.04	2.47	0.27
UV	5.56	0.48	1.01	0.04	1.82	0.17
Thermo	5.52	0.50	1.01	0.04	1.83	0.18
Background	4.41	0.37	1.01	0.03	2.29	0.21
Best Fits	5.56	0.43	1.01	0.04	1.81	0.15

Table 8.5. Slopes, Intercepts, $k_{\text{isom}}/k_{\text{O}_2}$, and Standard Errors for 2-pentoxy Data Fits

Scaling Method	Slope (10^{-20} cm^3)	St. Error (2σ) (10^{-20} cm^3)	y-Intercept	St. Error (2σ)	<i>int/slope</i> (10^{19} cm^{-3})	St. Error (2σ) (10^{19} cm^{-3})
Unscaled	1.20	0.29	1.00	0.03	8.35	2.05
UV	2.64	0.30	1.00	0.03	3.79	0.45
Thermo	2.60	0.36	1.00	0.03	3.86	0.55
Background	1.67	0.38	1.00	0.04	5.99	1.37
Best Fits	2.59	0.29	1.00	0.03	3.86	0.45

Required Parameters and Rate Constants

As shown in the *Methods* section, our relative kinetics data are expected to fit to Equation 8.29. We can extract $k_{\text{isom}}/k_{\text{O}_2}$ from this function by using Equations 8.35–8.37.

$$\frac{A_0}{A} = \frac{\left(\frac{k_{\text{O}_2}}{k_{\text{isom}}} \right)}{\left(1 + \frac{k_{\text{NO}} [\text{NO}\cdot]}{k_{\text{isom}}} + \frac{k_{\text{decomp}}}{k_{\text{isom}}} \right)} [\text{O}_2] + 1 \quad (8.29)$$

$$\frac{A_0}{A} = \frac{\left(\phi_{\text{pi}} \frac{k_{\text{O}_2}}{k_{\text{isom}}} \right)}{\left(1 + \phi_{\text{pi}} \left(\frac{k_{\text{NO}} [\text{NO}\cdot]}{k_{\text{isom}}} + \frac{k_{\text{decomp}}}{k_{\text{isom}}} \right) \right)} [\text{O}_2] + 1$$

$$\frac{k_{\text{isom}}}{k_{\text{O}_2}} = \left[\left(\frac{\partial \left(\frac{A_0}{A} \right)}{\partial [\text{O}_2]} \right)_{[\text{O}_2]=0} \right]^{-1} \times X_{\text{kin}} \times X_{\text{prompt}} \quad (8.35)$$

$$X_{kin} = \frac{1}{1 + \frac{k_{decomp}}{k_{isom}} + \frac{k_{NO} [\text{NO}\cdot]}{k_{isom}}} \quad (8.36)$$

$$X_{prompt} = \frac{(1 - \phi_{pi})}{1 + \phi_{pi} \left(\frac{k_{decomp}}{k_{isom}} + \frac{k_{NO} [\text{NO}]}{k_{isom}} \right)} \quad (8.37)$$

The parameters k_{decomp} , k_{isom} , k_{NO} , and ϕ_{pi} are summarized in Table 8.6. The justification for each rate constant is below the table. The justification for ϕ_{pi} is in the next section.

Table 8.6. – Rate constants, prompt process parameters, and 2σ uncertainties for *n*-butoxy and 2-pentoxy

		<i>n</i> -butoxy		2-pentoxy	
	Units	Best Value	Uncertainty (2σ)	Best Value	Uncertainty (2σ)
$\left[\left(\frac{\partial \left(\frac{A_0}{A} \right)}{\partial [\text{O}_2]} \right)_{[\text{O}_2]=0} \right]^{-1}$	10^{19} cm^{-3}	1.81	0.15	3.86	0.45
$k_{\text{O}_2}^{28, 142, 193}$	$10^{-14} \text{ cm}^3 \text{ s}^{-1}$	1.40	0.70	0.80	0.40
k_{isom} (derived)	10^5 s^{-1}	2.53	1.28	3.09	1.59
$k_{decomp}^{117, 149}$	s^{-1}	600	300	2.0×10^4	1.0×10^4
$k_{NO} \times [\text{NO}]^{32}$	s^{-1}	6640	3320	6640	3320
ϕ_{pi}		0.038	0.018	0.049	0.024

$\left[\left(\frac{\partial \left(\frac{A_0}{A} \right)}{\partial [\text{O}_2]} \right)_{[\text{O}_2]=0} \right]^{-1}$: Obtained from the fits presented in Figures 8.3 and 8.4.

k_{O_2} : The recommended value and uncertainty for *n*-butoxy are taken from Atkinson's 2007 review paper.¹⁴² The recommended value of the rate constant for 2-pentoxy is based on Balla's 1985 study of isopropoxy.¹⁹³ Atkinson recommends that all secondary alkoxy

radicals should have similar O₂ reaction rates.¹⁴² Balla reports a 4% uncertainty on his value. However, I choose to use 50% uncertainty (same as *n*-butoxy) because of the possible differences between 2-pentoxy and isopropoxy. It can be shown that the effect of this choice on the overall uncertainty is negligible, less than a 1% change in the overall reported error on the final value of $k_{\text{isom}}/k_{\text{O}_2}$.

k_{decomp} : The value and uncertainty of k_{decomp} for *n*-butoxy is taken from Curran's 2006 review paper, estimated as the difference between Curran's recommendation and Orlando's previous study.¹⁴⁹ Curran does not actually report an uncertainty, so the uncertainty was estimated on the basis of the Arrhenius plot in their paper (Figure 8.32). For 2-pentoxy, the uncertainty was estimated as the scatter in the theoretical rate constants available in the NIST kinetics database.¹¹⁷ We chose a value of k_{decomp} that fell in the middle of the available rate constants.

$k_{\text{NO}} \times [\text{NO}]$: Heicklen's recommendation is to use $3.32 \times 10^{-11} \text{ cm}^3 \text{ molec}^{-1} \text{ s}^{-1}$ for all alkoxies.³² The reported experimental data within his review paper have a scatter of roughly $\pm 0.4 \times 10^{-11} \text{ cm}^3 \text{ molec}^{-1} \text{ s}^{-1}$. [NO] is taken to be equal to our [RO•] ($2.0 \times 10^{14} \text{ molec cm}^{-3}$). With few available studies on alkoxy recombination with NO, we choose to use an overall factor of 50% uncertainty. Similar to the uncertainty choice on k_{O_2} , this increased uncertainty makes only a small difference in the overall reported uncertainty on $k_{\text{isom}}/k_{\text{O}_2}$.

Prompt Isomerization: Determination of ϕ_{pi}

We have already observed that prompt isomerization will cause nonlinearities in the plot of A_0/A vs [O₂] at high [O₂] (Equation 8.29).

$$\frac{A_0}{A} = \frac{\left(\frac{\frac{k_{O_2}}{k_{isom}}}{1 + \frac{k_{NO} [NO]}{k_{isom}} + \frac{k_{decomp}}{k_{isom}}} \right) [O_2] + 1}{\left(\frac{\phi_{pi} \frac{k_{O_2}}{k_{isom}}}{1 + \phi_{pi} \left(\frac{k_{NO} [NO]}{k_{isom}} + \frac{k_{decomp}}{k_{isom}} \right)} \right) [O_2] + 1} \quad (8.29)$$

We can determine the best value of ϕ_{pi} by performing a fit of the entire alkoxy data sets to both the simple linear function (Equation 8.31) and the full non-linear form (Equation 8.29). We then calculate the reduced chi-squared variable, χ_v^2 , for the linear and nonlinear fits, defined by Equation 8.38:

$$\chi_v^2 = \frac{\chi^2}{\nu} = \frac{1}{N-p-1} \sum \frac{[y_i - y(x_i)]^2}{\sigma_i^2}, \quad (8.38)$$

where $\nu = N-p-1$ is the number of degrees of freedom, N is the number of data points in the overall alkoxy data set, p is the number of parameters to fit to, y_i is the measured value of the i^{th} point, $y(x_i)$ is the expected value of the i^{th} point based on the function being fit to, and σ_i is variance associated with the i^{th} point. In our cases, $N = 177$ for *n*-butoxy and $N = 95$ for 2-pentoxy. The number of parameters for each fit is 2 for the linear fits (k_{isom} , k_{O_2}) and 3 for the nonlinear fits (k_{isom} , k_{O_2} , and ϕ_{pi}). We then assume that each data point has the same fractional uncertainty on A_0/A , expressed in Equation 8.39:

$$\sigma_i = a \times \left(\frac{A_0}{A} \right), \quad (8.39)$$

where a is a multiplicative constant ($a < 1$). It can be shown that while the value of a affects the values of χ^2 , it does not affect the final result for ϕ_{pi} . The best value of ϕ_{pi} is calculated by Equation 8.40:

$$\left[\chi_v^2\right]_{non-linear} = \left[\chi_v^2\right]_{linear} \times \left(1 + \frac{1}{v}\right). \quad (8.40)$$

The uncertainty is chosen to be the difference between the ϕ_{pi} determined from Equation 8.40 and the ϕ_{pi} which minimizes $\left[\chi_v^2\right]_{non-linear}$.

When we apply Equations 8.39 and 8.40 to the two alkoxy data sets, we obtain $\left[\chi_v^2\right]_{linear} = 0.830$ for *n*-butoxy, and $\left[\chi_v^2\right]_{linear} = 0.365$ for 2-pentoxy. The ϕ_{prompt} necessary to obtain the $\left[\chi_v^2\right]_{non-linear}$ described in Equation 8.40 are **$\phi_{pi} = 0.038 \pm 0.018$** for *n*-butoxy and **$\phi_{pi} = 0.049 \pm 0.024$** for 2-pentoxy.

Calculation of k_{ison}/k_{O2} , Comparison of Data Fits

With best values and uncertainties for each parameter in hand, we can calculate k_{ison}/k_{O2} and its uncertainty. The uncertainty is calculated by propagating the individual parameter uncertainties through Equation 8.29 using standard statistical equations.¹⁹⁴ For two uncorrelated variables u, v , with uncertainties σ_u, σ_v , the uncertainty on $x(u, v)$ (σ_x) is calculated as

$$x = au \pm bv, \quad \sigma_x = \sqrt{a^2 \sigma_u^2 + b^2 \sigma_v^2}, \quad (8.41)$$

$$x = \pm auv, \quad \sigma_x = x \sqrt{\frac{\sigma_u^2}{u^2} + \frac{\sigma_v^2}{v^2}}, \quad (8.42)$$

where a and b are constants.

Table 8.7 summarizes the parameters, uncertainties, and correction factors used for calculating $k_{\text{isom}}/k_{\text{O}_2}$. We obtain $X_{\text{kin}} \times X_{\text{prompt}}$ of 0.93 ± 0.03 for *n*-butoxy and 0.87 ± 0.04 for 2-pentoxy. Using these correction factors and their uncertainties, we report $k_{\text{isom}}/k_{\text{O}_2}$ as $(1.69 \pm 0.15) \times 10^{19} \text{ cm}^{-3}$ for *n*-butoxy and $(3.37 \pm 0.43) \times 10^{19} \text{ cm}^{-3}$ for 2-pentoxy.

Table 8.7. Parameters, correction factors, 2σ uncertainties, and derived $k_{\text{isom}}/k_{\text{O}_2}$ for *n*-butoxy and 2-pentoxy

		<i>n</i> -butoxy		2-pentoxy	
	Units	Best Value	Uncertainty (2σ)	Best Value	Uncertainty (2σ)
$\left[\left(\frac{\partial \left(\frac{A_0}{A} \right)}{\partial [\text{O}_2]} \right)_{[\text{O}_2]=0} \right]^{-1}$	10^{19} cm^{-3}	1.81	0.15	3.86	0.45
$k_{\text{decomp}}/k_{\text{isom}}$		0.0024	0.0017	0.0648	0.0464
$k_{\text{NO}}[\text{NO}]/k_{\text{isom}}$		0.0262	0.0187	0.0215	0.0154
ϕ_{pi}		0.038	0.018	0.049	0.024
X_{kin}		0.97	0.02	0.92	0.04
X_{prompt}		0.96	0.02	0.95	0.02
$X_{\text{kin}} \times X_{\text{prompt}}$		0.93	0.03	0.87	0.04
$k_{\text{isom}}/k_{\text{O}_2}$	10^{19} cm^{-3}	1.69	0.15	3.37	0.43

With the parameters, correction factors, and $k_{\text{isom}}/k_{\text{O}_2}$ calculated for each system, we can compare how well Equation 8.31 (simple linear equation) and Equation 8.29 (full dependence of A_0/A on $[\text{O}_2]$) fit to our relative kinetics data. Figure 8.5 compares four different fits to the *n*-butoxy and 2-pentoxy data: the simple linear fit using only the

derivative $\left[\left(\frac{\partial \left(\frac{A_0}{A} \right)}{\partial [\text{O}_2]} \right)_{[\text{O}_2]=0} \right]^{-1}$ (Equation 8.31), and the full dependence (Equation 8.29)

for three different values of ϕ_{pi} : 0%, the best value (4% for *n*-butoxy, 5% for 2-pentoxy), and 20%. These values were chosen to illustrate the extent to which prompt isomerization will cause nonlinearity in the relative kinetics plots.

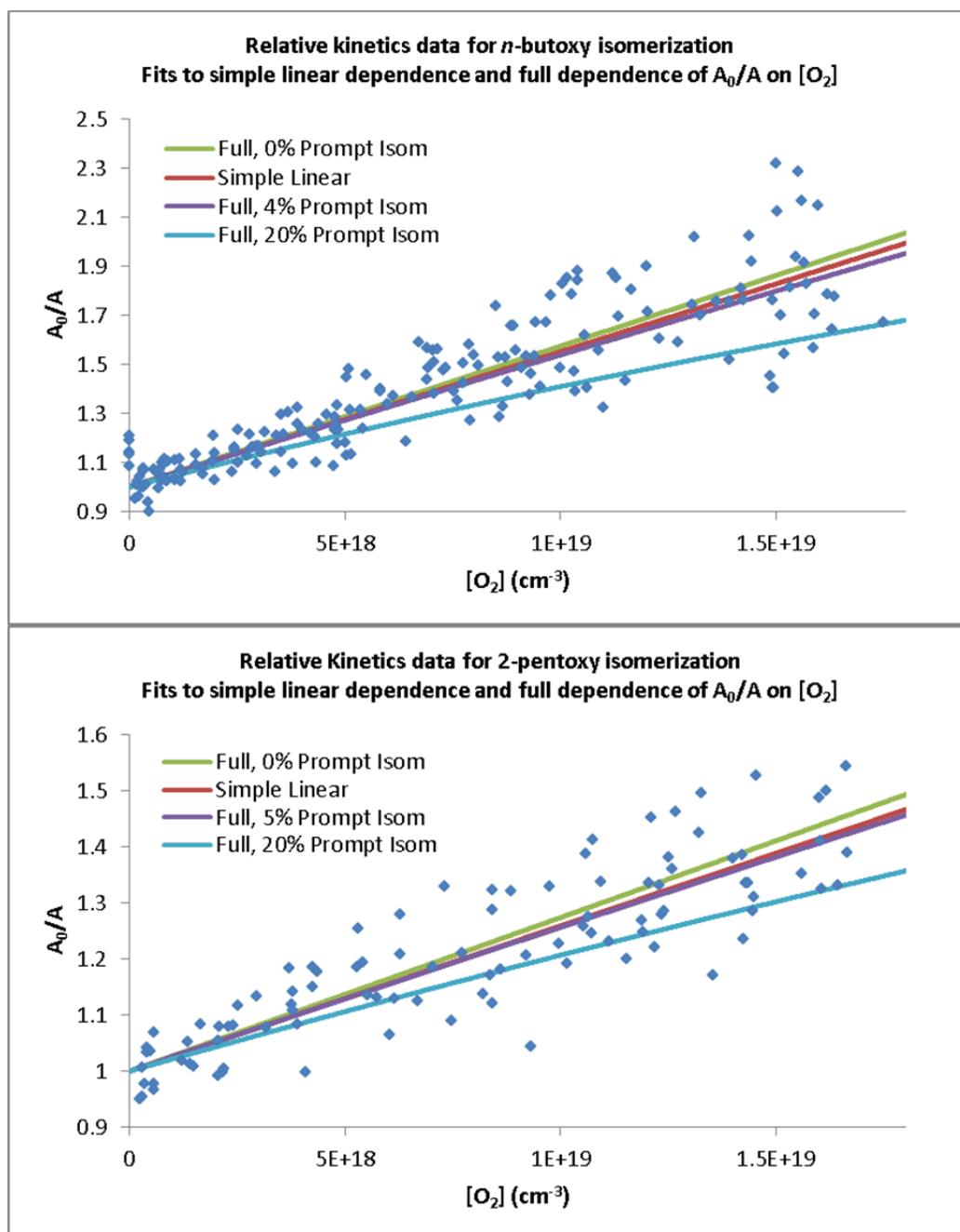


Figure 8.5. Fits of the functional forms of A_0/A vs $[O_2]$ to our CRDS relative kinetics for isomerization of *n*-butoxy (top) and 2-pentoxy (bottom). The simple linear fits (assuming only isomerization and reaction with O_2 are important, Equation 8.31 in the main text) are shown in red. The fits to the full form of A_0/A vs $[O_2]$ (Equation 8.29 in the main text) are

shown for 0% prompt isomerization (green), the best values of prompt isomerization (purple), and 20% prompt isomerization (blue). Adapted with permission from Sprague et al.³¹ Copyright 2012 American Chemical Society.

There are two key features of the fits presented in Figure 8.5. First, the simple linear fit and the full fits using the best value of prompt isomerization are in very good agreement across the entire range of $[O_2]$. This result is to be expected; the slopes of both lines at $[O_2] = 0$ are the same, and the relatively small fraction of prompt isomerization causes a small amount of nonlinearity. Second, large values of prompt isomerization (blue curves, $\phi_{pi}=20\%$) cause too much nonlinearity to model our CRDS data well. This supports our estimates of only 4%–5% of the alkoxy radicals undergoing prompt isomerization.

Discussion

With the new gas concentrations, photolysis ratios, and A_0/A vs $[O_2]$ data, we can readdress three points of interest: comparison of our relative rate k_{isom}/k_{O_2} to the values in the literature, the sensitivity of our correction factors to the rate constants and parameters used, and the nature of the products being detected 110 μs after formation of the alkoxy radicals (the time at which our CRDS measurements were made).

Comparison of k_{isom}/k_{O_2} Values to the Literature

Table 8.8 contains a comparison of our reanalyzed k_{isom}/k_{O_2} values for *n*-butoxy and 2-pentoxy to the rest of the chemical literature (in essence, an updated version of Table 8.1). Our reanalyzed value of k_{isom}/k_{O_2} for *n*-butoxy, $(1.69 \pm 0.15) \times 10^{19} \text{ cm}^{-3}$, fall on the lower end of the literature values ($1.9 \times 10^{19} \text{ cm}^{-3}$), while the initial analysis

($2.3 [+0.2, -0.3] \times 10^{19} \text{ cm}^{-3}$) fell at the upper end of the previously reported uncertainties. Our CRDS measurement has lower uncertainty on $k_{\text{isom}}/k_{\text{O}_2}$ (8%, 2σ) than any of the other measured values (minimum of 20%, 2σ) because we can directly detect the primary products of isomerization (HOR•, HOROO•), and their immediate secondary products (shown in Chapter 7 to be HORO•, HOROOH, HOROH, HORROH, and HOR'CHO). Previous experimental studies of the *n*-butoxy radical at 1 atm have obtained values for $k_{\text{isom}}/k_{\text{O}_2}$ ranging from 1.5×10^{19} to $2.1 \times 10^{19} \text{ cm}^{-3}$.^{148, 154-156, 159, 160} The IUPAC data evaluation reports a preferred value of $(2.1 \pm 1.8) \times 10^{19}$ for $k_{\text{isom}}/k_{\text{O}_2}$ at 298 K and 1 bar pressure, assuming k_{O_2} of $(1.4 \pm 0.7) \times 10^{-14} \text{ cm}^3 \text{ molecule}^{-1} \text{ s}^{-1}$.¹¹⁸ The majority of these studies^{28, 148, 154, 156, 159, 160} relied on detection of *n*-butanal (the product of alkoxy reaction with O₂) with no detection of the isomerization pathway. Cassanelli et al.¹⁵⁵ quantify the isomerization pathway by measuring 4-hydroxy butanal, a secondary product generated from further reaction of $\delta\text{-HOC}_4\text{H}_8\text{OO}\cdot$. These secondary product analyses are in good agreement with our measured $k_{\text{isom}}/k_{\text{O}_2}$ for *n*-butoxy of $(1.69 \pm 0.15) \times 10^{19} \text{ cm}^{-3}$ via direct detection of the isomerization product. This suggests that the secondary chemistry used in previous studies is well modeled, or that the errors in each secondary step cancel each other out. The results of the fast flow study by Hein,¹⁵⁹ which measured NO₂ in real time, were performed at lower pressures (38 torr) and cannot be compared directly to our results. Similarly, our measured $k_{\text{isom}}/k_{\text{O}_2}$ for 2-pentoxy of $(3.37 \pm 0.43) \times 10^{19} \text{ cm}^{-3}$ is in good agreement with Atkinson's previous measurements ($3.1 \times 10^{19} \text{ cm}^{-3}$, factor of 2 uncertainty).¹⁴⁵ Both our and Atkinson's $k_{\text{isom}}/k_{\text{O}_2}$ disagree with Dóbé's result by a factor of 20 ($k_{\text{isom}}/k_{\text{O}_2} = 0.15 \times 10^{19} \text{ cm}^{-3}$, uncertainty not reported).¹⁵⁷ Dóbé's study used methyl radicals to convert the $\delta\text{-HO-1-C}_5\text{H}_{10}\cdot$ to

2-hexanol, and it is possible that additional secondary chemistry could significantly alter their results.

Our reanalyzed value of $k_{\text{isom}}/k_{\text{O}_2}$ for 2-pentoxy is now higher than the value obtained from the initial analysis, and larger than Atkinson's best value. However, Atkinson's value of $k_{\text{isom}}/k_{\text{O}_2}$ has a large uncertainty (reported as a factor of 2), so our reanalyzed value still comfortably agrees with the only literature value available while having a far lower uncertainty.

Table 8.8. Comparison of relative rate constant determinations $k_{\text{isom}}/k_{\text{O}_2}$ and derived k_{isom} for *n*-butoxy and 2-pentoxy using our reanalysis of Mollner's CRDS data

	$k_{\text{isom}}/k_{\text{O}_2}$ (10^{19} cm^{-3}) ^a	k_{isom} (10^5 s^{-1}) ^b	Molecules detected	Method	<i>P</i> (<i>torr</i>)	Ref
<i>n</i>-butoxy	1.69 ± 0.15	2.4 ± 1.2	δ-hydroxy-<i>n</i>-butyl peroxy	Slow flow, CRDS (OH Str)	670	This work
	1.96 ± 0.25	2.7 ± 1.4	δ-hydroxy- <i>n</i> -butyl peroxy	Slow flow, CRDS (OH Str)	330	Chapter 7
	1.39 ± 0.47	2.0 ± 1.2	δ-hydroxy- <i>n</i> -butyl peroxy	Slow flow, CRDS (A-X)	330	Chapter 10
	2.0 ± 0.4	2.7 ± 1.5	Butyl nitrite, Butanal,	Static, FTIR	700	Cassanelli ¹⁵⁵
	1.5 ± 0.4	2.1 ± 1.2	4-hydroxy butanal	Static, GC	760	Cox ¹⁵⁶
	1.9 ± 0.4	2.7 ± 1.4	Butane, Butanal	Static, FTIR	700	Niki ¹⁴⁸
	2.1 ± 0.5	2.9 ± 1.6	Butyl nitrite, Butanal	Slow flow, GC	760	Cassanelli ¹⁶⁰
	1.8 ± 1.1	2.5 ± 2.0	Butyl nitrite, Butanal	Slow flow, GC	760	Cassanelli ¹⁶⁰
	1.8 ± 0.6	2.5 ± 1.5	Butane, Butanal	Static, FTIR	760	Geiger ¹⁶¹
	0.25 ± 0.19 ^c	0.35 ± 0.20 ^c	Butanal, 4-hydroxy butanal	Fast flow, LIF	38	Hein ¹⁵⁹
	1.6	2.2	OH and NO ₂	Static, GC	740	Carter ¹⁵⁴
	2.1 ± 1.8 ^d	2.9 ± 1.4 ^d		Recommendation	760	IUPAC ¹¹⁸
2-pentoxy	3.37 ± 0.43^e	2.7	δ-hydroxy-<i>n</i>-pentyl peroxy	Slow flow, CRDS (OH Str)	670	This work
	3.78 ± 1.62	3.0	δ-hydroxy- <i>n</i> -pentyl peroxy	Slow flow, CRDS (OH Str)	330	Chapter 7
	3.1 ^e	2.5 ^e	2-pentanone	Static, GC	700	Atkinson ¹⁴⁵
	0.15	0.12 ^f	Acetone, Acetaldehyde, 2-hexanol	Static, GC	760	Dóbe ¹⁵⁷

a) All uncertainties are 2σ . All studies other than the current work treat all alkoxy reactions besides isomerization and reaction with O₂ as negligible.

b) Computed k_{isom} assuming literature value of $k_{\text{O}_2} = (1.4 \pm 0.7) \times 10^{-14} \text{ cm}^3 \text{ molec}^{-1} \text{ s}^{-1}$ for *n*-butoxy,²⁸ and $k_{\text{O}_2} = 8 \times 10^{-15} \text{ cm}^3 \text{ molec}^{-1} \text{ s}^{-1}$ for 2-pentoxy (no estimate available for the uncertainty).¹⁴²

c) Unlike the other studies, Hein directly measured k_{isom} . In this table, we calculate the ratio $k_{\text{isom}}/k_{\text{O}_2}$ from Hein's measurement using the literature value of k_{O_2} .

d) The IUPAC recommendation for $k_{\text{isom}}/k_{\text{O}_2}$ is computed from their individual recommendations of the isomerization and O₂ reactions

e) The uncertainty on $k_{\text{isom}}/k_{\text{O}_2}$ is reported by Atkinson as a factor of 2.

f) Dóbe's study calculates k_{isom} from the relative rate $k_{\text{isom}}/k_{\text{decomp}}$ and their measured rate $k_{\text{decomp}} = 1.2 \times 10^4 \text{ s}^{-1}$. The $k_{\text{isom}}/k_{\text{O}_2}$ reported in this table uses the literature value of $k_{\text{O}_2} = 8 \times 10^{-15} \text{ cm}^3 \text{ s}^{-1}$ for 2-pentoxy.¹⁴²

While there is good agreement between our $k_{\text{isom}}/k_{\text{O}_2}$ values with the existing literature values, it should be noted that previous studies did not consider how additional alkoxy reactions (decomposition, recombination with NO, prompt isomerization) would affect the calculated value of $k_{\text{isom}}/k_{\text{O}_2}$. In our experiment, the difference between including and ignoring these three reactions is a factor of $X_{\text{kin}} \times X_{\text{prompt}}$ (0.93 ± 0.03 for

n-butoxy and 0.87 ± 0.04 for 2-pentoxy). Ignoring these corrections would cause us to systematically overestimate $k_{\text{isom}}/k_{\text{O}_2}$ (by 7% for *n*-butoxy or 13% for 2-pentoxy). It may be necessary to apply similar correction factors to the previous alkoxy relative kinetics experiments. For example, some of the previous *n*-butoxy experiments made use of elevated [NO], as high as 9×10^{14} molec cm^{-3} in order to drive secondary chemistry to completion.¹⁵⁵ For this [NO], the relative rate of reaction with NO to isomerization is $\frac{k_{\text{NO}}[\text{NO}\cdot]}{k_{\text{isom}}} = 0.12$, roughly equal to the 1σ uncertainties on the previously reported $k_{\text{isom}}/k_{\text{O}_2}$ values. It would be worthwhile to determine whether the previously reported $k_{\text{isom}}/k_{\text{O}_2}$ values for *n*-butoxy require revision in light of the correction factors $X_{\text{kin}} \times X_{\text{prompt}}$.

The reported correction factors and contributions are valid for our experimental conditions, $[\text{NO}] = 2 \times 10^{14}$ molec cm^{-3} ; changing [NO] will change the importance of the NO recombination reaction on the relative kinetics analysis. For example, if $[\text{NO}] = 9 \times 10^{14}$ molec cm^{-3} , alkoxy recombination with NO becomes very important compared to isomerization ($k_{\text{NO}}[\text{NO}]/k_{\text{isom}} = 0.12$). The change in [NO] from 2×10^{14} molec cm^{-3} to 9×10^{14} molec cm^{-3} will cause a significant change in X_{kin} , from 0.97 to 0.89. A separate correction factor X_{kin} must be computed for each of the previous studies due to the differing [NO] in each experiment.

Sensitivity of Correction Factors to Parameters

The parameters in Table 8.7 show that the major contributions to the correction factors are different for *n*-butoxy and 2-pentoxy. For *n*-butoxy, X_{kin} and X_{prompt} are roughly equal (0.97 and 0.96 respectively). The major contribution to X_{kin} is

recombination with NO ($\frac{k_{NO}[\text{NO}]}{k_{isom}} = 0.026$), while the effects of decomposition are negligible ($\frac{k_{decomp}}{k_{isom}} = 0.002$). In contrast, for 2-pentoxy, X_{kin} is a more significant correction than X_{prompt} (0.92 compared to 0.95). Decomposition is the major contributor to X_{kin} ($\frac{k_{decomp}}{k_{isom}} = 0.065$), although recombination with NO still remains significant ($\frac{k_{NO}[\text{NO}]}{k_{isom}} = 0.022$). The reported correction factors and contributions are valid for our experimental conditions, $[\text{NO}] = 2 \times 10^{14}$ molec cm^{-3} ; changing $[\text{NO}]$ will change the importance of the NO recombination reaction on the relative kinetics analysis.

The parameters within Table 8.7 are subject to somewhat large uncertainties. k_{decomp} is taken as the midpoint of aggregate kinetics experimental data,¹¹⁷ while k_{NO} is taken from a single experimental study.³² k_{isom} must be calculated from preliminary values of k_{isom}/k_{O_2} (discussed above as possibly being too large) and the value of k_{O_2} in the literature, determined from a single experimental study.²⁸ It is instructive to see how the correction factors X_{kin} and X_{prompt} , and therefore k_{isom}/k_{O_2} , vary as a function of each parameter.

Table 8.9 contains the partial derivatives of the correction factors with respect to each parameter at the optimal parameter values (found in Table 8.7). Figure 8.6 shows how the correction factors X_{kin} , X_{prompt} , and $X = X_{kin} \times X_{prompt}$ vary with respect to k_{decomp}/k_{isom} , $k_{NO}[\text{NO}]/k_{isom}$, and ϕ_{pi} , for both *n*-butoxy and 2-pentoxy. The derivatives of X with respect to the rate constant parameters are -0.944 for *n*-butoxy and -0.845 for 2-pentoxy. For both systems, the derivatives of X with respect to ϕ_{pi} are approximately 1.

Table 8.9. Sensitivity of Correction Factors X_{kin} , X_{prompt} , and X to parameters $k_{\text{decomp}}/k_{\text{isom}}$, $k_{\text{NO}}[\text{NO}]/k_{\text{isom}}$, and ϕ_{pi}

	<i>n</i> -butoxy			2-pentoxy		
	X_{kin}	X_{prompt}	X	X_{kin}	X_{prompt}	X
$\frac{\partial X}{\partial \left(\frac{k_{\text{decomp}}}{k_{\text{isom}}} \right)}$	-0.945	-0.036	-0.944	-0.847	-0.046	-0.845
$\frac{\partial X}{\partial \left(\frac{k_{\text{NO}}[\text{NO}]}{k_{\text{isom}}} \right)}$	-0.945	-0.036	-0.944	-0.847	-0.046	-0.845
$\frac{\partial X}{\partial \phi_{\text{pi}}}$	0	-1.026	-0.998	0	-1.077	-0.992

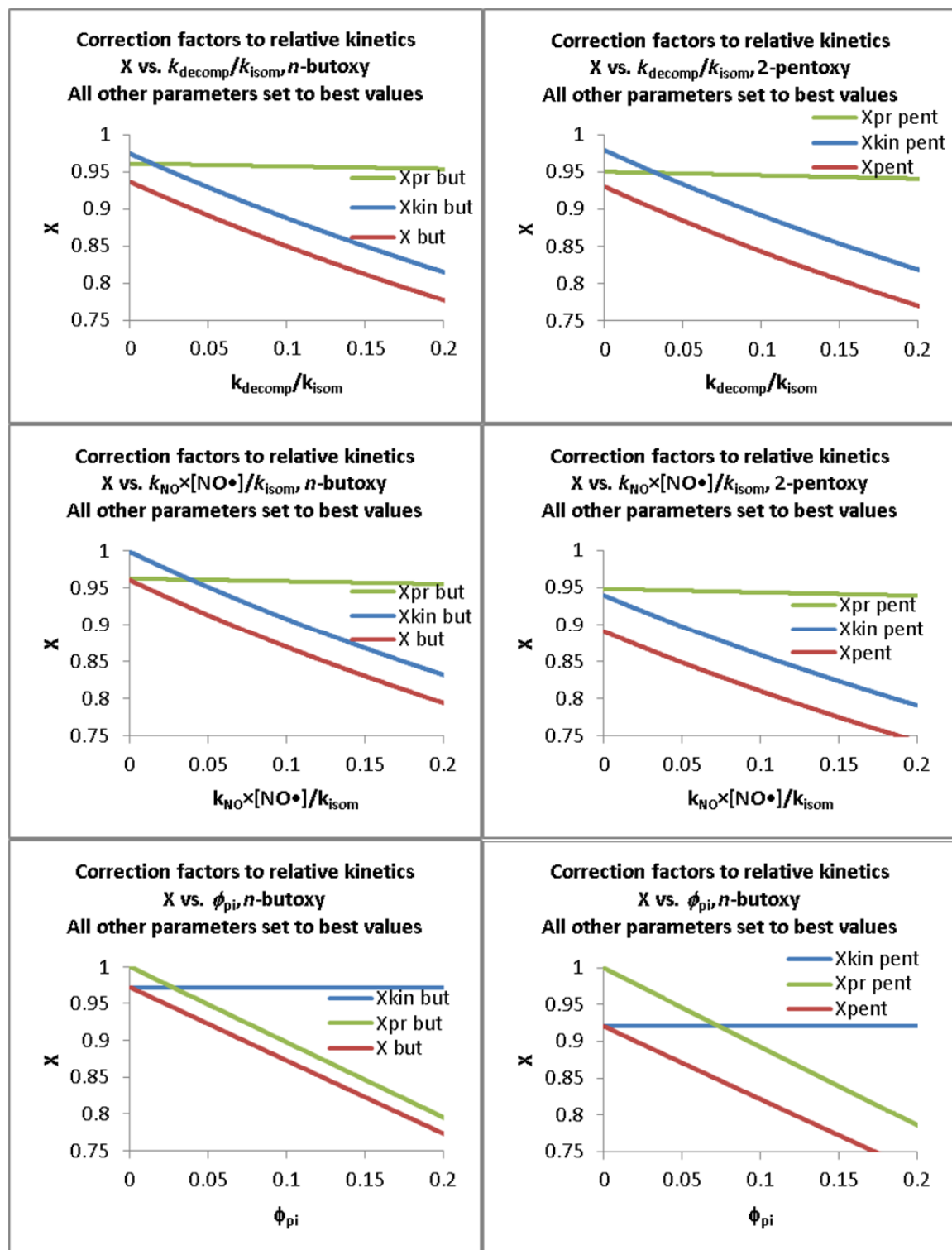


Figure 8.6. Variation of the correction factors X_{kin} , X_{prompt} , and X with respect to the parameters $k_{\text{decomp}}/k_{\text{isom}}$ (top), $k_{\text{NO}^\times}[\text{NO}]/k_{\text{isom}}$ (middle), and ϕ_{pi} (right), for *n*-butoxy (left) and 2-pentoxy (right). The correction factors are defined in the main text. For each plot, the remaining parameters are held constant at their best values, defined in the main text.

Large changes in any of the parameters will cause large changes in X . Of particular note are changes in $k_{\text{decomp}}/k_{\text{isom}}$ for 2-pentoxy (due to the scatter in values calculated from theoretical studies)¹¹⁷ and changes in $k_{\text{NO}\times[\text{NO}]} / k_{\text{isom}}$ (due to variances in $[\text{NO}]$ in the experiments found in the literature).^{28, 148, 154, 156, 159, 160} If we compare $k_{\text{decomp}} = 1 \times 10^4 \text{ s}^{-1}$ to $3 \times 10^4 \text{ s}^{-1}$ for 2-pentoxy (a factor of 3 difference), $k_{\text{decomp}}/k_{\text{isom}}$ changes from 0.032 to 0.097. The resulting change in X is -0.055 , significant with respect to the 2σ uncertainty of 0.05. A change in $[\text{NO}]$ from $2 \times 10^{14} \text{ molec cm}^{-3}$ to $4 \times 10^{14} \text{ molec cm}^{-3}$ (a factor of 2 increase in $[\text{NO}]$) changes $k_{\text{NO}[\text{NO}]} / k_{\text{isom}}$ from 0.026 to 0.052 (*n*-butoxy). This corresponds to a change in X of -0.037 , significant compared to the reported 2σ uncertainty on X of 0.03. The range of $[\text{NO}]$ in the literature is much larger than the example presented here, with some experiments using $[\text{NO}] = 1 \times 10^{15} \text{ molec cm}^{-3}$.^{155, 160} It is therefore not possible to define a single, approximate, correction factor that can be used across multiple alkoxy experiments to quickly reanalyze previous studies. Rather, each study must be treated separately with respect to experimental conditions to derive accurate correction factors.

Products Being Detected at 110 μs

In theory, one of the advantages to studying alkoxy isomerization using cavity ringdown spectroscopy is the ability to detect the primary products of isomerization: $\text{HOR}\cdot$ (and its dimer HORROH) and $\text{HORO}\cdot$. As observed in Chapter 7, significant secondary chemistry occurs in the first 110 μs after formation of the alkoxy radicals, the point at which the relative kinetics data collected by Mollner³⁰ and presented in this chapter were measured. **Therefore, we cannot claim that the relative kinetics that we**

measured in this chapter's OH stretch experiment are solely due to the primary products of isomerization. However, the direct kinetics measurements (Chapter 7) of the OH stretch peaks for both alkoxy isomerizations (n -C₄H₉O• and 2-C₅H₁₁O•) show that the OH stretch intensity remains constant for at least 800 μ s, indicating that regardless of secondary chemistry, the ν_1 band is a good measure of the isomerization pathway. These ideas give us confidence that **our reported $k_{\text{isom}}/k_{\text{O}_2}$ values are still valid, despite the fact that a significant fraction of the measured products were actually secondary products.** Computed intensities and modeled relative kinetics data are discussed in Chapter 9 to support the idea that secondary reactions will not affect the relative kinetics experiment.

To determine the products being detected 110 μ s after alkoxy generation, we use the same kinetics models that were used to analyze the spectroscopy experiment in Chapter 7. The model is described in detail in Chapter 9, here we only cite the results of the modeling. Rate constants used in the model were taken directly from the JPL Data Evaluation, NIST Kinetics Database, or the IUPAC Gas Kinetic Data Evaluation.^{27, 117, 118} For reactions where no kinetic information was available, best estimates were made from analogous reactions within the databases. All modeling was performed using the Kintecus 3.95 software.¹⁹¹

A separate model for 2-pentoxy was not created, given the lack of available rate constants and the added complexity due to the presence of an extra carbon. While the exact nature of the secondary products will differ between the n -butoxy and 2-pentoxy systems, it is expected that the relative concentrations of primary to secondary products should remain roughly the same.

Figure 8.7 shows the -OH containing products over the first 110 μs after $\text{C}_4\text{H}_9\text{O}\cdot$ formation for one set of typical experimental conditions used in the OH stretch experiment ($[\text{C}_4\text{H}_9\text{ONO}] = 2.0 \times 10^{16} \text{ molec cm}^{-3}$, $[\text{C}_4\text{H}_9\text{O}\cdot] = 2.0 \times 10^{14} \text{ molec cm}^{-3}$, $[\text{NO}] = 2.0 \times 10^{14} \text{ molec cm}^{-3}$, $p = 670 \text{ torr}$) for $[\text{O}_2] = 0$ (bath gas N_2) and $[\text{O}_2] = 2.2 \times 10^{19} \text{ molec cm}^{-3}$.

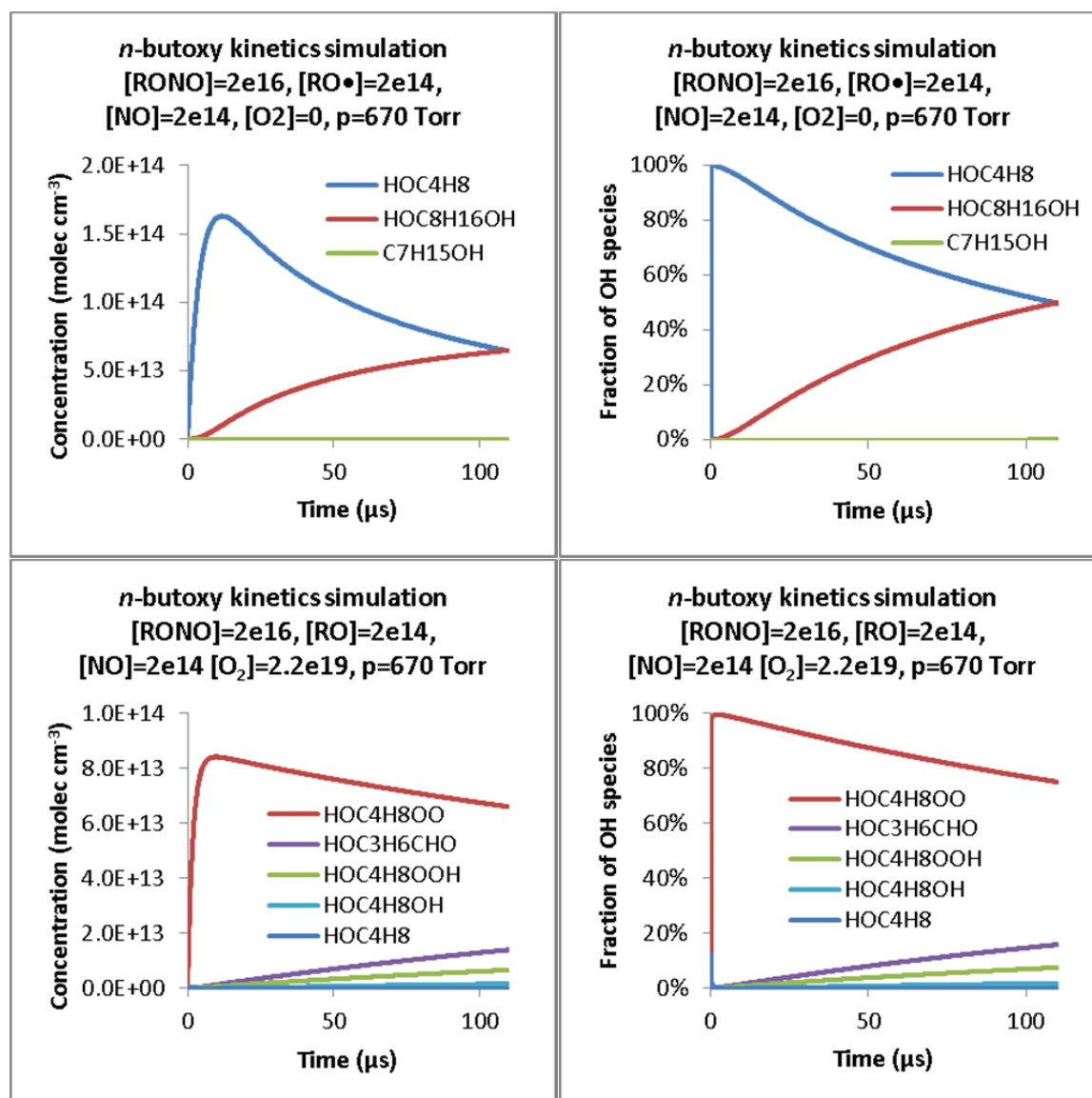


Figure 8.7. Kinetics model of the chemical species contributing to the OH stretch peak in the *n*-butoxy isomerization experiment, for $[O_2] = 0$ (top) and $[O_2] = 2.2 \times 10^{19} \text{ molec cm}^{-3}$ (bottom), at $p = 670$ torr, 298 K. The left panels show absolute concentrations, while the right panels show the fraction of total OH molecules that each chemical species makes up. In the absence of O_2 , the main products being detected at 110 μs are the direct isomerization product $\text{HOC}_4\text{H}_8\bullet$ (50%) and its dimer, $\text{HOC}_8\text{H}_{16}\text{OH}$ (50%). For 670 torr of O_2 , the main products being detected are the direct isomerization product with O_2 association, $\text{HOC}_4\text{H}_8\text{OO}\bullet$ (75%), and three end-products: $\text{HOC}_3\text{H}_6\text{CHO}$ (16%), $\text{HOC}_4\text{H}_8\text{OOH}$ (7%), and $\text{HOC}_4\text{H}_8\text{OH}$ (2%). Simulations run for $[\text{RONO}] = 2 \times 10^{16} \text{ molec cm}^{-3}$, $[\text{RO}\bullet] = 2 \times 10^{14} \text{ molec cm}^{-3}$, and $[\text{NO}] = 2 \times 10^{14} \text{ molec cm}^{-3}$.

Significant secondary chemistry has taken place 110 μs after formation of the initial $\text{C}_4\text{H}_9\text{O}\cdot$ radicals. In the absence of O_2 , only 50% of the OH stretch peak being detected is due to $\text{HOC}_4\text{H}_8\cdot$. The remaining isomerization product has dimerized into $\text{HOC}_8\text{H}_{16}\text{OH}$. A very small fraction (0.06%) exists as $\text{C}_7\text{H}_{15}\text{OH}$, formed from the reaction of $\text{HOC}_4\text{H}_8\cdot$ with the decomposition product $\text{C}_3\text{H}_7\cdot$.

In the presence of $[\text{O}_2]$, the nature of the products being detected changes. For $[\text{O}_2] = 2.2 \times 10^{19} \text{ molec cm}^{-3}$ (670 torr of O_2 , shown in Figure 8.7), four major products contribute to the OH stretch peak. Only 75% of this contribution is due to the primary isomerization product $\text{HOC}_4\text{H}_8\text{OO}\cdot$. The remainder of the OH stretch intensity comes from stable end-products of the isomerization reaction pathways: $\text{HOC}_3\text{H}_6\text{CHO}$ (16%), $\text{HOC}_4\text{H}_8\text{OOH}$ (7%), and $\text{HOC}_4\text{H}_8\text{OH}$ (2%). It should be noted that previous experiments by Cassanelli et al.^{155, 160} used FTIR detection of $\text{HOC}_3\text{H}_6\text{CHO}$ to measure $k_{\text{isom}}/k_{\text{O}_2}$. Our kinetics model agrees with their experiment: at very long times (10 ms after $\text{C}_4\text{H}_9\text{O}\cdot$ formation), nearly all of the isomerization product has been converted to $\text{HOC}_3\text{H}_6\text{CHO}$.

The effects of secondary chemistry can be minimized by detecting the isomerization products at an earlier time following generation of the alkoxy radicals, and reducing the absolute radical concentrations used. For example, for the $[\text{O}_2] = 2.2 \times 10^{19} \text{ molec cm}^{-3}$ simulation in Figure 8.7, 97% of the products being detected are $\text{HOC}_4\text{H}_8\text{OO}\cdot$ at 20 μs (as opposed to only 75% at 110 μs). Running the experiment at earlier times would allow for clean spectra of $\text{HOC}_4\text{H}_8\cdot$ or $\text{HOC}_4\text{H}_8\text{OO}\cdot$ to be obtained. However, care must be taken not to measure the ν_1 band before it has grown in completely (20 μs), as shown in Chapter 7. We have also observed in Chapter 7 that

reducing $[\text{RO}\cdot]$ by a factor of 2 leads to even cleaner spectra at 20 μs : >98% $\text{HOC}_4\text{H}_8\text{OO}\cdot$ as opposed to 97%.

Conclusions

Reanalysis of the *n*-butoxy and 2-pentoxy isomerization data sets (OH stretch CRDS experiment) have led to a drastic revision to $k_{\text{isom}}/k_{\text{O}_2}$, due to previous errors in calculations of $[\text{O}_2]$, $[\text{RONO}]$, photolysis flux, and data scaling. Furthermore, the effects of additional alkoxy reactions have been shown to be non-negligible, and have now been accounted for. After reanalysis, the $k_{\text{isom}}/k_{\text{O}_2}$ value for *n*-butoxy, $(1.69 \pm 0.15) \times 10^{19} \text{ cm}^{-3}$ (−26% revision), is in much better agreement with the rest of the chemical literature. Our value for 2-pentoxy, $(3.37 \pm 0.43) \times 10^{19} \text{ cm}^{-3}$ (+3% revision), has considerably less uncertainty than the only other value in the literature. We have also re-evaluated the amount of prompt isomerization that occurs following photolysis of the alkyl nitrites, and show that a significant amount of the alkoxy radicals do undergo prompt isomerization (4% for *n*-butoxy, 5 % for 2-pentoxy). Because the previous relative kinetics data were taken 110 μs after photolysis, a mixture of primary and secondary products were detected in the OH stretch experiments. In the absence of O_2 , the major products being detected were the primary isomerization product $\text{HOC}_4\text{H}_8\cdot$ (50%), and its dimer $\text{HOC}_8\text{H}_{16}\text{OH}$ (50%). In the presence of 670 torr of O_2 , the major products being detected were the primary isomerization product $\text{HOC}_4\text{H}_8\text{OO}\cdot$ (75%) and three end-products: $\text{HOC}_3\text{H}_6\text{CHO}$ (16%), $\text{HOC}_4\text{H}_8\text{OOH}$ (7%), and $\text{HOC}_4\text{H}_8\text{OH}$ (2%).

The alkoxy studies reported in the literature do not consider reactions besides isomerization and reaction with O_2 . It is currently unknown to what extent these previous

studies are affected by other alkoxy reaction pathways. It is possible that the correction factors reported in this chapter must be applied to the previously reported $k_{\text{isom}}/k_{\text{O}_2}$, although this idea has not yet been explored.

Acknowledgements

We thank Andrew K. Mollner for his work on the initial alkoxy relative kinetics experiments. The experiments and reanalysis performed in this chapter were funded under NASA Upper Atmosphere Research Program Grants NAG5-11657, NNG06GD88G, and NNX09AE21G2, California Air Resources Board Contract 03-333 and 07-730, National Science Foundation CHE-0515627, and a Department of Defense National Defense Science and Engineering Graduate Fellowship (NDSEG).

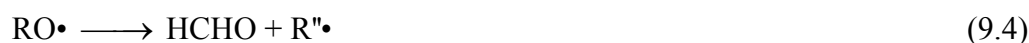
Chapter 9—A Quantum Chemistry Explanation of the Alkoxy Relative Kinetics “Low [O₂] Anomaly”

Abstract

In Chapter 7, we observed that the primary products of alkoxy isomerization, HOR• (absence of O₂) and HOROO• (presence of O₂), have ν_1 (OH stretch) bands with different peak shapes and intensities. We used these peaks to measure the relative kinetics of alkoxy isomerization to reaction with O₂ ($k_{\text{isom}}/k_{\text{O}_2}$) in Chapter 8 by measuring the relative absorbance A_0/A vs [O₂]. This relationship is expected to be approximately linear, with A_0/A increasing with O₂. However, for very low [O₂] ($0 < [\text{O}_2] < 3 \times 10^{16}$ molec cm⁻³), we observe anomalous behavior: A_0/A is not equal to 1 at [O₂] = 0, and A_0/A decreases as [O₂] increases. The work in this thesis chapter explains the cause of this anomalous behavior for A_0/A , and the general factors affecting the OH stretch frequency and intensity in alkoxy systems. The difference in absorption cross sections for the OH stretch of HOR• and HOROO• is the main factor causing the observed anomalous behavior for A_0/A . The OH stretch absorption behavior is governed by the relative location of the hydroxy group to the radical center of HOR• or the peroxy group of HOROO•. Quantum chemistry calculations were performed on alcohols (ROH), hydroxyalkyl radicals (HOR•), and hydroxyalkylperoxy radicals (HOROO•), for R = methyl, ethyl, propyl, butyl, and pentyl. OH stretch frequencies and integrated absorption cross sections were calculated at the B3LYP/6-31+G(d,p) level of theory and basis. The results were combined with a kinetics model of the *n*-butoxy system to simulate the apparent A_0/A as a function of [O₂].

Introduction

We have shown in Chapters 7 and 8 that CRDS is capable of measuring the relative kinetics of alkoxy isomerization to reaction with O_2 (k_{isom}/k_{O_2}) via the ν_1 (OH stretch band of the primary isomerization products, HOR• (absence of O_2) and HOROO• (presence of O_2). A summary of the results of Chapter 8 are provided here. We measure the relative absorbance A_0/A of the ν_1 band as a function of $[O_2]$, where A is the absorbance for a given O_2 , and A_0 is the absorbance for “[O_2] = 0” (intercept of regression lines). Considering all of the reactions of alkoxy radicals (RO•, Reactions 9.1–9.5) and hot radicals (RO•*, Reactions 9.6 and 9.7)



we obtain Equations 9.8–9.11: the relationship of A_0/A vs $[O_2]$ and the value of k_{isom}/k_{O_2} .

$$\frac{A_0}{A} = \frac{\left(\frac{\frac{k_{O_2}}{k_{isom}}}{1 + \frac{k_{NO}[NO]}{k_{isom}} + \frac{k_{decomp}}{k_{isom}}} \right) [O_2] + 1}{\left(\frac{\phi_{pi} \frac{k_{O_2}}{k_{isom}}}{1 + \phi_{pi} \left(\frac{k_{NO}[NO]}{k_{isom}} + \frac{k_{decomp}}{k_{isom}} \right)} \right) [O_2] + 1} \quad (9.8)$$

$$\frac{k_{isom}}{k_{O_2}} = \left[\left(\frac{\partial \left(\frac{A_0}{A} \right)}{\partial [O_2]} \right)_{[O_2]=0} \right]^{-1} \times X_{kin} \times X_{prompt}, \quad (9.9)$$

where

$$X_{kin} = \frac{1}{1 + \frac{k_{decomp}}{k_{isom}} + \frac{k_{NO} [NO]}{k_{isom}}}, \quad (9.10)$$

$$X_{prompt} = \frac{(1 - \phi_{pi})}{1 + \phi_{pi} \left(\frac{k_{decomp}}{k_{isom}} + \frac{k_{NO} [NO]}{k_{isom}} \right)}. \quad (9.11)$$

Since ϕ_{pi} (prompt isomerization fraction) was determined to be much less than 1 (4% for *n*-butoxy, 5% for 2-pentoxy), Equation 9.8 shows that A_0/A will increase as $[O_2]$ increases. Figure 9.1 shows the relative kinetics data for *n*-butoxy, as measured by the ν_1 bands of HOR• and HOROO•. For $[O_2] > 3 \times 10^{16}$ molec cm^{-3} , we observe the trend predicted by Equation 9.8: an increase in A_0/A with increasing $[O_2]$. However, we do not observe the trend predicted by Equation 9.8 at low $[O_2]$. For $0 < [O_2] < 3 \times 10^{16}$ molec cm^{-3} , we observe a decrease in A_0/A with increasing $[O_2]$. Furthermore, Equation 9.8 predicts $A_0/A = 1$ for $[O_2] = 0$; however, in Figure 9.1, we observe $A_0/A = 1.2$ at $[O_2] = 0$.

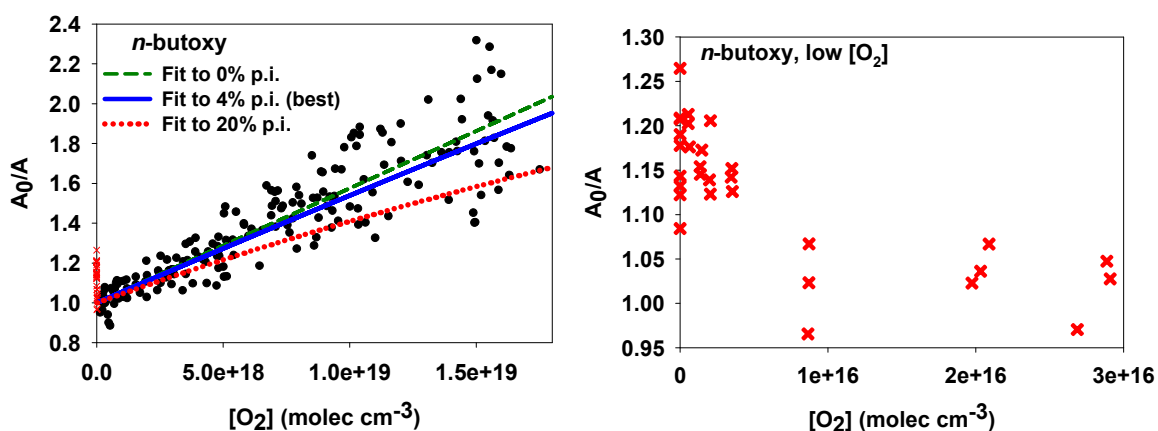


Figure 9.1. A_0/A plotted as a function of $[O_2]$ for *n*-butoxy using the ν_1 CRDS absorbance (Chapter 7). For $[O_2] > 3 \times 10^{16}$ molec cm^{-3} (black markers), we observe the expected decrease in A/A_0 with $[O_2]$. For $0 < [O_2] < 3 \times 10^{16}$ molec cm^{-3} , the *n*-butoxy data show an apparent increase in A/A_0 with $[O_2]$ (points marked by red Xs on the left panel, expanded in the right panel). Because of this effect, only absorbance data with $[O_2] > 1 \times 10^{17}$ molec cm^{-3} were used in the fits to determine k_{isom}/k_{O_2} (Chapter 8). Adapted with permission from Sprague et al.³¹ Copyright 2012 American Chemical Society.

One explanation for this behavior is that different isomerization products are detected in each $[O_2]$ regime. When $[O_2]$ far exceeds $[HOR\bullet]$, then addition of O_2 to the isomerization product (Reaction 9.2) is immediate. Thus, any spectroscopic measurement of the “isomerization product” is actually a measurement of $HOROO\bullet$. In contrast, at very low O_2 , the amount of $HOR\bullet$ that reacts with O_2 is small (or none, for $[O_2] = 0$). In this case, the primary “isomerization product” being detected is $HOR\bullet$. We have already observed in Chapter 7 that the ν_1 bands of $HOR\bullet$ and $HOROO\bullet$ have different intensities and shapes. This effect may be one of the causes of nonlinearity in the plot of A_0/A vs $[O_2]$ at low $[O_2]$, where the identity of the isomerization product changes from $HOR\bullet$ to $HOROO\bullet$. Additionally, these two species are only the primary products of alkoxy isomerization. The relative kinetics measurements presented in Figure 9.1 were made 110 μs after the initial formation of alkoxy radicals. As discussed in Chapter 8, secondary

products form in appreciable quantities on this timescale. For example, at $[\text{RO}\cdot] = 2 \times 10^{14} \text{ molec cm}^{-3}$ and $[\text{O}_2] = 0$, 50% of the isomerization product $\text{HOR}\cdot$ can self-react to form HORROH (Chapter 8). If the spectroscopic properties of these secondary products differ significantly from $\text{HOR}\cdot$ and $\text{HOROO}\cdot$, then we must account for the presence of these products. Thus, in order to fully interpret the relative kinetics data presented in Chapter 8, a theoretical analysis of the primary and secondary products is necessary (spectroscopy, modeled concentrations, simulated A_0/A vs $[\text{O}_2]$).

If the OH stretch absorption changes between the $\text{HOR}\cdot$ and $\text{HOROO}\cdot$ formed from alkoxy chemistry, a larger chemical physics question is presented: how does the OH stretch absorption vary as a function of the relative positions of the hydroxy group and peroxy group/radical center? This question arises due to the contrasting behavior observed for $\delta\text{-HOC}_4\text{H}_8\cdot/\delta\text{-HOC}_4\text{H}_8\text{OO}\cdot$ (Chapter 7) and $\text{HOCH}_2\text{OO}\cdot$ (HMP) (Chapter 4). We have observed that the OH stretch frequencies of $\delta\text{-HOC}_4\text{H}_8\cdot$, $\delta\text{-HOC}_4\text{H}_8\text{OO}\cdot$ and *n*-butanol are all approximately the same (3675 cm^{-1} for the radicals, 3671 cm^{-1} for *n*-butanol). In contrast, the OH stretch of HMP is red shifted by 70 cm^{-1} compared to methanol (3611 cm^{-1} for HMP, 3681 cm^{-1} for methanol). It is possible that the band position changes because of the relative location of the peroxy and hydroxy groups (far apart for the butoxy case, on the same carbon for HMP). This idea makes sense based on the argument that the dipole derivative should change greatly if the peroxy group is interacting with the hydroxy group, either through the overall electronic structure or by hydrogen bonding. However, no calculations on these hydroxyalkylperoxy systems have been performed to support this idea. Although other groups have computed harmonic

vibrational frequencies,^{19-21, 108, 111, 136-138} these calculations were used only to obtain a zero-point vibrational energy: individual frequencies and intensities were not reported.

In this thesis chapter, we describe a combined quantum chemical and kinetics modeling study to determine the spectroscopic properties of the chemical species formed during alkoxy reactions. Our focus is on the harmonic frequency and integrated intensity of the OH stretch vibrational mode. Although the motivation for this study comes from our work on *n*-butoxy and 2-pentoxy, we also seek to answer the larger chemical physics questions of whether similar behavior persists with different sized alkoxy radicals, and what factors determine the OH stretch absorption behavior. To determine the effect of carbon chain length on the spectroscopic properties, we examine the species ROH, HOR•, and HOROO• for R = methyl, ethyl, *n*-propyl, *n*-butyl, *n*-pentyl, and isopentyl. To determine the effect of the relative positions of the hydroxy group and the peroxy group/radical center, we examine ROH, HOR•, and HOROO• for various straight chain isomers of R = pentyl. We then constructed a kinetics model for the reactions of *n*-butoxy, performed further quantum chemical calculations on any -OH containing species within the model, and simulated the strength of the OH stretch spectroscopic band based on the kinetics model and harmonic frequencies. These results were used to construct a plot of the apparent A_0/A vs $[O_2]$ for comparison to the relative kinetics data presented in Chapter 8.

Methods

Kinetics Model

As observed by the modeling in Chapters 7 and 8, secondary products of alkoxy isomerization contribute to the observed OH stretch intensity. It is necessary to determine what products form and to what extent they form over the entire range of $[O_2]$ used in the relative kinetics experiment, so that all of the observed intensity is accounted for. In order to determine what chemical species are being detected, we constructed a kinetics model for the reactions of *n*-butoxy radical. All kinetics modeling was performed in Kintecus 3.95.¹⁹¹ Table 9.1 summarizes the reactions and rate constants used in the kinetics model. Most of the rate constants are taken from the JPL Data Evaluation, IUPAC Kinetics database, and the NIST Kinetics database.^{27, 117, 118} The rate constant for *n*-butoxy isomerization is based on our measured k_{isom}/k_{O_2} from Chapter 8, since it is these data that we seek to explain. The impact of choosing a different k_{isom}/k_{O_2} is explored in the *Discussion* section.

Note that this model is much larger than necessary to correctly model alkoxy chemistry over 110 μs . This design was intentional; the model is capable of modeling chemistry over milliseconds, as was illustrated in Chapters 7 and 8.

Table 9.1. Kinetics Model for *n*-butoxy. Rate constants were taken from JPL,²⁷ IUPAC,¹¹⁸ or estimated from similar reactions in NIST,¹¹⁷ unless otherwise specified

$A^{a,b}$	E_a/R (K)	reaction	source
1) Alkoxy Primary Reactions			
2.37E+05	0	C4H9O \rightleftharpoons HOC4H8	Chapter 8
5.80E+02	0	C4H9O \rightleftharpoons C3H7+HCHO	Atkinson ¹⁴²
1.40E-14	0	C4H9O+O2 \rightleftharpoons C3H7CHO+HO2	Atkinson ¹⁴²
2) Association with O ₂			
7.50E-12	0	HOC4H8+O2 \rightleftharpoons HOC4H8OO	IUPAC

8.00E-12	0	$C_3H_7+O_2 \Rightarrow C_3H_7OO$	IUPAC
3) Additional peroxy formation by HO_2+HCHO			
9.70E-15	-625	$HO_2+HCHO \Rightarrow HOCH_2OO$	JPL
4) Peroxy destruction by NO			
9.00E-12	0	$HOC_4H_8OO+NO \Rightarrow HOC_4H_8O+NO_2$	IUPAC, NIST
4.00E-13	0	$HOC_4H_8OO+NO \Rightarrow HOC_4H_8ONO_2$	NIST
9.00E-12	0	$C_3H_7OO+NO \Rightarrow C_3H_7O+NO_2$	IUPAC, NIST
4.00E-13	0	$C_3H_7OO+NO \Rightarrow C_3H_7ONO_2$	NIST
2.80E-12	-300	$HOCH_2OO+NO \Rightarrow HOCH_2O+NO_2$	JPL
4.00E-13	0	$HOCH_2OO+NO \Rightarrow HOCH_2ONO_2$	JPL
5) Alkyl radical dimerization or association			
5.00E-11	0	$HOC_4H_8+HOC_4H_8 \Rightarrow HOC_8H_{16}OH$	NIST
1.69E-11	0	$C_3H_7+C_3H_7 \Rightarrow C_6H_{14}$	NIST
1.55E-10	0	$C_4H_9+C_4H_9 \Rightarrow C_4H_{10}+C_4H_8$	NIST
1.70E-11	0	$HOC_3H_6+HOC_3H_6 \Rightarrow HOC_6H_{12}OH$	similar to NIST
1.00E-12	0	$HOC_3H_6CH(OH)+HOC_3H_6CH(OH) \Rightarrow HOC_3H_6CHO+HOC_4H_8OH$	similar to NIST
1.70E-11	0	$HOC_4H_8+C_3H_7 \Rightarrow C_7H_{15}OH$	similar to NIST
1.70E-11	0	$HOC_4H_8+C_4H_9 \Rightarrow C_8H_{17}OH$	similar to NIST
1.70E-11	0	$HOC_4H_8+HOC_3H_6 \Rightarrow HOC_7H_{14}OH$	similar to NIST
5.00E-12	0	$HOC_4H_8+HOC_3H_6CH(OH) \Rightarrow C_4H_9OH+HOC_3H_6CHO$	similar to NIST
1.70E-11	0	$C_3H_7+C_4H_9 \Rightarrow C_7H_{16}$	similar to NIST
1.70E-11	0	$C_3H_7+HOC_3H_6 \Rightarrow C_6H_{13}OH$	similar to NIST
5.00E-12	0	$C_3H_7+HOC_3H_6CH(OH) \Rightarrow C_3H_8+HOC_3H_6CHO$	similar to NIST
1.70E-11	0	$C_4H_9+HOC_3H_6 \Rightarrow C_7H_{15}OH$	similar to NIST
5.00E-12	0	$C_4H_9+HOC_3H_6CH(OH) \Rightarrow C_4H_{10}+HOC_3H_6CHO$	similar to NIST
5.00E-12	0	$HOC_3H_6+HOC_3H_6CH(OH) \Rightarrow C_3H_7OH+HOC_3H_6CHO$	similar to NIST
6) Peroxy Self Reactions			
5.00E-13	0	$HOC_4H_8OO+HOC_4H_8OO \Rightarrow HOC_4H_8O+HOC_4H_8O+O_2$	NIST
7.80E-14	-1000	$C_3H_7OO+C_3H_7OO \Rightarrow C_3H_7O+C_3H_7O+O_2$	IUPAC
5.50E-12	0	$HOCH_2OO+HOCH_2OO \Rightarrow HOCH_2O+HOCH_2O+O_2$	IUPAC
5.70E-14	-750	$HOCH_2OO+HOCH_2OO \Rightarrow HCOOH+HOCH_2OH+O_2$	IUPAC
3.50E-13	-430	$HO_2+HO_2 \Rightarrow H_2O_2+O_2$	JPL
1.70E-33	-1000	$HO_2+HO_2+M \Rightarrow H_2O_2+O_2+M$	JPL
7) Peroxy Cross Reactions			
5.00E-13	0	$HOC_4H_8OO+C_3H_7OO \Rightarrow HOC_4H_8O+C_3H_7O+O_2$	NIST
5.00E-13	0	$HOC_4H_8OO+HOCH_2OO \Rightarrow HOC_4H_8O+HOCH_2O+O_2$	NIST
8.00E-12	0	$HOC_4H_8OO+HO_2 \Rightarrow HOC_4H_8OOH+O_2$	JPL
5.00E-13	0	$C_3H_7OO+HOCH_2OO \Rightarrow C_3H_7O+HOCH_2O+O_2$	NIST
8.00E-12	0	$C_3H_7OO+HO_2 \Rightarrow C_3H_7OOH+O_2$	JPL
1.20E-11	0	$HOCH_2OO+HO_2 \Rightarrow HOCH_2OOH+O_2$	IUPAC
8) $RONO_2$ Eliminations			
1.60E-12	0	$HOC_4H_8ONO_2+OH \Rightarrow HONO_2+HOC_4H_8O$	IUPAC
5.80E-13	0	$C_3H_7ONO_2+OH \Rightarrow HONO_2+C_3H_7O$	IUPAC
3.00E-13	0	$HOCH_2ONO_2+OH \Rightarrow HONO_2+HOCH_2O$	NIST
9) HORO and smaller RO reactions			
1.58E+11	3270	$HOC_4H_8O \Rightarrow HOC_3H_6CH(OH)$	NIST
2.00E+13	9560	$HOC_4H_8O \Rightarrow HCHO+HOC_3H_6$	NIST
1.40E-14	0	$HOC_4H_8O+O_2 \Rightarrow HO_2+HOC_3H_6CHO$	NIST
2.60E-11	0	$HOC_3H_6CH(OH)+O_2 \Rightarrow HOC_3H_6CHO+HO_2$	NIST
5.00E+13	7850	$C_3H_7O \Rightarrow HCHO+C_2H_5$	NIST
2.60E-14	253	$C_3H_7O+O_2 \Rightarrow HO_2+C_2H_5CHO$	IUPAC
7.80E-12	0	$C_2H_5+O_2 \Rightarrow C_2H_5OO$	IUPAC
3.80E-15	0	$C_2H_5+O_2 \Rightarrow C_2H_4+HO_2$	IUPAC

7.50E-12	0	HOC3H6+O2==>HOC3H6OO	IUPAC
10) Reactions with NO: Alkoxy and small peroxies			
3.32E-11	0	C4H9O+NO==>C4H9ONO	NIST
3.30E-11	0	HOC4H8O+NO==>HOC4H8ONO	NIST
4.00E-11	0	HOCH2O+NO==>HOCH2ONO	NIST
3.80E-11	0	C3H7O+NO==>C3H7ONO	IUPAC
9.00E-12	0	C2H5OO+NO==>C2H5O+NO2	NIST
1.60E-15	16.78	C2H5OO+NO==>C2H5ONO2	NIST
9.00E-12	0	HOC3H6OO+NO==>HOC3H6O+NO2	NIST
4.00E-13	0	HOC3H6OO+NO==>HOC3H6ONO2	NIST
11) Alkyl Reactions with NO			
6.64E-14	0	HOC4H8+NO==>HOC4H8NO	NIST
6.64E-14	0	C3H7+NO==>C3H7NO	NIST
6.51E-12	0	HOC3H6CH(OH)+NO==>HOC3H6CHO+HNO	NIST
6.64E-14	0	HOC3H6+NO==>HOC3H6NO	NIST
2.30E-13	0	C2H5+NO==>C2H5NO	NIST
12) Alkyl Reactions with HO ₂			
4.00E-11	0	C4H9+HO2==>C4H9O+OH	NIST
4.00E-11	0	HOC4H8+HO2==>HOC4H8O+OH	NIST
4.00E-11	0	C3H7+HO2==>C3H7O+OH	NIST
4.00E-11	0	HOC3H6+HO2==>HOC3H6O+OH	NIST
2.60E-11	0	HOC3H6CH(OH)+HO2==>HOC3H6CHO+H2O2	NIST
13) Alkyl Nitrite reaction with OH			
2.00E-12	0	C4H9ONO+OH==>C4H9+HONO2	NIST
2.00E-12	0	C4H9ONO+OH==>C4H9O+HONO	NIST
14) Butyl and butyl peroxy reactions with NO, OH, and other peroxies			
6.64E-14	0	C4H9+NO==>C4H9NO	NIST
7.50E-12	0	C4H9+O2==>C4H9OO	IUPAC
9.00E-12	0	C4H9OO+NO==>C4H9O+NO2	IUPAC
4.00E-13	0	C4H9OO+NO==>C4H9ONO2	NIST
1.60E-12	0	C4H9ONO2+OH==>C4H9O+HONO2	IUPAC
4.00E-13	0	C4H9OO+C4H9OO==>C4H9O+C4H9O+O2	NIST
5.00E-13	0	C4H9OO+HOC4H8OO==>C4H9O+HOC4H8O+O2	NIST
5.00E-13	0	C4H9OO+C3H7OO==>C4H9O+C3H7O+O2	NIST
5.00E-13	0	C4H9OO+HOCH2OO==>C4H9O+HOCH2O+O2	NIST
15) Peroxy reactions with alkyl			
4.00E-11	0	C4H9OO+C4H9==>C4H9O+C4H9O	NIST
4.00E-11	0	C4H9OO+HOC4H8==>HOC4H8O+C4H9O	NIST
4.00E-11	0	C4H9OO+C3H7==>C3H7O+C4H9O	NIST
4.00E-11	0	C4H9OO+HOC3H6==>C4H9O+HOC3H6O	NIST
4.00E-11	0	HOC4H8OO+C4H9==>HOC4H8O+C4H9O	NIST
4.00E-11	0	HOC4H8OO+HOC4H8==>HOC4H8O+HOC4H8O	NIST
4.00E-11	0	HOC4H8OO+C3H7==>HOC4H8O+C3H7O	NIST
4.00E-11	0	HOC4H8OO+HOC3H6==>HOC4H8O+HOC3H6O	NIST
4.00E-11	0	C3H7OO+C4H9==>C3H7O+C4H9O	NIST
4.00E-11	0	C3H7OO+HOC4H8==>C3H7O+HOC4H8O	NIST
4.00E-11	0	C3H7OO+C3H7==>C3H7O+C3H7O	NIST
4.00E-11	0	C3H7OO+HOC3H6==>C3H7O+HOC3H6O	NIST
4.00E-11	0	HOCH2OO+C4H9==>HOCH2O+C4H9O	NIST
4.00E-11	0	HOCH2OO+HOC4H8==>HOCH2O+HOC4H8O	NIST
4.00E-11	0	HOCH2OO+C3H7==>HOCH2O+C3H7O	NIST
4.00E-11	0	HOCH2OO+HOC3H6==>HOCH2O+HOC3H6O	NIST
1.00E-11	0	C4H9OO+HOC3H6CH(OH)==>C4H9OOH+HOC3H6CHO	NIST

1.00E-11	0	HOC4H8OO+HOC3H6CH(OH) \rightleftharpoons HOC4H8OOH+HOC3H6CHO	NIST
1.00E-11	0	C3H7OO+HOC3H6CH(OH) \rightleftharpoons C3H7OOH+HOC3H6CHO	NIST
1.00E-11	0	HOCH2OO+HOC3H6CH(OH) \rightleftharpoons HOCH2OOH+HOC3H6CHO	NIST
16) Peroxy reactions with alkoxy			
2.00E-12	0	HOC4H8OO+C4H9O \rightleftharpoons HOC4H8OOH+C3H7CHO	NIST
2.00E-12	0	HOC4H8OO+HOC4H8O \rightleftharpoons HOC4H8OOH+HOC3H6CHO	NIST
2.00E-12	0	HOC4H8OO+C3H7O \rightleftharpoons HOC4H8OOH+C2H5CHO	NIST
2.00E-12	0	HOC4H8OO+HOCH2O \rightleftharpoons HOC4H8OOH+HCOOH	NIST
2.00E-12	0	C4H9OO+C4H9O \rightleftharpoons C4H9OOH+C3H7CHO	NIST
2.00E-12	0	C4H9OO+HOC4H8O \rightleftharpoons C4H9OOH+HOC3H6CHO	NIST
2.00E-12	0	C4H9OO+C3H7O \rightleftharpoons C4H9OOH+C2H5CHO	NIST
2.00E-12	0	C4H9OO+HOCH2O \rightleftharpoons C4H9OOH+HCOOH	NIST
2.00E-12	0	C3H7OO+C4H9O \rightleftharpoons C3H7OOH+C3H7CHO	NIST
2.00E-12	0	C3H7OO+HOC4H8O \rightleftharpoons C3H7OOH+HOC3H6CHO	NIST
2.00E-12	0	C3H7OO+C3H7O \rightleftharpoons C3H7OOH+C2H5CHO	NIST
2.00E-12	0	C3H7OO+HOCH2O \rightleftharpoons C3H7OOH+HCOOH	NIST
2.00E-12	0	HOCH2OO+C4H9O \rightleftharpoons HOCH2OOH+C3H7CHO	NIST
2.00E-12	0	HOCH2OO+HOC4H8O \rightleftharpoons HOCH2OOH+HOC3H6CHO	NIST
2.00E-12	0	HOCH2OO+C3H7O \rightleftharpoons HOCH2OOH+C2H5CHO	NIST
2.00E-12	0	HOCH2OO+HOCH2O \rightleftharpoons HOCH2OOH+HCOOH	NIST
17) Peroxy reactions with OH			
1.00E-10	0	C4H9OO+OH \rightleftharpoons C4H9OH+O2	NIST
1.00E-10	0	HOC4H8OO+OH \rightleftharpoons HOC4H8OH+O2	NIST
1.00E-10	0	C3H7OO+OH \rightleftharpoons C3H7OH+O2	NIST
1.00E-10	0	HOCH2OO+OH \rightleftharpoons HOCH2OH+O2	NIST
1.00E-10	0	C2H5OO+OH \rightleftharpoons C2H5OH+O2	NIST
18) HO _x and NO _x chemistry (from the Global Kinetics Model used for Part 3 of this thesis)			
1.61E-12	0	OH+NO2 \rightleftharpoons HOONO	JPL
7.22E-01	0	HOONO \rightleftharpoons OH+NO2	JPL
1.07E-12	0	HO2+NO2 \rightleftharpoons HO2NO2	JPL
6.67E-02	0	HO2NO2 \rightleftharpoons HO2+NO2	JPL
6.73E-15	0	NO+NO2 \rightleftharpoons N2O3	JPL
3.22E+05	0	N2O3 \rightleftharpoons NO+NO2	JPL
2.59E-14	0	NO2+NO2 \rightleftharpoons N2O4	JPL
9.13E+04	0	N2O4 \rightleftharpoons NO2+NO2	JPL
1.17E-12	0	NO2+NO3 \rightleftharpoons N2O5	JPL
4.02E-02	0	N2O5 \rightleftharpoons NO2+NO3	JPL
5.88E-12	0	OH+OH \rightleftharpoons H2O2	JPL
6.90E-12	0	OH+NO \rightleftharpoons HONO	JPL
9.99E-12	0	OH+NO2 \rightleftharpoons HONO2	JPL
1.80E-12	0	OH+OH \rightleftharpoons H2O+O	JPL
4.80E-11	-250	OH+HO2 \rightleftharpoons H2O+O2	JPL
1.80E-12	0	OH+H2O2 \rightleftharpoons H2O+HO2	JPL
3.50E-12	-250	HO2+NO \rightleftharpoons OH+NO2	JPL

a) Units of A are cm³ molec⁻¹ s⁻¹ for bimolecular reactions, and s⁻¹ for unimolecular reactions

b) Termolecular reactions have already been converted to the effective bimolecular rate constant: the listed rate constants are valid at 670 torr, 298 K only

The initial conditions used for the kinetics simulations are summarized in Table

9.2. These conditions (gas concentrations, temperature, total pressure) were chosen to

match the experimental conditions used in the experiments described in Chapter 8. Briefly, *n*-butoxy was formed in the reaction cell by photolysis of *n*-butyl nitrite (C_4H_9ONO) using 351 nm light. Approximately 1% of C_4H_9ONO was photolyzed. For typical $[C_4H_9ONO]_0$ of 2×10^{16} molec cm^{-3} , the resulting *n*-butoxy concentration was 2×10^{14} molec cm^{-3} . We ran simulations for $[O_2] = 0$ and for the range 1×10^{13} molec cm^{-3} to 2×10^{19} molec cm^{-3} (four $[O_2]$ values per order of magnitude). Simulations were run for 110 μs , with an integration step size of 5 ns. The concentration of all OH containing species at 110 μs was recorded for each $[O_2]$.

Table 9.2. Kinetics Model Parameters

Parameter	Value
$[C_4H_9ONO]_0$	2×10^{16} molec cm^{-3}
$[C_4H_9O]_0$	2×10^{14} molec cm^{-3}
$[NO]_0$	2×10^{14} molec cm^{-3}
$[O_2]_0$	$(0-2.17) \times 10^{19}$ molec cm^{-3} ^a
$[N_2]_0$	$(0-2.17) \times 10^{19}$ molec cm^{-3} ^a
Total Pressure	670 torr
Temperature	298 K
Simulation Time	110 μs
Integration Step Size	5 ns

a) The sum of $[O_2]$ and $[N_2]$ was kept constant at 2.17×10^{19} molec cm^{-3}

Quantum Chemistry Calculations

Our strategy for choosing which chemical species to run calculations on consists of three parts. We would like to examine whether carbon chain length affects the OH stretch absorption properties amongst hydroxyalkyl and hydroxyalkylperoxy radicals. We therefore chose to run calculations on the primary products (HOR• and HOROO•) and parent alcohols (ROH), for a variety of alkane chain lengths (up to five carbons). To obtain chemical species similar to the ones observed in alkoxy isomerization, we placed

the hydroxy group and radical center/peroxy group on opposite ends of the carbon chain. Secondly, we wish to investigate how the relative positions of the hydroxy group and the peroxy group/radical center affect the OH stretch position and intensity. To accomplish this, we ran calculations on all of the straight carbon chain isomers of pentanol, hydroxypentyl, and hydroxypentylperoxy. Finally, we would like to determine the OH stretch absorption properties of all relevant species within our kinetics model. We therefore chose to run calculations on all species within the *n*-butoxy kinetics model that contain an OH stretch.

Table 9.3 contains the chemical species that we examined for this study. All quantum chemistry calculations were performed in Gaussian 03W,⁷⁹ on a single processor, dual core workstation. Geometry optimizations and harmonic frequency calculations were performed at the B3LYP/6-31+G(d,p) level of theory and basis. Molecules with three or fewer carbons were also analyzed at CCSD/6-31+G(d,p) to ensure that the relative intensities were independent of the level of theory. We did not choose to scale any of the frequencies or intensities, as we are only interested in the relative OH stretch band positions and absorption cross sections. The “Density=Current” command was used in all calculations to ensure that the B3LYP or CCSD wavefunction was used to perform orbital population and electric dipole analysis (details in Appendix C). Additionally, multiple conformers of the *n*-butoxy system were analyzed to determine whether or not different conformers would have different relative intensities.

Table 9.3. Chemical Species Calculated for This Study

Part 1: Carbon Chain Size Study (ROH, HOR•, HOROO•) B3LYP/6-31+G(d,p)		
Alcohol	Hydroxyalkyl	Hydroxyalkylperoxy
CH ₃ OH	HOCH ₂ •	HOCH ₂ OO•
CH ₃ CH ₂ OH	HOCH ₂ CH ₂ •	HOCH ₂ CH ₂ OO•
CH ₃ CH ₂ CH ₂ OH	HOCH ₂ CH ₂ CH ₂ •	HOCH ₂ CH ₂ CH ₂ OO•
CH ₃ CH ₂ CH ₂ CH ₂ OH	HOCH ₂ CH ₂ CH ₂ CH ₂ •	HOCH ₂ CH ₂ CH ₂ CH ₂ OO•
CH ₃ CH ₂ CH ₂ CH ₂ CH ₂ OH	HOCH ₂ CH ₂ CH ₂ CH ₂ CH ₂ •	HOCH ₂ CH ₂ CH ₂ CH ₂ CH ₂ OO•
CH ₃ CH ₂ CH ₂ CH(OH)CH ₃	CH ₃ CH(OH)CH ₂ CH ₂ CH ₂ •	CH ₃ CH(OH)CH ₂ CH ₂ CH ₂ OO•
Part 2: Check that B3LYP and CCSD give similar results CCSD/6-31+G(d,p)		
Alcohol	Hydroxyalkyl	Hydroxyalkylperoxy
CH ₃ OH	HOCH ₂ •	HOCH ₂ OO•
CH ₃ CH ₂ OH	HOCH ₂ CH ₂ •	HOCH ₂ CH ₂ OO•
CH ₃ CH ₂ CH ₂ OH	HOCH ₂ CH ₂ CH ₂ •	HOCH ₂ CH ₂ CH ₂ OO•
Part 3: Change relative positions of OO and OH groups on pentoxy system B3LYP/6-31+G(d,p)		
Alcohol	Hydroxyalkyl	Hydroxyalkylperoxy
CH ₃ CH ₂ CH ₂ CH ₂ CH ₂ OH	•CH ₂ CH ₂ CH ₂ CH ₂ CH ₂ OH	•OOCH ₂ CH ₂ CH ₂ CH ₂ CH ₂ OH
	CH ₃ CH(•)CH ₂ CH ₂ CH ₂ OH	CH ₃ CH(OO•)CH ₂ CH ₂ CH ₂ OH
	CH ₃ CH ₂ CH(•)CH ₂ CH ₂ OH	CH ₃ CH ₂ CH(OO•)CH ₂ CH ₂ OH
	CH ₃ CH ₂ CH ₂ CH(•)CH ₂ OH	CH ₃ CH ₂ CH ₂ CH(OO•)CH ₂ OH
	CH ₃ CH ₂ CH ₂ CH ₂ CH(•)OH	CH ₃ CH ₂ CH ₂ CH ₂ CH(OO•)OH
CH ₃ CH ₂ CH ₂ CH(OH)CH ₃	•CH ₂ CH ₂ CH ₂ CH(OH)CH ₃	•OOCH ₂ CH ₂ CH ₂ CH(OH)CH ₃
	CH ₃ CH(•)CH ₂ CH(OH)CH ₃	CH ₃ CH(OO•)CH ₂ CH(OH)CH ₃
	CH ₃ CH ₂ CH(•)CH(OH)CH ₃	CH ₃ CH ₂ CH(OO•)CH(OH)CH ₃
	CH ₃ CH ₂ CH ₂ C(•)(OH)CH ₃	CH ₃ CH ₂ CH ₂ C(OO•)(OH)CH ₃
	CH ₃ CH ₂ CH ₂ CH(OH)CH ₂ •	CH ₃ CH ₂ CH ₂ CH(OH)CH ₂ OO•
CH ₃ CH ₂ CH(OH)CH ₂ CH ₃	•CH ₂ CH ₂ CH(OH)CH ₂ CH ₃	•OOCH ₂ CH ₂ CH(OH)CH ₂ CH ₃
	CH ₃ CH(•)CH(OH)CH ₂ CH ₃	CH ₃ CH(OO•)CH(OH)CH ₂ CH ₃
	CH ₃ CH ₂ C(•)(OH)CH ₂ CH ₃	CH ₃ CH ₂ C(OO•)(OH)CH ₂ CH ₃
Part 4: OH containing molecules in the <i>n</i> -butoxy system B3LYP/6-31+G(d,p)		
Alcohols, Diols	Hydroxyalkyl, Hydroxyalkylperoxy	Hydroxyalkoxy, Hydroxyalkylperoxide
C ₃ H ₇ OH	HOC ₄ H ₈ •	HOC ₄ H ₈ O•
C ₇ H ₁₅ OH	HOC ₄ H ₈ OO•	HOC ₄ H ₈ OOH
HOC ₄ H ₈ OH		C ₃ H ₇ OOH
HOC ₈ H ₁₆ OH		

The frequencies and integrated intensities for each OH stretch mode were recorded. For the *n*-butoxy system, these integrated intensities were entered into the kinetics model to determine the overall OH stretch absorption. These overall absorptions

were scaled to the cross section of $\delta\text{-HOC}_4\text{H}_8\text{OO}\cdot$ to obtain an apparent A_0/A for use in our plots of A_0/A vs $[\text{O}_2]$.

Results

We present the results of this study in three parts. First, we present the kinetics simulations of the *n*-butoxy system at $[\text{O}_2] = 0$ and $[\text{O}_2] = 2.17 \times 10^{19}$ molec cm^{-3} . The results of the kinetics simulations show us that only 50%–81% of the $-\text{OH}$ containing products at 110 μs exist as the primary isomerization products $\text{HOR}\cdot$ or $\text{HORO}\cdot$, depending on $[\text{O}_2]$. The results show that self-reaction of $\text{HOR}\cdot$ at low $[\text{O}_2]$ is very important. At high $[\text{O}_2]$, secondary products make up 25% of the total $-\text{OH}$ containing species, attributable to the stable end-products $\text{HOR}'\text{CHO}$, HOROOH , and HOROH . Second, we present the quantum chemical calculations on the ν_1 (OH stretch) harmonic frequencies and intensities. These results give us insight into how carbon chain length and relative position of the hydroxy group and the peroxy group/radical center affect the OH stretch absorption properties. We observe that addition of the peroxy group to a hydroxyalkyl radical will increase the OH stretch intensity by 15%–20%, with deviant behavior observed when both the hydroxy and peroxy groups are located on the same or adjacent carbons. Most of the secondary products have cross sections similar to the hydroxyalkyl radicals: only the hydroxyalkylperoxy radicals have a higher cross section. Finally, we combine the quantum chemical cross sections with the *n*-butoxy kinetics simulations to build up the plot of A_0/A vs $[\text{O}_2]$, analogous to the plot presented in Chapter 8. Our simulations are able to simultaneously reproduce the low $[\text{O}_2]$ anomaly and provide a good fit to the relative kinetics data, indicating that the primary cause of

the low $[O_2]$ anomaly in Figure 9.1 is the change in products being detected as $[O_2]$ is increased.

Kinetics Model for *n*-butoxy

The concentrations of OH containing species from our kinetics model are shown in Figure 9.2, for $[O_2] = 0$ (left) and $[O_2] = 2.17 \times 10^{19}$ molec cm^{-3} (right), for the first 110 μs after formation of the *n*-butoxy radicals. Although full kinetics data exist for all of the $[O_2]$ that we examined, we examine these two concentrations in full detail to determine the major products and important secondary chemistry for low and high $[O_2]$.

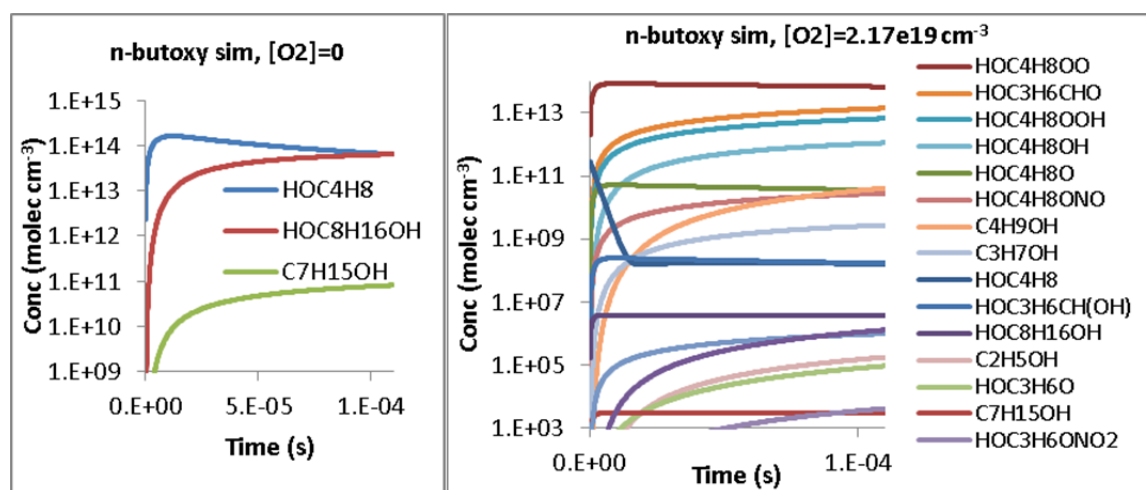


Figure 9.2. Concentration (log scale) vs time for the OH containing chemical species in the *n*-butoxy kinetics model, for $[O_2] = 0$ (left) and $[O_2] = 2.17 \times 10^{19}$ molec cm^{-3} (right).

The kinetics simulations allow us to answer the question “What isomerization product is being detected at 110 μs ?” At $[O_2] = 0$, only three products are being detected. 50% of the isomerization product exists as $HOC_4H_8\bullet$, the direct product of isomerization (Reaction 9.1). 50% of the isomerization product exists as 1,8-octanediol ($HOC_8H_{16}OH$), formed from the self-reaction of $HOC_4H_8\bullet$ (Reaction 9.12).

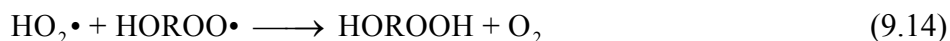


n-heptanol (C₇H₁₅OH), a minor product accounting for less than 0.05% of the total isomerization product, forms from reaction of the decomposition product C₃H₇• with the direct isomerization product HOC₄H₈• (Reaction 9.13).



In contrast to the low [O₂] kinetics data, we observe the formation of many different secondary products for [O₂] = 2.17 × 10¹⁹ molec cm⁻³. Most of these products are present in small concentrations: the four products in highest concentration account for 99.9% of the OH stretch containing species. As expected, very little of the isomerization product exists as HOC₄H₈•, and the major product observed is HOC₄H₈OO• (Reaction 9.2), accounting for 75% of the observed products with OH groups.

The remaining three species are stable end-products on the isomerization pathway. 16% of the products exist as hydroxybutanal (HOC₃H₆CHO), formed through multiple series of reactions. This product is one of the “classic” molecules detected in end-product studies,^{155, 161} yet it forms in appreciable quantities even within 110 μs. 7% of the isomerization product exists as a hydroperoxide, HOC₄H₈OOH. The hydroperoxide forms from the reaction of HOC₄H₈OO• with the HO₂ formed from reaction of the alkoxy radical with O₂ (Reactions 9.3 and 9.14).



1% of the products exist as 1,4-*n*-butyldiol (HOC₄H₈OH), formed from the reaction of HOROO• with OH. The OH is formed when one of the decomposition products (C₃H₇•) reacts with the HO₂ from Reaction 9.9 (Reactions 9.4, 9.3, 9.15, 9.16).



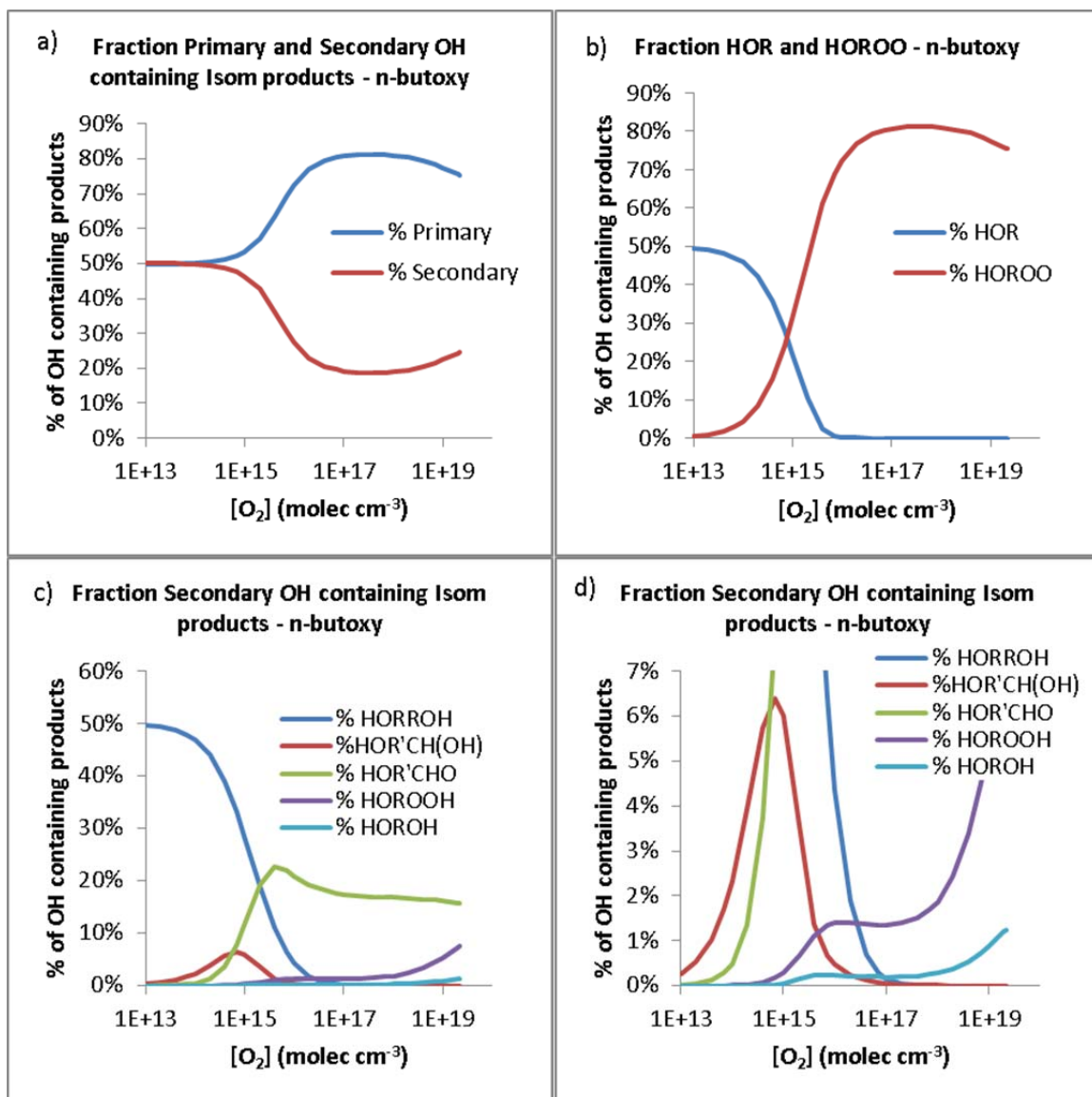


Figure 9.3. Description of the -OH containing products of the *n*-butoxy chemical system at 110 μs , as a function of O_2 . The plots show the percentage of -OH containing species that each individual chemical contributes. Part (a) shows the percentage of -OH containing molecules that exist as primary isomerization products ($HOR\bullet$, $HOROO\bullet$) and secondary isomerization products ($HORROH$, $HOROH$, $HOR'CHO$, $HOR'CH\bullet(OH)$ and $HOROOH$), where $R = C_4H_8$. Part (b) shows the distribution of primary products. Parts (c) and (d) show the distribution of secondary products.

On the basis of Figure 9.3, we can describe what isomerization products are being detected for each $[O_2]$. For $[O_2] < 10^{14}$ molec cm^{-3} , 50% of the product exists as $HOR\bullet$, and 50% exists as $HOC_8H_{16}OH$. In the range 10^{14} molec $cm^{-3} < [O_2] < 10^{17}$ molec cm^{-3} ,

the distribution of isomerization products changes rapidly. The percentage of secondary products decreases rapidly (to 20% at $[\text{O}_2] = 10^{17} \text{ molec cm}^{-3}$). Meanwhile, the primary products change from $\text{HOR}\cdot$ to $\text{HORO}\cdot$, with nearly all primary product existing as $\text{HORO}\cdot$ at $[\text{O}_2] = 10^{16} \text{ molec cm}^{-3}$. For $[\text{O}_2] > 10^{16} \text{ molec cm}^{-3}$, most of the products remain as $\text{HORO}\cdot$, with a slight decrease in relative abundance with $[\text{O}_2]$ (81% at $[\text{O}_2] = 10^{17} \text{ molec cm}^{-3}$, 75% at $[\text{O}_2] = 2.17 \times 10^{19} \text{ molec cm}^{-3}$). The secondary products are present in significant concentrations, and their relative abundances change with $[\text{O}_2]$. The dominant secondary product for $[\text{O}_2] > 10^{16} \text{ molec cm}^{-3}$ is the stable end-product $\text{HOR}'\text{CHO}$. For $[\text{O}_2] > 10^{18} \text{ molec cm}^{-3}$, $[\text{HORO}\cdot\text{H}]$ becomes appreciable, rising from 2%–7% over the range $(1\text{--}21) \times 10^{18} \text{ molec cm}^{-3}$.

Considering all of the kinetics data in Figure 9.3, we observe that secondary chemistry effects affect the 110 μs CRDS experiment at all $[\text{O}_2]$, with the largest fraction of secondary products observed for $[\text{O}_2] < 10^{16} \text{ molec cm}^{-3}$. We also note that the identity of the primary product changes rapidly from $\text{HOR}\cdot$ to $\text{HORO}\cdot$ as $[\text{O}_2]$ is increased over the range $10^{14}\text{--}10^{16} \text{ molec cm}^{-3}$. Careful attention is needed when interpreting alkoxy isomerization data for $[\text{O}_2] < 10^{16} \text{ molec cm}^{-3}$. In contrast, we note that the distribution of products remains relatively constant over the range $10^{17} \text{ molec cm}^{-3} < [\text{O}_2] < 10^{19} \text{ molec cm}^{-3}$. For these values of $[\text{O}_2]$, minimal changes in the OH spectrum due to changing products will be observed. This justifies the procedures in Chapter 8 of only performing linear regression on relative kinetics data with $10^{17} \text{ molec cm}^{-3} < [\text{O}_2] < 10^{19} \text{ molec cm}^{-3}$.

Quantum Chemical Calculations

The results of the quantum chemical calculations can be divided into five parts. First, we examine how the carbon chain length affects the OH stretch absorption properties for species with up to five carbons. In order to obtain compounds most relevant to alkoxy isomerization studies, we only look at isomers with the hydroxy group and radical center/peroxy group as far away as possible. Second, we show that the relative frequencies and intensities of the OH stretch do not change when the level of theory is increased from B3LYP to CCSD. This result allows us to use the faster B3LYP calculations to accurately analyze the OH stretch properties. Third, we show that the OH stretch properties are not significantly changed amongst different conformers of the *n*-butoxy isomerization products. Fourth, we examine the dependence of the OH stretch properties on the relative positions of the hydroxy and radical center/peroxy groups for a straight chain pentyl backbone. The results show that the main factor governing the relative OH stretch properties is the relative positions of the hydroxy group and radical center/peroxy groups, while the second most important factor is the absolute position of the groups on the carbon chain. Fifth, we calculate the OH stretch frequencies and intensities of all –OH containing species in the *n*-butoxy chemical system. These data will then be combined with the kinetics model to interpret Garland's CRDS measurements.

Effect of carbon chain size on OH stretch properties

One of the goals of this study was to answer the general chemical physics question of how the OH stretch frequency and intensity differs between an alcohol

(ROH), a hydroxyalkyl radical (HOR•), and a hydroxyalkyl peroxy radical (HORO•), and how the OH stretch is affected by alkyl chain length. Table 9.4 summarizes the harmonic frequencies (ω_e) and intensities (I) of these chemical species, for R = methyl, ethyl, *n*-propyl, *n*-butyl, *n*-pentyl, and isopentyl. For these species, the hydroxy group and radical center/peroxy group were placed on opposite ends of the carbon chain, in order to obtain chemical species that best resemble products of alkoxy isomerization. In particular, the *n*-butyl and isopentyl chemical species were reported in Chapters 7 and 8, and these calculations provide insight into what factors affect those experiments.

Table 9.4. Harmonic frequencies and intensities for straight chain alcohols, alkoxy radicals, and hydroxyalkylperoxy radicals, at B3LYP/6-31+G(d,p).

R	ROH		HOR•		HORO•		$I_{\text{HORO•}}/I_{\text{HOR•}}$
	ω_e^a	I^a	ω_e^a	I^a	ω_e^a	I^a	
Methyl	3839	28	3839	59	3799	53	0.9
Ethyl	3836	26	3836	26	3844	46	1.8
<i>n</i> -propyl	3836	26	3839	30	3836	35	1.2
<i>n</i> -butyl	3841	29	3841	30	3842	35	1.2
<i>n</i> -pentyl	3835	25	3834	25	3836	30	1.2
isopentyl	3828	20	3828	21	3829	25	1.2

a) Harmonic frequencies are in cm^{-1} , intensities are in km mol^{-1}

Examination of the frequencies and intensities in Table 9.4 reveals different behavior for R = methyl, R = ethyl, and all larger R groups. Considering R = methyl, we notice that the OH stretch position is the same for CH_3OH and $\text{HOCH}_2\bullet$, while the OH stretch is red shifted for $\text{HOCH}_2\text{OO}\bullet$ by 40 cm^{-1} . This is in qualitative agreement with the OH stretch spectrum of HMP presented in Chapter 4, where we observed a 60 cm^{-1} red shift compared to methanol. We also notice that the integrated intensities of the OH stretch for $\text{HOCH}_2\bullet$ and $\text{HOCH}_2\text{OO}\bullet$ are nearly twice as large as for CH_3OH . In contrast to this behavior, for R = ethyl, we notice that the OH stretch frequencies of $\text{C}_2\text{H}_5\text{OH}$ and

$\text{HOC}_2\text{H}_4\bullet$ are roughly equal, while $\text{HOC}_2\text{H}_4\text{OO}\bullet$ is blue shifted by 8 cm^{-1} . The integrated intensity of the OH stretch is roughly constant for $\text{C}_2\text{H}_5\text{OH}$ and $\text{HOC}_2\text{H}_4\bullet$, while the intensity nearly doubles for $\text{HOC}_2\text{H}_4\text{OO}\bullet$. It is likely that the relative proximity of the hydroxyl group to the radical center or peroxy group is causing the large changes in intensity and frequencies (as will be shown later for the different isomers for $\text{R} = \text{pentyl}$).

The remaining species in Table 9.4 ($\text{R} = n\text{-propyl}$, $n\text{-butyl}$, $n\text{-pentyl}$, isopentyl) exhibit similar behavior when comparing ROH , $\text{HOR}\bullet$, and $\text{HORO}\bullet$. For these R groups, the OH stretch frequency does not change between the three chemical species. In all cases, addition of the peroxy group increases the integrated intensity by a factor of 15–20%. For all of these R groups except $n\text{-C}_3\text{H}_7$, ROH and $\text{HOR}\bullet$ have the same integrated intensity. The similarity in OH stretch behavior amongst the different alkyl groups suggests that when the hydroxyl group and radical center or peroxy group are far enough apart, the OH stretch is only affected by the large change in dipole that occurs upon addition of a peroxy group.

Spectroscopic Properties as a Function of Level of Theory and Basis

Before embarking on any further analysis of the calculations, we must ensure that the relative trends in OH stretch frequency and intensity are not affected by the level of theory that we are using. B3LYP is a relatively cheap method, and can be used to study larger alkoxy systems without the need for a supercomputer. More sophisticated methods, such as CCSD, will presumably be more accurate with respect to spectroscopic properties. The problem is that CCSD frequency calculations are relatively expensive due to the lack of analytical gradients in Gaussian 03W,⁷⁹ and can only be used to study smaller alkoxy

systems. As an illustration of this point, the harmonic frequency calculation for $\text{HOC}_3\text{H}_6\text{OO}\cdot$ took 2100 times as much cpu time at CCSD/6-31+G(d,p) than at B3LYP/6-31+G(d,p). Because the cpu scaling of CCSD is of order N^6 (where N = number of basis functions), CCSD calculations on butyl and pentyl systems are both outside of the reach of our 32-bit, single processor workstation. However, if the OH stretch properties are in agreement between the two methods, then we can feel comfortable using the B3LYP results for larger systems (butyl or larger) where CCSD calculations would be unfeasible.

Table 9.5 contains the OH stretch harmonic frequencies and intensities at B3LYP/6-31+G(d,p) and CCSD/6-31+G(d,p) for ROH, $\text{HOR}\cdot$, and $\text{HORO}\cdot$, for R = methyl, ethyl, and *n*-propyl. For these species, the hydroxy group and radical center/peroxy group were placed on opposite ends of the carbon chain in order to obtain chemical species that best resemble products of alkoxy isomerization. The B3LYP results are listed normally while the CCSD results are in parentheses. We expect the absolute frequencies and intensities to differ between the two methods; however, if B3LYP is an acceptable level of theory, the relative intensities amongst ROH, $\text{HOR}\cdot$, and $\text{HORO}\cdot$ should be the same for B3LYP and CCSD. We immediately notice that the trends in harmonic frequencies between ROH, $\text{HOR}\cdot$, and $\text{HORO}\cdot$ is the same between the two methods. Additionally, the ratio of intensities is roughly the same between the two methods. The generally good agreement between the two methods suggests that we can trust our B3LYP results for all of the systems being studied.

Table 9.5. Harmonic frequencies and intensities for straight chain alcohols, alkoxy radicals, and hydroxyalkylperoxy radicals, at B3LYP/6-31+G(d,p) (top), and CCSD/6-31+G(d,p) (bottom, in parentheses).

R	ROH		HOR•		HORO•		$I_{\text{HORO•}}/I_{\text{HOR•}}$
	ω_e^a	I^a	ω_e^a	I^a	ω_e^a	I^a	
Methyl	3839 (3912)	28 (26)	3839 (3913)	59 (53)	3799 (3884)	53 (50)	0.9 (1.0)
Ethyl	3836 (3905)	26 (24)	3835 (3904)	26 (24)	3844 (3913)	46 (42)	1.8 (1.7)
<i>n</i> -propyl	3836 (3903)	26 (24)	3839 (3905)	30 (27)	3836 (3902)	35 (32)	1.2 (1.2)

a) Harmonic frequencies are in cm^{-1} , intensities are in km mol^{-1}

Similarly, we can also investigate how sensitive the relative frequencies and relative intensities are to the choice of basis set. Table 9.6 compares the B3LYP frequencies and intensities for two basis sets: 6-31+G(d,p) (plain numbers) and aug-cc-pVTZ (in parentheses). We observe very little change in relative frequencies and intensities upon changing the basis set, indicating that our choice of 6-31+G(d,p) will be adequate for our study.

Table 9.6. Harmonic Frequencies and Intensities for straight chain alcohols, alkoxy radicals, and hydroxyalkylperoxy radicals, at B3LYP/6-31+G(d,p) (top), and B3LYP/aug-cc-pVTZ (bottom, in parentheses).

R	ROH		HOR•		HORO•		$I_{\text{HORO•}}/I_{\text{HOR•}}$
	ω_e^a	I^a	ω_e^a	I^a	ω_e^a	I^a	
Methyl	3839 (3829)	28 (31)	3839 (3824)	59 (62)	3799 (3785)	53 (53)	0.9 (0.9)
Ethyl	3836 (3825)	26 (29)	3835 (3827)	26 (31)	3844 (3833)	46 (49)	1.8 (1.6)
<i>n</i> -propyl	3836 (3827)	26 (30)	3839 (3829)	30 (34)	3836 (3826)	35 (39)	1.2 (1.1)

a) Harmonic frequencies are in cm^{-1} , intensities are in km mol^{-1}

Comparison of n-butoxy Conformer OH Stretch Properties

It is also possible that the relative OH stretch frequencies and intensities of ROH, HOR•, and HOROO• change based on the conformation of the molecule. It is important to account for this effect, since in our cavity ringdown experiments, alkoxy radicals are formed from photolysis of an alkyl nitrite (Reaction 9.17, $\Delta H = 40 \text{ kcal mol}^{-1}$),¹⁸⁶ giving 40 kcal mol^{-1} of excess energy to be distributed between the RO• and NO fragments.



Excess energy leading to population of multiple conformers is not limited to our study; any experiment utilizing photolysis of alkyl nitrites will have the same issue, notably if the photolysis energy is much higher than 40 kcal mol^{-1} .^{29, 30} It is therefore plausible that multiple conformers of HOR• and HOROO• will be present in the experiment. We must check whether or not the ratio of intensities for our primary products, $I_{\text{HOROO}\cdot}/I_{\text{HOR}\cdot}$, remains constant amongst different conformers. If $I_{\text{HOROO}\cdot}/I_{\text{HOR}\cdot}$ remains constant or only changes slightly, then the observed OH stretch intensity will be a simple function of which chemical species are present. If $I_{\text{HOROO}\cdot}/I_{\text{HOR}\cdot}$ changes greatly, then the observed OH stretch intensity will be convoluted by the conformational distribution, which would have to be accounted for in our analysis.

Table 9.7 contains the OH stretch harmonic frequencies and intensities for four different conformers of $\delta\text{-HOC}_4\text{H}_8\cdot$ and $\delta\text{-HOC}_4\text{H}_8\text{OO}$ radical, calculated at B3LYP/6-31+G(d,p). To differentiate between conformers, the energy relative to Conformer 1 (the lowest energy conformer of $\delta\text{-HOC}_4\text{H}_8\cdot$ examined) is also reported. We notice that amongst the first three conformers, the OH stretch harmonic frequencies remains nearly constant, only changing by $\pm 2 \text{ cm}^{-1}$. The intensities also remain nearly

constant, and so does $I_{\text{HOROO}\cdot}/I_{\text{HOR}\cdot}$. All three of these conformers have some bending in the carbon backbone. In contrast, the fourth conformer has its harmonic frequencies red shifted by about 10 cm^{-1} compared to the other conformers. Additionally, the OH stretch intensity of $\delta\text{-HOC}_4\text{H}_8\cdot$ is only 25 km mol^{-1} , much lower than the other conformers (30 km mol^{-1}). This reduction in OH stretch intensity leads to a larger intensity ratio $I_{\text{HOROO}\cdot}/I_{\text{HOR}\cdot}$ (1.3 for Conformer 4, 1.2 for the other three). A more exhaustive search of conformers would be necessary to obtain a single value of $I_{\text{HOROO}\cdot}/I_{\text{HOR}\cdot}$ that would best represent the OH stretch intensity change between $\delta\text{-HOC}_4\text{H}_8\text{OO}\cdot$ and $\delta\text{-HOC}_4\text{H}_8\cdot$. However, most of our calculated conformers yield the same absolute intensities and $I_{\text{HOROO}\cdot}/I_{\text{HOR}\cdot}$. We will therefore use the intensities for Conformer 1 in our kinetics analysis, with the caveat that a larger conformer search must be performed in order to obtain more accurate cross sections.

Table 9.7. Relative energies (no zero-point energy correction), harmonic frequencies, and intensities for conformers of $\delta\text{-HOC}_4\text{H}_8\cdot$ and $\delta\text{-HOC}_4\text{H}_8\text{OO}\cdot$, at B3LYP/6-31+G(d,p).

Conformer	energy ^a	HOC ₄ H ₈ •		HOC ₄ H ₈ OO•		$I_{\text{HOROO}\cdot}/I_{\text{HOR}\cdot}$
		ω_e^b	I^b	ω_e^b	I^b	
1	0	3841	30	3842	35	1.2
2	93	3843	31	3839	35	1.2
3	94	3843	31	3841	35	1.2
4	169	3833	25	3836	32	1.3

a) The listed energies are the energy of $\delta\text{-HOC}_4\text{H}_8\cdot$ relative to Conformer 1, in cm^{-1} .

b) Harmonic frequencies are in cm^{-1} , intensities are in km mol^{-1} .

Effect of functional group positions on the OH stretch properties

We now turn our attention to how the relative positions of the hydroxy group and the radical center/peroxy group affect the trends in OH stretch frequency and intensity. In Table 9.4, we observed that the relative OH stretch properties for ROH, HOR•, and HOROO• were different for R = methyl, R = ethyl, and R = propyl or larger. It is

plausible that the different behavior is due to the strength of interaction between the hydroxy group and the radical center/peroxy group, whether this interaction is a hydrogen bond or simply an electrostatic interaction. One way to test this idea is to compute the OH stretch frequencies and intensities for a large number of isomers with the same carbon backbone (in this case, *n*-pentyl), where each isomer differs in the placement of the hydroxy group and the radical center/peroxy group. If proximity of the two functional groups is the main reason for the different behavior between R = methyl, R = ethyl, and R = propyl or larger, then we should see a similar result in our pentyl isomer calculations. When the hydroxy and radical center/peroxy group are on the same carbon, we should see OH stretch behavior similar to that of R = methyl. Likewise, when the hydroxy group and radical center/peroxy groups are on adjacent carbons, we should see OH stretch behavior similar to R = ethyl. When the two groups are even further apart, we should see OH stretch behavior similar to R = propyl or larger.

Table 9.8 contains the harmonic frequencies and intensities for the straight carbon chain isomers of pentanol, hydroxypentyl radical, and hydroxypentylperoxy. The positions of the hydroxy group and radical center/peroxy group for each isomer are listed in the first two columns. The data in the table have been sorted according to how far away the hydroxy group and radical center/peroxy groups are. In addition, the frequencies and intensities of the smaller hydroxyalkylperoxy radicals from Table 9.4 have also been included in order to compare radicals of different sizes.

Note: It is useful to adopt a numbering scheme to make discussing these molecules easier. Let {*x*, *y*} represent the straight chain isomer of $\text{HOC}_5\text{H}_{10}\bullet$ or

$\text{HOC}_5\text{H}_{10}\text{OO}\cdot$ with the OH group on carbon x , and the radical center or OO group on carbon y .

Table 9.8. Harmonic Frequencies and Intensities for straight chain isomers of pentanol, hydroxypentyl radicals, and hydroxypentylperoxy radicals, at B3LYP/6-31+G(d,p).

Positions		$\text{C}_5\text{H}_{11}\text{OH}$		$\text{HOC}_5\text{H}_{10}\cdot$		$\text{HOC}_5\text{H}_{10}\text{OO}\cdot$		
OH	OO	ω_e^a	I^a	ω_e^a	I^a	ω_e^a	I^a	$I_{\text{HOROO}\cdot}/I_{\text{HOR}\cdot}$
OH on same carbon as radical/peroxy								
methyl		3839	28	3839	59	3799	53	0.9
1	1	3835	25	3839	57	3780	53	0.9
2	2	3828	20	3824	36	3749	53	1.5
3	3	3838	20	3826	39	3652	86	2.2
OH one carbon away from radical/peroxy								
ethyl		3836	26	3836	26	3844	46	1.8
1	2	3835	25	3835	24	3848	43	1.8
2	3	3828	20	3820	15	3835	29	1.9
2	1	3828	20	3819	23	3755	69	3.0
3	2	3838	20	3812	10	3839	27	2.8
OH two carbons away from radical/peroxy								
<i>n</i> -propyl		3836	26	3839	30	3836	35	1.2
1	3	3835	25	3838	29	3839	34	1.2
2	4	3828	20	3827	22	3826	25	1.2
3	1	3838	20	3839	22	3836	26	1.2
OH three carbons away from radical/peroxy								
<i>n</i> -butyl		3841	29	3841	30	3842	35	1.2
1	4	3835	25	3835	26	3837	30	1.2
2	5	3828	20	3828	21	3829	25	1.2
OH four carbons away from radical/peroxy								
1	5	3835	25	3834	25	3835	30	1.2

a) Harmonic frequencies are in cm^{-1} , intensities are in km mol^{-1}

To first order, the data in Table 9.8 show different OH stretch behavior depending on the relative location of the hydroxy group and the radical center/peroxy group. We group these results into three categories: OH and OO are 1) on the same carbon, 2) on adjacent carbons, or 3) further than one carbon apart.

OH and OO on same carbon: For all three of these molecules, we notice that the OH stretch of $\text{HOROO}\cdot$ is red shifted compared to $\text{HOR}\cdot$. The magnitude of the red shift increases as the functional groups are moved toward the center of the chain (40 cm^{-1} for

{1, 1}, 75 cm⁻¹ for {2, 2}, and 175 cm⁻¹ for {3, 3}). This red shift is due to a hydrogen bond between the OH and OO groups, analogous to the red shifts observed in the OH stretch spectra of HOONO (Chapter 3)^{12, 15, 42, 43, 70, 74-76, 88} and HMP (Chapter 4). Furthermore, we can also make a comparison between R = methyl and the {1, 1} isomer, since both molecules have the two functional groups on the end carbon. The harmonic frequencies follow the same trend (ROH = HOR•, HOROO• red shifted by 40 cm⁻¹). Additionally, the OH stretch intensities follow the same ratio (intensity of HOR• and HOROO• is twice as large as ROH, and $I_{\text{HOROO}\bullet}/I_{\text{HOR}\bullet} = 0.9$). Evidently, when both functional groups are on the end carbon, the OH stretch behavior is exactly the same as the R = methyl case. However, when a middle carbon holds both functional groups, vastly different trends for the OH stretch are observed. For the {2, 2} isomer, the OH stretch intensity of HOR• is twice as large as ROH, while $I_{\text{HOROO}\bullet}$ is three times as large as I_{ROH} . Meanwhile, the harmonic frequencies of ROH and HOR• are the same, while HOROO• is red shifted by 75 cm⁻¹. In contrast, for the {3, 3} isomer, the OH stretch intensity of HOR• is less than that of ROH, while HOROO• has an intensity twice as large as ROH. The harmonic frequencies also follow a different pattern, with ROH > HOR• > HOROO•. Additionally, the ratio $I_{\text{HOROO}\bullet}/I_{\text{HOR}\bullet}$ increases as the functional groups move towards the middle of the carbon chain (0.9 for {1, 1}, 1.5 for {2, 2}, and 2.2 for {3, 3}). When both functional groups are on the same carbon, the absolute position of the functional groups along the carbon chain determines the properties of the OH stretch.

OH and OO on adjacent carbons: We notice two separate trends based on the absolute ordering of the functional groups: one when the hydroxy group is closer to the end of the carbon chain than the radical center/peroxy group ({1, 2} and {2, 3}), and a

second when the radical center/peroxy group is closer to the end of the carbon chain than the hydroxy group ($\{2, 1\}$ and $\{3, 2\}$). First consider the $\{1, 2\}$ and $\{2, 3\}$ isomers. The OH stretch harmonic frequency of HOROO• is blue shifted by 15 cm^{-1} compared to HOR•. Additionally, the ratio $I_{\text{HOROO}\bullet}/I_{\text{HOR}\bullet}$ is approximately the same for both of these molecules (1.8 for $\{1, 2\}$, 1.9 for $\{2, 3\}$). We also notice that comparing HOR• to HOROO•, both $\{1, 2\}$ and $\{2, 3\}$ have similar changes to the R = ethyl case from Table 9.4. The ratio $I_{\text{HOROO}\bullet}/I_{\text{HOR}\bullet}$ is similar in magnitude for all three species, and all three species have HOROO• blue shifted compared to HOR•, suggesting similar properties for the OH stretch. However, the trends between ROH and HOR• differ between the two isomers. The $\{1, 2\}$ isomer shows no change in harmonic frequency, and only a 5% decrease in intensity. In contrast, the $\{2, 3\}$ isomer has the OH stretch of HOR• red shifted by 7 cm^{-1} compared to ROH, while the intensity decreased by 20%.

Very different behavior is observed when the radical center/peroxy group is closer to the end of the carbon chain than the hydroxy group, as is the case for the $\{2, 1\}$ and $\{3, 2\}$ isomers. Both isomers have roughly the same $I_{\text{HOROO}\bullet}/I_{\text{HOR}\bullet}$ (3.0 for $\{2, 1\}$, 2.8 for $\{3, 2\}$), and both isomers have HOR• blue shifted compared to ROH (8 cm^{-1} for $\{2, 1\}$, 65 cm^{-1} for $\{3, 2\}$). The similarities between the $\{2, 1\}$ and $\{3, 2\}$ isomers end here, however. The $\{2, 1\}$ isomer has the HOROO• harmonic frequency blue shifted by 65 cm^{-1} compared to HOR•, while the $\{3, 2\}$ isomer has the HOROO• harmonic frequency red shifted by 25 cm^{-1} compared to HOR•. Additionally, the OH stretch intensities do not follow the same patterns. The $\{2, 1\}$ isomer has $I_{\text{ROH}} < I_{\text{HOR}\bullet} \ll I_{\text{HOROO}\bullet}$, while the $\{3, 2\}$ isomer has $I_{\text{HOR}\bullet} \ll I_{\text{HOROO}\bullet} < I_{\text{ROH}}$. Although the intensity trend for HOR• and HOROO•

is the same between the {2, 1} and {3, 2} isomers, most of the properties follow different trends.

OH and OO on nonadjacent carbons: All of the chemical species in this section ({1, 3}, {2, 4}, {3, 1} {1, 4}, {2, 5}, {1, 5}) follow the same OH stretch trends. The harmonic frequencies of ROH, HOR•, and HOROO• are all the same to $\pm 3 \text{ cm}^{-1}$. The absorption intensities all follow the same pattern, with $I_{\text{ROH}} < I_{\text{HOR}\cdot} < I_{\text{HOROO}\cdot}$. The ratio $I_{\text{HOROO}\cdot} / I_{\text{HOR}\cdot}$ is the same for all of these chemical species (1.2). Finally, these isomers have essentially the same properties as the *n*-propyl and *n*-butyl species calculated in Table 9.4. Our conclusion is that the OH stretch properties behave in the same manner when the hydroxy group and radical center/peroxy group are further than one carbon apart.

Looking at the entire data set, we note that there are two main factors affecting the OH stretch behavior. First, the distance between the hydroxy group and the radical center/peroxy group is the dominant factor determining the OH stretch behavior. When the two functional groups are sufficiently far enough apart (two or more carbons), the same harmonic frequency and intensity relationships are observed between ROH, HOR•, and HOROO•, regardless of chain length or absolute positions of the functional groups. When the functional groups are closer (same carbon or adjacent carbons), a second factor comes into play: how close the functional groups are to the end of the carbon chain. We notice very different behavior in the adjacent carbon cases when the peroxy group is closer to the end of the chain than when the hydroxy group is closer to the end of the chain. Similarly, for the same carbon case, the absolute position of the functional groups changes the OH stretch behavior between ROH, HOR•, and HOROO•.

Calculation of OH Stretch Properties for the Kinetics Model

We now examine the –OH containing chemical species in our *n*-butoxy kinetics model. Two types of OH groups are present: alcohols (–OH) and peroxides (–OOH), and both groups must be accounted for in our calculations. As seen in the *Kinetics Model* section, the dominant products contributing to the OH stretch band will be $\text{HOC}_4\text{H}_8\bullet$ and $\text{HOC}_4\text{H}_8\text{OO}\bullet$, both of which have a similar harmonic frequency (3841 cm^{-1} for $\text{HOC}_4\text{H}_8\bullet$, 3842 cm^{-1} for $\text{HOC}_4\text{H}_8\text{OO}\bullet$). If any other chemical species in the reaction mechanism also have OH stretches with similar frequencies, then they will contribute intensity to the observed OH stretch band. On the other hand, if the OH stretch frequencies are far from $\text{HOC}_4\text{H}_8\bullet$ and $\text{HOC}_4\text{H}_8\text{OO}\bullet$, then the species will not contribute any intensity to the observed peak. Table 9.9 contains the OH stretch harmonic frequencies and intensities for the –OH containing species in the *n*-butoxy kinetics model.

Table 9.9. Harmonic Frequencies and Intensities for the hydroxyl containing species in the *n*-butoxy kinetics model, at B3LYP/6-31+G(d,p).

Molecule	$\omega_{e,1}$ ^a	I_1 ^a	$\omega_{e,2}$ ^a	I_2 ^a	Total <i>I</i> at OH str. peak ^b	<i>I</i> per OH group
Major Products, $[O_2] = 0$						
HOC ₄ H ₈ •	3841	30	--	--	30	30
HOC ₈ H ₁₆ OH	3835	51	3835	0	51	26
C ₇ H ₁₅ OH	3835	25	--	--	25	25
Major Products, $[O_2] > 10^{17}$ molec cm ⁻³						
HOC ₄ H ₈ OO•	3842	35	--	--	35	35
HOC ₃ H ₆ CHO	3837	32	--	--	32	32
HOC ₄ H ₈ OOH	3836	29	3772	48	29	29
HOC ₄ H ₈ OH	3834	54	3834	0	54	27
HOC ₄ H ₈ O•	3836	28	--	--	28	28
C ₄ H ₉ OH	3835	25	--	--	25	25
HOC ₃ H ₆ CH•OH	3843	64	3832	22	86	43
Minor Products (total intensity contribution < 0.1%), $[O_2] > 10^{17}$ molec cm ⁻³						
C ₃ H ₇ OH	3836	26	--	--	26	26
C ₃ H ₇ OOH	--	--	3773	47	0	0.0
C ₈ H ₁₇ OH	3835	25	--	--	25	25
HOC ₃ H ₆ O	3833	29	--	--	29	29
HOCH ₂ OH	3837	33	3807	34	33	33
C ₆ H ₁₃ OH	3834	25	--	--	25	25
HOC ₇ H ₁₄ OH	3835	48	3835	3	51	26
HOC ₄ H ₈ ONO	3837	31	--	--	31	31
C ₂ H ₅ OH	3836	26	--	--	26	26
HOC ₃ H ₆ ONO ₂	3836	37	--	--	37	37
HOC ₃ H ₆ NO	3836	34	--	--	34	34

a) Harmonic frequencies are in cm⁻¹, intensities are in km mol⁻¹

b) The total intensity column is the sum of all OH stretch intensities that fall under the HOC₄H₈• peak.

Most of the OH stretches have frequencies within 10 cm⁻¹ of HOC₄H₈• and HOC₄H₈OO•, and will therefore contribute intensity to the observed OH stretch peak. These OH stretches are listed in the $\omega_{e,1}$ and I_1 columns. On the other hand, the symmetric OH stretches in the diols, and the peroxide OH stretches (OO-H) do not contribute to the observed OH stretch peak, and are listed in the $\omega_{e,2}$ and I_2 columns. The diol symmetric stretches have near zero intensity, while the peroxide OH stretches are red

shifted from the $\text{HOC}_4\text{H}_8\bullet$ peak by 60 cm^{-1} . As a result, none of these motions can contribute to the observed OH stretch peak. Note, however, that the hydroxy OH stretches of the peroxide molecules do contribute intensity; only the peroxide OH stretch is red shifted.

Simulation of A_0/A vs $[\text{O}_2]$

Now that the chemical kinetics and properties of the OH stretch absorption have been calculated, we can simulate the plot of A_0/A vs $[\text{O}_2]$ to show that our analysis can fully explain the low $[\text{O}_2]$ anomaly in Chapter 8. We do this in the following steps. First, we tabulate the concentrations of all $-\text{OH}$ containing species in the kinetics model at $110\text{ }\mu\text{s}$, for the values of $[\text{O}_2]$ used in the *Chemical Kinetics* section. Second, we multiply each of these concentrations by the absorption intensities calculated in the *Quantum Chemistry* section to obtain an overall absorbance. Third, we convert the overall absorbance at each $[\text{O}_2]$ to A_0/A using Equation 9.18:

$$\frac{A_0}{A} = \frac{[\text{HOR}\bullet]_0 I_{\text{HOROO}\bullet}}{\sum_i c_i I_i}, \quad (9.18)$$

where $[\text{HOR}\bullet]_0$ is the initial concentration of the hydroxybutyl radical (equal to $2 \times 10^{14}\text{ molec cm}^{-3}$), $I_{\text{HOROO}\bullet}$ is the B3LYP/6-31+G(d,p) integrated intensity of the OH stretch for $\text{HOC}_4\text{H}_8\text{OO}\bullet$ (34.9 km mol^{-1}), c_i are the individual concentrations of each OH containing species, and I_i are the integrated intensities of the OH stretches for each OH containing species. The numerator of Equation 9.18 represents the absorbance if 100% of the alkoxy reactant isomerizes ($A_0/A = 1$), while the denominator represents the observed absorbance. The numerator uses $I_{\text{HOROO}\bullet}$ rather than $I_{\text{HOR}\bullet}$ because 1) at large $[\text{O}_2]$, nearly all of the

products exists as HOROO•, and 2) we used this region of the relative kinetics plot in Chapter 8 to extract $k_{\text{isom}}/k_{\text{O}_2}$. We therefore write the apparent A_0/A in terms of HOROO•.

Figure 9.4a shows the apparent A_0/A vs $[\text{O}_2]$ data from the simulations performed in this chapter (green line) and our cavity ringdown spectroscopy data (Chapter 8, blue diamonds and red squares), for $[\text{O}_2] = (0-1.7) \times 10^{19}$ molec cm^{-3} . In order to better visualize the low $[\text{O}_2]$ anomaly, Figure 9.4b zooms in on the region $[\text{O}_2] = (0-3) \times 10^{16}$ molec cm^{-3} (CRDS data in the anomaly region in red squares). We notice excellent quantitative agreement between the simulation and our CRDS data. Assuming 10% uncertainty in A_0/A on each data point, the reduced chi-squared statistic (χ_v^2) is 0.80 over the entire $[\text{O}_2]$ range, and 0.64 for $[\text{O}_2] < 4 \times 10^{16}$ molec cm^{-3} . Since the values of χ_v^2 are reasonably close to 1, we have evidence that our kinetics simulation fits well to our CRDS data, and that the estimated error on A_0/A (10%) is appropriate. **The data in Figure 9.4 are good evidence that the combination of quantum chemistry and kinetics modeling can fully explain the low $[\text{O}_2]$ anomaly.**

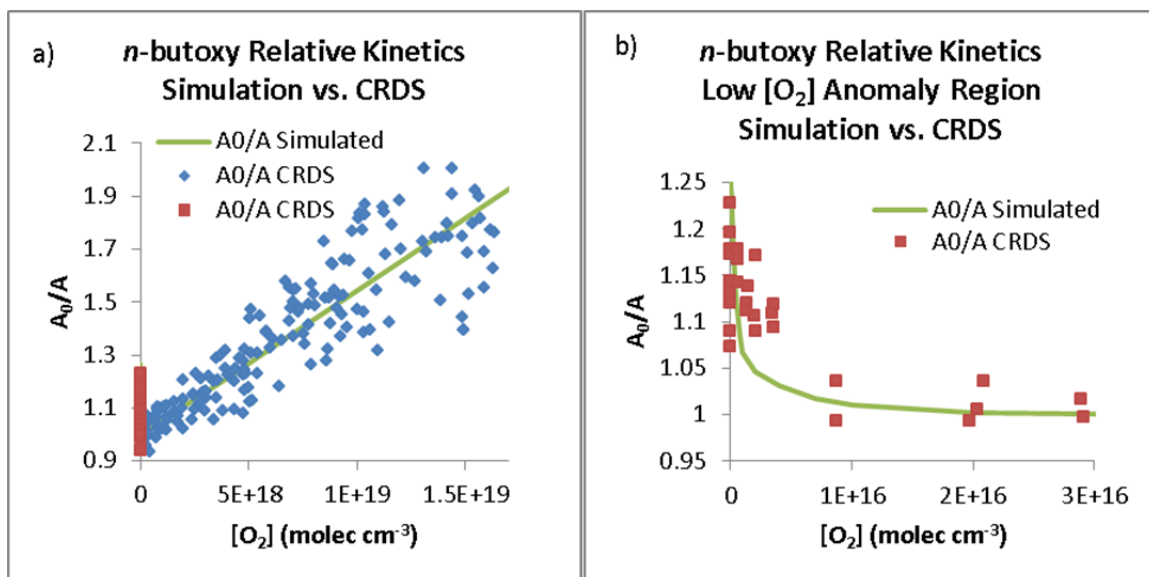


Figure 9.4. Comparison of A_0/A vs $[O_2]$ of *n*-butoxy for the relative kinetics simulation (green line) and our cavity ringdown study (blue diamonds and red squares), for $[O_2] = (0\text{--}1.7) \times 10^{19} \text{ molec cm}^{-3}$ (a), and $[O_2] = (0\text{--}3) \times 10^{16} \text{ molec cm}^{-3}$ (b). Figure 9.4a shows good quantitative agreement between the simulation and the CRDS data, while Figure 9.4b shows that the kinetics model contains all of the information necessary to explain the low $[O_2]$ anomaly observed in our CRDS measurements (Chapter 8). The reduced chi-squared statistic (χ_v^2) is 0.80 over the entire $[O_2]$ range, and 0.64 for $[O_2] < 4 \times 10^{16} \text{ molec cm}^{-3}$.

Despite the very good agreement observed in Figure 9.4, it is possible that the CRDS relative kinetics data collection method does not permit a fair comparison between simulation and experiment. About 50% of the relative kinetics data were obtained solely using the OH stretch peak height as a measure of the amount of isomerization product. However, the kinetics modeling presented in this chapter shows that the isomerization products being detected change relative quantities as a function of $[O_2]$. Additionally, the quantum chemical calculations show that the OH stretch frequencies of each isomerization product do not match exactly; the products can differ by as much as $\pm 5 \text{ cm}^{-1}$ (see Table 9.9). Although the observed peaks are very wide (FWHM 35–45 cm^{-1} , as shown in Chapter 7), small changes in band position may cause the observed A_0/A to

depend on the species being detected. As shown in Figure 9.3, this is most important for $[\text{O}_2] > 10^{19} \text{ molec cm}^{-3}$, where $\text{HORO}\cdot$ (35 km mol^{-1}) is converted to HOROOH (29 km mol^{-1}).

We can attempt to quantify this change in $k_{\text{isom}}/k_{\text{O}_2}$ by refitting our relative kinetics data using only data points that are both unaffected by the low $[\text{O}_2]$ anomaly and in the regime where the composition of secondary products is relatively constant (Figure 9.3d). The data points in the region $1 \times 10^{17} \text{ molec cm}^{-3} < [\text{O}_2] < 5 \times 10^{18} \text{ molec cm}^{-3}$ satisfy these criteria. The effect of reducing the data set being fit is small. Using the analysis presented in Chapter 8 (correction factor $X_{\text{tot}} = 0.93$) the full data set gives $k_{\text{isom}}/k_{\text{O}_2} = (1.69 \pm 0.15) \times 10^{19} \text{ molec cm}^{-3}$, while the reduced data set gives $k_{\text{isom}}/k_{\text{O}_2} = (1.72 \pm 0.30) \times 10^{19} \text{ molec cm}^{-3}$, a change of less than 2%. Since this change is smaller than the statistical scatter in our CRDS data (9%, 2σ), we conclude that our relative rate value $k_{\text{isom}}/k_{\text{O}_2}$ is not affected by the changing OH stretch peak positions amongst the isomerization products.

Discussion

With the kinetics and quantum chemistry simulation fully set up, we can address three points of interest. First, it is possible that some of the $-\text{OH}$ containing species are not formed from isomerization, but rather through secondary reactions of the O_2 or decomposition pathways. While it may seem plausible that the “extra” OH intensity may partially cause the low $[\text{O}_2]$ anomaly, we show that this additional OH stretch intensity is negligible, and thus cannot account for the low $[\text{O}_2]$ anomaly. Second, we can compare the results of our full kinetics model to two reduced kinetics model that ignore secondary

chemistry. We show that the low $[O_2]$ anomaly persists when we ignore secondary reactions in our model, further evidence that the anomaly is due to the intensity differences between $\bullet ROH$ and $\bullet OOROH$. Finally, we show that any of the literature k_{isom}/k_{O_2} will still yield a low $[O_2]$ anomaly, rather than only our value of k_{isom}/k_{O_2} .

Further points of discussion that are worth exploring are the effects of a contaminated sample of *n*-butyl nitrite (in particular, what happens if extra NO is present in the initial nitrite sample), and whether $HOC_4H_8OO\bullet$ can react with the precursor *n*-butyl nitrite. These discussions will be saved for Chapter 10, where they can be put into context based on the kinetics data obtained using the A-X electronic band of $HOC_4H_8OO\bullet$.

OH groups Formed Through Nonisomerization Pathways

In Chapter 8, we used the OH stretch peak height as a measure of how much alkoxy radical undergoes isomerization. However, not all of the hydroxy groups present 110 μs after alkoxy formation are from the isomerization channel. HO_2 is one of the products from the O_2 channel. This HO_2 can react with NO to form OH and NO_2 (Reaction 9.19). The resulting OH can then react with propylperoxy (Reaction 9.20) or hydroxybutylperoxy (Reaction 9.21) to form species with an OH group. This “extra” OH group will contribute to the absorption peak, but was not formed from isomerization.



The analysis of alkoxy chemistry presented by Sprague et al. states that at high $[O_2]$, less than 2% error in k_{isom}/k_{O_2} is introduced.³¹ This error is below the statistical uncertainty in k_{isom}/k_{O_2} (9%), leading them to conclude that extra OH groups do not impact their analysis of k_{isom}/k_{O_2} . One remaining question is whether or not the introduction of “extra” OH groups can account for the low $[O_2]$ anomaly. As $[O_2]$ is increased, the presence of extra OH groups could cause an artificial reduction in A_0/A . At high enough $[O_2]$, if no further extra OH is formed, then the apparent A_0/A will be dominated by the actual k_{isom}/k_{O_2} .

To determine whether or not the non-isomerization OH production accounts for the low $[O_2]$ anomaly, we can calculate the fraction of the OH stretch signal that arises from pathways other than isomerization. The only two species in the kinetics model that will contribute nonisomerization intensity are C_3H_7OH and HOC_4H_8OH . We therefore determine the nonisomerization contribution from Equation 9.22:

$$f_{\text{non-isom}} = \frac{[C_3H_7OH] \times I_{C_3H_7OH} + [HOC_4H_8OH] \times \frac{1}{2} \times I_{HOC_4H_8OH}}{\sum c_i I_i}, \quad (9.22)$$

where $f_{\text{non-isom}}$ is the fraction of OH stretch intensity from nonisomerization channels, $I_{C_3H_7OH}$ and $I_{HOC_4H_8OH}$ are the OH stretch intensities of the two nonisomerization products, c_i are the individual concentrations of the OH containing species, and I_i are the OH stretch intensities for each OH containing species. The factor of $\frac{1}{2}$ accounts for the fact that one of the OH groups on HOC_4H_8OH does form from isomerization. Figure 9.5 shows how $f_{\text{non-isom}}$ varies with $[O_2]$, 100 μs after formation of the *n*-butoxy radical. Figure 9.5a shows the entire range of $[O_2]$, $(0-2) \times 10^{19}$ molec cm^{-3} , while Figure 9.5b zooms in on the $[O_2]$ anomaly region, $(0-4) \times 10^{16}$ molec cm^{-3} . The plots show that

$f_{\text{non-isom}}$ increases nearly monotonically with $[\text{O}_2]$, but is less than 1% even at $[\text{O}_2] = 2.17 \times 10^{19} \text{ molec cm}^{-3}$. In the $[\text{O}_2]$ anomaly region, $f_{\text{non-isom}}$ is less than 0.2%, making a negligible contribution to the observed peak. We therefore conclude that nonisomerization –OH containing products are not the cause of the low $[\text{O}_2]$ anomaly.

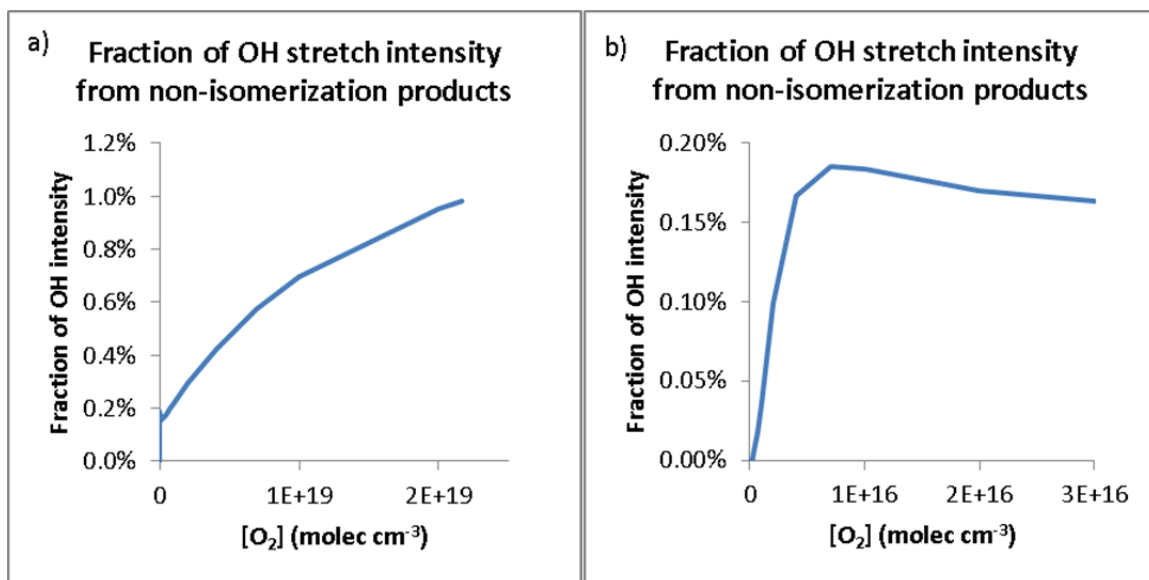


Figure 9.5. Fraction of OH stretch intensity that comes from products formed through non-isomerization reaction pathways, for $[\text{O}_2] = (0-2.17) \times 10^{19} \text{ molec cm}^{-3}$ (a), and $[\text{O}_2] = (0-4) \times 10^{16} \text{ molec cm}^{-3}$ (b). Part a shows that the nonisomerization intensity fraction increases nearly monotonically with $[\text{O}_2]$. Part b shows that the nonisomerization product contribution to the OH stretch intensity is too small to explain the low $[\text{O}_2]$ anomaly.

Reduced Kinetics Model Simulations of A_0/A vs $[\text{O}_2]$

Based on the results in the *Quantum Chemistry* section, we postulated that the large change in OH stretch intensity between $\text{HOR}\cdot$ and $\text{HORO}\cdot$ was causing the low $[\text{O}_2]$ anomaly. The kinetics model also shows that secondary chemistry effects are also important, with the main contributions being from the self-reaction of $\text{HOR}\cdot$ to form HORROH at $[\text{O}_2] = 0$ and formation of three stable end-products for $[\text{O}_2] > 10^{17} \text{ molec cm}^{-3}$. It is worthwhile to determine whether the primary alkoxy chemistry alone

can fully explain the low $[O_2]$ anomaly, despite not correctly capturing the nature of the secondary products being detected. To test this, we wrote two reduced kinetics models containing only the primary reactions for reaction of *n*-butoxy. These models are listed in Tables 9.10 and 9.11. The reactions included in both models are decomposition, isomerization, reaction with O_2 , reaction with NO , and association of O_2 with the isomerization product. The second model also contains the self-reaction of the isomerization product. Both models make use of Mollner's k_{isom}/k_{O_2} value obtained before the reanalysis of the kinetics data;³⁰ however, we show in the next section that the exact value of k_{isom}/k_{O_2} is irrelevant. By examining only these reactions, we can determine if the low $[O_2]$ anomaly persists in the absence of secondary chemistry.

Table 9.10. First Reduced Kinetics Model for *n*-butoxy (primary reactions only)

$A^{a,b}$	Ea/R (K)	Reaction	Source
5.80E+02	0	$C_4H_9O \rightleftharpoons C_3H_7 + HCHO$	Atkinson ¹⁴²
3.20E+05	0	$C_4H_9O \rightleftharpoons HOC_4H_8$	Mollner ³⁰
1.40E-14	0	$C_4H_9O + O_2 \rightleftharpoons C_3H_7CHO + HO_2$	Atkinson ¹⁴²
3.80E-11	0	$C_4H_9O + NO \rightleftharpoons C_4H_9ONO$	IUPAC ¹¹⁸
7.50E-12	0	$HOC_4H_8 + O_2 \rightleftharpoons HOC_4H_8OO$	IUPAC ¹¹⁸

a) Units of A are $\text{cm}^3 \text{molec}^{-1} \text{s}^{-1}$ for bimolecular reactions, and s^{-1} for unimolecular reactions

b) Termolecular reactions have already been converted to the effective bimolecular rate constant: the listed rate constants are valid at 670 torr, 298 K only

Table 9.11. Second Reduced Kinetics Model for *n*-butoxy (includes $HOR\cdot$ dimerization)

$A^{a,b}$	Ea/R (K)	reaction	source
5.80E+02	0	$C_4H_9O \rightleftharpoons C_3H_7 + HCHO$	Atkinson ¹⁴²
3.20E+05	0	$C_4H_9O \rightleftharpoons HOC_4H_8$	Mollner ³⁰
1.40E-14	0	$C_4H_9O + O_2 \rightleftharpoons C_3H_7CHO + HO_2$	Atkinson ¹⁴²
3.80E-11	0	$C_4H_9O + NO \rightleftharpoons C_4H_9ONO$	IUPAC ¹¹⁸
7.50E-12	0	$HOC_4H_8 + O_2 \rightleftharpoons HOC_4H_8OO$	IUPAC ¹¹⁸
5.00E-11	0	$HOC_4H_8 + HOC_4H_8 \rightleftharpoons HOC_8H_{16}OH$	NIST ¹¹⁷

a) Units of A are $\text{cm}^3 \text{molec}^{-1} \text{s}^{-1}$ for bimolecular reactions, and s^{-1} for unimolecular reactions

b) Termolecular reactions have already been converted to the effective bimolecular rate constant: the listed rate constants are valid at 670 torr, 298 K only

Plots of A_0/A vs $[O_2]$ were generated in the same manner as described in the *Results* section for the full kinetics model, shown in Figure 9.6. Figures 9.6a and 9.6b make use of the first reduced kinetics model (no self-reaction of HOR•), while Figures 9.6c and 9.6d make use of the second reduced kinetics model (includes self-reaction of HOR•). The full $[O_2]$ range is shown in Figures 9.6a and 9.6c, and the $[O_2]$ anomaly region shown in Figures 9.6b and 9.6d. Over the entire $[O_2]$ range, the agreement between the two reduced kinetics models and Garland's CRDS data is quite good. Ignoring the $[O_2] = 0$ data points and assuming 10% uncertainty in A_0/A on each data point, the reduced chi-squared statistic (χ_v^2) is 0.73 for the first kinetics model, and 0.72 for the second kinetics model. The full kinetics model (Figure 9.4) had $\chi_v^2 = 0.80$ (including all data points), essentially the same χ_v^2 as the reduced model. This confirms that secondary chemistry effects are minimal across the full range of $[O_2]$. At low $[O_2]$, we notice that inclusion of HOR• self-reaction affects the agreement between the kinetics models and the CRDS data. Both reduced kinetics models qualitatively fit the CRDS data, but the agreement between simulation and CRDS data is poorer in the first kinetics model, where HOR• self-reaction is not accounted for. Ignoring the $[O_2] = 0$ data points and assuming 10% uncertainty in A_0/A on each data point, the reduced chi-squared statistic (χ_v^2) is 0.41 for the first kinetics model, and 0.31 for the second kinetics model. The full kinetics model had $\chi_v^2 = 0.64$ (all data points used), in good agreement with the both of the reduced kinetics models. We conclude that the cause of the low $[O_2]$ anomaly lies in the primary alkoxy chemistry, and is mostly due to the change in OH stretch intensity between HOR• and HOROO•.

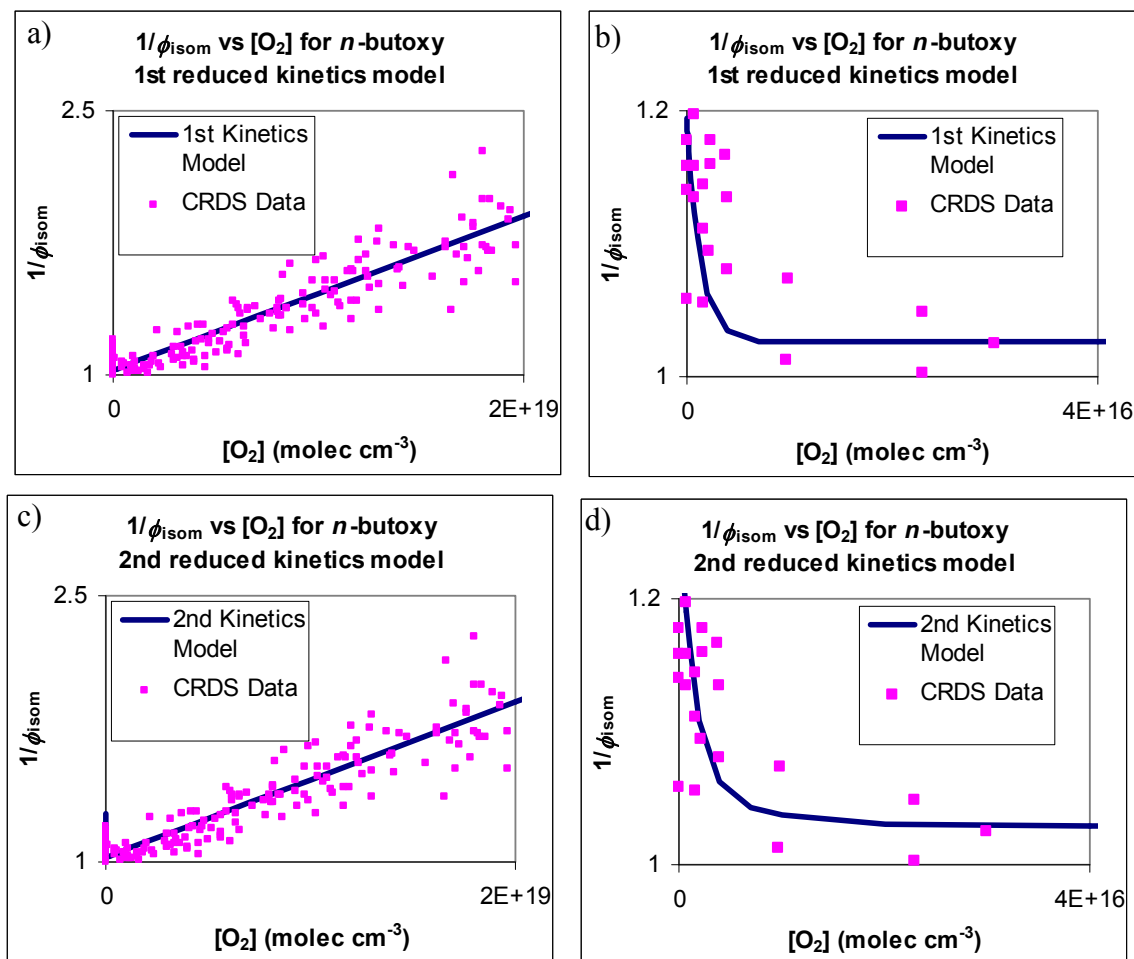


Figure 9.6 Comparison of A_0/A (labeled $1/\phi_{\text{isom}}$) vs $[\text{O}_2]$ of *n*-butoxy for the reduced kinetics/quantum chemistry simulation (blue line) and our cavity ringdown study prior to reanalysis (pink squares), for $[\text{O}_2] = (0\text{--}2) \times 10^{19}$ molec cm^{-3} (a and c), and $[\text{O}_2] = (0\text{--}4) \times 10^{16}$ molec cm^{-3} (b and d). Parts a and b use a kinetics model that ignores self-reaction of $\text{HOR}\cdot$, while parts c and d use a kinetics model including self-reaction of $\text{HOR}\cdot$. The four plots show good agreement between the reduced kinetics model simulation and the CRDS data, indicating that most of the low $[\text{O}_2]$ anomaly can be explained by the primary alkoxy chemistry, and thus the different OH stretch intensity of $\text{HOR}\cdot$ and $\text{HOROO}\cdot$.

Persistence of Low $[\text{O}_2]$ Anomaly for Other Values of $k_{\text{isom}}/k_{\text{O}_2}$

The analysis of the low $[\text{O}_2]$ anomaly up to this point has made exclusive use of our value for $k_{\text{isom}}/k_{\text{O}_2}$ of 1.69×10^{19} cm^{-3} . However, the scatter in $k_{\text{isom}}/k_{\text{O}_2}$ from previous experiments yields values over the range $(1\text{--}3) \times 10^{19}$ cm^{-3} . This raises the question of

whether or not the low $[O_2]$ anomaly will persist in our kinetics simulations for smaller values of k_{isom}/k_{O_2} . Since k_{isom}/k_{O_2} is predicted to be temperature dependent,¹²⁹⁻¹⁴⁰ such information will be useful for future spectroscopists.

To test this idea, we re-ran our full *n*-butoxy kinetics model using a different rate constant for the isomerization reaction. We chose to use one of the lowest value for the ratio of rate constants in Table 9.1 including uncertainty $k_{\text{isom}}/k_{O_2} = 1.1 \times 10^{19}$ molec cm⁻³.¹⁵⁶ To apply this new ratio to our kinetics model, we kept k_{O_2} constant,¹¹⁸ and changed the rate constant for isomerization from 3.2×10^5 s⁻¹ to 1.5×10^5 s⁻¹. The rest of the kinetics model remained unchanged. We then generated new plots of A_0/A vs $[O_2]$ as described above. Figure 9.7 compares the simulated A_0/A vs $[O_2]$ for Cox's value of k_{isom}/k_{O_2} (1.1×10^{19} molec cm⁻³, blue curve) to Mollner's value (2.3×10^{19} molec cm⁻³, pink curve).

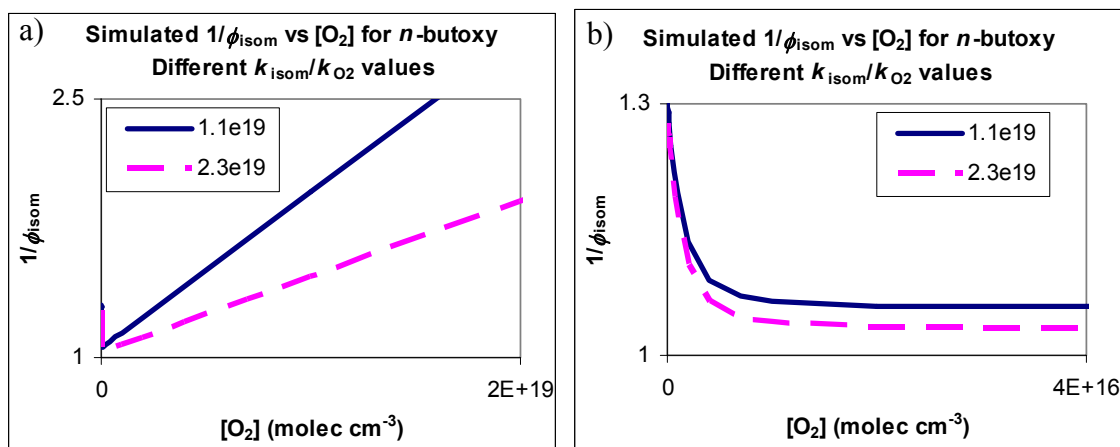


Figure 9.7. Comparison of simulated A_0/A vs $[O_2]$ for *n*-butoxy, using two different values of k_{isom}/k_{O_2} . The blue curve uses Cox's value of 1.1×10^{19} molec cm⁻³,¹⁵⁶ while the pink dashed curve uses Mollner's value of 2.3×10^{19} molec cm⁻³.³⁰ The full range of $[O_2]$, $(0-2) \times 10^{19}$ molec cm⁻³, is shown in part a, while the $[O_2]$ anomaly region, $(0-4) \times 10^{16}$ molec cm⁻³ is shown in part b. Although the curves have different slopes and values in each region, we observe that the low $[O_2]$ anomaly still appears at the reduced value of k_{isom}/k_{O_2} .

In Figure 9.7a, we immediately notice a steeper slope for the $k_{\text{isom}}/k_{\text{O}_2} = 1.1 \times 10^{19}$ molec cm^{-3} case, as predicted by Equation 9.8. Of greater interest to us is the curvature shown in Figure 9.7b. For both values of $k_{\text{isom}}/k_{\text{O}_2}$, the apparent A_0/A decreases sharply as $[\text{O}_2]$ is increased to 10^{14} molec cm^{-3} , followed by a slow and steady decrease as $[\text{O}_2]$ is further increased to 4×10^{16} molec cm^{-3} . Although the specific values of A_0/A differ between the two simulations, the low $[\text{O}_2]$ anomaly still appears in the same $[\text{O}_2]$ region. This observation agrees with our idea that the change in OH stretch intensity between $\text{HOR}\cdot$ and $\text{HORO}\cdot$ is the dominant cause of the low $[\text{O}_2]$ anomaly. Any future spectroscopic experiments should be able to observe the low $[\text{O}_2]$ anomaly, regardless of the specific value of $k_{\text{isom}}/k_{\text{O}_2}$ that is measured. Because Figure 9.7b shows that the curvature is dependent on $k_{\text{isom}}/k_{\text{O}_2}$, it may be possible to use the low $[\text{O}_2]$ region in rate constant fitting to obtain values of $k_{\text{isom}}/k_{\text{O}_2}$ with lower uncertainties.

Conclusions

We have generated a combined chemical kinetics and quantum chemistry model to determine the products being detected in our alkoxy relative kinetics experiment, develop a general framework for the OH stretch absorption properties of ROH, $\text{HOR}\cdot$, and $\text{HORO}\cdot$ isomers, and explain the anomalous behavior of the ν_1 relative absorption A_0/A at low $[\text{O}_2]$. We have shown that after 110 μs , only 50%–80% of the products being detected are the primary products of isomerization $\text{HOR}\cdot$ or $\text{HORO}\cdot$, with the remainder belonging to stable end-products. By examining alkoxy systems of different chain lengths and functional group positions, we also show that the relative positions of

the hydroxy group and radical center/peroxy group govern how the OH stretch position and intensity will change. We have shown that the anomalous behavior of A_0/A at low $[O_2]$ can be explained solely due to the change in the OH stretch intensities of the products being detected (HOR• at low $[O_2]$, HOROO• at high $[O_2]$). Our kinetics and quantum chemistry simulations produce A_0/A vs $[O_2]$ plots in excellent agreement with the CRDS data presented in Chapter 8, indicating that our model fully captures the essential chemistry occurring in the alkoxy system. The low $[O_2]$ anomaly occurs independently of the specific value of k_{isom}/k_{O_2} measured, indicating that general spectroscopic studies on the OH stretch of alkoxy products will exhibit the same anomaly.

Acknowledgements

The models developed in this chapter were funded under NASA Upper Atmosphere Research Program Grants NAG5-11657, NNG06GD88G, and NNX09AE21G2, California Air Resources Board Contract 03-333 and 07-730, and a Department of Defense National Defense Science and Engineering Graduate Fellowship (NDSEG).

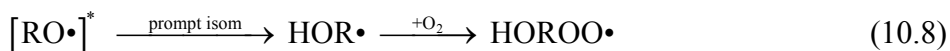
Chapter 10—Cavity Ringdown Spectroscopy and Kinetics of *n*-Butoxy Isomerization: The A-X Electronic Spectrum of HOC₄H₈OO•

Abstract

In Chapters 7 and 8, we have presented the ν_1 spectra of the primary products of alkoxy isomerization (HOR•, HOROO•) and used these absorption bands to measure the relative rate of isomerization to reaction with O₂, $k_{\text{isom}}/k_{\text{O}_2}$. In Chapter 9, we successfully explained the anomalous behavior in the ν_1 absorbance at low [O₂] by showing that the integrated intensities of HOR•, HOROO•, and secondary products differ from each other. Although the spectra in Chapter 7 are relatively clean (93% HOR•, 98% HOROO•), the ideal spectroscopic measurement of HOROO• would come from a clean, unique band free from interference of any secondary products. As we have observed in Chapter 4 (HOCH₂OO•), the A-X spectrum characteristic of all peroxy radicals will satisfy this condition. In this thesis chapter, we present the first detection of the A-X electronic spectrum of the HOC₄H₈OO• radical using cavity ringdown spectroscopy. The spectrum is similar in shape to the A-X spectrum of *n*-butyl peroxy: a broad spectroscopic band due to the multiple molecular conformers that are present. There are two small peaks within this broad band at 7355 and 7556 cm⁻¹, and a shoulder (or possibly a weak peak) at 7500 cm⁻¹. Using the A-X band, we measure the relative absorbance as a function of [O₂] (as in Chapter 8), and obtain $k_{\text{isom}}/k_{\text{O}_2} = (1.39 \pm 0.47) \times 10^{19} \text{ cm}^{-3}$ (2 σ), in good agreement with the ν_1 measurements. Finally, we directly measure the rate of destruction of HOC₄H₈OO•, and determine the kinetic lifetime to be 150 μs in our experiment, in reasonable agreement with our kinetics model.

Introduction

Let us begin with a brief summary of alkoxy radical chemistry and our relative kinetics analysis from Chapters 7–9. In our experiments, thermalized alkoxy radicals ($\text{RO}\cdot$) and hot alkoxy radicals ($[\text{RO}\cdot]^*$) are generated through photolysis of an alkyl nitrite (Reactions 10.1 and 10.2). Once formed, these radicals can undergo isomerization to form a hydroxyalkyl ($\text{HOR}\cdot$, Reaction 10.3), isomerization and rapid association with O_2 to form a hydroxyalkylperoxy ($\text{HOROO}\cdot$, Reaction 10.4), react with O_2 to form HO_2 and an aldehyde (Reaction 10.5), decompose to formaldehyde and an alkyl radical (followed by rapid association to form an alkylperoxy, Reaction 10.6), or recombine with NO to form the alkyl nitrite (Reaction 10.7). Hot alkoxy radicals can promptly isomerize (Reaction 10.8) or decompose (Reaction 10.9).



In Chapter 8, we showed that by measuring the absorbance of a spectroscopic band (A , or A_0 at $[O_2] = 0$) as a function of $[O_2]$, we can determine k_{isom}/k_{O_2} from Equations 10.10–10.13:

$$\frac{A_0}{A} = \frac{\left(\frac{\frac{k_{O_2}}{k_{isom}}}{1 + \frac{k_{NO}[NO]}{k_{isom}} + \frac{k_{decomp}}{k_{isom}}} \right) [O_2] + 1}{\left(\frac{\phi_{pi} \frac{k_{O_2}}{k_{isom}}}{1 + \phi_{pi} \left(\frac{k_{NO}[NO]}{k_{isom}} + \frac{k_{decomp}}{k_{isom}} \right)} \right) [O_2] + 1}, \quad (10.10)$$

$$\frac{k_{isom}}{k_{O_2}} = \left[\left(\frac{\partial \left(\frac{A_0}{A} \right)}{\partial [O_2]} \right)_{[O_2]=0} \right]^{-1} \times X_{kin} \times X_{prompt}, \quad (10.11)$$

where

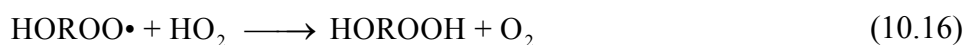
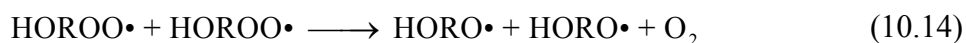
$$X_{kin} = \frac{1}{1 + \frac{k_{decomp}}{k_{isom}} + \frac{k_{NO}[NO]}{k_{isom}}}, \quad (10.12)$$

$$X_{prompt} = \frac{(1 - \phi_{pi})}{1 + \phi_{pi} \left(\frac{k_{decomp}}{k_{isom}} + \frac{k_{NO}[NO]}{k_{isom}} \right)}. \quad (10.13)$$

One possible problem with using the ν_1 band is that it is not a truly unique measure of HOROO•. In Chapter 9, we showed that secondary products formed in appreciable quantities over timescales of even 100 μ s. These products do not necessarily have the same absorption cross section as HOROO•. The effect of these secondary products is likely minimal due to two observations: 1) the ν_1 absorbance is constant over

1 ms (Chapter 7), and 2) the simulation of relative kinetics (Chapter 9) is in excellent agreement with our CRDS data (Chapter 8).

Nonetheless, measurement of a spectroscopic band unique to HOROO• presents many benefits. First, the problem of varying absorption cross sections as a function of [O₂] disappears, eliminating one possible confounding factor in our analysis of $k_{\text{isom}}/k_{\text{O}_2}$. Second, and perhaps more importantly, direct kinetics measurements can be made on HOROO•. We have already shown in Chapter 7 that measuring the formation of HOROO• is not possible at room temperature because the isomerization lifetime (5 μs) is on the same order as our ringdown lifetime (7 μs). On the other hand, destruction of HOROO• is expected to take place on much longer timescales (lifetimes > 100 μs), and measuring this should be possible, with the major destruction pathways being self-reaction (Reaction 10.14, $k = 5 \times 10^{-13} \text{ cm}^3 \text{ molec}^{-1} \text{ s}^{-1}$), reaction with NO (Reaction 10.15, $k = 9 \times 10^{-12} \text{ cm}^3 \text{ molec}^{-1} \text{ s}^{-1}$), and reaction with HO₂ (Reaction 10.16, $k = 8 \times 10^{-12} \text{ cm}^3 \text{ molec}^{-1} \text{ s}^{-1}$).^{27, 117, 118} Under most experimental conditions ([O₂] < 1 atm), the NO destruction pathway should dominate, underscoring the need to obtain a reasonably accurate [NO], notably the NO present in the *n*-butyl nitrite sample.



As stated in Chapter 4, hydroxyalkylperoxy molecules have distinct A-X electronic spectra, similar in shape and position to the corresponding alkylperoxy spectra. It is therefore expected that HOROO• will have a similar A-X spectrum to the corresponding ROO•. As a starting point, the smallest possible alkoxy isomerization

product, δ -HOC₄H₈OO•, will have a similar A-X spectrum to *n*-butylperoxy:¹⁹⁰ a broad band over 7200–7700 cm⁻¹ with two or three small peaks. The decomposition of C₄H₉O• is slow (lifetime 2 ms), and Mollner³⁰ and Sprague³¹ have shown that the prompt decomposition yield (Reaction 10.9) following 351 nm photolysis of *n*-butyl nitrite is less than 5%. Therefore, on short timescales, we expect to only observe the A-X transition of HOC₄H₈OO•, and not the decomposition product C₃H₇OO•.

This thesis chapter describes the first detection of the A-X electronic band of HOC₄H₈OO•, direct kinetics measurements on the destruction of HOC₄H₈OO•, determination of the relative kinetic rate constants $k_{\text{isom}}/k_{\text{O}_2}$ for *n*-butoxy using this spectroscopic band, and FTIR experiments to determine [NO] in the *n*-butyl nitrite used to generate the butoxy radicals. Similar to the experiments in Chapters 7 and 8, HOC₄H₈OO• was generated through pulsed laser photolysis of *n*-butyl nitrite in the presence of O₂. Cavity ringdown spectroscopy was used to measure the resulting spectrum over the range 7150–7700 cm⁻¹, 10 μs after photolysis. The resulting peak heights were measured over the first 500 μs after photolysis in order to assess the rate of destruction of HOC₄H₈OO•. The A-X peak heights were measured as a function of [O₂] to obtain $k_{\text{isom}}/k_{\text{O}_2}$. FTIR spectra of *n*-butyl nitrite were taken before and after purification (freeze-pump-thaw cycles) to determine the presence and nature of contaminants in our cavity ringdown experiments.

Methods

Apparatus and Chemicals

The cavity ringdown spectrometer, laser system, and gas kinetics flow cell have been described in detail in Chapter 2 (Figures 2.5, 2.7, 2.8). Briefly, the tunable near-infrared light used to measure the spectrum ($6900\text{--}7800\text{ cm}^{-1}$, $100\text{ }\mu\text{J/pulse}$) was generated by sending the output from a Nd:YAG (532 nm, 370 mJ/pulse, 10 Hz) pumped dye laser (DCM dye, 620–660 nm, 35 mJ/pulse peak) into a H₂ filled Raman shifter. The infrared light was sent into an optical cavity consisting of two highly reflective mirrors (Los Gatos Research, 1.35 μm peak, R = 99.98%). Ringdown traces were collected with an amplified InGaAs detector (ThorLabs PDA400 or PDA10CS) connected to a PC oscilloscope card (GageScope CS1450). 80 μs of ringdown data were collected per shot, and 16 ringdowns were collected and averaged before being fit. The first eighth of the ringdown lifetime was removed before the data were refit in order to eliminate errors caused from noise near the peak of the ringdown.

$\delta\text{-HOC}_4\text{H}_8\text{OO}\cdot$ radicals were formed by photolysis of *n*-butyl nitrite (95%, Sigma-Aldrich) in the presence of O₂ (Reactions 10.1 and 10.4). Photolysis was initiated by 351 nm light from the excimer laser described in Chapter 2. Typical UV flux was kept at 2.5×10^{17} photons cm^{-2} . The absorption cross section of *n*-butyl nitrite at 351 nm is $\sigma_{351\text{nm}} = 8.0 \times 10^{-20}$ $\text{cm}^2\text{ molec}^{-1}$,³² resulting in 2.0% of the alkyl nitrite being photolyzed.

n-butyl nitrite was introduced to the gas kinetics cell by flowing N₂ gas through a bubbler kept at 0 °C. Prior to usage, the *n*-butyl nitrite went through a minimum of three freeze-pump-thaw cycles in order to degas the sample of oxygen and to reduce the concentration of impurities (such as NO, nitrous oxides, aldehydes, and acids). Briefly,

one cycle consists of freezing the nitrite in liquid nitrogen, vacuum pumping on the sample for 10–20 minutes, then isolating the sample and thawing. The gas bubbles that evolve represent impurities that have a higher vapor pressure than the nitrite. Cycles were repeated until minimal to no gas evolved during thawing.

Experimental and Flow Conditions

Four experiments were conducted on the *n*-butoxy chemical system. First, the A-X electronic spectrum of $\text{HOC}_4\text{H}_8\text{OO}\cdot$ was measured by scanning across a range of frequencies (7150–7700 cm^{-1} , step size 1 cm^{-1}) while at a constant time after photolysis of the *n*-butyl nitrite (10 μs). Second, the A-X band was used to directly measure the rate of destruction of $\text{HOC}_4\text{H}_8\text{OO}\cdot$ by keeping the laser at one frequency (7556 cm^{-1}) and measuring the change in absorption with time after photolysis of the *n*-butyl nitrite (0–400 μs). Although these two experiments were conducted at two different pressures (670 and 330 torr), one set of common chemical concentrations was used to show that the destruction of $\text{HOC}_4\text{H}_8\text{OO}\cdot$ is pressure independent. This experiment was repeated for two different values of $[\text{C}_4\text{H}_9\text{ONO}]$ (3.4×10^{16} and 1.6×10^{16} molec cm^{-3}) and three different values of photolysis ratio (2.0%, 1.0%, 2.8%), for a total of six experimental conditions. Third, the relative rate constant $k_{\text{isom}}/k_{\text{O}_2}$ was measured by varying $[\text{O}_2]$, $(0\text{--}8) \times 10^{18}$ molec cm^{-3} at constant pressure (330 torr) and measuring the resulting absorption at a constant frequency (7556 cm^{-1}) and time after photolysis (10 μs).

The conditions for the three experiments are summarized in Table 10.1. Gas flows were measured using the flowmeters discussed in Chapter 2. The temperature of the gas

kinetics cell was taken to be room temperature: no temperature control of any kind was attempted.

Table 10.1. Experimental conditions (gas flows, photolysis parameters, chemical concentrations, and spectrometer performance) for alkoxy experiments

	Spectrum and direct kinetics, 670 torr	Spectrum and direct kinetics, 330 torr	Relative rate, 330 torr
N ₂ Purge Flow—Left Mirror	700 sccm	650 sccm	650 sccm
N ₂ Purge Flow—Right Mirror	900 sccm	450 sccm	450 sccm
N ₂ Bubbler Flow	250 sccm	250 sccm 125 sccm ^b	225 sccm
N ₂ Dilution Flow	6500 sccm	2900 sccm	0–2900 sccm ^a
O ₂ Flow	70 sccm	70 sccm	0–2900 sccm ^a
Cell Pressure	670 torr	330 torr	330 torr
Temperature (room)	293 ± 2 K	293 ± 2 K	293 ± 2 K
Flush Time	57 ms	28 ms	28 ms
Photolysis Window Length	5 cm	5 cm	5 cm
Excimer Energy at 351 nm	162 ± 10 mJ/pulse	162 ± 10 mJ/pulse 84 ± 5 mJ/pulse ^b 240 ± 15 mJ/pulse ^b	162 ± 10 mJ/pulse
% Alkoxy Photolyzed	1.98%	1.98% 0.95% ^b 2.83% ^b	1.98%
[C ₄ H ₉ ONO] _{cell}	3.4 × 10 ¹⁶ cm ⁻³	3.4 × 10 ¹⁶ cm ⁻³ 1.6 × 10 ¹⁶ cm ⁻³ ^b	3.4 × 10 ¹⁶ cm ⁻³
[C ₄ H ₉ O•]	6.5 × 10 ¹⁴ cm ⁻³	6.5 × 10 ¹⁴ cm ⁻³ 3.2 × 10 ¹⁴ cm ⁻³ ^b 9.1 × 10 ¹⁴ cm ⁻³ ^b 1.6 × 10 ¹⁴ cm ⁻³ ^b 4.6 × 10 ¹⁴ cm ⁻³ ^b	6.5 × 10 ¹⁴ cm ⁻³
[O ₂]	2.0 × 10 ¹⁷ cm ⁻³	2.0 × 10 ¹⁷ cm ⁻³	0–8 × 10 ¹⁸ cm ⁻³
Optical Cell Length	52 cm	52 cm	52 cm
1/τ ₀ (7500 cm ⁻¹ , vacuum)	1.1 × 10 ⁵ Hz	1.2 × 10 ⁵ Hz	0.9 × 10 ⁵ Hz
1/τ (7500 cm ⁻¹ , all gases and C ₄ H ₉ ONO)	1.3 × 10 ⁵ Hz	1.3 × 10 ⁵ Hz	0.9 × 10 ⁵ Hz
Δτ/τ ^c	0.7%	0.7%	0.7%
Sensitivity, 7500 cm ⁻¹	2.0 ppm Hz ^{-1/2}	2.0 ppm Hz ^{-1/2}	1.4 ppm Hz ^{-1/2}

a) The sum of O₂ and N₂ dilution flows was kept at 2900 sccm for the relative rate experiments to keep a constant pressure and flush time

b) Excimer flux and concentrations used only for direct kinetics measurements

c) Δτ/τ reported for averaging 16 ringdown traces per point

The cell flush time, [RONO], and [RO•] are calculated from the experimental parameters Table 10.1. Derivations of these equations were presented in Chapter 8; therefore, only the final results are presented here. The flush time is defined as the amount of time to remove the chemicals within the photolysis length from the ringdown cavity, and is calculated from Equation 10.17:

$$t_{flush} = \left(\frac{V_{in-out}}{\sum_{flush} f_i} \right) \times \left(\frac{p_{cell}}{p_{st}} \right), \quad (10.17)$$

where t_{flush} is the flush time for the chemical sample, V_{in-out} is the volume between the inlet for butyl nitrite and vacuum outlet ($V_{in-out} = 3.93 \text{ cm}^3$ for the cell used in this experiment), $\sum_{flush} f_i$ is the total flow rate of gases in the direction of flushing (in sccm), p_{cell} is the pressure in the CRDS cell, and p_{st} is the standard pressure (760 torr).

[RONO] in the CRDS cell is determined by the vapor pressure of the alkyl nitrite and the dilution of the butyl nitrite carrier gas within the CRDS cell, and can be calculated from Equation 10.18:

$$\left(\frac{N}{V} \right)_{RONO,CRDS} = p_{vap} \left(\frac{N/V}{P} \right)_{conv} \left(\frac{T_{bubbler}}{T_{cell}} \right) \left(\frac{f_{bubbler}}{\sum f_i} \right), \quad (10.18)$$

where $\left(\frac{N}{V} \right)_{RONO,CRDS}$ is the concentration of butyl nitrite in the CRDS cell, p_{vap} is the vapor pressure of RONO in the bubbler, $T_{bubbler}$ is the temperature of the bubbler (273 K),

$\left(\frac{N/V}{P} \right)_{conv}$ is the conversion factor between pressure and number density of a gas

$(3.24 \times 10^{16} \text{ molec cm}^{-3}/\text{torr})$, T_{cell} is the temperature of the gas kinetics cell (293 K), f_{bubbler} is the gas flow through the bubbler, and Σf_i is the sum of all gas flows through the gas kinetics cell. The vapor pressure of $\text{C}_4\text{H}_9\text{ONO}$ (20.3 torr at 273 K) can be computed based on known thermodynamic properties (ΔH_{vap} , $T_{\text{boil,1atm}}$).

The fraction of RONO that is photolyzed can be calculated from Equation 10.19:

$$\%_{\text{photolysis}} = \frac{\left(\frac{P_{\text{excimer}}}{A_{\text{meter}}} \right)}{F_{\text{excimer}}} \left(\frac{\lambda}{hc} \right) (\sigma_{\text{RONO},\lambda}) (X) \left(\frac{A_{\text{UV,laser}}}{A_{\text{UV,CRDS}}} \right), \quad (10.19)$$

where $\%_{\text{photolysis}}$ is the fraction of RONO that is photolyzed, $(P_{\text{excimer}}/A_{\text{meter}})$ is the power per unit area of the UV light (read directly from the power meter), F_{excimer} is the rep rate of the excimer laser (10 Hz), h is Planck's constant, c is the speed of light, λ is the wavelength of the excimer light (351 nm), $\sigma_{\text{RONO},\lambda}$ is the absorption cross section of RONO at the excimer wavelength ($8 \times 10^{-20} \text{ cm}^2 \text{ molec}^{-1}$ at 351 nm for *n*-butyl nitrite), X is the quantum yield for photolysis (taken to be 1), $A_{\text{UV,laser}}$ is the area of excimer beam measured at the excimer laser output, and $A_{\text{UV,CRDS}}$ is the area of excimer beam measured at the CRDS cell. For these experiments, $\frac{A_{\text{UV,laser}}}{A_{\text{UV,CRDS}}} = 2$.

FTIR—Apparatus, Chemicals, Methods

Gas phase FTIR spectra of *n*-butyl nitrite (95%, Sigma-Aldrich) were acquired using the Nicolet FTIR instrument in Paul Wennberg's lab (path length 19 cm). The nitrite samples were placed in a flask and atmospheric gas was pumped off (freezing the nitrite, pumping off gas for 1 minute, then thawing the nitrite) before use. The vapor from the butyl nitrite was sent into the FTIR cell: no gas was bubbled through the liquid

sample. Butyl nitrite samples were injected and pumped out of the FTIR three times before the gas to be measured was injected to ensure that no residual air was present in the FTIR.

Four different *n*-butyl nitrite samples were measured to assess how purification, storage, and sample age affect nitrite purity. The four samples that were measured were freshly purchased nitrite that was freeze pumped, freshly purchased nitrite that was not freeze pumped, 4-week-old nitrite stored at 4 °C that was not freeze pumped, and 8-week-old nitrite stored at room temperature that was not freeze pumped. The pressure of the nitrite vapor in the FTIR was measured using a Baratron (MKS). The experimental conditions for each sample are summarized in Table 10.2.

Table 10.2. Experimental conditions for FTIR spectra of butyl nitrite samples

	Units	1	1a	1b	2	2a	3	4
Sample Age		Fresh	Fresh	Fresh	Fresh	Fresh	4 wks	8 wks
Storage Temp	K	277	277	277	277	277	277	293
Freeze Pump?		yes	yes	yes	no	no	no	no
Pressure	torr	148	62	77	68	66	65	65

The FTIR spectra were compared to reference spectra⁴⁰ of NO and C₂H₅ONO to determine the purity of the butyl nitrite, similar to the methods of assessing our 2-pentyl nitrite in Chapter 7. The resulting concentrations were used to calculate [NO] in the CRDS experiment.

Results

We present the results of this study in four parts. First, the A-X spectrum of HOC₄H₈OO• is reported. The spectrum is similar in shape to the literature spectrum of C₄H₉OO•:¹⁹⁰ a broad absorption band over the range 7200–7700 cm⁻¹ with two small

peaks. Second, the kinetics of $\text{HOC}_4\text{H}_8\text{OO}\cdot$ destruction are reported by using the A-X spectroscopic band for six combinations of $[\text{C}_4\text{H}_9\text{ONO}]$ and photolysis ratios. In all cases, the lifetime of $\text{HOC}_4\text{H}_8\text{OO}\cdot$ is 150 μs , in reasonable agreement with our kinetics model. Third, the relative rate $k_{\text{isom}}/k_{\text{O}_2}$ is reported by using the A-X spectroscopic band to obtain A_0/A as a function of $[\text{O}_2]$. The relative rate obtained with the A-X band is in agreement with all of the previous literature studies, including our OH stretch CRDS measurements (Chapter 8). This result gives us further confidence in assigning the measured NIR spectrum to $\text{HOC}_4\text{H}_8\text{OO}\cdot$. Fourth, the FTIR spectra of the *n*-butyl nitrite samples are presented, and the amount of NO present in the CRDS experiments is calculated. We calculate a small but observable amount of NO that comes from the *n*-butyl nitrite sample.

A-X Spectrum of $\text{HOC}_4\text{H}_8\text{OO}\cdot$

Figure 10.1 shows the A-X spectrum of $\text{HOC}_4\text{H}_8\text{OO}\cdot$. This spectrum was taken 10 μs after photolysis of *n*-butyl nitrite, over the range 7150–7700 cm^{-1} , with a step size of 1 cm^{-1} . Background water absorptions increase the noise in the spectrum, rendering some of the scans across the region 7150–7400 cm^{-1} unusable. Therefore, two regions of the spectrum have different amounts of averaging per point. Each point in the range 7150–7400 cm^{-1} has 6.4 s of averaging (4 scans), while each point in the range 7400–7700 cm^{-1} has 24 s of averaging (15 scans). The spectrum inset in the upper right corner is the A-X cavity ringdown spectrum of *n*-butylperoxy obtained by Glover and Miller.¹⁹⁰

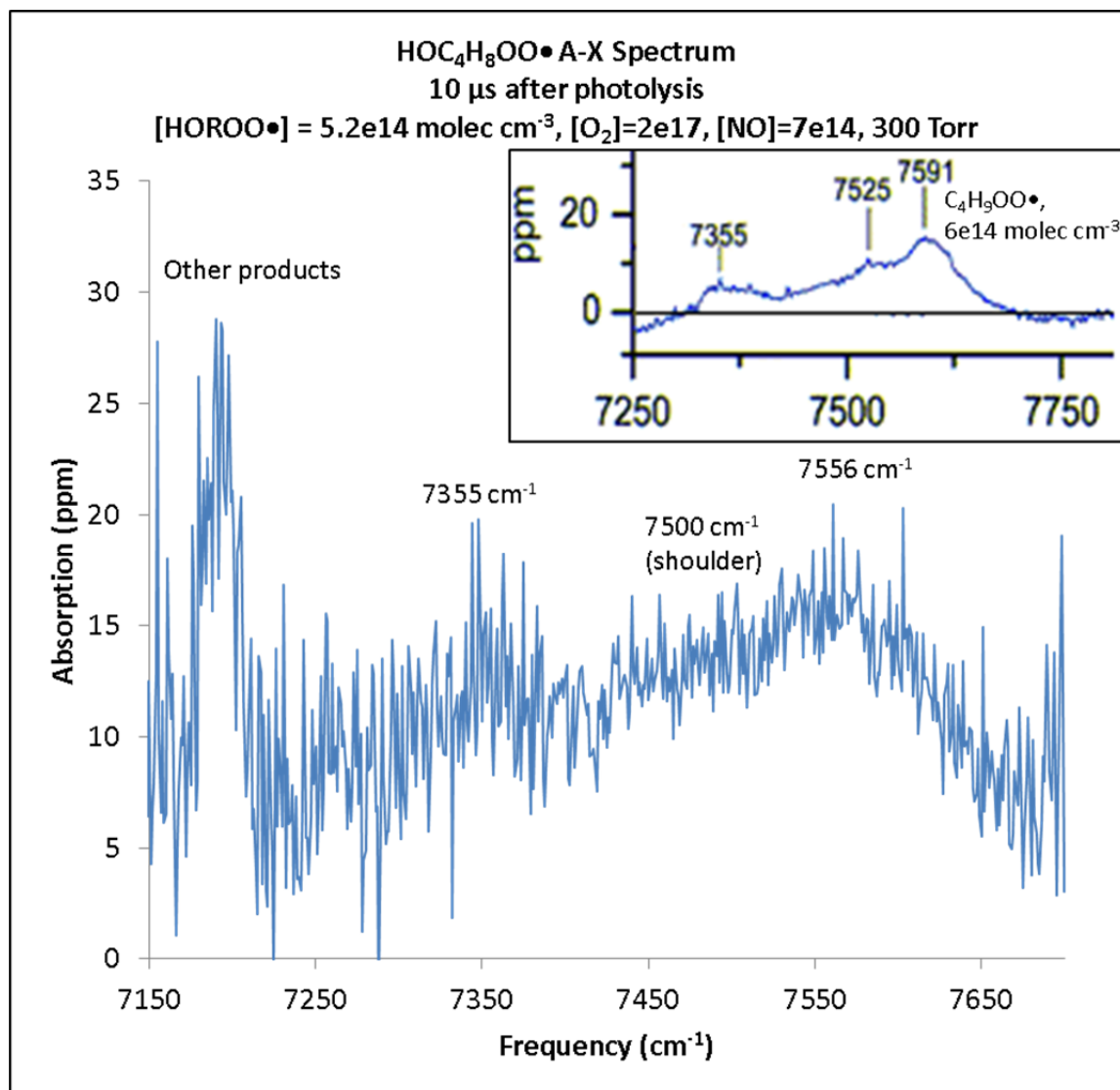


Figure 10.1. Cavity ringdown spectrum of the A-X electronic transition for the δ -hydroxybutylperoxy radical (HOC₄H₈OO•). A broad absorption is observed over the range 7200–7700 cm⁻¹, with two peaks at 7355 and 7556 cm⁻¹. A shoulder is also present at 7500 cm⁻¹. These three features are similar in position and intensity to the three peaks found in the spectrum of *n*-butylperoxy, inset in the upper right corner for reference.¹⁹⁰ The peak at 7190 cm⁻¹ is assigned to other, stable, photolysis products. Inset spectrum adapted with permission from Glover *et al.*¹⁹⁰ Copyright 2005 American Chemical Society.

There are a few features of the A-X spectrum of HOC₄H₈OO• to note. We observe a broad absorption over the range 7200–7700 cm⁻¹, with two peaks (7355 cm⁻¹, 12 ppm; and 7556 cm⁻¹, 16 ppm) and a shoulder (centered at 7500 cm⁻¹; 13 ppm). No

rotational lines can be observed (in contrast to the spectrum of HOCH₂OO• presented in Chapter 4) due to the large number of molecular conformers present. As observed in other alkyl peroxy studies,^{184, 190, 195} a large absorption at 7190 cm⁻¹ is observed. This peak is attributed to stable photolysis products, and not to alkyl peroxies, including HOC₄H₈OO•. This can be confirmed by examination of the kinetics of this peak, presented later in this chapter.

A comparison of the spectrum of HOC₄H₈OO• to Glover and Miller's spectrum of C₄H₉OO• shows that both peroxies have very similar spectral features. Both spectra have three similar features in very similar regions. The spectrum of HOC₄H₈OO• has a small broad peak at 7355 cm⁻¹, a shoulder at 7500 cm⁻¹, and a large broad peak at 7556 cm⁻¹. Similarly, the spectrum of C₄H₉OO• has a small broad peak at 7355 cm⁻¹, a very weak peak/shoulder at 7525 cm⁻¹, and a larger broad peak at 7591 cm⁻¹. The small shifts in peak positions are likely due to energy shifts in the valence orbitals from interactions between the OH and OO• groups, similar to the HOCH₂OO• vs CH₃OO• transition frequencies presented in Chapter 5.

Finally, the peak intensities and relative intensities are summarized in Table 10.3. We note similar absolute absorbances. Our kinetics model (presented later in the *Kinetics* section) predicts that we will form [HORO•] = 5 × 10¹⁴ molec cm⁻³, and that 99% of the chemical species with a peroxy group in the system are HOROO•. Glover and Miller's A-X spectrum of C₄H₉OO• was taken by photolysis of C₄H₉I in the presence of O₂.¹⁹⁰ Typical C₄H₉• formed was 6 × 10¹⁴ molec cm⁻³, with no estimate of how much was converted to C₄H₉OO•. Still, we expect Glover's [C₄H₉OO•] to be approximately equal to our [HOC₄H₈OO•] (within a factor of 2), and our absorbance data support this.

Table 10.3. Absolute and relative absorbances for the A-X peaks in δ -HOC₄H₈OO• and *n*-C₄H₉OO•.

	A_{7355}^a	A_{7500}^a	A_{7550}^a	A_{7500}/A_{7355}	A_{7550}/A_{7355}	A_{7550}/A_{7355}
δ -HOC ₄ H ₈ OO•	12	13	16	1.1	1.3	1.2
<i>n</i> -C ₄ H ₉ OO•	6	10	14	1.7	2.3	1.4

a) Absorbances in ppm

We also note that the relative intensities of the three features differ between the two spectra. In our δ -HOC₄H₈OO• spectrum, the absorption at 7355 cm⁻¹ is nearly as strong as the other two features. In contrast, the 7355 cm⁻¹ absorption in *n*-C₄H₉OO• is a factor of 2 weaker than the other two features.¹⁹⁰ This could be explained in a number of ways: different conformers being populated for each molecule, different Franck-Condon factors, or different dipole-derivatives. It would be interesting and worthwhile to examine this behavior in detail with a quantum chemistry study similar to the one in Chapter 5.

Kinetics

One of the major benefits of measuring the A-X band is that we can measure the kinetics of HOC₄H₈OO• destruction. Figure 10.2 shows six plots of the A-X absorbance (7556 cm⁻¹) as a function of time after RONO photolysis. A combination of two [RONO] (3.4×10^{16} molec cm⁻³ and 1.4×10^{16} molec cm⁻³) and three photolysis ratios (2.83%, 1.98%, 0.95%) gave rise to six different experimental conditions, allowing us to observe whether the kinetics were affected by [RO•] or [RONO]. For all scans, [O₂] = 2×10^{17} molec cm⁻³. The HOC₄H₈OO• lifetimes (1/e time for absorbance) were calculated by drawing an average line through the kinetics data, and are summarized in Table 10.4. The large noise level in each kinetics plot causes our lifetime estimates to have at least 20% error.

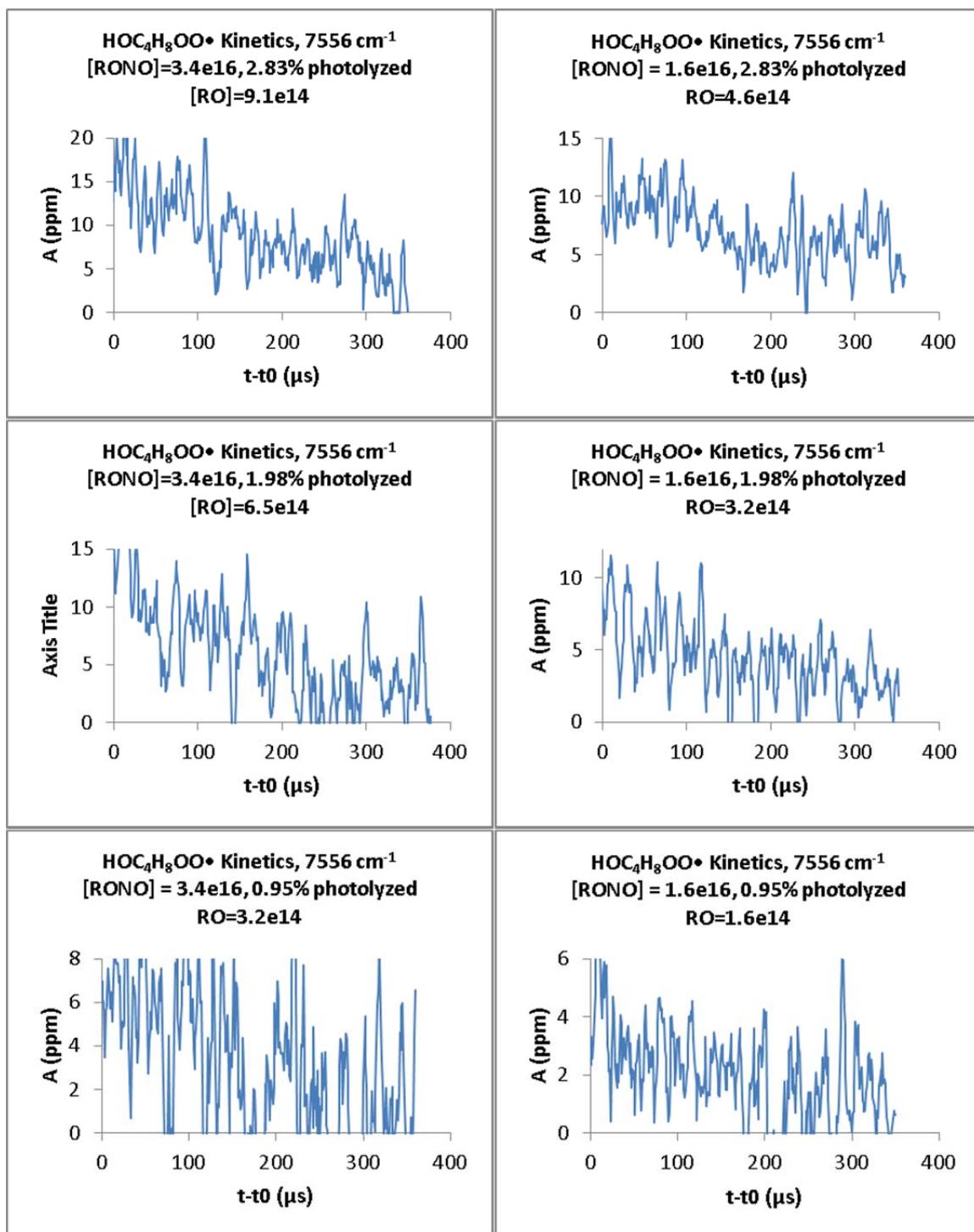


Figure 10.2. Direct kinetics measurements of $\text{HOC}_4\text{H}_8\text{OO}\cdot$ via the A-X band (7556 cm^{-1}), 0–350 μs after $\text{C}_4\text{H}_9\text{O}\cdot$ formation. Various $[\text{RONO}]$ and photolysis ratios were used (see individual plots for details). For all experiments, $[\text{O}_2] = 2 \times 10^{17}\text{ molec cm}^{-3}$, $p = 300\text{ torr}$. The low $[\text{RO}\cdot]$ experiments give rise to low $[\text{HOROO}\cdot]$, and therefore noisy kinetics data, making interpretation of the data difficult. The lifetimes of $\text{HOROO}\cdot$ are on the order 200–400 μs , and are summarized in Table 10.4.

Table 10.4. Observed and modeled $\text{HOC}_4\text{H}_8\text{OO}\cdot$ lifetimes ($1/e$ time), $[\text{O}_2] = 2 \times 10^{17}$ molec cm^{-3} , $p = 300$ torr.

[RONO] (molec cm^{-3})	[RO•] (molec cm^{-3})	[NO] ^a (molec cm^{-3})	$\tau_{\text{HOROO}\cdot}$ obs. (μs)	$\tau_{\text{HOROO}\cdot}$ model (μs)
3.4×10^{16}	9.1×10^{14}	9.6×10^{14}	200	170
3.4×10^{16}	6.5×10^{14}	7.0×10^{14}	200	250
3.4×10^{16}	3.2×10^{14}	3.7×10^{14}	275	450
1.6×10^{16}	4.6×10^{14}	4.8×10^{14}	300	310
1.6×10^{16}	3.2×10^{14}	3.4×10^{14}	300	425
1.6×10^{16}	1.6×10^{14}	1.8×10^{14}	>350	>500

a) Assumes RONO:NO=700:1 in sample

b) Error on observed lifetimes is at least $\pm 20\%$

We observe lifetimes of $\text{HOROO}\cdot$ on the order of 200–400 μs . The lifetime increases as we reduce radical concentrations (RO• or NO). These compare favorably to the lifetimes obtained from our kinetics simulations, summarized in the final column. We conclude that the secondary chemistry of $\text{HOROO}\cdot$ is reasonably well modeled.

Kinetics simulations are shown in Figure 10.3 for $\text{HOC}_4\text{H}_8\text{OO}\cdot$ and other peroxies under our experimental conditions. At 500 μs , we observe formation of $\text{C}_4\text{H}_9\text{OO}\cdot$ (up to 25% of the $\text{HOC}_4\text{H}_8\text{OO}\cdot$ concentration). At these times, we expect two contributions to the A-X spectrum and our measured kinetics in Figure 10.2: $\text{HOC}_4\text{H}_8\text{OO}\cdot$ (major product) and $\text{C}_4\text{H}_9\text{OO}\cdot$ (minor product). Formation of additional peroxies implies that we cannot make meaningful kinetics measurements of $\text{HOC}_4\text{H}_8\text{OO}\cdot$ at long times ($>500 \mu\text{s}$).

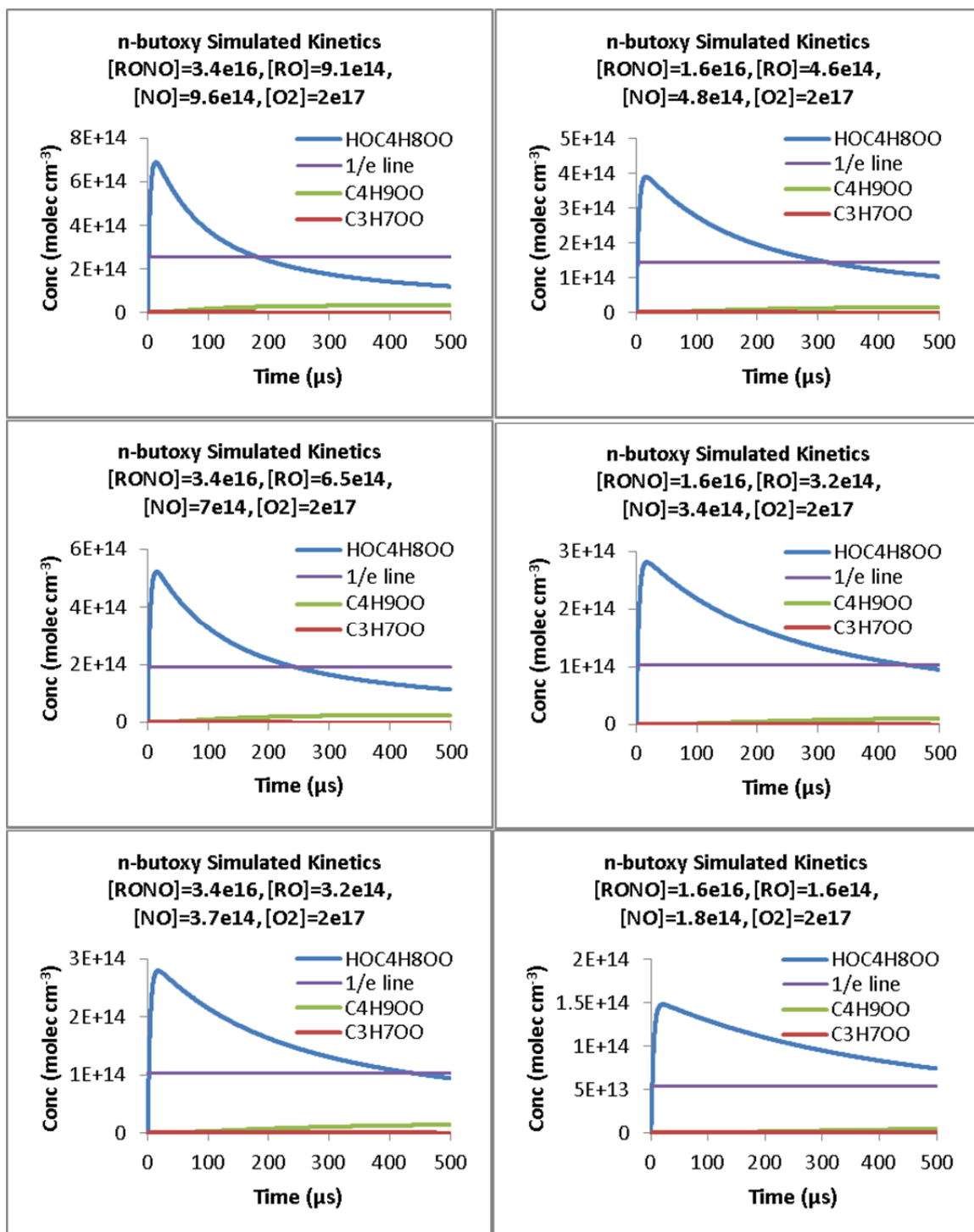


Figure 10.3 Kinetics simulations of HOC₄H₈OO• and peroxy species for our alkoxy experiments, 0–500 μs after C₄H₉O• formation. Various [RONO] and photolysis ratios were used (see individual plots for details). For all experiments, [O₂] = 2 × 10¹⁷ molec cm⁻³, *p* = 300 torr. The lifetime of HOC₄H₈OO• is indicated by the intersection of the kinetics trace (blue line) with the 1/e concentration (purple line). The lifetimes are in good agreement with our experiment (Figure 10.2).

Determination of the Relative Rate Constant $k_{\text{isom}}/k_{\text{O}_2}$

The main goals of the study presented in this chapter were to measure the A-X electronic spectrum of $\text{HOC}_4\text{H}_8\text{OO}\cdot$ and direct kinetics of $\text{HOC}_4\text{H}_8\text{OO}\cdot$ destruction. To date, limited relative kinetics data have been obtained. The reported $k_{\text{isom}}/k_{\text{O}_2}$ should be considered preliminary.

As described in the *Introduction* section, the relative rate constants of the isomerization channel (Reaction 10.2) and the O_2 channel (Reaction 10.3) can be determined by varying $[\text{O}_2]$ and measuring the absorptions of $\text{HOC}_4\text{H}_8\text{OO}\cdot$. $k_{\text{isom}}/k_{\text{O}_2}$ can be extracted by measuring the absorbance (A) relative to “[O_2] = 0” (A_0), then applying Equations 10.10–10.13.

There are two items of note for our relative kinetics experiment. First, at $[\text{O}_2] = 0$, we do not form any $\text{HOROO}\cdot$, and any absorbance measurements that we make are meaningless. We therefore define A_0 as the y-intercept of the regression line fit to the rest of the absorbance data (same procedure as used in our ν_1 experiment in Chapter 8). Second, we are using a much higher $[\text{RO}\cdot]$ than in the ν_1 experiment, and therefore a much higher $[\text{NO}]$. Consequently, the correction factors X_{kin} and X_{prompt} will not be the same as in Chapter 8, and will be recalculated here.

To determine $k_{\text{isom}}/k_{\text{O}_2}$, A_0/A was measured at the largest peak of the A-X spectrum, 7556 cm^{-1} , for the range $2 \times 10^{17}\text{ molec cm}^{-3} < [\text{O}_2] < 8 \times 10^{18}\text{ molec cm}^{-3}$. The peak was measured 10 μs after photolysis to ensure that $\text{HOC}_4\text{H}_8\text{OO}\cdot$ was not being destroyed, as shown in the *Kinetics* section above. 800 ringdown traces, or 80 seconds of data, were averaged for each $[\text{O}_2]$ concentration (16 shots per point, 50 data points). The resulting absorbances were then scaled to $[\text{C}_4\text{H}_9\text{ONO}]$ concentration by scaling to the gas

flows and pressure in the CRDS cell. We then used Equations 10.10–10.13 to determine $k_{\text{isom}}/k_{\text{O}_2}$.

Figure 10.4 shows the plot of A_0/A vs $[\text{O}_2]$ for *n*-butoxy, measured using the A-X spectrum peak at 7556 cm^{-1} . The linear fit is reasonable given the low number of data points taken ($R^2 = 90.4\%$). With 2σ errors, the slope of the plot is $(6.3 \pm 2.1) \times 10^{-20}\text{ cm}^{-3}$ and the intercept is (1.00 ± 0.08) .

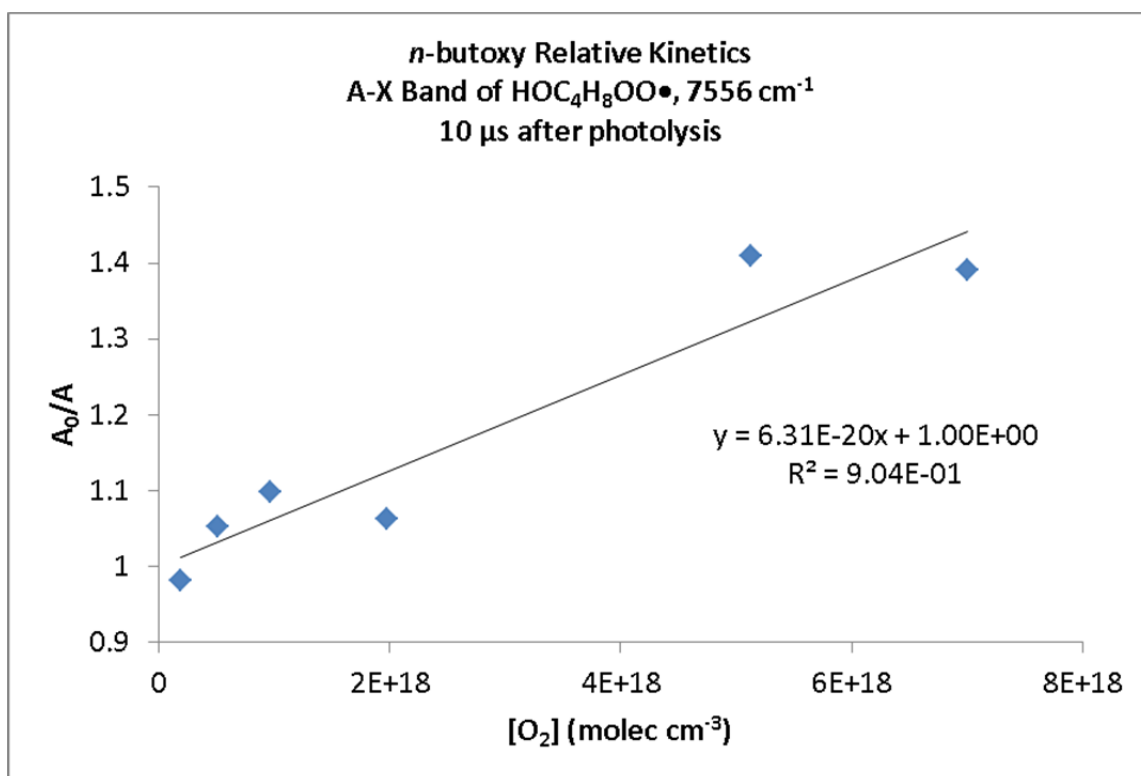


Figure 10.4. Plot of A_0/A vs $[\text{O}_2]$ for *n*-butoxy as measured by the A-X electronic spectrum peak of $\delta\text{-HOC}_4\text{H}_8\text{OO}\bullet$ at 7556 cm^{-1} . With 2σ errors, this plot has a slope of $(6.3 \pm 2.1) \times 10^{-20}\text{ cm}^{-3}$, and an intercept of (1.00 ± 0.08) . Including the correction factor $X = (0.88 \pm 0.05)$, the resulting $k_{\text{isom}}/k_{\text{O}_2}$ value for *n*-butoxy is determined to be $(1.39 \pm 0.47) \times 10^{19}\text{ cm}^{-3}$, with 2σ error.

As noted earlier, we must recalculate the correction factors X_{kin} and X_{prompt} (Equations 10.12 and 10.13) with our elevated NO ($6.8 \times 10^{14}\text{ molec cm}^{-3}$). This [NO] is the sum of the calculated $[\text{RO}\bullet]$ (Table 10.1) and the additional NO present in the *n*-butyl

nitrite (see the *FTIR* section for more information). The relevant parameters and derived values of X_{kin} , X_{prompt} , and the overall correction factor X_{tot} are summarized in Table 10.5.

Our results show that $X_{\text{kin}} = 0.92 \pm 0.05$, $X_{\text{prompt}} = 0.96 \pm 0.02$, and $X_{\text{tot}} = 0.88 \pm 0.05$ (2σ).

Using this correction factor and our A_0/A , we obtain $k_{\text{isom}}/k_{\text{O}_2} = (1.39 \pm 0.47) \times 10^{19} \text{ cm}^{-3}$.

Table 10.5. Parameters used for calculation of correction factors and $k_{\text{isom}}/k_{\text{O}_2}$ for A-X band

	Units	Best Value	Uncertainty (2σ)
$\left[\left(\frac{\partial \left(\frac{A_0}{A} \right)}{\partial [\text{O}_2]} \right)_{[\text{O}_2]=0} \right]^{-1}$	10^{19} cm^{-3}	1.58	0.53
$k_{\text{decomp}}/k_{\text{isom}}$		0.0024	0.0017
$k_{\text{NO}}[\text{NO}]/k_{\text{isom}}$		0.0262	0.0187
ϕ_{pi}		0.038	0.018
X_{kin}		0.92	0.05
X_{prompt}		0.96	0.02
$X_{\text{kin}} \times X_{\text{prompt}}$		0.88	0.05
$k_{\text{isom}}/k_{\text{O}_2}$	10^{19} cm^{-3}	1.39	0.47

Table 10.6 contains a summary of the relative rate constants $k_{\text{isom}}/k_{\text{O}_2}$ for *n*-butoxy found in the literature and compares our value measured from the A-X band. We observe that the preliminary value of $k_{\text{isom}}/k_{\text{O}_2}$ as determined from the A-X band is in good agreement with all of the previous studies in the literature, although subject to somewhat large uncertainty (34%) compared to our ν_1 CRDS experiment from Chapter 8 (9%).

Table 10.6. Comparison of relative rate constant determinations $k_{\text{isom}}/k_{\text{O}_2}$ and derived k_{isom} for *n*-butoxy and 2-pentoxy

	$k_{\text{isom}}/k_{\text{O}_2}$ (10^{19} cm^{-3}) ^a	k_{isom} (10^5 s^{-1}) ^b	Molecules detected	Method	<i>P</i> (<i>torr</i>)	Ref
<i>n</i> -butoxy	1.39 ± 0.47	2.0 ± 1.2	δ -hydroxy- <i>n</i> -butyl peroxy	Slow flow, CRDS (A-X)	330	This work
	1.96 ± 0.25	2.7 ± 1.4	δ -hydroxy- <i>n</i> -butyl peroxy	Slow flow, CRDS (OH Str)	330	Chapter 7
	1.69 ± 0.15	2.4 ± 1.2	δ -hydroxy- <i>n</i> -butyl peroxy	Slow flow, CRDS (OH Str)	670	Chapter 8
	2.0 ± 0.4	2.7 ± 1.5	Butyl nitrite, Butanal,	Static, FTIR	700	Cassanelli ¹⁵⁵
	1.5 ± 0.4	2.1 ± 1.2	4-hydroxy butanal	Static, GC	760	Cox ¹⁵⁶
	1.9 ± 0.4	2.7 ± 1.4	Butane, Butanal	Static, FTIR	700	Niki ¹⁴⁸
	2.1 ± 0.5	2.9 ± 1.6	Butyl nitrite, Butanal	Slow flow, GC	760	Cassanelli ¹⁶⁰
	1.8 ± 1.1	2.5 ± 2.0	Butyl nitrite, Butanal	Slow flow, GC	760	Cassanelli ¹⁶⁰
	1.8 ± 0.6	2.5 ± 1.5	Butane, Butanal	Static, FTIR	760	Geiger ¹⁶¹
	0.25 ± 0.19^c	0.35 ± 0.20^c	Butanal, 4-hydroxy butanal	Fast flow, LIF	38	Hein ¹⁵⁹
	1.6	2.2	OH and NO ₂	Static, GC	740	Carter ¹⁵⁴
	2.1 ± 1.8^d	2.9 ± 1.4^d		Recommendation	760	IUPAC ¹¹⁸

a) All uncertainties are 2σ . All studies other than the current work treat all alkoxy reactions besides isomerization and reaction with O₂ as negligible.

b) Computed k_{isom} assuming literature value of $k_{\text{O}_2} = (1.4 \pm 0.7) \times 10^{-14} \text{ cm}^3 \text{ s}^{-1}$ for *n*-butoxy.²⁸

c) Unlike the other studies, Hein directly measured k_{isom} . In this table, we calculate the ratio $k_{\text{isom}}/k_{\text{O}_2}$ from Hein's measurement using the literature value of k_{O_2} .

d) The IUPAC recommendation for $k_{\text{isom}}/k_{\text{O}_2}$ is computed from their individual recommendations of the isomerization and O₂ reactions

FTIR Analysis of *n*-butyl nitrite

Four samples of *n*-butyl nitrite were measured in the FTIR, and will be presented in order of decreasing purification (fresh and freeze pumped, fresh but not freeze pumped, old but not freeze pumped, and old but stored at room temperature).

Figure 10.5 shows the FTIR spectrum for the purest sample: a freshly opened bottle of butyl nitrite from Sigma-Aldrich, stored at 4 °C, and freeze pumped 3 times prior to use. Three FTIR spectra were taken of this sample: the first spectrum with 148 torr of butyl nitrite, the second spectrum with 62 torr, and the third spectrum of 78 torr. Time was allowed to pass between when the FTIR spectra were taken: the second

spectrum was taken 15 minutes after the first, and the third was taken 45 minutes after the first.

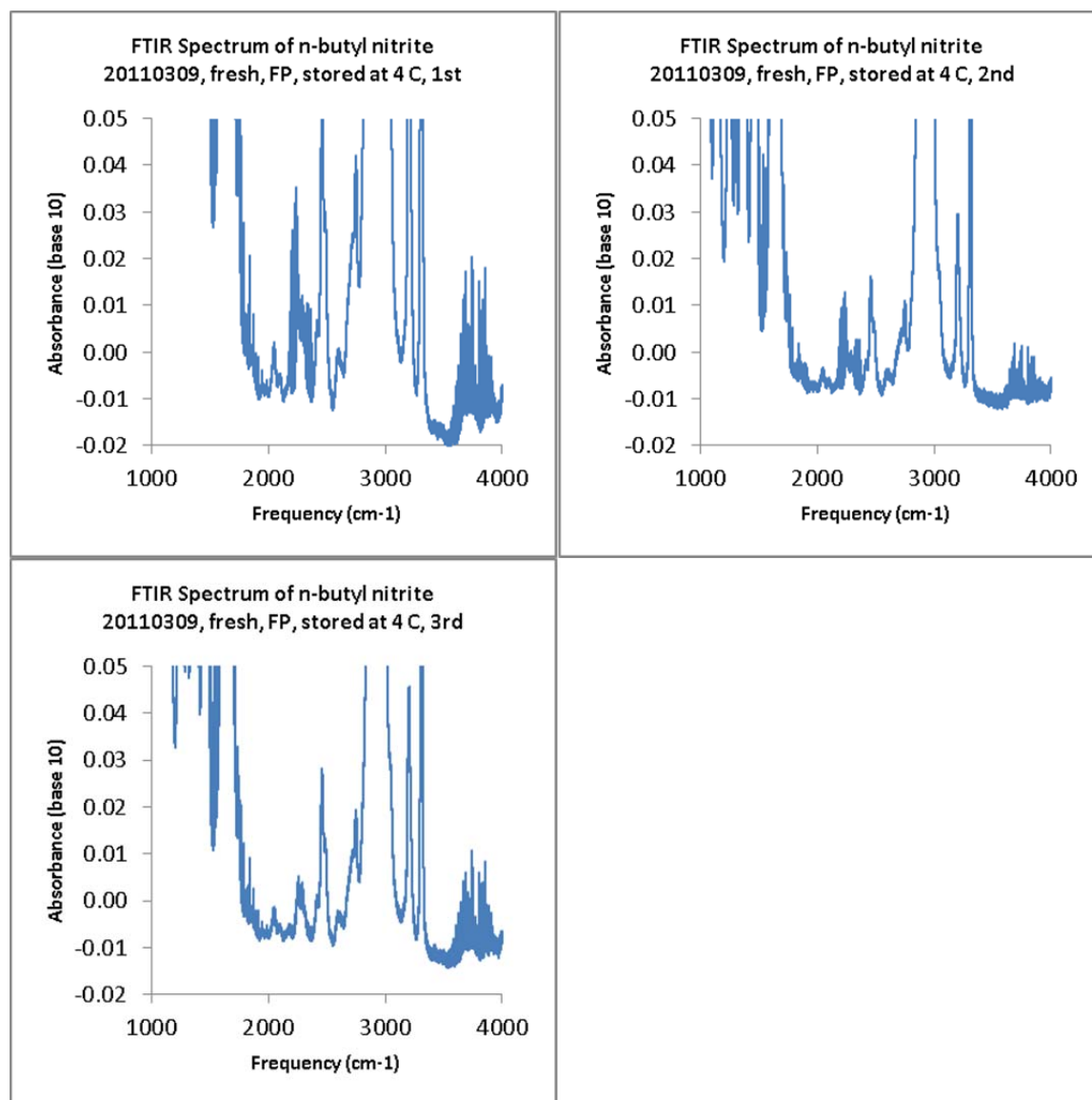


Figure 10.5. FTIR Spectra of *n*-butyl nitrite (March 2011 sample). The butyl nitrite was a freshly opened sample from Aldrich, stored at 4 °C, and freeze pumped 3 times prior to use. Part a (upper left): first spectrum (148 torr). Part b (upper right): second spectrum (62 torr), 15 minutes after first sample. Part c (lower left): third spectrum (78 torr), 45 minutes after first sample.

The spectra in Figure 10.5 show peaks that vary in height as a function of the pressure in the FTIR cell (and therefore the amount of sample injected). These are the

peaks at 1600 cm^{-1} (RONO), 2050 cm^{-1} , 2350 cm^{-1} (CO_2), 2970 cm^{-1} (RONO), and 3860 cm^{-1} (CO_2). There is also a peak at 2315 cm^{-1} that is present in the first two spectra, but not in the third.

Figure 10.6 shows the NO band region for all three spectra that were taken (centered at 1875 cm^{-1}). Weak NO peaks are observed in the first spectrum, much stronger NO lines are observed in the second spectrum and much weaker peaks are observed in the third spectrum. No purification was performed between the scans: it appears that $[\text{NO}]$ is varying over time.

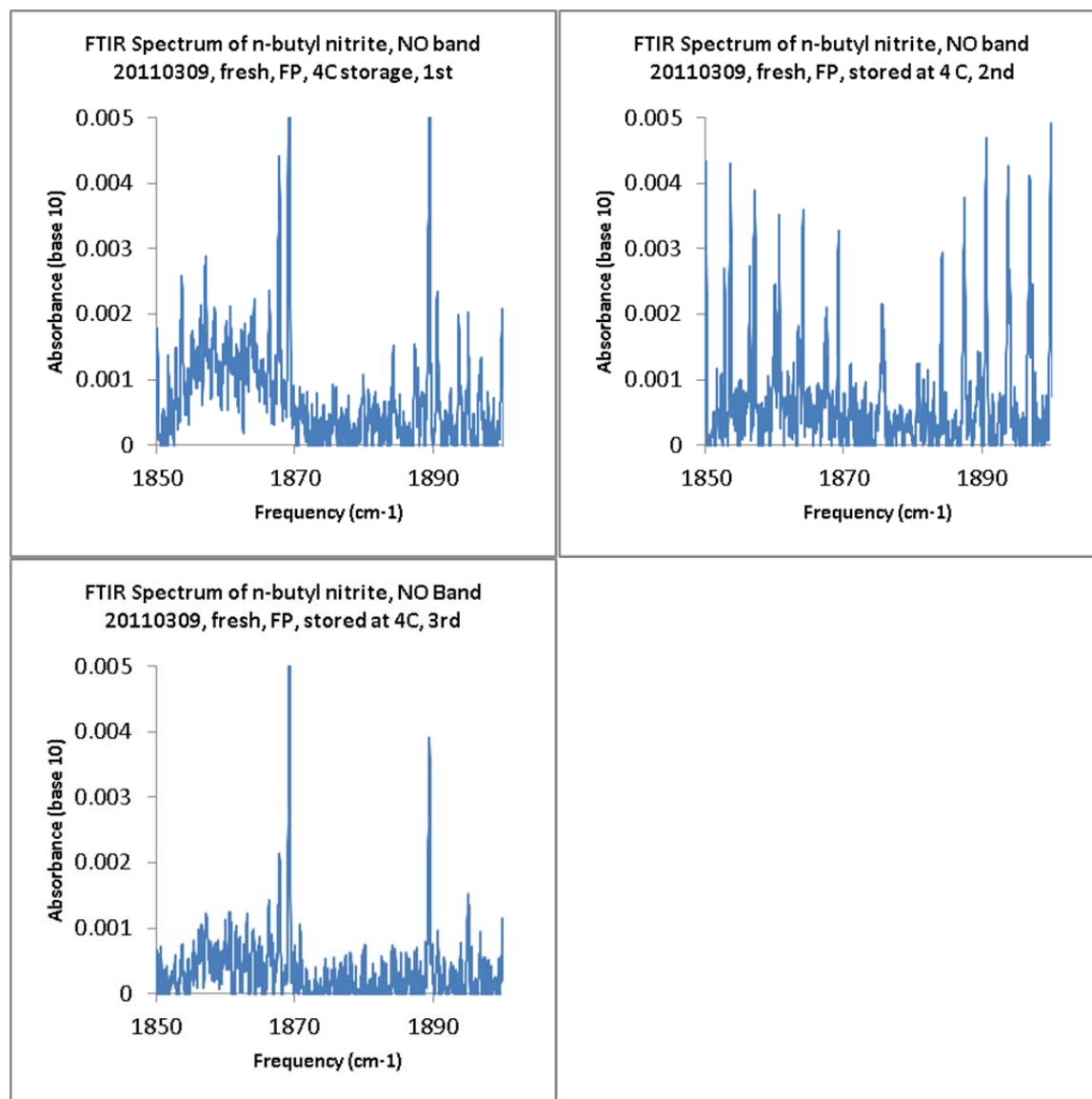


Figure 10.6. FTIR Spectra of the NO vibrational band region of *n*-butyl nitrite. The butyl nitrite was a freshly opened sample from Aldrich, stored at 4 °C, and freeze pumped 3 times prior to use. Part a (upper left): first spectrum (148 torr). Part b (upper right): second spectrum (62 torr), 15 minutes later. Part c (lower left): third spectrum (78 torr), 45 minutes after first sample.

The FTIR spectra of the other three samples and their associated NO bands are shown in Figures 10.7 and 10.8, with Figure 10.7 representing a purer sample than the ones presented in Figure 10.8. The second sample (Figure 10.7) was the same freshly opened butyl nitrite as the first sample discussed above, but not freeze pumped (besides

pumping the atmosphere off prior to FTIR injection). Two FTIR spectra of this sample were taken, 10 minutes apart. The third sample (Figure 10.8, top) was a 4 week old sample of butyl nitrite stored at 4 °C, not freeze pumped prior to measurement. The fourth sample (Figure 10.8, bottom) was an 8 week old sample of butyl nitrite stored at 25 °C, measured to assess the effects of decomposition.

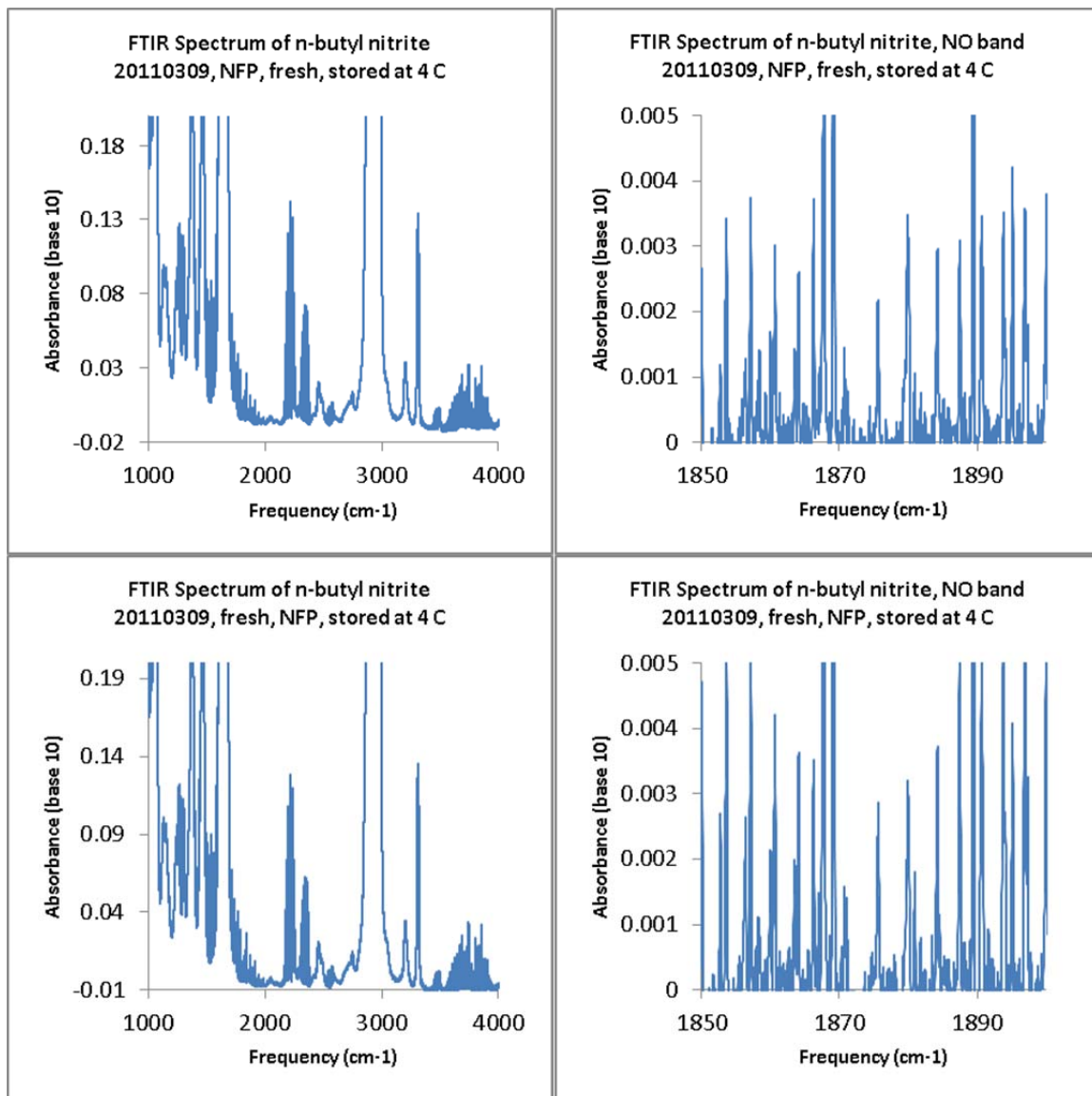


Figure 10.7. FTIR spectra of the full scan and NO vibrational band region of *n*-butyl nitrite. The butyl nitrite was a freshly opened sample from Aldrich, stored at 4 °C, and not freeze pumped. Part a (upper left): first spectrum (68 torr), full range. Part b (upper right): first spectrum (68 torr), NO band. Part c (lower left): second spectrum (66 torr), 10 minutes after first sample, full range. Part d (lower right): second spectrum (66 torr), NO band.

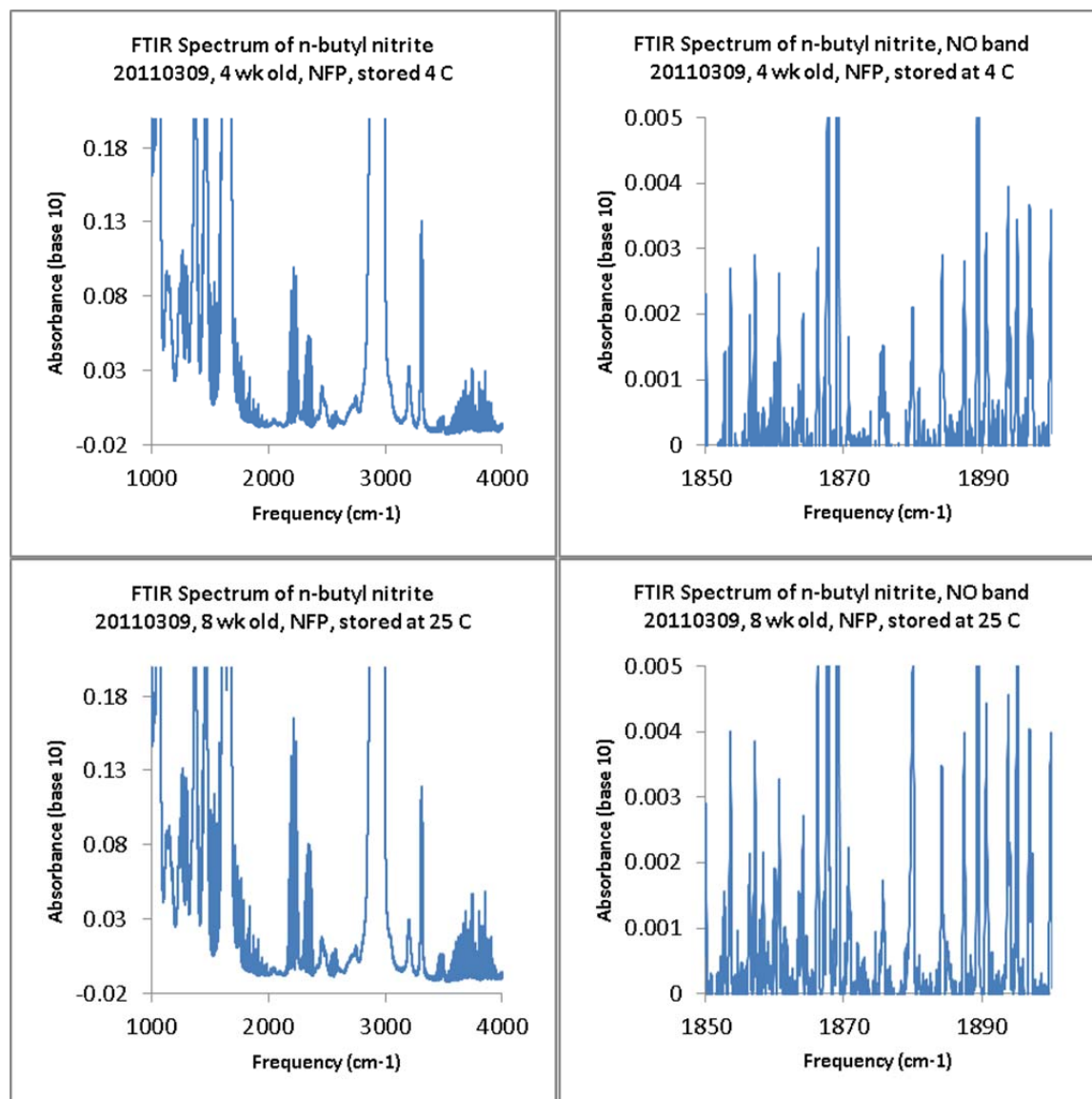


Figure 10.8. FTIR spectra of the full scan and NO vibrational band region of *n*-butyl nitrite. Part a (upper left): 4 week old sample stored at 4 °C, not freeze pumped prior to measurement (65 torr), full range. Part b (upper right): same as part a, NO band. Part c (lower left): 8 week old sample stored at room temperature, not freeze pumped prior to measurement (65 torr), full range. Part d (lower right): same as part c, NO band.

With the FTIR spectra from each sample recorded, we can now fit the PNNL reference spectrum of NO to each *n*-butyl nitrite spectrum. Figure 10.9 shows the fitting to the NO band for the three spectra taken for the first sample (fresh nitrite, freeze pumped, stored at 4 °C). The other three samples had NO bands most similar to the

second spectrum of the first sample (Figure 10.9b), and thus their fits will not be shown here.

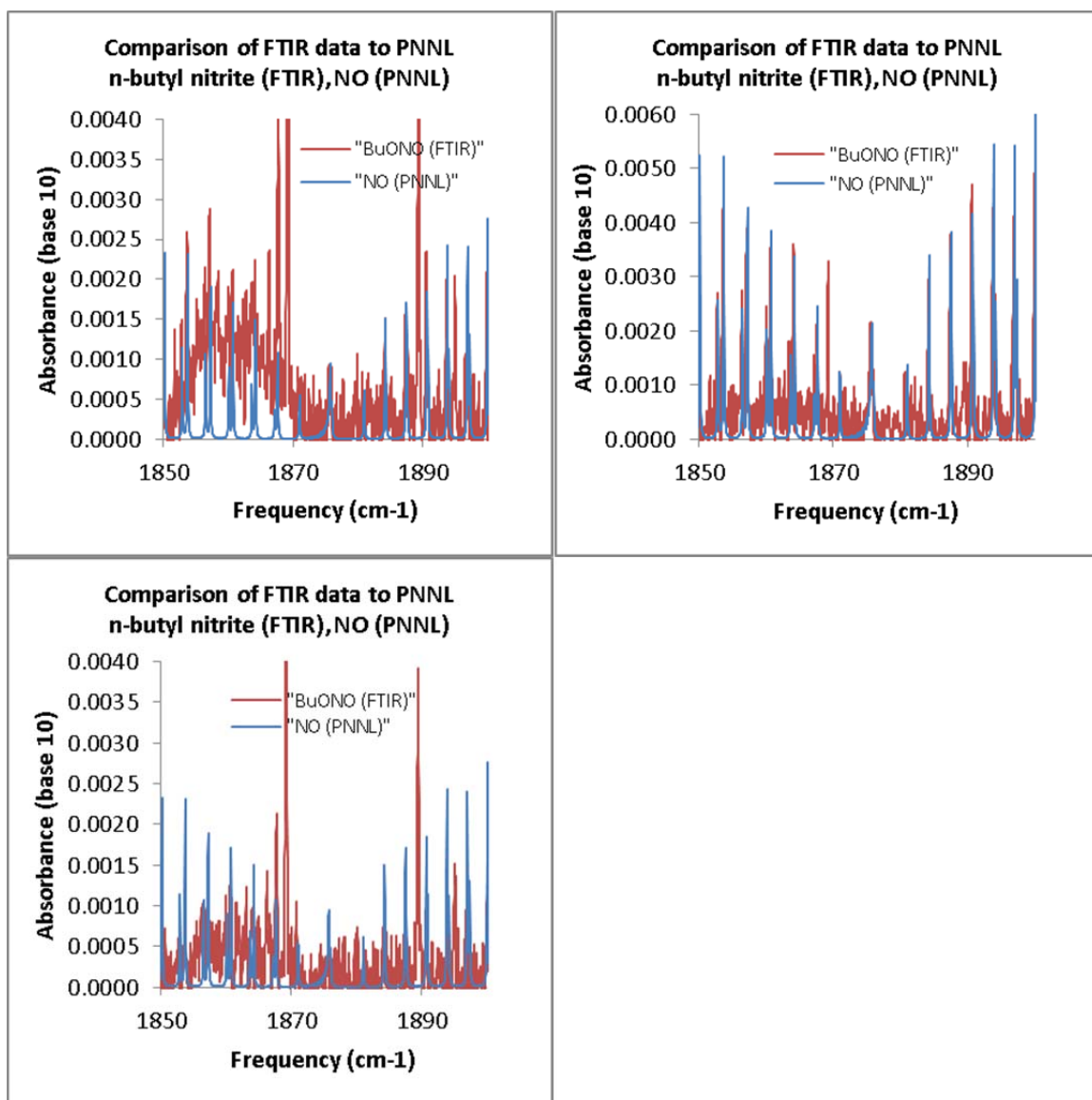


Figure 10.9. FTIR spectra of the NO bands in *n*-butyl nitrite (March 2011 sample, freshly opened, freeze pumped, stored at 4 °C) compared to PNNL reference spectra of NO. Part a (upper left): first spectrum taken (PNNL scaled by a factor of 4). Part b (upper right): second spectrum taken (15 minutes after first, PNNL scaled by a factor of 9). Part c (lower left): third spectrum taken (45 minutes after first, PNNL scaled by a factor of 4).

The fit of the PNNL reference band to the FTIR band in Figure 10.9b is good. However, the fits in Figures 10.9a and 10.9c show inconsistencies between fitting the P

and R branches. The peak ratios in the experimental spectrum do not match the peak ratios in the reference spectrum, leading to extra uncertainty on the amount of NO present in the cell. Additionally, the FTIR instrument was not able to produce a totally correct baseline for any of the spectra. Despite best efforts to manually produce better baselines, inconsistencies still appear in regions of the spectra (in this case, between 1850 and 1870 cm^{-1}). It is also possible that there is an absorber in this region, although it appears to vary inversely with the amount of NO present. Despite these problems, best estimates of [NO] were made, with the stipulation that all reported [NO] values should have around a factor of 5 uncertainty.

Finally, the concentration of $\text{C}_4\text{H}_9\text{ONO}$ was determined by measuring the ON-O stretch peak (1575–1725 cm^{-1}) and comparing to the integrated absorbance calculated in Chapter 7 ($I_{\text{base e}} = 194 \text{ km mol}^{-1}$, or $3.22 \times 10^{-17} \text{ cm molec}^{-1}$). This corresponds to a cross section in the FTIR of $I_{\text{base10}} = 84.2 \text{ km mol}^{-1}$, or $1.4 \times 10^{-17} \text{ cm molec}^{-1}$. The largest peak at 1670 cm^{-1} is very strong, and perhaps in the non-linear absorption region (shown in Figure 10.10), causing us to underestimate [RONO]. Thus, the NO contamination that we report is an upper limit.

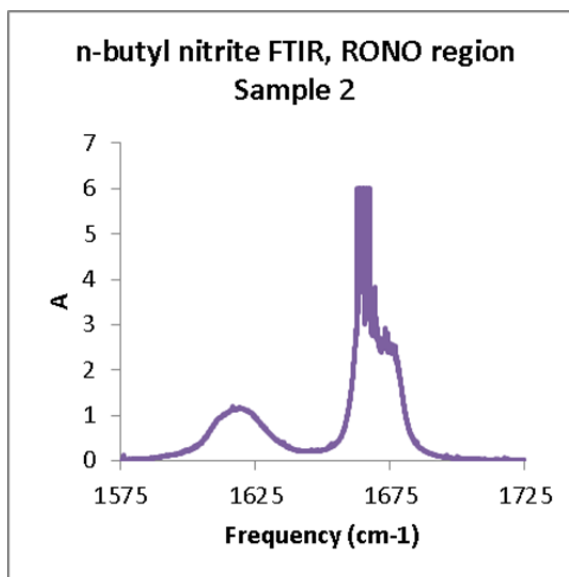


Figure 10.10. – Sample ON-O stretch spectrum (FTIR) of *n*-butyl nitrite. For this sample, the integrated absorbance is 92.7 cm^{-1} , or $[\text{RONO}] = 3.5 \times 10^{17} \text{ molec cm}^{-3}$.

We can determine $[\text{NO}]$ in the CRDS experiment based on the FTIR spectra by using the following procedure. All reference spectra reported by PNNL are scaled by the authors to an effective burden ($[\text{gas}] \times \text{path length}$) of $2.48 \times 10^{15} \text{ molec cm}^{-2}$. $[\text{NO}] \times \text{path length}$ in the experimental FTIR spectrum was calculated by scaling the PNNL NO spectrum to the NO vibrational band at 1875 cm^{-1} , then multiplying the scaling factor by $2.48 \times 10^{15} \text{ molec cm}^{-2}$. Dividing by the FTIR path length (19 cm) gives us $[\text{NO}]$.

The *n*-butyl nitrite sample descriptions, FTIR conditions, scaling factors of the reference spectra to the FTIR spectra, and calculated $[\text{NO}]$ in the CRDS experiment are summarized in Table 10.7. Our FTIR data suggest that using a freeze pumped sample of butyl nitrite will yield excess $[\text{NO}]_{\text{CRDS}} = (0.3\text{--}1) \times 10^{14} \text{ molec cm}^{-3}$, and that not freeze pumping the sample (regardless of storage conditions) will yield excess $[\text{NO}]_{\text{CRDS}} = (1\text{--}2) \times 10^{14} \text{ molec cm}^{-3}$. The values reported from this study have large uncertainties associated with them due to inconsistencies in the measured NO bands and nonlinearities

in the RONO spectrum. The derived excess $[\text{NO}]_{\text{CRDS}}$ should be considered an upper limit, and may be high by a factor of 2–5.

Based on the FTIR analysis, we expect that the extra $[\text{NO}]$ introduced from the nitrite sample itself is 5%-10% of the $[\text{NO}]$ generated from the nitrite photolysis (Reactions 10.1 and 10.2).

Table 10.7. Scale factors for FTIR and PNNL spectra and determination of $[\text{NO}]$ in the CRDS experiment

	Units	1	1a	1b	2	2a	3	4
Sample Age		Fresh	Fresh	Fresh	Fresh	Fresh	4 wks.	8 wks.
Storage Temp	K	277	277	277	277	277	277	293
Freeze Pump?		yes	yes	yes	no	no	no	no
Pressure	torr	148	62	77	68	66	65	65
[RONO] (by ON-O str, 1575-1725 cm^{-1})	molec cm^{-3}	8.6×10^{17}	4.4×10^{17}	6.0×10^{17}	5.1×10^{17}	5.1×10^{17}	5.1×10^{17}	4.5×10^{17}
NO scale factor (FTIR/PNNL)		4	9	4	10	12	7	8
$[\text{NO}]_{\text{FTIR}}$	molec cm^{-3}	6.6×10^{14}	1.5×10^{15}	6.6×10^{14}	1.7×10^{15}	2.0×10^{15}	1.2×10^{15}	1.3×10^{15}
[RONO]:[NO]		1300	290	910	300	250	420	350
$[\text{NO}]_{\text{CRDS}}$	molec cm^{-3}	3.3×10^{13}	1.4×10^{14}	4.7×10^{13}	1.4×10^{14}	1.7×10^{14}	9.7×10^{13}	1.3×10^{14}

Discussion

Measuring the A-X Spectrum of $\delta\text{-HO-1-C}_5\text{H}_{10}\text{OO}\cdot$

Given the studies in Chapters 7 and 8, the next logical extension of the alkoxy A-X spectroscopy studies would be the product of 2-pentoxy isomerization: $\delta\text{-HO-1-C}_5\text{H}_{10}\text{OO}\cdot$. Unfortunately, such a study would be complicated by prompt decomposition and the large decomposition rate of 2-pentoxy ($k_{\text{decomp}} = 2 \times 10^4 \text{ s}^{-1}$)¹¹⁷ compared to isomerization ($k_{\text{isom}} = 2.7 \times 10^5 \text{ s}^{-1}$, Chapter 8). Since decomposition (Reactions 10.6 and 10.9) will lead to the formation of other peroxy radicals, the

observed spectrum will be a mixture of δ -HO-1-C₅H₁₀OO• and the decomposition product C₃H₇OO•.

To determine the extent of this interference, we modeled the kinetics of the 2-pentoxy system using the same parameters (k_{isom} , k_{O_2} , k_{decomp}) as in Chapter 8. We used the same chemical concentrations as for the A-X spectrum of *n*-butoxy in Figure 10.1 ($[\text{RONO}] = 3.4 \times 10^{16}$ molec cm⁻³, $[\text{RO}\cdot] = 6.5 \times 10^{14}$ molec cm⁻³, $[\text{NO}] = 7.0 \times 10^{14}$ molec cm⁻³, $[\text{O}_2] = 2 \times 10^{17}$ molec cm⁻³). The simulation is shown in Figure 10.11.

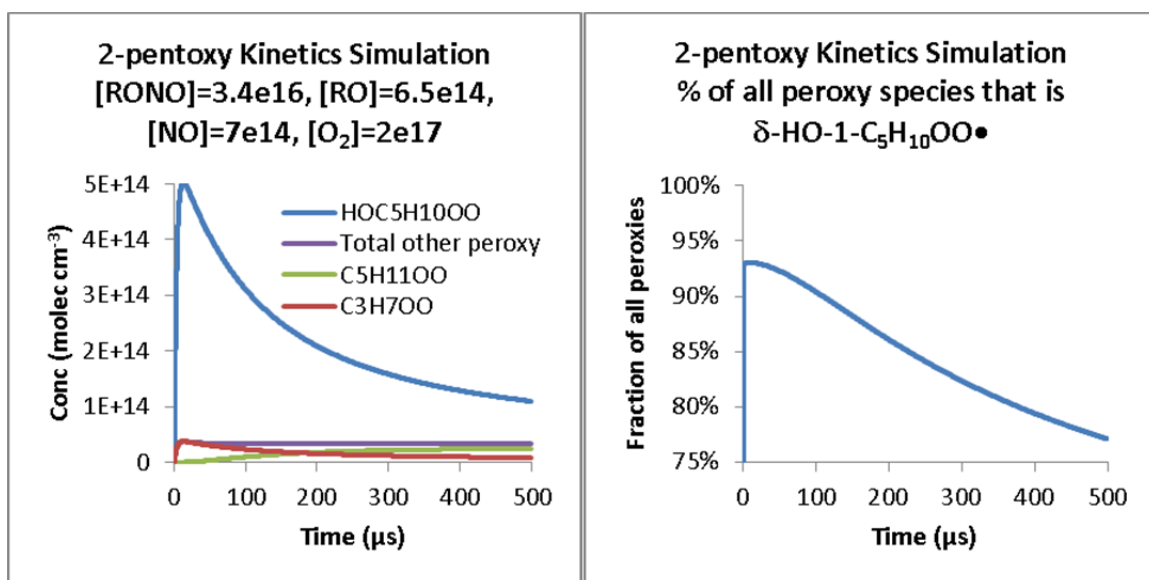


Figure 10.11. Kinetics simulations for 2-pentoxy system: concentrations of peroxy species and fraction of peroxies that are the isomerization product δ -HO-1-C₅H₁₀OO•, 0–500 μs after 2-pentoxy formation (chemical concentrations listed on the plot). Over 0–500 μs , 7%–20% of the peroxy species belong to non-isomerization products.

The isomerization product δ -HO-1-C₅H₁₀OO• reaches its maximum concentration 15 μs after alkoxy formation. We note that even within this short timescale, the decomposition product C₃H₇OO• forms in appreciable quantities, 7% of the total peroxy species in the system. (In the *n*-butoxy system, we expected less than 1%) At later times,

we observe formation of $C_5H_{11}OO\cdot$ while $\delta\text{-HO-1-C}_5\text{H}_{10}OO\cdot$ is destroyed, causing the spectrum to become contaminated. At 500 μs , over 20% of the peroxy species are products other than the alkoxy isomerization product.

The overall conclusion is that the A-X spectrum of $\delta\text{-HO-1-C}_5\text{H}_{10}OO\cdot$ obtained from alkoxy chemistry will be contaminated by other peroxy species. Since decomposition is temperature dependent, it is likely that reducing the temperature of the CRDS cell will allow for purer A-X spectra to be obtained.¹¹⁷ Room temperature experiments must contain the caveat that other peroxy species are contributing to the reported spectrum.

Conclusions

In this chapter, we have reported the first clean A-X electronic spectrum of the primary product of *n*-butoxy isomerization in the presence of oxygen: $\delta\text{-HOC}_4\text{H}_8\text{OO}\cdot$. The spectrum is similar in shape and intensity to *n*-butyl peroxy: a broad absorption in the near-IR with three features in the range 7200-7700 cm^{-1} . The relative intensities of these three features are different between $\delta\text{-HOC}_4\text{H}_8\text{OO}\cdot$ and *n*- $C_4H_9OO\cdot$. Under our experimental conditions, the recorded spectrum is expected to be at least 99% $\delta\text{-HOC}_4\text{H}_8\text{OO}\cdot$. We can measure the kinetics of $\delta\text{-HOC}_4\text{H}_8\text{OO}\cdot$ directly using the A-X band, observing $\delta\text{-HOC}_4\text{H}_8\text{OO}\cdot$ of 200–400 μs , in agreement with kinetics modeling. We have shown that the A-X band can be used for measurement of alkoxy relative kinetics, and obtain a preliminary k_{isom}/k_{O_2} , $(1.39 \pm 0.47) \times 10^{19} \text{ cm}^{-3}$, in agreement with the CRDS study in Chapter 8 (ν_1 band). Finally, we have assessed the purity of the *n*-butyl

nitrite used in our alkoxy experiments, and have shown that the [NO] contributed from the *n*-butyl nitrite sample is 5%–10% of the NO generated from alkyl nitrite photolysis.

Acknowledgements

We thank Ralph H. Page for improvements to the optical setup and assistance with experiments, and Nathan C. Eddingsaas for assistance with acquiring the FTIR spectrum of *n*-butyl nitrite. The experiments performed in this chapter were funded under NASA Upper Atmosphere Research Program Grant NNX09AE21G2.

Part 5—Appendices

Appendix A—Classification of Laser System Performance

This appendix contains a description of the methods used to classify the performance of the lasers used in the infrared cavity ringdown (IR-CRD) spectrometer (described in Chapter 2). In general, our lasers should perform as well as listed for daily use. If the energy per pulse or energy fluctuations do not meet the listed specifications, the user should replace the flashlamps in the Nd:YAG and/or realign the laser system. If performance is still unacceptable, one or more lasers may require repair. A list of repairs made to the previous Nd:YAG laser (Quantel YG-661) can be found in Appendix B, though by no means is this an exhaustive list of fixes for a broken laser.

Introduction

As described in Chapter 2, the performance of a pulsed IR-CRD spectrometer is dependent on both the average energy per laser pulse, and the pulse-to-pulse energy fluctuations. The average energy per pulse will determine the ringdown amplitude, according to Equation A.1:

$$V_0 = \mathfrak{R} \times A \times \frac{(1-R)^2 c E_{IR}}{L_{opt}} (X), \quad (\text{A.1})$$

where V_0 is the ringdown amplitude, \mathfrak{R} is the photovoltaic responsivity of the photodiode (in A/W), A is the transimpedance amplification (in V/A), R is the cavity ringdown mirror reflectivity, L_{opt} is the cavity length, c is the speed of light, E_{IR} is the energy per pulse of the incident infrared light, and X is the fraction of light entering the cavity that couples to cavity modes. As E_{IR} becomes larger, the ringdown amplitude also becomes larger, allowing for a larger quantity of ringdown data to be collected before reaching the noise

limit of the detector. Additionally, increasing E_{IR} allows for higher reflectivity mirrors can be used, which increases the sensitivity of the instrument.

Cavity ringdown spectroscopy is theoretically insensitive to energy fluctuations; nonetheless, it is important to keep these fluctuations to a minimum because of data collection considerations. Ringdown data are sent to a 14-bit digital oscilloscope (Gage CompuScope CS1450), with a variable maximum detectable voltage ($\pm 0.1, 0.2, 0.5, 1, 2,$ or 5 V). In order to obtain high quality ringdown data, the oscilloscope's data range is set so that the ringdown amplitude is nearly equal to the maximum detectable voltage. If very large fluctuations in incident energy are present, successive pulses may either exceed the selected data range (causing clipping of the ringdown signal at short times), or have an amplitude well below the selected data range (leading to lower quality ringdown data). Both cases can lead to incorrectly fit ringdown traces, and thus noisy or incorrect spectra.

Average Energy Measurement Methods

The average pulse energy out of the YAG and dye lasers was measured using a volume absorbing power meter (Scientech AC2501). The power meter was calibrated at 1064 nm, and no corrections were made to the reported energies for other wavelengths of light. It was observed that this power meter had a slow response time before “settling into” the actual power reading. To account for this, laser light was allowed to strike the power meter for 15 seconds before recording the average power.

The average pulse energy of the NIR and MIR light (out of the Raman shifter and OPA respectively) were measured with a joulemeter (Newport 818E) connected to an

oscilloscope with 1 M Ω termination (see the next section for a discussion of impedance choice). When IR light strikes the joulemeter, a voltage is sent to the oscilloscope. This voltage can be converted to pulse energy using Equation A.2:

$$E_{IR} = V_{IR} \left(\frac{E}{V} \right)_{1064} \left(\frac{A_{1064}}{A_{IR}} \right), \quad (\text{A.2}),$$

where E_{IR} is the energy per pulse of the IR light, V_{IR} is the voltage reported by the oscilloscope, $(E/V)_{1064}$ is the conversion factor from voltage to energy for 1064 nm light, and A_{1064}/A_{IR} is the absorbance ratio of the joulemeter for 1064 nm light and the IR light of interest. For our joulemeter, $(E/V)_{1064} = 1 \text{ J} / 104.7 \text{ V}$. A typical value of A_{1064}/A_{IR} is 1.15 for 1370 nm light (central wavelength of the NIR range). A full chart is provided in the joulemeter manual for conversion to other wavelengths.

Table A.1 contains the performance data for the first laser setup used in this thesis (fully repaired Quantel YG-661 Nd:YAG laser, longitudinally pumped DCM dye laser), while Table A.2 contains the performance data for the second laser setup (Continuum Surelite III Nd:YAG laser, transversely pumped DCM dye laser). Both tables report the energy and energy fluctuations (1σ) for the Nd:YAG laser (oscillator, amplifier, and second harmonic generator), dye laser (at 640 nm, the center of DCM dye's range), and the Raman shifter (7283 cm^{-1}). To control the energy out of the Nd:YAG lasers, we adjusted either the flashlamp voltage (YG-661) or the q-switch delay time (Surelite III). The average energy and fluctuations were recorded on separate days. However, long term measurements of our laser data show that the data reported in Tables A.1 and A.2 are reproducible, and are thus representative of the overall laser system performance.

Table A.1. Laser Performance with Quantel YG-661 Nd:YAG laser^a

Flashlamps (kV)	1064 nm osc (mJ)	1064 nm amp (mJ)	532 nm (mJ)	Dye ^b 640 nm (mJ)	IR 7283 cm ⁻¹ 140 psi H ₂ (μJ)	IR 7283 cm ⁻¹ 200 psi H ₂ (μJ)
1.00	18.1 (±1.2%) ^c	111	14.4 (±6.4%)	0.1 (±18%)	—	—
1.05	38.2 (±0.8%)	205	49.4 (±3.5%)	2.3 (±8.0%)	—	—
1.10	60.1 (±0.7%)	290	94 (±2.4%)	6.3 (±5.5%)	—	—
1.15	84.1 (±0.6%)	371	146 (±1.5%)	10.8 (±4.5%)	—	—
1.20	111 (±0.5%)	450	192 (±1.3%)	15.0 (±4.7%)	—	—
1.25	137 (±0.5%)	523	234 (±1.2%)	18.2 (±5.0%)	24 (±23%)	35 (±29%)
1.30	169 (±0.5%)	—	285	20.2	41 (±13%)	51 (±16%)

a) Q-switch delay kept constant at 355 μs

b) DCM dye, longitudinally pumped amplifier, no preamp installed. Oscillator 175 mg/L, amplifier 28 mg/L

c) Fluctuations are reported as 1σ

Table A.2. Laser Performance with Continuum Surelite III Nd:YAG laser^a

Q-sw delay (int, μ s)	1064 nm (mJ)	532 nm ^b (mJ)	Dye ^c 640 nm (mJ, w/preamp)	IR 7283 cm^{-1} 245 psi H ₂ (μ J)
160	140 ($\pm 2.5\%$) ^d	24 ($\pm 10.5\%$)	1.4	—
170	248 ($\pm 1.0\%$)	72 ($\pm 3.3\%$)	7.8	—
180	394 ($\pm 0.7\%$)	160 ($\pm 2.2\%$)	18.9	19 ($\pm 51\%$)
190	501	225	25.4	74 ($\pm 25\%$)
200	607 ($\pm 0.6\%$)	288 ($\pm 1.3\%$)	30.0	92 ($\pm 20\%$)
220	721 ($\pm 0.4\%$)	348	33.0	89 ($\pm 22\%$)
240	756 ($\pm 0.3\%$)	365 ($\pm 1.5\%$)	34.0	—

a) Flashlamp voltage kept constant at 1.39 kV

b) External second harmonic generation: Inrad 5-302 SHG (Type II) with temp controller

c) DCM dye, transversely pumped amplifier, preamp installed. Oscillator and preamp 270 mg/L, amplifier 90 mg/L.

d) Fluctuations are reported as 1σ

Pulse-to-Pulse Energy Fluctuation Measurement Methods

It is impossible to use the volume absorbing power meter to measure pulse-to-pulse fluctuations of the YAG or dye lasers due to its slow response time (15 seconds) compared to the time between pulses (0.1 seconds). Instead, a Si photodiode (ThorLabs DET210) was used to collect scattered laser light. NIR and MIR light was still collected with a joulemeter (Newport 818E). 255 consecutive pulses were sent to the CompuScope 1450 card (50 MS/s sampling rate, 20 ns period between samples), and saved to disk using GageScope 3.0 software (see the next section for a caveat on saving the pulses to disk). The height and timing of these pulses were analyzed to determine the standard deviation for shot-to-shot energy.

The Si photodiode and joulemeter are both designed to be 50 Ω terminated. However, using the correct termination cause problems when the laser pulse being observed is as short as or shorter than the period between consecutive samples (20 ns). Artificial changes in amplitude will be observed due to the timing jitter, resulting in an apparent energy fluctuation that is larger than the actual distribution.

The above point can be proven very easily. A function generator was used to generate a sine wave (269 ns period, 3.84 MHz frequency, 245 mV peak-to-peak amplitude). The sine wave was sent to the CompuScope card, and the signal was recorded for sampling rates of 50, 25, 10, and 5 MS/s. Figure A.1 shows the recorded waveforms.

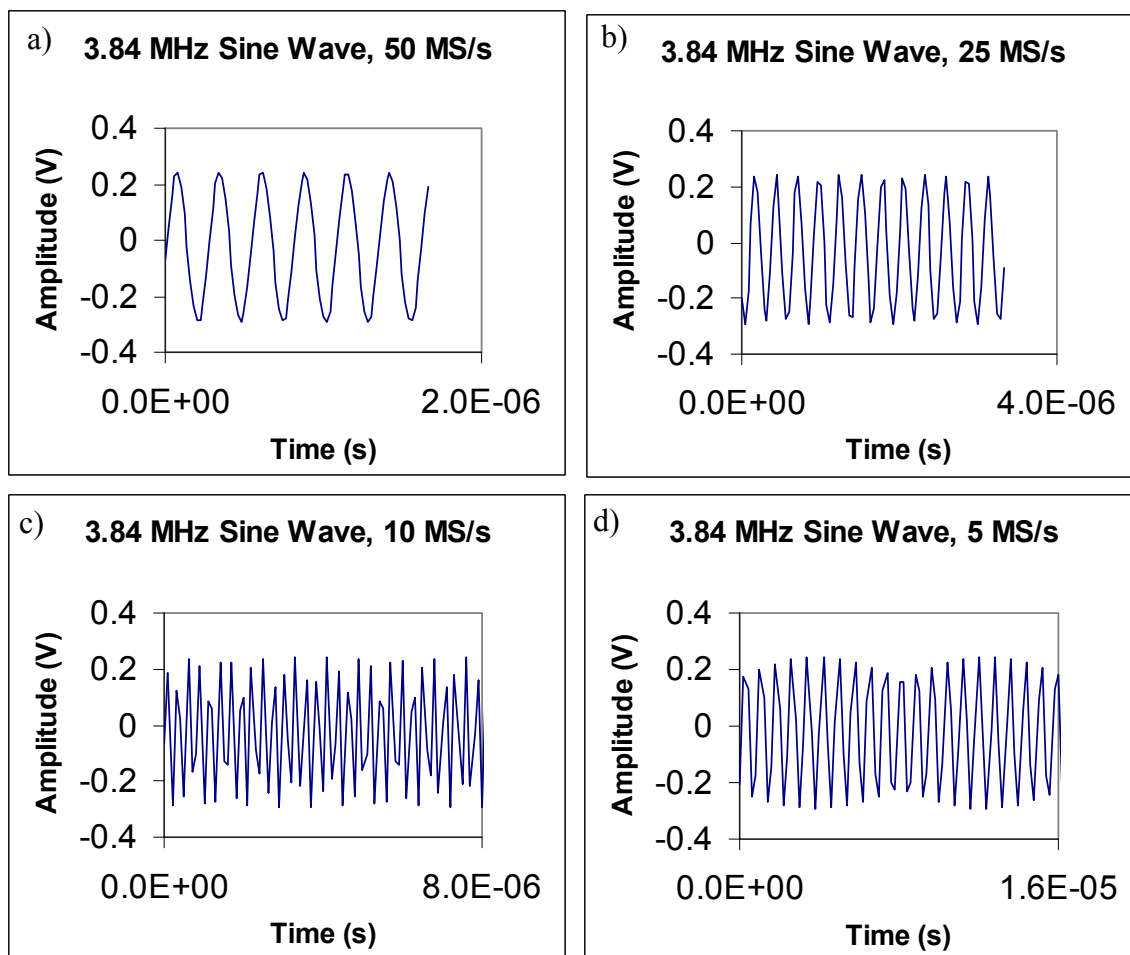


Figure A.1. Waveforms collected for a sine wave input (3.84 MHz frequency) to our PC oscilloscope card (GaGe CompuScope CS1450) set to sampling rates of 50 MS/s (a), 25 MS/s (b), 10 MS/s (c), and 5 MS/s (d).

At 50 and 25 MS/s, the constant amplitude out of the function generator is reproduced reasonably well. At 10 and 5 MS/s, the peak amplitude appears to be fluctuating, despite not adjusting the function generator. This is not surprising: since the sine frequency and the scope sampling rate do not match (and also are not multiples of each other), the CompuScope card samples different parts of the sine wave during each period. The result is that the sine wave's amplitude appears to be fluctuating.

Based on this analysis, it should be clear that the same sampling issue will occur when measuring peak heights of our laser pulses on the oscilloscope. The FWHM of our laser pulses is less than 10 ns, as confirmed on an oscilloscope with a very high sampling rate (2.5 GS/s, 0.4 ns period between samples). Because the CompuScope can only sample every 20 ns, we expect that the limited sampling rate of the CompuScope will make the apparent peak fluctuation larger than the actual fluctuation.

Our solution to this problem is to “spread out” the peak over a time period greater than 20 ns. We can do this by changing the impedance of the oscilloscope to 1 M Ω , rather than the expected 50 Ω . When light strikes the photodiode, the voltage produced will charge the BNC cable due to impedance mismatching. This has the effect of creating a “signal plateau,” as shown in Figure A.2. It can be shown that the average height of this plateau (after subtracting out the nonzero baseline) is proportional to the average energy measured with our power meter. This indicates that the plateau height is a measure of shot energy, and can be used as a substitute for peak height in our energy fluctuation analysis.

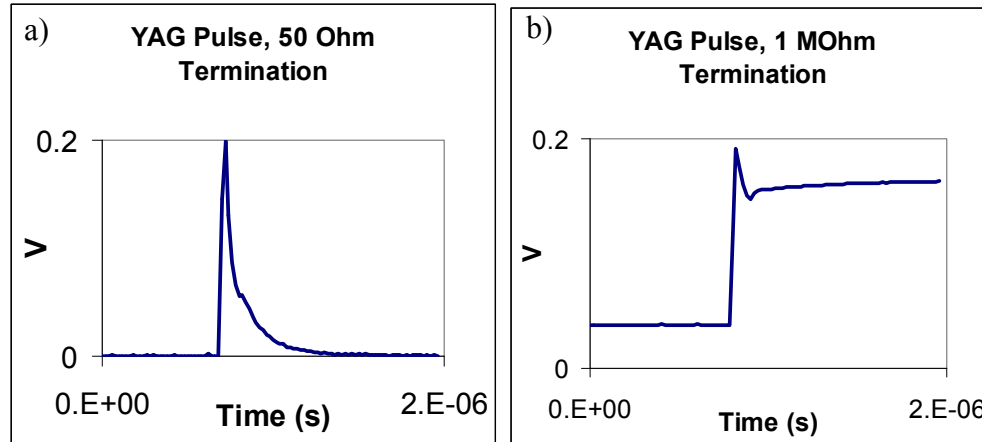


Figure A.2. Comparison of measurements of 532 nm light scattered to a Si photodiode, with CompuScope termination of 50 Ω (a) and 1 M Ω (b). After subtracting out the baseline, the average plateau height is proportional to the average power measured with a power meter, indicating that plateau height is a measure of shot-to-shot energy.

Issue with Saving “MultiRec” ASCII Waveforms

As described above, in order to measure pulse-to-pulse fluctuations, 255 consecutive pulses were collected, saved to disk using GageScope 3.0 software (Build 494), and analyzed. Consecutive pulses can be recorded using the “MultiRec” function of the GageScope software. However, a bug in the software prevents saving all 255 pulses to a single file in ASCII format. If the MultiRec feature is used, the user must save each pulse as a separate file.

In order to illustrate this bug, 255 consecutive near IR pulses were collected by a PDA400 InGaAs detector, and recorded by our CompuScope CS1450 board. The signals from these 255 pulses were displayed in GageScope, and the signal was saved to disk in the GageScope native file format (SIG), as well as to ASCII format (ASC). When saving a multirecord file, the user is given the option to save all of the records appended to one large file, or to split into many single-record files.

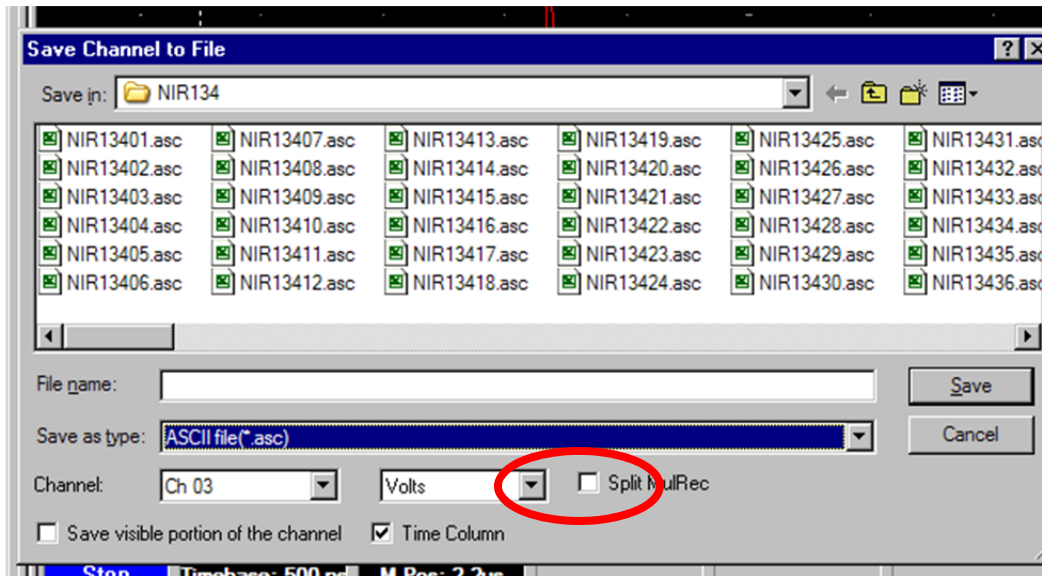


Figure A.3. The “Split MulRec” checkbox (circled) in the GageScope program determines whether or not multiple oscilloscope traces are saved as one large file (unchecked), or split into individual files (checked).

There are no issues saving multiple pulses to one SIG file, and consequently only one SIG file is needed to store the 255 pulses. However, there are issues saving ASC files. Consider the first four records in the set of 255 pulses, saved as a SIG file and displayed in GageScope (Figure A.4). We notice that although the amplitude of the ringdown varies (due to laser fluctuations), the program is able to record each pulse properly.

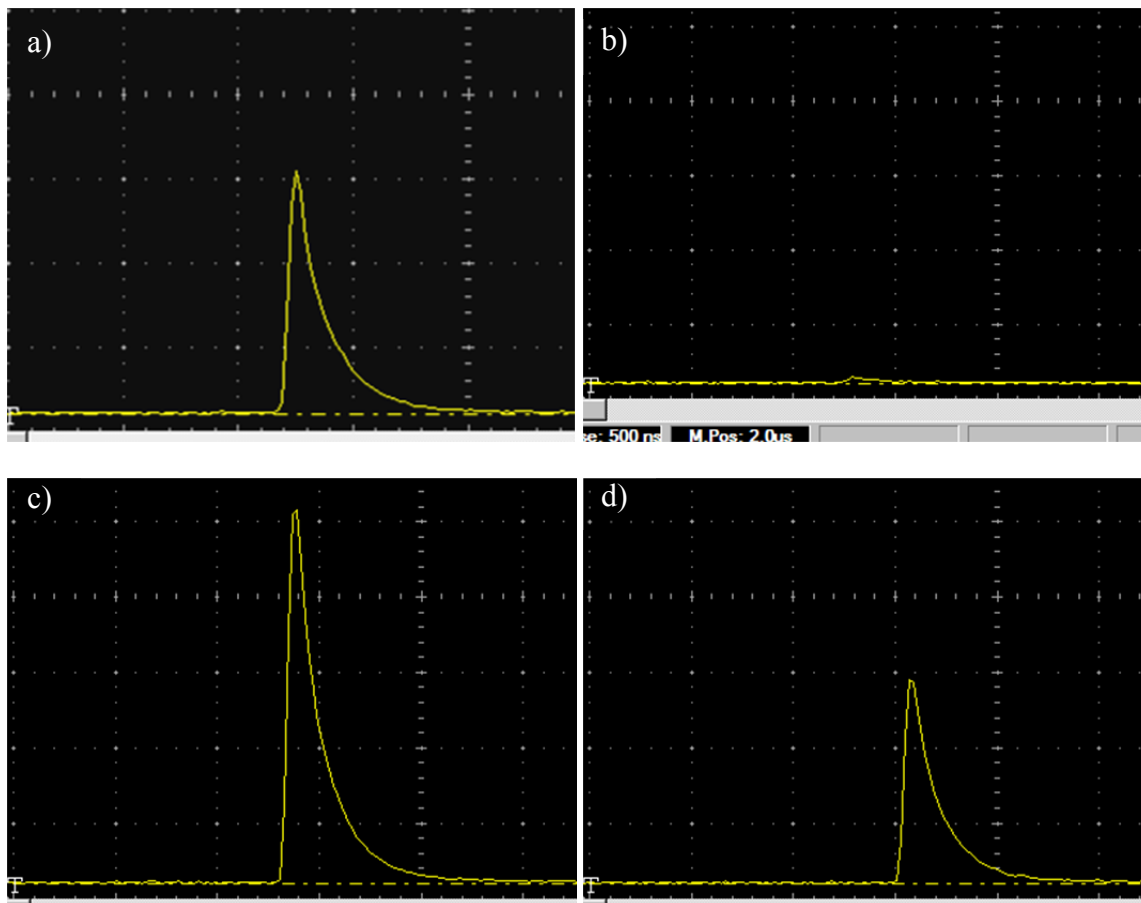


Figure A.4. Records 1 (a), 2 (b), 3 (c), and 4 (d) of the 255 consecutive NIR pulses collected, displayed in GageScope 3.0. The records were saved in GageScope’s native SIG file format. The width of each window is roughly 3 μ s.

Now consider the same records when saved into ASC files. The waveforms can be plotted in Excel. If we check the “Split MulRec” button, then we obtain 255 files with one waveform stored in each. The first four records obtained this way are presented in Figure A.5. Note that when saving the waveforms in ASC format and enabling “Split MulRec,” the ASC waveforms match the SIG waveforms. This indicates that GageScope is saving the individual records properly.

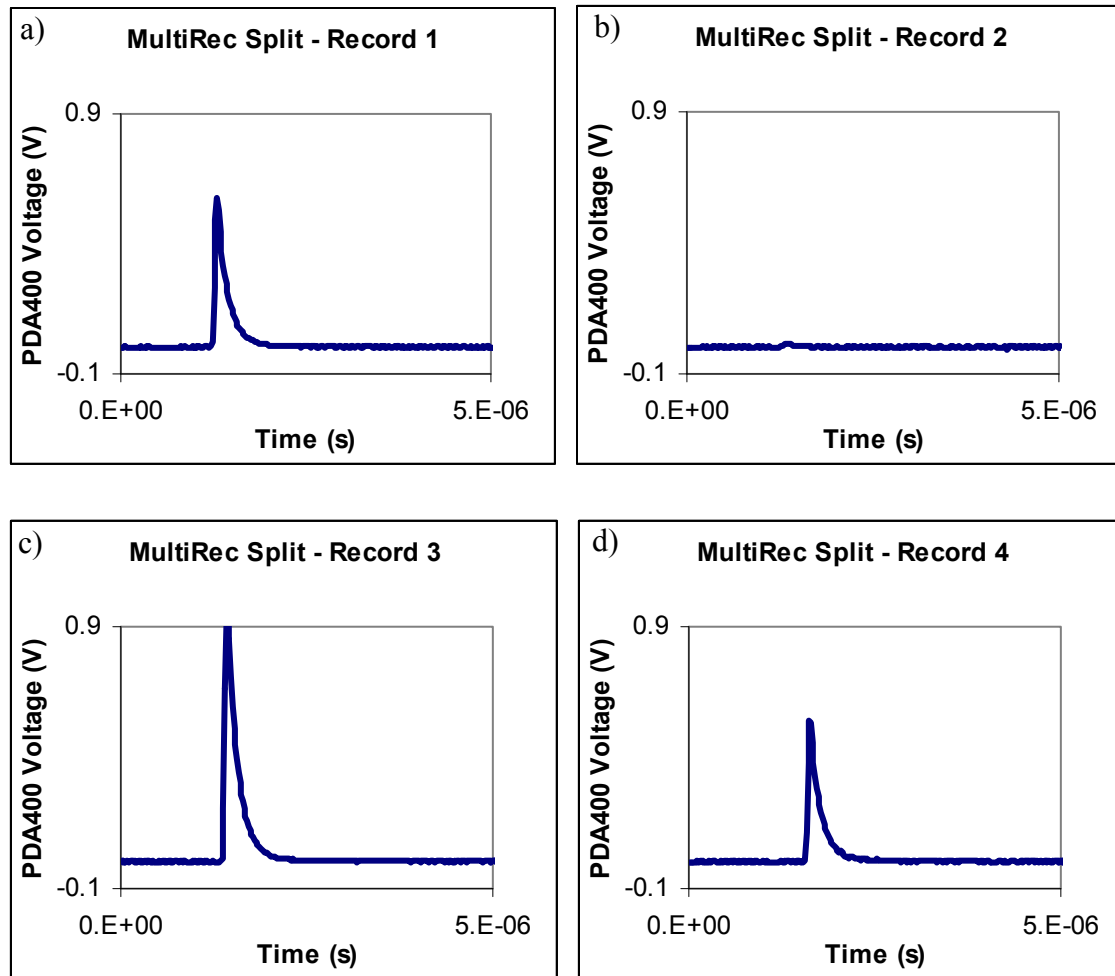


Figure A.5. Pulse records 1 (a), 2 (b), 3 (c), and 4 (d) in ASC format, using the “Split MulRec” option. The shapes of these records match the shapes in Figure A.4.

On the other hand, if we save the waveforms to ASC format without using “Split MulRec,” then we obtain the plots in Figure A.6. Note that only the first record is recorded properly in Figure A.6. All further records in the single file are corrupted, and do not show the measured pulse. This issue persists regardless of voltage range, time scale, or most other settings on the CompuScope board. However, the bug disappears when the CompuScope is set to certain sampling rates (50 MS/s, 100 kS/s). It is possible that this bug has been corrected in later versions or builds of the GageScope software.

However, the current software used in 17 Noyes suffers from this bug. In order to do correct analyses of multiple record files, we must split the file first, and then use a LabVIEW program to recompile the data.

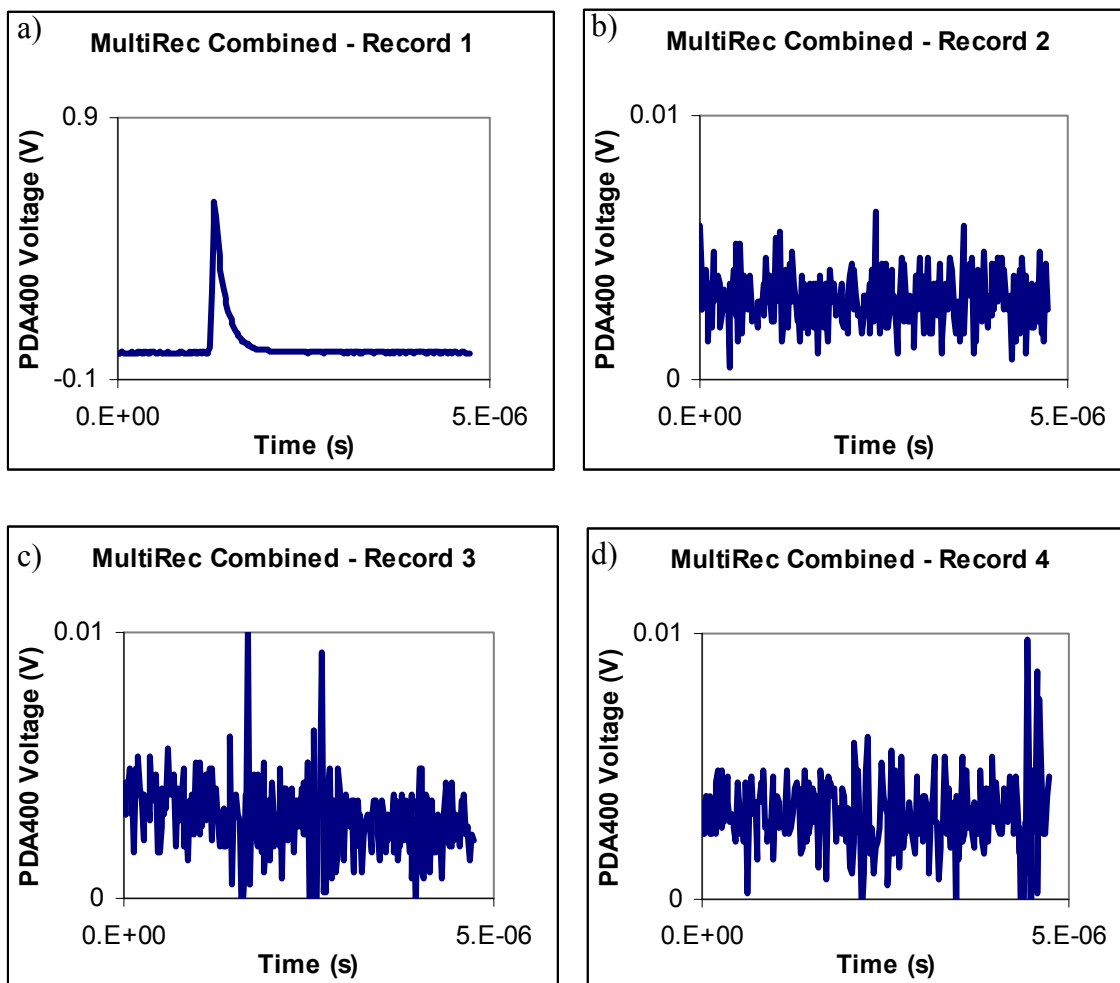


Figure A.6. Pulse records 1 (a), 2 (b), 3 (c), and 4 (d) in ASC format, saved to one single file. The shapes do not match the records in Figure A.4, indicating an error when saving all data to one ASC file.

Appendix B—Nd:YAG Laser Stability Issues and Repairs

This appendix contains information regarding performance issues and repairs to the Quantel YG-661 Nd:YAG laser used in our laboratory from July 2004 until August 2009. The primary issues described here are incorrect installation of the laser, a damaged q-switch trigger circuit, a malfunctioning capacitor bank, and physical damage to the laser head. The first part of the appendix describes the symptoms exhibited by the laser that indicated malfunctioning equipment and improper setup. The second part describes the repairs made to the laser, and the improvement in laser performance. It is my hope that this information will be of value to future graduate students.

Introduction

Our interest in the energy and temporal stability of our laser light comes from the initial HO₂ + HCHO near-infrared (NIR) cavity ringdown spectrum (Figure B.1). The spectrum was much noisier than anticipated, making any spectroscopic or kinetics measurements impossible.

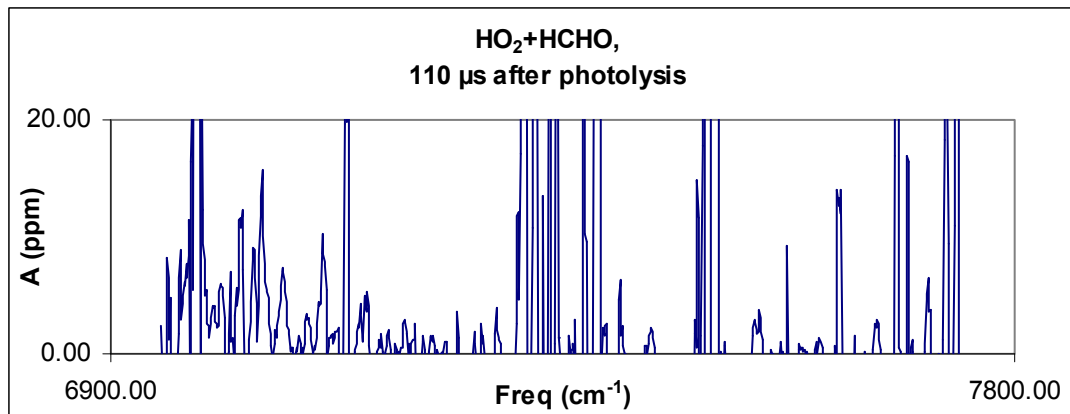


Figure B.1. NIR spectrum of HO₂ + HCHO products 110 μs after reaction. The considerable noise in the spectrum prevents accurate spectroscopy or kinetics measurements from being performed.

The apparent cause of this spectral noise was very large power fluctuations in the near infrared (NIR) light. Although cavity ringdown spectroscopy (CRDS) is theoretically independent of laser intensity (see Chapter 2), the data acquisition program will not operate properly if very large intensity fluctuations are present. The ringdown fitting program selects a voltage scale for the CompuScope board (CS1450) by measuring the peak voltage for one pulse, then recording 16 pulses on that voltage scale. Problems occur if the pulse that sets the scale is much lower in intensity than the other 16 pulses. If this problem occurs, the beginning of the averaged ringdown trace will be a saturated signal, and the expected exponential decay is only observed at the end of the signal.

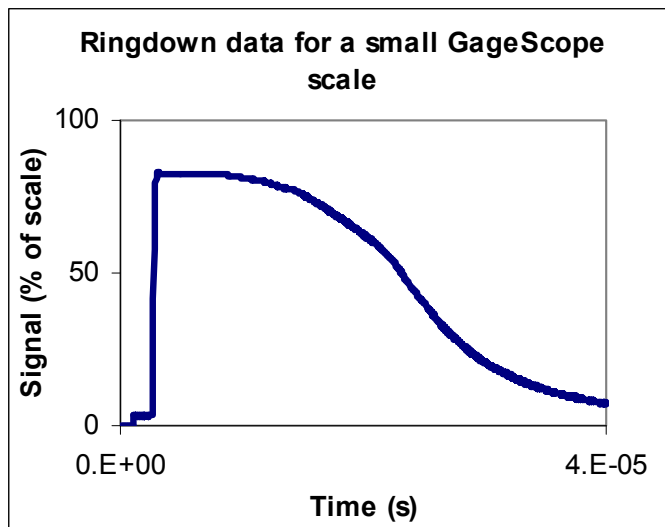


Figure B.2. Sample ringdown data acquired when the peak ringdown voltage exceeds the voltage scale of the CompuScope board. The first 25 μs has saturated signals averaged in. Exponential decay is only observed for the final 15 μs of the signal.

When we first observed this issue, it was unclear which optical component was causing the large intensity fluctuations. If any one piece of equipment (laser or optic) in the entire optical chain is malfunctioning, then the light reaching the detector will exhibit severe power fluctuations. Since the NIR light is generated through multiple nonlinear optical processes, we must check the power of light throughout the entire optical system (see Chapter 2 for a diagram of the entire system). The main places to check the light intensities are

- 1) The 1064 nm light emitted from the Nd:YAG oscillator and amplifier rods
- 2) The 532 nm light emitted from the second harmonic generator
- 3) The 640 nm light emitted from the dye laser (DCM dye)
- 4) The 1370 nm near IR light emitted from the H₂ Raman shifter

We used the methods described in Appendix A to collect 255 consecutive pulse energies at each point. We then analyze the energy distributions (and when possible, temporal distributions). These data tell us which part of the optical chain is causing the power fluctuations (YAG, dye laser, Raman shifter).

Initial Measurements and Classification of the Unrepaired Laser System

Energy Distribution Results and Analysis

The first data to examine are the distributions of pulse energies at two separate Nd:YAG flashlamp voltages. These data allow us to see how the distribution changes with average pulse energy, and allow us to correlate problems in one laser with problems in a previous laser. The energy distributions are illustrated in Figure B.3 for the YAG laser (a), dye laser (b), and NIR light (c). All data were taken at a flashlamp voltage of 1.28 kV. The measured photodiode or joulemeter voltage (x-axis) is directly correlated to the pulse energy, as described in Appendix A.

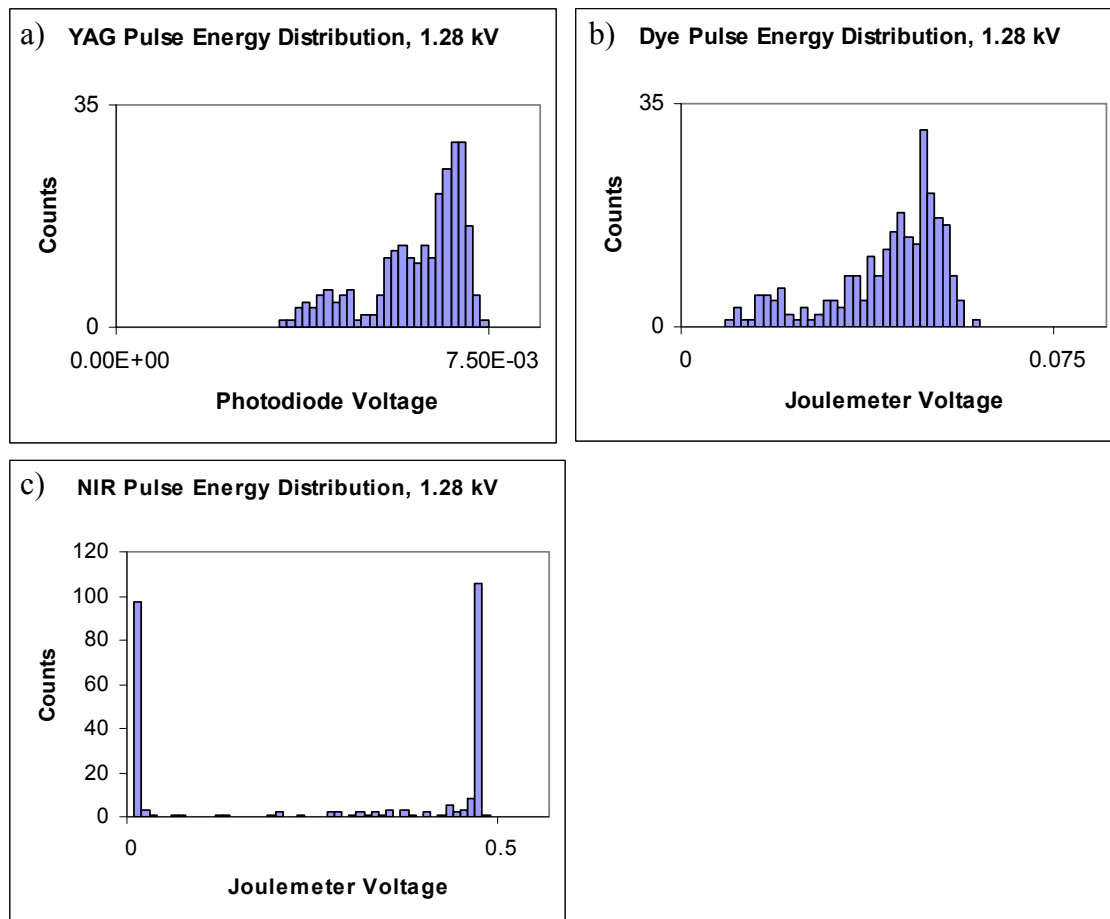


Figure B.3. Energy distributions for 255 consecutive pulses from the Nd:YAG laser (a), dye laser (b), and NIR light (c) at a flashlamp voltage of 1.28 kV. The YAG and dye distributions both have a main peak and a smaller peak at lower voltage. The NIR distribution shows a peak corresponding to saturation of the detector, and a large number of zero energy pulses. The number of “zero” counts in the NIR plot is approximately equal to the number of counts below the main peaks in the YAG and dye laser plots.

The YAG distribution contains 40 pulses (16%) in the low energy peak centered near 4 mV, 88 pulses (34%) in the midenergy peak centered near 5.6 mV, and 127 pulses (50%) in the high energy peak centered near 6.9 mV. Similar observations can be made for the dye laser pulses (50% of the pulses are in the high energy peak near 50 mV, while the other 50% are scattered below this peak). Finally, when we examine the NIR, we note

that roughly half of the pulses have near-zero intensity, while the other half saturate the detector.

Figure B.4 shows the energy distributions for the YAG, dye laser, and NIR light at 1.34 kV. At a higher flashlamp voltage, we expect the average pulse energy to increase, and the Nd:YAG laser to become more stable. We observed in Figure B.3 that the NIR light was saturating the detector. We therefore attenuated the light with a 99.98% reflective mirror to get a better idea of the actual energy distribution (Figure B.4d).

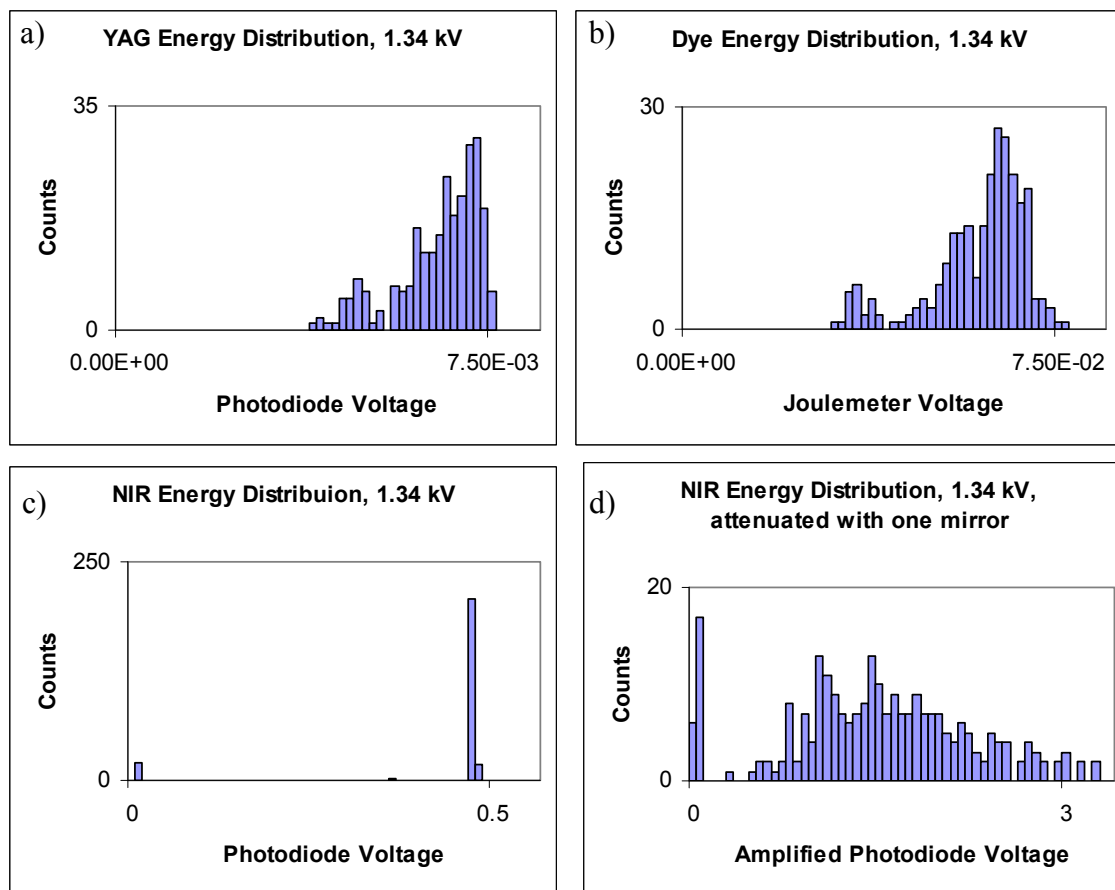


Figure B.4. Energy distributions for 255 consecutive pulses from the Nd:YAG laser (a), dye laser (b), and NIR light (c) at a flashlamp voltage of 1.34 kV. In order to get a better description of the NIR energy fluctuations, the NIR light was attenuated with one highly reflective mirror (d, $R = 99.98\%$), then amplified. The general shape of the YAG and dye distributions is the same as observed in Figure B.3. Although fewer zero energy pulses are observed in the NIR light, the energy distribution is very wide. The number of “zero” pulses in the NIR is nearly equal to the number of pulses in the smaller peaks of the YAG and dye distributions.

At the higher flashlamp voltage, we still observe the same two-peak features in the YAG and dye distributions. In the YAG distribution, there are 33 points (13%) in the small peak centered at 4.5 mV, while the rest of the pulses exceed 5.6 mV. Similar results are observed for the dye laser (21 pulses, or 8%, have a peak signal less than 40 mV). The NIR data show approximately 22 pulses (9%) with roughly zero intensity, and the

rest in a roughly Gaussian distribution. Figure B.4d shows that the NIR energy distribution is very wide, likely causing the GageScope scale problem described earlier.

Both the 1.28 and 1.34 kV distributions contain a cluster of low energy pulses in the YAG and dye laser, and roughly the same number of “zero intensity” pulses in the NIR distribution. **These data indicate that fluctuations in the YAG laser are causing the noise observed in the CRD spectrum.**

Temporal Distribution Results and Analysis

The conclusion from the energy distribution data was that fluctuations in the YAG are causing the energy drop-offs in the NIR. The question now becomes what is causing these energy drop-offs. One possibility is timing jitter between the firing of the flashlamps and opening of the Q-switch. Such timing jitter was observed on the GageScope while collecting energy data: the relative timing between the trigger and the pulse peak varied shot to shot. In theory, the laser should be controlled exclusively by two high precision digital delay generators (see Chapter 2). Since these delay generators were verified to be working properly, **the conclusion is that some part of the YAG is set up incorrectly.**

The first step to determining the cause of the laser pulse jitter is to characterize the time distribution of pulses. This can be done by reanalyzing the pulse distributions described above, but by picking out the timing of the peak rather than the peak voltage. It is possible to do this in Excel by judicious use of the VLOOKUP command. Note that the GageScope was triggered by the delay generators, so any measured distribution of times reflects a difference between flashlamp fire (controlled by the DDGs), and q-switch

opening (possibly controlled elsewhere). The timing analysis results are shown in Figure B.5 (flashlamp voltage of 1.28 kV) and Figure B.6 (flashlamp voltage of 1.34 kV)

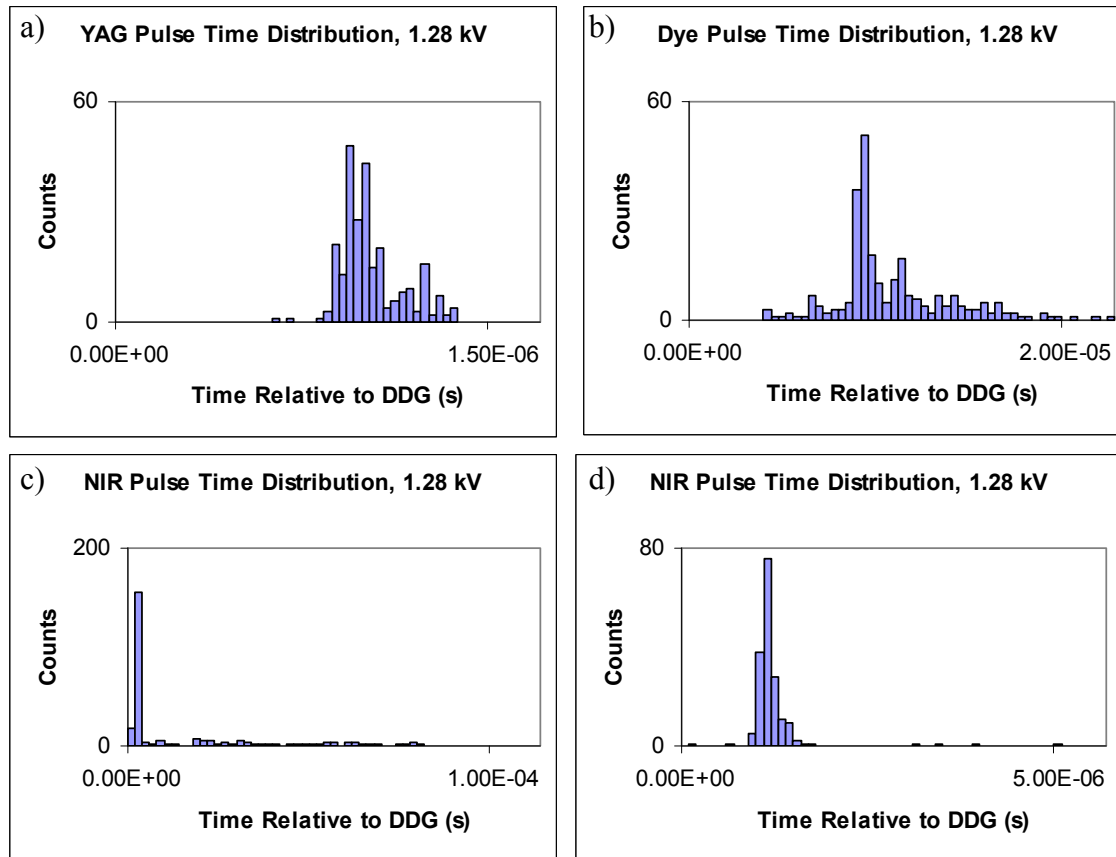


Figure B.5. Timing distributions for 255 consecutive pulses from the Nd:YAG laser (a), dye laser (b), and NIR light (c) at a flashlamp voltage of 1.28 kV. Pulse times are relative to the trigger signal from the DDG. In order to get a better description of the NIR timing fluctuations, we zoomed in on the first 50 μ s of the NIR distribution (d). The Nd:YAG distribution width is on the order of tens of nanoseconds, wider than expected.

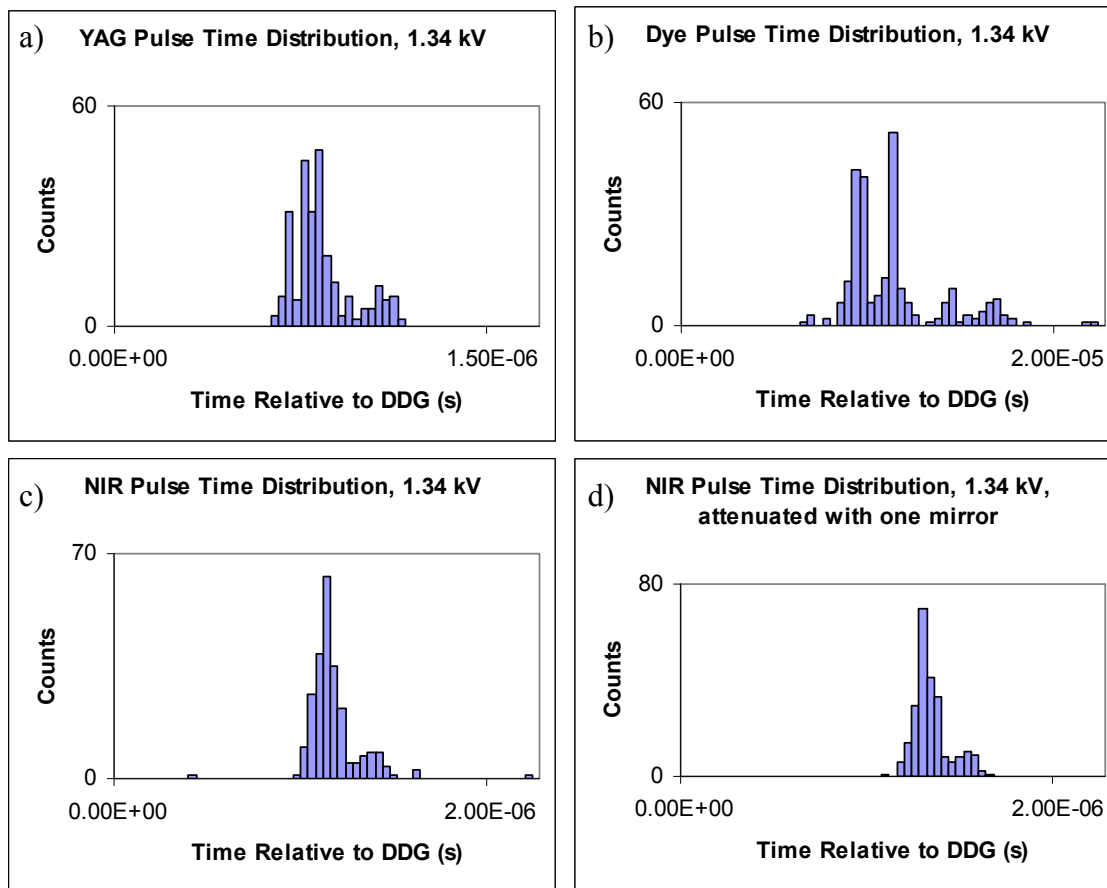


Figure B.6. Timing distributions for 255 consecutive pulses from the Nd:YAG laser (a), dye laser (b), and NIR light (c) at a flashlamp voltage of 1.34 kV. Pulse times are relative to the trigger signal from the DDG. The timing of the NIR pulses was not affected by the attenuation mirror (d). The Nd:YAG distribution width is on the order of tens of nanoseconds. Despite improvement compared to the 1.28 kV distributions in Figure B.5, this width is still larger than expected.

At 1.28 kV (Figure B.5), we notice that the YAG distribution contains a large main peak ($0.9 \mu\text{s}$), followed by a smaller peak out at later times ($1.2 \mu\text{s}$) containing 57 pulses (22%). The total width of the YAG distribution is on the order of $1 \mu\text{s}$. The dye distribution is much wider than the YAG distribution (on the order of $10 \mu\text{s}$), but the NIR distribution is similar in width to the YAG distribution. Similar results are observed at 1.34 kV (Figure B.6), though the YAG distribution appears to be somewhat narrower

than at 1.28 kV. At both voltages, the timing widths are much larger than the timing jitter in the laser specifications (7–9 ns).

We can also try to correlate when the laser pulse is emitted (from the timing distributions) with the energy of the pulse (from the energy distributions). Figure B.7 shows scatter plots of the pulse time vs pulse width for the Nd:YAG laser at 1.28 and 1.34 kV.

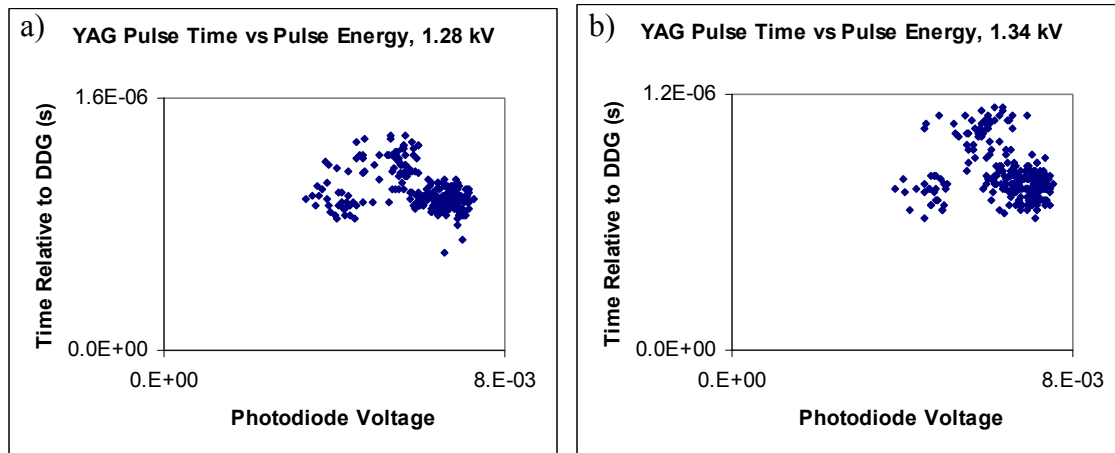


Figure B.7. Pulse timing vs pulse energy for the Nd:YAG laser at flashlamp voltages of 1.28 kV (a) and 1.34 kV (b). Three clusters of points are observed at both voltages, with the majority of points in the top cluster and lower right cluster. The clustering of points indicates a possible correlation between pulse time and pulse energy.

Both plots appear to contain three clusters of peaks. While it is hard to tell what the correlation is between pulse timing and pulse energy, the plots do indicate that the two concepts are somehow related based on the clustering. It appears that the majority of points lie in the top cluster and bottom right cluster, indicating a possible negative correlation. Regardless of the exact correlation, **the conclusion that we reach is that errors in when the q-switch opens is causing instability in pulse energy, and thus is the cause of the noise in the CRD spectrum.**

Laser Repair Information

Based on the pulse energy and timing analysis, we chose to re-examine how the q-switch was being triggered. We took the following six steps to improve the YAG timing and performance:

- First, the jitter between the Marx Bank signal and the DDG was measured, and was found to be unacceptably large. These measurements prompted us to trigger the Marx Bank directly from the DDG.
- The Marx Bank requires a 15 V trigger pulse, a larger voltage than our DDG can supply. Our second step was to build a pulse amplification circuit.
- Considerable ringing was observed on the charge and fire signal lines, so our third step was to repair and modify the optoisolator circuits for the charge and fire lines, as well as to add correct termination to the two lines.
- A 60 V spike was observed on all lines when the flashlamps fired. The cause of this spike was eventually identified as a problem with the YAG capacitor bank. Our fourth step was to swap the capacitor bank for a working spare bank.
- The cooling water running to the laser head during laser operation was observed to be warmer than 35 °C, the specified temperature. In order to correct this, our fifth step was to replace the “power pill” thermostat unit in the cooling unit.
- After making the first five changes, we still noticed that the energy out of the YAG laser would drop by 30% over the first two hours of operation, and continue to steadily drop afterwards. The cause of this is likely corroded o-rings and

buildup of minerals in the laser head. Our sixth step was to clean the laser head and replace all of the o-rings.

Jitter Between the Marx Bank Signal and the DDG

The original setup of our YG-661 had the Marx Bank being triggered by either the “Fixed Sync” or “Var Sync” outputs on the LU660 logic unit. However, this is not the correct way to trigger the Marx Bank. Normally, the Marx Bank is triggered by a different connection: the “J24” connector from the laser head cables. The normal setup allows for external triggering of the Q-switch (by passing an external signal directly through the laser), while the LU660 connection does not. The previous owners of the YG-661 set up the Marx Bank to be triggered by the LU660 because the signal out of J24 was being corrupted.

In “external mode,” the SB660 control box accepts a DDG trigger signal, and passes it directly through to the Marx Bank (as shown on the circuit diagram) via J24. We verified this by turning the laser off, and showing that the signal from the DDG is still passed through to J24. However, the laser would not fire when a 15 V signal was sent through J24, despite adjusting the timing of the Q-switch signal in relation to the flashlamp emission. Additionally, the laser would not fire when the Q-switch was controlled internally via J24, but *would* fire when controlled internally via the LU660. This led us to conclude that the signal out of J24 was being corrupted.

Finally, the Q-switch pulse out of the LU660 was compared to the DDG in order to determine the extent of jitter between the two. This jitter was on the order of microseconds, which is enough to explain the energy fluctuations previously observed.

We therefore conclude that the LU660 is an unacceptable Q-switch trigger. The Q-switch should be triggered directly by the DDG, ensuring a constant delay between flashlamp fire and opening of the Q-switch.

Amplification Circuit for the Marx Bank

Note: The Marx Bank used in our YG-661 is a Continuum Marx Bank, and DOES NOT MATCH the Marx Bank diagram in the YG-661 manual. These Marx Banks are a newer design, and information about them can be found in the NY-61 manual (YAG laser used in our other CRDS laboratory in Linde-Robinson).

The Marx Bank requires a 15 V positive edge trigger signal. The rise time of this signal must be fast (order of nanoseconds), and the signal shape must be stable from pulse to pulse in order to open the Q-switch at a constant time after the flashlamp emission. Unfortunately, none of the delay generators in the lab are able to provide a 15 V pulse. The Stanford DG535 delay generators in use can only provide a 4 V pulse. Likewise, the EG&G 9650 delay generators can only provide 10 V, and these generators do not work properly.

In order to obtain a 15 V pulse, we built an amplification circuit. The circuit takes a 4 V pulse from the DDG. This pulse is sent through a 6N137 high-speed optoisolator, and then series of two transistors in an emitter-follower configuration (VN10KLS first, then IRF510 second). In this circuit, the optoisolator will protect the DDGs from any energy spikes produced by the YAG. Additionally, the optoisolator will invert the DDG pulse. The two transistors will invert and amplify the pulse. The overall result of the circuit is that a 0–4 V square pulse is converted to a 0–15 V square pulse. We found that

using a slower optoisolator (such as a 6N135) or a slower first transistor would cause the rise time of the output pulse to be unacceptable. An 18 V power supply was connected to the drains of the two transistors, with a 515 Ω resistor between the 18 V line and the drain of the VN10KLS. A 5 V power supply was used to provide power to the 6N137. Figure B.8 shows the full circuit diagram for the amplification circuit.

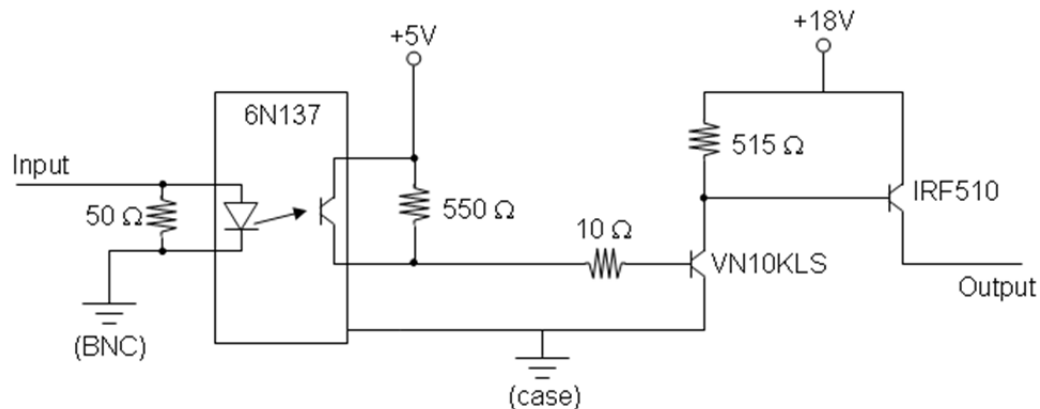


Figure B.8. Q-switch amplification circuit for the YG-661 laser. A 0–4 V square pulse is sent into a high speed optoisolator (6N137), then into two transistors in an emitter-follower combination (VN10KLS, IRF510). The output of the circuit is a 0–15 V square pulse.

The circuit performance was determined to be acceptable for use with our Marx Bank. The pulse rise time to 15 V was 400 ns (0–11 V in 100 ns). We also measured the firing of the Marx Bank inductively, by holding clip leads near the Marx Bank (flashlamps off), and observing the inducted pulse on an oscilloscope. The circuit was observed to trigger the Marx Bank properly.

Modifications to Charge and Fire Signal Lines

During the testing of the Marx Bank circuit, we also examined the flashlamp signals (charge and fire) being sent from the delay generator to the SB660 control unit via an optoisolator box. It is crucial that little or no noise is present on these lines, and that the signals being sent to the laser exhibit little to no timing jitter. Any corruption in these signals will lead to the flashlamps being fired at the incorrect time. Since the Marx Bank is being fired by the delay generator, the end result will be the Marx Bank being triggered at the “wrong” time relative to the flashlamps, resulting in a reduction in lasing power, or no lasing at all.

The charge and fire signals are first sent from the DDG to an optoisolator box. The outputs from the optoisolator box are then converted to a 9-pin D-sub connector, and fed into the SB660 supply box. Without the optoisolator box, DDG channels can be destroyed by electrical noise (this has happened in the past in 17 Noyes, when the laser was first installed in 2004).

After investigation of the optoisolator box, we observed two problems. First, the signals being sent out of the optoisolator box exhibited severe ringing. This was most likely due to the charge and fire lines not being terminated correctly. Second, the optoisolator circuit was wired up very poorly. Very thin wires were connected to balls of solder in midair to connect grounds to each other. Most of the components in the box were not mounted to a circuit board, making modification or repair to the circuit very difficult. Eventually, one of the two channels stopped working due to wires being disconnected and optoisolators burning out. Clearly a surface mounted circuit was needed, as well as correct termination for the optoisolator channels and output signals.

The new circuit for the optoisolator box is shown in Figure B.9. A positive DDG signal is sent into a 6N135 optoisolator. The output from this IC is sent into a 74128 NOR line driver to provide enough current to the Marx Bank. The output is terminated to 50 Ω at the D-sub converter box before being sent to the laser. All components are mounted to a circuit board. When this circuit is used for charge and fire signals, no ringing is observed.

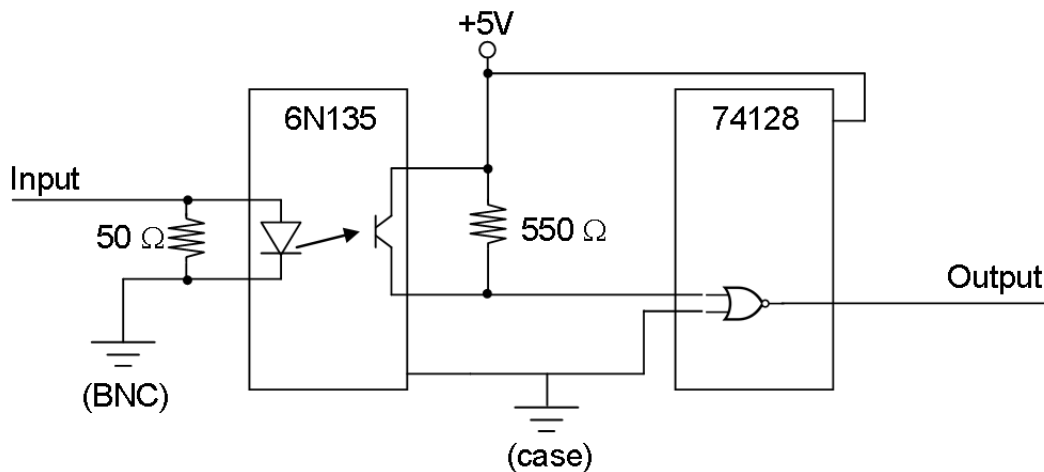


Figure B.9. Circuit diagram for the optoisolator box. The box contains two channels. Each channel has a copy of the above circuit. A 0–4 V square pulse is sent to a medium speed optoisolator (6N135). The pulse is then sent to a NOR line driver (74128). The output of the circuit is a 0–5 V square pulse.

The 60 V Spike and Replacement of the CB631 Capacitor Bank

Since installation of the YG-661 in 2004, a 15–60 V spike was observed on most of the laser lines (Charge, Fire, and “J24” Q-switch) at the time of flashlamp emission. This spike is not observed on the LU660 sync out. The amplitude of the spike is not affected by flashlamp voltage, varies shot to shot, and is always present at flashlamp emission. In the initial setup (Marx Bank triggered by LU660 sync out), this spike did not

affect lasing. However, the spike did cause a few DDG channels to be destroyed, prompting the creation of the initial optoisolator box.

The spike becomes a large problem when triggering the Q-switch via the DDG. When measuring the Marx Bank firing inductively using clip leads, we discovered that the Marx Bank was being triggered by the 60 V spike as well as our circuit. As a result, the Pockels cell was opening at the wrong time, and no lasing was observed. In order for the YG-661 to operate properly, the 60 V spike must be eliminated.

By swapping parts with another YG-661 (Jay Winkler's lab in the Beckman Institute), we determined that the original capacitor bank (CB631) was damaged. Changing capacitor banks for another CB631 results in the 60 V spike disappearing. We also showed that a third, smaller, capacitor bank (CB630) does not exhibit a 60 V spike at the time of flashlamp firing. It may be possible to repair the original CB631 by replacing the thyristor (C158PB). This part has been ordered and resides uninstalled in 17 Noyes; however, we will use the working CB631 in our laser for the time being. It is not possible to use the CB630 in the laser, because its capacitance (18 μF) is much lower than the CB631 (32 μF). The flashlamps would have to be turned up much higher when using the CB630, placing too much of a thermal strain on the Nd:YAG rods.

Replacing the Power Pill Thermostat

After the above repairs were performed, it was observed that the lasing power would decrease over time. Figure B.10 shows the energy per pulse of the 532 nm light from the YAG vs the amount of time that the flashlamps were firing. In the first three hours after the flashlamps were started, the energy out of the oscillator cavity would drop

by 30%. Even after the first three hours of flashing, the power would continue to steadily drop.

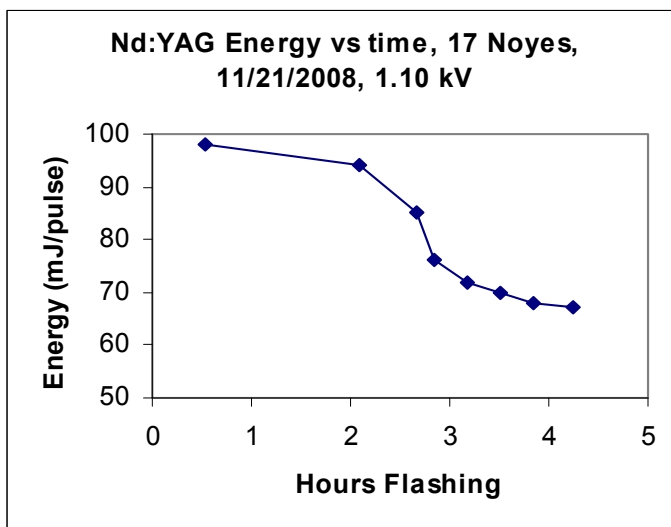


Figure B.10. Energy per pulse for the Nd:YAG vs flashlamp fire time. The plotted energies are for the 532 nm light; however, the same trend is observed for the 1064 nm oscillator light. Over the first three hours, the YAG energy drops by 30%. After three hours, the energy continues to slowly decrease.

Because the power out of the oscillator was behaving abnormally, we concluded that parts of the laser head needed to be repaired. Two ideas came to mind: incorrect cooling of the laser head (described in this section), and physical/chemical damage to the laser head (described in the next section).

The YG-661 manual specifies that for unseeded operation of the laser, the cooling water sent to the laser head should be no greater than 35 °C. If the water temperature exceeds this limit, then the YAG rods can overheat, changing the thermal lensing properties of the rods, leading to a reduction of lasing efficiency. We measured the cooling water temperature by placing a thermocouple into the DI reservoir. This reservoir

is located just prior to the laser head, so the reservoir temperature is a good measure of the water being sent to the YAG rods. Figure B.11 shows the temperature data.

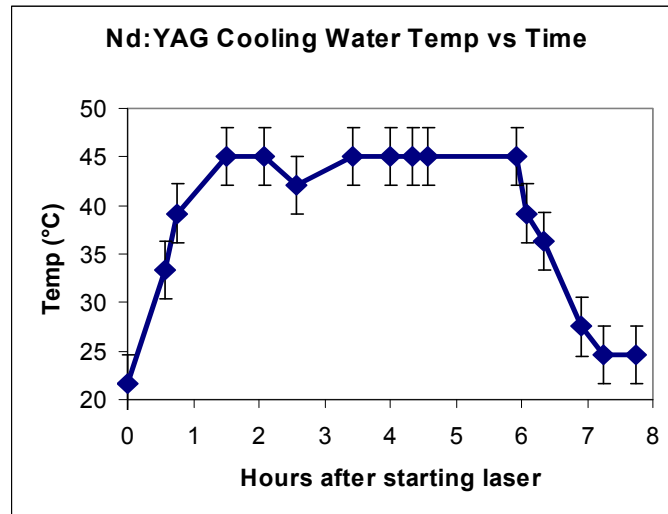


Figure B.11. Cooling water temperature in the Nd:YAG laser vs time since the laser flashlamps were started. The flashlamps were turned off 6 hours after starting the laser. During the time that the laser was flashing, the temperature rose to 45 °C and then stayed constant. Based on the voltage scale for the thermocouple, the uncertainty on each temperature measurement is ± 3 °C.

We notice that the water temperature increases to 45 °C over the first hour, then remains constant for the duration of laser operation. This temperature exceeds the manual’s specifications, so we must reduce the cooling water temperature in order to ensure proper operation of the laser. Note also that after 6 hours, the flashlamps were turned off, and the water temperature decreased back to room temperature.

The laser head is cooled by a reservoir of deionized water that exchanges heat with the building’s chilled water. The amount of heat transfer is controlled by changing the flow of the chilled water: if the deionized water becomes too warm, more chilled water is flowed to the heat exchanger. The flow of building water is controlled by a “power pill” thermostat: a ceramic thermostat with a wax reservoir and a small metal

extension separated by a flexible barrier. When the deionized water becomes too warm, the wax in the power pill melts. The expanding wax moves the barrier and forces the metal extension to press against a lever, increasing the flow of building chilled water to the heat exchanger. When the deionized water cools down, the wax resolidifies (and is compressed), the metal extension recedes, and the flow of building chilled water decreases. Each power pill has its own melting point, and therefore maintains one specific water temperature. The only way to change the cooling water temperature is to replace the power pill unit.

The power pill inside of our cooling unit was rated for 113 °F (45 °C) by the manufacturer. This power pill is appropriate for a seeded YAG, but not an unseeded one. By replacing the power pill with one rated for 95 °F (35 °C), we were able to reduce the laser head temperature back to 35 °C, the value specified in the manual.

Laser Head Cleaning and Replacement of O-rings

In addition to incorrect cooling, chemical deposits in the laser head or damage to the o-ring seals could also cause the 30% drop in energy over time observed in the previous section. If the head is coated with mineral deposits (formed from using impure deionized water), then the thermal properties of the head will change. The same principle holds for the o-ring seals: damaged or deformed o-rings will expand differently at elevated temperatures than undamaged o-rings. The end result for either problem is deviation from normal behavior in the physical and optical properties of the oscillator cavity at elevated temperatures. Therefore, it is critical to ensure that the laser head is clean, and that the o-rings are in good condition.

Upon opening the laser head, we noticed large calcium deposits on the ends of the head and inside the YAG rod reflector cavities. The o-rings were discolored and brittle, and likely had never been replaced since the laser was manufactured in 1989. We cleaned the laser head by disassembling as many parts as possible, then placing the laser head parts into household vinegar. The YAG rod reflector cavities were cleaned by dipping a cotton swab in vinegar, and lightly brushing the inside of the cavities. All of the o-rings inside of the laser head were replaced with new Viton o-rings (McMaster-Carr). After cleaning and replacing the o-rings, the laser head was reassembled and installed into the laser.

Result of Repairs

A full listing of the average energies and energy fluctuations as a function of flashlamp voltage for the repaired YG-661 laser can be found in Appendix A. In Table B.1, we present a comparison of the laser system performance before and after repairs (YAG, dye laser, Raman shifter). We immediately notice an improvement in both absolute energy and energy fluctuations. The pulse energy has increased by nearly a factor of three after repairs. The 1.2% fluctuation in 532 nm energy corresponds to a fluctuation of 0.5% at the oscillator rod, which matches the specs for the laser. We notice similar improvement in the dye laser output. The NIR light from the Raman shifter could not be measured at 1.24 kV prior to repair, but can be detected after repairs. The amount of NIR light produced (35 $\mu\text{J}/\text{pulse}$) is enough energy for use in cavity ringdown experiments.

Table B.1. Comparison of pulse energy and energy fluctuations at 1.24 kV for YG-661 (532 nm), dye laser (640 nm), and Raman shifter (1370 nm), before and after laser repairs

	E(YAG) (mJ/pulse)	σ_E/E_{avg} (YAG)	E(Dye) (mJ/pulse)	σ_E/E_{avg} (Dye)	E(Raman) (μ J/pulse)	σ_E/E_{avg} (Raman)
Before	78	41%	4.5	43%	— ^a	— ^a
After	225	1.2%	18	5%	35	29%

a) Energies too low to be measured

To get a better handle on the improvements in laser stability (both energy and timing), we can look at histograms of energy and pulse time with respect to the DDG, similar to those presented in Figures B.3–B.6. Shown below are histograms of energy (Figure B.12) and timing (Figure B.13) for the 1064 nm oscillator light, 532 nm light, dye laser light, and near-IR light. These plots were made at a flashlamp voltage of 1.25 kV.

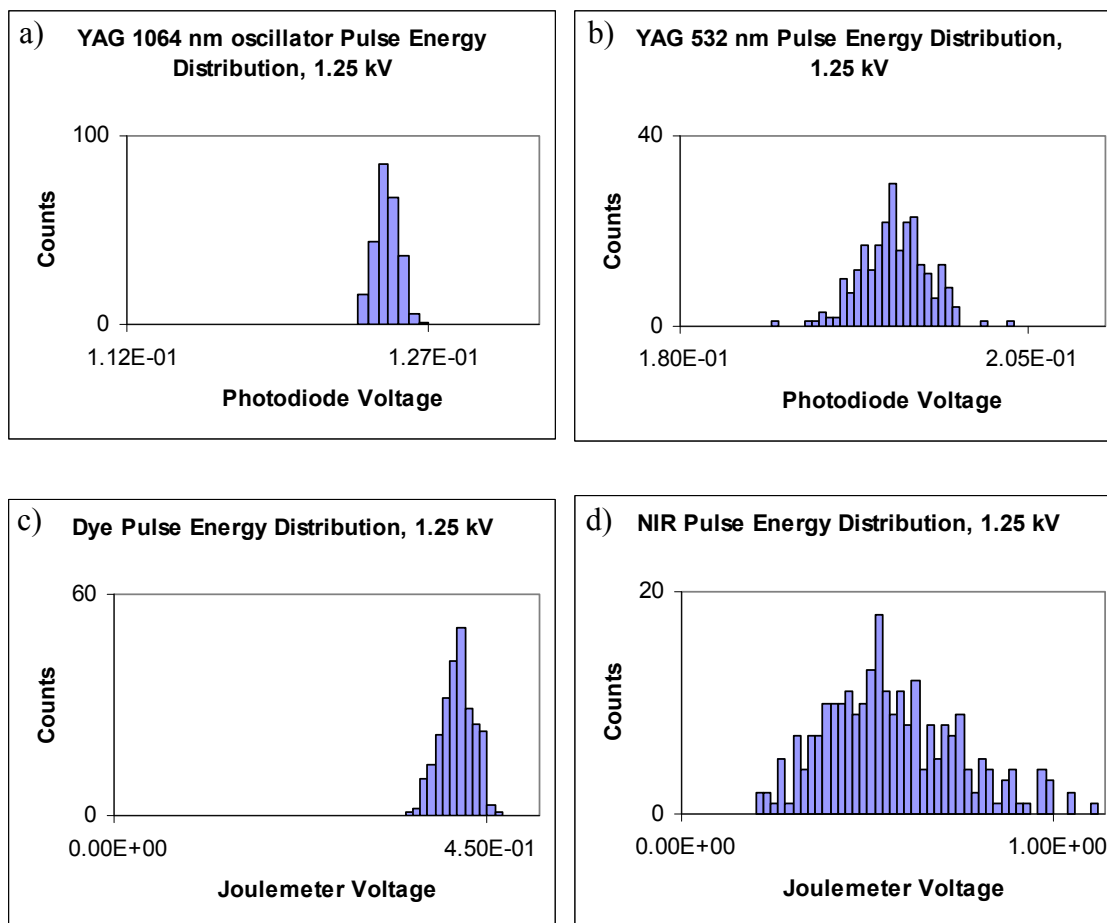


Figure B.12. Histograms of energy per shot for 255 pulses of 1064 nm oscillator light (a), 532 nm light (b), 640 nm dye laser light (c), and 7283 cm^{-1} near IR light (d). All light was collected at a flashlamp voltage of 1.25 kV. Plateau heights were analyzed for the 1064, 532, and 640 nm light, while peak height was analyzed for the 7283 cm^{-1} light. Note that the x-axis scales for the YAG light are much narrower than the axis scales in Figures B.3 and B.4. In comparison to Figures B.3 and B.4, no zero voltage pulses in NIR light are observed, nor is a bimodal distribution observed in YAG or dye laser light. Additionally, the width of the energy distributions appears to be narrower than in Figures B.3 and B.4.

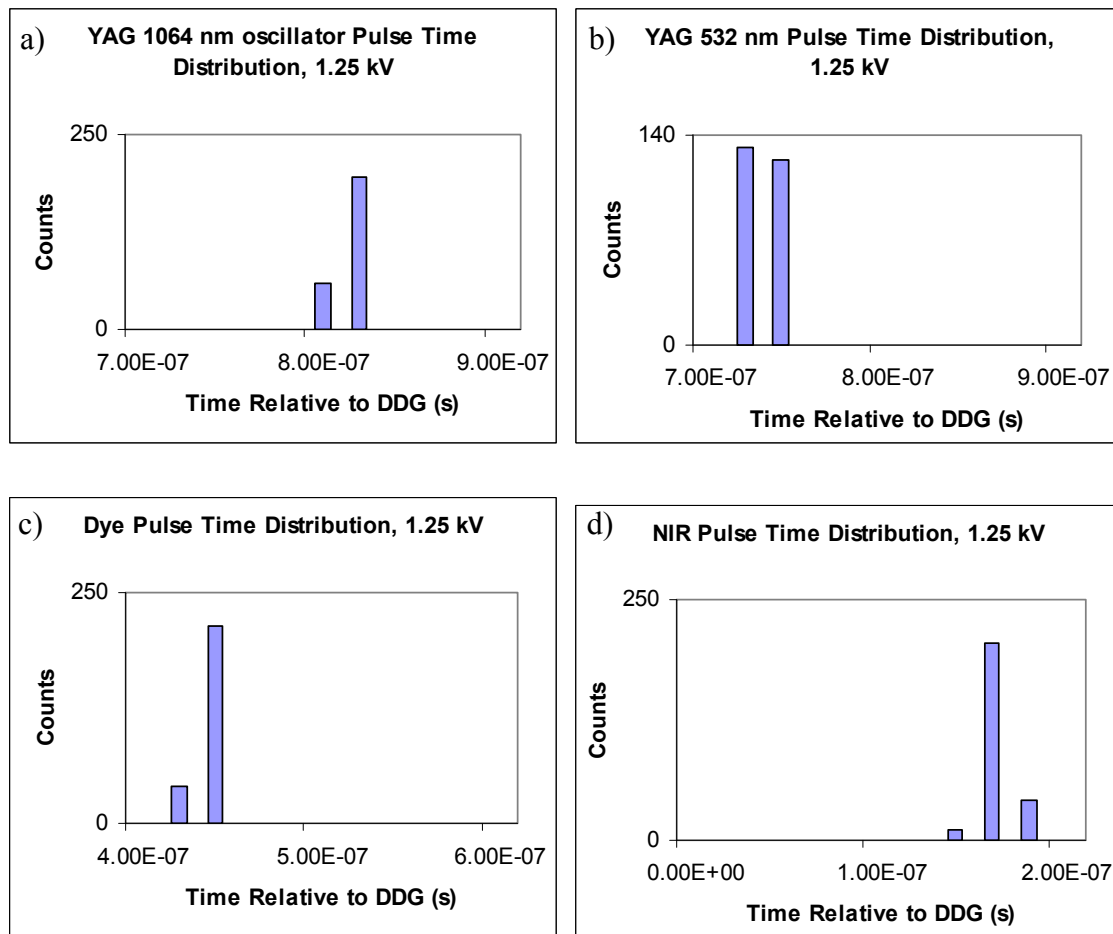


Figure B.13. Histograms of peak timing for 255 pulses of 1064 nm oscillator light (a), 532 nm light (b), 640 nm dye laser light (c), and 7283 cm^{-1} near IR light (d). All light was collected at a flashlamp voltage of 1.25 kV. In all plots, consecutive bars are 20 ns apart. This indicates that the jitter between pulses is shorter than the CompuScope sampling period of 20 ns. Further work with a higher sampling rate scope confirmed that timing jitter is less than 20 ns.

By comparing Figures B.12 and B.13 with Figures B.3–B.6, we notice two major improvements as a result of the laser repairs. First, the energy histograms reveal that the light at all stages (YAG, dye, NIR) has only one peak energy, as opposed to the original bimodal distributions. No zero energy pulses are observed in the NIR light, due to the reduced energy fluctuations in YAG and dye laser light. Second, the timing histograms show that the laser pulses have jitter of less than 20 ns at all stages (YAG, dye, NIR), a

vast improvement over the microsecond jitter in the unrepaired laser. Furthermore, our jitter now agrees with the YAG specification (8 ns). By using an oscilloscope with a higher sampling rate (2.5 GS/s, 0.4 ns between samples), we confirmed that the YAG jitter matched the 8 ns specification.

Conclusions

As stated repeatedly in this thesis, it is imperative that our cavity ringdown spectrometer's laser system is in proper working condition in order to obtain the best quality spectra possible. Incorrect installation of the Nd:YAG laser coupled with malfunctioning parts caused large power and timing fluctuations, leading to a reduction in the light pulse energy and unusable cavity ringdown spectra. By fixing the q-switch trigger circuits, capacitor bank, and laser head, we were able to repair the laser to a useful state. As a result, we observe increased absolute pulse energies out of the YAG, reduced pulse-to-pulse energy fluctuations, and a large reduction in timing jitter. The YAG laser now meets the manufacturer's specifications, an accomplishment given that the laser is 23 years old.

The take away lesson to future graduate students is to pay very close attention when installing new laboratory equipment, and to continually monitor the equipment's performance characteristics. Time should be taken to fix problems to the best of the student's ability, rather than performing quick workarounds that do not solve the problem, but merely ignore it. The YG-661 laser that was incorrectly set up was able to be used in a number of cavity ringdown spectroscopy projects including preliminary OH stretch spectra of the hydroxymethylperoxy radical discussed in Part 3 of this thesis. However,

402

the laser was performing far less than optimally, leading to ringdown spectra that were noisier than expected, and potentially rendering kinetics data useless. By spending the time determining the laser problems and fixing them, we were able to improve the quality of our data, and are now able to fully trust our kinetics measurements.

Appendix C—Calculating Excited States using Gaussian

This appendix contains methods for using Gaussian 03⁷⁸ and Gaussian 09¹²¹ to calculate excited states of molecules. Such methods are useful for estimating the electronic transition frequencies of molecules, particularly for the open shell peroxy radicals studied in our lab. In particular, these methods have been used to study hydroxymethylperoxy (HMP), described in Part 3 of this thesis. Testing and verification of these methods was performed on alkyl peroxy radicals, since extensive experimental and computational work has been performed on these species.⁴⁴

Methods described in this appendix:

- 1) Configuration Interaction Singles (CIS)
- 2) Time-Dependent HF and DFT (TD-HF and TD-DFT)
- 3) Exploiting Orbital Symmetry
- 4) Freezing the Initial Orbital Guess Using `Guess=(Alter,Always)`
- 5) Scaling of Transition Frequencies
- 6) Composite Quantum Chemistry Methods: G2, CBS-QB3, and W1
- 7) Generating Potential Energy Surfaces
- 8) A Caution on Using EOM-IP

1) Configuration Interaction Singles (CIS)

The Configuration Interaction Singles method (CIS) is a “zeroth order method” to approximate excited state energies.¹⁹⁶ Excited states are determined by combinations of single excitations from the Hartree Fock wavefunction. CIS calculations tend to give

very rough estimates of transition frequencies ($\pm 4000 \text{ cm}^{-1}$). In general, one should select a more accurate method to estimate electronic transition frequencies. On the other hand, CIS calculations are very cheap, and can be used on larger molecules where *ab initio* or DFT methods would be unfeasible.

A CIS calculation can be requested using the following route line in Gaussian:

```
#p opt CIS/6-31+g(d,p) geom=connectivity Density=Current
```

There are a few things to point out in this route line. First, CIS calculations cannot be paired with a higher level of theory (such as CCSD). Specifying both CIS and a level of theory will default to a CIS calculation. Second, a CIS calculation should always be run with the `Opt` keyword to ensure that the excited state analysis is performed on an optimized geometry. Finally, note that the `Density=Current` command requests that all analysis be done on the CIS wavefunction, rather than the HF wavefunction. **As a general rule, `Density=Current` should be included in all calculations where the dipole moment integrals are needed.**

The relevant CIS data are found near the end of the output file. These data include transition dipole moments, transition frequencies, oscillator strengths, and information on which orbitals are involved in the excitation. Shown below is the output for a CIS calculation on the HMP radical (discussed in Part 3 of this thesis).

```
*****
Excited states from <AA,BB:AA,BB> singles matrix:
*****

1PDM for each excited state written to RWF 633
Ground to excited state Transition electric dipole moments (Au):
```

state	X	Y	Z	Osc.
1	0.0043	0.0068	0.0048	0.0000
2	-0.0526	-0.1119	-0.1460	0.0058
3	-0.0183	0.0033	-0.0028	0.0001

Ground to excited state transition velocity dipole Moments (Au):

state	X	Y	Z	Osc.
1	0.0005	-0.0027	-0.0022	0.0003
2	0.0069	0.0121	0.0247	0.0023
3	-0.0109	-0.0028	0.0108	0.0006

Ground to excited state transition magnetic dipole Moments (Au):

state	X	Y	Z
1	-0.5531	0.7356	-0.3320
2	-0.7098	-0.2665	0.6301
3	0.0279	0.0486	0.0881

$\langle 0 | \text{del} | b \rangle * \langle b | \text{rxdel} | 0 \rangle$ (Au), Rotatory Strengths (R) in
cgs (10^{*-40} erg-esu-cm/Gauss)

state	X	Y	Z	R(velocity)
1	-0.0003	-0.0020	0.0007	-12.7346
2	-0.0049	-0.0032	0.0156	7.4106
3	-0.0003	-0.0001	0.0010	0.4657

$\langle 0 | r | b \rangle * \langle b | \text{rxdel} | 0 \rangle$ (Au), Rotatory Strengths (R) in
cgs (10^{*-40} erg-esu-cm/Gauss)

state	X	Y	Z	R(length)
1	-0.0024	0.0050	-0.0016	-0.2556
2	0.0374	0.0298	-0.0920	5.8450
3	-0.0005	0.0002	-0.0002	0.1418

$\langle 0 | \text{del} | b \rangle * \langle b | r | 0 \rangle$ (Au)

state	X	Y	Z	Osc.(frdel)
1	0.0000	0.0000	0.0000	0.0000
2	-0.0004	-0.0014	-0.0036	0.0036
3	0.0002	0.0000	0.0000	-0.0001

Ground to excited state transition densities written to RWF 633

Excitation energies and oscillator strengths:

Excited State	1:	?Spin	-A	0.7752 eV	1599.45 nm	f=0.0000
12B -> 17B			0.13373			
14B -> 17B			-0.27905			
14B -> 18B			0.19594			
14B -> 19B			0.16934			
14B -> 20B			-0.14236			
14B -> 21B			0.11446			
14B -> 26B			-0.11191			
15B -> 17B			0.23868			
15B -> 18B			-0.16647			
15B -> 19B			-0.14434			
15B -> 20B			0.12165			
16B -> 17B			-0.44498			
16B -> 18B			0.31356			
16B -> 19B			0.26832			
16B -> 20B			-0.22451			
16B -> 21B			0.17976			
16B -> 26B			-0.16624			
16B -> 29B			-0.12826			
16B -> 30B			0.11778			

This state for optimization and/or second-order correction.
Total Energy, E(CIS) = -264.047852507

In this case, the HMP A-X frequency is predicted to be 0.7752 eV (1599.45 nm, or 6252 cm^{-1}). This is 1100 cm^{-1} less than the experimental frequency, determined by CRDS (7391 cm^{-1}). It is predicted to have an oscillator strength of 0.0000, but Gaussian predicts this for many peroxy radicals (HO_2 , $\text{CH}_3\text{O}_2\bullet$, etc.). This is because the minimum oscillator strength that Gaussian will report is 0.0001, corresponding to an integrated cross section of $8.85 \times 10^{-17} \text{ cm molec}^{-1}$. Electronic transitions with integrated cross sections less than this will appear to have an oscillator strength of 0, a reasonable result for the weak A-X transition in peroxy radicals.⁴⁴

Table C.1 shows a comparison of CIS A-X transition frequency to experiment for HO_2 , $\text{CH}_3\text{OO}\bullet$, and HMP. The quantitative and qualitative agreement between theory and experiment is absolutely terrible. CIS calculations underestimate the A-X frequency by 1000–1500 cm^{-1} . Additionally, the CIS calculation places the A-X transition frequency of $\text{CH}_3\text{OO}\bullet$ lower than HO_2 , while experiment shows the A-X transition frequency of $\text{CH}_3\text{OO}\bullet$ is higher than HO_2 .

Table C.1. Comparison of CIS/6-31+G(d,p) to experiment for A-X electronic transitions of peroxy radicals

Molecule	A-X, CIS (cm^{-1})	A-X, Experiment (cm^{-1})
HO_2	6331	7029 ^{54,55}
$\text{CH}_3\text{OO}\bullet$	5857	7382 ⁴⁴
$\text{HOCH}_2\text{OO}\bullet$	6252	7391

2) Time-Dependent HF and DFT (TD-HF and TD-DFT)

The time-dependent versions of Hartree-Fock and Density Functional Theory (TD-HF and TD-DFT) can also predict excited state energies. Both methods are extensions of the respective time-independent theories (HF and DFT). While the

time-independent methods do not report excited state frequencies, the time dependent formulations do.

To request a time-dependent calculation in Gaussian, simply append the TD keyword to the rest of the route section. The program will automatically select TD-HF or TD-DFT based on the level of theory requested. Shown below is the route line for a TD-DFT calculation.

```
#p Opt B3LYP/6-31+G(d,p) TD geom=connectivity
```

The relevant section of the output looks similar to the CIS output. Shown below is the result of a TD-B3LYP calculation on HO₂.

```
*****
Excited states from <AA, BB:AA, BB> singles matrix:
*****

1PDM for each excited state written to RWF 633
Ground to excited state Transition electric dipole moments (Au):
  state      X      Y      Z      Osc.
  1          0.0000  0.0000 -0.0198  0.0000
  2         -0.0400 -0.5619  0.0000  0.0418
  3          0.0159  0.1112  0.0000  0.0017
Ground to excited state transition velocity dipole Moments (Au):
  state      X      Y      Z      Osc.
  1          0.0000  0.0000  0.0043  0.0003
  2          0.0078  0.1050  0.0000  0.0374
  3         -0.0041 -0.0206  0.0000  0.0015
Ground to excited state transition magnetic dipole Moments (Au):
  state      X      Y      Z
  1         -0.0795 -0.8866  0.0000
  2          0.0000  0.0000  0.0309
  3          0.0000  0.0000 -0.0447
<0|del|b> * <b|rxdel|0> (Au), Rotatory Strengths (R) in
cgs (10**-40 erg-esu-cm/Gauss)
  state      X      Y      Z      R(velocity)
  1          0.0000  0.0000  0.0000  0.0000
  2          0.0000  0.0000  0.0000  0.0000
  3          0.0000  0.0000  0.0000  0.0000
<0|r|b> * <b|rxdel|0> (Au), Rotatory Strengths (R) in
cgs (10**-40 erg-esu-cm/Gauss)
  state      X      Y      Z      R(length)
```

```

      1      0.0000      0.0000      0.0000      0.0000
      2      0.0000      0.0000      0.0000      0.0000
      3      0.0000      0.0000      0.0000      0.0000
<0|del|b> * <b|r|0> (Au)
      state      X      Y      Z      Osc.(frdel)
      1      0.0000      0.0000      -0.0001      0.0001
      2      -0.0003      -0.0590      0.0000      0.0395
      3      -0.0001      -0.0023      0.0000      0.0016
Ground to excited state transition densities written to RWF 633

Excitation energies and oscillator strengths:

Excited State 1: ?Spin -A" 0.9919 eV 1249.97 nm f=0.0000
      8B -> 9B 1.08132
This state for optimization and/or second-order correction.
Total Energy, E(RPA) = -150.876870963
Copying the excited state density for this state as the 1-particle
RhoCI density.

Excited State 2: ?Spin -A' 5.3799 eV 230.46 nm f=0.0418
      7A -> 10A -0.17402
      8A -> 13A 0.11876
      9A -> 10A -0.19873
      7B -> 9B 0.95400

Excited State 3: ?Spin -A' 5.4896 eV 225.85 nm f=0.0017
      9A -> 10A -0.63390
      9A -> 11A 0.25689
      9A -> 14A -0.15605
      7B -> 9B -0.17966
      8B -> 10B 0.65845
      8B -> 11B -0.35617
      8B -> 14B 0.20378
Leave Link 914 at Tue Apr 06 09:17:52 2010, MaxMem= 167772160 cpu:
4.0
(Enter C:\G03W\1114.exe)

```

There are a couple of things to note about the TD-DFT calculations. Similar to the CIS calculation, dipole moment integrals, excited state frequencies, oscillator strengths, and the molecular orbitals involved in excitation are reported. The above output reports the A-X frequency of HO₂ to be 0.9919 eV (1249.97 nm, or 8000 cm⁻¹). This overestimates the A-X frequency by 1000 cm⁻¹ (experimental value of 7029 cm⁻¹).^{54, 55} Additionally, the TD-DFT calculations are very computationally expensive when paired with the Opt keyword. One workaround is to optimize the geometry using

time-independent DFT, and then run a single point TD-DFT calculation. While this method will reduce the computational expense, it is also less accurate than a full TD-DFT optimization.

Table C.2 shows a comparison of TD-DFT A-X transition frequency to experiment for HO₂, CH₃OO•, and HMP. TD-DFT values were calculated both with and without the `Opt` keyword, as described above. When the `Opt` keyword was used on the calculations of CH₃OO• and HMP, Gaussian would crash after a few optimization steps, reporting that the Hessian structure was not correct. We do notice that the single point TD-DFT calculations are able to correctly predict the trend in A-X frequency amongst the three radicals, suggesting that the single point TD-DFT method can be used to predict relative positions in peroxy radicals.

Table C.2. Comparison of TD-DFT to experiment for A-X electronic transitions of peroxy radicals (TD-B3LYP/6-31+G(d,p))

Molecule	A-X, TDDFT SP (cm ⁻¹)	A-X, TDDFT Opt (cm ⁻¹)	A-X, Experiment (cm ⁻¹)
HO ₂	8932	8000	7029 ^{54,55}
CH ₃ OO•	9287	not computed	7382 ⁴⁴
HOCH ₂ OO•	9303	not computed	7391

The authors of NWChem,¹⁹⁷ a computational chemistry program published by Pacific Northwest National Laboratories, offer a comment on the accuracy of TD-DFT:

“The accuracy of TDDFT may vary depending on the exchange-correlation functional. In general, the exchange-correlation functionals that are widely used today and are implemented in NWChem work well for low-lying valence excited states. However, for high-lying diffuse excited states and Rydberg excited states in particular, TDDFT employing these conventional functionals breaks down and the excitation energies are substantially underestimated.”

TD-HF is roughly comparable in accuracy to CIS. My experience with TD-DFT is absolute accuracy of $\pm 1000 \text{ cm}^{-1}$ (based on the above calculations on HO_2 , $\text{CH}_3\text{OO}\cdot$, and HMP). In general, I would not ever run a TD-HF calculation, since the CIS calculation will be of comparable accuracy and less expensive. TD-DFT can be thought of as one step more accurate than CIS. However, the computational expense of TD-DFT calculations makes them generally unsuitable for anything with more than a few carbons.

3) Exploiting Orbital Symmetry

The optimization algorithm in Gaussian will do its best to keep the same molecular symmetry as the input geometry.⁷⁹ Thus, if the input file contains a molecule in C_s symmetry, the optimized structure will also be C_s . The same idea holds true for the symmetry of the electronic wavefunction. If the input file contains an electronic wavefunction with A'' symmetry, then the optimization will attempt to keep the electronic wavefunction in A'' symmetry at every step.

The idea of restricting symmetries can be exploited to obtain excited state geometries. Consider, for example, the first two states of HO_2 . The ground state has A'' symmetry, while the first excited state has A' symmetry. Suppose that the input file requests a geometry optimization, with an initial electronic state guess of A' symmetry. During the optimization, Gaussian will always keep the electronic state symmetry as A' . The result of the optimization will be the lowest energy structure with A' electronic symmetry, i.e., the first excited state.

The initial orbital population can be changed using `Guess=Alter` in the route line. This command allows users to switch pairs of orbitals that are to be populated. (For

example, switching orbitals 4 and 5 will cause Gaussian to populate the orbitals in this order: 1, 2, 3, 5, 4, 6, 7, ...) Switching two core orbitals will have no effect. (However, such an operation is not completely useless; it may be necessary to switch core orbital filling in a CASSCF job.) Switching a core or valence orbital with a virtual orbital will allow the user to change the electronic symmetry. These pairs of orbitals are listed at the end of the input file.

If the calculation uses a restricted method (RHF, RCCSD, etc.), then only one line is necessary to change orbitals. If the calculation uses an unrestricted method (UHF, UCCSD, etc.), then separate lines are necessary for α and β electrons. Both lines must be present in the input file. If no electrons of one type are to be changed, then the line should be blank.

The following example file calculates the first excited state of HO₂. Since HO₂ has 17 electrons (9 α , 8 β), we will change the order of β orbitals 8 and 9. Since no α electrons are being altered, we put a blank line before the β orbital line (**this is in addition to a blank line needed to separate the connectivity section from the orbital alteration section**).

412

```
%chk=HO2 B3LYP A Opt.chk
%nproc=1
#p opt B3LYP/6-31+g(d,p) geom=connectivity Guess=Alter
```

```
HO2 A State
MKS, 4/6/10
```

```
0 2
O
H          1          B1
O          1          B2      2          A1
```

```
B1=0.98052408
B2=1.33330037
A1=105.52948981
```

```
1 2 1.0 3 1.0
2
3
```

```
8 9
```

The output file will look exactly like a normal optimization file. **However, the user should ensure that the final symmetry is the excited state electronic symmetry, and not the ground state.** Sometimes, the optimization will “relax” down to the ground state symmetry. I am not sure what the reason for this is, but it does happen from time to time. The symmetry can be found in the final output (highlighted below).

```
(Enter C:\G03W\19999.exe)
Final structure in terms of initial Z-matrix:
O
H,1,B1
O,1,B2,2,A1
Variables:
B1=0.97637273
B2=1.39529609
A1=103.55791628
1|1|UNPC-UNK|FOpt|UB3LYP|6-31+G(d,p)|H1O2(2)|PCUSER|06-Apr-2010|4||#P
OPT B3LYP/6-31+G(D,P) GEOM=CONNECTIVITY GUESS=ALTER|Title Ca
rd Required||0,2|O,-0.6348300196,0.,0.1172381389|H,-0.6030213526,0.,1.
0930925935|O,0.7102076887,0.,-0.253874713|||8,9||Version=IA32W-G03RevC
.01|State=2-A'|HF=-150.8824122|S2=0.753042|S2-1=0.|S2A=0.750007|RMSD=3
.483e-009|RMSF=8.428e-005|Dipole=-0.1481518,0.,0.8045714|PG=CS [SG(H1O
2)]|@
```

In this case, the electronic state is listed as $2-A'$, which is the electronic symmetry of the first excited state. The final energy can be compared to the ground state (calculated separately), and the A-X frequency can be computed. For HO₂ at B3LYP/6-31+G(d,p), the A-X frequency is computed as 7251 cm⁻¹, 222 cm⁻¹ higher than the experimental value.

4) Freezing the Initial Orbital Guess Using `Guess=(Alter,Always)`

Note: The paper on alkyl peroxy spectra by Sharp et al. describe populating the electronic orbitals in a low level calculation, then running a high level calculation using the orbitals obtained from the previous calculation.⁴⁴ It is unknown to me whether Sharp uses a separate script or the method described below. As will be shown, our method can reproduce Sharp's results, and is, at a minimum, equivalent to their method. The discussion below should help future students perform these calculations.

Most conformations of the molecules that we are interested in do not have any point group symmetry (i.e., they belong to the C₁ point group). As such, there is no electronic wavefunction symmetry to take advantage of, and simply using the keyword `Guess=Alter` will result in the optimization relaxing back to the ground state. However, by changing this command to `Guess=(Alter,Always)`, Gaussian 03W will repopulate the electron orbitals at each step of the SCF calculation. The result of this is "freezing" the electrons in a non-ground-state configuration. Such a calculation will allow for the excited state energy of any molecule to be computed. Unlike a CIS calculation, the geometry and orbitals are optimized in the excited state as opposed to the

ground state, and thus the energies obtained should be vastly more accurate than a CIS calculation.

The syntax and output are the same as described in the previous section, with the exception of changing `Guess=Alter` to `Guess=(Alter,Always)`. The A-X transition frequencies obtained on C_1 conformers of a molecule are consistent with results obtained from C_s conformers (i.e., exploiting orbital symmetry as described in the previous section). This can be illustrated by mapping out the full potential energy surfaces, and showing that the C_s transition frequencies agree with the surrounding C_1 transition frequencies, as has been done for HMP (see the surfaces presented in Part 3 of this thesis). This consistency strongly implies that this method of obtaining excited states is valid for molecules with no symmetry.

Table C.3 shows a comparison of `Guess=(Alter,Always)` A-X transition frequency to experiment for HO_2 , $\text{CH}_3\text{OO}\cdot$, and HMP. The absolute transition frequencies are too high by 100–200 cm^{-1} , though this represents a vast improvement over CIS or TD-DFT. For the most part, the transition frequencies qualitatively follow the experimental trends. `Guess=(Alter,Always)` is able to predict the transition frequencies of both $\text{CH}_3\text{OO}\cdot$ and $\text{HOCH}_2\text{OO}\cdot$ to be higher than the transition frequency of HO_2 . Unfortunately, it also predicts $\text{HOCH}_2\text{OO}\cdot$ to have a lower frequency than $\text{CH}_3\text{OO}\cdot$. Sharp et al. make similar observations: the `Guess=(Alter,Always)` calculations become less accurate as the peroxy radical of interest becomes more complicated (either additional functional groups, or a longer carbon chain).

Table C.3. Comparison of the `Guess=(Alter,Always)` method to experiment for A-X electronic transitions of peroxy radicals (B3LYP/6-31+G(d,p))

Molecule	A-X, <code>Alter,Always</code> (cm^{-1})	A-X, Experiment (cm^{-1})
HO ₂	7251	7029 ^{54,55}
CH ₃ OO•	7622	7382 ⁴⁴
HOCH ₂ OO•	7501	7391

5) Scaling of Transition Frequencies

The calculation methods presented above can often get the correct qualitative behavior for the transition frequencies. For example, the `Guess=(Alter,Always)` method at B3LYP/6-31+G(d,p) is able to predict that CH₃OO• and HOCH₂OO• both have a higher A-X transition frequency than HO₂. However, the quantitative agreement between calculated and experimental transition frequencies is not very good, ranging in accuracy from $\pm 300 \text{ cm}^{-1}$ (`Guess=Alter,Always`) to $\pm 1500 \text{ cm}^{-1}$ (single point TD-DFT). As presented so far, the computed transition frequencies are of limited aid for predicting electronic transitions that have not yet been detected.

A careful look at Tables C.1–C.3 reveals that each particular method tends to overestimate or underestimate the transition frequency by a similar amount, regardless of the specific peroxy radical being studied. This observation suggests that if we scale the calculated frequencies to a well-studied peroxy radical, such as HO₂, we will be able to obtain quantitatively accurate transition frequencies. Scaling should eliminate systematic errors from the level of theory and basis being used. Additionally, if the reference molecule is chemically similar to the molecules of interest, we expect that the electronic surfaces will have similar curvature and harmonic frequencies. Thus, we will also account for any changes in the zero point vibrational energy (ZPVE).

Table C.4 contains the scaled A-X transition frequencies for $\text{CH}_3\text{OO}\cdot$ and $\text{HOCH}_2\text{OO}\cdot$, using each of the methods to obtain this frequency described above (CIS, TD-DFT, Guess=Alter, Always). The frequencies are scaled to the experimentally determined A-X transition of HO_2 of 7029 cm^{-1} .^{54, 55} The scaled frequencies are in general closer to the experimental values than the unscaled frequencies. While CIS still gives a poor prediction for the transition frequency, TD-DFT and Guess=(Alter, Always) are able to predict the A-X frequency within 100 cm^{-1} . Although this is still considered considerable error, both TD-DFT and Guess=(Alter, Always) can be used to aid in experimental detection of A-X transitions in peroxy radicals. In order to obtain better quantitative agreement, we must move on to more sophisticated (and thus more expensive) methods, described in the next section.

Table C.4. Comparison of scaled frequencies to experiment for A-X electronic transitions of peroxy radicals. Frequencies scaled to A-X (HO_2) = 7029 cm^{-1} . (B3LYP/6-31+G(d,p))

Molecule	CIS (cm^{-1})	TD-DFT, no opt (cm^{-1})	Guess=Alter, Always (cm^{-1})	Expt. (cm^{-1})
HO_2	—	—	—	7029 ^{54, 55}
$\text{CH}_3\text{O}_2\cdot$	6503	7309	7390	7382 ⁴⁴
$\text{HOCH}_2\text{O}_2\cdot$	6942	7321	7272	7391

6) Composite Quantum Chemistry Methods: G2, CBS-QB3, and W1

Composite quantum chemistry methods are designed for high-accuracy thermochemical calculations. The purpose of these calculations is to approximate the energy at a high level of theory and large basis by performing many smaller calculations

(high level and small basis, or low level and large basis). Three methods used in the current chemical literature are G2,^{123, 198-201} CBS-QB3,²⁰²⁻²⁰⁵ and W1.²⁰⁶⁻²¹¹ Of these, G2 has been used frequently in calculations of alkyl peroxy radicals. It has been shown to predict the A-X transition frequencies within $\pm 50 \text{ cm}^{-1}$ without the need for scaling.⁴⁴ Sharpe et al. show that as the alkyl chain gets larger, the frequencies predicted by the G2 method become less accurate. The accuracy may or may not get worse when additional functional groups are present.

The purpose of the G2 method is to estimate the QCISD(T)/6-311+G(3df,2p) energy by computing less expensive energies at lower levels of theory, or smaller basis sets. These energies are used to estimate the contributions to the energy due to increasing the basis set. A G2 calculation consists of the following steps:

- 1) Geometry optimization at HF/6-31G(d)
- 2) Frequency calculation at the geometry from step 1, to obtain the zero point energy
- 3) Geometry optimization at MP2(Full)/6-31G(d)
- 4) Using the geometry from step 3, single point calculations at
 - a) QCISD(T,E4T)/6-311G(d,p) (see below for explanation of “E4T”)
 - b) MP4(SDTQ)/6-311G(2df,p)
 - c) MP4(SDTQ)/6-311+G(d,p)
 - d) MP2/6-311+G(3df,2p)

Note that the MP4(SDTQ) and QCISD(T) calculations will also provide MP2 and MP4 energies, at no additional cost. **The user must request for triples to be calculated during the QCISD(T) calculation by using the method QCISD(T,E4T).**

The G2 energy can then be computed from Equation C.1, as defined in Pople's G1 and G2 papers:^{123, 198, 201}

$$\begin{aligned}
 E(\text{G2}) = & \{ \text{QCISD(T)/6-311G(d,p)} \} \\
 & + [\{ \text{MP4/6-311G(2df,p)} \} - \{ \text{MP4/6-311G(d,p)} \}] \\
 & + [\{ \text{MP4/6-311+G(d,p)} \} - \{ \text{MP4/6-311G(d,p)} \}] \\
 & + [\{ \text{MP2/6-311+G(3df,2p)} \} - \{ \text{MP2/6-311G(2df,p)} \}] \quad (\text{C.1}) \\
 & + [\{ \text{MP2/6-311G(d,p)} \} - \{ \text{MP2/6-311+G(d,p)} \}] \\
 & + 0.8929 \times \text{ZPVE} \\
 & + \text{HLC},
 \end{aligned}$$

where the terms labeled {xx/yy} denote the single point energy at xx/yy//MP2(Full)/6-31G(d), ZPVE is the zero point vibrational energy, 0.8929 is the HF/6-31(d) scaling factor for the harmonic frequencies, and HLC is a "high level correction." The HLC is defined as

$$\text{HLC} = (-4.81 \text{ mhartree}) \times N_V - (-0.19 \text{ mhartree}) \times N_U, \quad (\text{C.2})$$

where N_V is the total number of valence electrons, and N_U is the number of unpaired valence electrons. For example, in HMP, there are 33 total electrons. 8 of these 33 are core (1s) electrons, leaving 25 valence electrons (N_V), 1 of which is unpaired (N_U). The HLC is -60.19 mhartree.

For ground state molecules, the G2 method can be directly requested in G03W, via the following route line:

```
#p G2 geom=connectivity
```

Gaussian will automatically carry out the calculations described above. The end of the output file contains information on the G2 energies. Shown below is the output for a G2 calculation on HMP:

Temperature=	298.150000	Pressure=	1.000000
E(ZPE)=	0.047510	E(Thermal)=	0.051972
E(QCISD(T))=	-264.903868	E(Empiric)=	-0.073870
DE(Plus)=	-0.015881	DE(2DF)=	-0.141516
G1(0 K)=	-265.087624	G1 Energy=	-265.083162
G1 Enthalpy=	-265.082218	G1 Free Energy=	-265.115071
E(Delta-G2)=	-0.017592	E(G2-Empiric)=	0.013680
G2(0 K)=	-265.091536	G2 Energy=	-265.087074
G2 Enthalpy=	-265.086130	G2 Free Energy=	-265.118983
DE(MP2)=	-0.166853		
G2MP2(0 K)=	-265.083401	G2MP2 Energy=	-265.078938
G2MP2 Enthalpy=	-265.077994	G2MP2 Free Energy=	-265.110847

The G2 energy is listed as G2 (0 K). In this case, the G2 energy is -265.091536 au.

It is not possible to use the built in G2 method for calculating excited states, because Gaussian will not pass the `Guess=(Alter,Always)` command correctly to each step. Instead, the user must manually request the calculations described above (steps 1-4), and extract the correct energies from each file. I wrote a G2 calculator in Excel to automatically calculate the G2 energy: the user types in the energies from each part, and the program determines the G1 and G2 energies (Figure C.1 shows a screenshot of the calculator). Typically, the G2 energy obtained through the calculator only differs from the G2 energy directly reported by G03W by a few microhartree ($<1 \text{ cm}^{-1}$). Once the X and A states have been calculated, the energy difference should be used directly as the transition frequency. No further energy scaling is required (such as the scaling described in the previous section), because differences in the ZPVE for the X and A states have already been accounted for.

HMP G2 through Gaussian						
A1	A	B	C	D	E	G
1	HMP G2 through Gaussian					
2	Level	Basis	E (au)		Molecule	
3	QCISD(T)	6-311G(d,p)	-264.9038679		ncore	8
4	MP4	6-311G(2df,p)	-265.0426343		nalpha	13
5	MP4	6-311G(d,p)	-264.9011185		nbeta	12
6	MP4	6-311+G(d,p)	-264.9169993			
7	MP2	6-311+G(3df,2p)	-265.0151013			
8	MP2	6-311G(d,p)	-264.8482486			
9	MP2	6-311G(2df,p)	-264.9827944			
10	MP2	6-311+G(d,p)	-264.8629634			
11	MP2	6-311+G(d,p)	-264.8629634			
12						
13	ZPVE	HF/6-31G(d)	0.053212			
14						
15		E(G1, 0K)	-265.0876215			
16		E(G2, 0K)	-265.0915336			
17						
18						
19	G1:	MP4(Full)/6-311G**/MP2(Full)/6-31G*				-264.9011185
20	(Pople 89)	dE(+)=MP4/6311+G** - MP4/6-311G**				-0.0158808 DE(Plus)
21		dE(2df) = MP4/6-311G**(2df) - MP4/6-311G**				-0.1415158 DE(2DF)
22		dE(QCJ) = QCISD(T)/6-311G** - MP4/6-311G**				-0.0027494
23		E combined				-265.0612645
24		dE(HLC) = -0.00019*nalpha+0.00595*nbeta				-0.07387 (E Empiric)
25		0.8929*ZPE				0.047512995 E(ZPE)
26		E(G1)				-265.0876215 G1 (0K)
27						
28						
29						

Figure C.1. Screenshot of the G2 energy calculator spreadsheet. The calculated G1 and G2 energies are circled.

Table C.5 shows a comparison of G2 A-X transition frequency to experiment for HO₂, CH₃OO•, and HOCH₂OO•. The quantitative agreement between calculation and experiment is quite good. HO₂ and HOCH₂OO• are calculated to within 40 cm⁻¹ of their experimental values, while CH₃OO• is calculated to better than 10 cm⁻¹. It should be

noted that G2 is generally a much more expensive method than using `Guess=(Alter, Always)`, although this depends on the level of theory and basis used. It may be unfeasible to run G2 calculations on larger alkyl peroxies without access to a supercomputer.

Table C.5. Comparison of G2 calculated frequencies to experiment for A-X electronic transitions of peroxy radicals

Molecule	A-X (G2) (cm ⁻¹)	A-X, Experiment (cm ⁻¹)
HO ₂	7060	7029 ^{54, 55}
CH ₃ OO•	7375	7382 ⁴⁴
HOCH ₂ OO•	7424	7391

As shown in Part 3 of this thesis, the G2 method cannot locate all three conformers (local minima) of the HMP radical. The MP2(Full)/6-31+G(d,p) potential energy surface of HMP reveals that one of the local minima from CCSD and B3LYP calculations becomes a shelf at MP2(Full). Because the CCSD calculation is likely more accurate than the MP2(Full) calculation, my thought is that the G2 method is inadequate for conformer searches of substituted peroxy radicals.

Two other composite chemistry methods are also available in Gaussian 03: the complete basis set methods by Petersson (denoted as CBS methods),²⁰²⁻²⁰⁵ and the Weizmann-1 method (W1).²⁰⁶⁻²¹¹ In particular, two methods of interest are CBS-QB3 (based on a B3LYP geometry optimization) and W1U (based on a UB3LYP geometry optimization and UCCSD energy corrections). The work described in Part 3 of this thesis shows that the B3LYP and CCSD potential energy surfaces of HMP are in qualitative agreement. Furthermore, both methods are able to predict the A-X transition of HMP to within ± 80 cm⁻¹ when scaled to HO₂ (as seen in the previous section). Thus, composite

chemistry methods based on these levels of theory could lead to improvements in A-X transition predictions.

I wrote a CBS-QB3 energy calculator in Excel (similar to the G2 calculator described above), allowing for the computation of A-X transition frequencies. Table C.6 contains the CBS-QB3 calculated A-X transition frequencies for HO₂, CH₃OO•, and HOCH₂OO•. CBS-QB3 is able to calculate both HO₂ and CH₃OO• to within 20 cm⁻¹ of the experimental values. However, the accuracy is worse with substituted alkyl peroxies. The calculated A-X transition for HMP is 90 cm⁻¹ higher than the experimental frequency. It is unclear at the moment whether the accuracy will be better or worse than G2.

Table C.6. Comparison of CBS-QB3 calculated frequencies to experiment for A-X electronic transitions of peroxy radicals

Molecule	A-X (CBS-QB3) (cm ⁻¹)	A-X, Experiment (cm ⁻¹)
HO ₂	7042	7029 ^{54,55}
CH ₃ OO•	7411	7382 ⁴⁴
HOCH ₂ OO•	7479	7391

W1U calculations make use of a B3LYP geometry and use CCSD(T) calculations to obtain complete basis set corrections. I've already written a calculator in Excel for W1U calculations, and I can reproduce the W1U energies for H₂ and OH. The W1U calculated A-X frequency for HMP is within 60 cm⁻¹ of the experimental value (7443 cm⁻¹ calculated, 7391 cm⁻¹ experimental). More expensive (and more accurate) methods are available (W2, W3, W4); however, these are likely out of range of our computational resources without access to a supercomputer.

It should be noted that the 32-bit version of Gaussian cannot perform a W1 calculation on HO₂ (or anything larger), due to the CCSD and CCSD(T) calculations exceeding the 16 GB scratch space limit for 32-bit programs. There are no problems running the W1 calculations on the 64-bit version of Gaussian in Linux. Furthermore, other 64-bit programs are also capable of these calculations (CFour, Molpro, Q-Chem, etc.). Significant amounts of memory are required for these calculations: the W1 calculation on HMP exceeded the 10 GB of RAM that I initially had allocated to Gaussian.

7) Generating Potential Energy Surfaces

It is generally useful to determine the potential energy surface (PES) of a molecule as a function of molecular coordinates (bond distances, bond angles, dihedral angles). These potential energy functions can be used to assess energy barriers to molecular motion or reaction, coupling of vibrational and torsional normal modes due to intramolecular interactions such as hydrogen bonding, and explicit calculation of wavefunctions and quantum energy levels. As has been shown repeatedly in this thesis (HOONO, HMP, 2-HIPP), normal mode coupling causes additional complexity in the IR spectra, and must be explicitly modeled in order to correctly simulate the spectra.

Two types of potential energy scans can be requested in Gaussian: a rigid scan in which all other molecular coordinates remain fixed, or a relaxed scan in which all other molecular coordinates are optimized at each step. Rigid scans are useful in the adiabatic approximations: fast vibrational modes can be completely separated from slow modes. This is true when separating OH stretch motions from torsional motions in many

molecules, including HOONO and HMP. Relaxed scans are useful when an adiabatic approximation cannot be made. This is true when scanning over dihedral angles in a molecule: the torsional normal modes associated with these angles are typically of low frequency, and many other low frequency modes are generally present.

Scans are typically performed across internal coordinates rather than a Cartesian coordinate; therefore, it is easiest to request the potential energy scan directly from the Z-matrix input. The following example requests a relaxed potential energy scan across the two torsional angles (HOCO, OOCO) on the A state of the 2-HIPP radical, with the essential parts of requesting the scan highlighted.

```
%chk=C:\G09W\MKS\2-HIPP PES\2-HIPP A B3LYP PES.chk
#p Opt=Z-matrix B3LYP/6-31+g(d,p) Guess=(Alter,Always) NoSymm
```

Title Card Required

0 2

C							
C	1	B1					
H	2	B2	1	A1			
H	2	B3	1	A2	3	D1	0
H	2	B4	1	A3	4	D2	0
C	1	B5	2	A4	5	D3	0
H	6	B6	1	A5	2	D4	0
H	6	B7	1	A6	2	D5	0
H	6	B8	1	A7	2	D6	0
O	1	B9	2	A8	6	D7	0
H	10	B10	1	A9	2	D8	0
O	1	B11	10	A10	11	HOCO	0
O	12	B12	1	A11	10	OOCO	0

```
B1=1.52722762
B2=1.0933087
B3=1.09422741
B4=1.09247629
B5=1.51904907
B6=1.09171903
B7=1.09207247
B8=1.09289496
B9=1.39714561
B10=0.96792656
B11=1.48479112
B12=1.37990918
A1=109.09594428
A2=111.00707754
A3=110.52283361
A4=114.39312339
A5=110.61869101
A6=109.68521782
A7=108.76323525
A8=112.59779458
A9=109.77029369
A10=109.73656718
A11=112.28122574
D1=119.77962987
D2=120.04129575
D3=-60.2624729
D4=55.87981057
D5=176.84253762
D6=-64.27682433
D7=-123.2116855
D8=-120.0
HOCO=0.0 S 18 10.0
OOCO=0.0 S 35 10.0
```

24 25

There are four essential features to this input file. First, the keyword `Opt=Z-matrix` must be entered in the route line. This ensures that all optimization proceeds using Z-matrix coordinates. If only `Opt` is entered, the scan will fail. Second, the command `NoSymm` must be entered in the route line. If the scan breaks point group symmetry and `NoSymm` has not been requested, the scan will fail and Gaussian will exit with an error message. Third, all of the coordinates within the Z-matrix have been entered as variables (R1, A1, D1, etc.). The variables of interest have been specially labeled (HOCO and OOCO for the dihedral angles). Although this is not strictly necessary, it is good practice to highlight which variables are being scanned. Fourth, the entries for the variables being scanned over are not a single number; rather, they specify the initial parameter, number of steps, and step size. For example, the line `HOCO=0.0 S 18 10.0` requests that the variable HOCO start at a value 0.0, and then be scanned (S) with 18 steps of size 10.0 (final value of 180.0).

Gaussian will run all of the geometries consecutively and print the energies at the end of the file. It is more useful to compile all of the energies into one text file for further use in Excel (for data manipulation) and SigmaPlot (for surface plotting). GaussView can compile all of the energies, although versions 3 and 5 do this differently. Version 3 compiles the energies in the same order in which Gaussian ran them, while version 5 reorders them in ascending order by coordinate. Additionally, GaussView 5 will display a 3-dimensional surface for multidimensional scans. Figure C.2 shows the graphical output of GaussView 3.09 and GaussView 5.09 for scans of the X state of 2-HIPP.

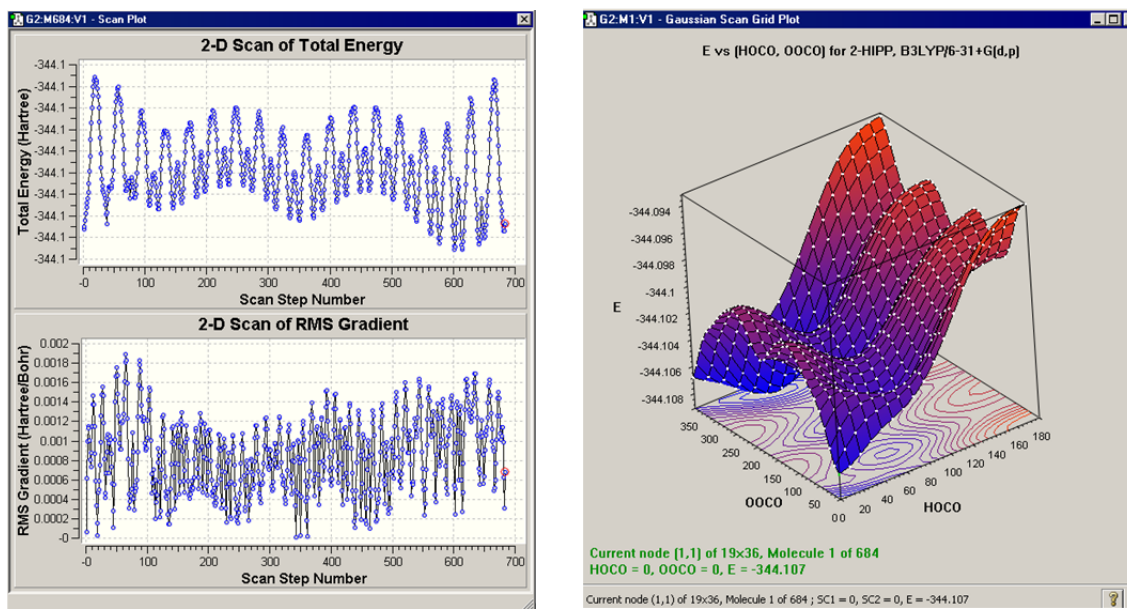


Figure C.2. Visualization of energies generated from a 2-D potential energy scan of 2-HIPP in GaussView 3.09 (left) and GaussView 5.09 (right). GaussView 3.09 simply displays the energies in the order in which they were calculated, while GaussView 5.09 generates a contour plot.

The 2-dimensional potential energy surfaces presented in this thesis were generated in SigmaPlot. SigmaPlot requires a periodic arrangement of data. In other words, to generate a plot across 2 dihedral angles of 360° apiece, the input data must be arranged in the form $(-180^\circ, -180^\circ)$, $(-180^\circ, -170^\circ)$, ..., $(-180^\circ, 180^\circ)$, $(-170^\circ, -180^\circ)$, $(-170^\circ, -170^\circ)$, etc. For many scans, only half of these points are explicitly calculated (the other half are equal in energy by symmetry). Before inputting energies into SigmaPlot, the user must generate all of the necessary energies in Excel by exploiting symmetry. Afterwards, the energies should be sorted into a periodic form, typically achieved by sorting one variable followed by a second variable. Finally, the sorted values can be copied into SigmaPlot to generate a contour plot similar to the ones presented in Parts 2 and 3 of this thesis.

8) A Caution on Using Equation of Motion (EOM) Methods

Note that a full discussion of Equation of Motion (EOM) methods is not included here because Gaussian 03 does not contain these methods. Gaussian 09 as well as many other programs (such as CFour and Q-Chem) do support EOM methods. These methods may prove useful for future calculations; however, future students are advised to use caution with these methods. Terry Miller's group found that EOM-IP overestimated the A-X transition frequency for alkyl peroxies by $\sim 1000 \text{ cm}^{-1}$.⁴⁴ Even if these values are scaled to experimental results on HO₂ or CH₃OO•, the transition frequencies do not follow the experimental trends any better than the previously described methods. The Miller group attributes the poor agreement to EOM methods not properly accounting for electron correlation.

Acknowledgements

We thank J. Sigrid Barklund and Leah G. Dodson for suggestions on how to improve the readability and utility of this appendix.

Appendix D—Simulating Spectroscopic Bands Using Gaussian and PGopher

This appendix contains methods for using Gaussian 09¹²¹ and PGopher¹²⁰ to simulate vibrational and electronic bands of molecules. These methods are useful for confirming spectroscopic band assignments based on band width, shape, and strength. The examples provided in this appendix are for simple molecules: the ν_1 vibrational spectrum of methanol and the A-X electronic spectrum of HOCH₂OO• (HMP) from Chapter 4.

Sections in this appendix:

- 1) Calculation of Vibrational Dipole Derivatives
- 2) Estimation of the A-X Dipole Derivative
- 3) Calculation of Anharmonic Rotational Constants
- 4) Simulation of the Spectroscopic band

1) Calculation of Vibrational Dipole Derivatives

By default, Gaussian 03 or 09 will not print the dipole derivatives associated with vibrational modes. However, adding the command `iop(7/33=1)` to the route line will request the dipole derivatives to be printed. The command is entered as follows:

```
#p freq rb3lyp/6-31+g(d,p) geom=connectivity iop(7/33=1)
```

Note that `iop(7/33=1)` will not work if you request an optimization and a frequency job in the same file (i.e., `opt freq`), because it will not be passed correctly

to the frequency calculation. Only specify `iop(7/33=1)` with “frequency only” calculations.

Also, `iop(7/33=1)` makes use of normal modes only; anharmonic corrections are irrelevant. Running an anharmonic frequency calculation will not yield different or more accurate dipole derivatives.

Below is an excerpt from the relevant output from a frequency calculation on methanol using the `iop(7/33=1)` command.

```
Dipole derivatives wrt mode 1: 1.81379D-08 2.40612D-08 -1.18744D+01
Vibrational polarizability contributions from mode 1 0.0000000
0.0000000 38.0275286
Vibrational hyperpolarizability contributions from mode 1
0.0000000 0.0000000 0.0000000
Dipole derivatives wrt mode 2: -5.06359D-01 1.15450D+01 -1.96119D-08
Vibrational polarizability contributions from mode 2 0.0063052
3.2777142 0.0000000
Vibrational hyperpolarizability contributions from mode 2
0.0000000 0.0000000 0.0000000
...
Dipole derivatives wrt mode 12: -4.09757D+00 -3.36931D+00 -6.58556D-08
Vibrational polarizability contributions from mode 12 0.0306689
0.0207361 0.0000000
Vibrational hyperpolarizability contributions from mode 12
0.0000000 0.0000000 0.0000000
```

Of interest to us are the lines marked `Dipole derivatives wrt mode xxx`, where `xxx` is the normal mode number. The modes are numbered from lowest to highest frequency (same listings as in the harmonic frequency output, but NOT the anharmonic frequency output). For methanol, mode 12 is the OH stretch. Presumably, the components listed are (a, b, c) (although with little documentation on this command, I am not sure if this generally holds true). As a check, the sum of the squares of the three components should equal the IR intensity (in this case, 28.1 km mol^{-1}) for the normal mode of interest.

2) Estimation of the A-X Dipole Derivative

There are two problems with calculating the A-X dipole derivatives. First, the A-X bands of peroxy radicals are weak (oscillator strengths less than 0.0001), so the magnitude of the transition moment cannot be estimated from a CIS calculation (see Appendix C). Second, our higher-level calculations on the X and A states are performed separately, and Gaussian will not report a transition dipole moment from the independent calculations.

Instead, we estimate the dipole derivative on the basis of the visualized molecular orbitals in GaussView 5.0. In Figure D.1, we show the relevant molecular orbitals involved in the A-X transition of HOCH₂OO• (HMP, Chapters 4–6). These orbitals were generated using the unrestricted canonical wavefunction with a 6-31+G(d,p) basis set. HMP has 33 electrons (17 α , 16 β); therefore, the A-X transition involves promotion of an electron from the 16 β orbital to the 17 β orbital.

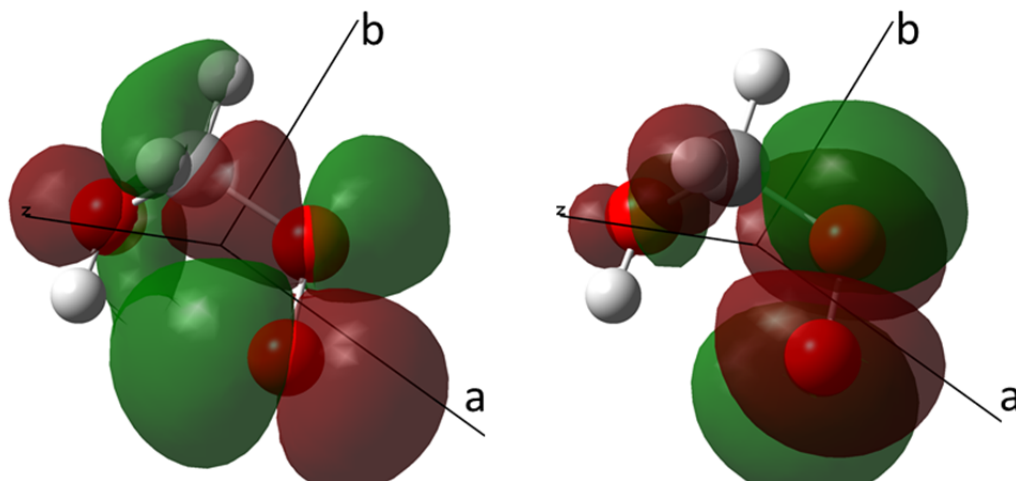


Figure D.1. Molecular orbitals involved in the A-X transition of HMP: 16 β (left) and 17 β (right). The c-axis is out of the plane of the paper. Unrestricted canonical orbitals were generated using the 6-31+G(d,p) basis set.

We already know that the electron density is located on the peroxy group (if we did not, we would have to generate a surface plot of electron density). We can simply look at the change in the π^* orbital on the OO group to determine the dipole derivative direction. In this case, the dipole change is nearly all on the a- and c-axes, with a small contribution along the b-axis. To a first approximation, we only enter a and c components into our transition dipole moment. (To a second approximation, we can add in a small contribution from the b component. However, since the transition intensity is proportional to the square of the dipole derivative, we do not expect the small b component to make an appreciable difference in the spectrum)

3) Calculation of Anharmonic Rotational Constants

A major component to accurate spectrum simulations is to use the appropriate rotational constant for each state. This is absolutely crucial when modeling electronic transitions, as the excited states may have significantly different geometries than the ground state. Differences in rotational constants between vibrationally excited states and the ground state are much smaller; however, these differences will have a small yet observable effect on the simulated spectrum.

In general, Gaussian will only report the rotational constants for the equilibrium geometry. By requesting an anharmonic frequency calculation, Gaussian will determine zero point energies, anharmonicities, and the average geometry/rotational constants in the ground state and all vibrational states (including the first overtones and combination bands). This is requested by entering `freq=anharmonic`. Note that anharmonic frequencies are only available for HF, DFT, CIS, and MP2.¹²¹ Calculation of anharmonic

frequencies requires multiple energy evaluations along the normal mode coordinates, and therefore is much more expensive than the corresponding harmonic frequency calculation.

Below is an excerpt of the relevant information from an anharmonic frequency calculation on methanol (B3LYP/6-31+G(d,p)):

Vibrational Energies and Rotational Constants (cm ⁻¹)					
Mode(Quanta)	E(harm)	E(anharm)	Aa(z)	Ba(x)	Ca(y)
Equilibrium Geometry					
Ground State	11243.115	11068.551	4.201436	0.810130	0.783960
Fundamental Bands (DE w.r.t. Ground State)					
1(1)	3838.340	3657.078	4.166657	0.809317	0.782149
2(1)	3132.414	2987.700	4.179411	0.810602	0.784141
3(1)	3002.706	2868.339	4.167406	0.810395	0.784668
4(1)	1511.279	1419.780	4.723076	0.812129	0.817227
5(1)	1484.215	1509.763	4.209302	0.752017	0.751135
6(1)	1354.473	1310.191	4.254842	0.808235	0.780542
7(1)	1071.906	1053.427	4.195495	0.805186	0.779969
8(1)	1046.125	1018.149	4.199339	0.803309	0.775287
9(1)	3055.148	2917.619	4.177511	0.811408	0.784924
10(1)	1500.580	1463.053	3.633543	0.867621	0.785489
11(1)	1173.087	1146.559	4.209320	0.807503	0.780678
12(1)	315.958	308.510	4.195842	0.803800	0.785240

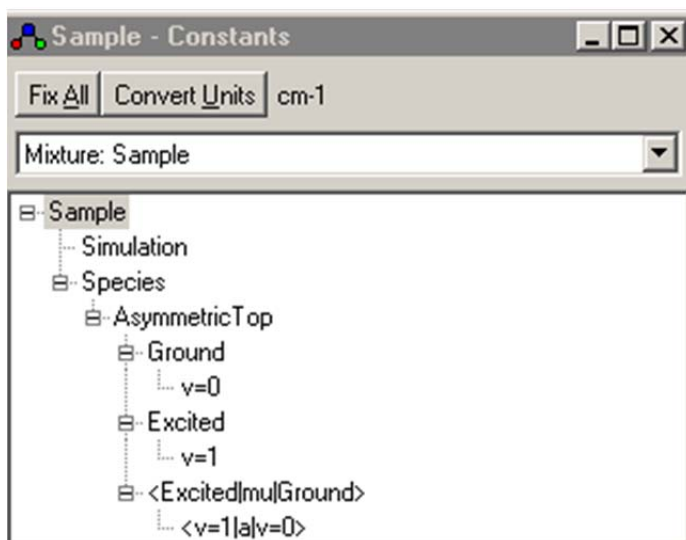
The rotational constants for each mode are listed on the right in cm⁻¹. Note that the modes are listed from highest frequency to lowest frequency, in opposite order than in the harmonic frequency listing. The OH stretch now corresponds to mode 1, not mode 12. Note also that for molecules with symmetry (such as CH₃OH, C_s), the modes are separated by symmetry. Modes 1–8 have A' symmetry, modes 9–12 have A'' symmetry.

In the absence of any other band position information, the anharmonic frequencies can be used in the spectrum simulations. However, these frequencies may have errors of up to 10% in the hydroxyalkylperoxy systems that we have studied (Chapter 5). When possible, experimental data or explicit modeling of the potential energy surface (Chapter 3) will give much more accurate results.

4) Simulation of the Spectroscopic Band

With the (absolute or relative) dipole derivatives (a, b, and c components) and rotational constants in hand, it is straightforward to simulate the bands using PGopher.¹²⁰ We have already seen the excellent agreement between simulation and CRD spectrum of the HMP A-X bands (Chapter 4); here, we compare the simulated CH₃OH ν_1 band to our CRD spectrum.

To begin our simulation, we open the PGopher program, create a new asymmetric top (File-New-Asymmetric Top), and open the list of constants (View-Constants). For now, we ignore the spectrum window and focus on entering our parameters in the Constants list.



There are four items to define before we can simulate our band: the simulation parameters (Simulation), the molecular symmetry (Asymmetric Top), the vibrational or electronic level properties ($v=0$ and $v=1$), and the transition moment integrals (listed under $\langle \text{Excited} | \mu | \text{Ground} \rangle$).

Clicking on Simulation brings up the following options:

	Value	Float	Increment	StdDev
Fmin	3600	no		
Fmax	3800	no		
Temperature	300	no		
Gaussian	1	no		
Lorentzian	0	no		
Foffset	0	no		
SMargin	-1	no		
OTThreshold	1e-6	no		
RefWidth	0	no		
Tvib	-1	no		
MinI	0	no		
Saturation	0	no		
Tspin	-1	no		
EField	0	no		
BField	0	no		
Doppler	0	no		

IntensityUnits	Normalized
LifeModel	ImNone
PlotUnits	cm1
nDF	20001
WidthMult	6
ShowSum	True
ShowParts	False
ShowFortrat	False
UseUpper	False
ShowSymmetry	True
ShowDeltaJ	False
ScaleMarkSize	True
UseSymmetry	False
UseStateNumber	False
FortratQno	J

The only items that need to be set are F_{\min} and F_{\max} (the frequency range), Temperature (K), Gaussian and Lorentzian (cm^{-1} , convolution of spectrum with these functions), and nDF (number of points within spectrum). For ease of exporting the plot, nDF should be set to $\frac{F_{\max} - F_{\min}}{\Delta\nu} + 1$. For example, if the range is 200 cm^{-1} and the desired step size is 0.1 cm^{-1} , nDF should be set to 2001. The frequencies (cm^{-1}) calculated for the main plot will be 0, 0.1, 0.2, ..., 200.

Clicking on Asymmetric Top brings up the following options:

	Value	Float	Increment	StdDev
Abundance	1	no		
nNuclei	0			
Jmin	-0.5			
Jmax	-0.5			
Colour	None			
JAdjustSym	True			
BlockMatrix	True			
PointGroup	Cs			
Representation	IIIr			
SReduction	False			
eeWt	1			
eoWt	1			
oeWt	1			
ooWt	1			
C2zAxis	c			
C2xAxis	a			
PseudoC2v	False			
FakeSym	False			

The options that need to be set are Point Group, Representation, C2zAxis, and C2aAxis. The Representation describes how a, b, c are related to x, y, z. In general, this will be set to IIIr ($x = a, y = b, z = c$), though this can be changed if necessary. C2zAxis and C2aAxis define the symmetry axes for C₂/C_{2v} molecules. For C_s molecules, C2z defines the axis through which the mirror plane passes through. C2aAxis is irrelevant for C_s molecules.

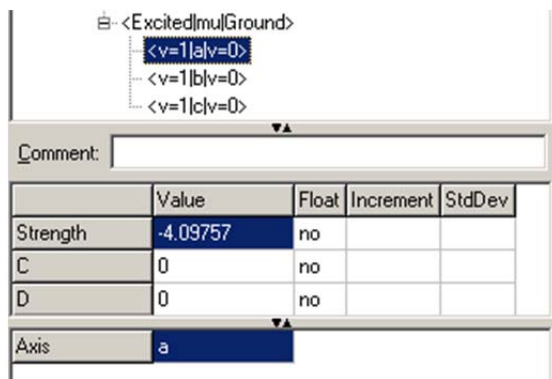
Clicking on either $v=0$ or $v=1$ will bring up similar options:

	Value	Float	Increment	StdDev
Origin	0	no		
Width	0	no		
A	4.201436	no		
B	.81013	no		
C	.78396	no		
BBar	0	no		
BDelta	0	no		
DK	0	no		
DJK	0	no		
DJ	0	no		
deltaK	0	no		
deltaJ	0	no		
HK	0	no		
HKJ	0	no		
HJK	0	no		
HJ	0	no		
phiK	0	no		
phiJK	0	no		
phiJ	0	no		
LK	0	no		
LKKJ	0	no		
LJK	0	no		
LJK	0	no		
LJ	0	no		
IK	0	no		
IKJ	0	no		
IJK	0	no		
II	0	no		
Colour	None			
RveSelect	all			
S	0			
Symmetry	A'			
Kmin	all			
Kmax	all			

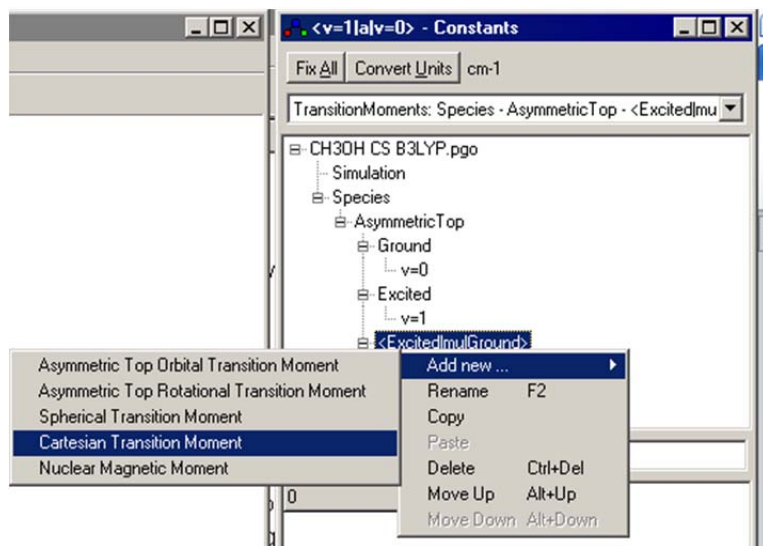
Show Tab Pane

Origin should be set to 0 in the ground state ($v=0$), and the transition frequency in the excited state ($v=1$). A, B, and C should be set individually for each state to the rotational constants calculated from Gaussian. The remaining parameters are distortion constants. These are reported in any anharmonic frequency calculation and can be entered, but I have found that they make very little difference in my spectrum simulations. At the bottom, S and Symmetry should be entered to be the electron spin and overall symmetry of the state (ground, vibrational, etc.)

Clicking on an individual transition moment brings up the following options:



Strength should be set to the value of the absolute dipole derivative calculated from Gaussian (vibrational spectra) or the relative dipole derivative from visual analysis of the molecular orbitals (electronic spectra). Axis defines the transition as a, b, or c type. In general, a given spectrum will contain contributions from more than one type, and multiple transition moments should be included. To add additional transition moments, right click $\langle \text{Excited}|\mu|\text{Ground} \rangle$ and select Add new – Cartesian Transition Moment. This will add a second (or third, or more) transition that can be edited. In this way, a single spectrum can contain contributions from a, b, and c transitions.



Once all of the parameters have been entered, click Plot-Simulate to generate the spectrum. Figure D.2 shows the simulation of the ν_1 band of methanol.

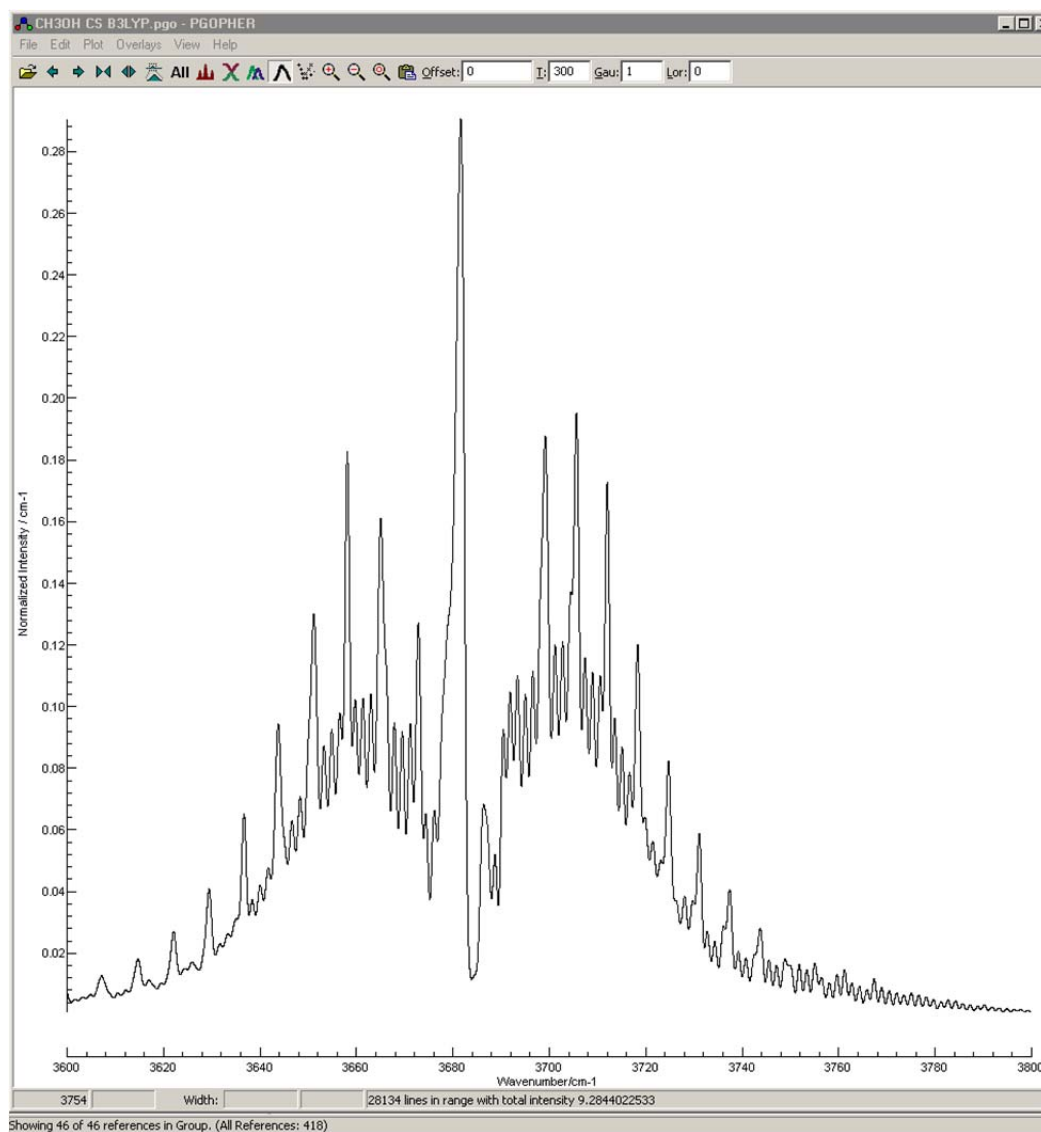


Figure D.2. Simulated ν_1 band of CH₃OH, B3LYP/6-31+G(d,p), anharmonic rotational constants. Screenshot directly out of the PGopher program.

We can export this plot to a text file (File-Export-Main Plot) for use in Excel or other graphing programs. This allows us to compare to an experimental spectrum. Figure D.3 compares our simulated CH₃OH band to one measured on our cavity ringdown

spectrometer. We observe good agreement between the two spectra, although in general, the very sharp spikes in the simulation are washed out in the cavity ringdown spectrum.

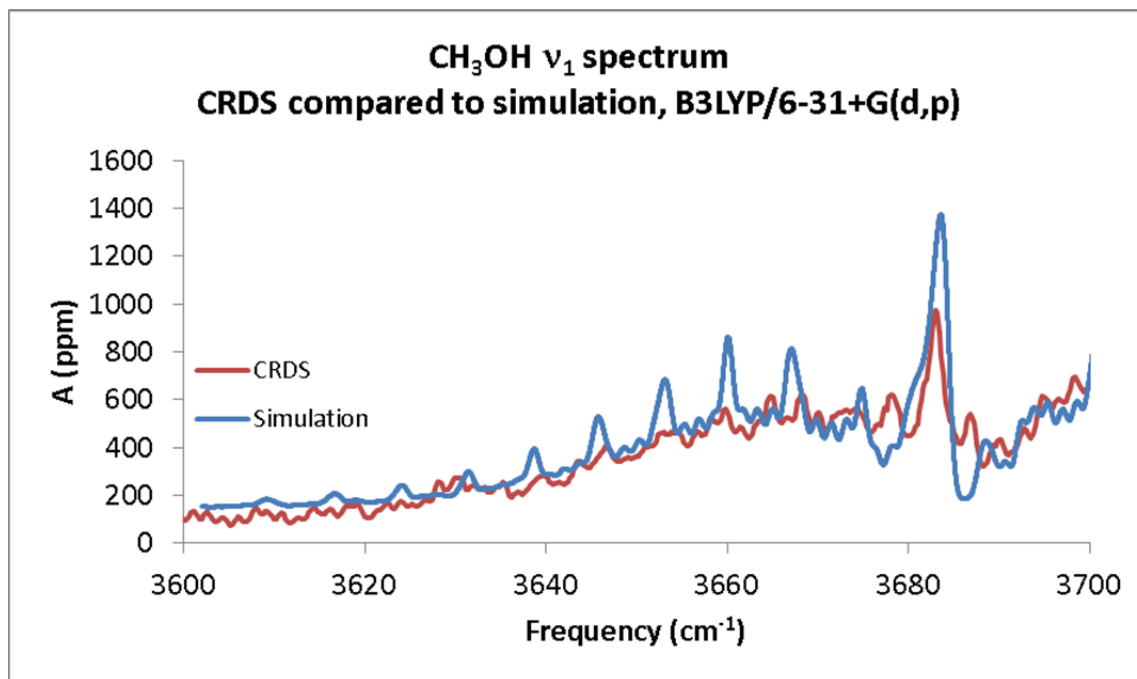


Figure D.3. Comparison of experimental (red, CRDS) and simulated (blue) ν_1 bands of CH₃OH.

Appendix E—The “Global Kinetics Model”: OH+(NO₂,CO,O₂) and HO₂+(HCHO,NO)

This appendix contains the kinetics model used for simulating a wide range of small molecule HO_x and NO_x chemistry: OH + (NO₂,CO,O₂) and HO₂ + (HCHO,NO). We use the Kintecus 3.95 program for all of our modeling (available free of charge to academic users at <http://www.kintecus.com>).¹⁹¹ This program allows for easy input of bimolecular reactions. We have made modifications to the standard input files to easily input special reactions from the NASA/JPL database:²⁷ termolecular reactions, reactions based on equilibrium constants, chemical activation reactions, and miscellaneous reactions with other dependences.

Items described in this chapter:

- 1) Setting up Kintecus 3.95
- 2) Calculation of Termolecular Rate Constants
- 3) Calculation of Other Reaction Rate Constants
- 4) Reactions Included in the “Global Kinetics Model”

1) Setting up Kintecus 3.95

At its core, Kintecus 3.95 is a numerical integrator that runs at the Windows NT command line. To permit ease of use, the author of the program has also written Microsoft Excel spreadsheets that contain all of the relevant simulation input (model, parameters) and compiled output. Figures E.1–E.3 show excerpts of the spreadsheets used to enter the model and specify simulation parameters.

	A	B	C	D	E	F
1	#	Model Description SpreadSheet				
2	#	Reactions can be entered in as				
3	# k	Reaction	Comments			
4	# 1.2345	A+B==>C	A sample reaction with rate constant			
5	#					
6	# OR					
7	#					
8	# A	T ⁿ	Ea	Reaction	Comments	
9	# 50600	2.67	6290	O+H2=OH+H	KLEMM,ET AL	
151	#	Section I - HO2+HCHO Reactions				
152		7.70E-15	0	-625 HO2+CH2O==>HOCH2O2	Veyret, 1989	
153		2.00E+12	0	7000 HOCH2O2==>HO2+CH2O	Veyret, 1989	
154		7.20E-12	0	0 HO2+HOCH2O2==>O2+HOCH2O2H	Burrows 1989, 298K	
155		4.80E-12	0	0 HO2+HOCH2O2==>HCO2H+H2O+O2	Burrows 1989, 298K	
156		5.20E-12	0	0 HOCH2O2+HOCH2O2==>HOCH2O+HOCH2O+O2	Burrows 1989, 298K	

Figure E.1. Portion of a kinetics model (“Model” tab) entered into a Kintecus Excel spreadsheet.

	A	B	C	D	E	F	G
1	#	Species Description Spreadsheet					
2	# Species	Residence	Initial	Display Output	External	SSA ?	Constant
3	#	Time in CSTR(s)	Conc.	(Y/N) ?	Conc.	(Y/N)	(Filename)
4	CH2O	0	0.00E+00	yes	0	No	No
5	Cl	0	7.50E+12	yes	0	no	no
6	Cl2	0	3.00E+15	yes	0	No	No
7	CH3OH	0	1.00E+15	yes	0	No	No
8	NO	0	4.00E+15	yes	0	No	No

Figure E.2. Portion of the initial chemical concentrations (“Species tab) entered into a Kintecus Excel spreadsheet.

	A	B	C	D	E
1	#	Parameter Description SpreadSheet			
2	#	See .pdf file for an explanation of each field			
3	#				
4	# Starting Integration Time	Maximum Integration Time	Ea UNITS (Kcal, KJ, J, CAL, K)	Conc. Units(moles/L, moles/cc, molecules/cc)	X0
5	1.00E-10	1.00E-06	Kelvin	Molecules/cm ³	0
6	#	External Heat Source/Sink # OR Profile (Filename)			
7	#Temperature (K) or Filename	Pressure (Constant ? (Yes/No))	Volume Profile (Filename/No)	OR Conductance:Extern. Temp OR Conductance:Ex	X0
8	300	NOPE	NO	No	0
9	# Simulation Length:				
10	# DAYS	Hours	Minutes	Seconds	PicoSeconds
11	0	0	0	3.00E-03	0
12	#				
13	#hv(filename)	Sampling Interval (s)	Percent(%)	Accuracy	X0
14	None1	1	0	1.00E-08	0
15	#	THESE FIELDS BELOW (X0) ARE CURRENTLY NOT USED, LEAVE THEM AT 0			
16	# CSTR/PFR inlet Flow				
17	Temperature	X0	X0	X0	X0
18	#				
19	END				
20					

Figure E.3. Kinetics simulation parameters (“Parm” tab) entered into a Kintecus Excel spreadsheet.

Figure E.1 shows that reaction temperature dependencies can be expressed in two ways: T^n or $\text{Exp}[-E_a/RT]$, where n or E_a are entered respectively (units of E_a specified on the “Parm” tab). The T^n column cannot be left blank: if there is no T^n dependence, 0

should be entered. Reactions based on equilibrium constants can be entered here (using \rightleftharpoons rather than \Rightarrow and entering K_{eq} in the A column); however, I have had terrible luck getting these reactions to work properly, especially in the case where the individual reactions are termolecular. Instead, I choose to use a rate constant calculator (described in Section 3 of this appendix).

Figure E.2 contains a list of all of the chemical species included in the kinetics model. This worksheet can be automatically generated by Kintecus on the “Control” tab (Make Species Spreadsheet from Model). The user needs to enter the initial concentrations (units specified on the “Parm” tab) and whether the concentration of that species should be written to the output file. All other options can be left as their defaults.

Figure E.3 contains all of the setting needed for the kinetics simulation, including the units of activation energy (“Ea units”) and concentration (“Conc Units”), temperature, simulation time (“Seconds”), and step size (“Maximum Integration Time”). The user should not change any of the other parameters. Typically, Ea units should be set to Kelvin (same units as in the NASA/JPL Data Evaluation) and Conc Units should be set to Molecules/cm³ (common units in atmospheric and gas phase chemistry). The maximum integration time should be set in relation to the simulation time; in general, no more than 30000 data points should be generated (plots in Excel 2003 or earlier cannot handle more than 32768 points).

2) Calculation of Termolecular Rate Constants

Termolecular reactions are typically modeled by “falloff” curves: i.e., linearly dependent on pressure at low pressures, and bimolecular at high pressure. This is represented in the NASA/JPL Data Evaluation by Equation E.1:

$$k = \left(\frac{k_0 [M]}{1 + \frac{k_0 [M]}{k_\infty}} \right) \times 0.6 \left\{ 1 + \left[\log_{10} \left(\frac{k_0 [M]}{k_\infty} \right) \right]^2 \right\}^{-1}, \quad (\text{E.1})$$

where k_0 and k_{infinity} are the termolecular and bimolecular rate constants in the limits of zero and infinite pressure respectively, and $[M]$ is the concentration of bath gas particles (pressure).

The problem is that Kintecus does not have the NASA/JPL form for termolecular falloff curves built in. Instead, Kintecus uses the IUPAC recommended form¹¹⁸

$$k = \left(\frac{k_0 [M]}{1 + \frac{k_0 [M]}{k_\infty}} \right) \times F, \quad (\text{E.2})$$

where

$$\log F = \left[1 + \frac{\log \left(\frac{k_0 [M]}{k_\infty} \right)}{n - 0.14 \left(\log \frac{k_0 [M]}{k_\infty} + c \right)} \right]^2 \right]^{-1} \log F_{\text{cent}}, \quad (\text{E.3})$$

$$c = -0.4 - 0.67 \log F_{\text{cent}}, \quad (\text{E.4})$$

$$n = 0.75 - 1.27 \log F_{\text{cent}}. \quad (\text{E.5})$$

Unfortunately, I cannot find a way to reconcile the NASA/JPL and Kintecus falloff curve formulations, especially because the k_0 and k_{infinity} derived from each formulation are not equal.¹¹⁸

To get around this problem, I wrote an Excel worksheet to calculate the effective bimolecular rate constant k from Equation E.1 and the NASA/JPL parameters. This worksheet is shown in Figure E.4. The user enters k_0 , n , k_{inf} , and m (from the NASA/JPL database). Based on the total pressure (calculated from the sum of concentrations in the “Species” spreadsheet) and the temperature (from the “Parm” spreadsheet), the effective bimolecular rate constant is reported in the “A” column. The reactions are automatically copied into the main “Model” spreadsheet: therefore, any changes to pressure, temperature, or falloff parameters will be immediately updated in the kinetics model. For reactions with no high pressure limit listed, k_{inf} should be set to 1.

#	A	T ⁿ m	Ea	Reaction	Comments	k0(300)	n	kinf(300)	m	
1	The user should enter k0(300), n, kinf(300), and m for each reaction									
2	For "chemical activation" reactions, the A column must be altered									
3	Temp (K)	300	DO NOT EDIT T or P, THEY ARE CALCULATED BASED ON THE SPECIES AND PARM WORKSHEETS							
4	p (torr)	524.9385								
5	#	A	T ⁿ m	Ea	Reaction	Comments	k0(300)	n	kinf(300)	m
6	1.26288E-12	0	0	0	OH+NO2==>HOONO	Sample Reaction	9.10E-32	3.9	4.20E-11	0.5
7	1.02E-14	0	0	0	O+O2==>O3	Termolecular, JPL15 2-4, no high pressure limit	6.00E-34	2.4	1.00E+00	
8	4.75315E-17	0	0	0	O1D+N2==>N2O	Termolecular, JPL15 2-4, no high pressure limit	2.80E-36	0.9		1
9	6.5288E-13	0	0	0	H+O2==>HO2	Termolecular, JPL15 2-4	4.40E-32	1.3	4.70E-11	0.2
10	5.12308E-12	0	0	0	OH+OH==>H2O2	Termolecular, JPL15 2-4	6.90E-31	1	2.60E-11	0
11	1.20279E-12	0	0	0	O+NO==>NO2	Termolecular, JPL15 2-4	9.00E-32	1.5	3.00E-11	0
12	2.54033E-12	0	0	0	O+NO2==>NO3	Termolecular, JPL15 2-4	2.50E-31	1.8	2.20E-11	0.7
13	5.90798E-12	0	0	0	OH+NO==>HONO	Termolecular, JPL15 2-4	7.00E-31	2.6	3.60E-11	0.1
14	8.7814E-12	0	0	0	OH+NO2==>HONO2	Termolecular, JPL15 2-4	1.80E-30	3	2.80E-11	0
15	7.36425E-13	0	0	0	CH3+O2==>CH3O2	Termolecular, JPL15 2-4	4.00E-31	3.6	1.20E-12	-1.1
16	2.69144E-11	0	0	0	CH3O+NO==>CH3ONO	Termolecular, JPL15 2-4	2.30E-29	2.8	3.80E-11	0.6
17	1.62727E-11	0	0	0	CH3O+NO2==>CH3ONO2	Termolecular, JPL15 2-5	5.30E-29	4.4	1.90E-11	1.8
18	2.13624E-13	0	0	0	Cl+C==>Cl2	Termolecular, NIST (no "falloff" listed, valid at 300	1.26E-32	1	1.00E+00	0
19	#DIV/0!	0	0	0	Termolecular					

Figure E.4. Termolecular falloff kinetics calculator worksheet. The effective bimolecular rate constants and reactions are automatically copied into the main kinetics model.

3) Calculation of other reaction rate constants

We can construct other worksheets to calculate rate constants similar to calculation of the termolecular falloff rate constants. We discuss two special reaction

types in this section: rate constants based on equilibrium constants, and treatment of OH + O₂.

Equilibrium constants are defined in the NASA/JPL database in terms of two parameters, *A* and *B*:

$$K_{eq} = A \exp\left[\frac{B}{T}\right], \quad 200 \text{ K} < T < 300 \text{ K}. \quad (\text{E.6})$$

Typically, either the forward or backward reaction is defined in terms of a bimolecular or termolecular rate constant. Using K_{eq} and one rate constant, we can define both the forward and backward rates. Figure E.5 shows the worksheet developed for these calculations. The user can input either bimolecular or termolecular rate constants for the forward rate, and the program will calculate effective bimolecular rate constants for both the forward and backward reactions. Note that if the user types in both bimolecular and termolecular rates, the bimolecular rate will take precedence. Similar to the termolecular falloff kinetics calculator, the rate constants are automatically copied to the main “Model spreadsheet,” any updates to the equilibrium constant page will be immediately reflected in the main model.

#	A	B	C	D	E	F	G	H	I	J	K	L	M	N	O	P
1	From JPL15 (p.3-1), $k(T) = A \cdot \exp(B/T)$, for $200K < T < 300K$															
2	This table assumes the units for Ea are in Kelvin (that is, the Ea column has Ea/R)															
3	If the bimolecular parameters are left blank, then the table will automatically use the termolecular parameters to obtain rate constants															
4	T	DO NOT EDIT T or P, THEY ARE CALCULATED BASED ON THE SPECIES AND PARM WORKSHEETS														
5	P	300 torr														
6		Equilibrium Values					Bimolecular									
7	# A	T ^m	Ea	Reaction	Comments	Keq A	Keq B	A	Ea/R	k0(300)	n	kin(300)	m	Termolecular		
8																
9																
10																
11	7.58E-13	0	0	OH+NO2==>HOONO	Sample Reaction	3.90E-27	10125			9.10E-32	3.9	4.20E-11	0.5			
12	4.28E-01	0	0	HOONO==>OH+NO2	Sample Reaction											
13	7.09E-13	0	0	HO2+NO2==>HO2NO2	JPL15, 2, 4, 3, 2	2.10E-27	10900			2.00E-31	3.4	2.90E-12	1.1			
14	5.61E-02	0	0	HO2NO2==>HO2+NO2	JPL15, 2, 4, 3, 2											
15	2.89E-15	0	0	NO+NO2==>N2O3	JPL15, 3, 2, and NIST Kine	3.30E-27	4667			3.10E-34	7.7	7.80E-12	-1.4			
16	1.54E+05	0	0	N2O3==>NO+NO2	JPL15, 3, 2, and NIST Kine											
17	1.20E-14	0	0	NO2+NO2==>N2O4	JPL15, 3, 2, and NIST Kine	5.90E-29	6643			1.40E-33	3.8	1.00E-12	0			
18	4.91E+04	0	0	N2O4==>NO2+NO2	JPL15, 3, 2, and NIST Kine											
19	1.05E-12	0	0	NO2+NO3==>N2O5	JPL15, 2, 4, 3, 2	2.70E-27	11000			2.00E-30	4.4	1.40E-12	0.7			
20	4.62E-02	0	0	N2O5==>NO2+NO3	JPL15, 2, 4, 3, 2											
21	2.50E-12	0	0	CH3O2+NO2==>CH3O2NO2	JPL15, 2, 5, 3, 2	9.50E-29	11234			1.00E-30	4.8	7.20E-12	2.1			
22	1.44E+00	0	0	CH3O2NO2==>CH3O2+NO2	JPL15, 2, 5, 3, 2											
23	5.70E-11	0	0	OH+O2==>HO3	Sridharan, and Stat Mech	3.95E-22	0	5.70E-11								
24	1.44E+11	0	0	HO3==>OH+O2	Sridharan, and Stat Mech											
25	2.07E-14	0	0	Cl+O2==>ClOO	JPL 15, 2, 5, 3, 2	6.60E-23	2502			2.20E-33	3.1	1.80E-10	0			
26	7.50E+04	0	0	ClOO==>Cl+O2	JPL 15, 2, 5, 3, 2											
27	1.26E-14	0	0	Cl+CO==>ClCO	JPL 15, 1, 8, 3, 2	3.50E-25	3730			1.30E-33	3.8	1.00E+00	0			
28	1.43E+05	0	0	ClCO==>Cl+CO	JPL 15, 1, 8, 3, 2											
29	1.15E-13	0	0	ClO+ClO==>Cl2O2	JPL 15, 1, 8, 3, 2	9.30E-28	8835			1.60E-32	4.5	2.00E-12	2.4			
30	2.00E+01	0	0	Cl2O2==>ClO+ClO	JPL 15, 1, 8, 3, 2											

Figure E.5. Equilibrium reaction rate kinetics calculator worksheet. The effective bimolecular rate constants and reactions are automatically copied into the main kinetics model.

It has been suggested that $\text{OH} + \text{O}_2$ will combine to form the HO_3 radical, with binding energy on the order of 3-5 kcal mol⁻¹.²¹²⁻²³² In our kinetics treatment, we estimate the rate constants for $\text{OH} + \text{O}_2 \rightarrow \text{HO}_3$ using a theoretical equilibrium constant (calculated partition functions combined with an experimental binding energy^{219, 224}) and a calculated forward rate constant.²³³

Further reactions of HO_3 are treated using $\text{OH} + \text{O}_2$ as the analogous reactant. For example, since $\text{OH} + \text{OH} \rightarrow \text{H}_2\text{O}_2$ is present in our kinetics model, we also include the reaction $\text{HO}_3 + \text{OH} \rightarrow \text{H}_2\text{O}_2 + \text{O}_2$. Bimolecular rate constants for HO_3 are taken to be equal to the OH reaction. Termolecular rate constants are taken to be equal to the high pressure limit (i.e., O_2 acts as the third body, and is always present for reaction).

4) Reactions included in the “Global Kinetics Model”

Our kinetics model includes over 150 reactions spanning small molecule HO_x and NO_x chemistry. We do not consider any organic species with more than one carbon. The model contains the chemistry necessary to model radical generation through O₃ photolysis in the presence of H₂ or CH₄ (OH) or Cl₂ photolysis in the presence of HCHO or CH₃OH (HO₂). The entire model is shown below in Table E.1. Rate constants are presented assuming 300 K, 760 torr (termolecular and specially calculated rate constants are updated when the pressure is varied).

Table E.1. Reactions included in the “Global Kinetics Model” used in this thesis. Termolecular and special rate constants calculated at 300 K, 760 torr for this table. All rate constants taken from NASA/JPL²⁷ or NIST Kinetics¹¹⁷ unless otherwise specified.

A (cm ³ molec ⁻¹ s ⁻¹)	Ea (K)	Reaction	Reference
Section A—Reactions defined by Equilibrium Constants			
7.58E-13		OH+NO2==>HOONO	
4.28E-01		HOONO==>OH+NO2	
7.09E-13		HO2+NO2==>HO2NO2	
5.61E-02		HO2NO2==>HO2+NO2	
2.89E-15		NO+NO2==>N2O3	
1.54E+05		N2O3==>NO+NO2	
1.20E-14		NO2+NO2==>N2O4	
4.91E+04		N2O4==>NO2+NO2	
1.05E-12		NO2+NO3==>N2O5	
4.62E-02		N2O5==>NO2+NO3	
2.50E-12		CH3O2+NO2==>CH3O2NO2	
1.44E+00		CH3O2NO2==>CH3O2+NO2	
5.70E-11		OH+O2==>HO3	Sridharan ²³³
1.44E+11		HO3==>OH+O2	D ₀ =-4.5 kcal mol ⁻¹ 220, 224
2.07E-14		Cl+O2==>ClOO	
7.50E+04		ClOO==>Cl+O2	
1.26E-14		Cl+CO==>ClCO	
1.43E+05		ClCO==>Cl+CO	
1.15E-13		ClO+ClO==>Cl2O2	
2.00E+01		Cl2O2==>ClO+ClO	
Section B—Termolecular Reactions following the Troe Falloff Curve			
5.82E-15		O+O2==>O3	
2.72E-17		O1D+N2==>N2O	
3.84E-13		H+O2==>HO2	
3.65E-12		OH+OH==>H2O2	
7.30E-13		O+NO==>NO2	
1.68E-12		O+NO2==>NO3	
4.09E-12		OH+NO==>HONO	

6.59E-12		OH+NO2==>HONO2	
6.11E-13		CH3+O2==>CH3O2	
2.36E-11		CH3O+NO==>CH3ONO	
1.55E-11		CH3O+NO2==>CH3ONO2	
1.22E-13		Cl+Cl==>Cl2	
Section C—Special Reactions			
1.49E-13		OH+HONO2==>H2O+NO3	
1.00E-13		OH+CO==>HOCO	
1.50E-13		OH+CO==>H+CO2	
2.40E-11		HOCO==>OH+CO	
9.30E-12		HOCO==>H+CO2	
Section D—O1D/H2 Chemistry			
8.00E-12	2060	O+O3==>O2+O2	
3.30E-11	-55	O1D+O2==>O+O2	
1.20E-10	0	O1D+O3==>O2+O2	
1.20E-10	0	O1D+O3==>O2+O+O	
1.10E-10	0	O1D+H2==>OH+H	
1.63E-10	-60	O1D+H2O==>OH+OH	
2.15E-11	-110	O1D+N2==>O+N2	
2.20E-11	-120	O+OH==>O2+H	
3.00E-11	-200	O+HO2==>OH+O2	
1.40E-12	2000	O+H2O2==>OH+HO2	
1.40E-10	470	H+O3==>OH+O2	
7.20E-11	0	H+HO2==>OH+OH	
1.60E-12	0	H+HO2==>O+H2O	
6.90E-12	0	H+HO2==>H2+O2	
1.70E-12	940	OH+O3==>HO2+O2	
2.80E-12	1800	OH+H2==>H2O+H	
1.80E-12	0	OH+OH==>H2O+O	
4.80E-11	-250	OH+HO2==>H2O+O2	
1.80E-12	0	OH+H2O2==>H2O+HO2	
1.00E-14	490	HO2+O3==>OH+O2+O2	
3.50E-13	-430	HO2+HO2==>H2O2+O2	
1.70E-33	-1000	HO2+HO2+M==>H2O2+O2+M	
Section E—O1D/CH4 Chemistry (O1D from N2O or O3)			
1.12E-10	0	O1D+CH4==>CH3+OH	
3.00E-11	0	O1D+CH4==>CH3O+H	
7.50E-12	0	O1D+CH4==>CH2O+H2	
4.70E-11	-20	O1D+N2O==>N2+O2	
6.70E-11	-20	O1D+N2O==>NO+NO	
5.10E-12	-210	O+NO2==>NO+O2	
1.00E-11	0	O+NO3==>O2+NO2	
4.00E-10	340	H+NO2==>OH+NO	
1.80E-11	390	OH+HONO==>H2O+NO2	
3.50E-12	-250	HO2+NO==>OH+NO2	
1.40E-14	-250	HO2+NO==>HONO2	Butkovskaya ²³⁴
3.00E-12	1500	NO+O3==>NO2+O2	
1.10E-10	0	O+CH3==>CH3O	
2.45E-12	1775	OH+CH4==>CH3+H2O	
5.50E-12	-125	OH+CH2O==>H2O+HCO	
2.90E-12	345	OH+CH3OH==>CH2OH+H2O	
5.20E-12	0	HCO+O2==>HO2+CO	
9.10E-12	0	CH2OH+O2==>CH2O+HO2	
3.90E-14	900	CH3O+O2==>CH2O+HO2	
4.00E-12	0	CH3O+NO==>CH2O+HNO	IUPAC ¹¹⁸

1.10E-11	1200	CH3O+NO2==>CH2O+HONO	
2.80E-12	-300	CH3O2+NO==>CH3O+NO2	
Section F—HOONO Chemistry			
3.00E-17	0	O+HONO2==>OH+NO3	
7.80E-11	3400	O+HO2NO2==>HO2+NO3	
2.20E-11	0	OH+NO3==>HO2+NO2	
1.30E-12	-380	OH+HO2NO2==>H2O+NO2+O2	
3.50E-12	0	HO2+NO3==>OH+NO2+O2	
1.50E-11	-170	NO+NO3==>NO2+NO2	
1.20E-13	2450	NO2+O3==>NO3+O2	
8.50E-13	2450	NO3+NO3==>NO2+NO2+O2	
5.00E-19	0	O3+HONO==>O2+HONO2	
2.00E-21	0	N2O5+H2O==>2HONO2	
5.00E-16	0	HO2+NO2==>HONO+O2	
Section G—HOCO Chemistry			
7.50E-11	-115	O1D+CO2==>O+CO2	
3.40E-11	1600	O+CH2O==>OH+HCO	
2.00E-12	0	O2+HOCO==>HO2+CO2	
2.70E-12	0	HOCO+NO==>HONO+CO	
1.03E-11	0	HOCO+OH==>CO2+H2O	
4.00E-19	0	NO3+CO==>NO2+CO2	
5.80E-16	0	NO3+CH2O==>HONO2+HCO	
Section H—Chlorine Chemistry (for Cl+MeOH)			
5.50E-11	0	Cl+CH3OH==>CH2OH+HCl	
9.10E-12	0	CH2OH+O2==>CH2O+HO2	
1.60E-13	6300	HOCH2O2+CH3OH==>HOCH2O2H+CH2OH	
2.00E-11	0	HOCH2O2+CH2OH==>HOCH2O2H+CH2O	
4.35E-13	345	CH3OH+OH==>CH3O+H2O	
8.10E-11	30	Cl+CH2O==>HCl+HCO	
1.80E-11	-170	HO2+Cl==>HCl+O2	
4.10E-11	450	HO2+Cl==>OH+ClO	
2.70E-12	-220	HO2+ClO==>HOCl+O2	
1.10E-11	980	Cl+H2O2==>HCl+HO2	
1.40E-12	900	OH+Cl2==>HOCl+Cl	
7.40E-12	-270	OH+ClO==>Cl+HO2	
6.00E-13	-230	OH+ClO==>HCl+O2	
2.60E-12	350	OH+HCl==>H2O+Cl	
3.00E-12	500	OH+HOCl==>H2O+ClO	
1.25E-12	130	Cl+HOCl==>Cl2+OH	
1.25E-12	130	Cl+HOCl==>HCl+ClO	
Section I—HO2+HCHO Reactions			
7.70E-15	-625	HO2+CH2O==>HOCH2O2	Veyret ²⁶
2.00E+12	7000	HOCH2O2==>HO2+CH2O	Veyret ²⁶
7.20E-12	0	HO2+HOCH2O2==>O2+HOCH2O2H	Burrows ²⁵
4.80E-12	0	HO2+HOCH2O2==>HCO2H+H2O+O2	Burrows ²⁵
5.20E-12	0	HOCH2O2+HOCH2O2==>HOCH2O+HOCH2O+O2	Burrows ²⁵
5.65E-14	-750	HOCH2O2+HOCH2O2==>HCO2H+CH2OH+OH+O2	Veyret ²⁶
3.50E-14	0	HOCH2O+O2==>HCO2H+HO2	Burrows ²⁵
Section J—CH3ONO Reactions			
2.32E-11	2620	CH3ONO+O==>OH+CH2O+NO	
3.00E-20	0	CH3ONO+HONO2==>CH3OH+NO2+NO2	
4.45E-13	0	CH3ONO+CH3O==>CH3OH+CH2O+NO	
2.09E-12	0	CH3ONO+Cl==>CH3O+ClNO	

Section K—HO₃ Reaction Analogs - O₁D/CH₄ Chemistry			
Part 1—Equilibrium Reaction Analogs			
4.20E-11		HO ₃ +NO ₂ ==>HOONO+O ₂	OH+NO ₂ → HOONO, high pressure limit
Part 2—Termolecular Reaction Analogs			
2.60E-11		HO ₃ +OH==>H ₂ O ₂ +O ₂	OH+OH high pressure limit
2.60E-11		HO ₃ +HO ₃ ==>H ₂ O ₂ +O ₂ +O ₂	OH+OH high pressure limit
3.60E-11		HO ₃ +NO==>HONO+O ₂	OH+NO high pressure limit
2.80E-11		HO ₃ +NO ₂ ==>HONO ₂ +O ₂	OH+NO ₂ → Nitric Acid, high pressure limit
Part 3—Special Reaction Analogs			
1.52E-13		HO ₃ +HONO ₂ ==>H ₂ O+NO ₃ +O ₂	OH+HONO ₂ high pressure limit
Part 4—O₁D/H₂ Chemistry Analogs			
2.20E-11	-120	O+HO ₃ ==>O ₂ +H+O ₂	O+OH analog
1.70E-12	940	HO ₃ +O ₃ ==>HO ₂ +O ₂ +O ₂	OH+O ₃ analog
2.80E-12	1800	HO ₃ +H ₂ ==>H ₂ O+H+O ₂	OH+H ₂ analog
1.80E-12	0	HO ₃ +OH==>H ₂ O+O+O ₂	OH+OH analog
1.80E-12	0	HO ₃ +HO ₃ ==>H ₂ O+O+O ₂ +O ₂	OH+OH analog
4.80E-11	-250	HO ₃ +HO ₂ ==>H ₂ O+O ₂ +O ₂	OH+HO ₂ analog
1.80E-12	0	HO ₃ +H ₂ O ₂ ==>H ₂ O+HO ₂ +O ₂	OH+H ₂ O ₂ analog
Part 5—O₁D/CH₄ Chemistry Analogs			
1.80E-11	390	HO ₃ +HONO==>H ₂ O+NO ₂ +O ₂	OH+HONO analog
2.45E-12	1775	HO ₃ +CH ₄ ==>CH ₃ +H ₂ O+O ₂	OH+CH ₄ analog
5.50E-12	-125	HO ₃ +CH ₂ O==>H ₂ O+HCO+O ₂	OH+CH ₂ O analog
2.90E-12	345	HO ₃ +CH ₃ OH==>CH ₂ OH+H ₂ O+O ₂	OH+CH ₃ OH analog
Part 6—HOONO Chemistry Analogs			
2.20E-11	0	HO ₃ +NO ₃ ==>HO ₂ +NO ₂ +O ₂	OH+NO ₃ analog
1.30E-12	-380	HO ₃ +HO ₂ NO ₂ ==>OHHO ₂ NO ₂ +O ₂	OH+HO ₂ NO ₂ analog
Part 7—Chlorine Chemistry Analogs			
4.35E-13	345	HO ₃ +CH ₃ OH==>CH ₃ O+O ₂ +H ₂ O	OH+CH ₃ OH analog
1.40E-12	900	HO ₃ +Cl ₂ ==>HOCl+Cl+O ₂	OH+Cl ₂ analog
7.40E-12	-270	HO ₃ +ClO==>Cl+HO ₂ +O ₂	OH+ClO analog
6.00E-13	-230	HO ₃ +ClO==>HCl+O ₂ +O ₂	OH+ClO analog
2.60E-12	350	HO ₃ +HCl==>H ₂ O+Cl+O ₂	OH+HCl analog

Part 6—References

1. Finlayson-Pitts, B. J.; Pitts, J. N., *Chemistry of the Upper and Lower Atmosphere*. Academic Press: New York, 1999; p 969.
2. Jacob, D. J., *Introduction to Atmospheric Chemistry*. Princeton University Press: Princeton, NJ, 1999.
3. Seinfeld, J. H.; Pandis, S. N., *Atmospheric Chemistry and Physics: From Air Pollution to Climate Change*. Wiley: New York, 2006; p 1203.
4. Jerrett, M.; Burnett, R. T.; Pope, C. A., 3rd; Ito, K.; Thurston, G.; Krewski, D.; Shi, Y.; Calle, E.; Thun, M., *New Engl. J. Med.* **2009**, *360* (11), 1085–1095.
5. Madsen, D. South Coast Air Basin Smog Trend. <http://www.aqmd.gov/smog/historicaldata.htm>.
6. Ball, S. M.; Jones, R. L., *Chem. Rev.* **2003**, *103* (12), 5239–5262.
7. Berden, G.; Peeters, R.; Meijer, G., *Int. Rev. Phys. Chem.* **2000**, *19* (4), 565–607.
8. O'Keefe, A.; Deacon, D. A. G., *Rev. Sci. Instrum.* **1988**, *59* (12), 2544–2551.
9. Scherer, J. J.; Voelkel, D.; Rakestraw, D. J.; Paul, J. B.; Collier, C. P., *Chem. Phys. Lett.* **1995**, *245* (2-3), 273–280.
10. Vallance, C., *New J. Chem.* **2005**, *29* (7), 867–874.
11. Zalicki, P.; Zare, R. N., *J. Chem. Phys.* **1995**, *102* (7), 2708–2717.
12. Mollner, A. K.; Valluvadasan, S.; Feng, L.; Sprague, M. K.; Okumura, M.; Milligan, D. B.; Bloss, W. J.; Sander, S. P.; Martien, P. T.; Harley, R. A.; McCoy, A. B.; Carter, W. P. L., *Science* **2010**, *330* (6004), 646–649.
13. Robertshaw, J. S.; Smith, I. W. M., *J. Phys. Chem.* **1982**, *86* (5), 785–790.
14. Nizkorodov, S. A.; Wennberg, P. O., *J. Phys. Chem. A* **2002**, *106* (6), 855–859.
15. Bean, B. D.; Mollner, A. K.; Nizkorodov, S. A.; Nair, G.; Okumura, M.; Sander, S. P.; Peterson, K. A.; Francisco, J. S., *J. Phys. Chem. A* **2003**, *107* (36), 6974–6985.
16. Zhang, X.; Nimlos, M. R.; Ellison, G. B.; Varner, M. E.; Stanton, J. F., *J. Chem. Phys.* **2006**, *124* (8), 084305.
17. Benson, S. W., *Int. J. Chem. Kinet.* **2001**, *33* (9), 509–512.
18. Dibble, T. S., *Chem. Phys. Lett.* **2002**, *355* (1-2), 193–200.
19. Hermans, I.; Muller, J. F.; Nguyen, T. L.; Jacobs, P. A.; Peeters, J., *J. Phys. Chem. A* **2005**, *109* (19), 4303–4311.
20. Hermans, I.; Nguyen, T. L.; Jacobs, P. A.; Peeters, J., *J. Am. Chem. Soc.* **2004**, *126* (32), 9908–9909.
21. Anglada, J. M.; Domingo, V. M., *J. Phys. Chem. A* **2005**, *109* (47), 10786–10794.
22. Cours, T.; Canneaux, S.; Bohr, F., *Int. J. Quantum Chem* **2007**, *107* (6), 1344–1354.
23. Grieman, F. J.; Noell, A. C.; Davis-Van Atta, C.; Okumura, M.; Sander, S. P., *J. Phys. Chem. A* **2011**, *115* (38), 10527–10538.
24. Su, F.; Calvert, J. G.; Shaw, J. H.; Niki, H.; Maker, P. D., *Chem. Phys. Lett.* **1979**, *65* (2), 221–225.
25. Burrows, J. P.; Moortgat, G. K.; Tyndall, G. S.; Cox, R. A.; Jenkin, M. E.; Hayman, G. D.; Veyret, B., *J. Phys. Chem.* **1989**, *93* (6), 2375–2382.
26. Veyret, B.; Lesclaux, R.; Rayez, M. T.; Rayez, J. C.; Cox, R. A.; Moortgat, G. K., *J. Phys. Chem.* **1989**, *93* (6), 2368–2374.

27. Sander, S. P.; Abbatt, J.; Barker, J. R.; Burkholder, J. B.; Friedl, R. R.; Golden, D. M.; Huie, R. E.; Kolb, C. E.; Kurylo, M. J.; Moortgat, G. K.; Orkin, V. L.; Wine, P. H., Chemical Kinetics and Photochemical Data for Use in Atmospheric Studies, Evaluation No. 17, JPL Publication 10-6, *Jet Propulsion Laboratory, Pasadena* **2011**.
28. Atkinson, R., *Atmos. Environ.* **2007**, *41* (38), 8468–8485.
29. Garland, E. R. Laboratory Studies of Atmospheric Reactions Using Infrared Cavity Ringdown Spectroscopy. Ph.D. Thesis, California Institute of Technology, Pasadena, CA, **2002**.
30. Mollner, A. K. Cavity Ringdown Spectroscopy Studies of Atmospheric Reactions: Peroxynitrous Acid Formation and Alkoxy Radical Isomerization. Ph.D. Thesis, California Institute of Technology, Pasadena, CA, **2007**.
31. Sprague, M. K.; Garland, E. R.; Mollner, A. K.; Bloss, C.; Bean, B. D.; Weichman, M. L.; Mertens, L. A.; Okumura, M.; Sander, S. P., *J. Phys. Chem. A* **2012**, *Articles ASAP*, DOI 10.1021/jp212136r.
32. Heicklen, J., The Decomposition of Alkyl Nitrites and the Reactions of Alkoxy Radicals. In *Advances in Photochemistry*, John Wiley & Sons: **2007**; pp 177–272.
33. Brown, S. S., *Chem. Rev.* **2003**, *103* (12), 5219–5238.
34. Chance, K. V.; Park, K.; Evenson, K. M.; Zink, L. R.; Stroh, F.; Fink, E. H.; Ramsay, D. A., *J. Mol. Spectrosc.* **1997**, *183* (2), 418.
35. Hochanad, C. J.; Ogren, P. J.; Ghormley, J. A., *J. Chem. Phys.* **1972**, *56* (9), 4426–4432.
36. Yamada, C., *J. Chem. Phys.* **1983**, *78* (7), 4379.
37. Scherer, J. J.; Paul, J. B.; O'Keefe, A.; Saykally, R. J., *Chem. Rev.* **1997**, *97* (1), 25–51.
38. Engeln, R.; Berden, G.; Peeters, R.; Meijer, G., *Rev. Sci. Instrum.* **1998**, *69* (11), 3763–3769.
39. Ye, J.; Ma, L. S.; Hall, J. L., *J. Opt. Soc. Am. B* **1998**, *15* (1), 6–15.
40. Sharpe, S. W.; Johnson, T. J.; Sams, R. L.; Chu, P. M.; Rhoderick, G. C., *Appl. Spectrosc.* **2004**, *58* (12), 1452–1461.
41. NIST Mass Spec Data Center, S. E. S., director, "Infrared Spectra" in NIST Chemistry WebBook, NIST Standard Reference Database Number 69. Linstrom, P. J.; Mallard, W. G., Eds. 2011. <http://webbook.nist.gov> (accessed November 2, 2011).
42. McCoy, A. B.; Fry, J. L.; Francisco, J. S.; Mollner, A. K.; Okumura, M., *J. Chem. Phys.* **2005**, *122* (10), 104311.
43. McCoy, A. B.; Sprague, M. K.; Okumura, M., *J. Phys. Chem. A* **2010**, *114* (3), 1324–1333.
44. Sharp, E. N.; Rupper, P.; Miller, T. A., *PCCP* **2008**, *10* (27), 3955–3981.
45. Takematsu, K. Cavity Ringdown Spectroscopy of the Nitrate and Peroxy Radicals. Ph.D. Thesis, California Institute of Technology, Pasadena, CA, 2011.
46. Paschotta, R., *Encyclopedia of Laser Physics and Technology*. Wiley-VCH: Berlin, 2008.
47. Reid, S. A.; Tang, Y., *Appl. Opt.* **1996**, *35* (9), 1473–1477.
48. Demartino, A.; Frey, R.; Pradere, F., *IEEE J. Quantum Elect.* **1980**, *16* (11), 1184–1191.

49. Fuelberth, T. M. The Building of an Infrared Source for Use in Free Radical Kinetics Important in Stratospheric Ozone Depletion: Cavity Ringdown Detection. M.S. Thesis, California Institute of Technology, Pasadena, CA, 1997.
50. Barbieri, B.; Beverini, N.; Galli, M.; Inguscio, M.; Strumia, F., *Nuovo Cimento D* **1984**, *4* (2), 172–180.
51. Barbieri, B.; Beverini, N.; Sasso, A., *Rev Mod Phys* **1990**, *62* (3), 603–644.
52. Reisner, D. E.; Field, R. W.; Kinsey, J. L.; Dai, H. L., *J. Chem. Phys.* **1984**, *80* (12), 5968–5978.
53. Reisner, D. E.; Vaccaro, P. H.; Kittrell, C.; Field, R. W.; Kinsey, J. L.; Dai, H. L., *J. Chem. Phys.* **1982**, *77* (1), 573–575.
54. Fink, E. H.; Ramsay, D. A., *J. Mol. Spectrosc.* **1997**, *185* (2), 304–324.
55. Osmann, G.; Bunker, P. R.; Jensen, P.; Buenker, R. J.; Gu, J. P., *J. Mol. Spectrosc.* **1999**, *197* (2), 262–274.
56. Anastasi, C.; Smith, I. W. M., *J. Chem. Soc.-Faraday Trans. II* **1976**, *72*, 1459–1468.
57. Atkinson, R.; Perry, R. A.; Pitts, J. N., *J. Chem. Phys.* **1976**, *65* (1), 306–310.
58. Chen, W. J.; Lo, W. J.; Cheng, B. M.; Lee, Y. P., *J. Chem. Phys.* **1992**, *97* (10), 7167–7173.
59. Cheng, B. M.; Lee, J. W.; Lee, Y. P., *J. Phys. Chem.* **1991**, *95* (7), 2814–2817.
60. Lo, W. J.; Lee, Y. P., *Chem. Phys. Lett.* **1994**, *229* (4–5), 357–361.
61. Lo, W. J.; Lee, Y. P., *J. Chem. Phys.* **1994**, *101* (7), 5494–5499.
62. Barker, J. R.; Golden, D. M., *Chem. Rev.* **2003**, *103* (12), 4577–4591.
63. Chakraborty, D., *Chem. Phys.* **1998**, *231* (1), 39.
64. Doclo, K., *Chem. Phys. Lett.* **1998**, *297* (3–4), 205.
65. Golden, D. M.; Barker, J. R.; Lohr, L. L., *J. Phys. Chem. A* **2003**, *107* (50), 11057–11071.
66. Golden, D. M.; Smith, G. P., *J. Phys. Chem. A* **2000**, *104* (17), 3991–3997.
67. Matthews, J.; Sinha, A., *J. Chem. Phys.* **2005**, *122* (10).
68. Matthews, J.; Sinha, A.; Francisco, J. S., *J. Chem. Phys.* **2004**, *120* (22), 10543–10553.
69. Miller, Y.; Chaban, G. M.; Finlayson-Pitts, B. J.; Gerber, R. B., *J. Phys. Chem. A* **2006**, *110* (16), 5342–5354.
70. Pollack, I. B.; Konen, I. M.; Li, E. X. J.; Lester, M. I., *J. Chem. Phys.* **2003**, *119* (19), 9981–9984.
71. Williams, C. F.; Pogrebnya, S. K.; Clary, D. C., *J. Chem. Phys.* **2007**, *126* (15), 154321.
72. Zhang, J.; Donahue, N., *J. Phys. Chem. A* **2006**, *110* (21), 6898–6911.
73. Burkholder, J. B.; Hammer, P. D.; Howard, C. J., *J. Phys. Chem.* **1987**, *91* (8), 2136–2144.
74. Fry, J. L.; Nizkorodov, S. A.; Okumura, M.; Roehl, C. M.; Francisco, J. S.; Wennberg, P. O., *J. Chem. Phys.* **2004**, *121* (3), 1432–1448.
75. Konen, I. M.; Li, E. X. J.; Stephenson, T. A.; Lester, M. I., *J. Chem. Phys.* **2005**, *123* (20), 094320.
76. Li, E. X. J.; Konen, I. M.; Lester, M. I.; McCoy, A. B., *J. Phys. Chem. A* **2006**, *110* (17), 5607–5612.

77. M. J. Frisch, G. W. T., H. B. Schlegel, G. E. Scuseria, M. A. Robb, J. R. Cheeseman, G. Scalmani, V. Barone, B. Mennucci, G. A. Petersson, H. Nakatsuji, et al. *Gaussian 98W, Revision A.01*, Gaussian Inc.: 1998.
78. M. J. Frisch, G. W. T., H. B. Schlegel, G. E. Scuseria, M. A. Robb, J. R. Cheeseman, G. Scalmani, V. Barone, B. Mennucci, G. A. Petersson, H. Nakatsuji, et al. *Gaussian 03, Revision A.02*, Gaussian Inc.: 2003.
79. M. J. Frisch, G. W. T., H. B. Schlegel, G. E. Scuseria, M. A. Robb, J. R. Cheeseman, G. Scalmani, V. Barone, B. Mennucci, G. A. Petersson, H. Nakatsuji, et al. *Gaussian 03W, Revision C.01*, Gaussian Inc.: 2003.
80. Laidig, W. D.; Purvis, G. D.; Bartlett, R. J., *Int. J. Quantum Chem* **1982**, 561–573.
81. Purvis, G. D.; Bartlett, R. J., *J. Chem. Phys.* **1982**, 76 (4), 1910–1918.
82. Scuseria, G. E.; Janssen, C. L.; Schaefer, H. F., *J. Chem. Phys.* **1988**, 89 (12), 7382–7387.
83. Scuseria, G. E.; Schaefer, H. F., *J. Chem. Phys.* **1989**, 90 (7), 3700–3703.
84. Headgordon, M.; Pople, J. A.; Frisch, M. J., *Chem. Phys. Lett.* **1988**, 153 (6), 503–506.
85. Moller, C.; Plesset, M. S., *Phys. Rev.* **1934**, 46 (7), 0618–0622.
86. Pople, J. A.; Headgordon, M.; Raghavachari, K., *J. Chem. Phys.* **1987**, 87 (10), 5968–5975.
87. Donahue, N. M.; Mohrschladt, R.; Dransfield, T. J.; Anderson, J. G.; Dubey, M. K., *J. Phys. Chem. A* **2001**, 105 (9), 1515–1520.
88. Konen, I. M.; Pollack, I. B.; Li, E. X. J.; Lester, M. I.; Varner, M. E.; Stanton, J. F., *J. Chem. Phys.* **2005**, 122 (9), 094320.
89. Buendia-Atencio, C.; Leyva, V.; Gonzalez, L., *J. Phys. Chem. A* **2010**, 114 (35), 9537–9544.
90. Herbert, J. M.; McCoy, A. B.; Szalay, P. G.; Stanton, J. F.; Ellison, G. B., *Abstr Pap Am Chem S* **2004**, 228, U203–U204.
91. Lohr, L. L.; Barker, J. R.; Shroll, R. M., *J. Phys. Chem. A* **2003**, 107 (38), 7429–7433.
92. Renbaum, L. H.; Smith, G. D., *PCCP* **2009**, 11 (36), 8040–8047.
93. Zhang, J. Y.; Dransfield, T.; Donahue, N. M., *J. Phys. Chem. A* **2004**, 108 (42), 9082–9095.
94. Zhao, Y. L.; Houk, K. N.; Olson, L. P., *J. Phys. Chem. A* **2004**, 108 (27), 5864–5871.
95. Jensen, F., *Introduction to Computational Chemistry*. John Wiley and Sons: New York, NY, 1999.
96. Barnes, I.; Becker, K. H.; Fink, E. H.; Reimer, A.; Zabel, F.; Niki, H., *Chem. Phys. Lett.* **1985**, 115 (1), 1–8.
97. Gierczak, T.; Ravishankara, A. R., *Int. J. Chem. Kinet.* **2000**, 32 (9), 573–580.
98. Huie, R. E.; Clifton, C. L., *Chem. Phys. Lett.* **1993**, 205 (2-3), 163–167.
99. Su, F.; Calvert, J. G.; Shaw, J. H., *J. Phys. Chem.* **1979**, 83 (25), 3185–3191.
100. Tomas, A.; Villenave, E.; Lesclaux, R., *J. Phys. Chem. A* **2001**, 105 (14), 3505–3514.
101. Tyndall, G. S.; Cox, R. A.; Granier, C.; Lesclaux, R.; Moortgat, G. K.; Pilling, M. J.; Ravishankara, A. R.; Wallington, T. J., *J. Geophys. Res.—Atmos.* **2001**, 106 (D11), 12157–12182.

102. Veyret, B.; Rayez, J. C.; Lesclaux, R., *J. Phys. Chem.* **1982**, *86* (17), 3424–3430.
103. Rabani, J.; Klugroth, D.; Henglein, A., *J. Phys. Chem.* **1974**, *78* (21), 2089–2093.
104. Dóbé, S.; Temps, F.; Bohland, T.; Wagner, H. G., *Z Naturforsch A* **1985**, *40* (12), 1289–1298.
105. Gab, S.; Turner, W. V.; Wolff, S.; Becker, K. H.; Ruppert, L.; Brockmann, K. J., *Atmos. Environ.* **1995**, *29* (18), 2401–2407.
106. Horie, O.; Moortgat, G. K., *Fresenius J. Anal. Chem.* **1991**, *340* (10), 641–645.
107. Olivella, S.; Bofill, J. M.; Sole, A., *Chem.-Eur. J.* **2001**, *7* (15), 3377–3386.
108. Aloisio, S.; Francisco, J. S., *J. Phys. Chem. A* **2000**, *104* (14), 3211–3224.
109. Evleth, E. M.; Melius, C. F.; Rayez, M. T.; Rayez, J. C.; Forst, W., *J. Phys. Chem.* **1993**, *97* (19), 5040–5045.
110. Li, Q. S.; Zhang, X.; Zhang, S. W., *J. Phys. Chem. A* **2005**, *109* (51), 12027–12035.
111. Nguyen, T. L.; Vereecken, L.; Peeters, J., *Z. Phys. Chem.* **2010**, *224* (7-8), 1081–1093.
112. Zhao, Y. C.; Wang, B. X.; Li, H. Y.; Wang, L., *J. Mol. Struct—Theochem* **2007**, *818* (1–3), 155–161.
113. Roehl, C. M.; Marka, Z.; Fry, J. L.; Wennberg, P. O., *Atmos. Chem. Phys.* **2007**, *7*, 713–720.
114. Maricq, M. M.; Wallington, T. J., *J. Phys. Chem.* **1992**, *96* (2), 986–992.
115. Melnik, D.; Chhantyal-Pun, R.; Miller, T. A., *J. Phys. Chem. A* **2010**, *114* (43), 11583–11594.
116. Gratien, A.; Nilsson, E.; Doussin, J.-F.; Johnson, M. S.; Nielsen, C. J.; Stenstrom, Y.; Picquet-Varrault, B., *J. Phys. Chem. A* **2007**, *111* (45), 11506–11513.
117. Manion, J. A.; Huie, R. E.; Levin, R. D.; Jr., D. R. B.; Orkin, V. L.; Tsang, W.; McGivern, W. S.; Hudgens, J. W.; Knyazev, V. D.; Atkinson, D. B.; Chai, E.; Tereza, A. M.; Lin, C.-Y.; Allison, T. C.; Mallard, W. G.; Westley, F.; Herron, J. T.; Hampson, R. F.; Frizzell, D. H. NIST Chemical Kinetics Database, NIST Standard Reference Database 17, Version 7.0 (Web Version), Release 1.4.3, Data version 2008.12. <http://kinetics.nist.gov/>
118. Atkinson, R.; Baulch, D. L.; Cox, R. A.; Crowley, J. N.; Hampson, R. F.; Hynes, R. G.; Jenkin, M. E.; Rossi, M. J.; Troe, J., *Atmos. Chem. Phys.* **2006**, *6*, 3625–4055.
119. Fry, J. L.; Matthews, J.; Lane, J. R.; Roehl, C. M.; Sinha, A.; Kjaergaard, H. G.; Wennberg, P. O., *J. Phys. Chem. A* **2006**, *110* (22), 7072–7079.
120. Western, C. M. *PGopher, a Program for Simulating Rotational Structure*, University of Bristol: 2012.
121. M. J. Frisch, G. W. T., H. B. Schlegel, G. E. Scuseria, M. A. Robb, J. R. Cheeseman, G. Scalmani, V. Barone, B. Mennucci, G. A. Petersson, H. Nakatsuji, et al. *Gaussian 09, Revision C.01*, Gaussian, Inc.: 2009.
122. Chung, C.-Y.; Cheng, C.-W.; Lee, Y.-P.; Liao, H.-Y.; Sharp, E. N.; Rupper, P.; Miller, T. A., *J. Chem. Phys.* **2007**, *127* (4).
123. Curtiss, L. A.; Raghavachari, K.; Trucks, G. W.; Pople, J. A., *J. Chem. Phys.* **1991**, *94* (11), 7221–7230.
124. Zalyubovsky, S. J.; Wang, D. B.; Miller, T. A., *Chem. Phys. Lett.* **2001**, *335* (3–4), 298–304.
125. Dennington, R.; Keith, T.; Millam, J. *GaussView 3.09*, Semichem Inc.: Shawnee Mission, KS, 2003.

126. *SigmaPlot 8.0*, SPSS Inc.: Chicago, IL, 2002.
127. Just, G. M. P.; McCoy, A. B.; Miller, T. A., *J. Chem. Phys.* **2007**, *127* (4).
128. Johnson, R. D., NIST Computational Chemistry Comparison and Benchmark Database. NIST Standard Reference Database Number 101: 2011.
129. Caralp, F.; Forst, W., *PCCP* **2003**, *5* (20), 4653–4655.
130. Devolder, P., *J Photoch Photobio A* **2003**, *157* (2–3), 137–147.
131. Jungkamp, T. P. W.; Smith, J. N.; Seinfeld, J. H., *J. Phys. Chem. A* **1997**, *101* (24), 4392–4401.
132. Lendvay, G.; Viskolcz, B., *J. Phys. Chem. A* **1998**, *102* (52), 10777–10786.
133. Mereau, R.; Rayez, M. T.; Caralp, F.; Rayez, J. C., *PCCP* **2000**, *2* (9), 1919–1928.
134. Mereau, R.; Rayez, M. T.; Caralp, F.; Rayez, J. C., *PCCP* **2003**, *5* (21), 4828–4833.
135. Somnitz, H., *PCCP* **2008**, *10* (7), 965–973.
136. Somnitz, H.; Zellner, R., *PCCP* **2000**, *2* (9), 1907–1918.
137. Somnitz, H.; Zellner, R., *PCCP* **2000**, *2* (19), 4319–4325.
138. Somnitz, H.; Zellner, R., *PCCP* **2000**, *2* (9), 1899–1905.
139. Somnitz, H.; Zellner, R., *Z. Phys. Chem.* **2006**, *220* (8), 1029–1048.
140. Vereecken, L.; Peeters, J., *J. Chem. Phys.* **2003**, *119* (10), 5159–5170.
141. Caralp, F.; Forst, W.; Bergeat, A., *PCCP* **2008**, *10* (37), 5746–5753.
142. Atkinson, R., *Int. J. Chem. Kinet.* **1997**, *29* (2), 99–111.
143. Atkinson, R.; Arey, J., *Chem Rev* **2003**, *103* (12), 4605–4638.
144. Orlando, J. J.; Tyndall, G. S.; Wallington, T. J., *Chem. Rev.* **2003**, *103* (12), 4657–4689.
145. Atkinson, R.; Aschmann, S. M., *Environ. Sci. Technol.* **1995**, *29* (2), 528–536.
146. Atkinson, R.; Kwok, E. S. C.; Arey, J.; Aschmann, S. M., *Faraday Discuss.* **1995**, *100*, 23–37.
147. Kwok, E. S. C.; Arey, J.; Atkinson, R., *J. Phys. Chem.* **1996**, *100* (1), 214–219.
148. Niki, H.; Maker, P. D.; Savage, C. M.; Breitenbach, L. P., *J. Phys. Chem.* **1981**, *85* (18), 2698–2700.
149. Curran, H. J., *Int. J. Chem. Kinet.* **2006**, *38* (4), 250–275.
150. Johnson, D.; Cassanelli, P.; Cox, R. A., *Atmos. Environ.* **2004**, *38* (12), 1755–1765.
151. Mereau, R.; Rayez, M. T.; Caralp, F.; Rayez, J. C., *PCCP* **2000**, *2* (17), 3765–3772.
152. Vereecken, L.; Peeters, J., *PCCP* **2010**, *12* (39), 12608–20.
153. Kwok, E. S. C.; Atkinson, R.; Arey, J., *Abstr. Pap. Am. Chem. Soc.* **1995**, *209*, ENVR-106.
154. Carter, W. P. L.; Lloyd, A. C.; Sprung, J. L.; Pitts, J. N., *Int. J. Chem. Kinet.* **1979**, *11* (1), 45–101.
155. Cassanelli, P.; Cox, R. A.; Orlando, J. J.; Tyndall, G. S., *J. Photoch. Photobio. A* **2006**, *177* (2–3), 109–115.
156. Cox, R. A.; Patrick, K. F.; Chant, S. A., *Environ Sci Technol* **1981**, *15* (5), 587–592.
157. Dóbé, S.; Berces, T.; Marta, F., *Int. J. Chem. Kinet.* **1986**, *18* (3), 329–344.
158. Heiss, A.; Sahetchian, K., *Int. J. Chem. Kinet.* **1996**, *28* (7), 531–544.
159. Hein, H.; Hoffmann, A.; Zellner, R., *PCCP* **1999**, *1* (16), 3743–3752.

160. Cassanelli, P.; Johnson, D.; Cox, R. A., *PCCP* **2005**, 7 (21), 3702–3710.
161. Geiger, H.; Barnes, I.; Becker, K. H.; Bohn, B.; Brauers, T., *J Atmos Chem* **2002**, 42 (1), 323–357.
162. Bai, J. L.; Okabe, H.; Halpern, J. B., *Chem. Phys. Lett.* **1988**, 149 (1), 37–39.
163. Carter, C. C.; Atwell, J. R.; Gopalakrishnan, S.; Miller, T. A., *J. Phys. Chem. A* **2000**, 104 (40), 9165–9170.
164. Carter, C. C.; Gopalakrishnan, S.; Atwell, J. R.; Miller, T. A., *J. Phys. Chem. A* **2001**, 105 (13), 2925–2928.
165. Ebata, T.; Yanagishita, H.; Obi, K.; Tanaka, I., *Chem. Phys.* **1982**, 69 (1–2), 27–33.
166. Foster, S. C.; Misra, P.; Lin, T. Y. D.; Damo, C. P.; Carter, C. C.; Miller, T. A., *J. Phys. Chem.* **1988**, 92 (21), 5914–5921.
167. Gopalakrishnan, S.; Carter, C. C.; Zu, L.; Stakhursky, V.; Tarczay, G.; Miller, T. A., *J. Chem. Phys.* **2003**, 118 (11), 4954–4969.
168. Gopalakrishnan, S.; Zu, L.; Miller, T. A., *J. Phys. Chem. A* **2003**, 107 (26), 5189–5201.
169. Gopalakrishnan, S.; Zu, L.; Miller, T. A., *Chem. Phys. Lett.* **2003**, 380 (5–6), 749–757.
170. Inoue, G.; Okuda, M.; Akimoto, H., *J. Chem. Phys.* **1981**, 75 (5), 2060–2065.
171. Jin, J.; Sioutis, I.; Tarczay, G.; Gopalakrishnan, S.; Bezant, A.; Miller, T. A., *J. Chem. Phys.* **2004**, 121 (23), 11780–11797.
172. Lin, J. L.; Zu, L. L.; Fang, W. H., *J. Phys. Chem. A* **2011**, 115 (3), 274–279.
173. Liu, X. M.; Damo, C. P.; Lin, T. Y. D.; Foster, S. C.; Misra, P.; Yu, L.; Miller, T. A., *J. Phys. Chem.* **1989**, 93 (6), 2266–2275.
174. Lotz, C., *PCCP* **2001**, 3 (13), 2607–2613.
175. Ohbayashi, K.; Akimoto, H.; Tanaka, I., *J. Phys. Chem.* **1977**, 81 (8), 798–802.
176. Powers, D. E.; Pushkarsky, M. B.; Miller, T. A., *J. Chem. Phys.* **1997**, 106 (17), 6863–6877.
177. Stakhursky, V. L.; Zu, L. L.; Liu, J. J.; Miller, T. A., *J. Chem. Phys.* **2006**, 125 (9), 094316.
178. Zhang, L.; Callahan, K. M.; Derbyshire, D.; Dibble, T. S., *J. Phys. Chem. A* **2005**, 109 (41), 9232–9240.
179. Zhang, L.; Kitney, K. A.; Ferenac, M. A.; Deng, W.; Dibble, T. S., *J. Phys. Chem. A* **2004**, 108 (3), 447–454.
180. Zu, L.; Liu, J. J.; Gopalakrishnan, S.; Miller, T. A., *Can. J. Chem.* **2004**, 82 (6), 854–866.
181. Tan, X. Q.; Williamson, J. M.; Foster, S. C.; Miller, T. A., *J. Phys. Chem.* **1993**, 97 (37), 9311–9316.
182. Wendt, H. R.; Hunziker, H. E., *J. Chem. Phys.* **1979**, 71 (12), 5202–5205.
183. Noyes, W. A., *Organic Syntheses* **1943**, Coll. Vol. 2, 108.
184. Chen, M. W.; Just, G. M. P.; Codd, T.; Miller, T. A., *J. Chem. Phys.* **2011**, 135 (18), 184304.
185. Chhantyal-Pun, R.; Kline, N. D.; Thomas, P. S.; Miller, T. A., *J. Phys. Chem. Lett.* **2010**, 1 (12), 1846–1852.
186. Keller, B. A.; Felder, P.; Huber, J. R., *J. Phys. Chem.* **1987**, 91 (5), 1114–1120.
187. Bruhlmann, U.; Dubs, M.; Huber, J. R., *J. Chem. Phys.* **1987**, 86 (3), 1249–1257.

188. Mestdagh, J. M.; Berdah, M.; Dimicoli, I.; Mons, M.; Meynadier, P.; Doliveira, P.; PiuZZi, F.; Visticot, J. P.; Jouvet, C.; Lardeuxdedonder, C.; Martrenchardbarra, S.; Soep, B.; Solgadi, D., *J. Chem. Phys.* **1995**, *103* (3), 1013–1023.
189. Yue, X. F.; Sun, J. L.; Yin, H. M.; Wei, Q.; Han, K. L., *J. Phys. Chem. A* **2009**, *113* (14), 3303–3310.
190. Glover, B. G.; Miller, T. A., *J. Phys. Chem. A* **2005**, *109* (49), 11191–11197.
191. Ianni, J. C. *Kintecus, Windows Version 3.95*, 2008.
192. Fittschen, C.; Frenzel, A.; Imrik, K.; Devolder, P., *Int. J. Chem. Kinet.* **1999**, *31* (12), 860–866.
193. Balla, R. J.; Nelson, H. H.; McDonald, J. R., *Chem. Phys.* **1985**, *99* (2), 323–335.
194. Bevington, P. R., *Data Reduction and Error Analysis for the Physical Sciences*. McGraw-Hill: 1969.
195. Sharp, E. N.; Rupper, P.; Miller, T. A., *J. Phys. Chem. A* **2008**, *112* (7), 1445–1456.
196. Foresman, J. B.; Frisch, Æ., *Exploring Chemistry With Electronic Structure Methods*. Gaussian Inc.: 1996.
197. Valiev, M.; Bylaska, E. J.; Govind, N.; Kowalski, K.; Staraatsma, T. P.; van Dam, H. J. J.; Wang, D.; Nieplocha, J.; Apra, E.; Windus, T. L.; de Jong, W. A., *Comput. Phys. Commun.* **2010**, *181* (9), 1477–1489.
198. Curtiss, L. A.; Jones, C.; Trucks, G. W.; Raghavachari, K.; Pople, J. A., *J. Chem. Phys.* **1990**, *93* (4), 2537–2545.
199. Curtiss, L. A.; Raghavachari, K.; Redfern, P. C.; Rassolov, V.; Pople, J. A., *J. Chem. Phys.* **1998**, *109* (18), 7764–7776.
200. Curtiss, L. A.; Redfern, P. C.; Raghavachari, K., *J. Chem. Phys.* **2007**, *126* (8), 084108.
201. Pople, J. A.; Head-Gordon, M.; Fox, D. J.; Raghavachari, K.; Curtiss, L. A., *J. Chem. Phys.* **1989**, *90* (10), 5622–5629.
202. Montgomery, J. A.; Frisch, M. J.; Ochterski, J. W.; Petersson, G. A., *J. Chem. Phys.* **1999**, *110* (6), 2822–2827.
203. Montgomery, J. A.; Frisch, M. J.; Ochterski, J. W.; Petersson, G. A., *J. Chem. Phys.* **2000**, *112* (15), 6532–6542.
204. Montgomery, J. A.; Ochterski, J. W.; Petersson, G. A., *J. Chem. Phys.* **1994**, *101* (7), 5900–5909.
205. Wood, G. P. F.; Radom, L.; Petersson, G. A.; Barnes, E. C.; Frisch, M. J.; Montgomery, J. A., Jr., *J. Chem. Phys.* **2006**, *125* (9), 094106.
206. Barnes, E. C.; Petersson, G. A.; Montgomery, J. A., Jr.; Frisch, M. J.; Martin, J. M. L., *J. Chem. Theory Comput.* **2009**, *5* (10), 2687–2693.
207. Boese, A. D.; Oren, M.; Atasoylu, O.; Martin, J. M. L.; Kallay, M.; Gauss, J., *J. Chem. Phys.* **2004**, *120* (9), 4129–4141.
208. Karton, A.; Rabinovich, E.; Martin, J. M. L.; Ruscic, B., *J. Chem. Phys.* **2006**, *125* (14), 144108.
209. Martin, J. M. L.; de Oliveira, G., *J. Chem. Phys.* **1999**, *111* (5), 1843–1856.
210. Martin, J. M. L.; de Oliveira, G., *Abstr. Pap. Am. Chem. Soc.* **2000**, *219*, U591–U591.
211. Parthiban, S.; Martin, J. M. L., *J. Chem. Phys.* **2001**, *114* (14), 6014–6029.
212. Aloisio, S.; Francisco, J. S., *J. Am. Chem. Soc.* **1999**, *121* (37), 8592–8596.

213. Beames, J. M.; Lester, M. I.; Murray, C.; Varner, M. E.; Stanton, J. F., *J. Chem. Phys.* **2011**, *134* (4), 044314.
214. Braams, B.; Yu, H. G., *PCCP* **2008**, *10*, 3150–3155.
215. Cacace, F.; de Petris, C.; Pepi, F.; Troiani, A., *Science* **1999**, *285* (5424), 81–82.
216. Caridade, P.; Betancourt, M.; Garrido, J. D.; Varandas, A. J. C., *J. Phys. Chem. A* **2001**, *105* (31), 7435–7440.
217. Cooper, P. D.; Moore, M. H.; Hudson, R. L., *J. Phys. Chem. A* **2006**, *110* (26), 7985–7988.
218. Denis, P. A.; Kieninger, M.; Ventura, O. N.; Cachau, R. E.; Diercksen, G. H. F., *Chem. Phys. Lett.* **2003**, *377* (3–4), 483–484.
219. Derro, E. L.; Murray, C.; Sechler, T. D.; Lester, M. I., *J. Phys. Chem. A* **2007**, *111* (45), 11592–11601.
220. Derro, E. L.; Sechler, T. D.; Murray, C.; Lester, M. I., *J. Phys. Chem. A*, **2008**, *112* (39), 9269–9276.
221. Fabian, W. M. F.; Kalcher, J.; Janoschek, R., *Theor. Chem. Acc.* **2005**, *114* (1–3), 182–188.
222. Mansergas, A.; Anglada, J. M.; Olivella, S.; Ruiz-Lopez, M. F.; Martins-Costa, M., *PCCP* **2007**, *9* (44), 5865–5873.
223. Mazziotti, D. A., *J. Phys. Chem. A* **2007**, *111* (49), 12635–12640.
224. Murray, C.; Derro, E. L.; Sechler, T. D.; Lester, M. I., *J. Phys. Chem. A* **2007**, *111* (22), 4727–4730.
225. Nelander, B.; Engdahl, A.; Svensson, T., *Chem. Phys. Lett.* **2000**, *332* (3–4), 403–408.
226. Setokuchi, O.; Sato, M.; Matuzawa, S., *J. Phys. Chem. A* **2000**, *104* (14), 3204–3210.
227. Speranza, M., *Inorg. Chem.* **1996**, *35* (21), 6140–6151.
228. Speranza, M., *J. Phys. Chem. A* **1998**, *102* (38), 7535–7536.
229. Suma, K.; Sumiyoshi, Y.; Endo, Y., *Science* **2005**, *308* (5730), 1885–1886.
230. Varner, M. E.; Harding, M. E.; Vazquez, J.; Gauss, J.; Stanton, J. F., *J. Phys. Chem. A* **2009**, *113* (42), 11238–11241.
231. Yang, J.; Li, Q. S.; Zhang, S. W., *PCCP* **2007**, *9* (4), 466–469.
232. Yu, H. G.; Varandas, A. J. C., *Chem. Phys. Lett.* **2001**, *334* (1–3), 173–178.
233. Sridharan, U. C.; Klein, F. S.; Kaufman, F., *J. Chem. Phys.* **1985**, *82* (1), 592–593.
234. Butkovskaya, N.; Rayez, M. T.; Rayez, J. C.; Kukui, A.; Le Bras, G., *J. Phys. Chem. A* **2009**, *113* (42), 11327–11342.